Université de Strasbourg

UNIVERSITÉ DE STRASBOURG

École Doctorale des Sciences de la Vie et de la Santé STRASBOURG

ÉCOLE DOCTORALE des Sciences de la Vie et de la Santé (ED414)

Institut de biologie moléculaire des plantes, UPR2357 CNRS

THÈSE présentée par :

Philippe JOHANN TO BERENS

Soutenue le : **25 mars 2022**

Pour obtenir le grade de : **Docteur de l'Université de Strasbourg**

Discipline / Spécialité : Aspects moléculaires et cellulaires de la biologie

Dynamique et maintenance de l'hétérochromatine constitutive en réponse à l'exposition aux UV

Dynamic and maintenance of constitutive heterochromatin in response to UV exposure

RAPPORTEURS

Mme POLO Sophie	Directrice de Recherche, ECF, Paris
M. MATHIEU Olivier	Directeur de Recherche, GRED, Clermont Ferrand

EXAMINATEURS

M. NGONDO Patryk	Maître de Conférences, IBMP, Strasbourg
Mme BOURBOUSSE Clara	Chargée de Recherche, IBENS, Paris
M. GAQUEREL Emmanuel	Professeur, IBMP, Strasbourg

THÈSE dirigée par

M. MOLINIER Jean	Directeur de Recherche, IBMP, Strasbourg

Summary

1. Introduction

Living organisms are exposed to many environmental factors that can interfere with their development. Plants, due to their sessile lifestyle and their autotrophy, have to cope with the genotoxic stress associated with sunlight. Indeed, UV exposure recurrently damages DNA and consequently endangers the genetic integrity of the plant. While the fundamental repair processes of DNA have been extensively studied, the essential role of the epigenome in these processes only recently gained interest. The following research work aims at deciphering the DNA repair processes acting within constitutive heterochromatin in the model plant *Arabidopsis thaliana*. Subsequently, this introduction will present the current knowledge about the crosstalk between chromatin/epigenome, DNA damage, and DNA repair processes.

1.1. *Arabidopsis thaliana* as a model plant

Arabidopsis thaliana, also called the thale cress or the mouse-ear cress is an annual plant from the Brassicaceae family and a central model in the field of plant research (Fig. 1) (Meinke et al. 1998; Koornneef and Meinke 2010). *Arabidopsis thaliana* brings together several interesting characteristics such as a small size, a relatively fast life cycle (6 weeks from seed to seed), and a high seed yield in standardized lab-growth conditions (Meinke et al. 1998; Rivero et al. 2014). Additionally, *Arabidopsis thaliana*, in contrast to its close relatives (*i.e., Arabidopsis lyrata*), is a self-pollinator (Tang et al. 2007).

Its use as a model organism starts with the early Ph.D. work of Friedrich Laibach (1907), interested in the fundamental process of genetic inheritance and chromosome individuality (Laibach 1907). Four decades later, he further promoted the suitability of *Arabidopsis thaliana* for genetic studies and already mentioned at that time the potential advantages of studying the naturally occurring variability in between *Arabidopsis thaliana* accessions. (Laibach 1943; Koornneef and Meinke 2010). Indeed, another great advantage of *Arabidopsis thaliana* as a model plant is its geographic spreading that happened 120 to 45 thousand years ago (Fulgione and Hancock 2018).

This spreading all around the terrestrial globe gives rise to a large number of natural variants growing in a large range of ecosystems (ecological niches), going from Columbia (Fig. 1) (Provart et al. 2016), to the Madeiran island (Fulgione et al. 2018) or to the Tibetan plateau (Zeng et al. 2017).

The study of these natural variants is an interesting tool to follow adaptational development and are recurrently used to investigate the molecular actors linking phenotypes to environments (Kawakatsu et al. 2016; Takou et al. 2019).

Figure 1: The model plant *Arabidopsis thaliana*

Left panel: drawing of flowering *Arabidopsis thaliana* from K. Sutliff (Meinke et al. 1998). Central panel: picture of *Arabidopsis thaliana*. Right panel: pictures of *Arabidopsis thaliana* natural variants of Columbia, Moscow, and Cape Verde at rosette stage.

Since Laibach, thousands of scientists have contributed to the current understanding of *Arabidopsis thaliana*'s intrinsic mechanisms and consequently to depict the ubiquitous biological processes (Somerville and Koornneef 2002; Koornneef and Meinke 2010; Provart et al. 2016).

This accumulation of knowledge enables further understanding of the crosstalk between complex biological mechanisms and strengthens the position of *Arabidopsis thaliana* as model organism. In addition, decades of work provided many robust methods and tools (Rivero et al. 2014; Provart et al. 2016).

Among these facilities, several seed stock centers exist, such as the Arabidopsis Biological Resource Center (ABRC) in the United States, The Sendai Arabidopsis Seed Stock Center (SASSC) in Japan, and the Nottingham Arabidopsis Stock Centre (NASC) in the UK (Scholl et al. 2000). These stock centers give direct access to thousands of mutant lines and to all kinds of natural accessions, thereby furnishing the source of plant material for research (Scholl et al. 2000). The access to the collection of T-DNA insertions mutant lines has long been a considerable advantage compared to other model organisms such as *Mus musculus* and *Drosophila melanogaster* (Ülker et al. 2008). The genomic sequence of Arabidopsis was released in 2000 (The Arabidopsis Genome Initiative 2000), and the publicly accessible portals and databases such as TAIR (The Arabidopsis Information Resource) and Araport (The Arabidopsis Information Portal) (Reiser et al. 2017; Pasha et al. 2020), enable to browse through many different types of genomic and epigenomic resources (Cantó-Pastor et al. 2021).

1.2. The genome of Arabidopsis thaliana

The genome of *Arabidopsis thaliana* is composed of 5 chromosomes (2n=10) and has a total size of approximately 135 Megabases (Mb). As previously mentioned, the first nearly complete genome assembly was released in 2000 (The Arabidopsis Genome Initiative 2000). At that time, 120 Mb have been sequenced, leaving some gaps of uncertainty, mainly in regions with high sequence repetitions (The Arabidopsis Genome Initiative 2000). Recently, most gaps from this golden path of the genomic sequence have been filled thanks to a High-quality genome assembly following Nanopore, and HiFi-Long read sequencing (Michael et al. 2018; Wang et al. 2021a). Aside from the 27.500 annotated protein-coding genes(Wang et al. 2021a), the Arabidopsis genome also contains around 32.000 Transposable Elements (TE), representing approximately 20% of the genome (Quesneville 2020).

As described for most eukaryotic organisms, the four bases of the genetic code do not show an equivalent usage in the Arabidopsis genome, having global GC content of around 36% (The Arabidopsis Genome Initiative 2000; Wang et al. 2021a). The discrepancy between GC- and AT- contents was somehow linked to genome size and explained by different hypotheses, such as the uptake of usually AT-rich foreign DNA and the increased synthesis cost of G/C. (Šmarda et al. 2014; Bohlin and Pettersson 2019).

The genomic sequence can spatially be subdivided into 3 main regions: telomeres, (peri-)centromeres, and chromosome-arms (Fig. 2A) (The Arabidopsis Genome Initiative 2000). Telomeres are located at the extremity of chromosomes and shield the coding regions of degeneration (Riha and Shippen 2003). In *Arabidopsis thaliana*, 8 chromosome arms show a "classical" sequence pattern with telomeric repeats (CCCTAAA/TTTAGGG) of variable length ranging from 1862 to 3563 bp (Fig. 2A) (Wang et al. 2021a). In contrast, 2 chromosome arms, the short arms of chromosomes 2 and 4, show an atypical structure with 45S ribosomal-DNA (rDNA) clusters at the extremity (Copenhaver and Pikaard 1996; Wang et al. 2021a). This specificity can notably be explained by a recent chromosome breaking event, followed by *de novo* telomere formation (Copenhaver and Pikaard 1996).

Centromeres are localized in the chromosome, thereby defining the inner limit of both chromosome arms (Fig. 2A) (The Arabidopsis Genome Initiative 2000; Naish et al. 2021). The key function of centromeric regions is to direct the kinetochore formation in order to allow proper chromosome segregation upon cell division processes (Lermontova et al. 2014; Naish et al. 2021). In-plant centromeres contain specific tandem repeat sequences of a length ranging from 150 to 180 bp by unit, covering several Mb of the genome (Fig. 2A) (Oliveira and Torres 2018; Wang et al. 2021a). In *Arabidopsis thaliana,* the 178 bp pAL1 repeat (also named cen180 or 180bp) is the typical centromeric repeat (Wang et al. 2021a; Naish et al. 2021) and has no sequence homology but has the approximatively same size as the alpha-satellites of the Human centromeres (Oliveira and Torres 2018; Sullivan and Sullivan 2020). The five Arabidopsis centromeres are called CEN1 to 5, and have sizes of 9, 4, 4, 5.5 and 4.9 Mb, respectively (Hosouchi et al. 2002; Wang et al. 2021a). The composition of the five Arabidopsis centromeres slightly differs from each other depending on a mix of four different cen180 tandem repeat satellite clusters, transposons, and 5S rDNA arrays (Oliveira and Torres 2018; Wang et al. 2021a).

The predominant type of transposons that invaded the centromeres are long terminal repeat (LTR) Retrotransposons derived from Athila2 (106B and TSI, for example) and LTRs from the GYPSY family (Simon et al. 2015; Wang et al. 2021a). Aside from the TEs, a few genes could also be found in these regions (Wang et al. 2021a). An additional distinction is often made to describe the border of centromeres, also called the peri-centromeres (Fig. 2A) (Fransz et al. 2000; Talbert et al. 2002; Simon et al. 2015). These pericentromeric regions mostly contain TEs and 5S-rDNA clusters but no cen180 repeats (Fig. 2A) (Quesneville 2020; Wang et al. 2021a). Interestingly, pericentromeric areas build GC-rich isochores (~40% GC-Content) mainly because of 5S-rDNA clusters (Zhang and Zhang 2004; Wang et al. 2021a).

Finally, in-between telomeres and centromeres/peri-centromeres, there are the chromosome arms. The chromosome arms represent the largest part of the genome and contain a broad range of different sequences (The Arabidopsis Genome Initiative 2000; Wang et al. 2021a). The probably most essential components of the chromosome arms are the protein-coding genes (PCG) (Fig. 2A). Like a blueprint, these PCG encodes for the bricks building the whole complexity of the multicellular organism, including its adaptability to various environments (The Arabidopsis Genome Initiative 2000; Lynch and Conery 2003; Charlesworth and Barton 2004). Aside from these PCG, chromosome arms also contain several other components, such as sequences encoding for tRNAs (Hummel et al. 2020), Long-non-coding RNAs (Jampala et al. 2021), micro RNAs (Xu et al. 2018), particular TEs …. (Maumus and Quesneville 2014; Quesneville 2020; Yocca et al. 2021).

1.3. The epigenome of *Arabidopsis thaliana*

As presented here above, the Arabidopsis genome contains a large range of sequences whose expression and replication must be tightly regulated (Fig. 2A) (Gibney and Nolan 2010). For example, the expression of PCG needs to be spatially and temporarily framed to allow routine processes, tissue dedifferentiation (Ali et al. 2020), development (Wils and Kaufmann 2017), and specific responses to environmental stimuli (Chang et al. 2020). At the same time, TE needs to be silenced to avoid undesired genomic rearrangements (Quesneville 2020). In order to fine-tune the protein-DNA interactions responsible for locus-specific transcription (Gibney and Nolan 2010) and replication (Costas et al. 2011) a supplemental set of information, completing the DNA sequence, is needed. This additional set of information is called the epigenome.

The epigenome is defined as the sum of several epigenetic layers, including DNA methylation, nucleosome positioning, histone variant distribution, and histone Post-Translational Modifications (PTMs). Generally speaking, the sum of all epigenetic layers ends up in higher-chromatin structures, subdividing the genome in transcriptionally active euchromatin and transcriptionally silenced heterochromatin.

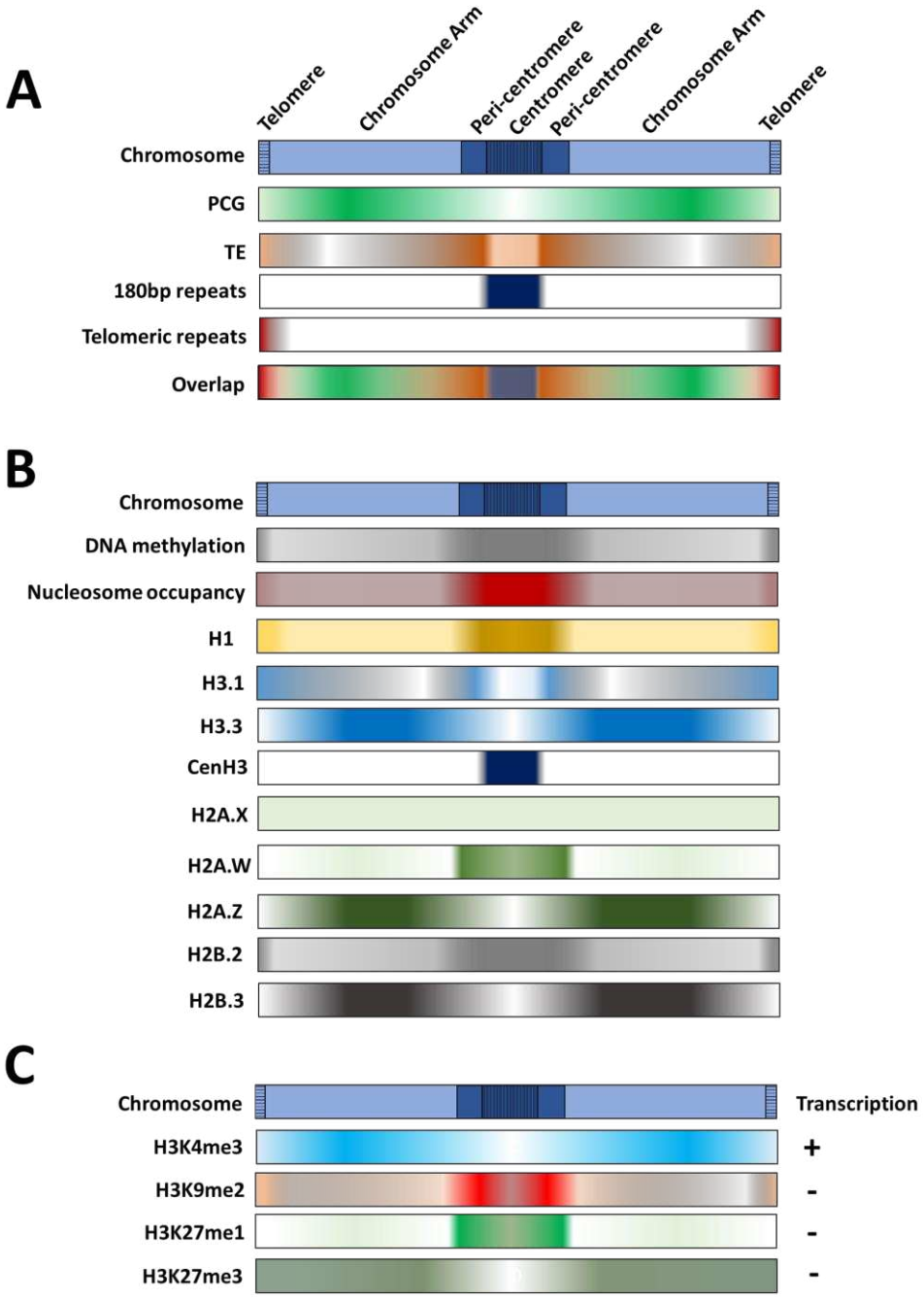

Figure 2: Distribution of genetic and epigenetic entities along chromosome 1

(A) Graphical representation of the global distribution of the protein-coding genes (PCG), transposable elements (TE), 180pb repeats, and telomeric repeats along chromosome 1 of *Arabidopsis thaliana*. Telomeres, chromosome arms, pericentromere, and centromere are annotated. **(B)** Graphical representation of the global distribution of DNA methylation, nucleosome positioning, and different histone variants along chromosome 1. **(C)** Graphical representation of the global distribution of the histone PTMs H3K4me3, H3K9me2, H3K27me1, and H3K27me3 along chromosome 1. Effect of PTMs on transcription. " + " activation ; " - " repression.

1.3.1. DNA methylation

A well-studied epigenetic mark is DNA methylation occurring at carbon 5 of Cytosine (5-mC) (Law and Jacobsen 2010; Zhang et al. 2018b). How DNA methylation is established, maintained, and erased in Arabidopsis was described in the part “Dynamics of DNA methylation” in our book chapter untitled “DNA damage and DNA methylation” (see § 1.5. “Attached reviews” for details).

1.3.2. Nucleosome positioning

The subsequent epigenetic layers are related to the compaction of genomic DNA in building blocks called nucleosomes. A nucleosome is defined as a unit of around 146 bp of DNA wrapped around a core histone octamer composed of 2 Histones 2A (H2A), 2 Histones 2B (H2B), 2 Histones 3 (H3), and 2 Histones 4 (H4; Fig. 3) (Probst et al. 2020). The DNA located between 2 nucleosomes has a variable size and is called linker DNA. In some cases, this linker DNA is bound by the Histone 1 (H1), which alternatively also binds on top of nucleosomes close to the DNA entry and exit sites (Fig. 3) (Probst et al. 2020). This complex DNA-histone structure is called chromatin (Probst et al. 2020). Core histones contain a central histone fold domain made of 3 α-helices and of more flexible N-tail regions that protrude out of the nucleosomes (Koyama and Kurumizaka 2018; Probst et al. 2020; Adhireksan et al. 2020). The linker histone H1, in turn, contains a globular domain and dynamic N- and C- terminal regions (Probst et al. 2020; Adhireksan et al. 2020).

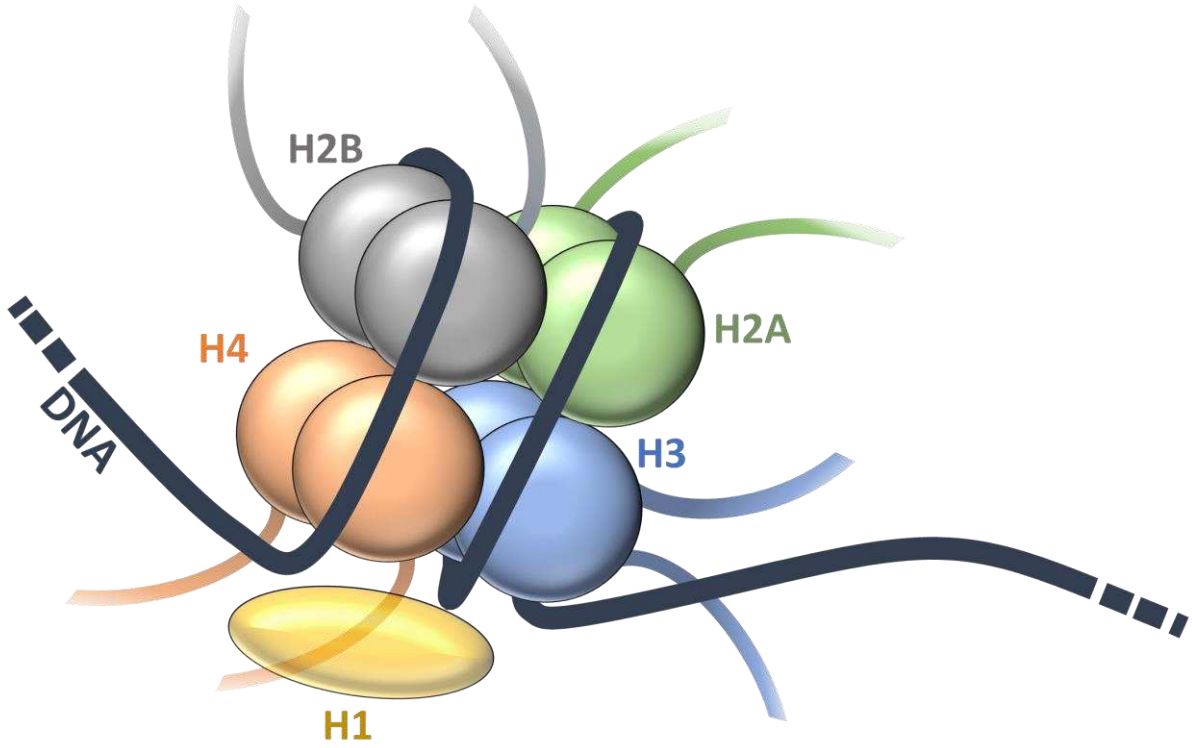

Figure 3: Schematic representation of a nucleosome

Schematic representation of DNA molecule wrapped around the histone core octamer composed of histones H2A, H2B, H4, and H3. The nucleosome is stabilized by the binding of a linker histone H1.

In Arabidopsis, like in most eukaryotes, the nucleosome positioning and H1 occupancy participate, among others, in the regulation of replication, transcription, and alternative splicing (Rutowicz et al. 2019; Jabre et al. 2021). Indeed, nucleosome and H1 packaging globally inhibit the accessibility of most DNA interacting proteins, thereby regulating the protein activity at bounded loci (Liu et al. 2015; Rutowicz et al. 2019).

The positioning of nucleosomes was shown to depend on at least two factors. Firstly, the nucleotide composition and secondly, the intervention of chromatin remodelers and histones chaperones (Liu et al. 2015; Yadav and Whitehouse 2016; Muñoz-Viana et al. 2017). In *Arabidopsis thaliana,* nucleosomes and histone H1 are enriched in centromeric- and pericentromeric- regions and participate in the transcriptional silencing of TEs (Fig. 2B) (Chodavarapu et al. 2010; Salih and Trifonov 2015; Pass et al. 2017; Rutowicz et al. 2019). Additionally, nucleosomes positioning and H1 are both involved in specifying the sites where DNA methylation should be deposited (Chodavarapu et al. 2010; Zemach et al. 2013).

Indeed, nucleosome and H1 rich regions are favorable targets of all 3 DNA methylation contexts: CG, CHG, and CHH, where H is A, C, or T (Chodavarapu et al. 2010; Zemach et al. 2013). The methylation of DNA wrapped around nucleosomes shows a periodicity of around ten bp (Chodavarapu et al. 2010). This correlates with the periodicity by which the major groove of the DNA helix, the target of DNA methyltransferases, is exposed away from nucleosomes core (Chodavarapu et al. 2010).

1.3.3. Histone variants and chaperones

Interestingly, to further enlarge the epigenetic multi-functionality of nucleosomes, eukaryotic organisms express different histone variants. They differ from each other in peptide sequence and genomic distribution (Fig. 2B) (Biterge and Schneider 2014; Probst et al. 2020). In *Arabidopsis thaliana,* 50 annotated genes encode for 9 H3 variants, 13 H2A variants, 11 H2B variants, and a single H4 variant (Table 1) (Probst et al. 2020).

The two predominant H3 variants are H3.1 and H3.3, differing by four amino acids (Probst et al. 2020). While H3.1 shows an S-phase specific expression indicating DNA-synthesis-dependent incorporation in chromatin, H3.3 incorporation apparently occurs in a DNA-synthesis-independent manner (Okada et al. 2005; Jiang and Berger 2017; Probst et al. 2020). Interestingly in whole seedlings, H3.1 and H3.3 are both expressed and mainly differ in their genomic distribution (Stroud et al. 2012).

In Arabidopsis, like in mammals, this distribution mainly relies on two histone chaperones, the CHROMATIN ASSEMBLY FACTOR 1 (CAF-1), which loads H3.1-H4 dimers explicitly upon replication, and the Histone Regulator A (HIRA), which predominantly loads H3.3-H4 dimers (Duc et al. 2015; Muñoz-Viana et al. 2017; Probst et al. 2020). The Arabidopsis CAF-1 complex interacts with the Proliferating Cell Nuclear Antigen (PCNA) at replication forks to primarily load H3.1 upon *de novo* DNA synthesis (Jiang and Berger 2017). H3.3, in turn, serves as replacement histone, which is later on incorporated, mainly as a consequence of transcriptional activity during interphase (Schneiderman et al. 2012; Duc et al. 2015).

H3.1 is found to be enriched in pericentromeric regions, whereas H3.3 is predominantly enriched in chromosome arms and positively correlates with transcriptional activity (Fig. 2B) (Stroud et al. 2012; Wollmann et al. 2012). The loading of H3.3 on the Arabidopsis genome mainly depends on HIRA; however alternative H3.3 loading mechanisms are expected, as HIRA loss of function does not abolish H3.3 incorporation (Duc et al. 2015). One known actor involved in an alternative H3.3 deposition pathway is the Alpha Thalassaemia/Mental Retardation Syndrome X-Linked protein (ATRX) (Duc et al. 2017; Wang et al. 2018). In mammals, ATRX seems to function as a recruitment platform for the chaperone Death Domain Associated Protein (DAXX) (Dyer et al. 2017). In Arabidopsis, DAXX homologs have not been identified, and the exact mechanisms by which ATRX allows the H3.3 loading remains unclear (Duc et al. 2017).

The role and specificity of the other more atypical H3 variants remain poorly understood apart from HTR12. Indeed, HTR12 encodes for the centromeric H3 variant of Arabidopsis (CenH3) (Nagaki et al. 2003; Stroud et al. 2012). CenH3 has a highly divergent amino-acid composition compared to all other H3 variants (Nagaki et al. 2003; Le Goff et al. 2020). In addition, CenH3 is associated with a unique role in centromeric 180 bp repeat binding (Fig. 2B) (Nagaki et al. 2003; Le Goff et al. 2020). This specific loading of CenH3 most likely depends on the shuttling by the orthologue of the mammalian NUCLEAR AUTOANTIGENIC SPERM PROTEIN (NASP) chaperone and on the incorporation by a yet unknown partner (Le Goff et al. 2020).

The H2A variants can be subdivided into four groups: the H2A, H2A.X, H2A.Z, and H2A.W variants, with the H2A.W type being specific to the plant kingdom (Yelagandula et al. 2014; Kawashima et al. 2015; Probst et al. 2020). At the scale of amino acid sequences most differences in between H2.A variants are found in the C-terminal, loop1, and docking domain (Kawashima et al. 2015). These structural differences induce significant changes in nucleosome stability. H2A.Z-H2B dimers are more rapidly displaced (Osakabe et al. 2018), whereas the H2A.W C-terminal interacts with the linker DNA (Stroud et al. 2012). H2A.X is found all over the genome and has an essential role in DNA Doubles Strand Break (DSB) repair (Fig. 2B) (Ismail and Hendzel 2008; Probst et al. 2020). H2A and H2A.Z are mostly localized on chromosome arms and are excluded from the pericentromeric region where H2A.W variants accumulate (Fig. 2B) (Yelagandula et al. 2014; Probst et al. 2020).

Less is known about the H2B variants (Probst et al. 2020). Recent work proposes to subdivide the 11 Arabidopsis variants into either two groups (based on their expression in reproductive tissues and evolutional apparition linked to seed production in plants) (Jiang et al. 2020) or three classes (based on multiple alignments) (Khadka et al. 2020) (Table 1). However, the first group of H2B variants (H2B.1, 2, 3, 4, 9 and 11) overlaps with the first class, and the 2nd group of the so-called H2B.S variants (H2B.5, 6, 7, 8 and 10) overlaps with the Class II, except for H2B.8 which is set apart in the Class III (Jiang et al. 2020; Khadka et al. 2020). First steps characterizing the genomic distribution of some H2B variants reveal that H2B.3 is enriched over PCG bodies and is somewhat positively correlated with transcription (Jiang et al. 2020). Conversely, H2B.2 mainly localizes in pericentromeric and transcriptionally inactive regions (Fig. 2B) (Jiang et al. 2020). In addition, H2B.3 was shown to primarily interact with H2A.Z and H3.3, whereas H2B.3 is poorly found in this conformation (Jiang et al. 2020). Consequently, the working model proposes that H2B.3 acts, like H3.3 and H2A.Z variants, as a replication-independent “replacement” histone (Stroud et al. 2012; Jiang et al. 2020).

The distribution of H2B-H2A dimers depends on five chaperones: NUCLEOSOME ASSEMBLY PROTEIN-1 (NAP1), FACILITATES CHROMATIN TRANSCRIPTION (FACT), NAP1-RELATED PROTEIN (NRP), Channels Modulator Chlorzoxazone (CHZ), and DECREASE IN DNA METHYLATION 1 (DDM1), with different specializations for each H2A variant (Zhou et al. 2015; Osakabe et al. 2021). Canonical H2B-H2A incorporation depends on an interplay between NAP1, NRP, and FACT (Zhou et al. 2015). H2B-H2A.Z incorporation depended on NAP1 FACT and CHZ (Zhou et al. 2015) and was shown to be assisted by the ATP-dependent chromatin remodeling complex SWR1 (Mizuguchi et al. 2004). H2B-H2A.Z removal, in turn, was recently shown to depend on NRP, thereby fine-tuning the H2A.Z occupancy (Wang et al. 2020). H2B-H2AX loading was for now described only for FACT (Zhou et al. 2015). Finally, the mechanism of incorporation of the plant-specific H2A.W was recently described to rely on the chromatin remodeler DDM1 (Osakabe et al. 2021).

Finally, the Arabidopsis genome encodes three H1 variants, H1.1, H1.2, and H1.3 (Probst et al. 2020). H1.3 significantly differs from the two others due to short N- and C- terminal tails and the lack of DNA binding domain. As a consequence, H1.3 appears to be relatively dynamic within chromatin (Rutowicz et al. 2015; Probst et al. 2020).

H1.3 was shown to be required for a substantial part of DNA methylation associated with environmental stimuli, suggesting that H1.3 may enable chromatin accessibility by entering in competition with the more stable H1 variants (Rutowicz et al. 2015). H1.1 and H1.2 are enriched in transcriptionally repressed regions and are nearly entirely depleted of H3.3 occupied territories (Fig. 2B) (Braunschweig et al. 2009; Probst et al. 2020).

Histone H3	Gene	Histone H4	Gene	Histone H2A	Gene	Histone H2B	Gene	Histone H1	Gene
H3.1	*At5g65360, HTR1*	H4	*At3g46320*	H2A.1	*At5g54640, HTA1*	H2B.1	*At1g07790, HTB1*	H1.1	*At1g06760, H1.1*
	At1g09200, HTR2		*At5g59690*	H2A.2	*At4g27230, HTA2*	H2B.2	*At5g22880, HTB2*	H1.2	*At2g30620, H1.2*
	At3g27360, HTR3		*At2g28740*	H2A.10	*At1g51060, HTA10*	H2B.3	*At2g28720, HTB3*	H1.3	*At2g18050, H1.3*
	At5g10400, HTR9		*At1g07820*	H2A.13	*At3g20670, HTA13*	H2B.4	*At5g59910, HTB4*		
	At5g10390, HTR13		*At3g53730*	H2A.X.3	*At1g54690, HTA3*	H2B.9	*At3g45980, HTB9*		
H3.3	*At4g40030, HTR4*		*At5g59970*	H2A.X.5	*At1g08880, HTA5*	H2B.11	*At3g46030, HTB11*		
	At4g40040, HTR5		*At3g45930*	H2A.W.6	*At5g59870, HTA6*	H2B.5	*At2g37470, HTB5*		
	At5g10980, HTR8		*At1g07660*	H2A.W.7	*At5g27670, HTA7*	H2B.6	*At3g53650, HTB6*		
H3.6	*At1g13370, HTR6*			H2A.W.12	*At5g02560, HTA12*	H2B.7	*At3g09480, HTB7*		
H3.7	*At1g75610, HTR7*			H2A.Z.4	*At4g13570, HTA4*	H2B.10	*At5g02570, HTB10*		
H3.10	*At1g19890, HTR10*			H2A.Z.8	*At2g38810, HTA8*	H2B.8	*At1g08170, HTB8*		
H3.11	*At5g65350, HTR11*			H2A.Z.9	*At1g52740, HTA9*				
H3.14	*At1g75600, HTR14*			H2A.Z.11	*At3g54560, HTA11*				
H3.15	*At5g12910, HTR15*								
CenH3	*At1g01370, HTR12*								

Table 1: *Arabidopsis thaliana* histone variants

List of all known *Arabidopsis thaliana* variants. Different subgroups are labeled by shades of the same color. The table was modified from (Probst et al. 2020).

1.3.4. Histones PTMs

Once histone variants are loaded all over the genome, their functionality is often completed by Post-translational modifications (PTMs). Indeed, an extensive range of PTMs can be added on core and H1 linker histones to allow a fine-tuned regulation of transcription and replication (Vergara and Gutierrez 2017; Ueda and Seki 2020; Leng et al. 2020). Most PTMs are covalently attached to the N- Tail of core Histones (Leung and Gaudin 2020). In animals at least 260 amino-acid histone positions were reported to be post-translationally modified (Sabari et al. 2017). A comparable number is expected to be found in plants (Zhang et al. 2007; Leung and Gaudin 2020).

The most prominent and well-documented PTMs are methylation, acetylation, phosphorylation, and ubiquitination (Leung and Gaudin 2020; Ueda and Seki 2020). However, many others are also involved in histone PTMs, such as SUMOylation and ADP-ribosylation (Leung and Gaudin 2020). The regulation and impact of this complex epigenetic layer is ruled by three classes of actors: the writers, erasers, and readers (Ueda and Seki 2020). Writers are proteins that deposit the modifying moiety. Conversely, erasers remove the modifying moiety. Finally, readers specifically recognize the PTMs to enable the regulatory effect (Zhao et al. 2018; Ueda and Seki 2020).

Given that our study only focuses on a set of PTMs, the following part will concentrate on a subset of the most studied histone PTMs in *Arabidopsis thaliana*: methylation at lysine (K) of histone H3 on positions K4, K9, and K27.

The lysine 4 of histone 3 (H3K4) was predominantly shown to be mono-, bi-, and tri-methylated. H3K4m2/3 localize near the Transcription Start Site (TSS), and H3K4me1 localizes all over the transcribed regions with a slight 3' bias (Cheng et al. 2020). In most eukaryotes, H3K4 methylation globally correlates with transcriptional activity and is depleted from TEs and highly methylated regions (Howe et al. 2017; Cheng et al. 2020). In Arabidopsis, the methylation of H3K4 depends on the Trithorax group (TrxG) Set-Domain group (SDG) proteins (Tamada et al. 2009; Chen et al. 2017; Cheng et al. 2020). In yeast, the H3K4 methylation is mainly triggered by nearby H2B mono-ubiquitination (H2Bub). Interestingly, in Arabidopsis, a significant part of H3K4 methylation appears to be independent of H2Bub, despite its colocalization in transcribed regions (Fiorucci et al. 2019). The demethylation of H3K4m1/me2/me3 depends on LSD1 homologs and several members of the lysine demethylase KDM5 group Jumonji (JMJ) proteins (Jiang et al. 2007; Liu et al. 2007; Lu et al. 2010; Liu et al. 2019; Cheng et al. 2020). H3K4 methylation was notably linked to transcriptional elongation through ATX1 (Arabidopsis Trithorax Homologue *1*) (Fromm and Avramova 2014).

In contrast to H3K4, the mono-, di- and tri-methylated Lysine 9 of Histone 3 (H3K9) were predominantly linked to expressional repression (Jackson et al. 2004; Lee et al. 2018; Cheng et al. 2020). H3K9me1 and H3K9me2 are enriched in pericentromeric regions with high DNA-methylation status (Fig. 2C) (Jackson et al. 2004; Cheng et al. 2020), whereas H3K9me3 localize all over the genome and repress the transcription of a subset of TEs and PCG (Veiseth et al. 2011; Lee et al. 2018). In mammals, drosophila, and yeast, H3K9me3 represents the main histone PTM in pericentromeric heterochromatin (Jih et al. 2017; Machida et al. 2018; Nicetto and Zaret 2019; Wei et al. 2021). Importantly, in *Arabidopsis thaliana*, H3K9me2 plays this role (Fig. 2C) (Xu and Jiang 2020).

The di-methylation of Arabidopsis H3K9 mainly depends on the SET-domain containing SU(VAR)3-9 HOMOLOGS SUVH4 (Suppressor of variegation 3-9 homolog protein 4; hereafter also called KRYPTONITE : KYP), SUVH5, and SUVH6 (Fig. 4 and 5) (Jackson et al. 2002; Ebbs and Bender 2006; Li et al. 2018). Interestingly, the SET and RING-Associated domain (SRA) of these methyltransferases show a high affinity for methylated DNA (Stroud et al. 2014; Li et al. 2018; Xu and Jiang 2020). At the same time, H3K9me2 serve as anchor signal enhancing non-CG DNA methylation either directly through CMT2 and CMT3 (CHROMOMETHYLASE 2/3) or indirectly through the H3K9me2 reader SHH1 (DNA TRANSCRIPTION FACTOR 1/SAWADEE HOMEODOMAIN HOMOLOG 1), further recruiting the RdDM machinery (Fig. 4) (Law et al. 2013; Stroud et al. 2014). Together these complementary mechanisms ensure the maintenance of a silenced environment. Aside from the canonical establishment of H3K9me2 landscape, the SU(VAR)3-9-RELATED proteins SUVR4 and SUVR5 were shown to convert H3K9me1 to H3K9me2/me3 *in vitro* and to establish H3K9me2 in a DNA methylation-independent manner, respectively (Fig. 5) (Thorstensen et al. 2006; Caro et al. 2012). In addition, a putative endosperm-specific methyltransferase activity was proposed for SUVH7 and SUVH8, albeit it requires further investigations (Gehring et al. 2011; Wolff et al. 2011; Xu and Jiang 2020).

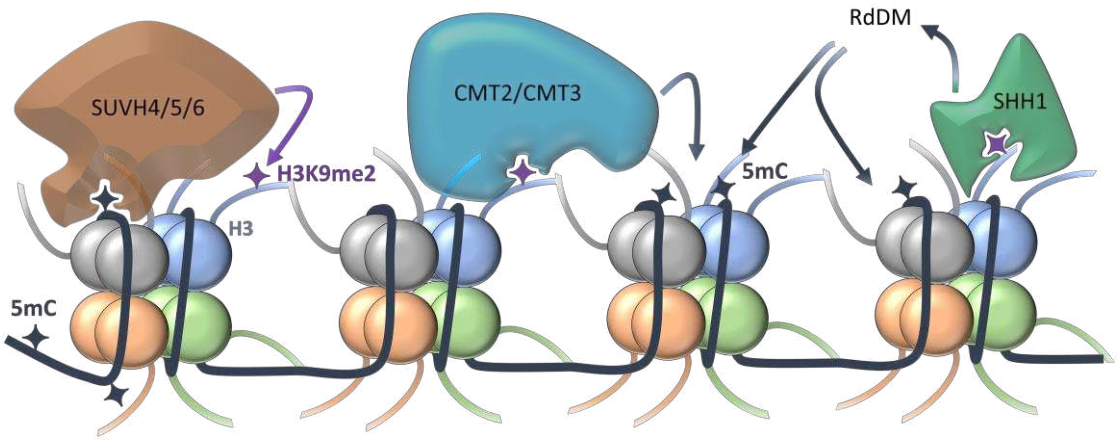

Figure 4: The feed-forward reinforcement loop between DNA methylation and H3K9me2

SUVH4/5/6 histone methyltransferases recognize methylated cytosines (5mC) on the DNA molecule as an anchor to di-methylate proximal Lysine 9 (K9) of histone H3. H3K9me2 is recognized by CMT2/CMT3 and SHH1, thereby triggering direct or indirect DNA methylation, respectively.

In Arabidopsis, the erasure of H3K9me2 is catalyzed by the demethylase activity of at least five Jumonji (JMJ) C domain-containing proteins, JMJ30, JMJ29, JMJ28, JMJ27, and JMJ25 (Fig. 5) (Hung et al. 2021). These demethylases are close homologues of the KDM3 group protein in Human and Drosophila which regulates H3K9me2 demethylation (Holowatyj et al. 2015). However, due to H3K9me3-like, pericentromeric localization of H3K9me2, the KDM4 group which demethylates H3K9me3 in Human, may be considered when comparing processes of heterochromatin regulation (Janssen et al. 2019). JMJ25, also called IBM1 (INCREASE IN BONSAI METHYLATION 1) was the first H3K9me1/me2 demethylase studied (Fig. 5) (Cheng et al. 2020). IBM1 was shown to prevent the spreading of heterochromatic H3K9 di-methylation in transcriptionally active genes (Saze et al. 2008; Miura et al. 2009), thereby participating in Arabidopsis immunity and RdDM (Fan et al. 2012; Chan and Zimmerli 2019) JMJ27 was reported to coordinate defense against Pseudomonas, to control flowering time (Dutta et al. 2017) and to regulate drought stress response (Fig. 5) (Wang et al. 2021b). JMJ28 is another H3K9me2 demethylase recently identified as a regulator of flowering through activation of the *CONSTANS* locus (Fig. 5) (Hung et al. 2021). Furthermore, JMJ30 was identified as an H3K9me3 specific demethylase, regulating a subset of genes responsible for the leaf to callus transition (Fig. 5) (Lee et al. 2018). Finally, JMJ29 was recently described for its H3K9me2 demethylase activity, regulating trichome development (Fig. 5) (Hung et al. 2020).

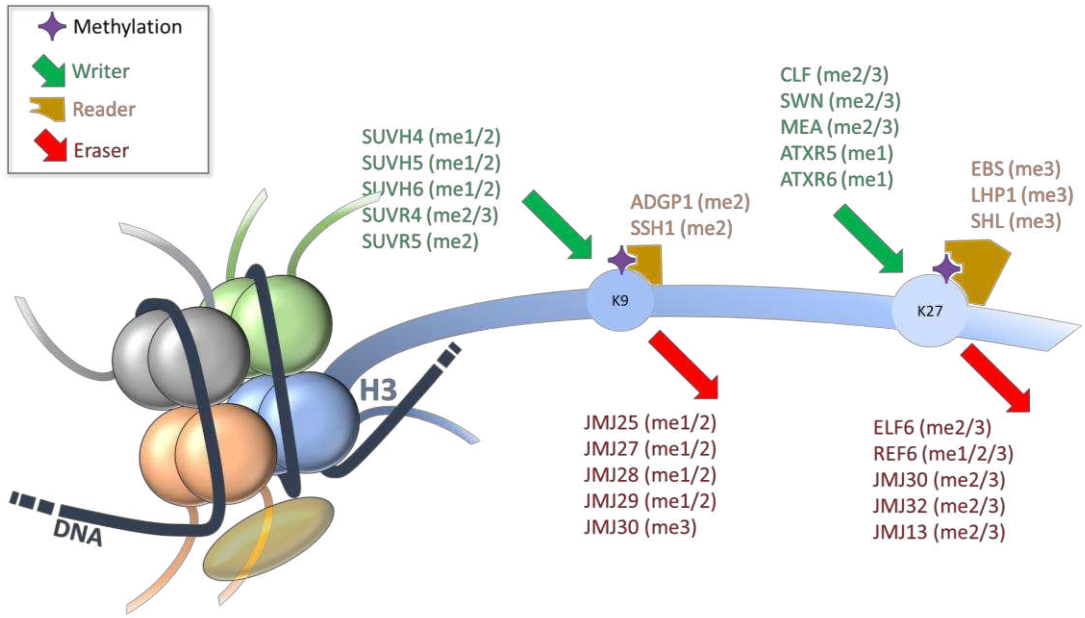

Figure 5: Writers, readers and erasers of H3K9me and H3K27me in *Arabidopsis thaliana*

Schematic representation of writers (green), readers (orange) and erasers (red) of the histone PTMs associated with methylation of Lysine 9 and Lysine 27 of histone H3. Degree of methylation is specified in brackets.

In Metazoan, an essential reader of the heterochromatic H3K9m3 was early identified and called Heterochromatin Protein 1 (HP1) (Bannister et al. 2001; Jacobs et al. 2001). Interestingly, the closest sequence homolog LHP1 (Like-HP1) in Arabidopsis is not associated *in vivo* to H3K9me2 but to the tri-methylated Lysine 27 of Histone 3 (H3K27) (Turck et al. 2007). Instead, recent studies identified the AGDP1 (Agenet domain (AGD)-containing protein 1), also known as ADCP1, as H3K9me2 reader and functional homolog of HP1 (Fig. 5) (Zhang et al. 2018a; Zhao et al. 2019). AGDP1 was shown to have a dual histone sensing faculty, reading, on the one hand, the H3K9me2, and on the other hand, the unmethylated H3K4me0. Consequently, AGDP1 is suspected to specifically target H3K9me2 in genomic regions that are clearly defined as transcriptionally silenced (*i.e.,* within heterochromatin) (Zhang et al. 2018a). Thus, AGDP1 mainly participates in the H3K9me2-dependent heterochromatin formation by promoting DNA methylation (Zhang et al. 2018a) thanks to a phase separation mechanism, as described for HP1-alpha in Human, and HP1a in Drosophila (Zhao et al. 2019).

Aside from H3K9 methylation, the methylation on the Lysine 27 of Histone 3 (H3K27) is responsible for another essential set of PTMs inducing transcriptional silencing (Fig. 5). H3K27 can be mono-, di- or tri-methylated. Interestingly like for H3K9, each methylation status has its own genome-wide distribution profile. H3K27me1 is enriched in silenced heterochromatin, consequently overlapping with H3K9me2 (Fig. 2C) (Jacob et al. 2010; Sequeira-Mendes et al. 2014). H3K27me2 is spread over the whole genome in gene-rich euchromatin as well as in regions with high TE density (Cheng et al. 2020). Finally, H3K27me3 predominantly localizes in transcribed regions of the genome, with a particular focus on the TSS (Fig. 2C) (Sequeira-Mendes et al. 2014; Carter et al. 2018). Surprisingly, H3K27me3 was also shown to be enriched in the telomeric sequences (Fig. 2C) (Vaquero-Sedas et al. 2012).

H3K27 di- and tri- methylation depends on the Polycomb Repressive Complex (PRC2), firstly identified in Drosophila (Kuzmichev et al. 2002; Cheng et al. 2020). In Arabidopsis, the alternative combination of different subunits forms a large set of combinations to form PRC2 complexes (Kradolfer et al. 2013; Kim and Sung 2013; Xiao and Wagner 2015; Cheng et al. 2020). Each PRC2 complex has distinct roles in the transcriptional repression of a subset of H3K27me3 regulated genes (Xiao and Wagner 2015; Cheng et al. 2020). The methyltransferase activity is carried by the core catalytic subunit, which can either be CURLY LEAF (CLF), SWINGER (SWN), or MEDEA (MEA) (Fig. 5) (Cheng et al. 2020). The different PRC2 complexes generally drive the transcriptional repression of developmental-transition genes and stress-responsive genes representing facultative heterochromatin (Xiao and Wagner 2015; Cheng et al. 2020).

In animals, unlike in Arabidopsis, H3K27 mono methylation, is also deposited by PRC2 complexes (Jacob and Michaels 2009). Indeed, in the model plant, H3K27me1 is established by 2 SET-domain containing methyltransferases, Trithorax-Related 5 and 6 (ATXR5 / ATXR6) mainly on H3.1 histone variants in a replication-dependent manner (Fig. 5) (Jacob et al. 2009; Jacob et al. 2014; Ma et al. 2018). Moreover, H3K27me1 was shown to prevent the release of silencing and re-replication events in heterochromatic regions by specific recruitment to the replication fork (Davarinejad et al. 2019).

More recent studies clarified this role, by highlighting the ATXR5/6- and H3.1K27me1-dependent repression of H3.1K27 acetylation by the Histone Acetyl transferase (HAT) GENERAL CONTROL NON DEREPRESSIBLE 5 GCN5 (Dong et al. 2021). Interestingly, ATXR5/6 methyl transferase activity was shown to be enhanced by SERRATE, which in parallel prevents RNA-dependent RNA polymerase 6 (RDR6)-dependent initiation of RdDM (Ma et al. 2018). The demethylation of H3K27 is mainly catalyzed by KDM4/JHDM3 group proteins (Fig. 5). Early Flowering 6 (ELF6/JMJ11) and Relative of Early Flowering 6 (REF6/JMJ12) function redundantly in H3K27me2/me3 demethylation during multiple developmental processes (Lu et al. 2011; Crevillén et al. 2014) and were shown to collaborate with the chromatin remodeler BRAHMA (BRM) (Li et al. 2016). In addition, JMJ13, JMJ30, and JMJ32 were shown to demethylate H3K27me3 and to regulate the flowering process through the control of Flowering locus T and C (*FT* and *FLC*) expressions (Fig. 5) (Gan et al. 2014; Zheng et al. 2019). REF6 was also shown to demethylate H3K27me1 in euchromatic regions (Fig. 5) (Antunez-Sanchez et al. 2020). Notably, this non-heterochromatic H3K27me1 is not deposited by ATXR5,6 but is a residual product associated with canonical PRC2 H3K27me2/me3 followed by uncompleted demethylation (Antunez-Sanchez et al. 2020).

Although H3K27me1 specific readers have not been described for now (Jacob and Michaels 2009), H3K27me3 is recognized by 3 different readers LHP1, EARLY BOLTING IN SHORT DAYS (EBS), and its homolog SHORT LIFE (SHL) (Fig. 5). Interestingly, LHP1 only affects a few loci, whereas EBS and SHL binding highly overlap with (H3K4me3 + H3K27m3)-rich regions due to their bivalent reading (Qian et al. 2018; Krause and Turck 2018; Yang et al. 2018). Both EBS and SHL were shown to be essential for the transcriptional repression of several Polycomb loci (Qian et al. 2018; Krause and Turck 2018; Yang et al. 2018). Interestingly, H3K9 and H3K27 positions can be both alternatively targeted by histone acetyl-transferases, thereby generating H3K9ac and H3K27ac (Benhamed et al. 2006). Histone acetylation activates gene expression and thus antagonizes K9 and K27 methylations (Benhamed et al. 2006; Rymen et al. 2019).

The hereabove described histone PTMs reflect a small proportion of the large repertoire of PTMs and their complexity to shape the epigenome landscape. However, the PTMs homeostasis contributes to the fine-tuning of DNA accessibility, thereby regulating replication, transcription, and other processes, including DNA repair.

1.3.5. *Arabidopsis thaliana* chromatin states

The combination of the different layers of the *Arabidopsis thaliana* epigenetic marks results in the formation of multiple "Chromatin States" (CS) (Roudier et al. 2011; Sequeira-Mendes et al. 2014; Liu et al. 2018). Defining a reduced number of chromatin states aims at simplifying the epigenetic annotation of the genome, by classifying together the combination of closely related epigenetic marks regulating specific biological processes (Roudier et al. 2011; Liu et al. 2018). The Arabidopsis epigenome was firstly divided into four and subsequently nine CS (Roudier et al. 2011; Sequeira-Mendes et al. 2014). More recently, Liu et al. (2018) collected a large number of publicly available ChIP data and defined 36 CS. In our investigations, we will refer to the CS defined by Sequeira-Mendes et al. (2014).

As summarized in Figure 6, CS1, CS2 and CS3 have a relatively high level in activating histone PTMs (H3K4me2/3, H3K36me4, H2Bub) (Sequeira-Mendes et al. 2014). However, CS1, due to its low nucleosome density and H3.3 / H2.AZ occupancy, tends to fit with TSSs, whereas CS3, with the presence of H3K4me1, is associated with transcriptional elongation (Sequeira-Mendes et al. 2014). CS2, in turn, shows an additional enrichment of H3K27me3 and is consequently related to Polycomb-regulated genes (Fig. 6) (Sequeira-Mendes et al. 2014). CS4 and 5 are centrally defined by a high H3K27me3, just like CS2, but lacking activating marks (Fig. 6) (Sequeira-Mendes et al. 2014). CS4 largely overlaps with non-coding and intergenic regions, and may regulate promoter activity in a distal manner whereas CS2 regulates promoters in a proximal manner (Sequeira-Mendes et al. 2014). CS5 Correspond to the canonical Polycomb signature, as described in Drosophila (Kharchenko et al. 2011), and is characterized by the nearly exclusive H3K27me3 loading in intergenic and genic regions (Fig. 6) (Sequeira-Mendes et al. 2014).

CS6 and CS7 are typical for intragenic areas, showing a high H2A.Z and H3K4me1 occupancy (in the case of CS6), and an important H3K4me1, H2Bub, and H3K36me3 load (in the case of CS7) (Fig. 6). Interestingly, state 7 was linked to transcription units, larger than the average length (Sequeira-Mendes et al. 2014). Finally, the so-called heterochromatin is defined by CS8 and CS9 which both show high CG methylation status, H3.1, H3K9me2 and H3K27me1 occupancy (Fig. 6). CS8 and CS9 can mainly be distinguished by their CG-rich or AT-rich contexts, respectively (Sequeira-Mendes et al. 2014). Consequently, CS9 is more closely related to pericentromeric regions.

However, the epigenetic landscape is often oversimplified and defined as Euchromatin (EC), Facultative-Heterochromatin (FHC), and Constitutive-Heterochromatin (CHC). These categories originate from cytogenetics (Trojer and Reinberg 2007). Euchromatin represents the transcriptionally active regions and is associated with high H3 acetylation and H3K4 methylation levels (Tamaru 2010). The facultative heterochromatin consists of the transcriptional inactive areas, which differ depending on cell type, developmental stage, and environmental stimuli and is generally related to the repressive mark H3K27me3 (Trojer and Reinberg 2007; Li and Zhou 2013). The constitutive heterochromatin is associated with DNA methylation, H3K9me2, and H3K27me1 in plants, and DNA methylation and H3K9me3 in mammals and Drosophila (Tamaru 2010).

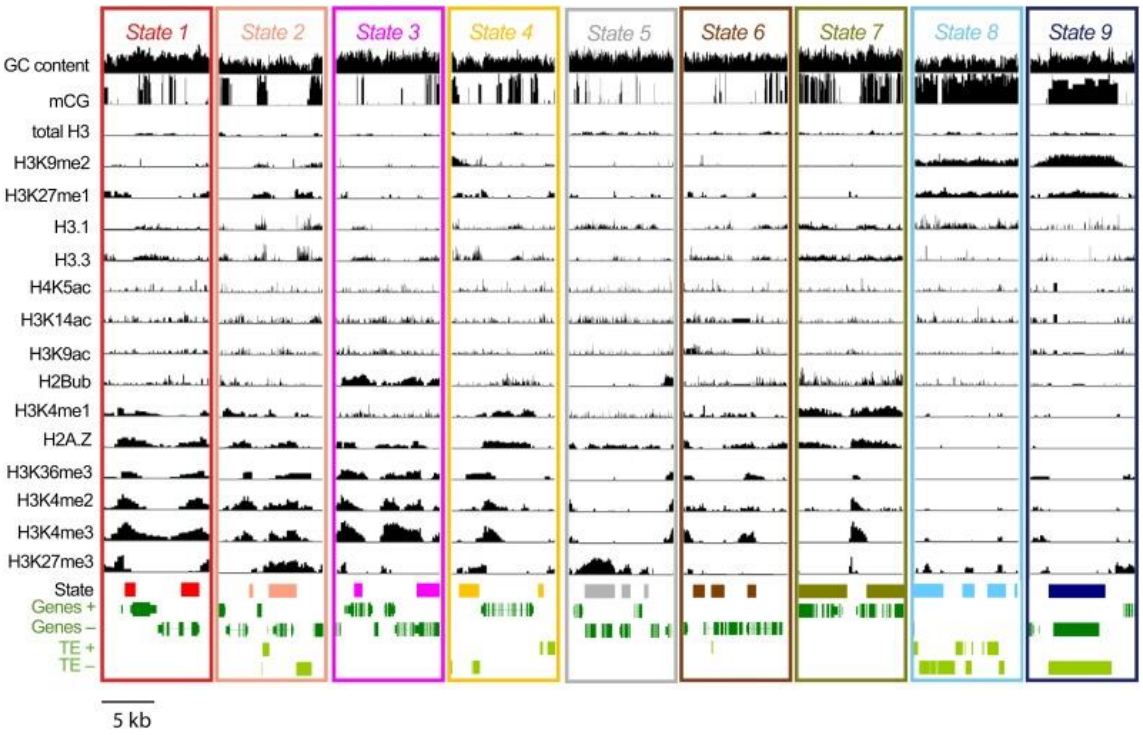

Figure 6: *Arabidopsis thaliana* chromatin states

Chromatin states are visualized through representative exemplary windows on the Integrated Genome Browser. Figure originates from the work of the Gutierrez Lab (Sequeira-Mendes et al. 2014).

1.3.6. 3D chromatin organization

Finally, to reach the complete picture of the Arabidopsis (epi-)genome, the spatial organization of the chromatin within the nucleus has to be considered. From early on, cytogenetic approaches showed the separation of euchromatin and heterochromatin in spatially distinct regions (Fig. 7A) (Passarge 1979; Berger 2019). Indeed, Emil Heitz started to describe that "some parts of the mitotic chromosomes are more densely stained than others" (Passarge 1979; Berger 2019). Since our understanding of the spatial distribution of chromatin considerably evolved, revealing another regulatory layer of the eukaryotic epigenome (Rowley and Corces 2018; Zhang and Wang 2021).

In Arabidopsis, each chromosome was shown to occupy a specific domain, the chromosomal territories (CTs) (Bi et al. 2017). However, the relative position of CTs to each other seems to be random in interphasic nuclei (Bi et al. 2017).

After CTs, the first spatial interaction units of chromatin at 1 to 10 Mb-scale are the A- and B-compartments where A- represents the euchromatic chromosome arms and B- the heterochromatic repeats in pericentromeric regions (Fig. 7B) (Pontvianne and Grob 2020). This compartment organization spatially put CS8 and CS9 apart from the others CS. Interestingly, these A- and B- compartments can be easily observed with cytogenetic approaches as nucleoplasm at the nuclear inner and chromocenters localized near the nuclear envelope, respectively (Fig. 7B) (Fransz et al. 2002).

When only considering the chromosome arms, sub-compartments called loose and closed structural domains (LSDs and CSDs) can be identified (Grob et al. 2014; Grob et al. 2014; Pontvianne and Grob 2020). LSDs are mainly constituted by active CS, whereas CSD contains the facultative heterochromatin, including the H3K27me3 repressive mark (Grob et al. 2014; Pontvianne and Grob 2020). In most eukaryotic species, further subdivision of each chromosome arm interaction allows defining the topologically associating domains (TADs) (Pontvianne and Grob 2020). TADs are Mb-sized interacting units in which several regions show a high interaction frequency to each other and a low interaction frequency with all other genomic loci (Pontvianne and Grob 2020; Zhang and Wang 2021). In animals, the TAD formation is mainly driven by the sequence motif CCCTC and its binding factor (CTCF) (Guo et al. 2015; Pontvianne and Grob 2020).

Interestingly, a plant homolog of CTCF has not been identified yet (Pontvianne and Grob 2020). Given that TADs have been described in several plant species (Dong et al. 2018; Zhang et al. 2018c; Hu et al. 2019b; Pontvianne and Grob 2020), it was assumed that the CTCF insulator function might be solely fulfilled by cohesins (Pontvianne and Grob 2020), that are known to collaborate with CTCF in mammals (Schwarzer et al. 2017). Interestingly, in Arabidopsis, the mutation of cohesin expressing genes leads to a disturbed chromatin organization (Schubert et al. 2009). However, *Arabidopsis thaliana* is not the optimal model to investigate 3D genome architecture due to a nearly complete absence of TADs (Feng et al. 2014; Grob et al. 2014).

Despite the absence of TADs, the role of chromatin folding on Arabidopsis gene expression can be observed, for example, at the KNOT structure (Grob et al. 2014; Grob and Grossniklaus 2019). KNOT is an interacting structure bringing together KNOT-Engaged Elements 1 to 10 (KEE1 to KEE10) loci which are distributed all over the five chromosomes (Fig. 7B) (Grob et al. 2014). Interestingly, KEEs show some sequence-specificities. Firstly, KEEs regions often harbored ATLANTYS3 and VANDAL6 TEs (Grob et al. 2014) and are thought to be under the regulatory processes related to TE biology (Grob et al. 2014). Indeed, a recent study demonstrated the role of KNOT in the silencing of foreign DNA (*i.e.,* T-DNA) through a process called "KNOT-linked silencing" (KLS) (Grob and Grossniklaus 2019). Upon KLS, the invasive DNA is spatially delocalized to the KNOT structure (Grob and Grossniklaus 2019). This spatial proximity appears to participate in the invasive DNA silencing independently of DNA methylation and canonical silencing pathways (Grob and Grossniklaus 2019). Interestingly, KNOT-like structures is shown to be conserved in other plant species and resemble the Flamenco Locus of Drosophila, indicating potential conservation of the KLS process (Grob et al. 2014; Grob and Grossniklaus 2019).

Aside from the KNOT, two other chromatin interaction hubs, which mainly depend on the relative position of chromatin compared to nuclear envelope or nucleoli, have been described: the plant lamina-associated chromatin domains (pLADS) and the nucleolus-associated chromatin domains (NADs; Fig 7B).

In Metazoan, the nuclear lamin fibers were shown to shape the interaction of large heterochromatin domains at the nuclear periphery, the LADs (Pickersgill et al. 2006; Vertii et al. 2019). Plants lack sequence homologs of lamins. However, the plant-specific CROWDED NUCLEI proteins (CRWN) appear to function as lamin orthologs, notably essential to anchor the heterochromatic pLADS to the nuclear envelope (Fig. 7B) (Bi et al. 2017; Hu et al. 2019a). Interestingly, aside from the typical constitutive heterochromatin feature characterizing chromocenters, in boundary regions, pLADs also contain a high level of H3K27me3 (Bi et al. 2017). This observation fits with the demonstrated interaction of CRWN1 and PWO1 (PROLINE-TRYPTOPHANE-TRYPTOPHANE-PROLINE (PWWP) INTERACTOR OF POLYCOMBS1), a newly discovered plant-specific PRC2 interacting protein (Mikulski et al. 2019).

On the “opposite” side, another hub of chromatin interaction domains is the periphery of the nucleolus (Fig. 7B) (Pontvianne and Grob 2020). The nucleolus is mainly shaped by the nucleoli organizer regions (NORs) and is a subnuclear spherical structure responsible for ribosome biogenesis in eucaryotes (Lo et al. 2006). In Human, subparts of all chromosomes were shown to interact with each other around the nucleolus, thereby forming the NADs (van Koningsbruggen et al. 2010). As in Human, the Arabidopsis NADs mainly contain heterochromatic regions (Fig. 7B) (Pontvianne et al. 2016; Pontvianne and Grob 2020). The short arm from chromosome 4, which contains transcriptionally active rDNA gene clusters (Fig. 7B), represents a main interacting fraction of the NAD structures (Pontvianne et al. 2016; Pontvianne and Grob 2020). However, NADs were also shown to contain telomeric repeats and several hundred genes (Fig. 7B) (Pontvianne et al. 2016; Pontvianne and Grob 2020). Interestingly, the transcriptionally inactive NAD genes are often developmentally regulated (Pontvianne et al. 2016; Pontvianne and Grob 2020). Working hypotheses propose that these genes could be moved away from NAD for their transcriptional activation (Pontvianne et al. 2016; Pontvianne and Grob 2020). In contrast to animal NADs and LADs, Arabidopsis NADs and pLADS do not show significant sequence overlap (Kind et al. 2013; Picart-Picolo et al. 2019). The unique exception to this rule is the short arm of chromosome 4, which interacts simultaneously with the nuclear envelope and the nucleoli, indirectly anchoring the nucleoli next to the envelope (Kind et al. 2013; Picart-Picolo et al. 2019; Pontvianne and Grob 2020).

Finally, the smallest interaction unit is the genomic loop. It was described as a conserved mechanism regulating gene expression in Arabidopsis (Jégu et al. 2014; Guo et al. 2018; Pontvianne and Grob 2020). A genomic loop is shaped by the interaction of at least two loci of distant genomic regions interacting at the base of an emerging chromatin loop (Guo et al. 2018; Pontvianne and Grob 2020; Boltsis et al. 2021). The regulation process of genomic loops has notably been demonstrated for the flowering repressor gene *Flowering Locus C* (Jégu et al. 2014) and for the bi-functional transcription factor WUSCHEL involved in the maintenance of stem cell populations in the shoot (Guo et al. 2018).

Despite the major advances in the field of chromatin organization, some points need to be further investigated. For example, does the epigenome shape the conformational structures, or vice versa? (Boltsis et al. 2021). As recently shown by computational polymer modeling approaches, the repulsive inter-chromocenter effect (Arpòn et al. 2021), combined with the positioning of heterochromatic NOR at the nucleolar periphery, was sufficient to reproduce a coherent spatial organization of the Arabidopsis genome (Arpòn et al. 2021; Di Stefano et al. 2021). Consequently, it seems that the phase separation effect associated with heterochromatin domain formation is an essential driver explaining the spatial chromatin organization in Arabidopsis (Sun et al. 2020; Salari et al. 2021; Di Stefano et al. 2021; Bourguet et al. 2021).

More recently, a growing interest in the influence of environmental stresses on 3D chromatin folding in Arabidopsis emerged (Sun et al. 2020; Yadav et al. 2021). For example, heat stress was shown to induce a significant decrease in the pericentromeric contact map, which goes ahead with the reactivation of TE (Sun et al. 2020).

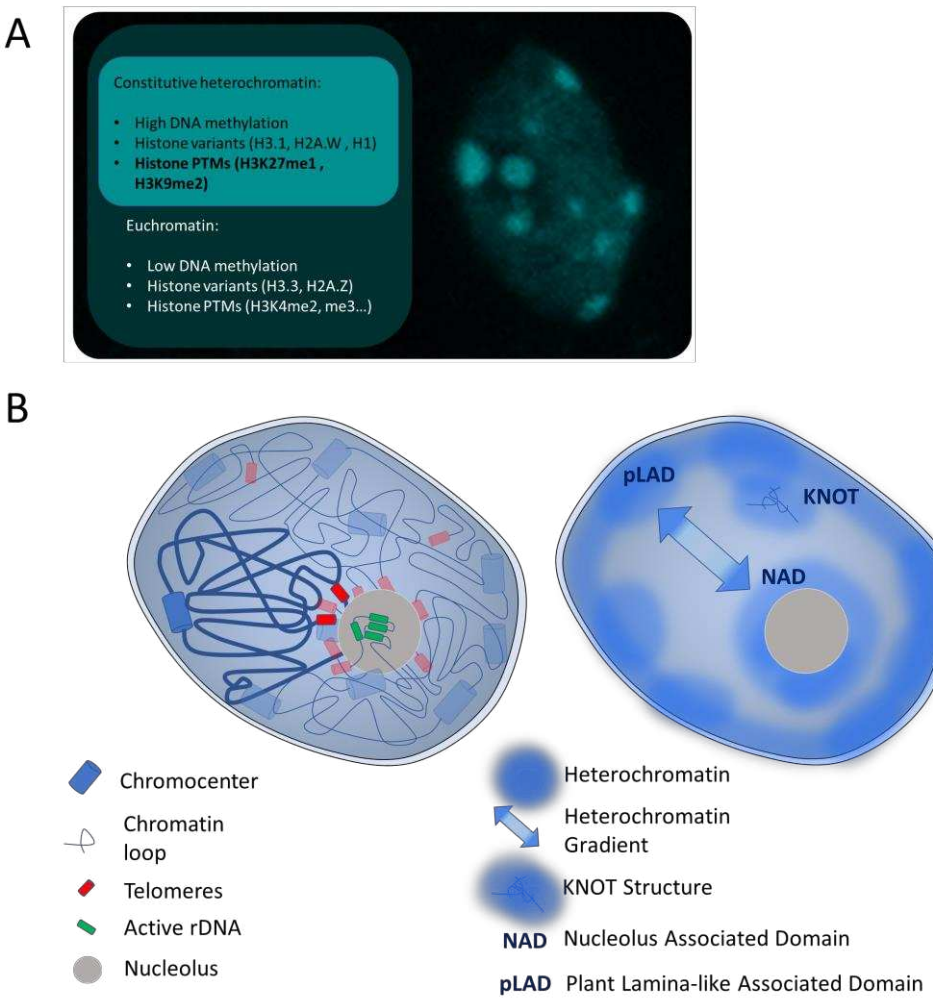

Figure 7: 3D organization of chromatin in interphasic Arabidopsis nucleus

(A) Description of the constitutive heterochromatin and euchromatin components (Left). Organization of chromocenter structures visible as a bright structure upon DAPI staining of interphasic Arabidopsis nuclei (Right). **(B)** Left panel: graphical representation of the spatial organization of chromocenters, chromatin loops, telomeres, active rDNA genes, and the nucleolus in an interphasic Arabidopsis nucleus. Right panel: spatial distribution of heterochromatic domains (dark blue) such as KNOT, NADs and pLADs. The intra-nuclear heterochromatin gradient is shown by the blue arrow.

1.4. DNA damages and epigenome

The daily growth of plants depends on the maintenance of genome integrity and the proper regulation of the transcriptional programs. Indeed, environmental cues recurrently endanger genome integrity by inducing different types of DNA damage. The signaling and repair of these damages may, in turn, disturb the epigenetic layers. Given that plants are recurrently exposed to the genotoxic effect of sunlight, they may have evolved sophisticated mechanisms to cooperatively maintain the integrity of genome and epigenome. The following parts introduce our current knowledge of the interplay between UV-induced DNA damages, epigenome, and DNA repair processes.

1.4.1. DNA damages

In the book chapter “DNA damage and DNA methylation” we reviewed several types of DNA damages associated with photolesions and bases modifications. We additionally focused on the crosstalk between DNA methylation and DNA repair.

1.4.2. Photodamage recognition and repair within different epigenomic landscapes

In the following part, we will focus on the DNA damages induced by UV light. In the review entitled “Formation and Recognition of UV-Induced DNA Damage within Genome Complexity” (Johann to Berens and Molinier 2020), the current knowledge about the influence of the epigenome landscape on DNA damage formation, recognition, and repair was summarized and discussed.

1.4.3. Oxidatively-induced DNA damage

As mentioned in our review, aside from the induction of photolesions, UV-light also generates oxidatively-induced DNA damage (Johann to Berens and Molinier 2020). Especially Guanine is prone to be oxidized, leading to the formation of 8-oxo-7,8-dihydro-2'-deoxyguanosine (8-Oxo-G) (Johann to Berens and Molinier 2020; Gorini et al. 2021).

As reviewed in our book chapter, 8-Oxo-G shows high guanine to thymine transversion mutation potential and may further react with surrounding proteins, thereby forming deleterious DNA-protein crosslinks. Interestingly, as reported for photolesions, recent studies in mammals provide the first evidence for an epigenome-dependent, non-random accumulation of 8-Oxo-G in promoters, 5'-UTRs, 3'-UTRs, exons, and introns (Ding et al. 2017; Gorini et al. 2020; Gorini et al. 2021). Furthermore, several studies reported that 8-Oxo-G accumulation preferentially occurs in transcriptionally active regions (Ding et al. 2017; Gorini et al. 2020; Gorini et al. 2021). This localization is consistent with the emerging role of 8-Oxo-G in the transcriptional activation of a specific subset of genes associated with oxidative stress response (Fleming et al. 2017a; Fleming et al. 2017b; Redstone et al. 2019; Fleming et al. 2019). This "epigenetic" role of 8-Oxo-G was shown to notably rely on DNA repair proteins (Fleming et al. 2017a; Gorini et al. 2021).

The primary repair mechanism of 8-Oxo-G is the removal by specific DNA glycosylases followed by either short- or long-patch Base Excision Repair process (BER), which is also responsible for repairing other nucleobase alterations and the single-strand breaks (Shinmura and Yokota 2001; Jansson et al. 2010). Alternatively, the DDB2 damage recognition protein was shown to bind 8-Oxo-G and Apurinic sites (AP) generated by DNA glycosylase activity (Jang et al. 2019). Consequently, DDB2 and NER process appear as a multifunctional pathway involved in the repair of most UV-induced lesions, thereby reinforcing the canonical BER pathway (Jang et al. 2019; Gorini et al. 2021).

The "epigenetic" effect of 8-Oxo-G is somehow sequence-specific and was mainly related to the activity of 8-OxoG Glycosylase1 (OGG1) in potentially G-quadruplex forming sequences (PQSs) (Fleming et al. 2017a; Ding et al. 2018; Gorini et al. 2021). The production of AP sites in PQSs leads to the formation of G-quadruplex structures that impair the enzymatic activity of Apurinic/Apyrimidinic Endonuclease 1 (APE1), thereby extending its binding. The extended binding of OGG1 and APE1 allows recruiting several TF, which regulates the transcriptional activity of proximal regions (Pan et al. 2016; Pan et al. 2017; Fleming et al. 2017b). Considering the fact that the UV-DDB complex was shown to transiently interact with OGG1 and APE1 to facilitate their dissociation from DNA, it can be expected that DDB2 may directly participate in the regulation of 8-Oxo-G contents (Jang et al. 2019).

Surprisingly in Arabidopsis, neither the localization nor the “epigenetic” role of 8-Oxo-G was investigated for now. However, the Arabidopsis DDB2 was shown to interact with APE1L (APE1-Like) and ZDP (ZINC 4 FINGER DNA 3'-PHOSPHOESTERASE) the functional homologs of APE1 stimulating their activities, indicating that a similar mode of action likely exists in plants (Córdoba-Cañero et al. 2017).

1.4.4. Reconstruction of chromatin upon damage repair

In previous parts, we focused on the interplay between the epigenome and DNA repair processes and highlighted the two first steps of the Access-Repair-Restore model (Fig. 8) (Green and Almouzni 2002; Polo and Almouzni 2015).

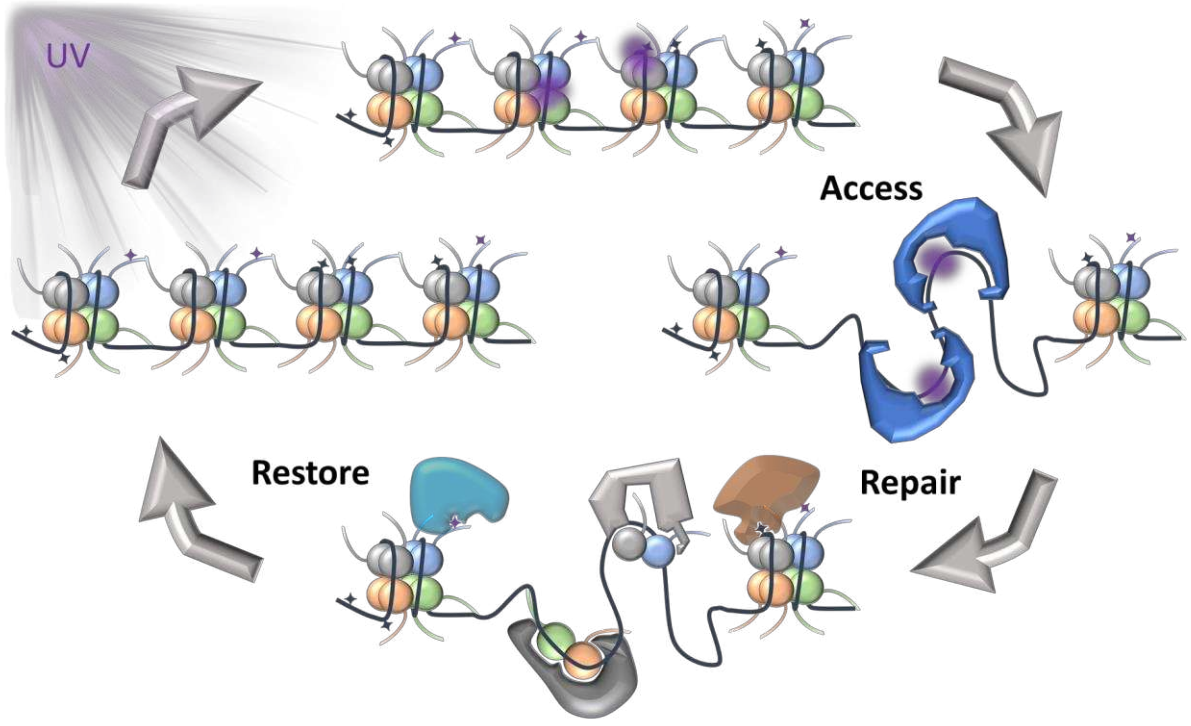

Figure 8: Access-Repair-Restore model

Graphical abstract of the successive chromatin opening and chromatin restoration steps occurring during DNA repair processes.

The following paragraph will discuss the re-establishment of chromatin structure upon repair called “Restoration”. This final step involves re-building of the epigenetic landscape at the damage site (Green and Almouzni 2002; Polo and Almouzni 2015). In DNA synthesis-dependent-DNA repair pathways, such as NER and long-patch BER, the restoration of the DNA methylation level is an important step for methylome maintenance (also discussed in our book chapter)(Johann to Berens and Molinier 2020).

Aside from DNA methylation, the other layers of the epigenome likely undergo a dynamic due to chromatin remodeling activities and specific histone modifiers involved in DNA repair (Johann to Berens and Molinier 2020). Interestingly, there are growing shreds of evidence that the restored epigenome may slightly differ from the initial one in terms of histone variants, nucleosome density, DNA methylation, and histone PTMs (Polo and Almouzni 2015; Fortuny et al. 2021). Indeed, in the mouse model, 6h upon UV-C irradiation an enrichment of H3 and genome compaction were observed (Schick et al. 2015). In addition, this study reveals significant changes in the localization of the activating mark H3K27ac, indicating that nucleosome positioning and histone PTMs are not accurately maintained (Schick et al. 2015). Later on, a more detailed study on Mouse and Human cell cultures, visualized the prominent role of DDB2 in successive decompaction, through H1 displacement, and re-compaction of UV-damaged heterochromatin (Fortuny et al. 2021). Interestingly, upon re-compaction, histone chaperones specifically delocalize to the damage site in a DDB2 -dependent manner, to reintroduce H3.1 and H3.3 histone variants (Fortuny et al. 2021).

Indeed, CAF-1, in collaboration with PCNA and with HIRA, were described to respectively incorporate new histones H3.1 and H3.3 to the repaired sites (Fig. 8) (Moggs et al. 2000; Adam et al. 2013). A recent study also reveals that the H3.3 histone chaperone DAXX is exclusively recruited at the heterochromatic damage site when assisted by ATRX (Wong et al. 2010; Fortuny et al. 2021). Surprisingly, DAXX did not show a strong H3.3 deposition activity in comparison to HIRA (Fortuny et al. 2021). Given that ATRX bound H3K9me3 and was shown to be somehow essential for its maintenance, it can be speculated that the DAXX ATRX complex participates in histone PTM maintenance on newly deposited histones in heterochromatin (Dyer et al. 2017).

Finally, the histone PTM H3K9me3, essential for silencing, is maintained upon DNA repair by the SET Domain Bifurcated Histone Lysine Methyltransferase 1 (SETDB1), that act on the newly integrated histones (Fig. 8) (Fortuny et al. 2021). This maintenance of H3K9me3 was also described as an essential feature of SIRT6 Deacetylase activity following recurrent DNA damaging events upon cell aging (Korotkov et al. 2021).

The mechanisms regulating the maintenance of the epigenetic landscape, genome-wide or at damaged sites, are gaining more and more interest. Indeed, interplays between DNA repair and DNA methylation factors were recently demonstrated (Schalk and Molinier 2016; Schalk et al. 2017; Jiang et al. 2021). This strongly suggests that related mechanisms (direct or indirect) likely exist to maintain other epigenetic marks. (*i.e.,* histone PTMs).

1.4.5. Epigenetic Inheritance

As discussed in the previous part, emerging notions strongly indicate that genotoxic stresses affect not only genetic integrity but also the epigenetic landscape (Schalk et al. 2017; Fortuny et al. 2021). Given that plants are submitted to recurrent UV-B exposure, it could be assumed that not only mutations are accumulated but also epi-mutations (Jiang et al. 2014). In order to further address the question of whether the epigenetic variation that may occur upon DNA repair can be inherited to the offspring and thus participates in the evolutionary adaptation (Stajic and Jansen 2021) we will briefly review the current knowledge about epigenetic inheritance upon sexual reproduction.

The mechanistic of parental epigenetic inheritance is supported by two main assumptions. The first one involves regulatory proteins, such as transcription factors and small regulatory RNAs that are transmitted through the cytoplasm of gametes and thus, from early on, act as regulatory control on the offspring's genome (Stajic and Jansen 2021). The second one relies on epigenetic marks (DNA methylation or histone PTMs) that are faithfully reintroduced during meiosis and somehow escape reprograming events linked to germline development, thereby imprinting the DNA of the offspring (Stajic and Jansen 2021).

In the last decades, several studies demonstrated that several epigenetic reprogramming events, in between germ cell development and seed germination, are essential for proper development of the offspring (Fig. 9) (Kawashima and Berger 2014; Borg et al. 2021; Ono and Kinoshita 2021). This reprogramming includes extensive DNA demethylation in pollen and endosperm as well as a replication-independent H3 replacement in male and female gametes (Fig. 9) (Hauser et al. 2011; Borg et al. 2021; Ono and Kinoshita 2021).

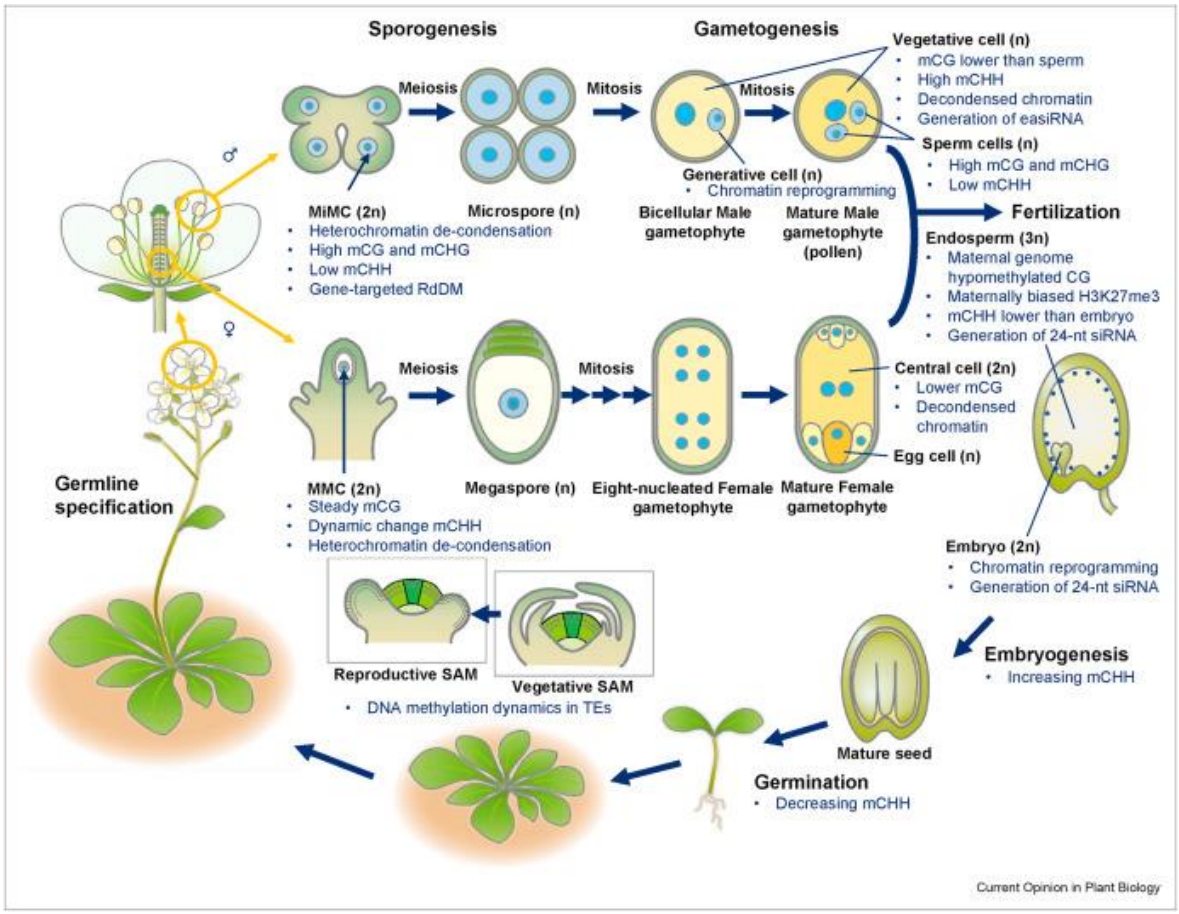

Figure 9: Arabidopsis Life-cycle and epigenetic reprogramming

Schematic view on the key steps of Arabidopsis life-cycle, including main epigenetic dynamics occurring upon sexual reproduction. The figure originates from Akemi Ono's and Tetsu Kinoshita's review (Ono and Kinoshita 2021).

Interestingly several examples of epi-mutations/epi-alleles have been described to be inherited upon several generations (Durand et al. 2012; Agorio et al. 2017; Blevins et al. 2017; He et al. 2018; Pignatta et al. 2018).

Most of these studies propose a central role for small RNAs and the RdDM machinery in epiallele inheritance (Durand et al. 2012; Pignatta et al. 2018; Mosher 2021). However, for some others, the feedforward loop between DNA and H3K9 methylation (Fig. 4) appears to be sufficient for transgenerational imprinting (Agorio et al. 2017). Despite this observation, few naturally occurring epimutations could, for now, be linked to traceable phenotypes (Silveira et al. 2013). However, the underlying molecular mechanisms ensuring epigenetic inheritance upon sexual reproduction remain poorly documented. Consequently, it is still debated to which extent epigenetic inheritance may participate in the naturally occurring adaptation process (Xavier et al. 2019; Stajic and Jansen 2021).

1.5. Attached reviews

CHAPTER 0001

DNA damage and DNA methylation

Salimata Ousmane Sall*, Philippe Johann To Berens* and Jean Molinier**
Institut de biologie moléculaire des plantes 12 rue du General Zimmer 67000 Strasbourg, France
*Equal contribution
**Corresponding author: jean.molinier@ibmp-cnrs.unistra.fr

Abstract

Exposure to genotoxic stress leads to the formation of various types DNA damages that alter genome integrity. Importantly, DNA lesions occur at particular nucleotides sequences and their reactivity is also under the influence of genome compaction and epigenetic marks such as DNA methylation. The DNA repair pathways that are activated in response to DNA damages rely predominantly on *de novo* DNA synthesis implying that the epigenomic landscape must also be accurately re-established. Therefore, complex interplays between bases composition, DNA methylation level and DNA repair pathways likely exist to efficiently maintain both genome and epigenome integrity at damaged and repaired genomic regions.

Keywords
Damageability, Base modifications, DNA repair, DNA methylation, plants

Introduction

Living organisms have to cope with environmental cues and with endogenous chemical compounds that are deleterious for their genetic information. Indeed, genotoxic stresses challenge genomes by inducing changes in the chemical structure of nucleotides. These alterations involving the four canonical bases (Adenine (A), Cytosine (C), Guanine (G) and Thymine (T)) or breaking the DNA strand(s) are defined as DNA damage/lesions and are specific of particular genotoxic agents [1]. Base modification is the addition of a chemical moiety resulting from either a reaction with a genotoxic agent (*i.e.* alkylation) or from an enzymatic reaction (*i.e.* DNA methylation). Thus, bases could be oxidized, deaminated, alkylated

or methylated leading to different types of modifications [2]. Importantly, methylation rather than being exclusively considered as a DNA lesion *per se* is also an epigenetic mark [2]. Indeed, one key component of the epigenome is cytosine methylation leading to 5-methyl cytosine (5-mC), which is required for the stable silencing of transposable elements (TE) as well as for the regulation of gene activity [3]. While in mammals DNA methylation occurs in the CG context, in plants, 5-mC is found in 2 additional sequence contexts: CHG and CHH (where H=A, T, or C) [4]. Such base modification likely adds another layer of complexity in the reactivity of genomic regions subjected to a genotoxic stress. Given that most of the DNA lesions occur at a particular base, the nucleotides composition of the genome is an important feature to take into account. Moreover, several studies highlighted that the epigenome landscape tends to play an important role in the ability of the DNA/genome to be damaged and to efficiently perform their repair [5].

Therefore, this chapter will be devoted to the presentation of the different types of bases modifications and their consequences on genome integrity. A particular emphasis will be placed on the influence of the DNA methylation profile on damage formation and on the maintenance of methylome integrity upon repair. We will focus on the emerging notion that complex interplays exist between genome, methylome, DNA damage and repair and, that plants have developed sophisticated strategies to simultaneously maintain (epi)genome integrity.

Bases modifications

Cellular processes as well as environmental factors induce genotoxic stress leading to the formation of a large repertoire of base modifications that affect genome stability. These modifications alter DNA structure and are sensed either as DNA lesions (*i.e.* base oxidation) or as epigenetic marks (*i.e.* DNA methylation) [2]. Several features of the genomic regions such as nucleotides composition, spatial organization may influence their ability to accumulate base modifications that must be accurately repaired (for DNA lesions) or fine-tuned (for DNA methylation). Upon detection, these modified bases are actively removed via DNA synthesis-dependent repair processes to maintain (epi)genome integrity (**Figure 1**).

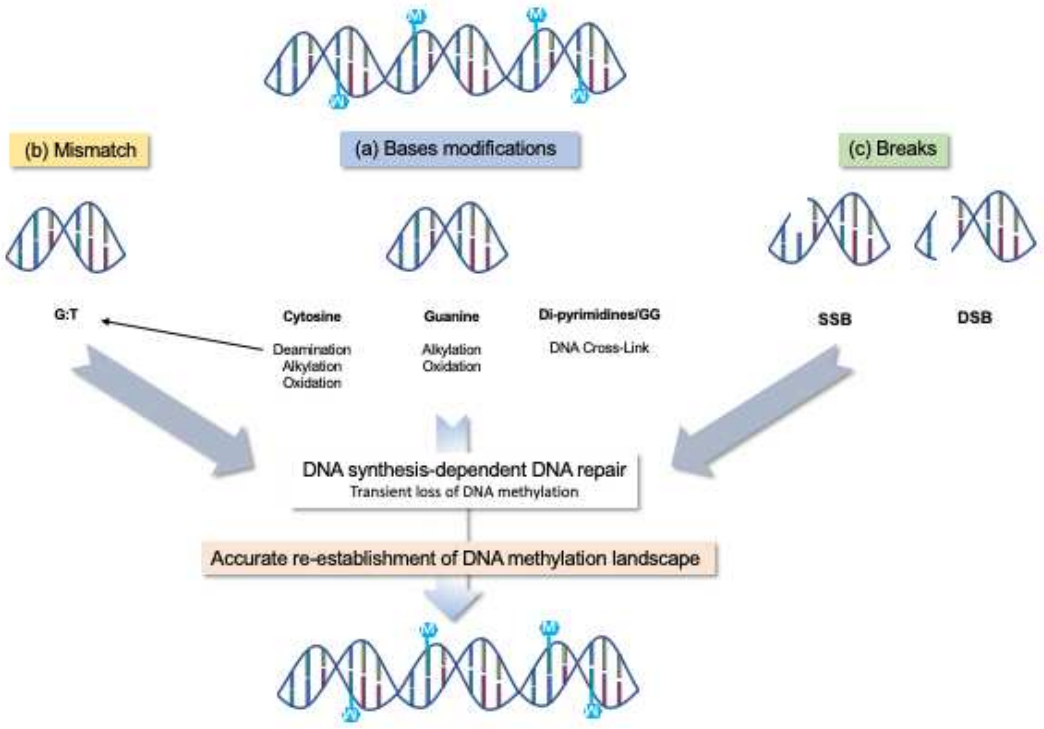

Figure 1. Types of DNA damages

DNA is subjected to various types of alterations that either lead to **(a)** bases modifications, **(b)** mismatch or **(c)** single/double strand breaks (SSB/DSB). These DNA damages are processed and repaired by different pathways that rely on *de novo* DNA synthesis. When the original DNA sequence is methylated (M), the processing of the damaged DNA leads to a transient loss of DNA methylation that must be accurately re-established to maintain methylome integrity.

DNA methylation

DNA methylation is the addition of a methyl group on either adenine to form 6-methyladenine (6-mA) or on cytosine to form 5-methylcytosine (5-mC) [3] . 5-mC is the most studied DNA methylation/epigenetic mark. 5-mC is detectable at different rates in plants, mammals, bacteria and is thought to be low in Drosophila or absent in yeast [6]. 5-mC changes DNA flexibility by enhancing stiffness and modulates DNA accessibility to different factors [7]. Moreover, the presence of 5-mC within a locus may favor the preferential formation of DNA damage (*i.e.* photolesions) [8,9].

Deamination

In addition to the enzymatic-mediated deamination [10–12], a significant amount of hydrolytic deamination can also occur especially on single stranded DNA [13–15]. The hydrolytic deamination of cytosine forms uracil (U) that is recognized as a DNA lesion. Deamination can also occur on 5-methylcytosine and

produces thymine (T) creating a T:G mismatch. Replication of these damaged sites including C:G to T:A transition prevents maintenance of DNA methylation at this particular genomic sequence and thus leads to alteration of both genome and methylome integrities [13]. To avoid such base transition and permanent loss of DNA methylation, the deamination product is removed by specific glycosylase, via the BER pathway [16,17].

Alkylation

DNA alkylation include all modifications induced by the binding of a new alkyl group on a non-canonical position of DNA after a monomolecular or bimolecular nucleophilic substitution (SN1/ SN2) reactions [18–20]. Alkylation can occur on the oxygen atoms in phosphodiesters backbone, as well as on Oxygen and Nitrogen atoms of the 4 nucleobases [18,21]. The site of DNA alkylation strongly depends on the alkylating agent which can be an endogenous metabolite such as S-adenosylmethionine (SAM) [22], or an exogenous agent, such as alkylating drugs currently used as chemotherapeutics (*i.e.* Busulfan) [18]. The most frequently transferred alkyl group is the methyl group, and the predominant alkylation products are N^7-methylguanine (N^7-meG), N^3-methyladenine (N^3-meA) and O^6-methylguanine (O^6-meG) [18–20]. N^7-meG and N^3-meA are cleaved by spontaneous depurination or by specific DNA glycosylases leaving in both case an abasic site with cytotoxic and mutagenetic potential that need further repair by Nucleotide Excision Repair (NER) or Base Excision Repair (BER; long- or short-patch BER) [23–25]. Conversely, the highly mutagenic O^6-methylguanine, allowing a preferential pairing with Thymine [26], can be repaired by direct reversion leading to the alkylation of a catalytic residue of O^6-methylguanine-DNA methyltransferase (MGMT) [27]. More recently, N3-methylcytosine (N3-meC), a usually rare side-product of classical alkylating agents (*i.e.* Methyl Methane Sulfonate) [20], was shown to be a significant byproduct of DNA methyltransferase enzymes (DNMTs) activity responsible for 5-mC synthesis in nematodes [28]. These results may notably explain the absence of DNA methylation in the nematode *Caenorhabditis elegans* and the observed coevolution of methylation and alkylation damage repair pathways all across eukaryotes [28].

Oxidation

Aside deamination and alkylation, DNA oxidation is another type of base modification, that affects genome integrity. Environmental factors, such as UV-light (UV-A and UV-B), as well as endogenous cellular processes (*i.e.* respiration) lead to the formation of reactive oxygen species (ROS): superoxide

anion (O_2^-), hydrogen peroxide (H_2O_2) and hydroxyl radical (• OH) [29–31]. ROS have a genotoxic effect by reacting with purines, pyrimidines and the deoxyribose backbone of DNA, to produce more than 20 different types of oxidatively-induced DNA lesions [31]. The yield of these different products is highly specific to the molecular redox context. Nevertheless, guanine is described as the major target of oxidation, especially at C8 position, thereby forming the highly mutagenetic 7,8-dihydro-8-oxoguanine (8-Oxo-G) [31–34]. When unrepaired, 8-Oxo-G can pair with the Hoogsteen face of adenine thereby generating a guanine to thymine transversion mutation upon replication, generating an un-methylatable A:T site [35,36]. Additionally, oxidation of 8-Oxo-G/lysine form bulky proteins-DNA cross-links that are deleterious [37]. As for alkylating damages, 8-Oxo-G is mainly removed by specific DNA glycosylases (*i.e.* MutY and MutT) and further processed by the BER machinery [38]. Theoretically, 5-mC can also undergo oxidative modification despite its relatively high reduction potential compared to guanine [31,36,39]. Especially the different oxidation products: 5-hydroxymethylcytosine (5-hmC), 5-formylcytosine (5-fC) or 5-carboxycytosine (5-caC) mainly gained in interest in the last decade. In mammals, the active removal of 5-mC occurs upon successive enzymatic-mediated oxidations [40,41]. These serial oxidations of 5-mC produce 5-hmC, 5-fC, and 5-caC and are catalyzed by the Ten-eleven translocation (TET) protein family members [42]. In absence of *bona fide* 5-mC glycosylases in mammals, this alternative process allows efficient active DNA demethylation [43]. The existence of a TET-like demethylation pathway in plants, as alternative strategy is as yet undetermined [44–46].

Cross-links

DNA-DNA cross-link (CL) has a great potential to alter genome integrity. CL can occur within one DNA strand (intra-strand crosslinks) or in between the 2 DNA strands (inter-strand crosslinks) [47]. Intra-strand crosslinks are very common for light-dependent living organisms. Indeed, the UV spectrum of sunlight induces crosslinks between di-pyrimidines [5,48,49]. Two successive pyrimidines (CC, TT, TC or CT) can be raised to their highly reactive singlet or triplet states when absorbing UV radiation, especially in the UV-C and UV-B wavelength ranging from 100 to 280 nm and 280 to 315 nm, respectively [48,49]. Once reached the reactive singlet or triplet states fast photochemical reactions lead to the formation of three main DNA intra-strand crosslink damages or photoproducts: cyclobutane pyrimidine dimers (CPDs), pyrimidine 6-4 pyrimidone photoproducts (6-4PPs) and the 6-4PPs Dewar isomer [49].

Conversely to intra-strand cross links, inter-strand crosslinks (ICLs) are relatively rare events, often thought to be a consequence of drug treatments [50]. For example, Mitomycin C induces inter-strand

crosslinks between the guanines of both strands and also shows specificity for CpG sequences [50,51]. Recently, the biological impact of the oxidation product of adenine, 7,8-dihydro-8-oxoadenine (8-Oxo-A) was shown to have significant potential to form ICL with adenine and guanine on the opposite strand [52]. The repair of ICL is complex and triggers *de novo* DNA synthesis of both strands in the vicinity of the damaged regions, endangering the maintenance of the DNA methylation footprints [47,53].

DNA methylation and DNA damageability

Endogenous and exogenous stimuli form directly or indirectly DNA lesions in a sequence specific context [20,32,49,54]. Recent studies highlighted the heterogenicity of the formation of DNA lesions within genome complexity, hereafter called as "damageability" [9,55–59]. DNA damageability can be defined as the degree of susceptibility of a locus, within a genome, to be damaged by a particular genotoxic agent. This damageability depends on the whole complexity of the local chemical context and should be considered as highly variable during lifespan and only partially predictable. The putative reverse-influence of the epigenome on the DNA damageability drew the attention of many research group in the last decade [5,55–57,60,61].

DNA methylation (5-mC), as main epigenetic mark, has the potential to influence the damageability of the genome. The influence of 5-mC on the formation of spontaneous hydrolytic deamination, was shown, *in vitro*, to occur twice more often compared to unmethylated cytosine [15]. Moreover, a 5-mC adjacent to a pyrimidine is more prone to form photoproducts than an unmethylated cytosine in combination with another pyrimidine [49]. *In vitro* ligation-mediated PCR, *in vitro* irradiation of genomic DNA and *in vivo* Immuno-precipitation of UV-Damaged DNA (IPOUD) experiments all highlighted a significant increased potential of methylated DNA to form photodamage upon UV exposure [9,55,62]. Given that 3/4 of the di-pyrimidines combinations (CC, TC or CT) involve at least one cytosine and that in plants, DNA methylation occurs also in CHG or the CHH contexts (where H is A, T or C), the highly methylated genomic regions may be more reactive to form photodamage. In other words, the sequence context in combination with the methylome landscape may influence the UV damageability and likely the repair machinery that act at particular loci [9,55,62].

Additionally, 5-mC can also indirectly influence DNA damageability through its role in the establishment of higher chromatin structures such as nucleosome occupancy, histone post-translational modifications (PTM) and genome folding [63,64]. Nucleosome displacement for example was shown to influence the formation of DNA strand break upon zeocin treatment [56]. 8-Oxo-G distribution was identified to

accumulate in H3 enriched regions of the Yeast genome [61], and was consistently more frequently observed in the rather compact lamina-associated-domains of chromatin, displaced at the nuclear periphery, in rat [57].

Finally, 5-mC can also indirectly impact the DNA damage dynamics, by controlling DNA repair. For example, when preventing transcription [64], 5-mC can hinder the damage recognition by the Transcription coupled repair (TCR) pathway [65].

Dynamics of DNA methylation

Establishment of DNA methylation

In plants, the mechanism called RNA-directed DNA methylation (RdDM) targets genomic DNA with small homologous interfering RNAs (siRNA of about 24-nt in length) and triggers, in *cis*, cytosine methylation in all sequence contexts [66]. This process is observed along the entire development of plants including both vegetative and reproductive phases [67–69]. The biogenesis of these 24-nt siRNAs depends on the plant specific RNA Polymerase IV (POL IV), on RNA-Dependent RNA Polymerase 2 (RDR2) and on DICER-Like 3 (DCL3) [4]. The siRNAs are incorporated into Argonaute 4 (AGO4) or its surrogate, AGO6, to direct cytosine methylation catalyzed by DRM2 [66]. Importantly, another plant specific RNA Polymerase V (POL V) is also required for siRNA accumulation at a subset locus [4]. In addition to the canonical RdDM pathway to initiate DNA methylation, RNA Polymerase II was also identified to be required to trigger transcriptional gene silencing in non-canonical pathways [70]. In these pathways AGO2, DCL2, DCL4, RNA-DEPENDENT RNA POLYMERASE 6 (RDR6), DRM2 and eventually POL IV/POL V are mobilized at some loci (**Figure 2**) [66,71].

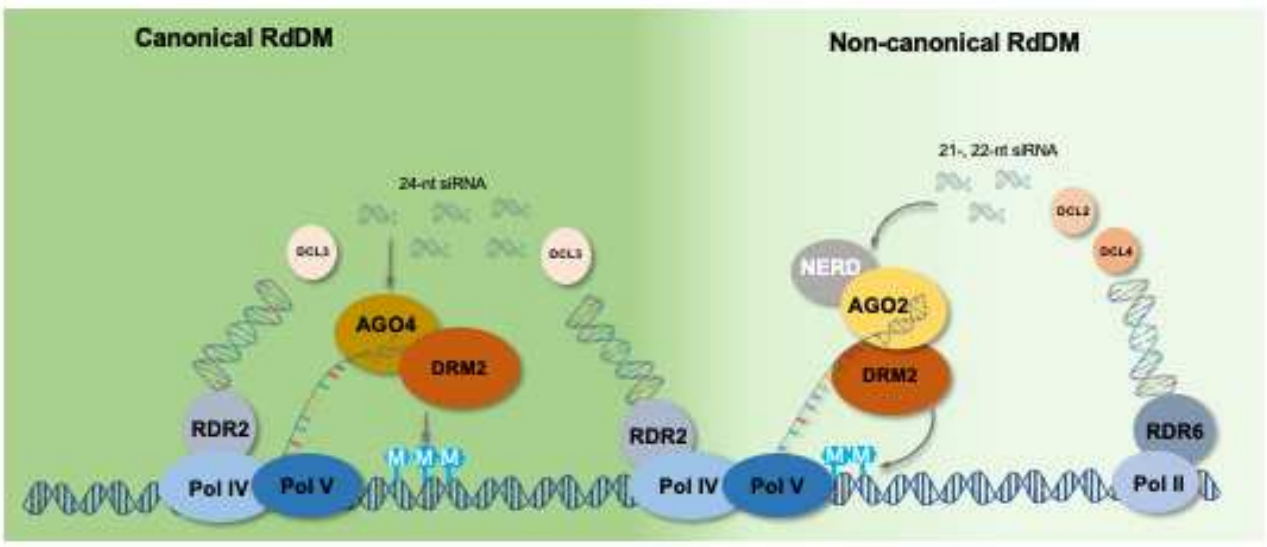

Figure 2. Canonical and non-canonical RdDM pathways

In the case of Canonical RdDM**, s**ingle-stranded RNAs transcribed by POL IV is copied by RDR2 into a dsRNA that is processed by DCL3 into 24-nt siRNAs. Following incorporation into AGO4 (left panel), the 24-nt siRNAs base-pair with Pol V scaffold transcripts, which results in DRM2 recruitment and dense methylation. SiRNAs are continuously produced from the methylated template by POL IV pathway components, which reinforces TGS that can be maintained in siRNA-independent manner by methyltransferases. In the case of non-canonical pathway (right panel), RNAs transcribed by POL II are processed by RDR6 to produce double-stranded RNAs (dsRNAs), which are transformed by DCL2 and DCL4 into small interfering RNAs (siRNAs) of 21-22 nucleotides (nt). Some if these siRNAs are loaded into AGO2 to trigger low levels of DNA methylation depending on DRM2 and RNA POL V, which interact with Needed for RDR2-independent DNA Methylation (NERD).

Maintenance of DNA methylation patterns

After establishment and upon cell division or synthesis-dependent DNA repair, DNA methylation must be maintained to ensure, for example, TE silencing or cell type identity [4]. Whilst in mammals DNA methylation occurs almost exclusively in the CG context, in plants, cytosines are additionally methylated in both CHG and CHH contexts (where H= A, T or C) [4]. The model plant *Arabidopsis thaliana* exhibits genomic DNA methylation rates of approximately 24%, 6.7%, and 1.7% for the CG, CHG and CHH contexts, respectively [72]. DNA methylation is maintained by context specific DNA methyltransferases [4]. CG is mediated by DNA methyltransferase 1 (MET1, orthologue of DNMT1 in mammals), CHG methylation is maintained by the Chromomethylase 3 (CMT3), a plant specific DNA methyltransferase, and finally CHH methylation is maintained by DRM2 through the RdDM pathway as well as

Chromomethylase 2 (CMT2) [73,74]. DRM2 is involved in CHH methylation in euchromatic regions, short TE and long TE border regions whilst CMT2 preferentially methylates pericentromeric heterochromatin and long TE bodies [75,76].

DNA methylation shows periodicity based on nucleotide resolution [77]. Indeed, DNA methylation is more prone to occur in core nucleosome compared to inter-nucleosomal regions [77]. Therefore, DNA methyltransferases tend to act preferentially at nucleosomes by entering the major groove to reach and methylate the cytosine on the outside of the nucleosome [78]. CHH methylation displays a genome-wide periodicity of about 10 bp whereas CHG methylation, exhibits a period of about one nucleosome size (167-nt) [72]. Importantly, it was recently shown that mammalian Dnmt3a (orthologue of DRM2 in plants) acts as a tetramer with Dnmt3L allowing methylation of two CG sequences separated by about 8 to10-nt [79].

Although DNA methylation is a stable epigenetic mark in most cases, a reduction in methylation level is observed during development. Two cases may account for this loss of methylation: either an absence of efficient/functional methylation maintenance upon replication (passive demethylation), or cytosine methylation is actively removed and this is referred to as active demethylation [4,43].

Active DNA demethylation

The model plant *Arabidopsis thaliana* contains four 5-mC specific DNA glycosylases that recognize and remove methylated cytosines from double strand DNA across all sequence contexts [80,81] : Repressor Of Silencing (ROS1) [82], Demeter (DME) [83], Demeter-like 2 and 3 (DML2 and DML3) [81,84]. Plants defective in expression of these 5-mC demethylases exhibit an increase in DNA methylation rate in all sequences contexts at specific genomic loci [80–82,85,86]. These demethylases have distinct biological roles. DME ensures the establishment of imprinting during gametogenesis [87] while ROS1 acts in vegetative tissues antagonizing the RdDM pathway [81,88,89]. Like ROS1, DML2 and DML3 are also expressed in vegetative tissues [82,84]. Although some specificity has been observed, ROS1, DML2 and DML3 work redundantly [88]. Like during all excision repair pathways (BER, NER, Mismatch Repair; enzymatic removal of 5-mC is also predicted to generate DSB [90].

DNA repair factors and DNA methylation

Interestingly, several DNA repair factors have been shown to regulate the shaping of DNA methylation landscape. In Arabidopsis, defect in expression of the Mismatch Repair factor MSH1 leads to heritable

alterations of DNA methylation profiles [91]. In mammals, NER contributes to active DNA demethylation [92,93]. Indeed, Growth Arrest and DNA Damage inducible 45 å protein (GADD45å) forms a complex with the NER factor XPG (Xeroderma pigmentosum, complementation group G) and influences the active DNA-demethylation process [94]. The two NER endonucleases, XPG and XPF (Xeroderma Pigmentosum, complementation group F) participate in active DNA demethylation and in the formation of transcriptionally permissive chromatin, thereby influencing gene expression [92]. Another NER factor, DDB2 has been demonstrated to influence both *de novo* DNA methylation and active DNA demethylation. Indeed, the loss of DDB2 function in Arabidopsis, alters DNA methylation patterns at many repeat loci [95]. DDB2 belongs to a protein complex with AGO4 that modulates the local abundance of 24-nt siRNAs and *de novo* DNA methylation at particular genomic sites [95]. Similarly, mammals depletions of cognate Arabidopsis NER factors also lead to alterations of DNA methylation profiles strengthening the identification of the interplays between repair factors and DNA methylation pathways [96]. Moreover, DDB2 was found to negatively regulate the expression and the activity of the DNA demethylase ROS1 highlighting a direct interconnection between the NER and the active demethylation machineries [97(p2)]. Altogether, DDB2 acts unexpectedly outside DNA repair as regulator of two antagonistic pathways: *de novo* DNA methylation and active DNA demethylation, likely controlling methylome homeostasis [95, 97(p2)]. Finally, DDB2, which predominantly exhibits high affinity for photodamage also senses abasic sites and G/T mismatches [98]. Interestingly, these damages are products of either the BER pathway or of 5-mC deamination. This allows considering that particular factors likely evolved sophisticated features to ensure both genome and epigenome stability upon direct or indirect formation of the broad spectrum of base modifications.

DNA methylation upon DNA repair

Most of the DNA repair pathways depends on the enzymatic removal of the damaged DNA fragment followed by *de novo* DNA synthesis. Indeed, BER, NER, mismatch repair and homologous recombination are repair pathways that entail DNA synthesis [99]. Therefore, in methylated genomic regions, the removal of methylated cytosines within the damaged fragment leads to a transient loss of DNA methylation. The efficient re-establishment of the DNA methylation landscape would rely on the maintenance pathways. In plants, it was recently established that DDB2 also forms a complex with the RNA silencing effector AGO1 and 21-nt siRNA overlapping genomic regions enriched in photo-lesions [100]. These 21-nt siRNAs, referred as uviRNAs (UV-induced small RNAs), are produced by a non-

canonical biogenesis pathway relying on the RdDM transcriptional machinery RNA POL IV-RDR2 and on the post-transcriptional gene silencing factor DCL4 (**Figure 3**) [100]. The DDB2-AGO1-uviRNA complex was shown to be loaded on chromatin upon UV exposure likely to recognize the UV-induced DNA lesions in a non-canonical NER pathway [100]. Interestingly the ribonucleotide sequences of these 21-nt uviRNAs share similarity with those of 24-nt siRNA involved in *de novo* DNA methylation, highlighting their common origins [100]. The discovery of such interconnections between core siRNAs biogenesis factors, leading to the widening of the repertoire of small RNAs, allows speculating that they may be used to cooperatively maintain genome/epigenome integrities.

Very little is known about the accuracy of the methylome integrity at damaged sites. Most of the studies either focused on the damageability or on the repair machinery mobilized at particular genomic regions. Recently, it has been reported that photolesions are sources of DNA methylation changes in repressive chromatin [62]. In addition, specific DNA repair pathways involved in the removal of photolesions prevent alterations of the DNA methylation landscape in Arabidopsis [62]. Altogether, these studies highlight that DNA repair and DNA methylation factors interplay, opening new perspectives in the decryption of the mechanisms controlling both genome and epigenome integrity.

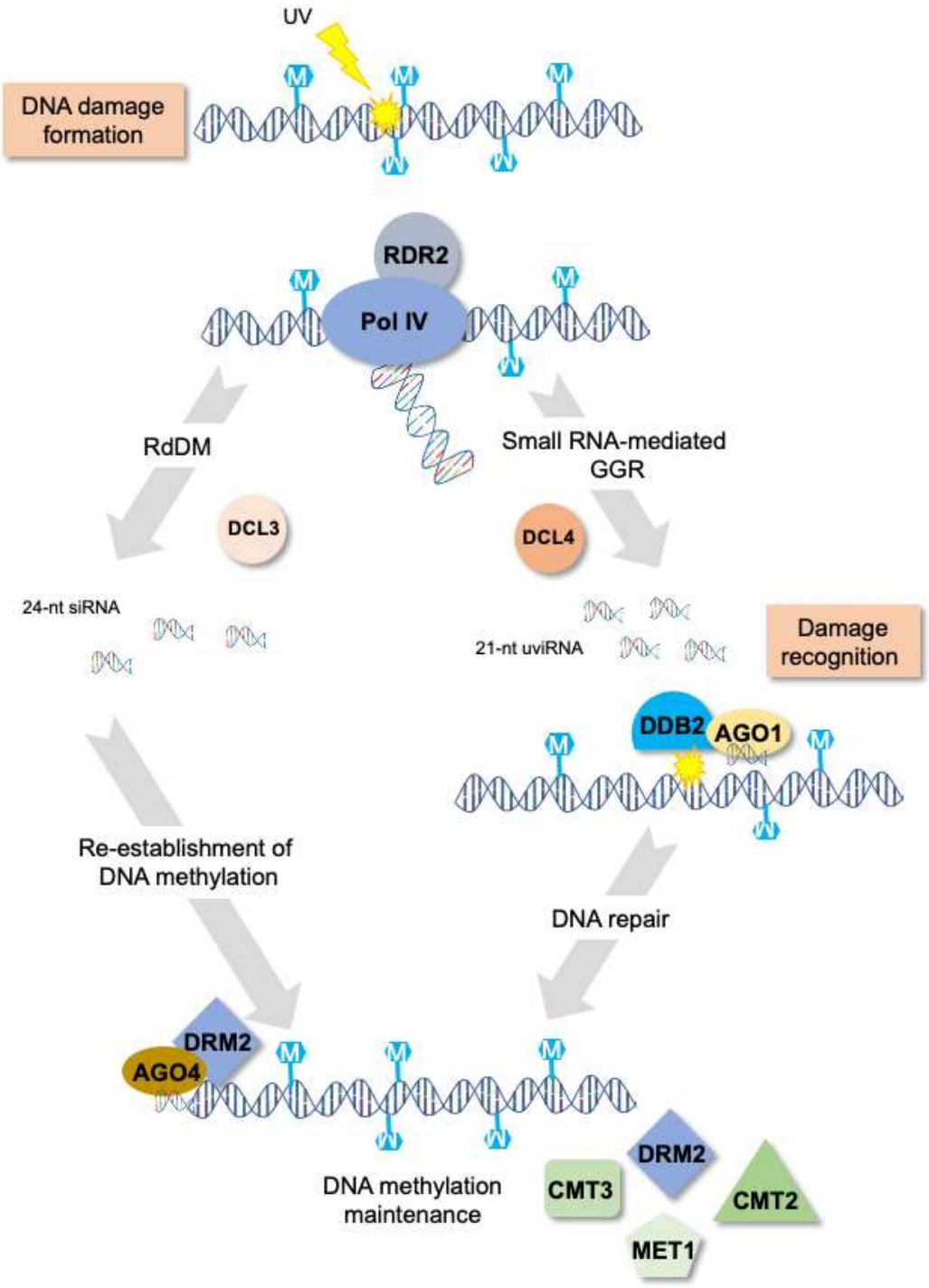
UV
DNA damage formation
RDR2
Pol IV
RdDM
Small RNA-mediated GGR
DCL3
DCL4
24-nt siRNA
21-nt uviRNA
Damage recognition
DDB2
AGO1
Re-establishment of DNA methylation
DNA repair
DRM2
AGO4
DNA methylation maintenance
DRM2
CMT3
CMT2
MET1

Figure 3. Canonical RdDM and interplay with the small-RNA mediated Global Genome Repair pathway

Particular methylated genomic regions are transcribed by the RNA POL IV and processed by RDR2 to form double strands RNA precursors (dsRNAs). These dsRNAs are diced by DCL3 into 24-nt siRNAs and loaded into AGO4 to trigger DNA methylation via the DNA methyltransferase DRM2. In parallel and upon UV exposure, damaged genomic regions produced dsRNAs in RNA POL IV-RDR2-dependent manner. These dsRNAs are diced by DCL4 into 21-nt uviRNAs and subsequently loaded into an AGO1 nuclear pool that forms a complex with DDB2, likely to recognize photolesions. Upon processing of the photodamage the methylome is re-established by the DNA methyltransferases (MET1, CMT2, CMT3 and DRM2) acting in different contexts (CG, CHG and CHH).

References

1. Jena NR. DNA damage by reactive species: Mechanisms, mutation and repair. *J Biosci*. 2012;37(3):503-517.

2. Bauer NC, Corbett AH, Doetsch PW. The current state of eukaryotic DNA base damage and repair. *Nucleic Acids Res*. 2015;43(21):10083-10101.

3. Kumar S, Chinnusamy V, Mohapatra T. Epigenetics of Modified DNA Bases: 5-Methylcytosine and Beyond. *Front Genet*. 2018;9.

4. Law JA, Jacobsen SE. Establishing, maintaining and modifying DNA methylation patterns in plants and animals. *Nature Reviews Genetics*. 2010;11(3):204-220.

5. Johann to Berens P, Molinier J. Formation and Recognition of UV-Induced DNA Damage within Genome Complexity. *Int J Mol Sci*. 2020;21(18).

6. Schmitz RJ, Lewis ZA, Goll MG. DNA Methylation: Shared and Divergent Features across Eukaryotes. *Trends Genet*. 2019;35(11):818-827.

7. Ngo TTM, Yoo J, Dai Q, et al. Effects of cytosine modifications on DNA flexibility and nucleosome mechanical stability. *Nat Commun*. 2016;7:10813.

8. Martinez-Fernandez L, Banyasz A, Esposito L, Markovitsi D, Improta R. UV-induced damage to DNA: effect of cytosine methylation on pyrimidine dimerization. *Signal Transduct Target Ther*. 2017;2:17021.

9. Rochette PJ, Lacoste S, Therrien J-P, Bastien N, Brash DE, Drouin R. Influence of cytosine methylation on ultraviolet-induced cyclobutane pyrimidine dimer formation in genomic DNA. *Mutat Res*. 2009;665(1-2):7-13.

10. Baute J, Depicker A. Base excision repair and its role in maintaining genome stability. *Crit Rev Biochem Mol Biol*. 2008;43(4):239-276.
11. Harris RS, Petersen-Mahrt SK, Neuberger MS. RNA editing enzyme APOBEC1 and some of its homologs can act as DNA mutators. *Mol Cell*. 2002;10(5):1247-1253.
12. Navaratnam N, Sarwar R. An overview of cytidine deaminases. *Int J Hematol*. 2006;83(3):195-200.
13. Barnes DE, Lindahl T. Repair and Genetic Consequences of Endogenous DNA Base Damage in Mammalian Cells. *Annu Rev Genet*. 2004;38(1):445-476.
14. Ehrlich M, Zhang XY, Inamdar NM. Spontaneous deamination of cytosine and 5-methylcytosine residues in DNA and replacement of 5-methylcytosine residues with cytosine residues. *Mutat Res*. 1990;238(3):277-286.
15. Shen JC, Rideout WM, Jones PA. The rate of hydrolytic deamination of 5-methylcytosine in double-stranded DNA. *Nucleic Acids Res*. 1994;22(6):972-976.
16. Alexeeva M, Moen MN, Grøsvik K, et al. Excision of uracil from DNA by hSMUG1 includes strand incision and processing. *Nucleic Acids Res*. 2019;47(2):779-793.
17. Neddermann P, Gallinari P, Lettieri T, et al. Cloning and expression of human G/T mismatch-specific thymine-DNA glycosylase. *J Biol Chem*. 1996;271(22):12767-12774.
18. Soll JM, Sobol RW, Mosammaparast N. Regulation of DNA Alkylation Damage Repair: Lessons and Therapeutic Opportunities. *Trends Biochem Sci*. 2017;42(3):206-218.
19. Boysen G, Pachkowski BF, Nakamura J, Swenberg JA. The Formation and Biological Significance of N7-Guanine Adducts. *Mutat Res*. 2009;678(2):76-94.
20. Peng Y, Pei H. DNA alkylation lesion repair: outcomes and implications in cancer chemotherapy. *J Zhejiang Univ Sci B*. 2021;22(1):47-62.
21. Drabløs F, Feyzi E, Aas PA, et al. Alkylation damage in DNA and RNA—repair mechanisms and medical significance. *DNA Repair*. 2004;3(11):1389-1407.
22. Rydberg B, Lindahl T. Nonenzymatic methylation of DNA by the intracellular methyl group donor S-adenosyl-L-methionine is a potentially mutagenic reaction. *The EMBO Journal*. 1982;1(2):211-216.
23. Drohat AC, Kwon K, Krosky DJ, Stivers JT. 3-Methyladenine DNA glycosylase I is an unexpected helix-hairpin-helix superfamily member. *Nat Struct Biol*. 2002;9(9):659-664.
24. Rubinson EH, Gowda ASP, Spratt TE, Gold B, Eichman BF. An unprecedented nucleic acid capture mechanism for excision of DNA damage. *Nature*. 2010;468(7322):406-411.

25. Rubinson EH, Christov PP, Eichman BF. Depurination of N7-methylguanine by DNA glycosylase AlkD is dependent on the DNA backbone. *Biochemistry*. 2013;52(42).
26. Eadie JS, Conrad M, Toorchen D, Topal MD. Mechanism of mutagenesis by O6-methylguanine. *Nature*. 1984;308(5955):201-203.
27. Kaina B, Christmann M, Naumann S, Roos WP. MGMT: key node in the battle against genotoxicity, carcinogenicity and apoptosis induced by alkylating agents. *DNA Repair (Amst)*. 2007;6(8):1079-1099.
28. Rošić S, Amouroux R, Requena CE, et al. Evolutionary analysis indicates that DNA alkylation damage is a byproduct of cytosine DNA methyltransferase activity. *Nature Genetics*. 2018;50(3):452-459.
29. Schuch AP, Moreno NC, Schuch NJ, Menck CFM, Garcia CCM. Sunlight damage to cellular DNA: Focus on oxidatively generated lesions. *Free Radic Biol Med*. 2017;107:110-124.
30. Kudryavtseva AV, Krasnov GS, Dmitriev AA, et al. Mitochondrial dysfunction and oxidative stress in aging and cancer. *Oncotarget*. 2016;7(29):44879-44905.
31. Dizdaroglu M, Jaruga P. Mechanisms of free radical-induced damage to DNA. *Free Radical Research*. 2012;46(4):382-419.
32. Kanvah S, Joseph J, Schuster GB, Barnett RN, Cleveland CL, Landman U. Oxidation of DNA: damage to nucleobases. *Acc Chem Res*. 2010;43(2):280-287.
33. Ravanat J-L, Di Mascio P, Martinez GR, Medeiros MHG, Cadet J. Singlet Oxygen Induces Oxidation of Cellular DNA*. *Journal of Biological Chemistry*. 2000;275(51):40601-40604.
34. Matter B, Malejka-Giganti D, Csallany AS, Tretyakova N. Quantitative analysis of the oxidative DNA lesion, 2,2-diamino-4-(2-deoxy-beta-D-erythro-pentofuranosyl)amino]-5(2H)-oxazolone (oxazolone), in vitro and in vivo by isotope dilution-capillary HPLC-ESI-MS/MS. *Nucleic Acids Res*. 2006;34(19):5449-5460.
35. Fleming AM, Burrows CJ. 8-Oxo-7,8-dihydroguanine, friend and foe: Epigenetic-like regulator versus initiator of mutagenesis. *DNA Repair (Amst)*. 2017;56:75-83.
36. Cooke MS, Evans MD, Dizdaroglu M, Lunec J. Oxidative DNA damage: mechanisms, mutation, and disease. *The FASEB Journal*. 2003;17(10):1195-1214.
37. Xu X, Muller JG, Ye Y, Burrows CJ. DNA-protein cross-links between guanine and lysine depend on the mechanism of oxidation for formation of C5 vs C8 guanosine adducts. *J Am Chem Soc*. 2008;130(2):703-709.

38. Jansson K, Blomberg A, Sunnerhagen P, Alm Rosenblad M. Evolutionary loss of 8-oxo-G repair components among eukaryotes. *Genome Integr*. 2010;1:12.
39. Wagner JR, Cadet J. Oxidation Reactions of Cytosine DNA Components by Hydroxyl Radical and One-Electron Oxidants in Aerated Aqueous Solutions.
40. Kriaucionis S, Heintz N. The nuclear DNA base 5-hydroxymethylcytosine is present in Purkinje neurons and the brain. *Science*. 2009;324(5929):929-930.
41. Tahiliani M, Koh KP, Shen Y, et al. Conversion of 5-methylcytosine to 5-hydroxymethylcytosine in mammalian DNA by MLL partner TET1. *Science*. 2009;324(5929):930-935.
42. Caldwell BA, Liu MY, Prasasya RD, et al. Functionally distinct roles for TET-oxidized 5-methylcytosine bases in somatic reprogramming to pluripotency. *Molecular Cell*. 2021;81(4):859-869.e8.
43. Zhu J-K. Active DNA Demethylation Mediated by DNA Glycosylases. *Annu Rev Genet*. 2009;43:143-166.
44. Parrilla-Doblas JT, Roldán-Arjona T, Ariza RR, Córdoba-Cañero D. Active DNA Demethylation in Plants. *Int J Mol Sci*. 2019;20(19).
45. Liu S, Dunwell TL, Pfeifer GP, Dunwell JM, Ullah I, Wang Y. Detection of Oxidation Products of 5-Methyl-2′-Deoxycytidine in Arabidopsis DNA. *PLoS One*. 2013;8(12).
46. Mahmood AM, Dunwell JM. Evidence for novel epigenetic marks within plants. *AIMS Genet*. 2019;6(4):70-87.
47. Enderle J, Dorn A, Puchta H. DNA- and DNA-Protein-Crosslink Repair in Plants. *Int J Mol Sci*. 2019;20(17).
48. Markovitsi D. UV-induced DNA Damage: The Role of Electronic Excited States. *Photochem Photobiol*. 2016;92(1):45-51.
49. Cadet J, Grand A, Douki T. Solar UV radiation-induced DNA Bipyrimidine photoproducts: formation and mechanistic insights. *Top Curr Chem*. 2015;356:249-275.
50. Bizanek R, McGuinness BF, Nakanishi K, Tomasz M. Isolation and structure of an intrastrand cross-link adduct of mitomycin C and DNA. *Biochemistry*. 1992;31(12):3084-3091.
51. Tomasz M. Mitomycin C: small, fast and deadly (but very selective). *Chem Biol*. 1995;2(9):575-579.
52. Rozelle AL, Cheun Y, Vilas CK, Koag M-C, Lee S. DNA interstrand cross-links induced by the major oxidative adenine lesion 7,8-dihydro-8-oxoadenine. *Nat Commun*. 2021;12.

53. Hlavin EM, Smeaton MB, Miller PS. Initiation of DNA Interstrand Cross-link Repair in Mammalian Cells. *Environ Mol Mutagen*. 2010;51(6):604-624.
54. Barciszewska A-M, Giel-Pietraszuk M, Perrigue PM, Naskręt-Barciszewska M. Total DNA Methylation Changes Reflect Random Oxidative DNA Damage in Gliomas. *Cells*. 2019;8(9).
55. Banyasz A, Esposito L, Douki T, et al. Effect of C5-Methylation of Cytosine on the UV-Induced Reactivity of Duplex DNA: Conformational and Electronic Factors. *J Phys Chem B*. 2016;120(18):4232-4242.
56. Zhu Y, Biernacka A, Pardo B, et al. qDSB-Seq is a general method for genome-wide quantification of DNA double-strand breaks using sequencing. *Nature Communications*. 2019;10(1):2313.
57. Yoshihara M, Jiang L, Akatsuka S, Suyama M, Toyokuni S. Genome-wide Profiling of 8-Oxoguanine Reveals Its Association with Spatial Positioning in Nucleus. *DNA Research*. 2014;21(6):603-612.
58. Akatsuka S, Aung TT, Dutta KK, et al. Contrasting Genome-Wide Distribution of 8-Hydroxyguanine and Acrolein-Modified Adenine during Oxidative Stress-Induced Renal Carcinogenesis. *The American Journal of Pathology*. 2006;169(4):1328-1342.
59. Mingard C, Wu J, McKeague M, Sturla SJ. Next-generation DNA damage sequencing. *Chem Soc Rev*. 2020;49(20):7354-7377.
60. Poetsch AR. The genomics of oxidative DNA damage, repair, and resulting mutagenesis. *Computational and Structural Biotechnology Journal*. 2020;18:207-219.
61. Wu J, McKeague M, Sturla SJ. Nucleotide-Resolution Genome-Wide Mapping of Oxidative DNA Damage by Click-Code-Seq. *J Am Chem Soc*. 2018;140(31):9783-9787.
62. Graindorge S, Cognat V, Johann to Berens P, Mutterer J, Molinier J. Photodamage repair pathways contribute to the accurate maintenance of the DNA methylome landscape upon UV exposure. Sale JE, ed. *PLoS Genet*. 2019;15(11):e1008476.
63. Cedar H, Bergman Y. Linking DNA methylation and histone modification: patterns and paradigms. *Nature Reviews Genetics*. 2009;10(5):295-304.
64. Tirado-Magallanes R, Rebbani K, Lim R, Pradhan S, Benoukraf T. Whole genome DNA methylation: beyond genes silencing. *Oncotarget*. 2016;8(3):5629-5637.
65. Hanawalt PC. Selective DNA repair in active genes. *Acta Biol Hung*. 1990;41(1-3):77-91.
66. Matzke MA, Mosher RA. RNA-directed DNA methylation: an epigenetic pathway of increasing complexity. *Nat Rev Genet*. 2014;15(6):394-408.
67. Henderson IR, Jacobsen SE. Epigenetic inheritance in plants. *Nature*. 2007;447(7143):418-424.

68. Matzke M, Kanno T, Daxinger L, Huettel B, Matzke AJM. RNA-mediated chromatin-based silencing in plants. *Curr Opin Cell Biol*. 2009;21(3):367-376.
69. Wassenegger M, Heimes S, Riedel L, Sänger HL. RNA-directed de novo methylation of genomic sequences in plants. *Cell*. 1994;76(3):567-576.
70. Cuerda-Gil D, Slotkin RK. Non-canonical RNA-directed DNA methylation. *Nat Plants*. 2016;2(11):16163.
71. Zheng B, Wang Z, Li S, Yu B, Liu J-Y, Chen X. Intergenic transcription by RNA polymerase II coordinates Pol IV and Pol V in siRNA-directed transcriptional gene silencing in Arabidopsis. *Genes Dev*. 2009;23(24):2850-2860.
72. Cokus SJ, Feng S, Zhang X, et al. Shotgun bisulphite sequencing of the Arabidopsis genome reveals DNA methylation patterning. *Nature*. 2008;452(7184):215-219.
73. Matzke MA, Kanno T, Matzke AJM. RNA-Directed DNA Methylation: The Evolution of a Complex Epigenetic Pathway in Flowering Plants. *Annu Rev Plant Biol*. 2015;66:243-267.
74. Zhang H, Lang Z, Zhu J-K. Dynamics and function of DNA methylation in plants. *Nat Rev Mol Cell Biol*. 2018;19(8):489-506.
75. Stroud H, Do T, Du J, et al. Non-CG methylation patterns shape the epigenetic landscape in Arabidopsis. *Nat Struct Mol Biol*. 2014;21(1):64-72.
76. Zemach A, Kim MY, Hsieh P-H, et al. The Arabidopsis nucleosome remodeler DDM1 allows DNA methyltransferases to access H1-containing heterochromatin. *Cell*. 2013;153(1):193-205.
77. Widom J. Role of DNA sequence in nucleosome stability and dynamics. *Q Rev Biophys*. 2001;34(3):269-324.
78. Chodavarapu RK, Feng S, Bernatavichute YV, et al. Relationship between nucleosome positioning and DNA methylation. *Nature*. 2010;466(7304):388-392.
79. Jurkowska RZ, Anspach N, Urbanke C, et al. Formation of nucleoprotein filaments by mammalian DNA methyltransferase Dnmt3a in complex with regulator Dnmt3L. *Nucleic Acids Res*. 2008;36(21):6656-6663.
80. Agius F, Kapoor A, Zhu J-K. Role of the Arabidopsis DNA glycosylase/lyase ROS1 in active DNA demethylation. *Proc Natl Acad Sci U S A*. 2006;103(31):11796-11801.
81. Penterman J, Uzawa R, Fischer RL. Genetic interactions between DNA demethylation and methylation in Arabidopsis. *Plant Physiol*. 2007;145(4):1549-1557.

82. Gong Z, Morales-Ruiz T, Ariza RR, Roldán-Arjona T, David L, Zhu JK. ROS1, a repressor of transcriptional gene silencing in Arabidopsis, encodes a DNA glycosylase/lyase. *Cell*. 2002;111(6):803-814.
83. Choi Y, Gehring M, Johnson L, et al. DEMETER, a DNA glycosylase domain protein, is required for endosperm gene imprinting and seed viability in arabidopsis. *Cell*. 2002;110(1):33-42.
84. Ortega-Galisteo AP, Morales-Ruiz T, Ariza RR, Roldán-Arjona T. Arabidopsis DEMETER-LIKE proteins DML2 and DML3 are required for appropriate distribution of DNA methylation marks. *Plant Mol Biol*. 2008;67(6):671-681.
85. Gehring M, Huh JH, Hsieh T-F, et al. DEMETER DNA glycosylase establishes MEDEA polycomb gene self-imprinting by allele-specific demethylation. *Cell*. 2006;124(3):495-506.
86. Lister R, O'Malley RC, Tonti-Filippini J, et al. Highly integrated single-base resolution maps of the epigenome in Arabidopsis. *Cell*. 2008;133(3):523-536.
87. Huh JH, Bauer MJ, Hsieh T-F, Fischer RL. Cellular programming of plant gene imprinting. *Cell*. 2008;132(5):735-744.
88. Penterman J, Zilberman D, Huh JH, Ballinger T, Henikoff S, Fischer RL. DNA demethylation in the Arabidopsis genome. *Proc Natl Acad Sci U S A*. 2007;104(16):6752-6757.
89. Zhu J, Kapoor A, Sridhar VV, Agius F, Zhu J-K. The DNA glycosylase/lyase ROS1 functions in pruning DNA methylation patterns in Arabidopsis. *Curr Biol*. 2007;17(1):54-59.
90. Hanai R, Yazu M, Hieda K. On the experimental distinction between ssbs and dsbs in circular DNA. *Int J Radiat Biol*. 1998;73(5):475-479.
91. Virdi KS, Laurie JD, Xu Y-Z, et al. Arabidopsis MSH1 mutation alters the epigenome and produces heritable changes in plant growth. *Nat Commun*. 2015;6:6386.
92. Le May N, Fradin D, Iltis I, Bougnères P, Egly J-M. XPG and XPF endonucleases trigger chromatin looping and DNA demethylation for accurate expression of activated genes. *Mol Cell*. 2012;47(4):622-632.
93. Naegeli H, Sugasawa K. The xeroderma pigmentosum pathway: decision tree analysis of DNA quality. *DNA Repair (Amst)*. 2011;10(7):673-683.
94. Barreto G, Schäfer A, Marhold J, et al. Gadd45a promotes epigenetic gene activation by repair-mediated DNA demethylation. *Nature*. 2007;445(7128):671-675.
95. Schalk C, Drevensek S, Kramdi A, et al. DNA DAMAGE BINDING PROTEIN2 Shapes the DNA Methylation Landscape. *Plant Cell*. 2016;28(9):2043-2059.

96. Schalk C, Molinier J. Global Genome Repair factors controls DNA methylation patterns in Arabidopsis. *Plant Signal Behav*. 2016;11(12):e1253648.

97. Córdoba-Cañero D, Cognat V, Ariza RR, Roldán Arjona T, Molinier J. Dual control of ROS1-mediated active DNA demethylation by DNA damage-binding protein 2 (DDB2). *Plant J*. 2017;92(6):1170-1181. d

98. Wittschieben BØ, Iwai S, Wood RD. DDB1-DDB2 (Xeroderma Pigmentosum Group E) Protein Complex Recognizes a Cyclobutane Pyrimidine Dimer, Mismatches, Apurinic/Apyrimidinic Sites, and Compound Lesions in DNA. *J Biol Chem*. 2005;280(48):39982-39989.

99. Kimura S, Sakaguchi K. DNA repair in plants. *Chem Rev*. 2006;106(2):753-766.

100. Schalk C, Cognat V, Graindorge S, Vincent T, Voinnet O, Molinier J. Small RNA-mediated repair of UV-induced DNA lesions by the DNA DAMAGE-BINDING PROTEIN 2 and ARGONAUTE 1. *Proc Natl Acad Sci U S A*. 2017;114(14):E2965-E2974.

International Journal of
Molecular Sciences

MDPI

Review

Formation and Recognition of UV-Induced DNA Damage within Genome Complexity

Philippe Johann to Berens and Jean Molinier *

Institut de Biologie Moléculaire des Plantes du CNRS, 12 rue du Général Zimmer, 67000 Strasbourg, France; philippe.johann-to-berens@etu.unistra.fr
* Correspondence: jean.molinier@ibmp-cnrs.unistra.fr

Received: 31 July 2020; Accepted: 9 September 2020; Published: 12 September 2020

Abstract: Ultraviolet (UV) light is a natural genotoxic agent leading to the formation of photolesions endangering the genomic integrity and thereby the survival of living organisms. To prevent the mutagenetic effect of UV, several specific DNA repair mechanisms are mobilized to accurately maintain genome integrity at photodamaged sites within the complexity of genome structures. However, a fundamental gap remains to be filled in the identification and characterization of factors at the nexus of UV-induced DNA damage, DNA repair, and epigenetics. This review brings together the impact of the epigenomic context on the susceptibility of genomic regions to form photodamage and focuses on the mechanisms of photolesions recognition through the different DNA repair pathways.

Keywords: ultraviolet; photolesions; photodamage recognition; chromatin; photolyase; nucleotide excision repair; transcription coupled repair; global genome repair

1. Introduction

Solar radiation that reaches the surface of the Earth consists of 3 main spectra: ultraviolet (UV; 100–400 nm), visible light (400–700 nm), and infrared (IR; 700 nm to over 1 mm). Each of these ranges of wavelengths plays essential roles in providing light, heat, and energy, allowing the proper development of life. In addition to their beneficial impacts for living organisms, these types of irradiation can lead to deleterious effects, affecting cellular structures, interfering with biological processes, and damaging DNA.

The genotoxic effect of UV radiation from sunlight (UV-R; UVA: 320–400 nm and UVB: 280–320 nm) has been studied for a long time [1]. UV-induced DNA damages are formed between dipyrimidines, leading to DNA helix distortion and alterations of transcriptional programs [2]. To prevent such dramatic changes as well as mutations and genome rearrangements, specific DNA repair pathways are mobilized [2,3]. Depending on the organism and on the growth conditions, photodamages are processed by light-dependent (photoreactivation) and/or by light-independent repair pathways (i.e., nucleotide excision repair, NER), allowing an efficient maintenance of genome integrity [2,3].

These specific DNA damage repair pathways rely on a photodamage recognition step within the complexity of genomic regions displaying variations in accessibility (i.e., chromatin compaction). The emergence of sophisticated approaches to map the photolesions genome wide, to decipher (epi)genome shapes and protein occupancy at particular loci, allowed considering that DNA damage formation, together with the choice and the efficiency of the repair pathways, could likely be under the multifactorial influence of genome and epigenome organizations.

This review will describe the different types of UV-induced DNA lesions and will present the current knowledge in the putative interconnections existing between epigenetic marks and photodamage formation. In addition, the mode of action and the structural features of photolesions recognition factors, acting in the different DNA repair pathways, will be highlighted.

2. Impact of UV Radiation on DNA

The DNA, as support of the genetic information, is the target of UV-R. Indeed, nucleotides absorb UV-R, especially in the wavelength ranging from 100 to 280 nm (UV-C) and from 280 to 315 nm (UV-B) [4]. These short UV-R wavelengths can raise DNA bases to their highly reactive singlet or triplet states, which are prone to undergo different photochemical reactions. Interestingly, recent studies propose that DNA adopts "collective" excitation states, delocalized over at least two bases, when irradiated with UV-C/UV-B and to some extent with UV-A (315–400 nm; [5]). Three main types of DNA lesions are formed by these photochemical reactions and involve two successive pyrimidine bases (CC, TT, TC, and CT): cyclobutane pyrimidine dimers (CPDs), pyrimidine 6-4 pyrimidone photoproducts (6-4PPs), and their Dewar isomers (Figure 1a). CPDs can be detected nearly instantly after UV-R (1 ps) as a result of the formation of a stable ring structure between the C5 and C6 atoms of two adjacent pyrimidines [6]. 6-4PPs are formed in a slightly slower process (4 ms) involving the C4 of an oxetane or azetidine intermediates (at the 3′-end) and the C6 of the (5′-end) pyrimidine to build a stable noncyclic bond [7]. The quantum yields (Φ) ratio ΦCPD/Φ6-4 PP upon UV-R was estimated in a range of seven double-stranded DNA by in vitro and in vivo assays [8,9].

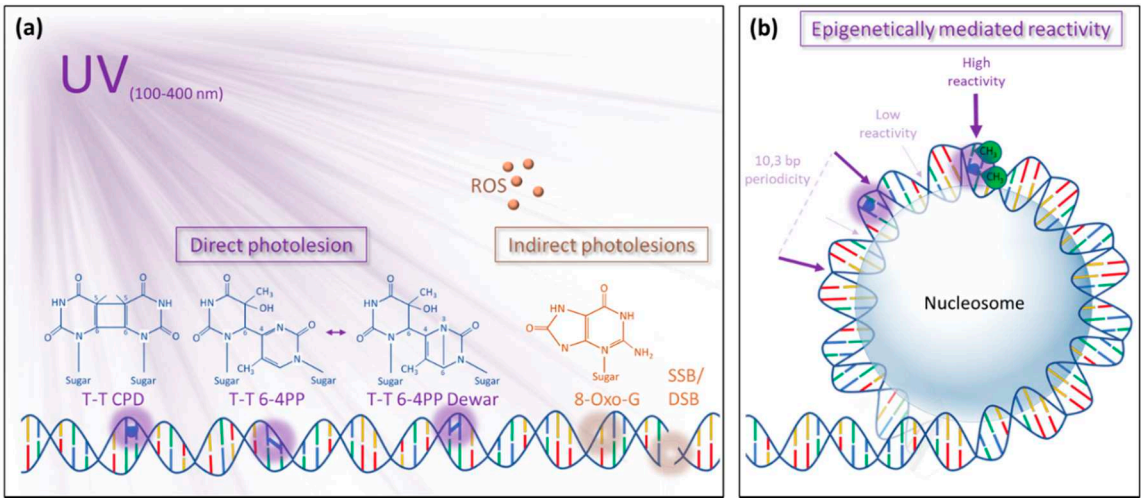

Figure 1. Photolesions and genome reactivity. (**a**) Schematic representation of the chemical structure of the most frequent direct and indirect photolesions induced upon UV exposure. From left to right: Cyclobutane pyrimidine dimer (example within two thymines T-T CPD), 6-4 photoproduct (example within two thymines T–T 6-4PP), Dewar valence isomer of the T-T 6-4PP (T-T 6-4PP Dewar), 8-oxo-7,8-dihydroguanine (8-oxo-G) indirectly induced by reactive oxygen species (ROS), single or double-strand breaks (SSB/DSB). (**b**) Schematic representation of the epigenetically mediated context reactivity to form photodamage upon UV radiation. Dark violet and light violet arrows signify a high or low sequence reactivity, respectively, compared to "naked DNA". Methylated cytosines are labelled with a green CH_3 group. CPD: cyclobutane pyrimidine dimers, 6-4PP: 6-4 pyrimidone photoproducts.

Upon absorption of UV-R, the 6-4PP photolesions can further evolve to their Dewar valence isomers in a fast (130 ps) electrocyclization reaction between the N3 and the C6 in the pyrimidine ring structure of the 3′ base of the 6-4PP (Figure 1a) [10]. The formation of these photolesions leads to weak base pairing reflected by changes in the helical DNA conformation [3]. Importantly, the DNA double helix distortion induced by the 6-4PP is much greater than that of the CPD [3]. In addition to the formation of direct photolesions, several indirect forms of DNA damage can occur by an interplay of photosensitization and oxidation reactions [11]. Through mechanisms of photosensitization, neighboring biomolecules excited by UV-R have the potential to directly or indirectly induce a chemical modification of the DNA. One example of such a photosensitization process is the triplet–triplet electron transfer (TTET) from UV-A excited benzophenone compounds to a nearly located thymidine to create

a CPD photolesion [12]. Photosensitization mechanisms involving non-DNA chromophores were also described, by the side of enzymatic activation and bystander effect, as a predominant source of reactive oxygen species (ROS) upon UV irradiation [11]. In further reactions, ROS and especially hydroxyl radicals (OH•) can induce the oxidation of purine and pyrimidine bases and of the deoxyribose backbone of DNA [11]. The predominant indirect photodamage caused by the oxidative burst is the highly mutagenetic 8-hydroxyguanine (8-oxo-G; Figure 1a) and in a smaller extent, DNA single and double-strand breaks (SSB and DSB; (Figure 1a) [11,13]. Additionally, UV-induced ROS can indirectly lead to base alkylation and DNA–protein or DNA–DNA cross-linking [14,15]. The recognition of 8-oxo-G, SSB, and DSB [16–19] will not be reviewed in the following parts.

3. Influence of (epi)Genomic Features on Photolesions Formation

3.1. Dipyrimidines Composition

For decades, the susceptibility of the genome to form photolesions upon exposure to UV-R was thought to be quite homogenous, although the frequency and the genome-wide distribution of pyrimidine dimers (CC, TT, CT, and TC) may significantly differ among living organisms [20]. In human, CPDs and 6-4PPs are mostly formed between TT and TC, and with a lower frequency at CT and CC sequences [21]. In the model plant *Arabidopsis thaliana*, CPDs are predominantly formed between CT and TC and to a lower extent between TT and CC [22,23]. Given that dipyrimidines frequencies are quite similar between human and Arabidopsis [21–23], such differences in reactivity cannot be only explained by a strong bias in dinucleotides composition. Other factors such as sequence context and chromatin structure should also be considered as putative parameters influencing the formation of UV-induced DNA damage.

Indeed, the composition of neighboring nucleotide sequence of pyrimidine dimers was also shown to impact damage frequency, which is in agreement with the hypothesis of a putative "collective" excitation state [24]. All together, these observations highlight that photolesions formation likely differs within a genome but also between kingdoms. The availability of whole-genome sequencing data and photoproducts maps may provide an added value to better assess the underlying features of genome reactivity.

3.2. DNA Methylation

Recent studies hypothesized that the epigenomic context may influence the susceptibility of particular loci to form photolesions (Figure 1b). Indeed, in addition to the nucleotidic sequence, epigenetic marks (DNA methylation, histone post-translational modifications [PTMs]) may affect the UV-R-associated damaging processes. In eukaryotic cells, the DNA is mostly packaged into chromatin fiber. The smallest repeating units of these chromatin fibers are the nucleosomes, which are composed of 145 to 147 DNA base pairs (bp) wrapped around histone core proteins, which are separated from each other by a "linker DNA" of 20 to 100 bp (organism dependent) often complexed with the H1 linker histone [25]. The DNA binding to histones serves as a platform for PTMs to regulate, amongst others processes, gene expression, higher chromatin structure, and DNA repair [26]. Several in vitro assays started considering the role of cytosine methylation, relative nucleosome positioning, and protein binding in the damage formation. Indeed, the methylation of DNA at C5 of cytosine (5-mC), an important epigenetic mark regulating gene expression [27], was shown to increase by 80% the CPD quantum yield and to decrease by a factor 3 the 6-4PP quantum yield [8]. The higher sensitivity of 5-mC to form CPD could be due to the redshift of its absorption spectrum and its diminished amplitude of conformational motions in a DNA duplex [8,28].

Regarding the relatively high quantum yield of CPD compared to 6-4PP, 5-mC could be considered as an epigenetic mark favorizing photolesion formation (Figure 1b). Unlike animals, where DNA methylation is predominantly found in CG islands, DNA methylation occurs in 3 different contexts in plants: CG, CHG, and CHH (where H is A, C, or T) [29]. Therefore, it is tempting to speculate

that plant genomes would be more prone to form photoproducts because of (i) their light-dependent lifestyle and (ii) the higher probability to find two consecutive pyrimidines in combination with a 5-mC (i.e., CTG or CCG in the CHG context). Such features have to be considered for deciphering genome responsiveness to UV-R (i.e., the formation of photolesions) and the complex interplays between DNA repair processes identified in plants [30].

The mapping of photolesions in a histone-loaded DNA context showed that upon UV-R, CPDs are formed around the core histone and in the linker DNA sequence, while 6-4PP is preferentially formed in the linker region of chromatin [31]. A deeper analysis at single-nucleotide resolution identified that CPD but not 6-4PPs occurred in a periodic pattern every 10.3 bp around the histone core [31] (Figure 1b). This periodicity reflects the conformational dynamics of DNA within chromatin. Every 10.3 bp, the DNA phosphate backbone is exposed away from the histone core, locally increasing its conformational motion potential and creating an energy "sink" [32,33]. Interestingly, due to the anisotropic bending preferences of the DNA, the more exposed sequences tend to be enriched in G and C, while the sequences close to the histone core tend to be enriched in A and T [34,35]. Interestingly, the ratio of CPD quantum yield in vivo versus naked DNA at sequences of strongly positioned nucleosomes appears to reach a maximum of around 1.2 for the exposed sequences and a minimum of around 0.9 for the sequence close to the nucleosome [31]. Thus, it is likely that DNA bound to nucleosomes is more prone to form CPDs than naked DNA. The in vivo impact of histone variants, histone PTMs, on DNA reactivity to form photolesions is a challenging area of research in the future.

3.3. Chromatin States

Taking into account the potential role of the above discussed genomic and epigenomic features in photoproducts formation, it could be expected that photolesions distribution may not occur randomly all over the genome in vivo.

According to the speculations of theoretical chemistry, in a biological system, a compacted DNA structure would be more reactive upon UV-R [5]. In the model plant *Arabidopsis thaliana*, this hypothesis seems to partially hold true. Indeed, CPD and 6-4PP mapping show significant enrichment in highly compacted heterochromatic regions [23].

In human, recent studies using HS (High Sensitivity)-damage-seq or ChIP (Chromatin Immuno-precipitation) assay followed by ELISA quantification did not reveal differences in CPD enrichment in specific chromatin states [21,36]. Nevertheless, CPD immune-staining assays show a non-homogeneous distribution of the photolesion upon acute UV-R, and several hotspots of photolesions have been identified [36,37]. How far the epigenetic context is involved in this hotspot formation, in humans, remain unclear. Similarly, in arabidopsis, genomic regions exhibiting heterochromatic features (high compaction, high DNA methylation levels) are more prone to form photoproducts, suggesting that particular epigenomic marks may contribute to such accurate reactivity [22,23].

Moreover, the impact of DNA binding proteins on photolesions formation was also taken into account. In vitro experiments showed altered reactivity of the binding sequences depending on the class of transcription factors (TF) [31]. In some cases, a subpart of the binding sequence even becomes a hotspot of photolesion, highlighting a putative role of DNA binding factors in genome damaging processes [38,39]. The UV reactivity of TF binding sites differs for each DNA binding protein and most probably depends on the conformational changes induced in the helical structure upon binding [39]. This hypothesis holds true in recent in vivo whole genome photolesion mapping assays, where the same TF binding sequence shows differential CPD enrichment at different loci depending on the secondary binding proteins [31]. In conclusion, protein binding is neither strictly correlated nor anticorrelated with a higher reactivity of DNA upon UV-R in vivo.

Considering these several lines of evidence supporting the idea that genomic and epigenomic contexts likely influence the formation of photolesions, the DNA repair pathways may have specifically evolved to efficiently recognize such damage in the complexity of the different chromatin landscapes.

4. Photolesion Repair Pathways

Two main strategies exist to repair UV-induced DNA lesions. A light-dependent process (referred as "light repair") that reverts photodamage using particular wavelengths and a light-independent process (referred as "dark repair") that excises the UV-damaged region followed by de novo synthesis of an intact DNA strand. Although most of the living organisms possess both pathways, the light repair pathway is predominantly used [40]. Importantly, growth conditions (i.e., full light versus shadow), tissue specificities (i.e., roots versus leaves), and the transcriptional level of particular genomic regions (i.e., euchromatin versus heterochromatin) are some examples of parameters that could determine the predominant use of one or the other pathway. For each of these pathways, specific factors/complexes recognize the photolesions and trigger the repair process.

4.1. Light Repair

An essential repair pathway of photon-induced damage is the direct repair (DR) pathway, which, interestingly, depends on photon-triggered enzymes called photolyases (PLs) (Figure 2a) [41,42]. Photolyases perform the repair of photolesions by reverting the damage [42]. In other words, this repair pathway does not rely on de novo DNA synthesis. According to phylogenetic analyses, it was proposed that 3.8 billion years ago, all living organisms possessed photolyase-like genes, making DR the oldest known DNA repair mechanism [43,44]. DNA photolyases genes evolved in all branches of life, including eukaryotes [44]. However, PLs are not found in placental mammals but exist in marsupials [44–46]. Despite their high sequence and structure similarities, photolyases with conserved DNA repair activity are distinct from cryptochromes (CRYs), which gained new functions as a light receptor involved in the regulation of gene expression or phototaxis [44,47]. PLs can further be classified as CPD- or 6-4-photolyases, according to their exclusive substrate specificity for CPDs or 6-4PPs, respectively [48]. Extensive studies in several model organisms such as *E. coli* [49,50], *S. cerevisiae* [51,52], *D. melanogaster* [53,54], and *A. thaliana* [55–57] allowed deciphering the specificities and the modes of action of several PLs. Surprisingly, a bifunctional photolyase, with a CPD and 6-4PP substrate recognition and repair activities, was recently identified [58].

PLs are structurally composed of an N-terminal dinucleotide binding domain and a C-terminal binding domain for the catalytic cofactor: flavin adenine dinucleotide (FAD) [42,47]. Besides FAD, many PLs also bind additional chromophore such as methenyltetrahydrofolate (MTHF) or 8-hydroxy-7,8-didemethyl-5-deazariboflavin (8-HDF) [42,47]. The electrostatic surface potential map shows an accumulation of positively loaded residues flanking a cavity localized in the vicinity of the flavin cofactor [59,60]. These positively charged residues bind the negatively loaded phosphate backbone of the DNA helix, whereas the hydrophobic cavity specifically binds the pyrimidine dimer [59,61]. Localization of the pyrimidine dimer in the enzymatic active binding pocket depends on a helical out-flipping of the damaged nucleotides (Figure 3a) [59–62]. The most recent study of CPD photolyase substrate binding kinetics suggests that conversely to other DNA repair proteins, CPD recognition does not rely on one-dimensional sliding or hopping along the DNA, but on the three-dimensional search for an extrahelical out-flipped photolesion [63,64]. Once out-flipped, the intrahelical bubble is stabilized by a bubble-intruding region (BIR) in Class II photolyases [65,66] and by a conserved Arg421 in 6-4PP photolyases (Figure 3a) [61,62]. In Class I photolyases, the structure is most probably stabilized by another type of interaction that remains to be further characterized [59,67].

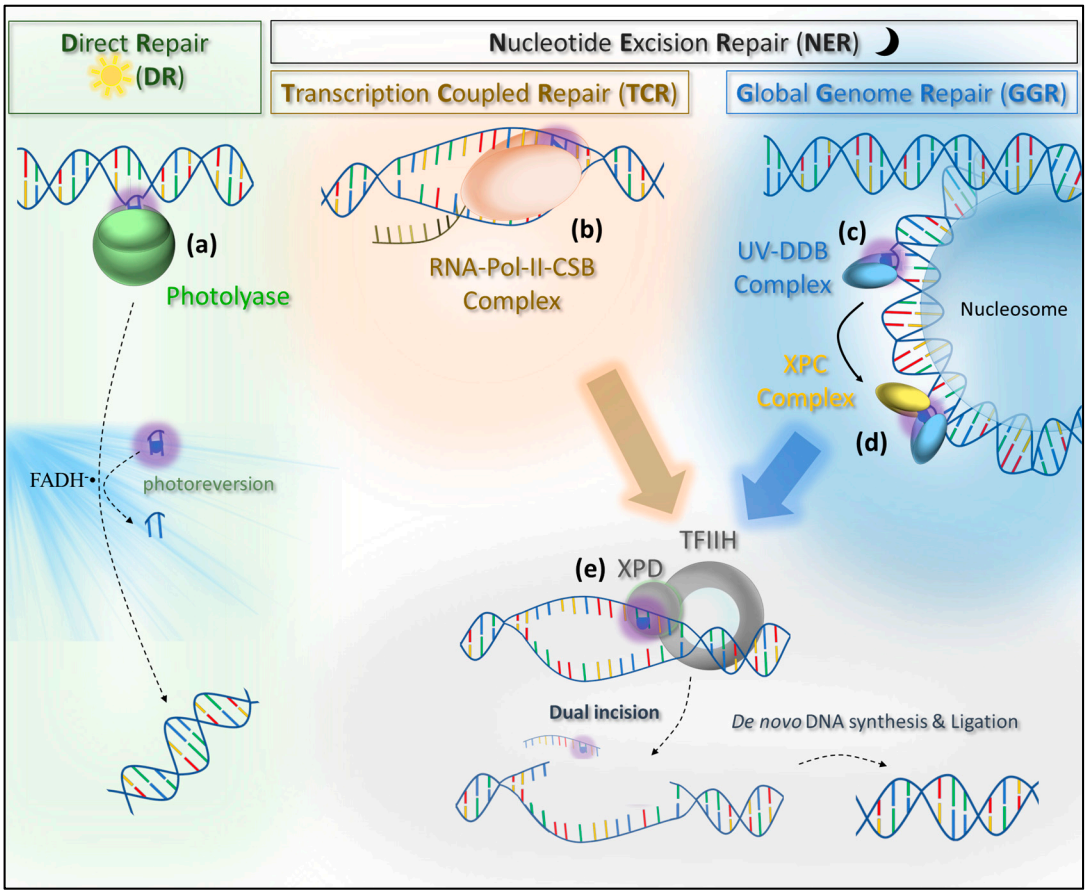

Figure 2. Photolesion recognition and repair pathways. (**a**) The direct repair pathway (light repair) relies on specific photolyases, which either recognize CPD or 6-4PP. The photolyase interne flavin adenine dinucleotide (FAD) cofactor, excited by blue light, catalyzes photoreversion to restore the initial undamaged sequence. (**b**) The transcription coupled repair (TCR) pathway (dark repair) is specific to transcribed genomic regions and depends on the RNA Pol II–CSB (RNA Polymerase II-Cockayne Syndrome protein B) complex for the recognition step. RNA Pol II stalls and arrests at the damage site. (**c**) The global genome repair (GGR) pathway (dark repair) primarily recognizes the photolesion by the damage sensor complex UV–DDB (DNA damage binding protein), which is able to scan DNA in compacted chromatin. (**d**) Once bound to the damage, UV–DDB recruits the Rad4/XPC (*Xeroderma Pigmentosum* complementation group C) complex for a second recognition step. The stalled RNA Pol II–CSB and The Rad4/XPC complex recruit the TFIIH (Transcription Factor II H) protein complex. (**e**) XPD (*Xeroderma Pigmentosum* complementation group D) proceeds to a damage validation step. Upon this final recognition step, the damaged DNA region is excised by a dual incision process, and the gap is filled by de novo DNA synthesis and nick ligation.

The above described binding structures were always determined in a nucleosome-free environment [59,61]. Given that the binding of photolyases induces a local DNA bending [59], the chromatin environment might be recalcitrant to such conformational change and hence would inhibit the recognition process [68]. Indeed, in yeast, in vivo photolyase-mediated photolesion repair is slowed down in nucleosome-bound regions [68]. However, photolesions located in the core regions of the nucleosome can also be repaired by PLs, but this process needs more time, arguing in favor of a chromatin remodeling mechanism [68]. Importantly, no shreds of evidence for a photolyase-specific chromatin remodeling mechanism have been described so far. Upon stable binding to the CPD or 6-4PP photolesions, the photolyase performs the "direct repair" reaction (Figure 2a). For this purpose, FAD and additional photo-antenna molecules collect energy through the absorption of a blue light spectrum photon [42]. The energy transfer generates excited $FADH^{-}\bullet$ [42]. In the case of CPD photolyases,

$FADH^{-}\bullet$ donates an electron to the CPD to catalyze the reversal repair reaction by cleaving the C5-C5 and C6-C-6 bonds of the cyclobutane ring [42,48]. The repair reaction of 6-4 photolyases also uses $FADH^{-}\bullet$ as an electron and proton donor to generate a transient oxetan-type residue followed by C6-C4 bond splitting [42,69]. In both cases, the result is the restoration of the native DNA sequence and photolyase release in a DNA synthesis-independent manner [42].

4.2. Dark Repair

The dark repair pathway, also called NER, promotes the repair of photolesions in a light-independent manner via two sub-pathways: transcription coupled repair (TCR) and global genome repair (GGR) processing photodamage along actively transcribed DNA strands or throughout the genome, respectively. NER is a DNA synthesis-dependent repair pathway. Thus, it implies that, in addition to the nucleotidic sequence, the epigenomic landscape (i.e., DNA methylation) must be accurately re-established.

4.2.1. Transcription Coupled Repair

The first experiments providing evidence for the existence of a TCR pathway in eukaryotes was performed on Chinese hamster ovary deficient in global genome repair [70]. The authors showed that CPD repair was more efficient in transcribed genomic regions compared to the transcriptionally silent upstream sequences [70]. The TCR damage recognition step was shown to rely on the stalling of RNA Polymerase II (RNA Pol II) [71]. As a consequence, TCR predominantly repair lesions on the transcribed DNA strand [71,72]. The RNA Pol II translocates along the DNA template strand, synthesizing the complementary RNA molecule. Gaps, breaks, and modified nucleotides can lead to stalling and arresting of the polymerase (Figure 2b) [73]. This stalling, identified to be the recognition step [71], mainly depends on the two highly conserved critical residues (R1386 and H1387) in the switch1 region of Pol II, which is described as a sensor of structural barriers in the minor groove of the DNA helix upstream of the polymerase (Figure 3b) [74]. However, RNA polymerase stalling can also be induced, in the absence of DNA damages, by extra-stable chromatin structures, a weak affinity between DNA and nascent RNA, or secondary structure in the nascent RNA [73].

Interestingly, a recent study investigated the role of early TCR factors in a potential differentiation mechanism, which can help to overcome some type of obstacles or lead to the recruitment of the damage repair machinery [75]. Considering these observations, the decisive recognition step only occurs by an interplay between RNA Pol II and the SWI2/SNF2 (SWitch 2/Sucrose Non fermenTable 2) protein Rad26 in *Saccharomyces cerevisiae*, which is the homolog of the human CSB (Cockayne Syndrome protein B) and the arabidopsis CHR8 proteins [75]. Mutations in the CSB gene result in a rare genetic disease called "Cockayne syndrome" [76]. In the proposed model, Rad26/CSB/CHR8 binds stalling RNA Pol II between the clamp (Rpb2 side) and stalk (Rpb4/7) regions, and it promotes its forward translocation, increasing the bypass efficiency at minor barriers [75,77]. While base alkylation [77], abasic sites [78], and 8-oxo-G [79] can be bypassed by the RNA Pol II, photolesions induce stalling and arrest [80,81]. In the example of (T<>T) CPD, the stalling occurs by the stacking above the bridge helix of Pol II (Figure 3b), slow incorporation of an A in front of the first T involved in the dimer, and an even slower misincorporation of a U in front of the second T [81,82]. This misincorporation finally leads to the arrest of transcription [81,82].

The persistent binding of Rad26/CSB/CHR8 to the arrested RNA Pol II signals the sequential recruitment of the NER machinery to complete the recognition step. The CSA (Cockayne Syndrome protein A)–Cullin 4 E3 ubiquitin ligase complex is recruited to ubiquitinate CSB and the Pol II subunit RPB_1 at position K1268 [75,83,84]. The stability of CSB seems to be regulated by a complex interplay between SUMOylation (Small Ubiquitin-like MOdifier) and ubiquitination homeostasis, opposing the CSA–Cullin 4 E3 ubiquitin ligase complex and the ubiquitin C-terminal hydrolase 7 (USP7) [85–87]. In parallel, the monoubiquitination of UVSSA (UV-sensitive syndrome (UV^SS) A), at position K414, triggers TFIIH (Transcription Factor II H) recruitment, leading to DNA unwinding (Figure 2b,e) [83,88]. TFIIH binding requires USP7 to leave the complex, enabling CSB polyubiquitination and release. At this point, TFIIH is proposed to forward-translocate on the DNA using its 5′–3′ XPD helicase promoting the Pol II backtracking, in order to efficiently access the damage site [89–91]. Importantly, RPB_1 polyubiquitination triggers RNA Pol II targeting to the 26S proteasome for degradation only when TCR is not functional in order to remove the arrested transcription complex from the DNA template [84,92]. After TFIIH binding and prior repair, a further step of validation of photodamage recognition is performed. This mechanism will be discussed in Section 4.2.3.

The core TCR process seems to be globally conserved in eukaryotes [93,94]. Even in drosophila lacking for CSB, CSA, and UVSSA homologs, a recent study revealed the existence of a TCR-like process [95]. Interestingly, in bacteria, the coupling factor Mfd (Mutation Frequency Decline) [96–98], which autonomously translocates on DNA, patrols for stalling polymerase [99]. Indeed, the binding of Mfd on a stalling RNA polymerase promotes its translocation [100]. If the arrest persists, because of severe obstacles, Mfd induces displacement of the RNA Pol and recruitment of UvrA, UvrB, and UvrC for NER. [97,98]. Alternatively, another TCR recruiting mechanism, independent of Mfd, was proposed to occur after RNA Pol II backtracking promoted by UvrD [101,102].

The RNA Pol II is not the only RNA polymerase stalling at UV-induced photolesions. A recent study showed that RNA Pol I stalled and arrested even earlier than the Pol II when encountering CPD [103]. In addition, RNA Pol I was also shown to form a complex with CSB [104] and to interact with TFIIH [105]. Besides, TCR was also observed in rDNA regions [106]. More recently, the analysis of the Pol I behavior upon UV irradiation revealed a considerable backtracking capacity but a low dissociation rate [107]. Altogether, these facts argue in favor of an alternative TCR pathway involving Pol I as a damage recognition platform that is so far poorly understood. Therefore, it may be of interest to reconsider the RNA Pol III involved in tDNA and in 5S rDNA transcription [108] and the plant-specific RNA Pol IV/Pol V [109], which are evolutionarily related to the RNA Pol II [110] as putative key players of the DNA repair machinery. Both RNA Pol IV/Pol V predominantly act in genomic regions containing high DNA methylation and compaction levels [29], suggesting that a non-canonical TCR process may exist in plants or that complex photodamage repair mechanisms may have evolved.

In brief, the TCR pathway acting in transcribed genomic regions displays an efficient recognition mechanism of UV-induced pyrimidine dimers. This process depends on the stalling of the RNA Pol II and the complexation with CSB at the damaged site (Figure 2b). This implies that transcriptional activation directly promotes the control of genome integrity. Consequently, epigenetic features impacting transcription initiation and elongation may also indirectly regulate genome surveillance pathways.

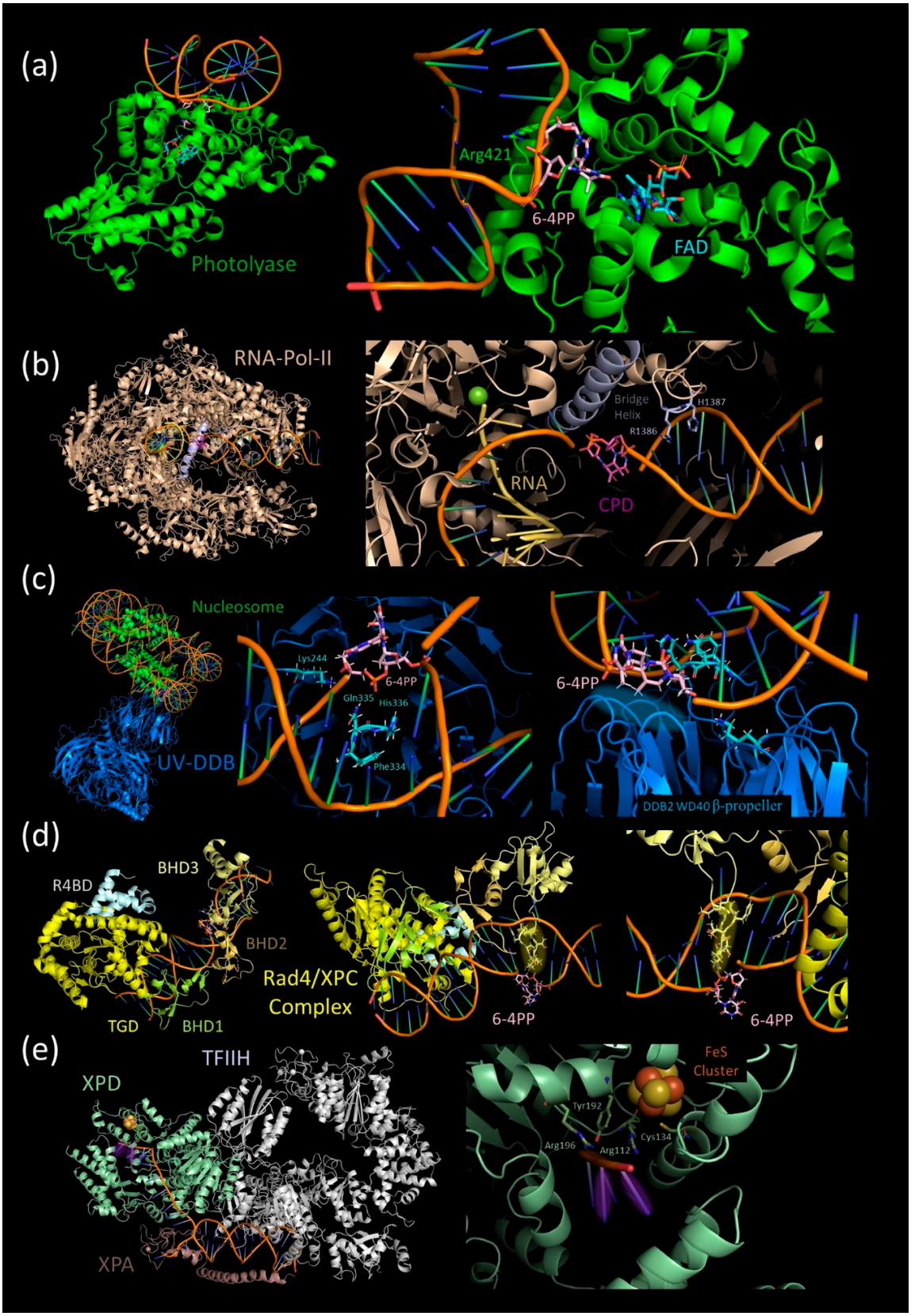

Figure 3. Structural views of the main photolesions recognition factors. (**a**) Left panel: in silico modeling of the *Drosophila melanogaster* (6-4) photolyase bound to double-stranded (ds) DNA with a "out-flipped" T-T 6-4PP. Figure is based on the PDB structure 3CVU [62]. The photolyase and these residue Arg421 are colored in green, the catalytic FAD ligand is colored in cyan blue, and the 6-4PP

is in light pink. Right panel: Zoomed-in detailed view of the photolyase–lesion interaction. (**b**) Left panel: in silico modeling of a *Saccharomyces cerevisiae* RNA polymerase II elongation complex arrested at a CPD lesion. Figure based on the PDB structure 6O6C [75]. The RNA Pol II is colored in salmon, the Pol II bridge helix and the residues R1386 and H1387 are colored in gray-blue, the nascent RNA is in gold, and the CPD is in violet. Right panel: Zoomed-in detailed view of the RNA Pol II–lesion interaction. (**c**) Left panel: In silico modeling of the *Homo sapiens* UV–DDB complex bound to a "out-flipped" 6-4PP in double-stranded DNA (dsDNA) wrapped around a nucleosome. Figure is based on the PDB structure 6R8Y [111]. The UV–DDB complex is colored in blue, the DDB2 residues Lys244, Phe34, Gln335, and His336 are in cyan, the nucleosome is in green, and the 6-4PP is in light pink. The photolesion binding pocket is highlighted with a blue hallow. Right panel: Zoomed-in detailed view of the DDB2–lesion interaction. (**d**) Left panel: In silico modeling of a *Saccharomyces cerevisiae* Rad4–Rad23 complex (XPC complex homologue) bound to a 6-4PP photoproduct. The figure is based on the PDB structure 6CFI [112]. The Rad4 TGD (Transglutaminase homology domain) is colored in yellow, the BHD1 (ß-hairpin domain 1) is in lime-yellow, the BHD2 domain is in gold, the BHD3 domain is in pale-yellow, the Rad23 R4BD domain is in white, and the 6-4PP is in light pink. Right panel: Zoomed-in detailed view of the *Xeroderma Pigmentosum* complementation group C (XPC)–lesion interaction. The helix insertion hairpin from the BHD3 domain is highlighted with a yellow hallow. (**e**) Left panel: In silico modeling of the *Homo sapiens* core TFIIH–XPA–DNA complex without photolesion. Figure is based on the PDB structure 6RO4 [113]. The TFIIH is colored in white, the XPA (*Xeroderma Pigmentosum* complementation group A) protein is in salmon, the FeS cluster is in yellow and orange, and the XPD protein and its Arg112, Cys134, Tyr192, and Arg196 residues are in pale green. Right panel: Zoomed-in detailed view of the XPD–lesion interaction. The theoretical localization of the photolesion during the recognition step is highlighted with a violet hallow. All figures were created using PyMOL (The PyMOL Molecular Graphics System, Version 2.0 Schrödinger, LLC.).

4.2.2. Global Genome Repair

In addition to TCR, the global genome repair pathway (GGR) acts in poorly transcribed/untranscribed genomic regions to efficiently repair photolesions. In this NER sub-pathway, the damage recognition is performed independently of RNA Pol II [3]. In GGR, the central actor is the *Xeroderma Pigmentosum* complementation group C (XPC)–RAD23 protein complex (hereafter called the XPC complex). This complex was identified as the initiator of GGR because of the ability of XPC to bind DNA lesions (Figure 2d) [114]. The XPC–RAD23 complex is well conserved in eukaryotes: RAD4–Rad23 in *Saccharomyces cerevisiae* [115], XPC–RAD23B in human [116], and XPC–RAD23 in *Arabidopsis* [117,118]. RAD23 binds RAD4 through its R4BD domain (Figure 3d) [112], thereby regulating RAD4 stabilization [119] and promoting lesion recognition activity [120]. Additionally, the XPC complex is stabilized at damage sites when associated with Cdc31 and Rad33 in yeast [121,122]/Centrin2 in human [123,124] and AtCentrin2 and CML19 [125,126] in Arabidopsis [121–126].

The first crystal structure of the RAD4–RAD23 complex binding a CPD containing DNA helix confirms the underlying recognition process previously described for the human XPC by Maillard et al. [127,128]. RAD4 contains TGD (Transglutaminase homology domain), BHD1 (ß-hairpin domain 1), BHD2, and BHD3 domains (Figure 3d). TGD and BHD1 regions bind to 11 bp of undamaged, double-stranded DNA (Figure 3d). Simultaneously, the BHD2 and BHD3 domains bind to a 4 bp DNA lesion site by insertion of a β-hairpin of the BHD3 in the helix (Figure 3d) and a groove of BHD2–BHD3 interacting with the backbone of the undamaged strand (Figure 3d) [127]. This structure forces the damaged dimers to flip out of the helix structure, leaving them accessible (Figure 3d) [127].

To stably adopt the bound conformation, the XPC complex needs to overcome a consequent energy barrier, which was described as a primary regulator for the recognition specificity [129,130]. Indeed, DNA damages induce structural changes of the DNA helix structure and weak base pairing, leading to a decrease of the energy barrier that the recognition complex needs to overcome for efficient binding [131]. In other words, XPC may patrol along the DNA until encountering a disturbed helical

structure with weak base pairing, allowing XPC to stably bind the lesion site [128–132]. This process likely explains how the XPC complex detects several different types DNA damages and why the identification of particular lesions is more efficient. For example, 6-4PP lesions causes a massive thermodynamic destabilization of the helical structure [133,134]. As a consequence, 6-4PP recognition by the XPC complex is preferred compared to CPD [135].

Additionally, the recognition efficiency is limited by the residence time of the XPC complex at lesion site [129]. By single-molecule tracking, XPC complex was shown in three different motions: (i) sliding on DNA, most probably scanning for damage site; (ii) in a constrained motion, approximatively 2 kb around the DNA lesion, and (iii) in the non-motile complexes [132]. As in TCR with the arrested RNA Pol II and CSB, the persistent binding of the XPC complex at the damage site recruits TFIIH and further NER factors (described hereafter in Section 4.2.3), ending the recognition step of the GGR.

Cell-free systems have significantly contributed to improving the understanding of the underlying mechanism of XPC photodamage recognition [127,129,132]. However, most of these systems used DNA substrates of relatively small sizes without nucleosomes and hence did not consider the substantial complexity of the recognition step in vivo. Unlike TCR, the GGR also acts in transcriptionally repressed regions with a high nucleosome density [136]. To efficiently fulfill its role in damage recognition in the context of chromatin, the XPC complex is assisted by damage pre-recognition and chromatin remodeling mechanisms.

The pre-recognition mechanisms involve the UV–DDB complex composed of DDB1 and DDB2 (DNA damage binding proteins 1 and 2), which are also known in human as p127 and p48, respectively (Figure 2c). Mutations in this complex lead to repair deficiency and UV sensitivity [137–139]. The UV–DDB complex enables a recognition of 6-4PP, CPD, mismatches, and apurinic/apyrimidinic sites in vivo [111,140,141]. The recognition of different damage is based on a mechanism of helical structure stability verification, resembling the scanning mechanism previously described for the XPC complex [111,142]. The human DDB2 contains a helix–loop–helix domain (residues 101 to 136) and a 7-bladed WD40 β-propeller domain (residues 137 to 455). The DNA binding of the UV–DDB complex is exclusively performed by the β-propeller. DDB2 binds 7 bp DNA by charge-stabilizing hydrogen bonds to the phosphodiester backbone [111,142]. This binding depends, among other residues, on a well-conserved Lysine (Lys244 in human) [111,142,143]. The point mutation of Lys244 causes DDB2 loss of function [143]. As described for the XPC complex, DDB2 can trigger a helical out-flipping of the lesion in the condition of helical structure distortion and weak base pairing (Figure 3c) [111,142]. This strand separation depends on the insertion of a 3 bp residue in DDB2 hairpin Phe334, Gln335, and His336 (Figure 3c) [111,142]. Unlike the XPC complex, which only interacts with the undamaged strand, DDB2 binds the displaced DNA lesion in a shallow pocket [111,142]. However, the shape and the composition of the pocket do not provide lesion binding specificity but limit the size and the chemical nature of the lesion that can be recognized [111,142]. This recognition mechanism holds true if the DNA is wrapped around a nucleosome, and a register shifting seems to be sufficient to allow DDB2 to stably bind the lesion (Figure 3c) [111]. In that way, DDB2 can act as UV-induced DNA damage pre-recognition platform, even in the context of dense chromatin [111].

The stable DDB2 binding to the lesion site activates the Cullin4 E3 ubiquitin ligase complex, which interacts with UV–DDB through the three β-propeller domains of DDB1 [144], leading to the ubiquitination of DDB2, XPC, and nearby histones [145,146]. Additionally, the UV–DDB complex was shown to recruit several chromatin remodelers [147–149] and histone methyltransferases: ASH1L [150] DOT1L [151], and NSD2 [152], suggesting that histone PTMs may also play a critical role in this recognition process [153].

The exact timing of interactions and the underlying interplays are only partially understood. ASH1L was shown to ensure the DNA lesion handoff between a DDB2 pre-recognition complex and the XPC recognition complex through H3K4 tri-methylation [150]. Additionally, the DDB2 dynamics are tightly regulated by PTMs, modulating its stability and retention time on chromatin [154]. Indeed, after stable damage recognition, DDB2 can be ubiquitinated [154], SUMOylated by PIASy (Protein

inhibitor of activated STAT Y) [155,156], and poly-ADP-ribosylated by PARP1 (Poly ADP-Ribose Polymerase) [149]. The poly-ADP-ribosylation of DDB2 increases its retention time on chromatin [149]. In contrast, the ubiquitination leads to the proteasomal degradation of DDB2 to complete the pre-recognition step [154,157].

Although the exact function of SUMOylation is as yet undetermined, a recent study highlighted the role of SUMOylation in DNA–protein cross-link (DPC) labeling and clearance in higher eukaryotes [158]. Considering the increased probability of DNA–protein cross-linking upon UV exposure [15] and the SUMOylation of several other NER proteins [159] such as XPC [160], SUMOylation may serve as priming mark for DPC surveillance. This hypothesis is reinforced by the recent evidence that DDB2 can recognize another type of UV-induced DNA lesion, 8-oxo-G [161], which shows a considerable DPC reactivity [14,15]. Alternatively, SUMOylation may feed the recently described SUMO-Targeted Ubiquitin Ligases (STUbL) process to promote protein ubiquitination [162].

Histone ubiquitination and chromatin remodelers likely play a promoting role for the efficiency of the following NER steps, as shown for the CHD1 chromatin remodeler, ensuring the XPC to TFIIH handover of UV photolesions bound to nucleosomes [163].

However, DDB2 was shown to spatially and temporally regulate XPC recruitment and thereby NER (Figure 2c,d) [164]. In the nucleosome-bound sequence, a close handover may occur through the interaction between DDB2 and the BHD1 domain of XPC at the damage site [164]. By this mechanism, XPC may access compact chromatin and stick the damaged site for a later repair [164]. Furthermore, DDB2 can also induce chromatin relaxation, which may prefer a contactless handover to XPC [165]. One working hypothesis would be that photolyases could also take advantage of this relaxed chromatin microenvironment formed by DDB2 to access photolesion in heterochromatic structures.

In *Saccharomyces cerevisiae*, Rad7 and Rad16 functionally substitute the UV–DDB2 complex by an ATP-dependent UV-damage sensor [166]. The Rad7–Rad16 complex interacts with elc1 and Cullin3 to form a Cullin-based E3 ubiquitin ligase necessary for Rad4 ubiquitination in response to UV radiation [167,168]. The exact mechanism and sequence context of Rad7–Rad16 lesions binding remains unclear.

Interestingly, Rad7–Rad16 and UV–DDB are both conserved in the model plant *Arabidopsis thaliana* [169]. The UV–DDB pathway was already extensively characterized [157]. Importantly, in addition to the canonical DDB2 recognition pathway, *Arabidopsis thaliana* evolved a small RNA-mediated photolesion detection mechanism [22]. The model proposes that upon UV exposure, small RNA, with sequence complementarity to DNA damaged sequences, accumulate. Upon UV exposure, these 21-nt UV-induced small RNAs (uviRNA) are loaded into ARGONAUTE 1 (AGO1) and form a complex with DDB2 to be targeted at damaged site, leading to efficient photolesions recognition [22].

To summarize, GGR is composed of an essential pre-recognition step performed by the UV–DDB/Rad7-16 complex, which enables, among other processes, the recognition of 6-4PP and CPD in DNA bonded to nucleosomes [111,166]. This pre-recognition step induces histone methylation [153] and chromatin remodeling [147–149] to promote the recruitment of the XPC complex for the central damage recognition step of the GGR pathway [150,164]. Alternatively, the damage handover between DDB2 and XPC may occur in a transient interaction at damage sites in nucleosome-rich regions [164]. DNA binding of the UV–DDB complex also activates the Cullin4 ubiquitin E3 ligase complex, which, ubiquitinated DDB2 and XPC to coordinate the end of the pre-recognition and recognition steps [145,154]. Once bound to the damage site, the XPC complex, in an interplay with the chromatin remodeler CHD, recruits TFIIH for the validation step of the NER recognition process [163].

4.2.3. Validation of NER Recognition Steps

Both TCR and GGR recognition steps end up by recruiting the TFIIH complex (Figure 2e), which is well conserved among eukaryotes [170–173]. In human, TFIIH is composed of a core complex with the 2 DNA helicases XPB and XPD as well as p62, p52, p44, p34, and p8 [174]. The additional

CDK-activating kinase subcomplex is formed by CDK7, cyclin H, and MAT1 subunits, which are required for transcription initiation but not for DNA repair [175]. In the context of NER, TFIIH interacts with XPA and XPG (*Xeroderma Pigmentosum* complementation group G) instead of MAT1, inducing a conformational change [113]. XPA clamps the TFIIH complex to DNA, whereas the endonuclease XPG competes with MAT1 [113]. XPA binds XPB with its extended helix, forming a tunnel for the DNA helix and promoting the translocation activity of XPB [113]. Simultaneously, XPA intercalating hairpin interacts with XPD at the 5′-edge of the DNA repair bubble, promoting strand separation and the 5 —> 3′ helicase activity of XPD [113].

XPD performs the final DNA lesion recognition step of NER, which is also called the "validation step". The mechanism by which the DNA strand is loaded into XPD was proposed to depend on the interaction between the HD2 domain of XPD and the ssDNA of the repair bubble [176]. This contact may subsequently initiate a transient opening of the interface between the Arch and the iron–sulfur cluster (FeS) domains to slip the DNA strand inside a cavity between the ATPase lobe1, the FeS cluster domain, and the Arch domain (Figure 3e) [176]. The damaged DNA strand is actively translocated through this cavity, enabling the proofreading DNA bases and the recognition of abnormal structures such as CPDs [113,176–178]. Indeed, the amino acids Y192 and R196 of the FeS domain, stabilizing the sugar–phosphate backbone, were shown to be essential for XPD retention at a bulky DNA lesion to (Figure 3e) [178]. The retention at the damaged site was proposed to depend on the lack of DNA-mediated charge transfer (CT) [179,180]. According to this hypothesis, electrons can be transferred between two FeS cluster proteins through the undamaged DNA duplex [179]. In the case of XPD, the amino acids R112 and C134, shaping a bridge between DNA and the FeS cluster, may allow the electron transfer, promoting the displacement of XPD (Figure 3e) [179]. In the presence of DNA damage, the CT through the DNA is altered, and XPD is stabilized, thereby labeling the damage site [179].

This last recognition step is followed by the recruitment of the endonucleases ERCC1–XPF and XPG in 5′ and 3′ of XPD, respectively [175]. These endonucleases perform a dual incision releasing a 30-nt DNA fragment containing the photolesion [175]. At the same time, the non-damaged strand is protected by the Replication Protein A (RPA) [175,181]. This excision step is followed by de novo DNA synthesis and nick ligation to restore the original DNA sequence (Figure 2) [175,182].

5. Conclusions and Perspectives

This review brought together several lines of evidence highlighting the existence of potential connections between the (epi)genomic landscapes, photolesions formation, and processing.

Indeed, genomic and epigenomic contexts (nucleotides composition, DNA methylation, nucleosome binding) lead to a differential reactivity of loci to form photolesions. A higher chromatin structure, determined by the epigenetic landscape, pins down the frame for recognition and repair specificities. In addition to the motif/amino acid-based recognition mechanisms of the core protein complexes, sequential handover between recognition and repair factors is partially mediated by chromatin remodelers and epigenome writers [150,153,183].

Given that the recognition step promotes histone eviction/sliding and also de novo DNA synthesis, it becomes evident that the accurate re-establishment of the epigenomic landscape is a part of the genome maintenance process. However, epigenome changes at damaged sites have been reported [23,184,185]. Such alterations may modulate the transcriptional programs, redirecting the choice of the photodamage repair pathway to be mobilized. Hence, it is likely that variabilities of DNA methylation, base composition, UV damage formation, recognition, and repair contribute to genome evolution [186]. This extended view on photodamage recognition mechanisms highlights the importance of future works to study the chromatin landscape at damaged loci upon UV exposure and repair, and it paves the way toward new concepts regarding the evolution of eukaryotic (epi)genomes.

Author Contributions: Conceptualization, P.J.t.B. and J.M.; writing—original draft preparation, P.J.t.B. and J.M.; writing—review and editing, P.J.t.B. and J.M. All authors have read and agreed to the published version of the manuscript.

Funding: This research received no external funding.

Acknowledgments: The authors would like to acknowledge the "Groupement De Recherche EPIPLANT" for helpful discussions.

Conflicts of Interest: The authors declare no conflict of interest.

Abbreviations

CPD	cyclobutane pyrimidine dimers
CS	Cockayne syndrome
DDB	DNA damage binding protein
DR	direct repair
GGR	global genome repair
6-4PP	pyrimidine 6-4 pyrimidone photoproducts
8-oxo-G	8-hydroxyguanine
NER	nucleotide excision repair
PL	photolyase
PTM	post-translational modification
ROS	reactive oxygen xpecies
SUMO	Small Ubiquitin-like MOdifier
TCR	transcription coupled repair
UV-R	ultraviolet radiation
uviRNA	UV-induced small RNAs
XP	*Xeroderma pigmentosum*

References

1. Schuch, A.P.; Menck, C.F.M. The genotoxic effects of DNA lesions induced by artificial UV-radiation and sunlight. *J. Photochem. Photobiol. B: Biol.* **2010**, *99*, 111–116. [CrossRef] [PubMed]
2. Mullenders, L.H.F. Solar UV damage to cellular DNA: From mechanisms to biological effects. *Photochem. Photobiol. Sci.* **2018**, *17*, 1842–1852. [CrossRef] [PubMed]
3. Rastogi, R.P.; Richa; Kumar, A.; Tyagi, M.B.; Sinha, R.P. Molecular Mechanisms of Ultraviolet Radiation-Induced DNA Damage and Repair. *J. Nucleic Acids* **2010**, *2010*. [CrossRef] [PubMed]
4. Cadet, J.; Wagner, J.R. DNA Base Damage by Reactive Oxygen Species, Oxidizing Agents, and UV Radiation. *Cold Spring Harb. Perspect. Biol.* **2013**, *5*. [CrossRef] [PubMed]
5. Markovitsi, D. UV-induced DNA Damage: The Role of Electronic Excited States. *Photochem. Photobiol.* **2016**, *92*, 45–51. [CrossRef]
6. Schreier, W.J.; Kubon, J.; Regner, N.; Haiser, K.; Schrader, T.E.; Zinth, W.; Clivio, P.; Gilch, P. Thymine dimerization in DNA model systems: Cyclobutane photolesion is predominantly formed via the singlet channel. *J. Am. Chem. Soc.* **2009**, *131*, 5038–5039. [CrossRef]
7. Marguet, S.; Markovitsi, D. Time-Resolved Study of Thymine Dimer Formation. *J. Am. Chem. Soc.* **2005**, *127*, 5780–5781. [CrossRef]
8. Banyasz, A.; Esposito, L.; Douki, T.; Perron, M.; Lepori, C.; Improta, R.; Markovitsi, D. Effect of C5-Methylation of Cytosine on the UV-Induced Reactivity of Duplex DNA: Conformational and Electronic Factors. *J. Phys. Chem. B* **2016**, *120*, 4232–4242. [CrossRef]
9. Wu, D.; Lai, W.; Lyu, C.; Hang, H.; Wang, H. UHPLC-Q-TOF/MS detection of UV-induced TpT dimeric lesions in genomic DNA. *J. Chromatogr. B Anal. Technol. Biomed. Life Sci.* **2018**, *1096*, 135–142. [CrossRef]
10. Haiser, K.; Fingerhut, B.P.; Heil, K.; Glas, A.; Herzog, T.T.; Pilles, B.M.; Schreier, W.J.; Zinth, W.; de Vivie-Riedle, R.; Carell, T. Mechanism of UV-Induced Formation of Dewar Lesions in DNA. *Angew. Chem. Int. Ed.* **2012**, *51*, 408–411. [CrossRef]
11. Schuch, A.P.; Moreno, N.C.; Schuch, N.J.; Menck, C.F.M.; Garcia, C.C.M. Sunlight damage to cellular DNA: Focus on oxidatively generated lesions. *Free Radic. Biol. Med.* **2017**, *107*, 110–124. [CrossRef] [PubMed]

12. Encinas, S.; Belmadoui, N.; Climent, M.J.; Gil, S.; Miranda, M.A. Photosensitization of Thymine Nucleobase by Benzophenone Derivatives as Models for Photoinduced DNA Damage: Paterno−Büchi vs Energy and Electron Transfer Processes. *Chem. Res. Toxicol.* **2004**, *17*, 857–862. [CrossRef]
13. Valko, M.; Rhodes, C.J.; Moncol, J.; Izakovic, M.; Mazur, M. Free radicals, metals and antioxidants in oxidative stress-induced cancer. *Chem. Biol. Interact.* **2006**, *160*, 1–40. [CrossRef] [PubMed]
14. Yu, Y.; Cui, Y.; Niedernhofer, L.J.; Wang, Y. Occurrence, Biological Consequences, and Human Health Relevance of Oxidative Stress-Induced DNA Damage. *Chem. Res. Toxicol.* **2016**, *29*, 2008–2039. [CrossRef] [PubMed]
15. Cadet, J.; Douki, T. Formation of UV-induced DNA damage contributing to skin cancer development. *Photochem. Photobiol. Sci.* **2018**, *17*, 1816–1841. [CrossRef]
16. Lhomme, J.; Constant, J.F.; Demeunynck, M. Abasic DNA structure, reactivity, and recognition. *Biopolymers* **1999**, *52*, 65–83. [CrossRef]
17. Mol, C.D.; Parikh, S.S.; Putnam, C.D.; Lo, T.P.; Tainer, J.A. DNA repair mechanisms for the recognition and removal of damaged DNA bases. *Annu. Rev. Biophys. Biomol. Struct.* **1999**, *28*, 101–128. [CrossRef]
18. Ohnishi, T.; Mori, E.; Takahashi, A. DNA double-strand breaks: Their production, recognition, and repair in eukaryotes. *Mutat. Res.* **2009**, *669*, 8–12. [CrossRef]
19. Andres, S.N.; Schellenberg, M.J.; Wallace, B.D.; Tumbale, P.; Williams, R.S. Recognition and repair of chemically heterogeneous structures at DNA ends. *Environ. Mol. Mutagen.* **2015**, *56*, 1–21. [CrossRef]
20. Mariño-Ramírez, L.; Spouge, J.L.; Kanga, G.C.; Landsman, D. Statistical analysis of over-represented words in human promoter sequences. *Nucleic Acids Res.* **2004**, *32*, 949–958. [CrossRef]
21. Hu, J.; Adebali, O.; Adar, S.; Sancar, A. Dynamic maps of UV damage formation and repair for the human genome. *Proc. Natl. Acad. Sci. USA* **2017**, *114*, 6758–6763. [CrossRef] [PubMed]
22. Schalk, C.; Cognat, V.; Graindorge, S.; Vincent, T.; Voinnet, O.; Molinier, J. Small RNA-mediated repair of UV-induced DNA lesions by the DNA DAMAGE-BINDING PROTEIN 2 and ARGONAUTE 1. *Proc. Natl. Acad. Sci. USA* **2017**, *114*, E2965–E2974. [CrossRef]
23. Graindorge, S.; Cognat, V.; Johann to Berens, P.; Mutterer, J.; Molinier, J. Photodamage repair pathways contribute to the accurate maintenance of the DNA methylome landscape upon UV exposure. *PLoS Genet.* **2019**, *15*, e1008476. [CrossRef] [PubMed]
24. Chung, L.H.; Murray, V. An extended sequence specificity for UV-induced DNA damage. *J. Photochem. Photobiol. B Biol.* **2018**, *178*, 133–142. [CrossRef] [PubMed]
25. McGinty, R.K.; Tan, S. Nucleosome Structure and Function. *Chem. Rev.* **2015**, *115*, 2255–2273. [CrossRef]
26. Cedar, H.; Bergman, Y. Linking DNA methylation and histone modification: Patterns and paradigms. *Nat. Rev. Genet.* **2009**, *10*, 295–304. [CrossRef] [PubMed]
27. Kumar, S.; Chinnusamy, V.; Mohapatra, T. Epigenetics of Modified DNA Bases: 5-Methylcytosine and Beyond. *Front. Genet.* **2018**, *9*. [CrossRef]
28. Rochette, P.J.; Lacoste, S.; Therrien, J.-P.; Bastien, N.; Brash, D.E.; Drouin, R. Influence of cytosine methylation on ultraviolet-induced cyclobutane pyrimidine dimer formation in genomic DNA. *Mutat. Res.* **2009**, *665*, 7–13. [CrossRef]
29. Law, J.A.; Jacobsen, S.E. Establishing, maintaining and modifying DNA methylation patterns in plants and animals. *Nat. Rev. Genet.* **2010**, *11*, 204–220. [CrossRef]
30. Molinier, J. Genome and Epigenome Surveillance Processes Underlying UV Exposure in Plants. *Genes* **2017**, *8*, 316. [CrossRef]
31. Mao, P.; Wyrick, J.J.; Roberts, S.A.; Smerdon, M.J. UV-Induced DNA Damage and Mutagenesis in Chromatin. *Photochem. Photobiol.* **2017**, *93*, 216–228. [CrossRef] [PubMed]
32. Gale, J.M.; Nissen, K.A.; Smerdon, M.J. UV-induced formation of pyrimidine dimers in nucleosome core DNA is strongly modulated with a period of 10.3 bases. *Proc. Natl. Acad. Sci. USA* **1987**, *84*, 6644–6648. [CrossRef] [PubMed]
33. Gale, J.M.; Smerdon, M.J. UV induced (6-4) photoproducts are distributed differently than cyclobutane dimers in nucleosomes. *Photochem. Photobiol.* **1990**, *51*, 411–417. [CrossRef] [PubMed]
34. Drew, H.R.; Travers, A.A. DNA bending and its relation to nucleosome positioning. *J. Mol. Biol.* **1985**, *186*, 773–790. [CrossRef]
35. Struhl, K.; Segal, E. Determinants of nucleosome positioning. *Nat. Struct. Mol. Biol.* **2013**, *20*, 267–273. [CrossRef]

36. Bérubé, R.; Drigeard Desgarnier, M.-C.; Douki, T.; Lechasseur, A.; Rochette, P.J. Persistence and Tolerance of DNA Damage Induced by Chronic UVB Irradiation of the Human Genome. *J. Investig. Dermatol.* **2018**, *138*, 405–412. [CrossRef]
37. Premi, S.; Han, L.; Mehta, S.; Knight, J.; Zhao, D.; Palmatier, M.A.; Kornacker, K.; Brash, D.E. Genomic sites hypersensitive to ultraviolet radiation. *Proc. Natl. Acad. Sci. USA* **2019**, *116*, 24196–24205. [CrossRef]
38. Tornaletti, S.; Pfeifer, G.P. UV Light as a Footprinting Agent: Modulation of UV-induced DNA Damage by Transcription Factors Bound at the Promoters of Three Human Genes. *J. Mol. Biol.* **1995**, *249*, 714–728. [CrossRef]
39. Pfeifer, G.P. Formation and processing of UV photoproducts: Effects of DNA sequence and chromatin environment. *Photochem. Photobiol.* **1997**, *65*, 270–283. [CrossRef]
40. Sancar, A. Photolyase and Cryptochrome Blue-Light Photoreceptors. In *Advances in Protein Chemistry*; DNA Repair and Replication; Academic Press: Cambridge, MA, USA, 2004; Volume 69, pp. 73–100.
41. Marmur, J.; Grossman, L. Ultraviolet light induced linking of deoxyribonucleic acid strands and its reversal by photoreactivating enzyme. *Proc. Natl. Acad. Sci. USA* **1961**, *47*, 778–787. [CrossRef]
42. Kavakli, I.H.; Ozturk, N.; Gul, S. Chapter One—DNA repair by photolyases. In *Advances in Protein Chemistry and Structural Biology*; Donev, R., Ed.; DNA Repair; Academic Press: Cambridge, MA, USA, 2019; Volume 115, pp. 1–19.
43. Eisen, J.A.; Hanawalt, P.C. A phylogenomic study of DNA repair genes, proteins, and processes. *Mutat. Res.* **1999**, *435*, 171–213. [CrossRef]
44. Vechtomova, Y.L.; Telegina, T.A.; Kritsky, M.S. Evolution of Proteins of the DNA Photolyase/Cryptochrome Family. *Biochem. Mosc.* **2020**, *85*, 131–153. [CrossRef] [PubMed]
45. Kato, T.; Todo, T.; Ayaki, H.; Ishizaki, K.; Morita, T.; Mitra, S.; Ikenaga, M. Cloning of a marsupial DNA photolyase gene and the lack of related nucleotide sequences in placental mammals. *Nucleic Acids Res.* **1994**, *22*, 4119–4124. [CrossRef]
46. Todo, T.; Tsuji, H.; Otoshi, E.; Hitomi, K.; Kim, S.T.; Ikenaga, M. Characterization of a human homolog of (6-4) photolyase. *Mutat. Res.* **1997**, *384*, 195–204. [CrossRef]
47. Sancar, A. Structure and function of DNA photolyase. *Biochemistry* **1994**, *33*, 2–9. [CrossRef]
48. Zhang, M.; Wang, L.; Zhong, D. Photolyase: Dynamics and Electron-Transfer Mechanisms of DNA repair. *Arch. Biochem. Biophys.* **2017**, *632*, 158–174. [CrossRef]
49. Harm, W. Analysis of photoenzymatic repair of UV lesions in E. coli by light flashes. *Res. Prog. Org. Biol. Med. Chem* **1972**, *3 Pt 1*, 402–420.
50. Lüdemann, G.; Woiczikowski, P.B.; Kubař, T.; Elstner, M.; Steinbrecher, T.B. Charge transfer in E. coli DNA photolyase: Understanding polarization and stabilization effects via QM/MM simulations. *J. Phys. Chem. B* **2013**, *117*, 10769–10778. [CrossRef]
51. Wulff, D.L.; Rupert, C.S. Disappearance of thymine photodimer in ultraviolet irradiated DNA upon treatment with a photoreactivating enzyme from baker's yeast. *Biochem. Biophys. Res. Commun.* **1962**, *7*, 237–240. [CrossRef]
52. Suter, B.; Thoma, F. DNA-repair by Photolyase Reveals Dynamic Properties of Nucleosome Positioning in Vivo. *J. Mol. Biol.* **2002**, *319*, 395–406. [CrossRef]
53. Browning, L.S.; Altenburg, E. The proportionality between mutation rate and ultraviolet dose after photoreactivation in Drosophila. *Genetics* **1962**, *47*, 361–366. [PubMed]
54. Kim, S.T.; Malhotra, K.; Ryo, H.; Sancar, A.; Todo, T. Purification and characterization of Drosophila melanogaster photolyase. *Mutat. Res.* **1996**, *363*, 97–104. [CrossRef]
55. Pang, Q.; Hays, J.B. UV-B-Inducible and Temperature-Sensitive Photoreactivation of Cyclobutane Pyrimidine Dimers in Arabidopsis thaliana. *Plant Physiol.* **1991**, *95*, 536–543. [CrossRef]
56. Ahmad, M.; Jarillo, J.A.; Klimczak, L.J.; Landry, L.G.; Peng, T.; Last, R.L.; Cashmore, A.R. An enzyme similar to animal type II photolyases mediates photoreactivation in Arabidopsis. *Plant Cell* **1997**, *9*, 199–207. [CrossRef]
57. Nakajima, S.; Sugiyama, M.; Iwai, S.; Hitomi, K.; Otoshi, E.; Kim, S.T.; Jiang, C.Z.; Todo, T.; Britt, A.B.; Yamamoto, K. Cloning and characterization of a gene (UVR3) required for photorepair of 6-4 photoproducts in Arabidopsis thaliana. *Nucleic Acids Res.* **1998**, *26*, 638–644. [CrossRef] [PubMed]

58. Marizcurrena, J.J.; Acosta, S.; Canclini, L.; Hernández, P.; Vallés, D.; Lamparter, T.; Castro-Sowinski, S. A natural occurring bifunctional CPD/(6-4)-photolyase from the Antarctic bacterium Sphingomonas sp. UV9. *Appl. Microbiol. Biotechnol.* **2020**. [CrossRef] [PubMed]
59. Mees, A.; Klar, T.; Gnau, P.; Hennecke, U.; Eker, A.P.M.; Carell, T.; Essen, L.-O. Crystal Structure of a Photolyase Bound to a CPD-Like DNA Lesion After in Situ Repair. *Science* **2004**, *306*, 1789–1793. [CrossRef]
60. Sancar, G.B.; Sancar, A. Purification and characterization of DNA photolyases. *Meth. Enzym.* **2006**, *408*, 121–156. [CrossRef]
61. Glas, A.F.; Schneider, S.; Maul, M.J.; Hennecke, U.; Carell, T. Crystal Structure of the T(6-4)C Lesion in Complex with a (6-4) DNA Photolyase and Repair of UV-Induced (6-4) and Dewar Photolesions. *Chem. A Eur. J.* **2009**, *15*, 10387–10396. [CrossRef]
62. Maul, M.J.; Barends, T.R.M.; Glas, A.F.; Cryle, M.J.; Domratcheva, T.; Schneider, S.; Schlichting, I.; Carell, T. Crystal structure and mechanism of a DNA (6-4) photolyase. *Angew. Chem. Int. Ed. Engl.* **2008**, *47*, 10076–10080. [CrossRef]
63. Wilson, T.J.; Crystal, M.A.; Rohrbaugh, M.C.; Sokolowsky, K.P.; Gindt, Y.M. Evidence from Thermodynamics that DNA Photolyase Recognizes a Solvent-Exposed CPD Lesion. *J. Phys. Chem. B* **2011**, *115*, 13746–13754. [CrossRef]
64. Schelvis, J.P.M.; Zhu, X.; Gindt, Y.M. Enzyme–Substrate Binding Kinetics Indicate That Photolyase Recognizes an Extrahelical Cyclobutane Thymidine Dimer. *Biochemistry* **2015**, *54*, 6176–6185. [CrossRef] [PubMed]
65. Kiontke, S.; Geisselbrecht, Y.; Pokorny, R.; Carell, T.; Batschauer, A.; Essen, L.-O. Crystal structures of an archaeal class II DNA photolyase and its complex with UV-damaged duplex DNA. *EMBO J.* **2011**, *30*, 4437–4449. [CrossRef] [PubMed]
66. Maestre-Reyna, M.; Yamamoto, J.; Huang, W.-C.; Tsai, M.-D.; Essen, L.-O.; Bessho, Y. Twist and turn: A revised structural view on the unpaired bubble of class II CPD photolyase in complex with damaged DNA. *IUCrJ* **2018**, *5*, 608–618. [CrossRef] [PubMed]
67. Essen, L.O.; Klar, T. Light-driven DNA repair by photolyases. *Cell. Mol. Life Sci.* **2006**, *63*, 1266–1277. [CrossRef]
68. Guintini, L.; Charton, R.; Peyresaubes, F.; Thoma, F.; Conconi, A. Nucleosome positioning, nucleotide excision repair and photoreactivation in Saccharomyces cerevisiae. *DNA Repair* **2015**, *36*, 98–104. [CrossRef] [PubMed]
69. Li, J.; Liu, Z.; Tan, C.; Guo, X.; Wang, L.; Sancar, A.; Zhong, D. Dynamics and Mechanism of Repair of UV-induced (6-4) Photoproduct by Photolyase. *Nature* **2010**, *466*, 887–890. [CrossRef] [PubMed]
70. Bohr, V.A.; Smith, C.A.; Okumoto, D.S.; Hanawalt, P.C. DNA repair in an active gene: Removal of pyrimidine dimers from the DHFR gene of CHO cells is much more efficient than in the genome overall. *Cell* **1985**, *40*, 359–369. [CrossRef]
71. Lainé, J.-P.; Egly, J.-M. Initiation of DNA repair mediated by a stalled RNA polymerase IIO. *EMBO J.* **2006**, *25*, 387–397. [CrossRef] [PubMed]
72. Hanawalt, P.C.; Spivak, G. Transcription-coupled DNA repair: Two decades of progress and surprises. *Nat. Rev. Mol. Cell Biol.* **2008**, *9*, 958–970. [CrossRef]
73. Belotserkovskii, B.P.; Mirkin, S.M.; Hanawalt, P.C. DNA sequences that interfere with transcription: Implications for genome function and stability. *Chem. Rev.* **2013**, *113*, 8620–8637. [CrossRef] [PubMed]
74. Xu, L.; Wang, W.; Gotte, D.; Yang, F.; Hare, A.A.; Welch, T.R.; Li, B.C.; Shin, J.H.; Chong, J.; Strathern, J.N.; et al. RNA polymerase II senses obstruction in the DNA minor groove via a conserved sensor motif. *Proc. Natl. Acad. Sci. USA* **2016**, *113*, 12426–12431. [CrossRef] [PubMed]
75. Xu, J.; Lahiri, I.; Wang, W.; Wier, A.; Cianfrocco, M.A.; Chong, J.; Hare, A.A.; Dervan, P.B.; DiMaio, F.; Leschziner, A.E.; et al. Structural basis for the initiation of eukaryotic transcription-coupled DNA repair. *Nature* **2017**, *551*, 653–657. [CrossRef] [PubMed]
76. Vélez-Cruz, R.; Egly, J.-M. Cockayne syndrome group B (CSB) protein: At the crossroads of transcriptional networks. *Mech. Ageing Dev.* **2013**, *134*, 234–242. [CrossRef]
77. Xu, L.; Wang, W.; Wu, J.; Shin, J.H.; Wang, P.; Unarta, I.C.; Chong, J.; Wang, Y.; Wang, D. Mechanism of DNA alkylation-induced transcriptional stalling, lesion bypass, and mutagenesis. *Proc. Natl. Acad. Sci. USA* **2017**, *114*, E7082–E7091. [CrossRef]

78. Wang, W.; Walmacq, C.; Chong, J.; Kashlev, M.; Wang, D. Structural basis of transcriptional stalling and bypass of abasic DNA lesion by RNA polymerase II. *Proc. Natl. Acad. Sci. USA* **2018**, *115*, E2538–E2545. [CrossRef]
79. Charlet-Berguerand, N.; Feuerhahn, S.; Kong, S.E.; Ziserman, H.; Conaway, J.W.; Conaway, R.; Egly, J.M. RNA polymerase II bypass of oxidative DNA damage is regulated by transcription elongation factors. *EMBO J.* **2006**, *25*, 5481–5491. [CrossRef]
80. Mei Kwei, J.S.; Kuraoka, I.; Horibata, K.; Ubukata, M.; Kobatake, E.; Iwai, S.; Handa, H.; Tanaka, K. Blockage of RNA polymerase II at a cyclobutane pyrimidine dimer and 6-4 photoproduct. *Biochem. Biophys. Res. Commun.* **2004**, *320*, 1133–1138. [CrossRef]
81. Brueckner, F.; Hennecke, U.; Carell, T.; Cramer, P. CPD damage recognition by transcribing RNA polymerase II. *Science* **2007**, *315*, 859–862. [CrossRef]
82. Walmacq, C.; Cheung, A.C.M.; Kireeva, M.L.; Lubkowska, L.; Ye, C.; Gotte, D.; Strathern, J.N.; Carell, T.; Cramer, P.; Kashlev, M. Mechanism of translesion transcription by RNA polymerase II and its role in cellular resistance to DNA damage. *Mol. Cell* **2012**, *46*, 18–29. [CrossRef]
83. Nakazawa, Y.; Hara, Y.; Oka, Y.; Komine, O.; van den Heuvel, D.; Guo, C.; Daigaku, Y.; Isono, M.; He, Y.; Shimada, M.; et al. Ubiquitination of DNA Damage-Stalled RNAPII Promotes Transcription-Coupled Repair. *Cell* **2020**, *180*, 1228–1244.e24. [CrossRef] [PubMed]
84. Tufegdžić Vidaković, A.; Mitter, R.; Kelly, G.P.; Neumann, M.; Harreman, M.; Rodríguez-Martínez, M.; Herlihy, A.; Weems, J.C.; Boeing, S.; Encheva, V.; et al. Regulation of the RNAPII Pool Is Integral to the DNA Damage Response. *Cell* **2020**, *180*, 1245–1261.e21. [CrossRef] [PubMed]
85. Groisman, R.; Kuraoka, I.; Chevallier, O.; Gaye, N.; Magnaldo, T.; Tanaka, K.; Kisselev, A.F.; Harel-Bellan, A.; Nakatani, Y. CSA-dependent degradation of CSB by the ubiquitin-proteasome pathway establishes a link between complementation factors of the Cockayne syndrome. *Genes Dev.* **2006**, *20*, 1429–1434. [CrossRef] [PubMed]
86. Zhu, Q.; Ding, N.; Wei, S.; Li, P.; Wani, G.; He, J.; Wani, A.A. USP7-mediated deubiquitination differentially regulates CSB but not UVSSA upon UV radiation-induced DNA damage. *Cell Cycle* **2020**, *19*, 124–141. [CrossRef] [PubMed]
87. Liebelt, F.; Schimmel, J.; Verlaan- de Vries, M.; Klemann, E.; van Royen, M.E.; van der Weegen, Y.; Luijsterburg, M.S.; Mullenders, L.H.; Pines, A.; Vermeulen, W.; et al. Transcription-coupled nucleotide excision repair is coordinated by ubiquitin and SUMO in response to ultraviolet irradiation. *Nucleic Acids Res.* **2020**, *48*, 231–248. [CrossRef] [PubMed]
88. van der Weegen, Y.; Golan-Berman, H.; Mevissen, T.E.T.; Apelt, K.; González-Prieto, R.; Goedhart, J.; Heilbrun, E.E.; Vertegaal, A.C.O.; van den Heuvel, D.; Walter, J.C.; et al. The cooperative action of CSB, CSA, and UVSSA target TFIIH to DNA damage-stalled RNA polymerase II. *Nat. Commun.* **2020**, *11*. [CrossRef]
89. Mullenders, L. DNA damage mediated transcription arrest: Step back to go forward. *Dna Repair* **2015**, *36*, 28–35. [CrossRef]
90. Lans, H.; Hoeijmakers, J.H.J.; Vermeulen, W.; Marteijn, J.A. The DNA damage response to transcription stress. *Nat. Rev. Mol. Cell Biol.* **2019**, *20*, 766–784. [CrossRef]
91. Wang, W.; Xu, J.; Chong, J.; Wang, D. Structural Basis of DNA Lesion Recognition for Eukaryotic Transcription-Coupled Nucleotide Excision Repair. *DNA Repair* **2018**, *71*, 43–55. [CrossRef]
92. Woudstra, E.C.; Gilbert, C.; Fellows, J.; Jansen, L.; Brouwer, J.; Erdjument-Bromage, H.; Tempst, P.; Svejstrup, J.Q. A Rad26–Def1 complex coordinates repair and RNA pol II proteolysis in response to DNA damage. *Nature* **2002**, *415*, 929–933. [CrossRef]
93. Spivak, G. Transcription-Coupled Repair: An update. *Arch. Toxicol.* **2016**, *90*, 2583–2594. [CrossRef] [PubMed]
94. Al Khateeb, W.M.; Sher, A.A.; Marcus, J.M.; Schroeder, D.F. UVSSA, UBP12, and RDO2/TFIIS Contribute to Arabidopsis UV Tolerance. *Front. Plant Sci.* **2019**, *10*. [CrossRef] [PubMed]
95. Deger, N.; Yang, Y.; Lindsey-Boltz, L.A.; Sancar, A.; Selby, C.P. Drosophila, which lacks canonical transcription-coupled repair proteins, performs transcription-coupled repair. *J. Biol. Chem.* **2019**, *294*, 18092–18098. [CrossRef] [PubMed]
96. Selby, C.P.; Witkin, E.M.; Sancar, A. Escherichia coli mfd mutant deficient in "mutation frequency decline" lacks strand-specific repair: In vitro complementation with purified coupling factor. *Proc. Natl. Acad. Sci. USA* **1991**, *88*, 11574–11578. [CrossRef]

97. Fan, J.; Leroux-Coyau, M.; Savery, N.J.; Strick, T.R. Reconstruction of bacterial transcription-coupled repair at single-molecule resolution. *Nature* **2016**, *536*, 234–237. [CrossRef] [PubMed]
98. Selby, C.P. Mfd Protein and Transcription-Repair Coupling in Escherichia coli. *Photochem. Photobiol.* **2017**, *93*, 280–295. [CrossRef]
99. Le, T.T.; Yang, Y.; Tan, C.; Suhanovsky, M.M.; Fulbright, R.M.; Inman, J.T.; Li, M.; Lee, J.; Perelman, S.; Roberts, J.W.; et al. Mfd Dynamically Regulates Transcription via a Release and Catch-Up Mechanism. *Cell* **2018**, *172*, 344–357.e15. [CrossRef]
100. Park, J.-S.; Marr, M.T.; Roberts, J.W. E. coli Transcription repair coupling factor (Mfd protein) rescues arrested complexes by promoting forward translocation. *Cell* **2002**, *109*, 757–767. [CrossRef]
101. Epshtein, V.; Kamarthapu, V.; McGary, K.; Svetlov, V.; Ueberheide, B.; Proshkin, S.; Mironov, A.; Nudler, E. UvrD facilitates DNA repair by pulling RNA polymerase backwards. *Nature* **2014**, *505*, 372–377. [CrossRef]
102. Epshtein, V. UvrD helicase: An old dog with a new trick. *Bioessays* **2015**, *37*, 12–19. [CrossRef]
103. Sanz-Murillo, M.; Xu, J.; Belogurov, G.A.; Calvo, O.; Gil-Carton, D.; Moreno-Morcillo, M.; Wang, D.; Fernández-Tornero, C. Structural basis of RNA polymerase I stalling at UV light-induced DNA damage. *Proc. Natl. Acad. Sci. USA* **2018**, *115*, 8972–8977. [CrossRef] [PubMed]
104. Bradsher, J.; Auriol, J.; de Santis, L.P.; Iben, S.; Vonesch, J.-L.; Grummt, I.; Egly, J.-M. CSB Is a Component of RNA Pol I Transcription. *Mol. Cell* **2002**, *10*, 819–829. [CrossRef]
105. Iben, S.; Tschochner, H.; Bier, M.; Hoogstraten, D.; Hozák, P.; Egly, J.-M.; Grummt, I. TFIIH Plays an Essential Role in RNA Polymerase I Transcription. *Cell* **2002**, *109*, 297–306. [CrossRef]
106. Conconi, A.; Bespalov, V.A.; Smerdon, M.J. Transcription-coupled repair in RNA polymerase I-transcribed genes of yeast. *Proc. Natl. Acad. Sci. USA* **2002**, *99*, 649–654. [CrossRef]
107. Daniel, L.; Cerutti, E.; Donnio, L.-M.; Nonnekens, J.; Carrat, C.; Zahova, S.; Mari, P.-O.; Giglia-Mari, G. Mechanistic insights in transcription-coupled nucleotide excision repair of ribosomal DNA. *Proc. Natl. Acad. Sci. USA* **2018**, *115*, E6770–E6779. [CrossRef] [PubMed]
108. Willis, I.M.; Moir, R.D. Signaling to and from the RNA Polymerase III Transcription and Processing Machinery. *Annu. Rev. Biochem.* **2018**, *87*, 75–100. [CrossRef] [PubMed]
109. Huang, Y.; Kendall, T.; Forsythe, E.S.; Dorantes-Acosta, A.; Li, S.; Caballero-Pérez, J.; Chen, X.; Arteaga-Vázquez, M.; Beilstein, M.A.; Mosher, R.A. Ancient Origin and Recent Innovations of RNA Polymerase IV and V. *Mol. Biol. Evol.* **2015**, *32*, 1788–1799. [CrossRef]
110. Ream, T.S.; Haag, J.R.; Wierzbicki, A.T.; Nicora, C.D.; Norbeck, A.; Zhu, J.-K.; Hagen, G.; Guilfoyle, T.J.; Paša-Tolić, L.; Pikaard, C.S. Subunit Compositions of the RNA-Silencing Enzymes PoI IV and PoI V Reveal Their Origins as Specialized Forms of RNA Polymerase II. *Mol. Cell* **2009**, *33*, 192–203. [CrossRef]
111. Matsumoto, S.; Cavadini, S.; Bunker, R.D.; Grand, R.S.; Potenza, A.; Rabl, J.; Yamamoto, J.; Schenk, A.D.; Schübeler, D.; Iwai, S.; et al. DNA damage detection in nucleosomes involves DNA register shifting. *Nature* **2019**, *571*, 79–84. [CrossRef]
112. Paul, D.; Mu, H.; Zhao, H.; Ouerfelli, O.; Jeffrey, P.D.; Broyde, S.; Min, J.-H. Structure and mechanism of pyrimidine-pyrimidone (6-4) photoproduct recognition by the Rad4/XPC nucleotide excision repair complex. *Nucleic Acids Res.* **2019**, *47*, 6015–6028. [CrossRef]
113. Kokic, G.; Chernev, A.; Tegunov, D.; Dienemann, C.; Urlaub, H.; Cramer, P. Structural basis of TFIIH activation for nucleotide excision repair. *Nat. Commun.* **2019**, *10*, 2885. [CrossRef]
114. Sugasawa, K.; Ng, J.M.Y.; Masutani, C.; Iwai, S.; van der Spek, P.J.; Eker, A.P.M.; Hanaoka, F.; Bootsma, D.; Hoeijmakers, J.H.J. Xeroderma Pigmentosum Group C Protein Complex Is the Initiator of Global Genome Nucleotide Excision Repair. *Mol. Cell* **1998**, *2*, 223–232. [CrossRef]
115. Guzder, S.N.; Habraken, Y.; Sung, P.; Prakash, L.; Prakash, S. Reconstitution of yeast nucleotide excision repair with purified Rad proteins, replication protein A, and transcription factor TFIIH. *J. Biol. Chem.* **1995**, *270*, 12973–12976. [CrossRef] [PubMed]
116. van der Spek, P.J.; Eker, A.; Rademakers, S.; Visser, C.; Sugasawa, K.; Masutani, C.; Hanaoka, F.; Bootsma, D.; Hoeijmakers, J.H. XPC and human homologs of RAD23: Intracellular localization and relationship to other nucleotide excision repair complexes. *Nucleic Acids Res.* **1996**, *24*, 2551–2559. [CrossRef] [PubMed]
117. Britt, A.B. Molecular genetics of DNA repair in higher plants. *Trends Plant Sci.* **1999**, *4*, 20–25. [CrossRef]
118. Kunz, B.A.; Anderson, H.J.; Osmond, M.J.; Vonarx, E.J. Components of nucleotide excision repair and DNA damage tolerance in Arabidopsis thaliana. *Environ. Mol. Mutagenesis* **2005**, *45*, 115–127. [CrossRef] [PubMed]

119. Mao, P.; Smerdon, M.J. Yeast deubiquitinase Ubp3 interacts with the 26 S proteasome to facilitate Rad4 degradation. *J. Biol. Chem.* **2010**, *285*, 37542–37550. [CrossRef]
120. Bergink, S.; Toussaint, W.; Luijsterburg, M.S.; Dinant, C.; Alekseev, S.; Hoeijmakers, J.H.J.; Dantuma, N.P.; Houtsmuller, A.B.; Vermeulen, W. Recognition of DNA damage by XPC coincides with disruption of the XPC–RAD23 complex. *J. Cell Biol.* **2012**, *196*, 681–688. [CrossRef]
121. Chen, L.; Madura, K. Centrin/Cdc31 is a novel regulator of protein degradation. *Mol. Cell. Biol.* **2008**, *28*, 1829–1840. [CrossRef]
122. den Dulk, B.; van Eijk, P.; de Ruijter, M.; Brandsma, J.A.; Brouwer, J. The NER protein Rad33 shows functional homology to human Centrin2 and is involved in modification of Rad4. *Dna Repair* **2008**, *7*, 858–868. [CrossRef]
123. Araki, M.; Masutani, C.; Takemura, M.; Uchida, A.; Sugasawa, K.; Kondoh, J.; Ohkuma, Y.; Hanaoka, F. Centrosome protein centrin 2/caltractin 1 is part of the xeroderma pigmentosum group C complex that initiates global genome nucleotide excision repair. *J. Biol. Chem.* **2001**, *276*, 18665–18672. [CrossRef] [PubMed]
124. Nishi, R.; Okuda, Y.; Watanabe, E.; Mori, T.; Iwai, S.; Masutani, C.; Sugasawa, K.; Hanaoka, F. Centrin 2 stimulates nucleotide excision repair by interacting with xeroderma pigmentosum group C protein. *Mol. Cell. Biol.* **2005**, *25*, 5664–5674. [CrossRef] [PubMed]
125. Liang, L.; Flury, S.; Kalck, V.; Hohn, B.; Molinier, J. CENTRIN2 interacts with the Arabidopsis homolog of the human XPC protein (AtRAD4) and contributes to efficient synthesis-dependent repair of bulky DNA lesions. *Plant Mol. Biol.* **2006**, *61*, 345–356. [CrossRef] [PubMed]
126. La Verde, V.; Trande, M.; D'Onofrio, M.; Dominici, P.; Astegno, A. Binding of calcium and target peptide to calmodulin-like protein CML19, the centrin 2 of Arabidopsis thaliana. *Int. J. Biol. Macromol.* **2018**, *108*, 1289–1299. [CrossRef] [PubMed]
127. Min, J.-H.; Pavletich, N.P. Recognition of DNA damage by the Rad4 nucleotide excision repair protein. *Nature* **2007**, *449*, 570–575. [CrossRef]
128. Maillard, O.; Solyom, S.; Naegeli, H. An Aromatic Sensor with Aversion to Damaged Strands Confers Versatility to DNA Repair. *PLoS Biol.* **2007**, *5*. [CrossRef]
129. Chen, X.; Velmurugu, Y.; Zheng, G.; Park, B.; Shim, Y.; Kim, Y.; Liu, L.; Van Houten, B.; He, C.; Ansari, A.; et al. Kinetic gating mechanism of DNA damage recognition by Rad4/XPC. *Nat. Commun.* **2015**, *6*. [CrossRef]
130. Camenisch, U.; Träutlein, D.; Clement, F.C.; Fei, J.; Leitenstorfer, A.; Ferrando-May, E.; Naegeli, H. Two-stage dynamic DNA quality check by xeroderma pigmentosum group C protein. *EMBO J.* **2009**, *28*, 2387–2399. [CrossRef]
131. Panigrahi, A.; Vemuri, H.; Aggarwal, M.; Pitta, K.; Krishnan, M. Sequence specificity, energetics and mechanism of mismatch recognition by DNA damage sensing protein Rad4/XPC. *Nucleic Acids Res.* **2020**, *48*, 2246–2257. [CrossRef]
132. Kong, M.; Liu, L.; Chen, X.; Driscoll, K.I.; Mao, P.; Böhm, S.; Kad, N.M.; Watkins, S.C.; Bernstein, K.A.; Wyrick, J.J.; et al. Single-molecule imaging reveals that Rad4 (XPC) employs a dynamic DNA damage recognition process. *Mol. Cell* **2016**, *64*, 376–387. [CrossRef]
133. Kim, J.-K.; Patel, D.; Choi, B.-S. Contrasting structural impacts induced by cis-syn cyclobutane dimer and (6–4) adduct in dna duplex decamers: Implication in mutagenesis and repair activity. *Photochem. Photobiol.* **1995**, *62*, 44–50. [CrossRef] [PubMed]
134. Jing, Y.; Kao, J.F.; Taylor, J.S. Thermodynamic and base-pairing studies of matched and mismatched DNA dodecamer duplexes containing cis-syn, (6-4) and Dewar photoproducts of TT. *Nucleic Acids Res.* **1998**, *26*, 3845–3853. [CrossRef] [PubMed]
135. Batty, D.; Rapic'-Otrin, V.; Levine, A.S.; Wood, R.D. Stable binding of human XPC complex to irradiated DNA confers strong discrimination for damaged sites11Edited by M. Yaniv. *J. Mol. Biol.* **2000**, *300*, 275–290. [CrossRef]
136. Han, C.; Srivastava, A.K.; Cui, T.; Wang, Q.-E.; Wani, A.A. Differential DNA lesion formation and repair in heterochromatin and euchromatin. *Carcinogenesis* **2016**, *37*, 129–138. [CrossRef] [PubMed]
137. Zolezzi, F.; Fuss, J.; Uzawa, S.; Linn, S. Characterization of a Schizosaccharomyces pombe strain deleted for a sequence homologue of the human damaged DNA binding 1 (DDB1) gene. *J. Biol. Chem.* **2002**, *277*, 41183–41191. [CrossRef]
138. Itoh, T. Xeroderma pigmentosum group E and DDB2, a smaller subunit of damage-specific DNA binding protein: Proposed classification of xeroderma pigmentosum, Cockayne syndrome, and ultraviolet-sensitive syndrome. *J. Dermatol. Sci.* **2006**, *41*, 87–96. [CrossRef]

139. Koga, A.; Ishibashi, T.; Kimura, S.; Uchiyama, Y.; Sakaguchi, K. Characterization of T-DNA insertion mutants and RNAi silenced plants of Arabidopsis thaliana UV-damaged DNA binding protein 2 (AtUV-DDB2). *Plant Mol. Biol.* **2006**, *61*, 227–240. [CrossRef]
140. Wang, Q.-E.; Zhu, Q.; Wani, G.; Chen, J.; Wani, A.A. UV radiation-induced XPC translocation within chromatin is mediated by damaged-DNA binding protein, DDB2. *Carcinogenesis* **2004**, *25*, 1033–1043. [CrossRef]
141. Wittschieben, B.Ø.; Iwai, S.; Wood, R.D. DDB1-DDB2 (Xeroderma Pigmentosum Group E) Protein Complex Recognizes a Cyclobutane Pyrimidine Dimer, Mismatches, Apurinic/Apyrimidinic Sites, and Compound Lesions in DNA. *J. Biol. Chem.* **2005**, *280*, 39982–39989. [CrossRef]
142. Scrima, A.; Koníčková, R.; Czyzewski, B.K.; Kawasaki, Y.; Jeffrey, P.D.; Groisman, R.; Nakatani, Y.; Iwai, S.; Pavletich, N.P.; Thomä, N.H. Structural basis of UV DNA damage recognition by the DDB1-DDB2 complex. *Cell* **2008**, *135*, 1213–1223. [CrossRef]
143. Tang, J.; Chu, G. Xeroderma pigmentosum complementation group E and UV-damaged DNA-binding protein. *Dna Repair* **2002**, *1*, 601–616. [CrossRef]
144. Cavadini, S.; Fischer, E.S.; Bunker, R.D.; Potenza, A.; Lingaraju, G.M.; Goldie, K.N.; Mohamed, W.I.; Faty, M.; Petzold, G.; Beckwith, R.E.J.; et al. Cullin–RING ubiquitin E3 ligase regulation by the COP9 signalosome. *Nature* **2016**, *531*, 598–603. [CrossRef] [PubMed]
145. Sugasawa, K.; Okuda, Y.; Saijo, M.; Nishi, R.; Matsuda, N.; Chu, G.; Mori, T.; Iwai, S.; Tanaka, K.; Tanaka, K.; et al. UV-induced ubiquitylation of XPC protein mediated by UV-DDB-ubiquitin ligase complex. *Cell* **2005**, *121*, 387–400. [CrossRef] [PubMed]
146. Wang, H.; Zhai, L.; Xu, J.; Joo, H.-Y.; Jackson, S.; Erdjument-Bromage, H.; Tempst, P.; Xiong, Y.; Zhang, Y. Histone H3 and H4 Ubiquitylation by the CUL4-DDB-ROC1 Ubiquitin Ligase Facilitates Cellular Response to DNA Damage. *Mol. Cell* **2006**, *22*, 383–394. [CrossRef]
147. Zhao, Q.; Wang, Q.-E.; Ray, A.; Wani, G.; Han, C.; Milum, K.; Wani, A.A. Modulation of Nucleotide Excision Repair by Mammalian SWI/SNF Chromatin-remodeling Complex. *J. Biol. Chem.* **2009**, *284*, 30424–30432. [CrossRef]
148. Jiang, Y.; Wang, X.; Bao, S.; Guo, R.; Johnson, D.G.; Shen, X.; Li, L. INO80 chromatin remodeling complex promotes the removal of UV lesions by the nucleotide excision repair pathway. *Proc. Natl. Acad. Sci. USA* **2010**, *107*, 17274–17279. [CrossRef]
149. Pines, A.; Vrouwe, M.G.; Marteijn, J.A.; Typas, D.; Luijsterburg, M.S.; Cansoy, M.; Hensbergen, P.; Deelder, A.; de Groot, A.; Matsumoto, S.; et al. PARP1 promotes nucleotide excision repair through DDB2 stabilization and recruitment of ALC1. *J. Cell Biol* **2012**, *199*, 235–249. [CrossRef]
150. Balbo Pogliano, C.; Gatti, M.; Rüthemann, P.; Garajovà, Z.; Penengo, L.; Naegeli, H. ASH1L histone methyltransferase regulates the handoff between damage recognition factors in global-genome nucleotide excision repair. *Nat. Commun.* **2017**, *8*. [CrossRef]
151. Zhu, B.; Chen, S.; Wang, H.; Yin, C.; Han, C.; Peng, C.; Liu, Z.; Wan, L.; Zhang, X.; Zhang, J.; et al. The protective role of DOT1L in UV-induced melanomagenesis. *Nat. Commun.* **2018**, *9*, 259. [CrossRef]
152. Chitale, S.; Richly, H. DICER- and MMSET-catalyzed H4K20me2 recruits the nucleotide excision repair factor XPA to DNA damage sites. *J. Cell Biol.* **2018**, *217*, 527–540. [CrossRef]
153. Gsell, C.; Richly, H.; Coin, F.; Naegeli, H. A chromatin scaffold for DNA damage recognition: How histone methyltransferases prime nucleosomes for repair of ultraviolet light-induced lesions. *Nucleic Acids Res.* **2020**, *48*, 1652–1668. [CrossRef]
154. El-Mahdy, M.A.; Zhu, Q.; Wang, Q.; Wani, G.; Praetorius-Ibba, M.; Wani, A.A. Cullin 4A-mediated proteolysis of DDB2 protein at DNA damage sites regulates in vivo lesion recognition by XPC. *J. Biol. Chem.* **2006**, *281*, 13404–13411. [CrossRef] [PubMed]
155. Tsuge, M.; Masuda, Y.; Kaneoka, H.; Kidani, S.; Miyake, K.; Iijima, S. SUMOylation of damaged DNA-binding protein DDB2. *Biochem. Biophys. Res. Commun.* **2013**, *438*, 26–31. [CrossRef]
156. Han, C.; Zhao, R.; Kroger, J.; He, J.; Wani, G.; Wang, Q.-E.; Wani, A.A. UV radiation-induced SUMOylation of DDB2 regulates nucleotide excision repair. *Carcinogenesis* **2017**, *38*, 976–985. [CrossRef] [PubMed]
157. Molinier, J.; Lechner, E.; Dumbliauskas, E.; Genschik, P. Regulation and Role of Arabidopsis CUL4-DDB1A-DDB2 in Maintaining Genome Integrity upon UV Stress. *PLoS Genet.* **2008**, *4*. [CrossRef] [PubMed]

158. Borgermann, N.; Ackermann, L.; Schwertman, P.; Hendriks, I.A.; Thijssen, K.; Liu, J.C.; Lans, H.; Nielsen, M.L.; Mailand, N. SUMOylation promotes protective responses to DNA-protein crosslinks. *EMBO J.* **2019**, *38*. [CrossRef] [PubMed]
159. Silver, H.R.; Nissley, J.A.; Reed, S.H.; Hou, Y.-M.; Johnson, E.S. A role for SUMO in nucleotide excision repair. *Dna Repair* **2011**, *10*, 1243–1251. [CrossRef]
160. Akita, M.; Tak, Y.-S.; Shimura, T.; Matsumoto, S.; Okuda-Shimizu, Y.; Shimizu, Y.; Nishi, R.; Saitoh, H.; Iwai, S.; Mori, T.; et al. SUMOylation of xeroderma pigmentosum group C protein regulates DNA damage recognition during nucleotide excision repair. *Sci. Rep.* **2015**, *5*, 10984. [CrossRef]
161. Jang, S.; Kumar, N.; Beckwitt, E.C.; Kong, M.; Fouquerel, E.; Rapić-Otrin, V.; Prasad, R.; Watkins, S.C.; Khuu, C.; Majumdar, C.; et al. Damage sensor role of UV-DDB during base excision repair. *Nat. Struct. Mol. Biol.* **2019**, *26*, 695–703. [CrossRef]
162. Kumar, R.; Sabapathy, K. RNF4-A Paradigm for SUMOylation-Mediated Ubiquitination. *Proteomics* **2019**, *19*, e1900185. [CrossRef]
163. Rüthemann, P.; Balbo Pogliano, C.; Codilupi, T.; Garajovà, Z.; Naegeli, H. Chromatin remodeler CHD1 promotes XPC-to-TFIIH handover of nucleosomal UV lesions in nucleotide excision repair. *EMBO J.* **2017**, *36*, 3372–3386. [CrossRef] [PubMed]
164. Fei, J.; Kaczmarek, N.; Luch, A.; Glas, A.; Carell, T.; Naegeli, H. Regulation of nucleotide excision repair by UV-DDB: Prioritization of damage recognition to internucleosomal DNA. *PLoS Biol.* **2011**, *9*, e1001183. [CrossRef] [PubMed]
165. Luijsterburg, M.S.; Lindh, M.; Acs, K.; Vrouwe, M.G.; Pines, A.; van Attikum, H.; Mullenders, L.H.; Dantuma, N.P. DDB2 promotes chromatin decondensation at UV-induced DNA damage. *J. Cell Biol.* **2012**, *197*, 267–281. [CrossRef]
166. Guzder, S.N.; Sung, P.; Prakash, L.; Prakash, S. Yeast Rad7-Rad16 Complex, Specific for the Nucleotide Excision Repair of the Nontranscribed DNA Strand, Is an ATP-dependent DNA Damage Sensor. *J. Biol. Chem.* **1997**, *272*, 21665–21668. [CrossRef] [PubMed]
167. Guzder, S.N.; Sung, P.; Prakash, L.; Prakash, S. Synergistic interaction between yeast nucleotide excision repair factors NEF2 and NEF4 in the binding of ultraviolet-damaged DNA. *J. Biol. Chem.* **1999**, *274*, 24257–24262. [CrossRef] [PubMed]
168. Liu, L.; Huo, Y.; Li, J.; Jiang, T. Crystal structure of the yeast Rad7-Elc1 complex and assembly of the Rad7-Rad16-Elc1-Cul3 complex. *DNA Repair* **2019**, *77*, 1–9. [CrossRef] [PubMed]
169. Lahari, T.; Lazaro, J.; Marcus, J.M.; Schroeder, D.F. RAD7 homologues contribute to Arabidopsis UV tolerance. *Plant Sci.* **2018**, *277*, 267–277. [CrossRef]
170. Liu, Z.; Hong, S.-W.; Escobar, M.; Vierling, E.; Mitchell, D.L.; Mount, D.W.; Hall, J.D. Arabidopsis UVH6, a homolog of human XPD and yeast RAD3 DNA repair genes, functions in DNA repair and is essential for plant growth. *Plant Physiol.* **2003**, *132*, 1405–1414. [CrossRef]
171. Vonarx, E.J.; Tabone, E.K.; Osmond, M.J.; Anderson, H.J.; Kunz, B.A. Arabidopsis homologue of human transcription factor IIH/nucleotide excision repair factor p44 can function in transcription and DNA repair and interacts with AtXPD. *Plant J.* **2006**, *46*, 512–521. [CrossRef]
172. Luo, J.; Cimermancic, P.; Viswanath, S.; Ebmeier, C.C.; Kim, B.; Dehecq, M.; Raman, V.; Greenberg, C.H.; Pellarin, R.; Sali, A.; et al. Architecture of the Human and Yeast General Transcription and DNA Repair Factor TFIIH. *Mol. Cell* **2015**, *59*, 794–806. [CrossRef]
173. Rimel, J.K.; Taatjes, D.J. The essential and multifunctional TFIIH complex. *Protein Sci.* **2018**, *27*, 1018–1037. [CrossRef] [PubMed]
174. Greber, B.J.; Toso, D.B.; Fang, J.; Nogales, E. The complete structure of the human TFIIH core complex. *Elife* **2019**, *8*. [CrossRef] [PubMed]
175. Compe, E.; Egly, J.-M. Nucleotide Excision Repair and Transcriptional Regulation: TFIIH and Beyond. *Annu. Rev. Biochem.* **2016**, *85*, 265–290. [CrossRef] [PubMed]
176. Ghoneim, M.; Spies, M. Direct Correlation of DNA Binding and Single Protein Domain Motion via Dual Illumination Fluorescence Microscopy. *Nano Lett.* **2014**, *14*, 5920–5931. [CrossRef]
177. Sontz, P.A.; Mui, T.P.; Fuss, J.O.; Tainer, J.A.; Barton, J.K. DNA charge transport as a first step in coordinating the detection of lesions by repair proteins. *Proc. Natl. Acad. Sci. USA* **2012**, *109*, 1856–1861. [CrossRef]

178. Mathieu, N.; Kaczmarek, N.; Rüthemann, P.; Luch, A.; Naegeli, H. DNA quality control by a lesion sensor pocket of the xeroderma pigmentosum group D helicase subunit of TFIIH. *Curr. Biol.* **2013**, *23*, 204–212. [CrossRef]
179. Fuss, J.O.; Tsai, C.-L.; Ishida, J.P.; Tainer, J.A. Emerging critical roles of Fe-S clusters in DNA replication and repair. *Biochim. Biophys. Acta* **2015**, *1853*, 1253–1271. [CrossRef]
180. Service, R.F. Live wire. *Science* **2014**, *346*, 1284–1287. [CrossRef]
181. Overmeer, R.M.; Moser, J.; Volker, M.; Kool, H.; Tomkinson, A.E.; van Zeeland, A.A.; Mullenders, L.H.F.; Fousteri, M. Replication protein A safeguards genome integrity by controlling NER incision events. *J. Cell Biol.* **2011**, *192*, 401–415. [CrossRef]
182. Kemp, M.G. Damage removal and gap filling in nucleotide excision repair. *Enzymes* **2019**, *45*, 59–97. [CrossRef]
183. Hodges, A.J.; Plummer, D.A.; Wyrick, J.J. NuA4 acetyltransferase is required for efficient nucleotide excision repair in yeast. *DNA Repair* **2019**, *73*, 91–98. [CrossRef] [PubMed]
184. Schick, S.; Fournier, D.; Thakurela, S.; Sahu, S.K.; Garding, A.; Tiwari, V.K. Dynamics of chromatin accessibility and epigenetic state in response to UV damage. *J. Cell. Sci.* **2015**, *128*, 4380–4394. [CrossRef] [PubMed]
185. Ferrand, J.; Plessier, A.; Polo, S.E. Control of the chromatin response to DNA damage: Histone proteins pull the strings. *Semin. Cell Dev. Biol.* **2020**. [CrossRef] [PubMed]
186. Wang, J.; Li, X.; Do Kim, K.; Scanlon, M.J.; Jackson, S.A.; Springer, N.M.; Yu, J. Genome-wide nucleotide patterns and potential mechanisms of genome divergence following domestication in maize and soybean. *Genome Biol.* **2019**, *20*, 74. [CrossRef]

1.6. Objectives of the Ph.D. project

The formation of DNA damages depends on the chemical environment of the DNA molecule. As part of this environment, the epigenome would be able to act as shield or lightning rod to prevent or enhance the damage formation. In Arabidopsis, photodamage repair processes (DR and GGR) are involved in the maintenance and/or in the reshaping of the methylome landscape, genome-wide and at damaged sites (Graindorge et al. 2019). Thus, it could be assumed that such reshaping might participate in modulating the environment of the DNA to avoid further damage accumulation or to act as epigenetic memory to prevent, for example, undesired TE mobilization and thus ensuring genome integrity. Therefore, it is of prime interest to better understand the mechanisms related to DNA damage formation, recognition, and repair in the different chromatin states. In this project, the emphasis will be on the photodamage repair of constitutive heterochromatin and the dynamics of its associated epigenetic marks (Fig. 10). For this, we will use *Arabidopsis thaliana* as model organism and UV exposure as genotoxic stress to address the following questions:

- Where are formed photodamage?
- Does the epigenetic landscape influence DNA damageability?
- What are the epigenome dynamics during photodamage repair?
- What are the underlying molecular mechanisms?
- Do UV-induced DNA damages generate an epigenetic memory?

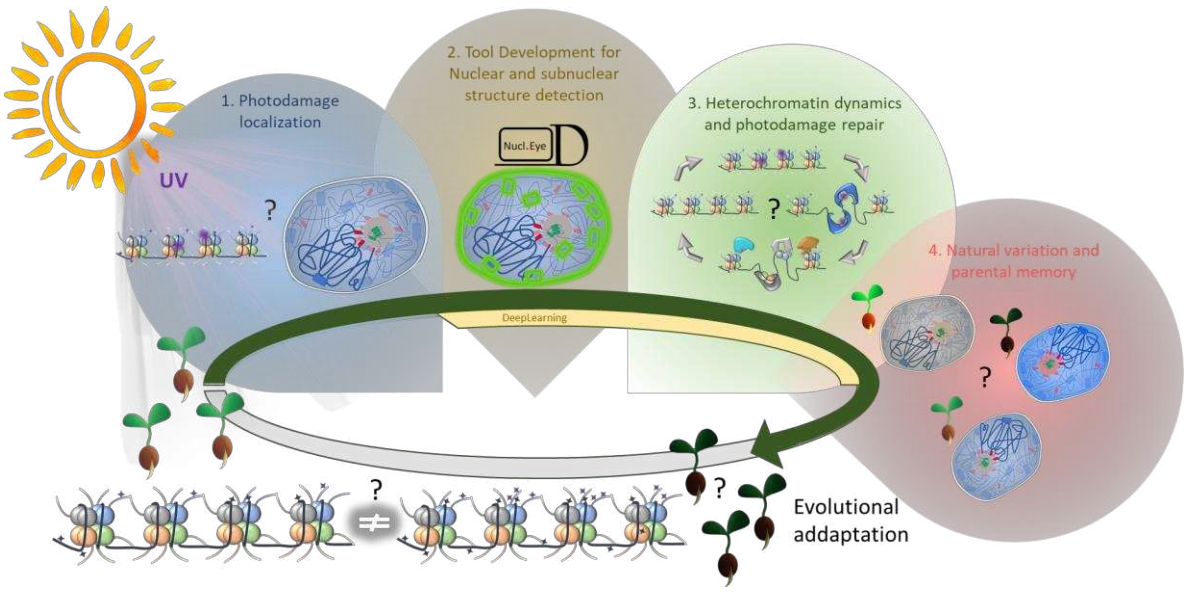

Figure 10: Graphical abstract of the 4 main research axes tackled in the following study.

1.7. References

Adam S, Polo SE, Almouzni G (2013) Transcription recovery after DNA damage requires chromatin priming by the H3.3 histone chaperone HIRA. Cell 155:94–106. https://doi.org/10.1016/j.cell.2013.08.029

Adhireksan Z, Sharma D, Lee PL, Davey CA (2020) Near-atomic resolution structures of interdigitated nucleosome fibres. Nat Commun 11:4747. https://doi.org/10.1038/s41467-020-18533-2

Agorio A, Durand S, Fiume E, Brousse C, Gy I, Simon M, Anava S, Rechavi O, Loudet O, Camilleri C, Bouché N (2017) An Arabidopsis Natural Epiallele Maintained by a Feed-Forward Silencing Loop between Histone and DNA. PLoS Genet 13:e1006551. https://doi.org/10.1371/journal.pgen.1006551

Ali S, Khan N, Xie L (2020) Molecular and Hormonal Regulation of Leaf Morphogenesis in Arabidopsis. International Journal of Molecular Sciences 21:5132. https://doi.org/10.3390/ijms21145132

Antunez-Sanchez J, Naish M, Ramirez-Prado JS, Ohno S, Huang Y, Dawson A, Opassathian K, Manza-Mianza D, Ariel F, Raynaud C, Wibowo A, Daron J, Ueda M, Latrasse D, Slotkin RK, Weigel D, Benhamed M, Gutierrez-Marcos J (2020) A new role for histone demethylases in the maintenance of plant genome integrity. eLife 9:e58533. https://doi.org/10.7554/eLife.58533

Arpòn J, Sakai K, Gaudin V, Andrey P (2021) Spatial modeling of biological patterns shows multiscale organization of Arabidopsis thaliana heterochromatin. Sci Rep 11:323. https://doi.org/10.1038/s41598-020-79158-5

Bannister AJ, Zegerman P, Partridge JF, Miska EA, Thomas JO, Allshire RC, Kouzarides T (2001) Selective recognition of methylated lysine 9 on histone H3 by the HP1 chromo domain. Nature 410:120–124. https://doi.org/10.1038/35065138

Benhamed M, Bertrand C, Servet C, Zhou D-X (2006) Arabidopsis GCN5, HD1, and TAF1/HAF2 interact to regulate histone acetylation required for light-responsive gene expression. Plant Cell 18:2893–2903. https://doi.org/10.1105/tpc.106.043489

Berger F (2019) Emil Heitz, a true epigenetics pioneer. Nat Rev Mol Cell Biol 20:572–572. https://doi.org/10.1038/s41580-019-0161-z

Bi X, Cheng Y-J, Hu B, Ma X, Wu R, Wang J-W, Liu C (2017) Nonrandom domain organization of the Arabidopsis genome at the nuclear periphery. Genome Res 27:1162–1173. https://doi.org/10.1101/gr.215186.116

Biterge B, Schneider R (2014) Histone variants: key players of chromatin. Cell Tissue Res 356:457–466. https://doi.org/10.1007/s00441-014-1862-4

Blevins T, Wang J, Pflieger D, Pontvianne F, Pikaard CS (2017) Hybrid incompatibility caused by an epiallele. Proc Natl Acad Sci U S A 114:3702–3707. https://doi.org/10.1073/pnas.1700368114

Bohlin J, Pettersson JH-O (2019) Evolution of Genomic Base Composition: From Single Cell Microbes to Multicellular Animals. Comput Struct Biotechnol J 17:362–370. https://doi.org/10.1016/j.csbj.2019.03.001

Boltsis I, Grosveld F, Giraud G, Kolovos P (2021) Chromatin Conformation in Development and Disease. Front Cell Dev Biol 9:723859. https://doi.org/10.3389/fcell.2021.723859

Borg M, Papareddy RK, Dombey R, Axelsson E, Nodine MD, Twell D, Berger F (2021) Epigenetic reprogramming rewires transcription during the alternation of generations in Arabidopsis. Elife 10:e61894. https://doi.org/10.7554/eLife.61894

Bourguet P, Picard CL, Yelagandula R, Pélissier T, Lorković ZJ, Feng S, Pouch-Pélissier M-N, Schmücker A, Jacobsen SE, Berger F, Mathieu O (2021) The histone variant H2A.W and linker histone H1 co-regulate heterochromatin accessibility and DNA methylation. Nat Commun 12:2683. https://doi.org/10.1038/s41467-021-22993-5

Braunschweig U, Hogan GJ, Pagie L, van Steensel B (2009) Histone H1 binding is inhibited by histone variant H3.3. EMBO J 28:3635–3645. https://doi.org/10.1038/emboj.2009.301

Cantó-Pastor A, Mason GA, Brady SM, Provart NJ (2021) Arabidopsis bioinformatics: tools and strategies. The Plant Journal 108:1585–1596. https://doi.org/10.1111/tpj.15547

Caro E, Stroud H, Greenberg MVC, Bernatavichute YV, Feng S, Groth M, Vashisht AA, Wohlschlegel J, Jacobsen SE (2012) The SET-domain protein SUVR5 mediates H3K9me2 deposition and silencing at stimulus response genes in a DNA methylation-independent manner. PLoS Genet 8:e1002995. https://doi.org/10.1371/journal.pgen.1002995

Carter B, Bishop B, Ho KK, Huang R, Jia W, Zhang H, Pascuzzi PE, Deal RB, Ogas J (2018) The Chromatin Remodelers PKL and PIE1 Act in an Epigenetic Pathway That Determines H3K27me3 Homeostasis in Arabidopsis. Plant Cell 30:1337–1352. https://doi.org/10.1105/tpc.17.00867

Chan C, Zimmerli L (2019) The Histone Demethylase IBM1 Positively Regulates Arabidopsis Immunity by Control of Defense Gene Expression. Front Plant Sci 10:1587. https://doi.org/10.3389/fpls.2019.01587

Chang Y-N, Zhu C, Jiang J, Zhang H, Zhu J-K, Duan C-G (2020) Epigenetic regulation in plant abiotic stress responses. Journal of Integrative Plant Biology 62:563–580. https://doi.org/10.1111/jipb.12901

Charlesworth B, Barton N (2004) Genome size: does bigger mean worse? Curr Biol 14:R233-235. https://doi.org/10.1016/j.cub.2004.02.054

Chen L-Q, Luo J-H, Cui Z-H, Xue M, Wang L, Zhang X-Y, Pawlowski WP, He Y (2017) ATX3, ATX4, and ATX5 Encode Putative H3K4 Methyltransferases and Are Critical for Plant Development. Plant Physiol 174:1795–1806. https://doi.org/10.1104/pp.16.01944

Cheng K, Xu Y, Yang C, Ouellette L, Niu L, Zhou X, Chu L, Zhuang F, Liu J, Wu H, Charron J-B, Luo M (2020) Histone tales: lysine methylation, a protagonist in Arabidopsis development. J Exp Bot 71:793–807. https://doi.org/10.1093/jxb/erz435

Chodavarapu RK, Feng S, Bernatavichute YV, Chen P-Y, Stroud H, Yu Y, Hetzel JA, Kuo F, Kim J, Cokus SJ, Casero D, Bernal M, Huijser P, Clark AT, Krämer U, Merchant SS, Zhang X, Jacobsen SE, Pellegrini M (2010) Relationship between nucleosome positioning and DNA methylation. Nature 466:388–392. https://doi.org/10.1038/nature09147

Copenhaver GP, Pikaard CS (1996) RFLP and physical mapping with an rDNA-specific endonuclease reveals that nucleolus organizer regions of Arabidopsis thaliana adjoin the telomeres on chromosomes 2 and 4. Plant J 9:259–272. https://doi.org/10.1046/j.1365-313x.1996.09020259.x

Córdoba-Cañero D, Cognat V, Ariza RR, Roldán Arjona T, Molinier J (2017) Dual control of ROS1-mediated active DNA demethylation by DNA damage-binding protein 2 (DDB2). Plant J 92:1170–1181. https://doi.org/10.1111/tpj.13753

Costas C, de la Paz Sanchez M, Stroud H, Yu Y, Oliveros JC, Feng S, Benguria A, López-Vidriero I, Zhang X, Solano R, Jacobsen SE, Gutierrez C (2011) Genome-wide mapping of Arabidopsis thaliana origins of DNA replication and their associated epigenetic marks. Nat Struct Mol Biol 18:395–400. https://doi.org/10.1038/nsmb.1988

Crevillén P, Yang H, Cui X, Greeff C, Trick M, Qiu Q, Cao X, Dean C (2014) Epigenetic reprogramming that prevents transgenerational inheritance of the vernalized state. Nature 515:587–590. https://doi.org/10.1038/nature13722

Davarinejad H, Joshi M, Ait-Hamou N, Munro K, Couture J-F (2019) ATXR5/6 Forms Alternative Protein Complexes with PCNA and the Nucleosome Core Particle. J Mol Biol 431:1370–1379. https://doi.org/10.1016/j.jmb.2019.02.020

Di Stefano M, Nützmann H-W, Marti-Renom MA, Jost D (2021) Polymer modelling unveils the roles of heterochromatin and nucleolar organizing regions in shaping 3D genome organization in Arabidopsis thaliana. Nucleic Acids Res 49:1840–1858. https://doi.org/10.1093/nar/gkaa1275

Ding Y, Fleming AM, Burrows CJ (2017) Sequencing the Mouse Genome for the Oxidatively Modified Base 8-Oxo-7,8-dihydroguanine by OG-Seq. J Am Chem Soc 139:2569–2572. https://doi.org/10.1021/jacs.6b12604

Ding Y, Fleming AM, Burrows CJ (2018) Case studies on potential G-quadruplex-forming sequences from the bacterial orders Deinococcales and Thermales derived from a survey of published genomes. Sci Rep 8:15679. https://doi.org/10.1038/s41598-018-33944-4

Dong J, LeBlanc C, Poulet A, Mermaz B, Villarino G, Webb KM, Joly V, Mendez J, Voigt P, Jacob Y (2021) H3.1K27me1 maintains transcriptional silencing and genome stability by preventing GCN5-mediated histone acetylation. Plant Cell 33:961–979. https://doi.org/10.1093/plcell/koaa027

Dong Q, Li N, Li X, Yuan Z, Xie D, Wang X, Li J, Yu Y, Wang J, Ding B, Zhang Z, Li C, Bian Y, Zhang A, Wu Y, Liu B, Gong L (2018) Genome-wide Hi-C analysis reveals extensive hierarchical chromatin interactions in rice. Plant J 94:1141–1156. https://doi.org/10.1111/tpj.13925

Duc C, Benoit M, Détourné G, Simon L, Poulet A, Jung M, Veluchamy A, Latrasse D, Le Goff S, Cotterell S, Tatout C, Benhamed M, Probst AV (2017) Arabidopsis ATRX Modulates H3.3 Occupancy and Fine-Tunes Gene Expression. Plant Cell 29:1773–1793. https://doi.org/10.1105/tpc.16.00877

Duc C, Benoit M, Le Goff S, Simon L, Poulet A, Cotterell S, Tatout C, Probst AV (2015) The histone chaperone complex HIR maintains nucleosome occupancy and counterbalances impaired histone deposition in CAF-1 complex mutants. Plant J 81:707–722. https://doi.org/10.1111/tpj.12758

Durand S, Bouché N, Perez Strand E, Loudet O, Camilleri C (2012) Rapid establishment of genetic incompatibility through natural epigenetic variation. Curr Biol 22:326–331. https://doi.org/10.1016/j.cub.2011.12.054

Dutta A, Choudhary P, Caruana J, Raina R (2017) JMJ27, an Arabidopsis H3K9 histone demethylase, modulates defense against Pseudomonas syringae and flowering time. Plant J 91:1015–1028. https://doi.org/10.1111/tpj.13623

Dyer MA, Qadeer ZA, Valle-Garcia D, Bernstein E (2017) ATRX and DAXX: Mechanisms and Mutations. Cold Spring Harb Perspect Med 7:a026567. https://doi.org/10.1101/cshperspect.a026567

Ebbs ML, Bender J (2006) Locus-specific control of DNA methylation by the Arabidopsis SUVH5 histone methyltransferase. Plant Cell 18:1166–1176. https://doi.org/10.1105/tpc.106.041400

Fan D, Dai Y, Wang X, Wang Z, He H, Yang H, Cao Y, Deng XW, Ma L (2012) IBM1, a JmjC domain-containing histone demethylase, is involved in the regulation of RNA-directed DNA methylation through the epigenetic control of RDR2 and DCL3 expression in Arabidopsis. Nucleic Acids Res 40:8905–8916. https://doi.org/10.1093/nar/gks647

Feng S, Cokus SJ, Schubert V, Zhai J, Pellegrini M, Jacobsen SE (2014) Genome-wide Hi-C analyses in wild type and mutants reveal high-resolution chromatin interactions in Arabidopsis. Mol Cell 55:694–707. https://doi.org/10.1016/j.molcel.2014.07.008

Fiorucci A-S, Bourbousse C, Concia L, Rougée M, Deton-Cabanillas A-F, Zabulon G, Layat E, Latrasse D, Kim SK, Chaumont N, Lombard B, Stroebel D, Lemoine S, Mohammad A, Blugeon C, Loew D, Bailly C, Bowler C, Benhamed M, Barneche F (2019) Arabidopsis S2Lb links AtCOMPASS-like and SDG2 activity in H3K4me3 independently from histone H2B monoubiquitination. Genome Biol 20:100. https://doi.org/10.1186/s13059-019-1705-4

Fleming AM, Ding Y, Burrows CJ (2017a) Oxidative DNA damage is epigenetic by regulating gene transcription via base excision repair. Proc Natl Acad Sci U S A 114:2604–2609. https://doi.org/10.1073/pnas.1619809114

Fleming AM, Zhu J, Ding Y, Burrows CJ (2017b) 8-Oxo-7,8-dihydroguanine in the Context of a Gene Promoter G-Quadruplex Is an On-Off Switch for Transcription. ACS Chem Biol 12:2417–2426. https://doi.org/10.1021/acschembio.7b00636

Fleming AM, Zhu J, Howpay Manage SA, Burrows CJ (2019) Human NEIL3 Gene Expression Regulated by Epigenetic-Like Oxidative DNA Modification. J Am Chem Soc 141:11036–11049. https://doi.org/10.1021/jacs.9b01847

Fortuny A, Chansard A, Caron P, Chevallier O, Leroy O, Renaud O, Polo SE (2021) Imaging the response to DNA damage in heterochromatin domains reveals core principles of heterochromatin maintenance. Nat Commun 12:2428. https://doi.org/10.1038/s41467-021-22575-5

Fransz P, De Jong JH, Lysak M, Castiglione MR, Schubert I (2002) Interphase chromosomes in Arabidopsis are organized as well defined chromocenters from which euchromatin loops emanate. Proc Natl Acad Sci U S A 99:14584–14589. https://doi.org/10.1073/pnas.212325299

Fransz PF, Armstrong S, de Jong JH, Parnell LD, van Drunen C, Dean C, Zabel P, Bisseling T, Jones GH (2000) Integrated cytogenetic map of chromosome arm 4S of A. thaliana: structural organization of heterochromatic knob and centromere region. Cell 100:367–376. https://doi.org/10.1016/s0092-8674(00)80672-8

Fromm M, Avramova Z (2014) ATX1/AtCOMPASS and the H3K4me3 marks: how do they activate Arabidopsis genes? Curr Opin Plant Biol 21:75–82. https://doi.org/10.1016/j.pbi.2014.07.004

Fulgione A, Hancock AM (2018) Archaic lineages broaden our view on the history of Arabidopsis thaliana. New Phytologist 219:1194–1198. https://doi.org/10.1111/nph.15244

Fulgione A, Koornneef M, Roux F, Hermisson J, Hancock AM (2018) Madeiran Arabidopsis thaliana Reveals Ancient Long-Range Colonization and Clarifies Demography in Eurasia. Molecular Biology and Evolution 35:564–574. https://doi.org/10.1093/molbev/msx300

Gan E-S, Xu Y, Wong J-Y, Geraldine Goh J, Sun B, Wee W-Y, Huang J, Ito T (2014) Jumonji demethylases moderate precocious flowering at elevated temperature via regulation of FLC in Arabidopsis. Nat Commun 5:5098. https://doi.org/10.1038/ncomms6098

Gehring M, Missirian V, Henikoff S (2011) Genomic analysis of parent-of-origin allelic expression in Arabidopsis thaliana seeds. PLoS One 6:e23687. https://doi.org/10.1371/journal.pone.0023687

Gibney ER, Nolan CM (2010) Epigenetics and gene expression. Heredity (Edinb) 105:4–13. https://doi.org/10.1038/hdy.2010.54

Gorini F, Scala G, Cooke MS, Majello B, Amente S (2021) Towards a comprehensive view of 8-oxo-7,8-dihydro-2'-deoxyguanosine: Highlighting the intertwined roles of DNA damage and epigenetics in genomic instability. DNA Repair (Amst) 97:103027. https://doi.org/10.1016/j.dnarep.2020.103027

Gorini F, Scala G, Di Palo G, Dellino GI, Cocozza S, Pelicci PG, Lania L, Majello B, Amente S (2020) The genomic landscape of 8-oxodG reveals enrichment at specific inherently fragile promoters. Nucleic Acids Res 48:4309–4324. https://doi.org/10.1093/nar/gkaa175

Graindorge S, Cognat V, Johann to Berens P, Mutterer J, Molinier J (2019) Photodamage repair pathways contribute to the accurate maintenance of the DNA methylome landscape upon UV exposure. PLoS Genet 15:e1008476. https://doi.org/10.1371/journal.pgen.1008476

Green CM, Almouzni G (2002) When repair meets chromatin. First in series on chromatin dynamics. EMBO Rep 3:28–33. https://doi.org/10.1093/embo-reports/kvf005

Grob S, Grossniklaus U (2019) Invasive DNA elements modify the nuclear architecture of their insertion site by KNOT-linked silencing in Arabidopsis thaliana. Genome Biol 20:120. https://doi.org/10.1186/s13059-019-1722-3

Grob S, Schmid MW, Grossniklaus U (2014) Hi-C analysis in Arabidopsis identifies the KNOT, a structure with similarities to the flamenco locus of Drosophila. Mol Cell 55:678–693. https://doi.org/10.1016/j.molcel.2014.07.009

Guo L, Cao X, Liu Y, Li J, Li Y, Li D, Zhang K, Gao C, Dong A, Liu X (2018) A chromatin loop represses WUSCHEL expression in Arabidopsis. Plant J 94:1083–1097. https://doi.org/10.1111/tpj.13921

Guo Y, Xu Q, Canzio D, Shou J, Li J, Gorkin DU, Jung I, Wu H, Zhai Y, Tang Y, Lu Y, Wu Y, Jia Z, Li W, Zhang MQ, Ren B, Krainer AR, Maniatis T, Wu Q (2015) CRISPR Inversion of CTCF Sites Alters Genome Topology and Enhancer/Promoter Function. Cell 162:900–910. https://doi.org/10.1016/j.cell.2015.07.038

Hauser M-T, Aufsatz W, Jonak C, Luschnig C (2011) Transgenerational epigenetic inheritance in plants. Biochim Biophys Acta 1809:459–468. https://doi.org/10.1016/j.bbagrm.2011.03.007

He L, Wu W, Zinta G, Yang L, Wang D, Liu R, Zhang H, Zheng Z, Huang H, Zhang Q, Zhu J-K (2018) A naturally occurring epiallele associates with leaf senescence and local climate adaptation in Arabidopsis accessions. Nat Commun 9:460. https://doi.org/10.1038/s41467-018-02839-3

Holowatyj A, Yang Z-Q, Pile LA (2015) Histone lysine demethylases in Drosophila melanogaster. Fly (Austin) 9:36–44. https://doi.org/10.1080/19336934.2015.1074787

Hosouchi T, Kumekawa N, Tsuruoka H, Kotani H (2002) Physical Map-Based Sizes of the Centromeric Regions of Arabidopsis thaliana Chromosomes 1, 2, and 3. DNA Research 9:117–121. https://doi.org/10.1093/dnares/9.4.117

Howe FS, Fischl H, Murray SC, Mellor J (2017) Is H3K4me3 instructive for transcription activation? Bioessays 39:1–12. https://doi.org/10.1002/bies.201600095

Hu B, Wang N, Bi X, Karaaslan ES, Weber A-L, Zhu W, Berendzen KW, Liu C (2019a) Plant lamin-like proteins mediate chromatin tethering at the nuclear periphery. Genome Biol 20:87. https://doi.org/10.1186/s13059-019-1694-3

Hu L, Xu Z, Wang M, Fan R, Yuan D, Wu B, Wu H, Qin X, Yan L, Tan L, Sim S, Li W, Saski CA, Daniell H, Wendel JF, Lindsey K, Zhang X, Hao C, Jin S (2019b) The chromosome-scale reference genome of black pepper provides insight into piperine biosynthesis. Nat Commun 10:4702. https://doi.org/10.1038/s41467-019-12607-6

Hummel G, Berr A, Graindorge S, Cognat V, Ubrig E, Pflieger D, Molinier J, Drouard L (2020) Epigenetic silencing of clustered tRNA genes in Arabidopsis. Nucleic Acids Research 48:10297–10312. https://doi.org/10.1093/nar/gkaa766

Hung F-Y, Chen J-H, Feng Y-R, Lai Y-C, Yang S, Wu K (2020) Arabidopsis JMJ29 is involved in trichome development by regulating the core trichome initiation gene GLABRA3. The Plant Journal 103:1735–1743. https://doi.org/10.1111/tpj.14858

Hung F-Y, Lai Y-C, Wang J, Feng Y-R, Shih Y-H, Chen J-H, Sun H-C, Yang S, Li C, Wu K (2021) The Arabidopsis histone demethylase JMJ28 regulates CONSTANS by interacting with FBH transcription factors. Plant Cell 33:1196–1211. https://doi.org/10.1093/plcell/koab014

Ismail IH, Hendzel MJ (2008) The gamma-H2A.X: is it just a surrogate marker of double-strand breaks or much more? Environ Mol Mutagen 49:73–82. https://doi.org/10.1002/em.20358

Jabre I, Chaudhary S, Guo W, Kalyna M, Reddy ASN, Chen W, Zhang R, Wilson C, Syed NH (2021) Differential nucleosome occupancy modulates alternative splicing in Arabidopsis thaliana. New Phytol 229:1937–1945. https://doi.org/10.1111/nph.17062

Jackson JP, Johnson L, Jasencakova Z, Zhang X, PerezBurgos L, Singh PB, Cheng X, Schubert I, Jenuwein T, Jacobsen SE (2004) Dimethylation of histone H3 lysine 9 is a critical mark for DNA methylation and gene silencing in Arabidopsis thaliana. Chromosoma 112:308–315. https://doi.org/10.1007/s00412-004-0275-7

Jackson JP, Lindroth AM, Cao X, Jacobsen SE (2002) Control of CpNpG DNA methylation by the KRYPTONITE histone H3 methyltransferase. Nature 416:556–560. https://doi.org/10.1038/nature731

Jacob Y, Bergamin E, Donoghue MTA, Mongeon V, LeBlanc C, Voigt P, Underwood CJ, Brunzelle JS, Michaels SD, Reinberg D, Couture J-F, Martienssen RA (2014) Selective methylation of histone H3 variant H3.1 regulates heterochromatin replication. Science 343:1249–1253. https://doi.org/10.1126/science.1248357

Jacob Y, Feng S, LeBlanc CA, Bernatavichute YV, Stroud H, Cokus S, Johnson LM, Pellegrini M, Jacobsen SE, Michaels SD (2009) ATXR5 and ATXR6 are H3K27 monomethyltransferases required for chromatin structure and gene silencing. Nat Struct Mol Biol 16:763–768. https://doi.org/10.1038/nsmb.1611

Jacob Y, Michaels SD (2009) H3K27me1 is E(z) in animals, but not in plants. Epigenetics 4:366–369. https://doi.org/10.4161/epi.4.6.9713

Jacob Y, Stroud H, LeBlanc C, Feng S, Zhuo L, Caro E, Hassel C, Gutierrez C, Michaels SD, Jacobsen SE (2010) Regulation of heterochromatic DNA replication by histone H3 lysine 27 methyltransferases. Nature 466:987–991. https://doi.org/10.1038/nature09290

Jacobs SA, Taverna SD, Zhang Y, Briggs SD, Li J, Eissenberg JC, Allis CD, Khorasanizadeh S (2001) Specificity of the HP1 chromo domain for the methylated N-terminus of histone H3. EMBO J 20:5232–5241. https://doi.org/10.1093/emboj/20.18.5232

Jampala P, Garhewal A, Lodha M (2021) Functions of long non-coding RNA in Arabidopsis thaliana. Plant Signal Behav 16:1925440. https://doi.org/10.1080/15592324.2021.1925440

Jang S, Kumar N, Beckwitt EC, Kong M, Fouquerel E, Rapić-Otrin V, Prasad R, Watkins SC, Khuu C, Majumdar C, David SS, Wilson SH, Bruchez MP, Opresko PL, Van Houten B (2019) Damage sensor role of UV-DDB during base excision repair. Nat Struct Mol Biol 26:695–703. https://doi.org/10.1038/s41594-019-0261-7

Janssen A, Colmenares SU, Lee T, Karpen GH (2019) Timely double-strand break repair and pathway choice in pericentromeric heterochromatin depend on the histone demethylase dKDM4A. Genes Dev 33:103–115. https://doi.org/10.1101/gad.317537.118

Jansson K, Blomberg A, Sunnerhagen P, Alm Rosenblad M (2010) Evolutionary loss of 8-oxo-G repair components among eukaryotes. Genome Integr 1:12. https://doi.org/10.1186/2041-9414-1-12

Jégu T, Latrasse D, Delarue M, Hirt H, Domenichini S, Ariel F, Crespi M, Bergounioux C, Raynaud C, Benhamed M (2014) The BAF60 subunit of the SWI/SNF chromatin-remodeling complex directly controls the formation of a gene loop at FLOWERING LOCUS C in Arabidopsis. Plant Cell 26:538–551. https://doi.org/10.1105/tpc.113.114454

Jiang C, Mithani A, Belfield EJ, Mott R, Hurst LD, Harberd NP (2014) Environmentally responsive genome-wide accumulation of de novo Arabidopsis thaliana mutations and epimutations. Genome Res 24:1821–1829. https://doi.org/10.1101/gr.177659.114

Jiang D, Berger F (2017) DNA replication-coupled histone modification maintains Polycomb gene silencing in plants. Science 357:1146–1149. https://doi.org/10.1126/science.aan4965

Jiang D, Borg M, Lorković ZJ, Montgomery SA, Osakabe A, Yelagandula R, Axelsson E, Berger F (2020) The evolution and functional divergence of the histone H2B family in plants. PLOS Genetics 16:e1008964. https://doi.org/10.1371/journal.pgen.1008964

Jiang D, Yang W, He Y, Amasino RM (2007) Arabidopsis relatives of the human lysine-specific Demethylase1 repress the expression of FWA and FLOWERING LOCUS C and thus promote the floral transition. Plant Cell 19:2975–2987. https://doi.org/10.1105/tpc.107.052373

Jiang J, Liu J, Sanders D, Qian S, Ren W, Song J, Liu F, Zhong X (2021) UVR8 interacts with de novo DNA methyltransferase and suppresses DNA methylation in Arabidopsis. Nat Plants 7:184–197. https://doi.org/10.1038/s41477-020-00843-4

Jih G, Iglesias N, Currie MA, Bhanu NV, Paulo JA, Gygi SP, Garcia BA, Moazed D (2017) Unique roles for histone H3K9me states in RNAi and heritable silencing of transcription. Nature 547:463–467. https://doi.org/10.1038/nature23267

Johann to Berens P, Molinier J (2020) Formation and Recognition of UV-Induced DNA Damage within Genome Complexity. Int J Mol Sci 21. https://doi.org/10.3390/ijms21186689

Kawakatsu T, Huang S-SC, Jupe F, Sasaki E, Schmitz RJ, Urich MA, Castanon R, Nery JR, Barragan C, He Y, Chen H, Dubin M, Lee C-R, Wang C, Bemm F, Becker C, O'Neil R, O'Malley RC, Quarless DX, 1001 Genomes Consortium, Schork NJ, Weigel D, Nordborg M, Ecker JR (2016) Epigenomic Diversity in a Global Collection of Arabidopsis thaliana Accessions. Cell 166:492–505. https://doi.org/10.1016/j.cell.2016.06.044

Kawashima T, Berger F (2014) Epigenetic reprogramming in plant sexual reproduction. Nat Rev Genet 15:613–624. https://doi.org/10.1038/nrg3685

Kawashima T, Lorković ZJ, Nishihama R, Ishizaki K, Axelsson E, Yelagandula R, Kohchi T, Berger F (2015) Diversification of histone H2A variants during plant evolution. Trends Plant Sci 20:419–425. https://doi.org/10.1016/j.tplants.2015.04.005

Khadka J, Pesok A, Grafi G (2020) Plant Histone HTB (H2B) Variants in Regulating Chromatin Structure and Function. Plants 9:1435. https://doi.org/10.3390/plants9111435

Kharchenko PV, Alekseyenko AA, Schwartz YB, Minoda A, Riddle NC, Ernst J, Sabo PJ, Larschan E, Gorchakov AA, Gu T, Linder-Basso D, Plachetka A, Shanower G, Tolstorukov MY, Luquette LJ, Xi R, Jung YL, Park RW, Bishop EP, Canfield TK, Sandstrom R, Thurman RE, MacAlpine DM, Stamatoyannopoulos JA, Kellis M, Elgin SCR, Kuroda MI, Pirrotta V, Karpen GH, Park PJ (2011) Comprehensive analysis of the chromatin landscape in Drosophila melanogaster. Nature 471:480–485. https://doi.org/10.1038/nature09725

Kim D-H, Sung S (2013) Coordination of the vernalization response through a VIN3 and FLC gene family regulatory network in Arabidopsis. Plant Cell 25:454–469. https://doi.org/10.1105/tpc.112.104760

Kind J, Pagie L, Ortabozkoyun H, Boyle S, de Vries SS, Janssen H, Amendola M, Nolen LD, Bickmore WA, van Steensel B (2013) Single-cell dynamics of genome-nuclear lamina interactions. Cell 153:178–192. https://doi.org/10.1016/j.cell.2013.02.028

Koornneef M, Meinke D (2010) The development of Arabidopsis as a model plant. The Plant Journal 61:909–921. https://doi.org/10.1111/j.1365-313X.2009.04086.x

Korotkov A, Seluanov A, Gorbunova V (2021) Sirtuin 6: linking longevity with genome and epigenome stability. Trends Cell Biol 31:994–1006. https://doi.org/10.1016/j.tcb.2021.06.009

Koyama M, Kurumizaka H (2018) Structural diversity of the nucleosome. J Biochem 163:85–95. https://doi.org/10.1093/jb/mvx081

Kradolfer D, Hennig L, Köhler C (2013) Increased Maternal Genome Dosage Bypasses the Requirement of the FIS Polycomb Repressive Complex 2 in Arabidopsis Seed Development. PLOS Genetics 9:e1003163. https://doi.org/10.1371/journal.pgen.1003163

Krause K, Turck F (2018) Plant H3K27me3 has finally found its readers. Nat Genet 50:1206–1208. https://doi.org/10.1038/s41588-018-0201-1

Kuzmichev A, Nishioka K, Erdjument-Bromage H, Tempst P, Reinberg D (2002) Histone methyltransferase activity associated with a human multiprotein complex containing the Enhancer of Zeste protein. Genes Dev 16:2893–2905. https://doi.org/10.1101/gad.1035902

Laibach F (1943) Arabidopsis thaliana (L.) Heynh. als Objekt für genetische und entwicklungsphysiologische Untersuchungen. https://scholar-google-com.scd-rproxy.u-strasbg.fr/scholar_lookup?title=Arabidopsis%20thaliana%20%28L.%29%20Heynh.%20als%20Objekt%20f%C3%BCr%20genetische%20und%20entwicklungsphysiologische%20Untersuchungen.&journal=Bot%20Arch&volume=44&pages=439-455&publication_year=1943&author=Laibach%2CF. Accessed 14 Feb 2022

Laibach F Zur Frage nach der Individualität der Chromosomen im Pflanzenreich. 22

Law JA, Du J, Hale CJ, Feng S, Krajewski K, Palanca AMS, Strahl BD, Patel DJ, Jacobsen SE (2013) Polymerase IV occupancy at RNA-directed DNA methylation sites requires SHH1. Nature 498:385–389. https://doi.org/10.1038/nature12178

Law JA, Jacobsen SE (2010) Establishing, maintaining and modifying DNA methylation patterns in plants and animals. Nature Reviews Genetics 11:204–220. https://doi.org/10.1038/nrg2719

Le Goff S, Keçeli BN, Jeřábková H, Heckmann S, Rutten T, Cotterell S, Schubert V, Roitinger E, Mechtler K, Franklin FCH, Tatout C, Houben A, Geelen D, Probst AV, Lermontova I (2020) The H3 histone chaperone NASPSIM3 escorts CenH3 in Arabidopsis. Plant J 101:71–86. https://doi.org/10.1111/tpj.14518

Lee K, Park O-S, Seo PJ (2018) JMJ30-mediated demethylation of H3K9me3 drives tissue identity changes to promote callus formation in Arabidopsis. Plant J 95:961–975. https://doi.org/10.1111/tpj.14002

Leng X, Thomas Q, Rasmussen SH, Marquardt S (2020) A G(enomic)P(ositioning)S(ystem) for Plant RNAPII Transcription. Trends Plant Sci 25:744–764. https://doi.org/10.1016/j.tplants.2020.03.005

Lermontova I, Sandmann M, Demidov D (2014) Centromeres and kinetochores of Brassicaceae. Chromosome Res 22:135–152. https://doi.org/10.1007/s10577-014-9422-z

Leung J, Gaudin V (2020) Who Rules the Cell? An Epi-Tale of Histone, DNA, RNA, and the Metabolic Deep State. Frontiers in Plant Science 11

Li C, Gu L, Gao L, Chen C, Wei C-Q, Qiu Q, Chien C-W, Wang S, Jiang L, Ai L-F, Chen C-Y, Yang S, Nguyen V, Qi Y, Snyder MP, Burlingame AL, Kohalmi SE, Huang S, Cao X, Wang Z-Y, Wu K, Chen X, Cui Y (2016) Concerted genomic targeting of H3K27 demethylase REF6 and chromatin-remodeling ATPase BRM in Arabidopsis. Nat Genet 48:687–693. https://doi.org/10.1038/ng.3555

Li G, Zhou L (2013) Genome-wide identification of chromatin transitional regions reveals diverse mechanisms defining the boundary of facultative heterochromatin. PLoS One 8:e67156. https://doi.org/10.1371/journal.pone.0067156

Li X, Harris CJ, Zhong Z, Chen W, Liu R, Jia B, Wang Z, Li S, Jacobsen SE, Du J (2018) Mechanistic insights into plant SUVH family H3K9 methyltransferases and their binding to context-biased non-CG DNA methylation. Proc Natl Acad Sci U S A 115:E8793–E8802. https://doi.org/10.1073/pnas.1809841115

Liu F, Quesada V, Crevillén P, Bäurle I, Swiezewski S, Dean C (2007) The Arabidopsis RNA-binding protein FCA requires a lysine-specific demethylase 1 homolog to downregulate FLC. Mol Cell 28:398–407. https://doi.org/10.1016/j.molcel.2007.10.018

Liu M-J, Seddon AE, Tsai ZT-Y, Major IT, Floer M, Howe GA, Shiu S-H (2015) Determinants of nucleosome positioning and their influence on plant gene expression. Genome Res 25:1182–1195. https://doi.org/10.1101/gr.188680.114

Liu P, Zhang S, Zhou B, Luo X, Zhou XF, Cai B, Jin YH, Niu D, Lin J, Cao X, Jin JB (2019) The Histone H3K4 Demethylase JMJ16 Represses Leaf Senescence in Arabidopsis. Plant Cell 31:430–443. https://doi.org/10.1105/tpc.18.00693

Liu Y, Tian T, Zhang K, You Q, Yan H, Zhao N, Yi X, Xu W, Su Z (2018) PCSD: a plant chromatin state database. Nucleic Acids Res 46:D1157–D1167. https://doi.org/10.1093/nar/gkx919

Lo SJ, Lee C-C, Lai H-J (2006) The nucleolus: reviewing oldies to have new understandings. Cell Res 16:530–538. https://doi.org/10.1038/sj.cr.7310070

Lu F, Cui X, Zhang S, Jenuwein T, Cao X (2011) Arabidopsis REF6 is a histone H3 lysine 27 demethylase. Nat Genet 43:715–719. https://doi.org/10.1038/ng.854

Lu F, Cui X, Zhang S, Liu C, Cao X (2010) JMJ14 is an H3K4 demethylase regulating flowering time in Arabidopsis. Cell Res 20:387–390. https://doi.org/10.1038/cr.2010.27

Lynch M, Conery JS (2003) The origins of genome complexity. Science 302:1401–1404. https://doi.org/10.1126/science.1089370

Ma Z, Castillo-González C, Wang Z, Sun D, Hu X, Shen X, Potok ME, Zhang X (2018) Arabidopsis Serrate Coordinates Histone Methyltransferases ATXR5/6 and RNA Processing Factor RDR6 to Regulate Transposon Expression. Dev Cell 45:769-784.e6. https://doi.org/10.1016/j.devcel.2018.05.023

Machida S, Takizawa Y, Ishimaru M, Sugita Y, Sekine S, Nakayama J-I, Wolf M, Kurumizaka H (2018) Structural Basis of Heterochromatin Formation by Human HP1. Mol Cell 69:385-397.e8. https://doi.org/10.1016/j.molcel.2017.12.011

Maumus F, Quesneville H (2014) Deep Investigation of Arabidopsis thaliana Junk DNA Reveals a Continuum between Repetitive Elements and Genomic Dark Matter. PLoS ONE 9:e94101. https://doi.org/10.1371/journal.pone.0094101

Meinke DW, Cherry JM, Dean C, Rounsley SD, Koornneef M (1998) Arabidopsis thaliana: a model plant for genome analysis. Science 282:662, 679–682. https://doi.org/10.1126/science.282.5389.662

Michael TP, Jupe F, Bemm F, Motley ST, Sandoval JP, Lanz C, Loudet O, Weigel D, Ecker JR (2018) High contiguity Arabidopsis thaliana genome assembly with a single nanopore flow cell. Nat Commun 9:541. https://doi.org/10.1038/s41467-018-03016-2

Mikulski P, Hohenstatt ML, Farrona S, Smaczniak C, Stahl Y, Kalyanikrishna null, Kaufmann K, Angenent G, Schubert D (2019) The Chromatin-Associated Protein PWO1 Interacts with Plant Nuclear Lamin-like Components to Regulate Nuclear Size. Plant Cell 31:1141–1154. https://doi.org/10.1105/tpc.18.00663

Miura A, Nakamura M, Inagaki S, Kobayashi A, Saze H, Kakutani T (2009) An Arabidopsis jmjC domain protein protects transcribed genes from DNA methylation at CHG sites. EMBO J 28:1078–1086. https://doi.org/10.1038/emboj.2009.59

Mizuguchi G, Shen X, Landry J, Wu W-H, Sen S, Wu C (2004) ATP-driven exchange of histone H2AZ variant catalyzed by SWR1 chromatin remodeling complex. Science 303:343–348. https://doi.org/10.1126/science.1090701

Moggs JG, Grandi P, Quivy JP, Jónsson ZO, Hübscher U, Becker PB, Almouzni G (2000) A CAF-1-PCNA-mediated chromatin assembly pathway triggered by sensing DNA damage. Mol Cell Biol 20:1206–1218. https://doi.org/10.1128/MCB.20.4.1206-1218.2000

Mosher RA (2021) Small RNAs on the move in male germ cells. Science 373:26–27. https://doi.org/10.1126/science.abj5020

Muñoz-Viana R, Wildhaber T, Trejo-Arellano MS, Mozgová I, Hennig L (2017) Arabidopsis Chromatin Assembly Factor 1 is required for occupancy and position of a subset of nucleosomes. The Plant Journal 92:363–374. https://doi.org/10.1111/tpj.13658

Nagaki K, Talbert PB, Zhong CX, Dawe RK, Henikoff S, Jiang J (2003) Chromatin immunoprecipitation reveals that the 180-bp satellite repeat is the key functional DNA element of Arabidopsis thaliana centromeres. Genetics 163:1221–1225. https://doi.org/10.1093/genetics/163.3.1221

Naish M, Alonge M, Wlodzimierz P, Tock AJ, Abramson BW, Schmücker A, Mandáková T, Jamge B, Lambing C, Kuo P, Yelina N, Hartwick N, Colt K, Smith LM, Ton J, Kakutani T, Martienssen RA, Schneeberger K, Lysak MA, Berger F, Bousios A, Michael TP, Schatz MC, Henderson IR (2021) The genetic and epigenetic landscape of the Arabidopsis centromeres. Science 374:eabi7489. https://doi.org/10.1126/science.abi7489

Nicetto D, Zaret KS (2019) Role of H3K9me3 heterochromatin in cell identity establishment and maintenance. Curr Opin Genet Dev 55:1–10. https://doi.org/10.1016/j.gde.2019.04.013

Okada T, Endo M, Singh MB, Bhalla PL (2005) Analysis of the histone H3 gene family in Arabidopsis and identification of the male-gamete-specific variant AtMGH3. Plant J 44:557–568. https://doi.org/10.1111/j.1365-313X.2005.02554.x

Oliveira LC, Torres GA (2018) Plant centromeres: genetics, epigenetics and evolution. Mol Biol Rep 45:1491–1497. https://doi.org/10.1007/s11033-018-4284-7

Ono A, Kinoshita T (2021) Epigenetics and plant reproduction: Multiple steps for responsibly handling succession. Curr Opin Plant Biol 61:102032. https://doi.org/10.1016/j.pbi.2021.102032

Osakabe A, Jamge B, Axelsson E, Montgomery SA, Akimcheva S, Kuehn AL, Pisupati R, Lorković ZJ, Yelagandula R, Kakutani T, Berger F (2021) The chromatin remodeler DDM1 prevents transposon mobility through deposition of histone variant H2A.W. Nat Cell Biol 23:391–400. https://doi.org/10.1038/s41556-021-00658-1

Osakabe A, Lorkovic ZJ, Kobayashi W, Tachiwana H, Yelagandula R, Kurumizaka H, Berger F (2018) Histone H2A variants confer specific properties to nucleosomes and impact on chromatin accessibility. Nucleic Acids Res 46:7675–7685. https://doi.org/10.1093/nar/gky540

Pan L, Hao W, Zheng X, Zeng X, Ahmed Abbasi A, Boldogh I, Ba X (2017) OGG1-DNA interactions facilitate NF-κB binding to DNA targets. Sci Rep 7:43297. https://doi.org/10.1038/srep43297

Pan L, Zhu B, Hao W, Zeng X, Vlahopoulos SA, Hazra TK, Hegde ML, Radak Z, Bacsi A, Brasier AR, Ba X, Boldogh I (2016) Oxidized Guanine Base Lesions Function in 8-Oxoguanine DNA Glycosylase-1-mediated Epigenetic Regulation of Nuclear Factor κB-driven Gene Expression. J Biol Chem 291:25553–25566. https://doi.org/10.1074/jbc.M116.751453

Pasha A, Subramaniam S, Cleary A, Chen X, Berardini T, Farmer A, Town C, Provart N (2020) Araport Lives: An Updated Framework for Arabidopsis Bioinformatics. Plant Cell 32:2683–2686. https://doi.org/10.1105/tpc.20.00358

Pass DA, Sornay E, Marchbank A, Crawford MR, Paszkiewicz K, Kent NA, Murray JAH (2017) Genome-wide chromatin mapping with size resolution reveals a dynamic sub-nucleosomal landscape in Arabidopsis. PLOS Genetics 13:e1006988. https://doi.org/10.1371/journal.pgen.1006988

Passarge E (1979) Emil Heitz and the concept of heterochromatin: longitudinal chromosome differentiation was recognized fifty years ago. Am J Hum Genet 31:106–115

Picart-Picolo A, Picault N, Pontvianne F (2019) Ribosomal RNA genes shape chromatin domains associating with the nucleolus. Nucleus 10:67–72. https://doi.org/10.1080/19491034.2019.1591106

Pickersgill H, Kalverda B, de Wit E, Talhout W, Fornerod M, van Steensel B (2006) Characterization of the Drosophila melanogaster genome at the nuclear lamina. Nat Genet 38:1005–1014. https://doi.org/10.1038/ng1852

Pignatta D, Novitzky K, Satyaki PRV, Gehring M (2018) A variably imprinted epiallele impacts seed development. PLoS Genet 14:e1007469. https://doi.org/10.1371/journal.pgen.1007469

Polo SE, Almouzni G (2015) Chromatin dynamics after DNA damage: The legacy of the access-repair-restore model. DNA Repair (Amst) 36:114–121. https://doi.org/10.1016/j.dnarep.2015.09.014

Pontvianne F, Carpentier M-C, Durut N, Pavlištová V, Jaške K, Schořová Š, Parrinello H, Rohmer M, Pikaard CS, Fojtová M, Fajkus J, Sáez-Vásquez J (2016) Identification of Nucleolus-Associated Chromatin Domains Reveals a Role for the Nucleolus in 3D Organization of the A. thaliana Genome. Cell Rep 16:1574–1587. https://doi.org/10.1016/j.celrep.2016.07.016

Pontvianne F, Grob S (2020) Three-dimensional nuclear organization in Arabidopsis thaliana. J Plant Res 133:479–488. https://doi.org/10.1007/s10265-020-01185-0

Probst AV, Desvoyes B, Gutierrez C (2020) Similar yet critically different: the distribution, dynamics and function of histone variants. J Exp Bot 71:5191–5204. https://doi.org/10.1093/jxb/eraa230

Provart NJ, Alonso J, Assmann SM, Bergmann D, Brady SM, Brkljacic J, Browse J, Chapple C, Colot V, Cutler S, Dangl J, Ehrhardt D, Friesner JD, Frommer WB, Grotewold E, Meyerowitz E, Nemhauser J, Nordborg M, Pikaard C, Shanklin J, Somerville C, Stitt M, Torii KU, Waese J, Wagner D, McCourt P (2016) 50 years of Arabidopsis research: highlights and future directions. New Phytologist 209:921–944. https://doi.org/10.1111/nph.13687

Qian S, Lv X, Scheid RN, Lu L, Yang Z, Chen W, Liu R, Boersma MD, Denu JM, Zhong X, Du J (2018) Dual recognition of H3K4me3 and H3K27me3 by a plant histone reader SHL. Nat Commun 9:2425. https://doi.org/10.1038/s41467-018-04836-y

Quesneville H (2020) Twenty years of transposable element analysis in the Arabidopsis thaliana genome. Mobile DNA 11:28. https://doi.org/10.1186/s13100-020-00223-x

Redstone SCJ, Fleming AM, Burrows CJ (2019) Oxidative Modification of the Potential G-Quadruplex Sequence in the PCNA Gene Promoter Can Turn on Transcription. Chem Res Toxicol 32:437–446. https://doi.org/10.1021/acs.chemrestox.8b00332

Reiser L, Subramaniam S, Li D, Huala E (2017) Using the Arabidopsis Information Resource (TAIR) to Find Information About Arabidopsis Genes. Curr Protoc Bioinformatics 60:1.11.1-1.11.45. https://doi.org/10.1002/cpbi.36

Riha K, Shippen DE (2003) Telomere structure, function and maintenance in Arabidopsis. Chromosome Res 11:263–275. https://doi.org/10.1023/a:1022892010878

Rivero L, Scholl R, Holomuzki N, Crist D, Grotewold E, Brkljacic J (2014) Handling Arabidopsis Plants: Growth, Preservation of Seeds, Transformation, and Genetic Crosses. In: Sanchez-Serrano JJ, Salinas J (eds) Arabidopsis Protocols. Humana Press, Totowa, NJ, pp 3–25

Roudier F, Ahmed I, Bérard C, Sarazin A, Mary-Huard T, Cortijo S, Bouyer D, Caillieux E, Duvernois-Berthet E, Al-Shikhley L, Giraut L, Després B, Drevensek S, Barneche F, Dèrozier S, Brunaud V, Aubourg S, Schnittger A, Bowler C, Martin-Magniette M-L, Robin S, Caboche M, Colot V (2011) Integrative epigenomic mapping defines four main chromatin states in Arabidopsis. EMBO J 30:1928–1938. https://doi.org/10.1038/emboj.2011.103

Rowley MJ, Corces VG (2018) Organizational principles of 3D genome architecture. Nat Rev Genet 19:789–800. https://doi.org/10.1038/s41576-018-0060-8

Rutowicz K, Lirski M, Mermaz B, Teano G, Schubert J, Mestiri I, Kroteń MA, Fabrice TN, Fritz S, Grob S, Ringli C, Cherkezyan L, Barneche F, Jerzmanowski A, Baroux C (2019) Linker histones are fine-scale chromatin architects modulating developmental decisions in Arabidopsis. Genome Biology 20:157. https://doi.org/10.1186/s13059-019-1767-3

Rutowicz K, Puzio M, Halibart-Puzio J, Lirski M, Kotliński M, Kroteń MA, Knizewski L, Lange B, Muszewska A, Śniegowska-Świerk K, Kościelniak J, Iwanicka-Nowicka R, Buza K, Janowiak F, Żmuda K, Jõesaar I, Laskowska-Kaszub K, Fogtman A, Kollist H, Zielenkiewicz P, Tiuryn J, Siedlecki P, Swiezewski S, Ginalski K, Koblowska M, Archacki R, Wilczynski B, Rapacz M, Jerzmanowski A (2015) A Specialized Histone H1 Variant Is Required for Adaptive Responses to Complex Abiotic Stress and Related DNA Methylation in Arabidopsis. Plant Physiol 169:2080–2101. https://doi.org/10.1104/pp.15.00493

Rymen B, Kawamura A, Lambolez A, Inagaki S, Takebayashi A, Iwase A, Sakamoto Y, Sako K, Favero DS, Ikeuchi M, Suzuki T, Seki M, Kakutani T, Roudier F, Sugimoto K (2019) Histone acetylation orchestrates wound-induced transcriptional activation and cellular reprogramming in Arabidopsis. Commun Biol 2:1–15. https://doi.org/10.1038/s42003-019-0646-5

Sabari BR, Zhang D, Allis CD, Zhao Y (2017) Metabolic regulation of gene expression through histone acylations. Nat Rev Mol Cell Biol 18:90–101. https://doi.org/10.1038/nrm.2016.140

Salari H, Di Stefano M, Jost D (2021) Spatial organization of chromosomes leads to heterogeneous chromatin motion and drives the liquid- or gel-like behavior of chromatin. Genome Research. https://doi.org/10.1101/2021.05.10.443375

Salih B, Trifonov EN (2015) Strong nucleosomes of A. thaliana concentrate in centromere regions. J Biomol Struct Dyn 33:10–13. https://doi.org/10.1080/07391102.2013.860624

Saze H, Shiraishi A, Miura A, Kakutani T (2008) Control of genic DNA methylation by a jmjC domain-containing protein in Arabidopsis thaliana. Science 319:462–465. https://doi.org/10.1126/science.1150987

Schalk C, Cognat V, Graindorge S, Vincent T, Voinnet O, Molinier J (2017) Small RNA-mediated repair of UV-induced DNA lesions by the DNA DAMAGE-BINDING PROTEIN 2 and ARGONAUTE 1. Proc Natl Acad Sci U S A 114:E2965–E2974. https://doi.org/10.1073/pnas.1618834114

Schalk C, Molinier J (2016) Global Genome Repair factors controls DNA methylation patterns in Arabidopsis. Plant Signal Behav 11:e1253648. https://doi.org/10.1080/15592324.2016.1253648

Schick S, Fournier D, Thakurela S, Sahu SK, Garding A, Tiwari VK (2015) Dynamics of chromatin accessibility and epigenetic state in response to UV damage. J Cell Sci 128:4380–4394. https://doi.org/10.1242/jcs.173633

Schneiderman JI, Orsi GA, Hughes KT, Loppin B, Ahmad K (2012) Nucleosome-depleted chromatin gaps recruit assembly factors for the H3.3 histone variant. Proc Natl Acad Sci U S A 109:19721–19726. https://doi.org/10.1073/pnas.1206629109

Scholl RL, May ST, Ware DH (2000) Seed and Molecular Resources for Arabidopsis. Plant Physiology 124:1477–1480. https://doi.org/10.1104/pp.124.4.1477

Schubert V, Weißleder A, Ali H, Fuchs J, Lermontova I, Meister A, Schubert I (2009) Cohesin gene defects may impair sister chromatid alignment and genome stability in Arabidopsis thaliana. Chromosoma 118:591–605. https://doi.org/10.1007/s00412-009-0220-x

Schwarzer W, Abdennur N, Goloborodko A, Pekowska A, Fudenberg G, Loe-Mie Y, Fonseca NA, Huber W, Haering CH, Mirny L, Spitz F (2017) Two independent modes of chromatin organization revealed by cohesin removal. Nature 551:51–56. https://doi.org/10.1038/nature24281

Sequeira-Mendes J, Aragüez I, Peiró R, Mendez-Giraldez R, Zhang X, Jacobsen SE, Bastolla U, Gutierrez C (2014) The Functional Topography of the Arabidopsis Genome Is Organized in a Reduced Number of Linear Motifs of Chromatin States. Plant Cell 26:2351–2366. https://doi.org/10.1105/tpc.114.124578

Shinmura K, Yokota J (2001) The OGG1 gene encodes a repair enzyme for oxidatively damaged DNA and is involved in human carcinogenesis. Antioxid Redox Signal 3:597–609. https://doi.org/10.1089/15230860152542952

Silveira AB, Trontin C, Cortijo S, Barau J, Del Bem LEV, Loudet O, Colot V, Vincentz M (2013) Extensive natural epigenetic variation at a de novo originated gene. PLoS Genet 9:e1003437. https://doi.org/10.1371/journal.pgen.1003437

Simon L, Voisin M, Tatout C, Probst AV (2015) Structure and Function of Centromeric and Pericentromeric Heterochromatin in Arabidopsis thaliana. Front Plant Sci 6. https://doi.org/10.3389/fpls.2015.01049

Šmarda P, Bureš P, Horová L, Leitch IJ, Mucina L, Pacini E, Tichý L, Grulich V, Rotreklová O (2014) Ecological and evolutionary significance of genomic GC content diversity in monocots. Proc Natl Acad Sci USA 111:E4096–E4102. https://doi.org/10.1073/pnas.1321152111

Somerville C, Koornneef M (2002) A fortunate choice: the history of Arabidopsis as a model plant. Nat Rev Genet 3:883–889. https://doi.org/10.1038/nrg927

Stajic D, Jansen LET (2021) Empirical evidence for epigenetic inheritance driving evolutionary adaptation. Philos Trans R Soc Lond B Biol Sci 376:20200121. https://doi.org/10.1098/rstb.2020.0121

Stroud H, Do T, Du J, Zhong X, Feng S, Johnson L, Patel DJ, Jacobsen SE (2014) Non-CG methylation patterns shape the epigenetic landscape in Arabidopsis. Nat Struct Mol Biol 21:64–72. https://doi.org/10.1038/nsmb.2735

Stroud H, Otero S, Desvoyes B, Ramírez-Parra E, Jacobsen SE, Gutierrez C (2012) Genome-wide analysis of histone H3.1 and H3.3 variants in Arabidopsis thaliana. Proc Natl Acad Sci USA 109:5370–5375. https://doi.org/10.1073/pnas.1203145109

Sullivan LL, Sullivan BA (2020) Genomic and functional variation of human centromeres. Exp Cell Res 389:111896. https://doi.org/10.1016/j.yexcr.2020.111896

Sun L, Jing Y, Liu X, Li Q, Xue Z, Cheng Z, Wang D, He H, Qian W (2020) Heat stress-induced transposon activation correlates with 3D chromatin organization rearrangement in Arabidopsis. Nat Commun 11:1886. https://doi.org/10.1038/s41467-020-15809-5

Takou M, Wieters B, Kopriva S, Coupland G, Linstädter A, De Meaux J (2019) Linking genes with ecological strategies in Arabidopsis thaliana. Journal of Experimental Botany 70:1141–1151. https://doi.org/10.1093/jxb/ery447

Talbert PB, Masuelli R, Tyagi AP, Comai L, Henikoff S (2002) Centromeric Localization and Adaptive Evolution of an Arabidopsis Histone H3 Variant. The Plant Cell 14:1053–1066. https://doi.org/10.1105/tpc.010425

Tamada Y, Yun J-Y, Woo SC, Amasino RM (2009) ARABIDOPSIS TRITHORAX-RELATED7 is required for methylation of lysine 4 of histone H3 and for transcriptional activation of FLOWERING LOCUS C. Plant Cell 21:3257–3269. https://doi.org/10.1105/tpc.109.070060

Tamaru H (2010) Confining euchromatin/heterochromatin territory: jumonji crosses the line. Genes Dev 24:1465–1478. https://doi.org/10.1101/gad.1941010

Tang C, Toomajian C, Sherman-Broyles S, Plagnol V, Guo Y-L, Hu TT, Clark RM, Nasrallah JB, Weigel D, Nordborg M (2007) The evolution of selfing in Arabidopsis thaliana. Science 317:1070–1072. https://doi.org/10.1126/science.1143153

The Arabidopsis Genome Initiative (2000) Analysis of the genome sequence of the flowering plant Arabidopsis thaliana. Nature 408:796–815. https://doi.org/10.1038/35048692

Thorstensen T, Fischer A, Sandvik SV, Johnsen SS, Grini PE, Reuter G, Aalen RB (2006) The Arabidopsis SUVR4 protein is a nucleolar histone methyltransferase with preference for monomethylated H3K9. Nucleic Acids Res 34:5461–5470. https://doi.org/10.1093/nar/gkl687

Trojer P, Reinberg D (2007) Facultative heterochromatin: is there a distinctive molecular signature? Mol Cell 28:1–13. https://doi.org/10.1016/j.molcel.2007.09.011

Turck F, Roudier F, Farrona S, Martin-Magniette M-L, Guillaume E, Buisine N, Gagnot S, Martienssen RA, Coupland G, Colot V (2007) Arabidopsis TFL2/LHP1 specifically associates with genes marked by trimethylation of histone H3 lysine 27. PLoS Genet 3:e86. https://doi.org/10.1371/journal.pgen.0030086

Ueda M, Seki M (2020) Histone Modifications Form Epigenetic Regulatory Networks to Regulate Abiotic Stress Response. Plant Physiol 182:15–26. https://doi.org/10.1104/pp.19.00988

Ülker B, Peiter E, Dixon DP, Moffat C, Capper R, Bouché N, Edwards R, Sanders D, Knight H, Knight MR (2008) Getting the most out of publicly available T-DNA insertion lines. The Plant Journal 56:665–677. https://doi.org/10.1111/j.1365-313X.2008.03608.x

van Koningsbruggen S, Gierlinski M, Schofield P, Martin D, Barton GJ, Ariyurek Y, den Dunnen JT, Lamond AI (2010) High-resolution whole-genome sequencing reveals that specific chromatin domains from most human chromosomes associate with nucleoli. Mol Biol Cell 21:3735–3748. https://doi.org/10.1091/mbc.E10-06-0508

Vaquero-Sedas MI, Luo C, Vega-Palas MA (2012) Analysis of the epigenetic status of telomeres by using ChIP-seq data. Nucleic Acids Res 40:e163. https://doi.org/10.1093/nar/gks730

Veiseth SV, Rahman MA, Yap KL, Fischer A, Egge-Jacobsen W, Reuter G, Zhou M-M, Aalen RB, Thorstensen T (2011) The SUVR4 histone lysine methyltransferase binds ubiquitin and converts H3K9me1 to H3K9me3 on transposon chromatin in Arabidopsis. PLoS Genet 7:e1001325. https://doi.org/10.1371/journal.pgen.1001325

Vergara Z, Gutierrez C (2017) Emerging roles of chromatin in the maintenance of genome organization and function in plants. Genome Biology 18:96. https://doi.org/10.1186/s13059-017-1236-9

Vertii A, Ou J, Yu J, Yan A, Pagès H, Liu H, Zhu LJ, Kaufman PD (2019) Two contrasting classes of nucleolus-associated domains in mouse fibroblast heterochromatin. Genome Res 29:1235–1249. https://doi.org/10.1101/gr.247072.118

Wang B, Yang X, Jia Y, Xu Y, Jia P, Dang N, Wang S, Xu T, Zhao X, Gao S, Dong Q, Ye K (2021a) High-quality Arabidopsis thaliana Genome Assembly with Nanopore and HiFi Long Reads. Genomics, Proteomics & Bioinformatics. https://doi.org/10.1016/j.gpb.2021.08.003

Wang H, Jiang D, Axelsson E, Lorković ZJ, Montgomery S, Holec S, Pieters BJGE, Al Temimi AHK, Mecinović J, Berger F (2018) LHP1 Interacts with ATRX through Plant-Specific Domains at Specific Loci Targeted by PRC2. Mol Plant 11:1038–1052. https://doi.org/10.1016/j.molp.2018.05.004

Wang Q, Liu P, Jing H, Zhou XF, Zhao B, Li Y, Jin JB (2021b) JMJ27-mediated histone H3K9 demethylation positively regulates drought-stress responses in Arabidopsis. New Phytol 232:221–236. https://doi.org/10.1111/nph.17593

Wang Y, Zhong Z, Zhang Y, Xu L, Feng S, Rayatpisheh S, Wohlschlegel JA, Wang Z, Jacobsen SE, Ausin I (2020) NAP1-RELATED PROTEIN1 and 2 negatively regulate H2A.Z abundance in chromatin in Arabidopsis. Nat Commun 11:2887. https://doi.org/10.1038/s41467-020-16691-x

Wei KH-C, Chan C, Bachtrog D (2021) Establishment of H3K9me3-dependent heterochromatin during embryogenesis in Drosophila miranda. eLife 10:e55612. https://doi.org/10.7554/eLife.55612

Wils CR, Kaufmann K (2017) Gene-regulatory networks controlling inflorescence and flower development in Arabidopsis thaliana. Biochim Biophys Acta Gene Regul Mech 1860:95–105. https://doi.org/10.1016/j.bbagrm.2016.07.014

Wolff P, Weinhofer I, Seguin J, Roszak P, Beisel C, Donoghue MTA, Spillane C, Nordborg M, Rehmsmeier M, Köhler C (2011) High-resolution analysis of parent-of-origin allelic expression in the Arabidopsis Endosperm. PLoS Genet 7:e1002126. https://doi.org/10.1371/journal.pgen.1002126

Wollmann H, Holec S, Alden K, Clarke ND, Jacques P-É, Berger F (2012) Dynamic Deposition of Histone Variant H3.3 Accompanies Developmental Remodeling of the Arabidopsis Transcriptome. PLOS Genetics 8:e1002658. https://doi.org/10.1371/journal.pgen.1002658

Wong LH, McGhie JD, Sim M, Anderson MA, Ahn S, Hannan RD, George AJ, Morgan KA, Mann JR, Choo KHA (2010) ATRX interacts with H3.3 in maintaining telomere structural integrity in pluripotent embryonic stem cells. Genome Res 20:351–360. https://doi.org/10.1101/gr.101477.109

Xavier MJ, Roman SD, Aitken RJ, Nixon B (2019) Transgenerational inheritance: how impacts to the epigenetic and genetic information of parents affect offspring health. Hum Reprod Update 25:518–540. https://doi.org/10.1093/humupd/dmz017

Xiao J, Wagner D (2015) Polycomb repression in the regulation of growth and development in Arabidopsis. Curr Opin Plant Biol 23:15–24. https://doi.org/10.1016/j.pbi.2014.10.003

Xu L, Hu Y, Cao Y, Li J, Ma L, Li Y, Qi Y (2018) An expression atlas of miRNAs in Arabidopsis thaliana. Sci China Life Sci 61:178–189. https://doi.org/10.1007/s11427-017-9199-1

Xu L, Jiang H (2020) Writing and Reading Histone H3 Lysine 9 Methylation in Arabidopsis. Frontiers in Plant Science 11

Yadav T, Whitehouse I (2016) Replication-Coupled Nucleosome Assembly and Positioning by ATP-Dependent Chromatin-Remodeling Enzymes. Cell Rep 15:715–723. https://doi.org/10.1016/j.celrep.2016.03.059

Yadav VK, Singh S, Yadav A, Agarwal N, Singh B, Jalmi SK, Yadav VK, Tiwari VK, Kumar V, Singh R, Sawant SV (2021) Stress Conditions Modulate the Chromatin Interactions Network in Arabidopsis. Front Genet 12:799805. https://doi.org/10.3389/fgene.2021.799805

Yang Z, Qian S, Scheid RN, Lu L, Chen X, Liu R, Du X, Lv X, Boersma MD, Scalf M, Smith LM, Denu JM, Du J, Zhong X (2018) EBS is a bivalent histone reader that regulates floral phase transition in Arabidopsis. Nat Genet 50:1247–1253. https://doi.org/10.1038/s41588-018-0187-8

Yelagandula R, Stroud H, Holec S, Zhou K, Feng S, Zhong X, Muthurajan UM, Nie X, Kawashima T, Groth M, Luger K, Jacobsen SE, Berger F (2014) The histone variant H2A.W defines heterochromatin and promotes chromatin condensation in Arabidopsis. Cell 158:98–109. https://doi.org/10.1016/j.cell.2014.06.006

Yocca AE, Lu Z, Schmitz RJ, Freeling M, Edger PP (2021) Evolution of Conserved Noncoding Sequences in Arabidopsis thaliana. Mol Biol Evol 38:2692–2703. https://doi.org/10.1093/molbev/msab042

Zemach A, Kim MY, Hsieh P-H, Coleman-Derr D, Eshed-Williams L, Thao K, Harmer SL, Zilberman D (2013) The Arabidopsis nucleosome remodeler DDM1 allows DNA methyltransferases to access H1-containing heterochromatin. Cell 153:193–205. https://doi.org/10.1016/j.cell.2013.02.033

Zeng L, Gu Z, Xu M, Zhao N, Zhu W, Yonezawa T, Liu T, Qiong L, Tersing T, Xu L, Zhang Y, Xu R, Sun N, Huang Y, Lei J, Zhang L, Xie F, Zhang F, Gu H, Geng Y, Hasegawa M, Yang Z, Crabbe MJC, Chen F, Zhong Y (2017) Discovery of A high-altitude ecotype and ancient lineage of Arabidopsis thaliana from Tibet. Science Bulletin 62:1628–1630. https://doi.org/10.1016/j.scib.2017.10.007

Zhang C, Du X, Tang K, Yang Z, Pan L, Zhu P, Luo J, Jiang Y, Zhang H, Wan H, Wang X, Wu F, Tao WA, He X-J, Zhang H, Bressan RA, Du J, Zhu J-K (2018a) Arabidopsis AGDP1 links H3K9me2 to DNA methylation in heterochromatin. Nat Commun 9:4547. https://doi.org/10.1038/s41467-018-06965-w

Zhang H, Lang Z, Zhu J-K (2018b) Dynamics and function of DNA methylation in plants. Nat Rev Mol Cell Biol 19:489–506. https://doi.org/10.1038/s41580-018-0016-z

Zhang K, Sridhar VV, Zhu J, Kapoor A, Zhu J-K (2007) Distinctive core histone post-translational modification patterns in Arabidopsis thaliana. PLoS One 2:e1210. https://doi.org/10.1371/journal.pone.0001210

Zhang L, Cai X, Wu J, Liu M, Grob S, Cheng F, Liang J, Cai C, Liu Z, Liu B, Wang F, Li S, Liu F, Li X, Cheng L, Yang W, Li M, Grossniklaus U, Zheng H, Wang X (2018c) Improved Brassica rapa reference genome by single-molecule sequencing and chromosome conformation capture technologies. Hortic Res 5:1–11. https://doi.org/10.1038/s41438-018-0071-9

Zhang R, Zhang C-T (2004) Isochore Structures in the Genome of the Plant Arabidopsis thaliana. J Mol Evol 59:227–238. https://doi.org/10.1007/s00239-004-2617-8

Zhang X, Wang T (2021) Plant 3D Chromatin Organization: Important Insights from Chromosome Conformation Capture Analyses of the Last 10 Years. Plant Cell Physiol 62:1648–1661. https://doi.org/10.1093/pcp/pcab134

Zhao S, Cheng L, Gao Y, Zhang B, Zheng X, Wang L, Li P, Sun Q, Li H (2019) Plant HP1 protein ADCP1 links multivalent H3K9 methylation readout to heterochromatin formation. Cell Res 29:54–66. https://doi.org/10.1038/s41422-018-0104-9

Zhao S, Zhang B, Yang M, Zhu J, Li H (2018) Systematic Profiling of Histone Readers in Arabidopsis thaliana. Cell Rep 22:1090–1102. https://doi.org/10.1016/j.celrep.2017.12.099

Zheng S, Hu H, Ren H, Yang Z, Qiu Q, Qi W, Liu X, Chen X, Cui X, Li S, Zhou B, Sun D, Cao X, Du J (2019) The Arabidopsis H3K27me3 demethylase JUMONJI 13 is a temperature and photoperiod dependent flowering repressor. Nat Commun 10:1303. https://doi.org/10.1038/s41467-019-09310-x

Zhou W, Zhu Y, Dong A, Shen W-H (2015) Histone H2A/H2B chaperones: from molecules to chromatin-based functions in plant growth and development. Plant J 83:78–95. https://doi.org/10.1111/tpj.12830

2. Material & Methods

2.1. Plant materials

Arabidopsis thaliana plants used in these studies are described in Table 1.

2.2. Plant growth conditions

Plants were cultivated *in vitro* on solid GM medium [MS salts (Duchefa), 1% sucrose, 0.8% Agar-agar ultrapure (Merck), pH 5.8] and grown in a culture chamber under a 16h light (light intensity ~150 µmol m^{-2} s^{-1}; 21°C) and 8h dark (19°C) photoperiod. Alternatively, plants were grown *in soil* under similar photoperiod and light intensity.

2.3. Exposure of plants to genotoxic stresses

2.3.1. UV-C irradiation

In vitro- or *soil*-grown, 21-day-old Arabidopsis plants were exposed to 3000 J/m^2 of UV-C using the Stratalinker 2400 (Stratagene). Plant material was harvested before irradiation for control (0) and during a time course upon irradiation (1'' 15', 30', 1h, 2h, 24h).

2.3.2. UV-B irradiation

Soil-grown 21-day-old Arabidopsis plants were exposed during 15 min to 4 Philips UV-B Broadband - TL 40W/12 RS SLV/25, delivering a total dose of 6.750 J/m^2. For "directed evolution" assays, a dose of 13.500 J/m^2 (30 min) was used. The material was harvested before irradiation for control (0) and during a time course upon irradiation (1'' 30', 1h, 2h, 24h).

2.3.3. Proton irradiation

One leaf of soil-grown 21-day-old Arabidopsis plants was exposed to 100 Gy of protons using a 25 MeV proton beam (Cyrcé, IPHC, Strasbourg). Irradiation was deposited on a single leaf on a surface of 5 mm in diameter. Leaves disks were harvested prior (0), 1'' and 24h upon irradiation. For some experiments, aside from irradiation targeted (Tar) leaves, un-irradiated opposite (Opo) leaves were also used to test the bystander effect.

2.3.4. Paraquat Treatment

Leaf disks (15 mm diameter) of soil-grown 21-day-old Arabidopsis plants were incubated 10h (light intensity ~150 µmol m^{-2} s^{-1}; 21°C) in 8 well plates in PBS solution (for control) or in 100 µM paraquat (SIGMA M-2254) solution. After incubation, leaf disks were washed twice in PBS and harvested in a fixative solution for immunolabeling.

2.4. Ecotypes UV-B dose regimes

Ecotypes specific longitude and latitude are extracted from https://1001genomes.org/ and used as a query for the glUV dataset (Beckmann et al. 2014) using the QGIS software (QGIS on GitHub). The results table is available in "Supplemental data" (https://tinyurl.com/JotoBe).

2.5. UV-C sensitivity assay

UV-C (λ = 254 nm) sensitivity was evaluated on 6-day-old *in vitro*-germinated Arabidopsis plants. Plants were transferred to square plates containing GM medium and grown vertically. Root length was measured 24h upon UV-C exposure (300, 600, and 900 J/m^2) using the Stratalinker 2400 (Stratagene). The relative root growth was calculated as follows: (root length treated/root length untreated) × 100 (± SD). Eight plants per replicate were used. Experiments were performed in triplicates.

2.6. Photodamage removal assay

21-day-old *in vitro*-grown Arabidopsis seedlings (n=40 per genotype) were irradiated with UV-C (3, 000 J/m^2). Half of the samples were harvested immediately after irradiation (0), and the other half was kept under normal light conditions and harvested 1h later. Genomic DNA was extracted using a plant DNA extraction kit (Macherey-Nagel). DNA samples were processed as described in Schalk et al. (2017). The repair efficiency was determined by the quantification of the remaining photodamage amounts after 1 h relative to the photodamage content at time 0.

2.7. Generation of transgenic plants

The Arabidopsis *JMJ27* coding genomic region was amplified by PCR using primers described in Supplemental Table 7. This region was cloned into the pEAQ_ΔP19 vector (Figure 1). The resulting plasmid was mobilized into *Agrobacterium tumefaciens* and used to transform *jmj27* mutant plants. The *pOEX2 DDB2-FLAG* plasmid (Molinier et al. 2008) was used to transform *ddb2* and *ddb2jmj27* plants.

2.8. 8-oxo-G detection and metabolome analysis

21-day-old Arabidopsis plants grown in soil and irradiated with UV-B (6, 750 J/m^2) were used. Directly upon irradiation, 16 replicates of 300 mg (+/- 5 mg) of control non-irradiated WT (Col-0) leaves and 16 replicates of 300 mg (+/- 5 mg) of irradiated WT (Col-0) leaves were collected in 1.5 ml Eppendorf tubes and shock froze in liquid nitrogen. The 16 controls and 16 treated replicates were divided into two groups, one for nucleoside preparation and the other for whole leaves extraction.

For nucleoside preparation, DNA was extracted for 8 control, and 8 UV-B treated replicates using the GenElute Plant Genomic DNA Miniprep Kit (G2N70-1KT). DNA was digested into nucleosides using the Zymo Research DNA Degradase Plus kit (E2020) following the manufacturer's instructions. Nucleoside samples were diluted in 4 volumes of ice-cooled methanol, and $^2H_6$ ABA (OlChemIm 034 2721) was added as an internal control to a final concentration of 1 µg/ml.

For whole leaves metabolite extraction, grinding of tissue was performed in ice-cooled methanol solution, using the tissue-lyser (4 times 2 min at 30 Hz). Samples were incubated 18h at -20°C and centrifuged at 4°C, 13, 200 rpm. Supernatants were transferred in vials and dried in a SpeedVac. 1.5 ml ice-cooled methanol was added on top of the pellets. Samples were vortexed and mixed 10 min at 4°C (1, 400 rpm) before being centrifugated at 4°C, 13, 200 rpm. Supernatants were transferred in the previously dried vials and put again for drying in the Speed vac. The pellet washing step was repeated twice more times. Finally, the dried vials were filled with 300 µl of an ice-cooled methanol solution containing 1 µg/ml $^{2}H_{6}$ ABA. In addition, nine different dilutions of 8-hydroxy-2'-deoxyguanosine standard (8-oxo-G; Sigma-H5653) samples were prepared as a control for targeted analysis.

Samples were analyzed by Liquide-Chromatography High-Resolution Mass-Spectrometry (LC-HRMS) using the QTOF for non-targeted whole metabolome analysis. A follow-up analysis was performed using the Bruker T-ReX® software to filter out molecules that appear in less than 80% of the replicates (less than 6 from 8). Detected metabolites were annotated querying 7 online libraries (KNApSAcK ,FoodDB ,PhenolExplorer ,LipidMaps ,Librairies spectrales ,PlantCyc and Natural products atlas (NPA)).

All samples were also analyzed by a Liquide-Chromatography followed by High sensitivity tandem quadrupole Mass Spectrometry approach (LC-TQ-MS/MS) specifically for nucleotide detection.

2.9. Immunolocalization of photolesions

Leaves 3 and 4 of *in vitro* 21-day-old Arabidopsis plants were incubated four times at least 5 min (4°C) in a fixative solution (3:1 ethanol/acetic acid; vol/vol). Leaves nuclei were extracted by chopping fixed tissue in LB-01 Buffer (15 mM Tris-HCl pH 7.5, 2 mM EDTA, 0.5 mM spermine, 80 mM KCl, 29 mM NaCl, 0.1% Triton X-100) with a razor blade. The nuclei-containing solution was filtered through 20 µm nylon mesh and centrifugated 1 min (1, 000g). The supernatant was spread on poly-lysine slides (Thermofisher 631-1349), and post-fixation was performed using a 1:1 acetone/methanol (vol/vol) solution for 2 min.

Slides were washed with Phosphate Buffer Saline x1 and incubated for 1h at room temperature in permeabilization buffer (8% BSA, 0.01% Triton-X in Phosphate Buffer Saline x1). Slides were incubated overnight at 4°C with anti-CPD or anti-6,4 PP primary antibodies (see Table 5) diluted in 1% BSA, Phosphate Buffer Saline x1 buffer. Upon incubation, slides were washed at least three times with PBS before and a secondary antibody coupled to Alexa fluor 488 or Alexa fluor 568 (diluted in 1% BSA, PBS) was added and incubated for 90 min at room temperature. Finally, slides were again washed three times with PBS, and 15 µl of Fluoromount-G (Southern Biotechnology CAT NO 0100–01) with 2 µg/ml DAPI were added as a mounting solution for the coverslip.

2.10. Immunolocalization of histone marks and proteins

For immunolocalization of histone marks and tagged proteins, leaves 3 and 4 from 21-days old Arabidopsis plants were fixed at 4°C in paraformaldehyde solution (4% in PBS). Leaves nuclei were extracted by chopping fixed tissue in LB-01 Buffer (15 mM Tris-HCl pH 7.5, 2 mM EDTA, 0.5 mM spermine, 80 mM KCl, 29 mM NaCl, 0.1% Triton X-100) with a razor blade. The nuclei-containing solution was filtered through 20 µm nylon mesh and centrifugated 1 min (1000g). The supernatant was spread on poly-lysine slides (Thermofisher 631-1349), and post-fixation was performed using paraformaldehyde (3.2% in PBS). Slides were washed with Phosphate Buffer Saline x1 and incubated for 1h at room temperature in permeabilization buffer (8% BSA, 0.01% Triton-X in Phosphate Buffer Saline x1). After the permeabilization step, slides were incubated overnight at 4°C with primary-antibody (see Table 5 for details) diluted in 1% BSA, Phosphate Buffer Saline x1 buffer. Upon incubation, slides were washed at least three times with PBS. Secondary antibody coupled to Alexa fluor 488 or Alexa fluor 568 (diluted in 1% BSA, PBS) was added and incubated for 90 min at room temperature. Finally, slides were washed three times with PBS, and 15 µl of Fluoromount-G (Southern Biotechnology CAT NO 0100–01) with 2 µg/ml DAPI were added as a mounting solution for the coverslip.

2.11. Microscopy Image acquisition, segmentation, and measurements

Image acquisition was entirely performed on a Zeiss LSM 780 confocal microscope using a 64X oil immersion objective. A 405 nm, 488 nm, and 568 laser excitation wavelengths were used for DAPI, Alexa Fluor 488/GFP, and Alexa Fluor 526, respectively. DAPI Emission was measured considering wavelengths in the range 410-585. Alexa Fluor 488/GFP emission was measured considering wavelengths in the range 493-630 nm. Alexa Fluor 568 emission was measured considering wavelengths in the range 590-645 nm. The same acquisition gain settings were used for all slides of the same experiment. Each image acquisition consists of a Z-stack capture with a 0.64 µm slice distance.

Regions of interest were segmented by different tools such as the ImageJ plug-ins Nucl.eye (https://github.com/mutterer/Nucl.Eye) or Icraq (https://github.com/gschivre/iCRAQ) or the DeepLearning script Nucl.Eye.D (https://tinyurl.com/NuclEyeD). Measurement of regions of interest was performed on ImageJ (Schroeder et al. 2021). Most measurements get automatized using ImageJ macros available in "ImageJ-macro-toolbox" (https://tinyurl.com/JotoBe). The final data display was mainly performed on Rstudio (http://www.rstudio.com/). The different macros used are available in "Rstudio-macro-toolbox" (https://tinyurl.com/JotoBe).

2.12. Protein extraction and immunoblotting

2.12.1. Total protein extraction

Whole protein extracts were prepared using denaturing buffer (Molinier et al. 2008). 20 µg of total protein were separated by 8% SDS-PAGE gel and blotted onto an Immobilon-P membrane (Millipore). Anti-bodies were used in PBST [PBS (PBS X 1), nonfat dry milk (5%, w:v) and Tween-20 (0.1%); (see Table 5 for details)].

2.12.2. Chromatin preparation and Mnase treatment

Fractions of soluble (S1)/insoluble (P1) proteins were extracted from 100 mg of 21-day-old seedlings using Nonidet P-40 lysis buffer (25 mM Tris-HCl, pH 8.0, 0.3 M NaCl, 1 mM EDTA, 10% [v/v] glycerol, Nonidet P-40 1% [v/v], 0.2 mM phenylmethylsulfonyl fluoride, and EDTA-free Protease Inhibitor Cocktail [1 tablet/50 mL]). After grinding, the powder was resuspended in 3 mL of Nonidet P-40 lysis buffer and incubated for 30 min on a rotating wheel at 4°C (8 rpm), and the solution was filtered through Miracloth. Removal of extra cell debris was performed by centrifugation (2.000*g*, 5 min, 4°C). Free chromatin-unbound proteins (S1 fraction) were recovered from the soluble fraction after centrifugation (13.000g, 10 min, 4°C). The pellet containing insoluble and chromatin-bound proteins (P1 fraction) was either resuspended in 75 µL of Nonidet P-40-containing resuspension buffer for immunoblot or washed twice with 0.5 ml ice-cold CS buffer (20 mM Tris-HCl, pH 7.5, 100 mM KCl, 2 mM $MgCl_2$, 1 mM $CaCl_2$, 0.3 M sucrose, 0.1% (v/v) Triton X-100) for Mnase treatment. The P1 fraction was resuspended in 40 µl of CS buffer. Mnase treatment was performed by adding 5 µl of 10× reaction buffer [500 mM Tris-HCl (pH 7.9), 50 mM $CaCl_2$], 1 µl of bovine serum albumin (BSA; 1 mg/ml) and MNase (4 U/µl in a volume of 50 µl) and incubated at 37 °C for 7 min. MNase digestion was stopped by the addition of EGTA (5 mM), and the internucleosomal fraction proteins (S2) were separated from insoluble core nucleosome fraction (P2) by centrifugation at 15.000 g (10 min, 4 °C). S2 and P2 fractions were loaded in denaturing buffer for SDS-PAGE separation and immunoblotting with the indicated antibodies (see Table 5 for details).

2.12.3. Co-immunoprecipitation

Proteins were extracted from 200 mg of 21-day-old Arabidopsis seedlings using 3 mL of IP buffer (50 mM Tris-HCl at pH 7.5, 150 mM NaCl, 5 mM $MgCl_2$, 0.1% v/v NP40, 10% glycerol, EDTA-free Protease Inhibitor Cocktail [1 tablet/50 mL]) and incubated for 30 min on a rotating wheel at 4°C (8 rpm). The solution is Miracloth-filtered, and immunoprecipitation was performed using anti-FLAG gel affinity (Sigma-Aldrich) overnight on a rotating wheel at 4°C (8 rpm). The precipitate was washed four times in IP buffer, resuspended in 50 µl of denaturing buffer, and heated for 5 min at 95°C prior to immunoblotting.

The DDB2-FLAG fusion protein was detected using the anti-FLAG HRP (A8592; Sigma-Aldrich) at a 1:5000 (v: v) dilution in PBST (1× PBS, nonfat dry milk [5%, w/v], and Tween 20 [0.1%, v/v; Sigma-Aldrich]).

2.13. RNA extraction and RT-qPCR

Total RNAs were extracted from 21-day-old *in vitro* Arabidopsis plants using Tri-Reagent (Sigma). Reverse transcription (RT) was performed on 5 µg of total RNA using the cDNA reverse transcription kit (Applied Biosystems) following the manufacturer's instructions. After RNaseH treatment, 100 ng of purified cDNA were used for quantitative PCR (qPCR). qPCR was performed, including technical triplicates, using a Light Cycler 480 and Light Cycler 480 SYBR Green I Master mix (Roche) following the manufacturer's instructions. All primers are listed in Supplemental Table 4.

2.14. Histochemical GUS assay

Histochemical GUS assay was performed on 21-days old *in vitro* grown pJMJ::JMJ27::GUS expressing plants (See Table 6 for details) in control condition (0) and in a time course following UV-C irradiation (3, 000 J/m^2). Plant samples were incubated for 15h at 37°C in 96 well plates filled with freshly prepared GUS mix (5 mM Potassium ferricyanide, 5 mM Potassium ferrocyanide, 1 mM EDTA, 1% Triton-X-100 and 1 mg/ml X-Gluc (resuspend in N,N-dimethylformamide). Before image acquisition, plants were dehydrated in 70%, 80% and 95 % ethanol solutions.

2.15. Statistics

Mann-Whitney U or Wilcoxon Matched-Pairs Signed-Ranks tests were used as non-parametric statistical hypothesis tests (http://astatsa.com/WilcoxonTest/). Chi 2 test was used to determine significant difference between categories distribution (https://goodcalculators.com/chi-square-calculator/). Representation factor (R) was used to determine the statistical significance of the overlap between 2 independent groups of genomic regions (http://nemates.org/MA/progs/overlap_stats.html). T-test was used as a parametric statistical hypothesis test.

Mutant	Reference
phrI	WiscDsLox466C12
uvr3	WiscDsLox334H05
rad10	SALK 077000
ddb2-3	WiscDsLoxHs195_05H
jmj27	SAIL_400_B08
ibm1	SALK_006042
kyp	SALK_069326
kyp suvh5/6	SALK_041474 GK-263C05 SAIL_1244_F04
atxr5/6	SAIL_240_H01 and SAIL_240_H01
nrpd1	SALK_583051
cmt2	SALK_201637
cmt3-11	SALK_148381
drm2-10	SALK_129477
dcl4-2	GABI_160G05
ago4-1	Zilberman et al., 2003
ddm1-2	Stokes et al., 1999

Table 1: *Arabidopsis thaliana* mutant lines used in the study

Ecotypes
C24 (CS906) from unknown.
Can-0 (CS6660) from Canary Islands, Spain. Longitude/Latitude/Elevation: W15/N28 at 1260m.
Cen-0 (CS6661) from Caen, France. Longitude/Latitude/Elevation: W0/N49 at 1-100m.
CIBC10 (CS22229) from United Kingdom.
Col-0 (N1092) from Columbia, Missouri, USA. Longitude/Latitude/Elevation: W93/N38 at 1-100m. Temp in C (Spr/Aut):15-16/21-2, Precipitation in mm (Spr/Aut):60-70/30-40.
Cvi-1 (CS8580) from Cape Verde Islands. Longitude/Latitude/Elevation: W24/N16 at 1-100m.
En-T (CS6176) from Tadjikistan.
Is-0 (CS6741) from Isenburg, Germany. Longitude/Latitude/Elevation: E7/N50 at 100-200m. Temp in C (Spr/Aut):7-8/11-12.
Kin-0 (CS6755) from Kindalville, Michigan, USA. Longitude/Latitude/Elevation: W85/N43 at 200-300m.
Ler-2 (CS8581) from Landsberg, Germany. Longitude/Latitude/Elevation: E15/N53 at 100-200m.
MS-0 (CS6797) from Moscow, Russia.
Nw-1 (CS6812) from Neuweilnau, Germany. Longitude/Latitude/Elevation: E8/N50 at 100-200m. Temp in C (Spr/Aut):5-6/9-10.
Old-2 (CS6821) from Oldenburg, Germany. Longitude/Latitude/Elevation: E8/N53 at 1-100m.
Ta-0 (CS6867) from Tabor, Czech Republic. Longitude/Latitude/Elevation: E14/N49 at 400-500m. Temp in C (Spr/Aut):3-4/9-10.

Table 2: *Arabidopsis thaliana* natural variants used in the study

Genotyping	LP 5‘-3‘	RP 5‘-3‘	
phrI	CCAACACAGGGCAAAGTAGTC	GATTCTTTGAAGGGAGCTTGG	
uvr3	AGGCTTCTGATTCACCACCTC	TCTTGAATACGCCTCAAAAGG	
rad10	TGTACCTTACGTTCGCCAATC	TGTGCCAACAGTCAGATTCAG	
ddb2-3	GCGCCACAAACAAACTTTATC	ATAGCAGGAGCTTTACCAGGC	
jmj27	ACAACAAGTCAACTGCGTAGG	TGGCAATACCAATGAGAGGTC	
ibm1	TACCTGCAACCATTACAAGCC	CTCTGGCATGTAAGGAGGATG	
kyp	CAATCTCGCGCTGCTTAGTC	CGCCTTAGCTTTTATCATCTGG	
nrpd1	GCACGGGTTCGAATACGGG	GTATCTGACACCGCGGACTC	
cmt2	CCATAGAACTTAAAAGCCGGG	CTTGTGGCCCTCCTTAGGTAC	
cmt3-11	TGCACTAGCTTCAGAAGTTTAA	ATAAGAGAAGGAGCTGCTGCC	
drm2-10	TCATTTTGTGGTGTGTGGACC	TTTTGAAGGACTTTTGGGAGC	
dcl4-2	GGCTGCACAGCTGATGATTACAA	GCCGCTCGAGATCATCAGCAAA GGAAT	
ago4-1	TGACTGACAGCTGAAAATGGGATGTG GAT	GCCACTCCCTAGAACTCACCACC TAAGTT	*Ava II* digestion
ddm1-2	ACG AAG CAA CCA AGG AAG AA	GAG CCA TGG GTT TGT GAA ACG TA	*Rsa I* digestion

T-DNA	5‘-3‘
Lba1	TGGTTCACGTAGTGGGCCATCG
LBb1	GCGTGGACCGCTTGCTGCAACT
L4	TGATCCATGTAGATTTCCCGG
LB1	GCCTTTTCAGAAATGGATAAATAGCCT TGCTTCC
LB2	GCTTCCTATTATATCTTCCCAAATTACC AATACA
LB3	TAGCATCTGAATTTCATAACCAATCTC GATACAC
GABI o8760	GGGCTACACTGAATTGGTAGCTC

Table 3: Primers used for genotyping

q-PCR	Fwd 5‘-3‘	Rev 5‘-3‘
GADPH	TTG GTG ACA ACA GGT CAA GCA	AAA CTT GTC GCT CAA TGC AAT
Hexo	GGC GTT TTC TGA TAG CGA AAA	ATG GAT CAG GCA TTG GAG CT
UbiCRed	ACA AGC CAA TTT TTG CTG AGC	ACA ACA GTC CGA GTG TCA TGG T
CSA	ATG CTG CTC AGG CGG TTG TG	CAG AGG CGA ACC TGG ACA TC
PHR1	TCC GGA GTA CTT CCC CTC AG	GCT CCA ACG AGT AAA TGT GTT CC
UVR3	ACC ATC TCT TGA GGA ACT TGG C	TGC CAC CCA TGC CTT ATC AC
DDB2	TGG GAC CCT AAG GAT ACC TCG	TTG GGT GAA GAG CAG TTC CG
180pb	ACC ATC AAA GCC TTG AGA AGC A	CCG TAT GAG TCT TTG TCT TTG TAT CTT CT
5S rDNA	GGATGCGATCATACCAG	CGAAAAGGTATCACATGCC
KYP	AGG TGC CAA CTG CAG GTT TAC TT	TTC AGA ACC CCA GTC TGC ATC C
JMJ27	GGT TAT CAA GGT AAG TGG GC	CAC TTG GAG GCT GAG ATT CAC

Table 4: q-PCR primers list

Immunostaining	Reference	Dilution
H3K9me2	Diagenode - C15200154	1/500
H3K27me1	Diagenode - C15410045-50	1/100
CPD	CosmoBio - CAC-NM-DND-001	1/1500
6-4PP	CosmoBio - CAC-NM-DND-002	1/300
5-mC	Diagenode - C15200003	1/1000
8-oxo-G	Abcam - ab206461	1/50
GFP	Takara - 632593	1/100
FLAG	Sigma - F3165	1/300
Goat anti mouse 488	ThermoFisher - A-11001	1/200
Goat anti mouse 568	ThermoFisher - A-11004	1/300
Goat anti Rabbit 488	ThermoFisher - A-11008	1/200
Immuno-blot	**Reference**	**Dilution**
DDB2	(Molinier et al., 2008) - anti-AtDDB2 antibody	1/2000
Flag Monoclonal	Sigma - A8592	1/1000
Myc	Sigma - AB3252	1/1000
H3	Abcam - ab10799	1/3000
H3K9me2	Diagenode - C15200154	1/1000
Pol-IV	Diagenode - C15200004	1/2000
GFP	Takara - 632593	1/2000
Dot-Blot	**Reference**	**Dilution**
CPD	CosmoBio - CAC-NM-DND-001	1/1000
6-4PP	CosmoBio - CAC-NM-DND-002	1/1000

Table 5: List of antibodies used in the study

Promoter	Protein	Tag	Plasmid	Ref.
Mas	DDB2	FLAG	pOEX2	(Molinier et al. 2004)
UBI	JMJ27	MYC	pEAQ_ΔP19	Figure 1
pJMJ27	JMJ27	GUS		(Wang et al. 2021)
35S	JMJ27	GFP		(Wang et al. 2021)
35S	JMJ27m	GFP		(Wang et al. 2021)
35S	UVR3	GFP		(Katarzyna Banas et al. 2018)

Table 6: List of constructs used in the study

Cloning pEAQ ΔP19	SapI jmj27-myc fwd 5'-3'	SapI jmj27-myc rev 5'-3'	
JMJ27	GGTGGTGCTCTTCAATGATGGAGAAAATGAGAGGGAAGC	GTGGTGGCTCTTCGTCATTACAGATCCTCTTCTGAGATGAGTTTTTGTTCGGTATCACTGCGTCGGGAGC	*Sap I* digestion

Table 7: JMJ27-MYC primers for *Sap*I cloning into pEAQ_ ΔP19 vector

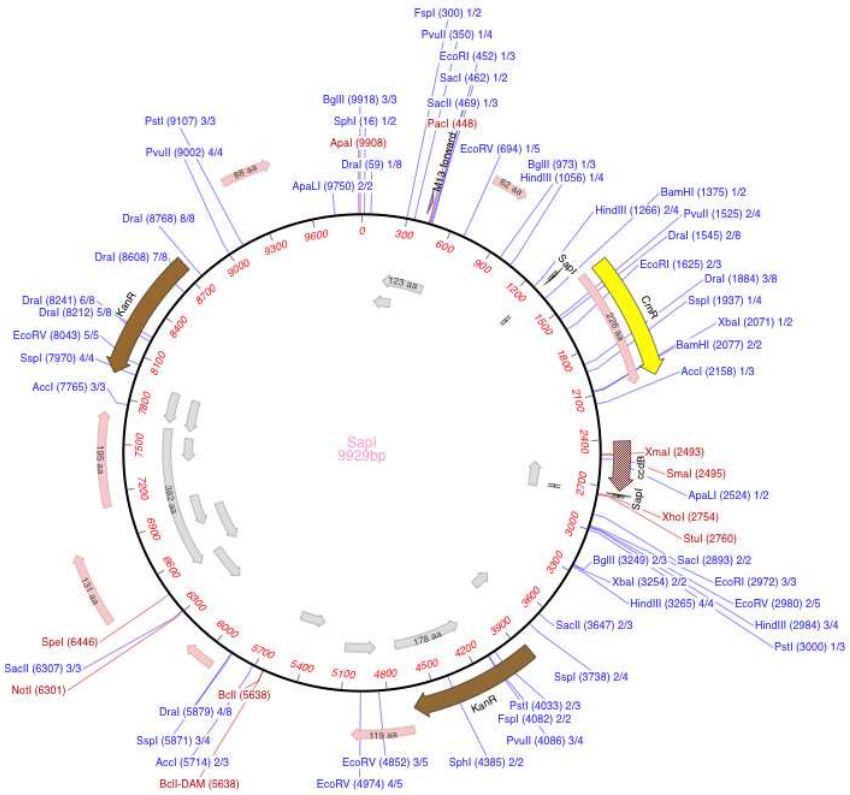

Figure 1: pEAQ_ ΔP19 vector map

Circular vector map of pEAQ_P19 which was used for the cloning of JMJ27-MYC fragment. Graphical representation was performed using MacVector™.

2.15. References

Beckmann M, Václavík T, Manceur AM, Šprtová L, von Wehrden H, Welk E, Cord AF (2014) glUV: a global UV-B radiation data set for macroecological studies. Methods in Ecology and Evolution 5:372–383. https://doi.org/10.1111/2041-210X.12168

Katarzyna Banas A, Hermanowicz P, Sztatelman O, Labuz J, Aggarwal C, Zglobicki P, Jagiello-Flasinska D, Strzalka W (2018) 6,4-PP Photolyase Encoded by AtUVR3 is Localized in Nuclei, Chloroplasts and Mitochondria and its Expression is Down-Regulated by Light in a Photosynthesis-Dependent Manner. Plant Cell Physiol 59:44–57. https://doi.org/10.1093/pcp/pcx159

Molinier J, Lechner E, Dumbliauskas E, Genschik P (2008) Regulation and Role of Arabidopsis CUL4-DDB1A-DDB2 in Maintaining Genome Integrity upon UV Stress. PLoS Genet 4. https://doi.org/10.1371/journal.pgen.1000093

Molinier J, Ramos C, Fritsch O, Hohn B (2004) CENTRIN2 modulates homologous recombination and nucleotide excision repair in Arabidopsis. Plant Cell 16:1633–1643. https://doi.org/10.1105/tpc.021378

Schalk C, Cognat V, Graindorge S, Vincent T, Voinnet O, Molinier J (2017) Small RNA-mediated repair of UV-induced DNA lesions by the DNA DAMAGE-BINDING PROTEIN 2 and ARGONAUTE 1. Proc Natl Acad Sci U S A 114:E2965–E2974. https://doi.org/10.1073/pnas.1618834114

Schroeder AB, Dobson ETA, Rueden CT, Tomancak P, Jug F, Eliceiri KW (2021) The ImageJ ecosystem: Open-source software for image visualization, processing, and analysis. Protein Sci 30:234–249. https://doi.org/10.1002/pro.3993

Wang Q, Liu P, Jing H, Zhou XF, Zhao B, Li Y, Jin JB (2021) JMJ27-mediated histone H3K9 demethylation positively regulates drought-stress responses in Arabidopsis. New Phytol 232:221–236. https://doi.org/10.1111/nph.17593

3. Chapter I - Photodamage localization and alteration in constitutive heterochromatin

3.1. Introduction

Ultraviolet (UV) light is a non-ionizing radiation that spans from 10 to 400 nm wavelength. Three main categories of UV are defined: UV-A (315-380nm), UV-B (280-315nm), and UV-C (280-100nm). UV-A induces oxidative stress that interferes with cellular processes by modifying metabolites, proteins, and DNA (Markovitsi 2016). The main oxidatively-induced DNA lesion is the 8-oxo-7,8-dihydro-2'-deoxyguanosine (8-oxo-G) (Schuch et al. 2017). Both UV-C and UV-B are known to induce the formation of photolesions on DNA molecules such as Cyclo-Pyrimidine-Dimers (CPD) and 6,4-Photoproducts (6,4-PP) (Markovitsi 2016). Importantly, UV-B also causes oxidative stress (Schuch et al. 2017).

Aside from UV, other genotoxic agents can be used to massively induce oxidative stress, as for example hydrogen peroxide (H_2O_2), Paraquat (Methyl-viologen), and ionizing radiations (*i.e.,* accelerated protons) (Moustaka and Moustakas 2014; Privett et al. 2017). Proton irradiation is a prominent innovative method, among others used in cancer therapy (Levin et al. 2005). The proton irradiation is generally performed using a cyclotron, enabling the particle acceleration giving to the proton its kinetic energy of around 70–250 MeV (for cancer treatment) (Privett et al. 2017). When going through tissue, the protons transfer this energy to surrounding molecules, in most cases water (H_2O) (Privett et al. 2017). Interestingly compared to conventional X-ray methods, the energy delivery is mainly restricted to a specific distance after entering the tissue. This maximal energy deposition, at the so-called Bragg peak, can be observed by plotting energy loss on the intra-tissular distance traveled by the protons (Solov'yov et al. 2009). The direct consequence is water radiolysis, triggering the production of Reactive Oxygen Species (ROS; *i.e.,* OH°), ions, and other reactive molecules, which may in turn damage the DNA by base fragmentation, base deletion, strand breaks, and oxidative base modification. (Girdhani et al. 2013; Privett et al. 2017).

Treatment with the herbicide Paraquat induces chronic oxidative stress (Moustaka and Moustakas 2014; Moustaka et al. 2015). In contrast to UV or proton irradiation, this stress has an endogenous source originating from the chloroplast (Moustaka and Moustakas 2014). Indeed, by transferring electrons from the respiratory chain of chloroplast to surrounding oxygen molecules, Paraquat generates ROS (Moustaka and Moustakas 2014).

As mentioned in the general introduction of this thesis manuscript, several studies provided evidence that the formation of photolesions is favored in particular epigenetic contexts. Indeed, cytosine methylation (5-mC) and nucleosome positioning were both shown to favor the damageability of DNA (Gale et al. 1987; Banyasz et al. 2016). In line with these findings, first *in vivo* studies characterizing DNA damage localization indicates that CPDs are not randomly distributed all-over the genome (Premi et al. 2019). In contrast, little is known about the influence of the epigenome on oxidatively-induced DNA damage. Aside from its impacts on damageability, the epigenetic context also influences DNA repair efficiency and speed (Bohr et al. 1985; Hanawalt and Spivak 2008). For example, Transcription Coupled Repair (TCR) is initiated by the stalling of the RNA polymerase II and consequently processes DNA damages in transcriptionally active genomic regions (Hanawalt and Spivak 2008). Conversely, the Global Genome Repair (GGR), initiated by DDB2 (DAMAGED DNA-BINDING 2), even allows damage recognition in DNA wrapped around nucleosomes and thus in poorly transcribed genomic regions (Matsumoto et al. 2019). Interestingly, the interplay between DNA damage, DNA repair, and the epigenomic landscape seems to act wider upon repair (Johann to Berens and Molinier 2020). For example, DDB2 was shown to induce change in chromatin compaction upon DNA repair in Human (Fortuny et al. 2021) and was shown as a potential regulator of DNA methylation homeostasis in Arabidopsis (Schalk and Molinier 2016; Córdoba-Cañero et al. 2017). In order to further study the potential crosstalk between DNA repair and epigenome, it requires to define in detail which damages are generated by different genotoxic stresses and where these damages are localized all over the genome.

The following chapter will report where UV-C and UV-B induce photolesions and where protons and paraquat induce 8-oxoG within the genome. In addition, we will show how the constitutive heterochromatin behaves upon ionic and non-ionic irradiation.

3.2. Results & Discussion

3.2.1. Genomic landscape of UV-C-induced CPDs and 6,4-PP

UV-C mainly induces the formation of CPDs and 6,4-PPs in di-pyrimidine contexts (CC, TT, TC, and CT). However, 5-mC and the presence of nucleosomes also appear to influence the reactivity of DNA upon UV-C irradiation. Using immunolabeling approaches with anti-CPD and anti-6,4-PP antibodies, the sub-nuclear distribution of CPDs and 6,4-PPs could be followed upon UV-C exposure on DAPI stained WT nuclei (Fig. 1A). Whereas no signal was observed before irradiation, CPDs and 6,4-PP look enriched in the treated nuclei for at least 2h (Fig. 1A). Interestingly, CPDs and 6,4 PPs show remarkable overlap with DAPI labeled chromocenter regions 30’ upon UV-C (Fig. 1A). Later on, 2h upon exposure, this overlap is less striking, especially for 6,4-PPs (Fig. 1A). This observation highlights a potential enrichment of UV-C-induced photolesions in heterochromatic regions. However, a remaining signal is still present at chromocenters at 2h, showing that photodamage repair is slower in heterochromatin. Comparing the mapping of CPD/6,4-PP obtained upon Immuno-precipitation of UV-induced DNA damage (IPOUD) with nucleosome and H3K9me2 positioning along the genome shows the damageability of the heterochromatic regions (Fig. 1B).Indeed, as shown by the genomic distribution on chromosome 1 (Fig. 1B) and Venn-diagram (Fig. 2), CPD/6,4-PP (Graindorge et al. 2019) and H3K9me2 (Costas et al. 2011) enriched regions tend to significantly overlap (Fig. 2). Indeed, around 1/3 of the CPDs and 1/5 of the 6,4-PPs overlap with H3K9me2-containing regions (Fig. 2). This holds true with the overlap with nucleosomes (Fig. 2). Consequently, photolesions formation upon UV-C exposure seems enriched in constitutive heterochromatin of *Arabidopsis thaliana* in agreement with the immunolocalization experiments. One possible explanation could be that higher chromatin compaction in such H3K9me2 regions favor photodamage formation (Mao et al. 2017; Johann to Berens and Molinier 2020). According to the DNA structure and its chemistry, such highly compacted conformation would be more reactive upon UV irradiation (Markovitsi 2016). In addition, H3K9me2 triggers DNA methylation (Stroud et al. 2014; Li et al. 2018; Xu and Jiang 2020), which is known to enhance photolesions formation (Banyasz et al. 2016). The chromatin structure of these predominantly damaged and repaired regions may undergo specific changes, enabling epigenome stability and flexibility.

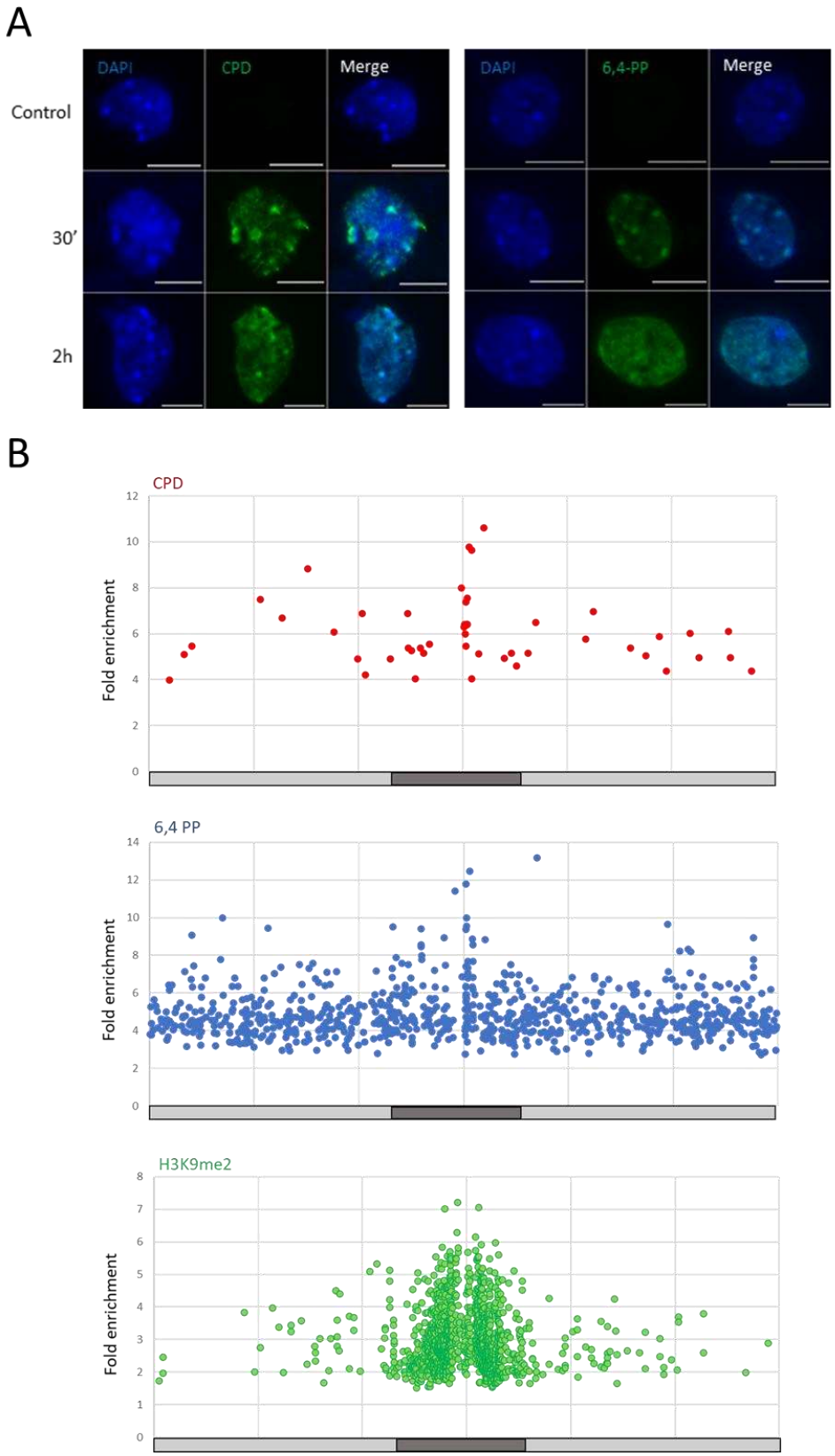

Figure 1: Genome-wide view of CPD and 6,4-PP localizations

(A) Immunolabeling of CPD or 6,4-PP (green) on DAPI stained (Blue) WT (Col-0) nuclei prepared prior, 30 min and 2h upon UV-C exposure. Scale bar = 5µm **(B)** CPDs and 6,4-PPs enrichment using IPOUD assay along the

Arabidopsis chromosome 1 (Graindorge et al. 2019). H3K9me2 enrichment along the Arabidopsis chromosome 1 according to ChIP seq data (Costas et al. 2011). Light grey: chromosome arms, dark grey: centromeric/pericentromeric region.

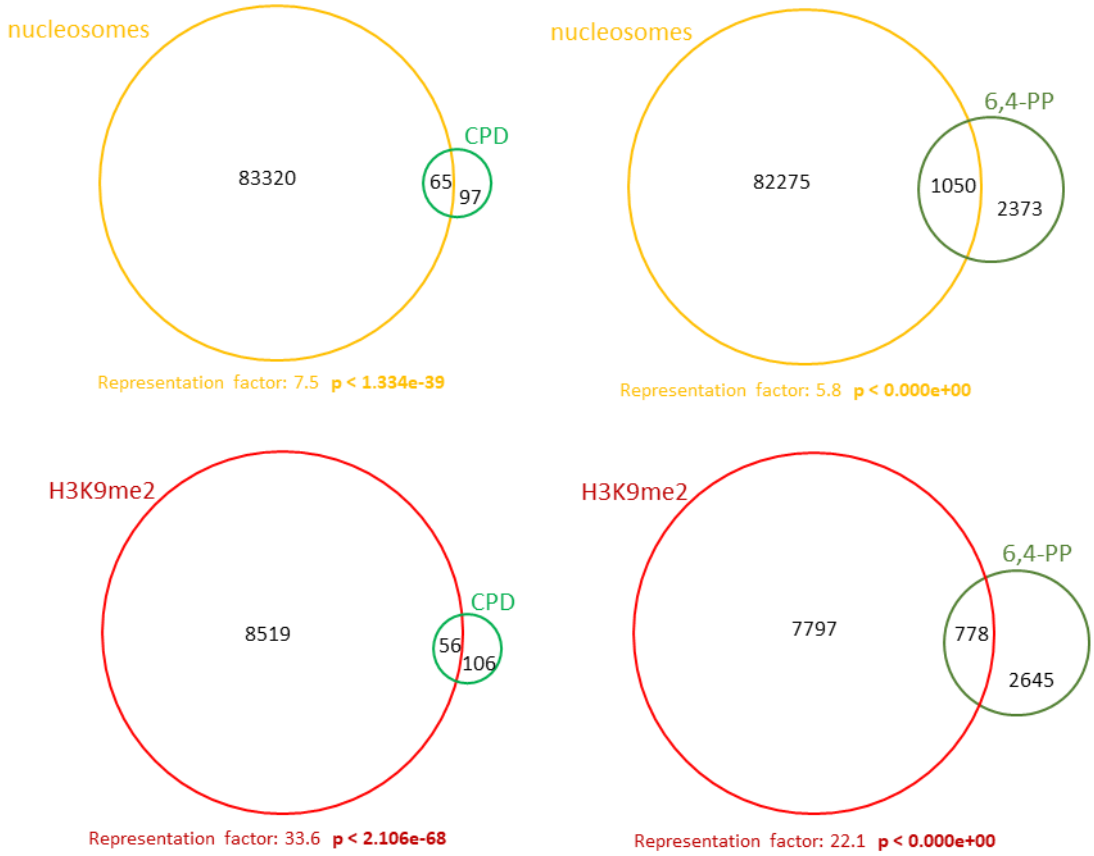

Figure 2: Venn-diagrams showing the overlap between photolesions, nucleosomes, and H3K9me2

Venn-diagrams showing the overlap between regions enriched in CPDs or 6,4-PPs, and regions enriched in nucleosomes or H3K9me2 according to IPOUD (Graindorge et al. 2019), MNase-seq (Zemach et al. 2013), and ChIP-seq assays (Costas et al. 2011), respectively. R factor and exact p-value are shown.

3.2.2. UV-C-induced methylome changes

A starting point, for the following parts of my thesis was my contribution to the characterization of DNA methylation and heterochromatin alterations of plants exposed to UV-C (Graindorge et al. 2019). We investigated the accuracy of the maintenance of the methylome and constitutive heterochromatin structure 24h upon UV-C irradiation. As described in our publication (Graindorge et al. 2019), we provided strong evidence that DNA repair processes modulate and maintain the DNA methylation landscape 24h upon UV-C (Graindorge et al. 2019). Additionally, we described that heterochromatin structures changes 24h upon UV-C, depending on the DNA repair processes used. Interestingly, we could observe that these structural changes are unlikely exclusively due to DNA methylation alterations (Graindorge et al. 2019). The full PDF is attached in § 3.5. Annex.

We decided to investigate earlier time points following UV-C irradiation to characterize a potential dynamic of the chromocenter structures. The Chromocenter Occupancy in WT and *ddb2* Arabidopsis plants significantly decreased 2h upon UV-C exposure (Fig. 3A and 3B), suggesting a precocious heterochromatin relaxation process. This change could be explained by modulation of histones PTMs and/or histone eviction/displacement and/or chromatin remodeling (Kim 2019).

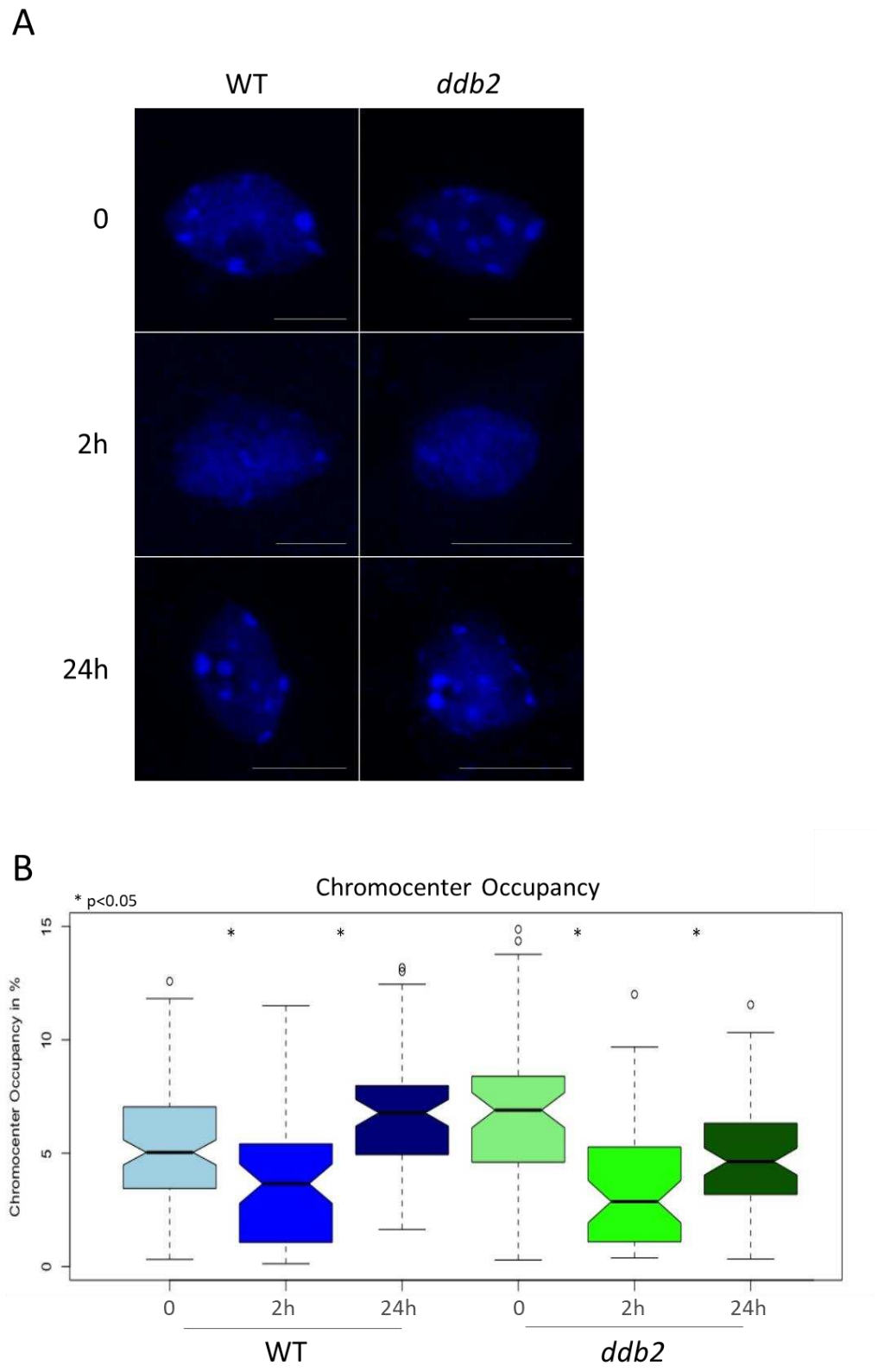

Figure 3: Chromocenter occupancy upon UV-C exposure in WT and *ddb2* plants

(A) Microscopy images of DAPI stained *Arabidopsis* WT (Col-0) and *ddb2* leaf nuclei in prior (0) and upon UV-C exposure (2h or 24h). Scale bar = 5µm. **(B)** Boxplots showing the Chromocenter Occupancies during the time course. N= at least 50 nuclei per time point. * p-value < 0.05. (Mann-Whitney U test.

3.2.3. UV-B-induced DNA damage

The previous part shows the formation of photolesion and the alterations of the methylome upon UV-C exposure. Given that the UV-C wavelength is filtered by the Ozon layer and thus does not reach the earth's surface, we did also use a more biological relevant UV wavelength: UV-B. Similar to UV-C, UV-B generates CPDs and 6-4 PP photolesions (Markovitsi 2016). However, UV-B also induces an oxidative burst through ROS production (Schuch et al. 2017). ROS are expected to react with DNA and to trigger the production of specialized metabolites involved in the defense mechanisms against ROS (Fischer et al. 2018). The predominant DNA modification generated by an oxidative burst is the 8-Oxo-G (Schuch et al. 2017).

To characterize the distribution of UV-B-induced DNA damages in Arabidopsis leaf nuclei, an Immunostaining of CPD and 8-Oxo-G was performed. As shown in Figure 4, an increased CPD signal could be observed. Upon UV-B exposure, CPDs appear enriched in chromocenter regions, like by UV-C (Fig .4).

Unfortunately, UV-B irradiated nuclei do not show significant enrichment of 8-Oxo-G when irradiated with 6750 J/m^2 (Fig. 4). Indeed, the residual signal observed is as strong as in control conditions in the absence of primary anti-8-oxo-G antibody (Fig. 4). This result could be explained by strong scavenging, preventing ROS from efficiently damaging DNA. Alternatively, it can be speculated that the used UV-B dose did not allow a strong oxidative burst.

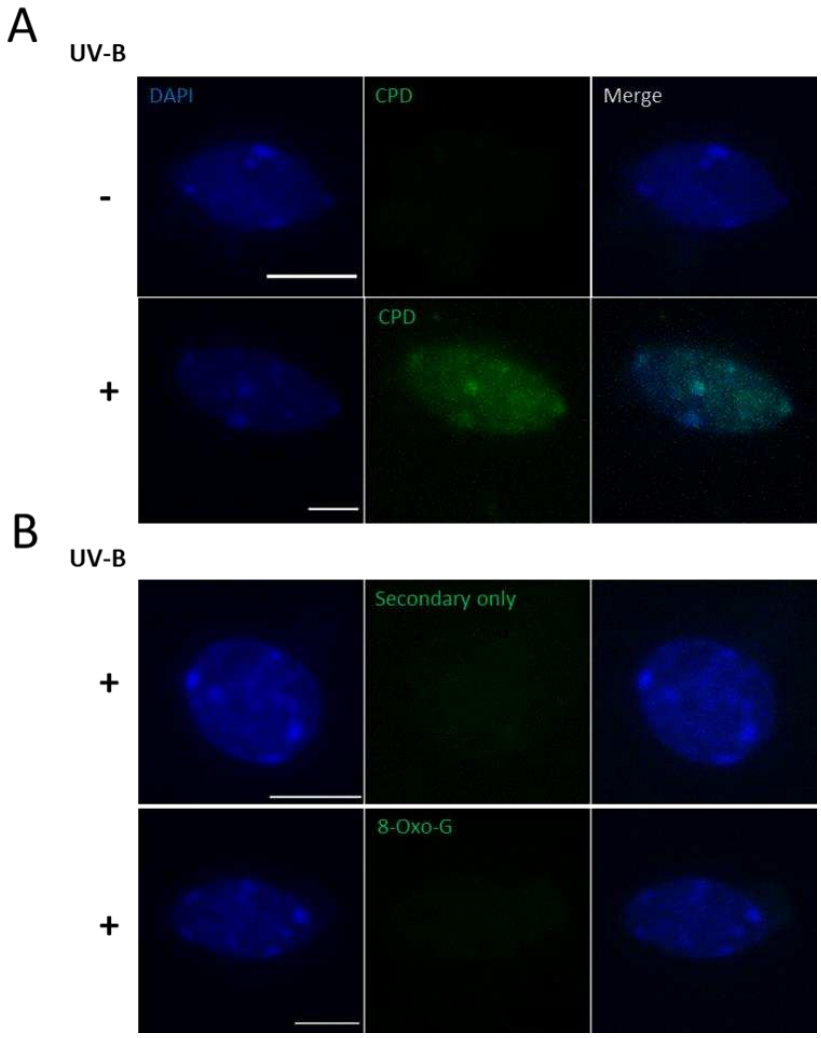

Figure 4: UV-B-induced DNA damage

Microscopy images representing immunolabeling of **(A)** CPD (green) and **(B)** 8-Oxo-G (green) on DAPI stained (Blue) WT (Col-0) nuclei prepared directly after UV-B exposure. Scale bar = 5µm.

In order to quantify more precisely the 8-Oxo-G and antioxidant metabolites induced upon UV-B exposure, a metabolome analysis approach was used. For this, leaves extracts and purified nucleosides of 8 independent biological replicates (8 controls and 8 UV-B-irradiated samples) have been analyzed by Liquide-Chromatography High-Resolution Mass-Spectrometry (LC-HRMS) using the QTOF.In a first step, a serial dilution of an 8-Oxo-G standard was used to precisely characterize its retention time and its MS-profile (Fig. 5). In a second step, the different samples were analyzed for the 8-oxo-G specific profile.

Unfortunately, 8-oxo-G could not be detected above the technical detection threshold (0.01 µg/mL), neither in whole plant extracts nor in the purified nucleoside samples (Fig. 5). To affine the analysis and overcome potential detection limits, we repeated the analysis with a Liquide-Chromatography followed by High sensitivity tandem quadrupole Mass Spectrometry approach (LC-TQ-MS/MS). Whereas guanosine and guanosine derivates such as N2, N2-dimethylguanosine, 2-O-methylguanosine, or 7-methylguanosine were easily detected, the 8-Oxo-Guanosine could only be observed in 3 samples at a concentration below 1 ng/ml (Fig. 6). Surprisingly, the highest 8-Oxo-G concentration was found in a control sample (Fig. 6). When analyzing the purified nucleoside fraction, relatively low amounts of guanosine could be detected, highlighting the need to improve the yield of our protocol for the analysis of purified nucleosides. Altogether, these observations may lead to the question, did our UV-B exposure induce an oxidative burst?

For answering this question, in a third step, we performed a non-targeted LC-HRMS strategy to identify metabolites related to mechanisms of ROS defense. The non-targeted LC-HR-MS QTOF approach shows a significant change in the concentration of 43 molecules in the metabolome extracted from irradiated leaves (Fig. 7). Among them, 23 molecules could be annotated, and several are related to potential oxidation processes or antioxidative activity (Fig. 7). For example, 5-Hydroxy-L-Tryptophan (5-HTP), an oxidation product of L-Tryptophan, shows an 80-fold increase compared to untreated samples (Fig. 7). Interestingly the role of 5-HTP in inhibiting oxidative damage was already largely described *in vitro* and other organisms but not yet in plants (Keithahn and Lerchl 2005). Tryptophan is an essential substrate for the 4-Methoxyglucobrassicin consequently, the observed decrease in concentration may be explained by competition with the, apparently, highly active 5-HTP synthesis pathway. Aside of 5-HTP, two other metabolites with antioxidant faculties increased in concentration upon treatment: 1,6-Dihydroxy-1,2,3,4-tetrahydro-beta-carboline the oxidation product of 1,2,3,4-tetrahydro-beta-carboline (Fig. 7) (Ichikawa et al. 2002) and Antrocinnamomin B (Wu et al. 2008).

In Sum, these approaches confirm that our UV-B treatment induces the formation of photolesions as well as metabolite involved in oxidative stress response, highlighting that an oxidative burst occurred.

However, the UV-B dose used was not sufficient to form detectable 8-Oxo-G. Therefore, more effort will be devoted to improve the irradiation conditions and further investigate the formation of oxidatively-induced DNA damage following UV-B exposure. The dynamics of constitutive heterochromatin upon UV-B, as a biological relevant UV wavelength inducing photodamages and intrinsic signaling through the photoreceptor UVR8 (Liang et al. 2019), will be further characterized in chapter IV.

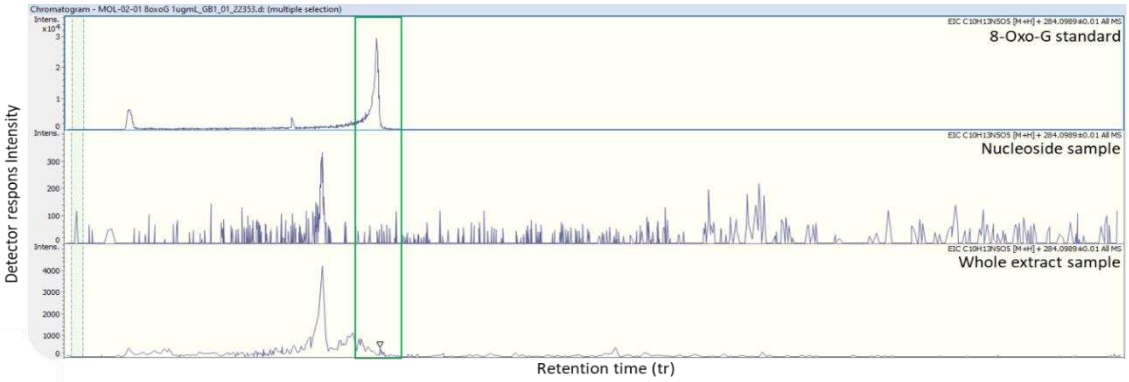

Figure 5: Targeted 8-oxo-G analysis upon UV-B exposure using QTOF

Chromatogram showing the expected peak of 8-Oxo-G in a standard sample, the absence of peaks in nucleoside and whole extract samples. The green square highlights the specific peak of 8-Oxo-G.

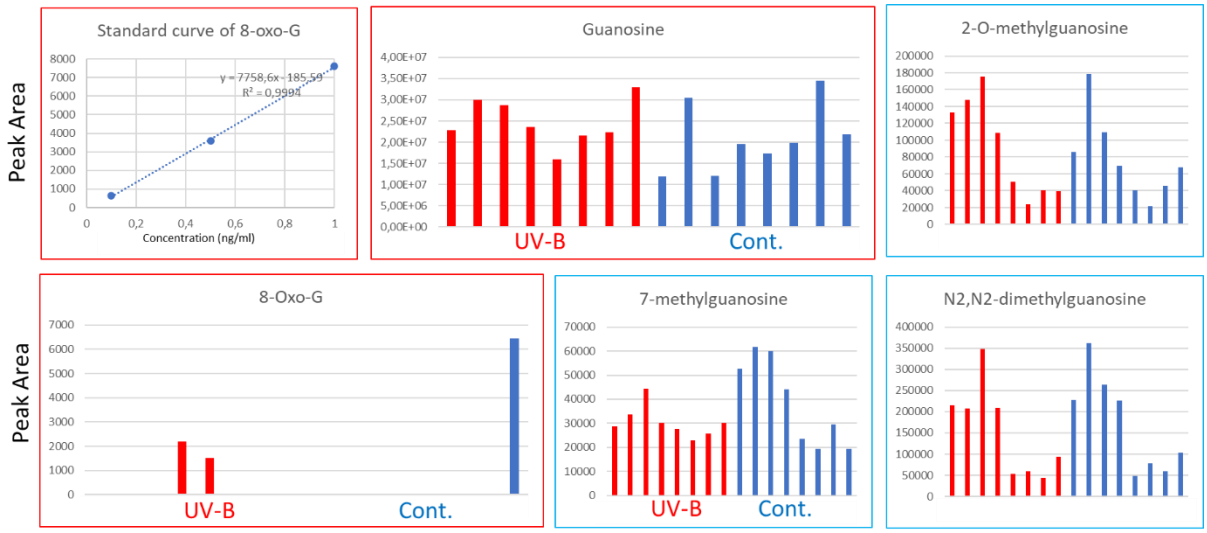

Figure 6: Targeted nucleoside analysis upon UV-B exposure using EvoQ

Standard curve of 8-oxo-G, for low concentrations (<1ng/ml). Histograms showing peaks areas (concentration) of Guanosine, N2, N2-dimethylguanosine,2-O-methylguanosine, 7-methylguanosine and 8-Oxo-G in UV-B and control samples.

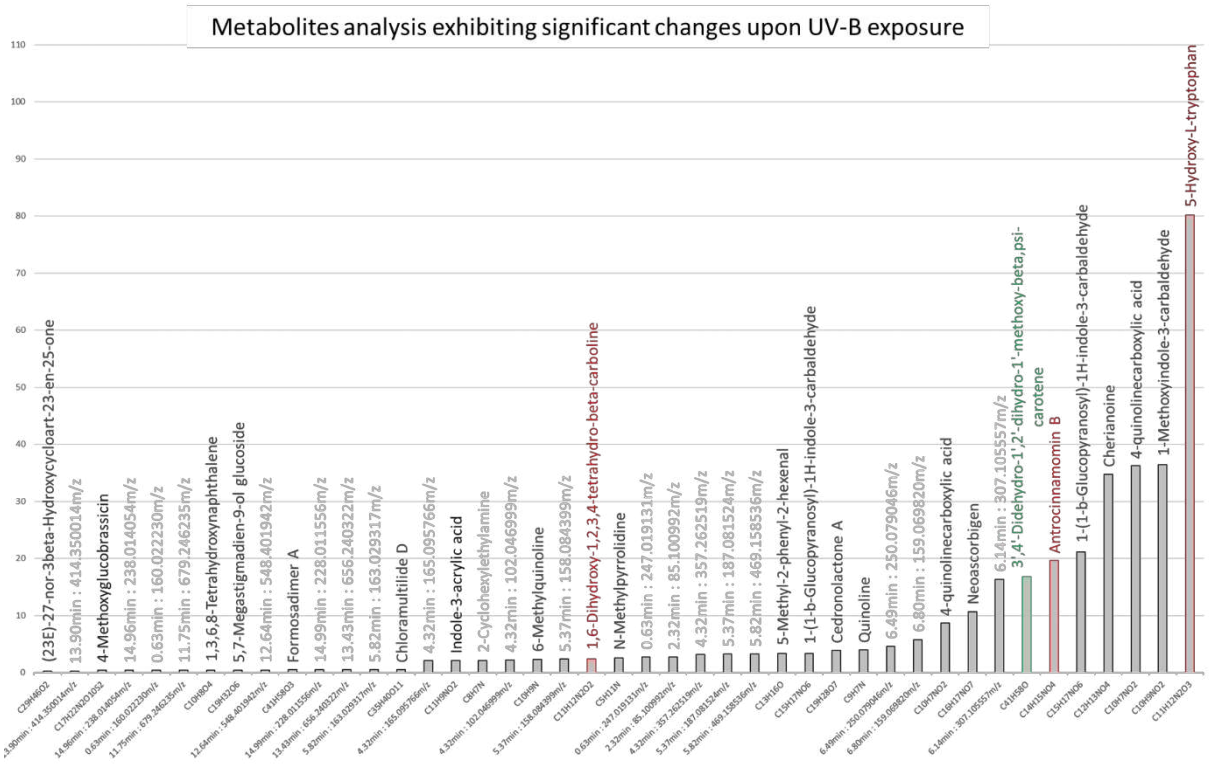

Figure 7: Non-targeted metabolome analysis of WT Arabidopsis leaves exposed to UV-B

Histogram showing the fold change concentrations of metabolites exhibiting significant differences in untreated *vs* UV-B treated samples (non-parametric t-test (FC>2; P-value<0,05)). In red, the metabolites with antioxidative potential. In green, the UV-B-induced metabolites (absent in all control samples and present in all UV-B-treated samples).

3.2.4. Oxidatively-induced DNA damage and heterochromatin reshaping

UV-B exposure induces oxidative stress but does not allow efficient detection of 8-oxo-G. In order to overtake this limitation and to determine the genomic localization of 8-Oxo-G, we decided to uncouple photolesion formation and oxidatively-induced DNA damage. For this, we used proton irradiations in collaboration with a team of physicists (Institut Pluridisciplinaire Hubert Curien). This fast energy deposition method is expected to induce water radiolysis in living tissues, thereby inducing a strong oxidative burst (Privett et al. 2017). Arabidopsis leaves were irradiated with a 100 Gy proton. As shown in Figure. 8A, a significant enrichment of 8-Oxo-G specific signal could be observed upon proton irradiation. This signal appears to be spread all over the nucleus (Fig. 8A) and resembles the results reported in human cells when observing the localization of 8-Oxo-G (D'Augustin et al. 2020).

In parallel we used a chemical treatment, Paraquat, to induce an oxidative burst. Following paraquat treatment, the 8-Oxo-G specific signal accumulates around chromocenter regions (Fig. 8A). This pattern is seldom observed in the proton-irradiated nuclei. Therefore, the source of oxidative stress seems to influence the damage localization.

Finally, as previously described for UV-C, the effect of proton irradiation on heterochromatic structures was analyzed in WT (Col-0) plant leaves nuclei 24h upon exposure. In this set of experiments, the chromocenter occupancy of control unirradiated plants was compared with the chromocenter occupancy of nuclei extracted from the leaves targeted by a 100 Gy proton beam as well as in nuclei prepared from opposite leaves (Fig. 8B). This would allow to identify a potential ROS signaling bystander effect (Jella et al. 2018). Interestingly, 24h upon irradiation, only nuclei extracted from targeted leaves show a significant increase in Chromocenter occupancy (Fig. 8B and 8C). Consequently, the proton irradiation, induces changes in heterochromatic structures in Arabidopsis, as previously described with UV-C exposure. One plausible explanation, would be that this increase in CO, depends on the DNA repair process more than on the damage that needs to be repaired.

According to our observations, it can be questioned how the epigenome of human cells evolves upon a proton beam therapy, which is notably used for the microtargeting of cancer cells (D'Augustin et al. 2020). Now ongoing work tries to follow the metabolomic and genomic changes induced by different proton irradiation protocols. The awaited results may provide more helpful insight in the cellular, genetic and epigenetic processes triggered upon proton irradiation of living tissues.

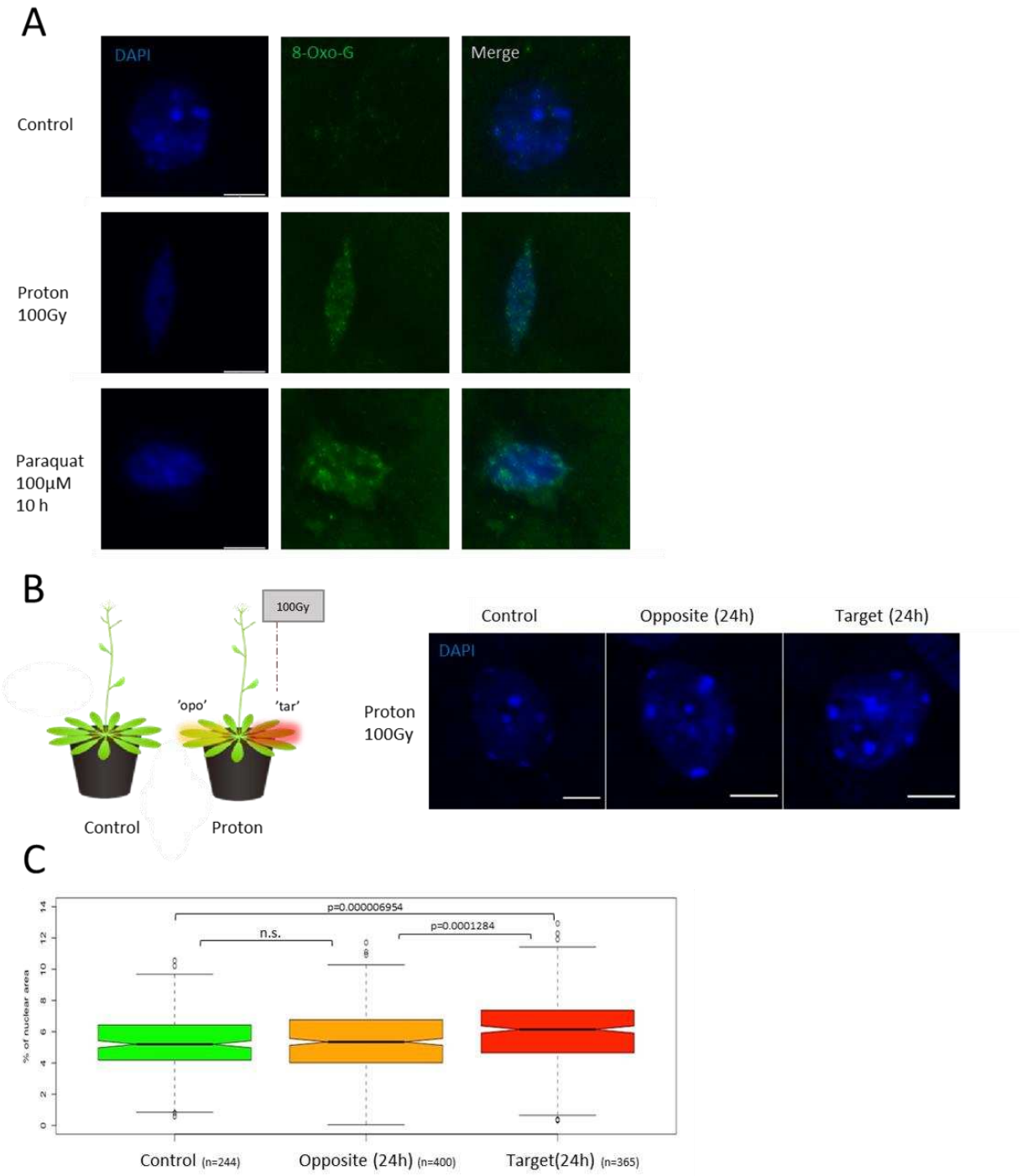

Figure 8: Immunolocalization of 8-oxo-G and measurements of Chromocenter Occupancy

(A) Microscopy images of immunolabeled 8-Oxo-G (green) WT (Col-0) Nuclei prepared directly after proton irradiation or after 10h of Paraquat treatment. DAPI stained (Blue). **(B)** Left panel: experimental procedure of proton irradiation. opo: opposite unirradiated leaf. tar: target irradiated leaf. Right panel: DAPI-stained nuclei of WT (Col-0) plants in the control condition(0) and 24h upon proton irradiation. Scale bar = 5µm **(C)** Boxplots showing the variation in chromocenter occupancies in WT nuclei in the control condition (0) and upon proton irradiation (24h). The exact p-values are shown. n.s: non-significant (Mann-Whitney U test).

3.3. Conclusions

While UV-C- and UV-B-induced photolesions showed a significant overlap with heterochromatic regions, the oxidative stress induced by proton irradiation seems to induce 8-Oxo-G formation all over the genome. However, in the case of chronic exposure to oxidative stress (using paraquat), the distribution of 8-Oxo-G becomes displaced to regions around chromocenters. However, both genotoxic stresses, induced by UV-C or by proton irradiation, alter in a similar way the shape of constitutive heterochromatin 24h upon treatment. These alterations may be the consequence of a complex dynamic and interplay between DNA repair and epigenome reshaping processes. The first evidence of such precocious events is supported by the analysis of Arabidopsis nuclei 2h upon UV-C, showing a massive decrease of the Chromocenter Occupancy. Based on these results we aim at deciphering the underlying molecular mechanisms involved in the reshaping of heterochromatin dynamics during and upon DNA repair.

3.4. References

Banyasz A, Esposito L, Douki T, Perron M, Lepori C, Improta R, Markovitsi D (2016) Effect of C5-Methylation of Cytosine on the UV-Induced Reactivity of Duplex DNA: Conformational and Electronic Factors. J Phys Chem B 120:4232–4242. https://doi.org/10.1021/acs.jpcb.6b03340

Bohr VA, Smith CA, Okumoto DS, Hanawalt PC (1985) DNA repair in an active gene: Removal of pyrimidine dimers from the DHFR gene of CHO cells is much more efficient than in the genome overall. Cell 40:359–369. https://doi.org/10.1016/0092-8674(85)90150-3

Córdoba-Cañero D, Cognat V, Ariza RR, Roldán Arjona T, Molinier J (2017) Dual control of ROS1-mediated active DNA demethylation by DNA damage-binding protein 2 (DDB2). Plant J 92:1170–1181. https://doi.org/10.1111/tpj.13753

Costas C, de la Paz Sanchez M, Stroud H, Yu Y, Oliveros JC, Feng S, Benguria A, López-Vidriero I, Zhang X, Solano R, Jacobsen SE, Gutierrez C (2011) Genome-wide mapping of Arabidopsis thaliana origins of DNA replication and their associated epigenetic marks. Nat Struct Mol Biol 18:395–400. https://doi.org/10.1038/nsmb.1988

D'Augustin O, Huet S, Campalans A, Radicella JP (2020) Lost in the Crowd: How Does Human 8-Oxoguanine DNA Glycosylase 1 (OGG1) Find 8-Oxoguanine in the Genome? Int J Mol Sci 21:E8360. https://doi.org/10.3390/ijms21218360

Fischer N, Seo E-J, Efferth T (2018) Prevention from radiation damage by natural products. Phytomedicine 47:192–200. https://doi.org/10.1016/j.phymed.2017.11.005

Fortuny A, Chansard A, Caron P, Chevallier O, Leroy O, Renaud O, Polo SE (2021) Imaging the response to DNA damage in heterochromatin domains reveals core principles of heterochromatin maintenance. Nat Commun 12:2428. https://doi.org/10.1038/s41467-021-22575-5

Gale JM, Nissen KA, Smerdon MJ (1987) UV-induced formation of pyrimidine dimers in nucleosome core DNA is strongly modulated with a period of 10.3 bases. Proc Natl Acad Sci USA 84:6644–6648. https://doi.org/10.1073/pnas.84.19.6644

Girdhani S, Sachs R, Hlatky L (2013) Biological effects of proton radiation: what we know and don't know. Radiat Res 179:257–272. https://doi.org/10.1667/RR2839.1

Graindorge S, Cognat V, Johann to Berens P, Mutterer J, Molinier J (2019) Photodamage repair pathways contribute to the accurate maintenance of the DNA methylome landscape upon UV exposure. PLoS Genet 15:e1008476. https://doi.org/10.1371/journal.pgen.1008476

Hanawalt PC, Spivak G (2008) Transcription-coupled DNA repair: two decades of progress and surprises. Nat Rev Mol Cell Biol 9:958–970. https://doi.org/10.1038/nrm2549

Ichikawa M, Ryu K, Yoshida J, Ide N, Yoshida S, Sasaoka T, Sumi S-I (2002) Antioxidant effects of tetrahydro-beta-carboline derivatives identified in aged garlic extract. Biofactors 16:57–72. https://doi.org/10.1002/biof.5520160302

Jella KK, Moriarty R, McClean B, Byrne HJ, Lyng FM (2018) Reactive oxygen species and nitric oxide signaling in bystander cells. PLoS One 13:e0195371. https://doi.org/10.1371/journal.pone.0195371

Johann to Berens P, Molinier J (2020) Formation and Recognition of UV-Induced DNA Damage within Genome Complexity. Int J Mol Sci 21. https://doi.org/10.3390/ijms21186689

Keithahn C, Lerchl A (2005) 5-hydroxytryptophan is a more potent in vitro hydroxyl radical scavenger than melatonin or vitamin C. J Pineal Res 38:62–66. https://doi.org/10.1111/j.1600-079X.2004.00177.x

Kim J-H (2019) Chromatin Remodeling and Epigenetic Regulation in Plant DNA Damage Repair. Int J Mol Sci 20:E4093. https://doi.org/10.3390/ijms20174093

Levin WP, Kooy H, Loeffler JS, DeLaney TF (2005) Proton beam therapy. Br J Cancer 93:849–854. https://doi.org/10.1038/sj.bjc.6602754

Li X, Harris CJ, Zhong Z, Chen W, Liu R, Jia B, Wang Z, Li S, Jacobsen SE, Du J (2018) Mechanistic insights into plant SUVH family H3K9 methyltransferases and their binding to context-biased non-CG DNA methylation. Proc Natl Acad Sci U S A 115:E8793–E8802. https://doi.org/10.1073/pnas.1809841115

Liang T, Yang Y, Liu H (2019) Signal transduction mediated by the plant UV-B photoreceptor UVR8. New Phytol 221:1247–1252. https://doi.org/10.1111/nph.15469

Mao P, Wyrick JJ, Roberts SA, Smerdon MJ (2017) UV-Induced DNA Damage and Mutagenesis in Chromatin. Photochem Photobiol 93:216–228. https://doi.org/10.1111/php.12646

Markovitsi D (2016) UV-induced DNA Damage: The Role of Electronic Excited States. Photochem Photobiol 92:45–51. https://doi.org/10.1111/php.12533

Matsumoto S, Cavadini S, Bunker RD, Grand RS, Potenza A, Rabl J, Yamamoto J, Schenk AD, Schübeler D, Iwai S, Sugasawa K, Kurumizaka H, Thomä NH (2019) DNA damage detection in nucleosomes involves DNA register shifting. Nature 571:79–84. https://doi.org/10.1038/s41586-019-1259-3

Moustaka J, Moustakas M (2014) Photoprotective mechanism of the non-target organism Arabidopsis thaliana to paraquat exposure. Pestic Biochem Physiol 111:1–6. https://doi.org/10.1016/j.pestbp.2014.04.006

Moustaka J, Tanou G, Adamakis I-D, Eleftheriou EP, Moustakas M (2015) Leaf Age-Dependent Photoprotective and Antioxidative Response Mechanisms to Paraquat-Induced Oxidative Stress in Arabidopsis thaliana. Int J Mol Sci 16:13989–14006. https://doi.org/10.3390/ijms160613989

Premi S, Han L, Mehta S, Knight J, Zhao D, Palmatier MA, Kornacker K, Brash DE (2019) Genomic sites hypersensitive to ultraviolet radiation. Proc Natl Acad Sci U S A 116:24196–24205. https://doi.org/10.1073/pnas.1907860116

Privett AJ, Teixeira ES, Stopera C, Morales JA (2017) Exploring water radiolysis in proton cancer therapy: Time-dependent, non-adiabatic simulations of H+ + (H2O)1-6. PLoS One 12:e0174456. https://doi.org/10.1371/journal.pone.0174456

Schalk C, Molinier J (2016) Global Genome Repair factors controls DNA methylation patterns in Arabidopsis. Plant Signal Behav 11:e1253648. https://doi.org/10.1080/15592324.2016.1253648

Schuch AP, Moreno NC, Schuch NJ, Menck CFM, Garcia CCM (2017) Sunlight damage to cellular DNA: Focus on oxidatively generated lesions. Free Radic Biol Med 107:110–124. https://doi.org/10.1016/j.freeradbiomed.2017.01.029

Solov'yov AV, Surdutovich E, Scifoni E, Mishustin I, Greiner W (2009) Physics of ion beam cancer therapy: a multiscale approach. Phys Rev E Stat Nonlin Soft Matter Phys 79:011909. https://doi.org/10.1103/PhysRevE.79.011909

Stroud H, Do T, Du J, Zhong X, Feng S, Johnson L, Patel DJ, Jacobsen SE (2014) Non-CG methylation patterns shape the epigenetic landscape in Arabidopsis. Nat Struct Mol Biol 21:64–72. https://doi.org/10.1038/nsmb.2735

Wu M-D, Cheng M-J, Wang B-C, Yech Y-J, Lai J-T, Kuo Y-H, Yuan G-F, Chen I-S (2008) Maleimide and maleic anhydride derivatives from the mycelia of Antrodia cinnamomea and their nitric oxide inhibitory activities in macrophages. J Nat Prod 71:1258–1261. https://doi.org/10.1021/np070634k

Xu L, Jiang H (2020) Writing and Reading Histone H3 Lysine 9 Methylation in Arabidopsis. Frontiers in Plant Science 11

Zemach A, Kim MY, Hsieh P-H, Coleman-Derr D, Eshed-Williams L, Thao K, Harmer SL, Zilberman D (2013) The Arabidopsis nucleosome remodeler DDM1 allows DNA methyltransferases to access H1-containing heterochromatin. Cell 153:193–205. https://doi.org/10.1016/j.cell.2013.02.033

3.5. Annex

PLOS GENETICS

RESEARCH ARTICLE

Photodamage repair pathways contribute to the accurate maintenance of the DNA methylome landscape upon UV exposure

Stéfanie Graindorge, Valérie Cognat, Philippe Johann to Berens, Jérôme Mutterer, Jean Molinier*

Institut de biologie moléculaire des plantes, UPR2357-CNRS, Strasbourg, France

* jean.molinier@ibmp-cnrs.unistra.fr

OPEN ACCESS

Citation: Graindorge S, Cognat V, Johann to Berens P, Mutterer J, Molinier J (2019) Photodamage repair pathways contribute to the accurate maintenance of the DNA methylome landscape upon UV exposure. PLoS Genet 15(11): e1008476. https://doi.org/10.1371/journal.pgen.1008476

Editor: Julian E. Sale, MRC Laboratory of Molecular Biology, UNITED KINGDOM

Received: July 1, 2019

Accepted: October 13, 2019

Published: November 18, 2019

Peer Review History: PLOS recognizes the benefits of transparency in the peer review process; therefore, we enable the publication of all of the content of peer review and author responses alongside final, published articles. The editorial history of this article is available here: https://doi.org/10.1371/journal.pgen.1008476

Data Availability Statement: WGBS, DNA-seq and small RNA-seq raw data generated in this work are

Abstract

Plants are exposed to the damaging effect of sunlight that induces DNA photolesions. In order to maintain genome integrity, specific DNA repair pathways are mobilized. Upon removal of UV-induced DNA lesions, the accurate re-establishment of epigenome landscape is expected to be a prominent step of these DNA repair pathways. However, it remains poorly documented whether DNA methylation is accurately maintained at photodamaged sites and how photodamage repair pathways contribute to the maintenance of genome/methylome integrities. Using genome wide approaches, we report that UV-C irradiation leads to CHH DNA methylation changes. We identified that the specific DNA repair pathways involved in the repair of UV-induced DNA lesions, Direct Repair (DR), Global Genome Repair (GGR) and small RNA-mediated GGR prevent the excessive alterations of DNA methylation landscape. Moreover, we identified that UV-C irradiation induced chromocenter reorganization and that photodamage repair factors control this dynamics. The methylome changes rely on misregulation of maintenance, *de novo* and active DNA demethylation pathways highlighting that molecular processes related to genome and methylome integrities are closely interconnected. Importantly, we identified that photolesions are sources of DNA methylation changes in repressive chromatin. This study unveils that DNA repair factors, together with small RNA, act to accurately maintain both genome and methylome integrities at photodamaged silent genomic regions, strengthening the idea that plants have evolved sophisticated interplays between DNA methylation dynamics and DNA repair.

Author summary

Living organisms have to efficiently respond to environmental cues that interfere with different cellular processes. Upon exposure to biotic/abiotic stresses, the coordinated maintenance of genome and epigenome integrity is crucial to allow the accurate progress of the developmental programs. In plants the sunlight used for photosynthesis also induces the formation of photodamage altering DNA structure. Although photolesions repair

publicly accessible through the GEO registration number: GSE132750.

Funding: JM was supported by the LABEX NetRNA (ANR-10-LABX-0036_NETRNA) The funders had no role in study design, data collection and analysis, decision to publish, or preparation of the manuscript

Competing interests: The authors have declared that no competing interests exist.

pathways are well characterized, the side effect of UV irradiation on epigenome integrity is yet-to-be fully investigated. Using genome wide approaches and several photodamage repair deficient Arabidopsis plants we determined that UV-C irradiation induces alterations of DNA methylation landscape and that all photodamage repair pathways contribute to the accurate maintenance of methylome integrity predominantly in silent genomic regions. These UV-induced methylation changes are accompanied by the modulation of constitutive heterochromatin organization. Moreover, our study highlighted that photolesions are source of DNA methylation alterations strengthening the idea that complex interplays between DNA damage, DNA repair and DNA methylation dynamics exist.

Introduction

DNA carries the genetic information that living organisms decrypt to efficiently ensure their developmental programs and their response/adaption to environmental cues. Exposure to biotic/abiotic stresses can directly or indirectly induce the formation of DNA damage such as bases modifications, DNA breaks, alterations of DNA structure all interfering with DNA replication and transcription [1]. Due to their lifestyle, photosynthetic organisms use the beneficial effect of sunlight [2]. However, they have to cope with the damaging effects of specific wavelengths that impact their genome integrity [3]. Indeed, ozone filtered ultraviolet (UV 315–400 nm) and infra-red (IR > 700 nm) induce different types of genomic alterations such as DNA damage, Transposable Elements (TE) mobilization and transposition [4, 5, 6]. In order to maintain genome stability, DNA repair pathways and tight suppression of transposition need to be efficiently activated to prevent DNA sequence alterations and/or genome rearrangements [7, 8, 9]. UV-B (environmental wavelength) and UV-C (experimental wavelength) directly react with DNA bases to produce photolesions [10, 11]. The induced photodamage are cyclobutane pyrimidine dimers (CPDs) and 6,4-photoproducts (6,4 PP; [4]). Both types of photolesions are formed between di-pyrimidines (TT, CC, TC and CT; [3]) and are localized in euchromatin and heterochromatin [12].

In plants, UV-induced DNA lesions are preferentially repaired by Direct Repair (DR) that is a light-dependent error-free process catalyzed by enzymes called DNA photolyases [13]. In *Arabidopsis thaliana*, two active photolyases act specifically on photolesions: PHR1 on CPDs and UVR3 on 6,4 PP [4]. Conversely, a light-independent mechanism, called Nucleotide Excision Repair (NER), repairs photolesions by the excision of the damaged DNA strand, followed by restoration of an intact double helix through *de novo* DNA synthesis [14]. NER is subdivided into two sub-pathways: Transcription-Coupled Repair (TCR) and Global Genome Repair (GGR), that process photolesions along actively transcribed DNA strands or throughout the genome, respectively [14]. The recognition of photolesions during TCR and GGR differ whereas the following steps, DNA unwinding, excision, gap filling and ligation share similar factors [14]. In actively transcribed genomic regions, the stalled RNA POLYMERASE II (RNA POL II) triggers the recognition signal that allows recruiting the COKAYNE SYNDROME proteins A and B (CSA, CSB; [14]). Conversely, during GGR, the DNA DAMAGE--BINDING PROTEIN 2 (DDB2) recognizes the UV-induced DNA lesions in un-transcribed or weakly transcribed genomic regions [14, 15].

Interestingly, DDB2 also associates with the silencing factor ARGONAUTE 1 (AGO1) to form a chromatin-bound complex with 21-nt small RNA (siRNAs, [16]). This class of small RNAs, called UV-induced siRNA (uviRNAs), originates from the photo-damaged regions (mainly TE and intergenic regions) and involves a non-canonical biogenesis pathway

requiring the plant specific RNA POLYMERASE IV (RNA POL IV), RNA-DEPENDENT RNA POLYMERASE 2 (RDR2) and DICER-LIKE 4 (DCL4, 16]). The DDB2-AGO1-uviRNA complex loads on chromatin upon UV irradiation and likely facilitates photo-damage recognition in an RNA/DNA complementary manner [16]. This recently unveiled DNA repair pathway is called small RNA-mediated GGR.

5-methyl cytosine (5-mC) is a base modification that is a component of the epigenome contributing, with histones post-translational modifications (PTM), to the silencing of TE and to the regulation of gene expression [17]. In plants, cytosines are methylated in the symmetric CG, CHG and asymmetric CHH sequence contexts (where H = A, T, or C; [18]). Upon DNA replication, DNA methylation status of the newly synthetized DNA strand needs to be properly maintained [18]. In Arabidopsis, the methyl moiety is deposited on cytosine by 4 DNA methyltransferases: METHYLTRANSFERASE 1 (MET1), CHROMOMETHYLASE 3 (CMT3), CHROMOMETHYLASE 2 (CMT2) and DOMAINS REARRANGED METHYLTRANSFERASE 2 (DRM2) [18]. These enzymes specifically maintain DNA methylation in the CG (MET1), CHG (CMT3) and CHH (CMT2 and DRM2) sequence contexts [18]. Additionally, cytosines can be methylated *de novo* by the RNA-directed DNA methylation (RdDM) pathway [19]. This process involves two plant-specific RNA POLYMERASES, RNA POL IV and RNA POL V [19]. RNA POL IV in association with RDR2 produces dsRNA precursors that are diced into 24-nt siRNAs by DCL3 [19]. These siRNAs are loaded into AGO4, which together with DRM2 are recruited to chromatin by the RNA POL V to methylate DNA in the 3 sequences contexts [19].

The DNA methylation profile is the result of the complex balance between gain (*de novo*), maintenance and loss/removal [20]. Indeed, DNA methylation can be passively lost upon DNA replication due to inefficient maintenance process [21]. Conversely, DNA methylation could be actively removed by specific 5-mC DNA glycosylases [21]. The Arabidopsis genome codes for 4 DNA demethylases: REPRESSOR OF SILENCING 1 (ROS1), DEMETER (DME), DEMETER LIKE-2 (DML2) and DEMETER LIKE-3 (DML3) which counteracts RdDM to prevent the spreading of DNA methylation [21]. Active DNA demethylation is related to Base Excision Repair (BER), highlighting that 5-mC is considered as a modified base like any other DNA lesions and thus strengthens the notion that DNA repair and DNA methylation dynamics are closely related [21].

Interestingly, several studies have uncovered that DNA repair factors control the shaping of the DNA methylation landscape. Arabidopsis plants defective in expression of the Mismatch Repair factor, mutS HOMOLOG1 (MSH1), exhibited heritable DNA methylation changes [22]. Arabidopsis DDB2 loss of function leads to DNA methylation alterations at many repeat loci [23]. Indeed, DDB2 forms a protein complex with AGO4 and ROS1 that controls *de novo* DNA methylation and expression/activity of ROS1 [23, 24]. Moreover, depletions of cognate GGR factors in plants and in mammals also lead to alterations of DNA methylation profiles at particular loci [25, 26]. Collectively, these studies robustly support the idea that direct interplays between DNA repair and DNA methylation dynamics exist [3]. Additionally, most of the DNA repair pathways, including NER, are DNA synthesis-dependent repair process [9]. Therefore, the re-establishment of proper DNA methylation landscape at damaged/repaired sites is a prominent part of these pathways that should not be under estimated. Ultimately, maintenance of genome and methylome integrities have to be considered as mechanistically interconnected.

The consequences of environmental cues on DNA methylation landscape as well as the putative role of DNA methylation/demethylation-related factors in response to biotic/abiotic stresses have been extensively reported [27, 28, 29, 30]. Biotic and abiotic stresses exposures alter DNA methylome to different extents, leading to the modulation of gene expression, thus

reflecting that DNA methylation mediates response to environmental stress [27, 31, 32]. However, it must also be taken into consideration that most of these stresses also induce DNA damage such as oxidatively-induced DNA modifications, Single and Double Strand Breaks (SSB and DSB) that need to be repaired in order to maintain genome integrity [3, 33]. The effect of genotoxic stress exposure on methylome integrity are yet-to-be fully investigated. Therefore, a major challenge would be to assess whether DNA damage could be sources of DNA methylation changes or not, and also to decipher to which extent particular DNA repair pathways could contribute to control methylome integrity not only genome wide but specifically at damaged sites and upon repair. To uncover this, we took advantage of plants that have to efficiently cope with the deleterious effects of UV radiation and that have evolved sophisticated interconnections between DNA methylation dynamics and DNA repair [3].

In this study, we used genome wide approaches to identify that UV-C irradiation leads to DNA methylation changes predominantly in asymmetric context. These changes are concomitant with the release of silencing of particular repeats and with alterations of chromocenters organization. We unveiled that the DNA repair pathways involved in the repair of UV-induced DNA lesions, namely, DR, GGR and small RNA-mediated GGR, prevent excessive alterations of DNA methylation upon UV-C irradiation. The methylome changes rely on the misregulation of maintenance, *de novo* and active DNA demethylation pathways highlighting that maintenance of genome and methylome integrities are interconnected. The genome wide mapping of UV-C induced photolesions revealed their predominant locations at centromeric/pericentromeric regions. The cross-comparison of methylome changes and of photodamaged regions allowed identifying that UV-C-induced DNA lesions are sources of DNA methylation alterations. Collectively, our data suggest that DNA repair factors, together with small RNA, act to accurately maintain genome and methylome integrities at damaged sites in repressive chromatin, including both constitutive and facultative heterochromatin.

Results

UV-C irradiation induces changes of the DNA methylation landscape

In order to characterize the effect of UV-C irradiation on DNA methylation landscape, we determined by whole-genome bisulfite sequencing (WGBS) the DNA methylome of WT Arabidopsis plants prior and 24h upon UV-C exposure. Importantly, the UV-C dose, the growth conditions and the time points used (see methods for details), were set up to favor an efficient induction of photolesions and to prevent significant changes in developmental phenotypes [34, 35].

Indeed, the photodamage repair is expected to be completed 24h upon UV-C exposure in WT and also in DNA repair deficient Arabidopsis plants, allowing the determination of the methylome landscape including repaired genomic regions.

In WT plants, comparison of the DNA methylation levels prior irradiation with those of 24h upon UV-C exposure revealed around 2,000 Differentially Methylated Regions (DMRs) including 55% of hyper-DMRs and 45% of hypo-DMRs, predominantly in the CHH asymmetric context (Figs 1A and S1A). These UV-C-induced DNA methylation changes are predominantly located within the centromeric and pericentromeric regions (Figs 1B, S2A and S3) mainly overlapping with chromatin state 6 (intergenic regions) and with constitutive heterochromatic states 8 and 9 (GC rich within intergenic regions and TE; S1B Fig, [36]). Importantly, the distribution of chromatin-states containing DMRs significantly differs from their overall distribution in the Arabidopsis genome, highlighting a strong bias for methylation changes within constitutive heterochromatin (S1B Fig).

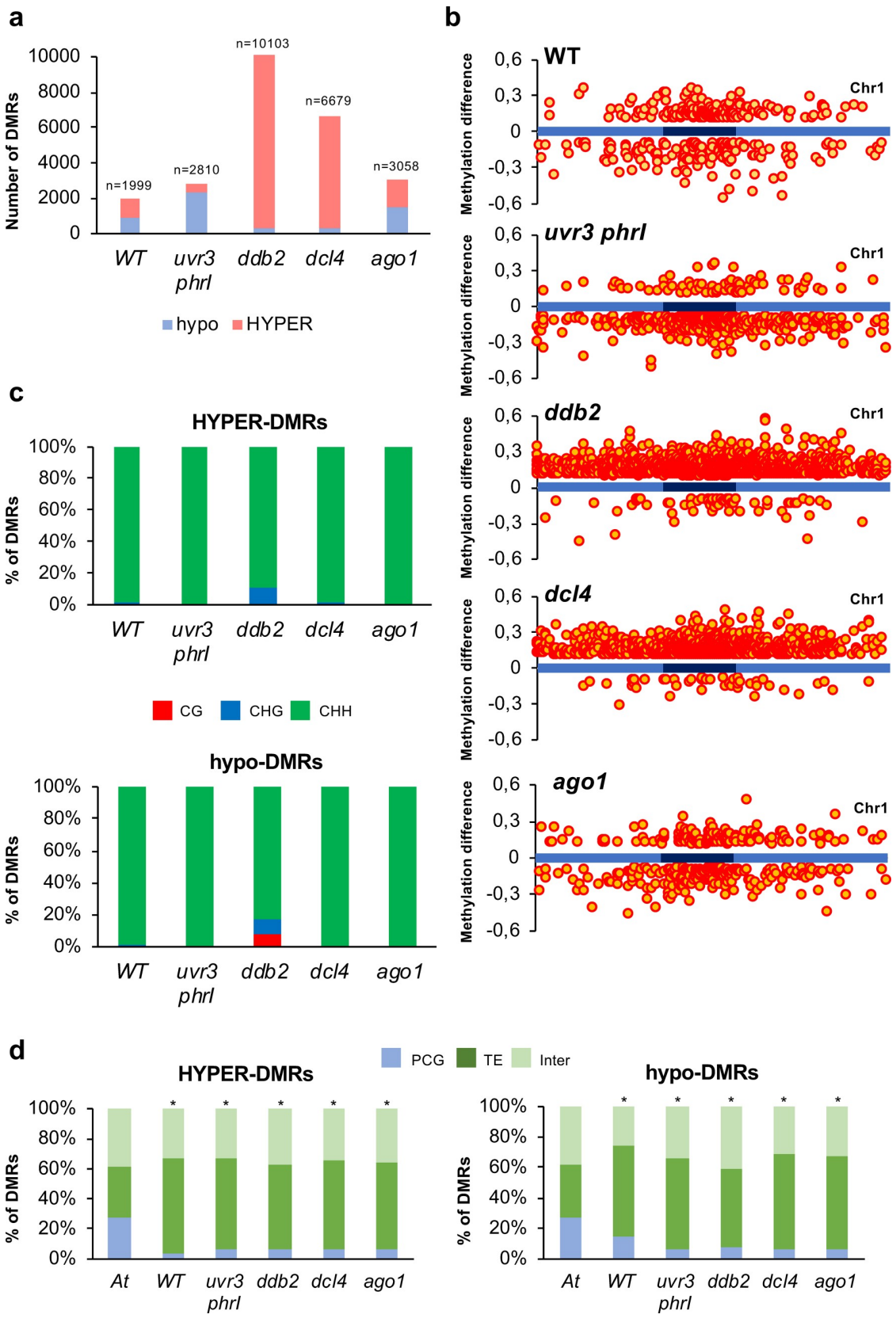
a
Number of DMRs
n=1999
n=2810
n=10103
n=6679
n=3058
WT
uvr3 phrI
ddb2
dcl4
ago1
hypo
HYPER
b
Methylation difference
WT
uvr3 phrI
ddb2
dcl4
ago1
Chr1
c
HYPER-DMRs
% of DMRs
CG
CHG
CHH
hypo-DMRs
d
PCG
TE
Inter
HYPER-DMRs
hypo-DMRs
At

Fig 1. DNA methylation differences induced by UV-C irradiation. a Histograms representing the total number of hypo-DMRs (red) and hyper-DMRs (blue) identified in WT, *uvr3 phrI*, *ddb2*, *dcl4* and *ago1* plants 24h upon UV-C exposure. DMRs were calculated relative to their corresponding untreated control. **b** Distributions of DMRs along chromosome 1 (light blue: chromosome arms, dark blue: pericentromeric regions) for the three sequence contexts. Hyper-DMRs and hypo-DMRs are shown above and below each chromosome, respectively. **c** Histograms representing the percentage of CG (red), CHG (blue) and CHH (green) of the hyper- and hypo-DMRs identified in WT, *uvr3 phrI*, *ddb2*, *dcl4* and *ago1* plants 24h upon UV-C exposure. DMRs were calculated relative to their corresponding untreated control. **d** Histograms representing the percentage of the identity (protein-coding genes: PCG, TE and intergenic) of the hyper- and hypo-DMRs identified in WT, *uvr3 phrI*, *ddb2*, *dcl4* and *ago1* plants. *A*. *t* represents the overall distribution of PCG, TE and intergenic regions in the *Arabidopsis thaliana* genome. * Chi square test < 0.01 compared to *A*. *t*.

https://doi.org/10.1371/journal.pgen.1008476.g001

Single resolution analyses of WGBS data allowed identifying that more than 97% of these changes occurred in the CHH context, exhibiting a trend of gain of DNA methylation (Figs 1C and S2B). These DMRs mainly overlapped with TE and intergenic genomic regions (Fig 1D), consistent with their enrichment in silent chromatin states. Interestingly, we could not identify genomic regions with concomitant changes of CHG and CHH methylation, highlighting that alterations of DNA methylation in both contexts are uncoupled in our experimental conditions (Fig 1C). This contrasts with the well characterized positive correlation between CHG and CHH methylation [37, 38] and thus suggests that UV-C irradiation may induce context specific changes of DNA methylation levels.

Collectively, our data showed that, in WT Arabidopsis plants, UV-C irradiation led to balanced gain and loss of DNA methylation in an CHH context that is largely distinct from CHG methylation. Importantly, theses changes in DNA methylation landscape were predominantly located within centromeric-pericentromeric regions representing constitutive heterochromatin.

Photodamage DNA repair pathways prevent excessive changes of DNA methylation landscape upon UV-C exposure

To assess the putative role of the DNA repair processes in the interplay between maintenance of genome and methylome integrities in response to UV irradiation, Arabidopsis plants deficient for the main pathways involved in the repair of UV-induced DNA photolesions were subjected to UV-C irradiation. DNA methylation profiles were determined by WGBS prior and 24h upon UV-C exposure in order to identify DMRs. We used the double *uvr3 phrI* mutant plants that are defective in both photolyases involved in the direct repair of photoproducts [39]. Therefore, in such plants, the NER pathway (TCR and GGR) would be expected to be the main process used to remove DNA photolesions. We also used *ddb2*, *dcl4* and *ago1* mutant plants that are defective in GGR (*ddb2*, [23, 40]) and/or in small RNA-mediated GGR (*ddb2*, *dcl4* and *ago1*, [16]). Thus, the DR would be expected to be predominantly used to repair photolesions as well as other pathways (i.e. homologous recombination) [33, 41]. Therefore, determining the genome-wide DNA methylation landscapes of these UV-C-treated mutant plants would allow identifying how each DNA repair pathway could, directly or indirectly, contribute to shape the DNA methylome upon UV-C exposure.

Comparative analyses of the DNA methylomes within each genotype, *uvr3 phrI* (0 *vs* 24h), *ddb2* (0 *vs* 24h), *dcl4* (0 *vs* 24h) and *ago1* (0 *vs* 24h) plants, revealed thousands of DMRs (Fig 1A). Indeed, *uvr3 phrI* mutant plants exhibited 2,379 hypo-DMRs upon UV-C exposure, representing more than 84% of the total DMRs (Figs 1A and S1A). Globally, UV-C exposure leads to loss of CHH DNA methylation in *uvr3 phrI* plants (S2B and S3 Figs). Both hyper- and hypo-DMRs are distributed all along the chromosomes arms albeit we can notice an enrichment within the centromeric and pericentromeric regions as observed in WT treated plants (Figs 1B, S2A and S3). Conversely, *ddb2* and *dcl4* mutant plants exhibited 9,750 and 6,350

hyper-DMRs, respectively, representing more than 95% of their total DMRs (Figs 1A and S1A). These observations are consistent with the role of DDB2 in the chaperoning of the RdDM factor AGO4 to control *de novo* DNA methylation [23]. Moreover, it suggests that the small RNA-mediated DNA repair of photolesions, involving DDB2 and DCL4, also controls DNA methylation. Finally, we identified in the *ago1* hypomorphic mutant plants (*ago1-27*, [42]), 3,058 DMRs including 52% of hyper-DMRs and 48% of hypo-DMRs (Figs 1A and S1A). These DMRs are located, like in the other tested plants, mostly in centromeric and pericentromeric regions (Figs 1B and S2A). Globally, UV-C exposure leads to gain of CHH DNA methylation in *ddb2*, *dcl4* and *ago1* plants (S2B and S3 Figs).

Similar to the results obtained in WT plants, the mutant's DMRs mainly overlap with TE (>55% of the total DMRs), intergenic genomic regions (around 30% of the total DMRs; Fig 1D) and with chromatin states (states 4, 5, 6, 8 and 9) that correspond to repressive contexts, as expected (S1B Fig, [36]).

Hyper-DMRs sizes of *ddb2*, *dcl4*, *ago1* plants and hypo-DMRs sizes of *uvr3 phrI* plants are significantly longer than those identified in WT plants (S4A and S4B Fig). This suggests that each DNA repair process restricts the length of regions exhibiting DNA methylation alterations. In addition, in all mutant plants, genomic regions giving rise to hyper-DMRs display higher methylation level prior UV-C treatment compared to WT plants and reciprocally with hypo-DMRs (S4C, S4D and S4E Fig). This would suggest that such regions are more prone to gain or to lose DNA methylation due to the pre-existing influence of particular DNA methylation/demethylation pathways. In all tested mutant plants, DNA methylation changes occurred predominantly in the CHH context although we found, in the *ddb2* mutant, around 10% of the DMRs in the symmetric contexts (CG and CHG; Fig 1C).

All together, these results suggest that, upon UV-C exposure, GGR and small RNA-mediated GGR prevent excessive gain of DNA methylation and that DR prevents excessive loss of DNA methylation. These methylome changes occurred predominantly in repressive chromatin where repeats and TE are abundant.

In WT and *dcl4* plants, LTR/Gypsy TE overlapping with DMRs are significantly over-represented compared to their distribution in the Arabidopsis genome (S1C Fig). In *uvr3 phrI*, *ddb2* and *ago1* plants, class II TE exhibiting DMRs are significantly over-represented compared to those of WT and *dcl4* plants (S1C Fig), suggesting that UV-C irradiation may have triggered TE mobilization. Interestingly, we found that the heat stress responsive LTR/Copia TE, *ONSEN* [43], displayed hyper-DMRs in WT plants upon UV-C irradiation (S5A Fig). This gain of DNA methylation at the edge of the TE as well as in intergenic regions is more pronounced in *ddb2* and *dcl4* plants (S5A, S6A, S6B and S6C Figs) and suggests that UV-C may have released *ONSEN* transcription. We can notice that, in all plants, the 24-nt abundances at the edge of *ONSEN* did not significantly change upon UV-C irradiation (S5A Fig). To test the effect of UV-C irradiation on *ONSEN* transcript level, we measured, 2h and 24h upon UV-C exposure, its RNA steady state level in WT and in DNA repair deficient plants. We found that in WT, *ddb2*, *dcl4* and *ago1* plants *ONSEN* transcripts were up-regulated whereas they were down-regulated in *uvr3 phrI* plants highlighting that UV-C exposure and DNA repair factors modulate its expression (S5B Fig). In agreement with our observations, UV-B stress was reported to precociously release gene silencing of transgene, of TE, as well as of endogenous loci in Arabidopsis and maize [44, 45].

Collectively, our data suggest that UV-C irradiation may have transiently released TEs expression and that changes in DNA methylation could act as a defense mechanism to prevent an additional burst of TE mobilization that would further lead to genome instability. Moreover, it allows considering that DNA repair pathways (DR, GGR and small RNA-mediated GGR) likely contribute to the regulation of the DNA methylation landscape at putative UV-reactivated loci.

UV response and methylation changes

In order to determine whether UV-C-induced DNA methylation changes are controlled by specific DNA repair processes or whether these methylome alterations result from a general "stress response" effect, we compared the DMRs identified in WT plants with those of each mutant. Additionally, we performed the same cross-comparison using WGBS data from WT plants subjected to drought stress [46]. Interestingly, we found significant overlap between DMRs (hyper and hypo) of WT (UV-C and drought) and of mutant plants as well as in between DNA defective plants as reflected by a representation factor >1 (S7 and S8 Figs). This suggests that DNA methylation levels of particular genomic regions are modulated in a stress-dependent manner and that photodamage repair processes controls the methylome landscape of a common set of regions.

Moreover, we re-analyzed the DNA methylation levels, in the CHH context, of each DMR for all the genotypes. Interestingly, we found that most of the DMRs in *ddb2*, *dcl4* and *ago1* plants display increased DNA methylation levels whilst in *uvr3 phrI* plants these profiles decreased (S9 Fig). These observations are consistent with the respective roles of these factors in the different pathways involved in the repair and in the response to UV-induced DNA lesions [3].

Hence, these data show that methylome changes are part of a general stress-response and that DNA repair pathways act synergistically to maintain DNA methylation landscape integrity in response to UV-C irradiation.

UV-C irradiation induces chromocenters reshaping

Using WGBS approach, we identified that UV-C irradiation induced genome wide alterations of DNA methylation landscape. Interestingly, many methylation changes overlapped with centromeric and pericentromeric regions suggesting that constitutive heterochromatin strongly reacts to such stress (Figs 1B, S1B and S2A). Given that chromocenters are highly compacted genomic regions, we examined whether UV-C irradiation may have affected their compaction and/or their shape and to which extend photodamage DNA repair pathways act to maintain their shape. For this, we developed an automated image quantification program using DAPI staining and confocal microscopy to determine the percentage of surface occupied by chromocenters in a corresponding nucleus. We defined this parameter as chromocenters occupancy (CO) and determined this value in untreated (time point 0) and UV-C treated leaves (24h upon exposure) of WT and DNA repair deficient plants. In addition, relative chromocenters fluorescence intensity, chromocenters and nucleus surfaces (see methods for details) were determined using the same samples. Interestingly, in WT and *dcl4* plants CO increased whilst it decreased in *uvr3 phrI* and *ddb2* mutant plants and remained unchanged in *ago1* plants (Fig 2A and 2B). UV-C-induced CO alterations are correlated with the significant modulation of chromocenters fluorescence intensity and of chromocenters-nucleus surfaces (S10A, S10B and S10C Fig). This reflects that UV-C irradiation triggers nucleus and heterochromatin reorganization and that DR and GGR factors contribute to different extents to the nuclear dynamics.

In order to determine whether 5-mC distribution follows UV-C-induced chromocenters reorganization and methylome alterations, as characterized by confocal microscopy and WGBS, respectively, we performed immunolocalization of 5-mC. We used untreated (time point 0) and UV-C treated leaves (24h upon exposure) of WT and DNA repair deficient plants. We found in all tested plants, and as expected, that 5-mC localized around chromocenters prior UV-C treatment [47]. We confirmed that 5-mC signal remained unchanged in WT and in *ago1* plants upon UV-C irradiation whereas the signal increased in *ddb2* and *dcl4* plants and decreased in *uvr3 phrI* plants, respectively (Fig 2B). Interestingly, in *ddb2* and in *dcl4* plants,

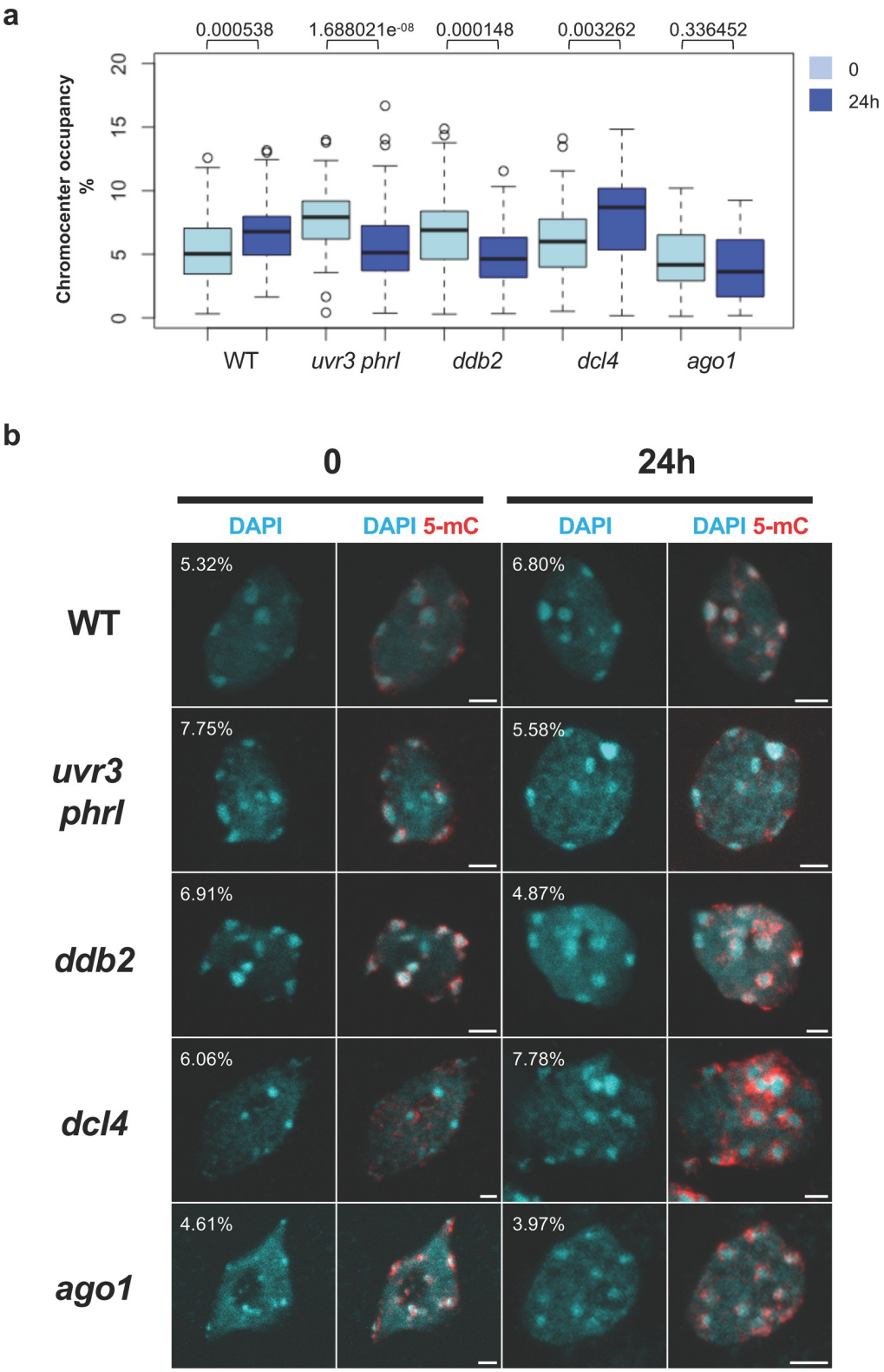

Fig 2. Chromocenters and 5-mC phenotypes upon UV-C exposure. a Boxplots representing the percentage of Chromocenters Occupancy (CO) in WT, *uvr3 phrI*, *ddb2*, *dcl4* and *ago1* plants before (0) and 24h upon UV-C exposure. CO was determined using DAPI staining, confocal microscopy and measured with an automated image quantification program. Exact p values according Mann Whitney test are indicated above each graph. Number of nuclei

analyzed: 44 to 109. **b** Chromocenters phenotypes of isolated leaf nuclei of WT, *uvr3 phrI*, *ddb2*, *dcl4* and *ago1* plants before (0) and 24h upon UV-C exposure. Representative DAPI staining (cyan) and 5-mC immunostaining (red) are shown for each genotype and time point. CO are indicated on the representative picture for each genotype and time point. Images were reconstructed from confocal image stacks. Scale bars = 2 μm.

https://doi.org/10.1371/journal.pgen.1008476.g002

5-mC spread over chromocenters consistent with our WGBS analyses (Figs 1B and 2B). UV-induced modulation of chromocenters shape may lead to transcriptional changes of particular sequences located in this area of the chromosome as already reported for heat-stress [45, 48]. Thus, to test this hypothesis, we analyzed by RT-qPCR the RNA steady state level of the centromeric 180 bp repeats and of the flanking pericentromeric heterochromatic domains containing 5S rRNA before (time point 0) and after UV-C irradiation (2h and 24h). We found that in WT plants the 180 bp and the 5S transcripts levels increased 2h upon UV-C exposure and come back to initial level at 24h (S11A and S11B Fig). In *ddb2*, *dcl4* and *ago1* plants we also measured an increase level of 180 bp and the 5S transcripts levels upon UV-C irradiation whilst in *uvr3 phrI* plants they decreased (S11A and S11B Fig). This shows that UV-C exposure released expression of particular centromeric and pericentromeric sequences and that this response relied on the DR pathway.

Collectively, our data highlighted that UV-C exposure induced the release of silencing of particular repeats as well as structural changes of chromocenters and 5-mC distribution. Moreover, we revealed that DNA repair factors involved in the repair of photodamage contribute to prevent excessive transcriptional reactivation and chromocenters changes in response to UV-C irradiation.

UV-induced DNA methylome changes rely on misregulation of DNA methylation/demethylation pathways

The methylome analysis of WT and DNA repair defective plants subjected to UV-C irradiation revealed thousands of DMRs (Fig 1A). Such DNA methylation alterations may result from local effects in *cis* and/or from expression changes of genes involved in DNA methylation/demethylation processes. To test the latter hypothesis, we measured by RT-qPCR in WT and DNA repair deficient plants the transcript levels of the main factors of Arabidopsis DNA methylation/demethylation pathways. UV-C induced up-regulation of *CMT2* and *DRM2* in WT, *uvr3 phrI*, *ddb2* and *ago1* plants in agreement with their roles in CHH methylation and with the gain of asymmetric methylation (S12 Fig). Conversely, in *dcl4* plants expression of all DNA methyltransferases was down-regulated whilst enhanced CHH methylation level was measured (S13 Fig). We also found that UV-C irradiation leads to the up-regulation of demethylases expression in all plants except for *DML3* in *uvr3phrI* and for *DML2* in *ddb2* mutant plants (S13 Fig). These results suggest that loss of DNA methylation could result from up-regulation the active DNA demethylation process.

In order to further determine the involvement of DNA methylation/demethylation pathways in these methylome changes, we re-analyzed the DNA methylation levels of each CHH-DMRs using publicly available data of mutant plants defective in the expression of the main Arabidopsis DNA methyltransferases: *met1*, *cmt2*, *cmt3*, *drm1 drm2* [38]. We found that DNA methylation levels at identified DMRs (hyper and hypo) rely mainly on CMT2 and on DRM1/2 DNA methyltransferases, consistent with their roles in maintenance and *de novo* CHH methylation (Fig 3A and 3B, [37]). We found that MET1, involved in maintenance of DNA methylation in the CG context, also influenced CHH methylation at few loci (Fig 3A). Indeed, in *met1* mutant plants many CHH hyper-DMR have been identified [38]. In agreement with this, we found that *MET1* RNA steady state level decreased in WT, *ddb2* and *dcl4* plants

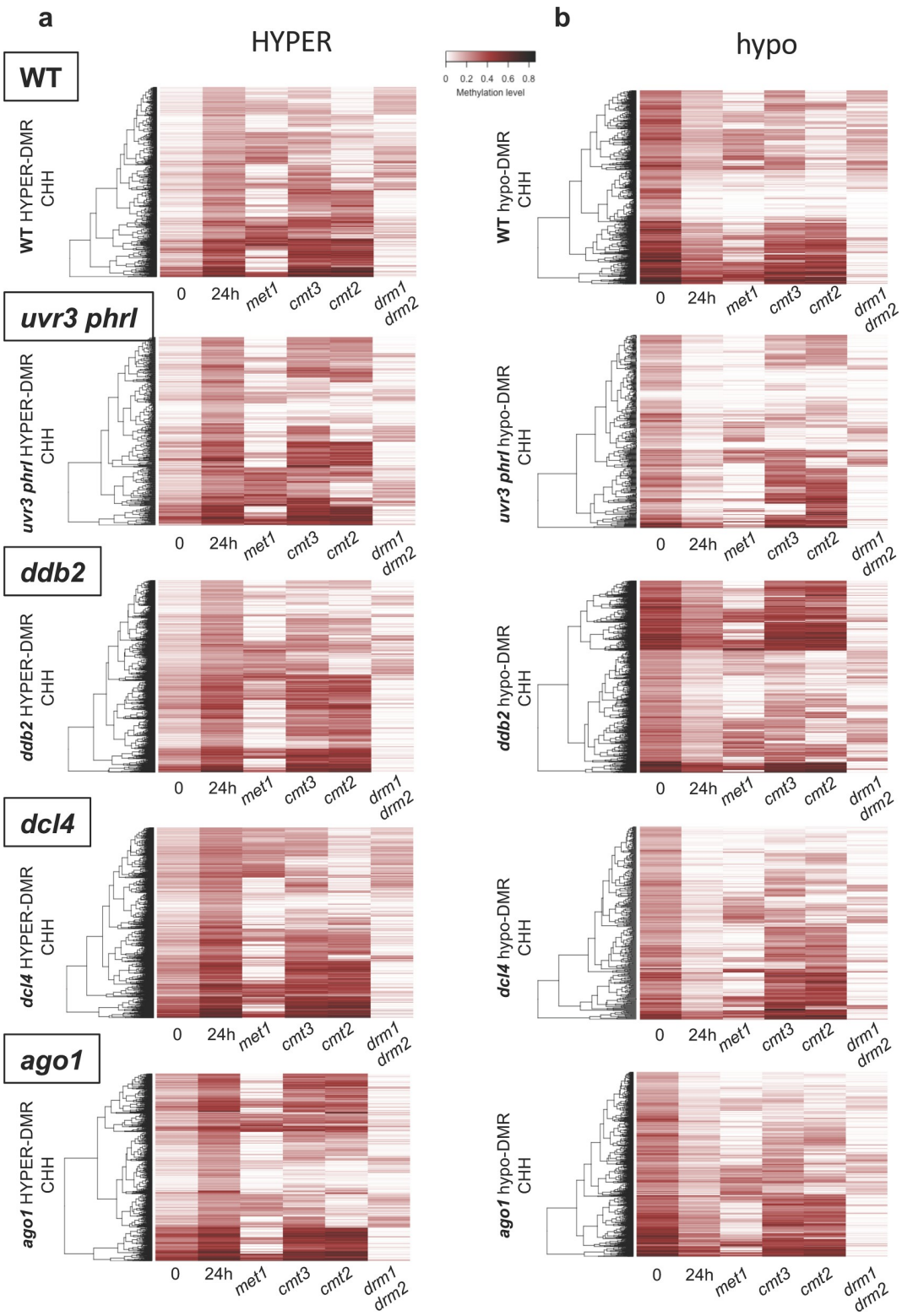

Fig 3. UV-induced DMRs and DNA methyltransferases. Heatmaps of CHH methylation levels within hyper-DMRs **(a)** and hypo-DMRs **(b)** identified in WT, *uvr3 phrI*, *ddb2*, *dcl4* and *ago1* plants 24h upon UV-C exposure. The CHH methylation levels of each of these hyper-DMR are reported for *met1*, *cmt2*, *cmt3* and *drm1/2* mutant plants. Columns represent data for each indicated genotype (white: 0; black: 1).

https://doi.org/10.1371/journal.pgen.1008476.g003

2h upon UV-C exposure supporting the idea that transient down regulation of *MET1* expression may have also contributed to an ectopic gain of CHH methylation (S12 Fig).

Surprisingly, in all tested plants we could not identify genomic regions with concomitant alterations of CHG and CHH methylation levels, strengthening the fact that changes of DNA methylation in both contexts are uncoupled (Fig 1C). These observations are in agreement with the data obtained in *met1* and *ddm1* mutant plants for which alterations of CHH methylation occurred at distinct sites compared to changes of CHG methylation [38].

We observed that DRM1/2 play a predominant role in the regulation of CHH DNA methylation levels at hyper- and hypo-DMRs upon UV-C exposure (Fig 3A and 3B). In order to further determine whether the canonical RdDM pathway is involved in this regulation, we analyzed the DNA methylation levels at hyper-/hypo-DMRs in *nrpd*1 and in *ago4* deficient plants [38]. Indeed, we confirmed that the RdDM pathway plays a major role in the regulation of CHH DNA methylation landscape at most identified DMRs (Figs 4A and S14A). These observations suggest that UV-C exposure induces RdDM dysfunction either stimulating *de novo* or altering maintenance of DNA methylation. Moreover, our results suggest that photodamage DNA repair pathways are, directly or indirectly involved in *de novo* and in DNA methylation maintenance processes.

Active DNA demethylation also leads to loss of DNA methylation [21]. We aimed at determining whether genomic regions exhibiting loss of DNA methylation are targeted by the active DNA demethylation pathway. For this, we compared our identified hypo-DMRs with hyper-DMRs found in plants defective in *ROS1*, *DML2* and *DML3* demethylases expression (*rdd* mutant, [38]). We observed between 35 and 55% overlap with *rdd* hyper-DMRs (S15A Fig) confirming that active DNA demethylation may have acted at these particular loci to reduce DNA methylation level upon UV-C exposure.

Collectively, these analyses revealed that alterations of DNA methylation could have as origin an UV-C-induced misregulation/dysfunction of actors of the DNA methylation pathways (*de novo* and maintenance) and/or of the active DNA demethylation process.

Small RNA populations upon UV-C exposure

To further decipher the role of the RdDM in the UV-induced regulation of DNA methylation landscape, we determined how canonical small RNA populations (21-, 22- and 24-nt) varied at DMRs. We first determined 24-nt siRNA abundance at hyper-/hypo-DMRs for all plants. In all the cases, and as expected, 24-nt siRNA population abundance is strongly reduced in RNA POL IV deficient plants (Figs 4B and S14B) strengthening the observation that canonical RdDM is involved in the biogenesis of these 24-nt siRNA. Surprisingly, only *ddb2* plants exhibit significant increase of 24-nt siRNA abundance at TE hyper-DMRs (Fig 4B) consistent with the role of DDB2 in the control of *de novo* DNA methylation [23]. Conversely, in all other mutant plants, we could either measure decreased or stabilization of small RNA abundances contrasting with the direct correlation between 24-nt siRNA quantity and gain of DNA methylation (Fig 4B, [19]). For hypo-DMRs, 24-nt siRNA abundance significantly decreased in WT, *uvr3 phrI* and *ago1* plants at TEs whereas no significant changes could be measured in *ddb2* and *dcl4* mutant (S14B Fig). Hence, our data suggest that either 24-nt siRNA abundances have been precociously and transiently modulated/used upon UV-C exposure and/or that other populations of small RNA (21-nt and 22-nt) may play a role in the regulation of DNA methylation. Using publicly available small RNA libraries [16] we found that in WT plants, 30 min following UV-C exposure, 24-nt siRNA abundance increased compared to the untreated time point 0 (S15B Fig) reflecting that transient enhancement of this population of small RNA may have occurred. To test the putative role of 21-nt and 22-nt siRNA in DNA methylation

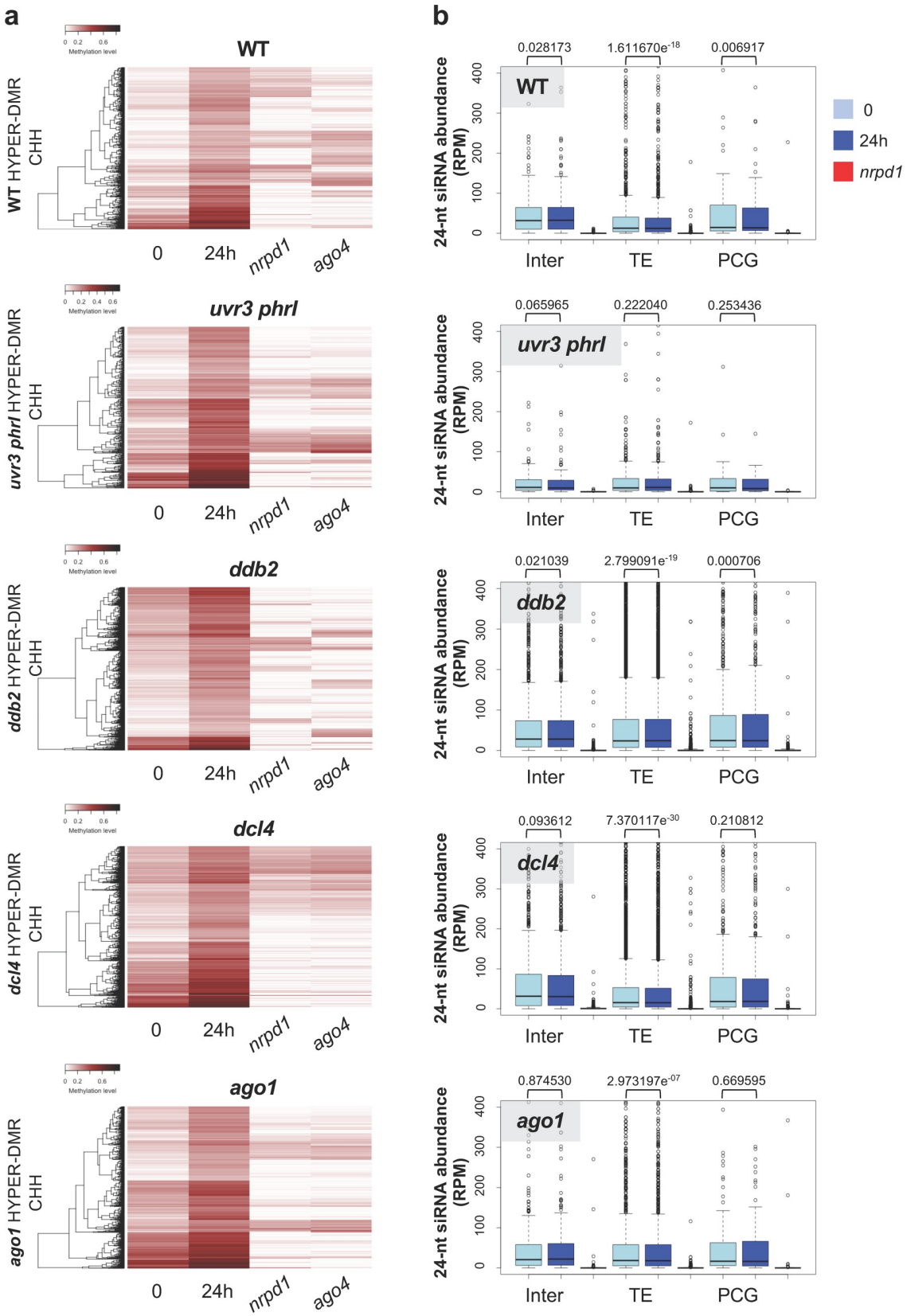

Fig 4. RNA-directed DNA methylation and DMRs. a Heatmaps of CHH methylation levels within hyper-DMRs identified in WT, *uvr3 phrI*, *ddb2*, *dcl4* and *ago1* plants before, 24h upon UV-C exposure. The CHH methylation levels of each of these hyper-DMR are

reported for RNA POL IV (*nrpd1*) and AGO4 (*ago4*) deficient plants. Columns represent data for each indicated genotype (white: 0; black: 1). **b** Boxplots representing the abundance of 24-nt siRNAs mapping to the CHH hyper-DMRs identified in WT, *uvr3 phrI*, *ddb2*, *dcl4*, *ago1* and plants. For each genotype the abundance of 24-nt siRNAs is shown in RNA POL IV deficient plants (*nrpd1*). The 24-nt siRNA abundance is normalized against global small RNA content and expressed as reads per million (RPM). p-values are calculated according to Wilcoxon Matched-Pairs Signed-Ranks.

https://doi.org/10.1371/journal.pgen.1008476.g004

changes we measured their abundances at hyper-/hypo-DMRs. Firstly, we noticed that both 21- and 22-nt siRNA abundances are strongly reduced in RNA POL IV deficient plants (S16A, S16B, S17A and S17B Figs) in agreement with the existence of non-canonical small RNA biogenesis pathways [49]. Secondly, in WT, *uvr3 phrI*, *ddb2* and *dcl4* mutant plants, 21-nt abundance increased for all types of genomic regions exhibiting hyper-/hypo-DMRs whilst in *ago*1 plants it decreased (S16A and S17A Figs). The 22-nt siRNA patterns are similar to those of 21-nt siRNA in *uvr3 phrI*, *ddb2* and *dcl4* mutant plants for hyper-/hypo-DMRs whereas their trends differ in WT plants (S16B and S17B Figs) strengthening the idea that DNA methylation may require different populations of small RNA [50]. 21- and 22-nt siRNA originating from up-regulation of TE RNA steady state level and of their degradation products are incorporated into a cognate AGO protein, namely AGO6, to target DNA methylation [51]. We found that DNA methylation level of several loci are under the control of both AGO4 and AGO6 consistent with their redundant functions (S18A and S18B Fig, [51]). Hence, our analyses suggest that POL IV-dependent siRNA (21-, 22- and 24-nt) mediate changes in DNA methylation landscape through complex interplays.

Genome wide mapping of UV-C-induced photolesions

UV-C exposure leads to the formation of photoproducts at di-pyrimidines [4]. In order to determine a genome-wide map of photolesions, genomic DNA was prepared from the same UV-C treated plants (WT, *uvr3 phrI*, *ddb2*, *dcl4* and *ago1*; see methods for details) used for the methylome analyses. Genomic DNA was subjected to immunoprecipitation using anti-CPD and anti-6,4 PPs antibodies and high throughput sequencing was performed on the immunoprecipitated DNA [16]. The resulting sequences were mapped on the nuclear Arabidopsis genome and the enriched genomic regions (IP/input) containing photolesions were identified using bioinformatic workflow (see methods for details, [16]). We found more than 3,500 regions enriched in photolesions in WT plants whereas these numbers are much more reduced in all tested mutant plants (Fig 5A). This could be due to the physiological adaptation of DNA repair deficient plants which are prone to produce more UV-screen compounds to prevent excessive photo-damage and also to the reduced leaves size of the *ago1-27* plants [39, 42]. In all tested plants, photolesions are located all along the chromosomes with a bias for TE and intergenic regions in mutant plants compared to WT plants (Fig 5B). Importantly, we can observe enhanced IP signals at centromeric/pericentromeric regions, suggesting that this part of the genome is more prone to form photodamage (Figs 5C and S19). Given that photolesions are formed between di-pyrimidines (CC, CT, TC and TT) we calculated their frequencies for each DNA strand of the identified damaged regions (intergenic, TE and Protein Coding Genes: PCG) and compared them to their overall frequencies in the Arabidopsis genome. We could not identify a significant bias for di-pyrimidines frequencies at damaged sites suggesting that other genomic or even epigenomic features may favor photolesions formation (S20 Fig; S1 Table). In order to characterize the epigenomic features of the photo-damaged regions we determined their overlap with chromatin states [36]. In WT plants we found a slight but significant enrichment of the photoproducts in chromatin states 2, 4, 5 containing high repressive H3K27me3 level, representative of facultative heterochromatin, in chromatin state 6 and in repressive chromatin states 8 and 9 representative of constitutive heterochromatin (S21 Fig).

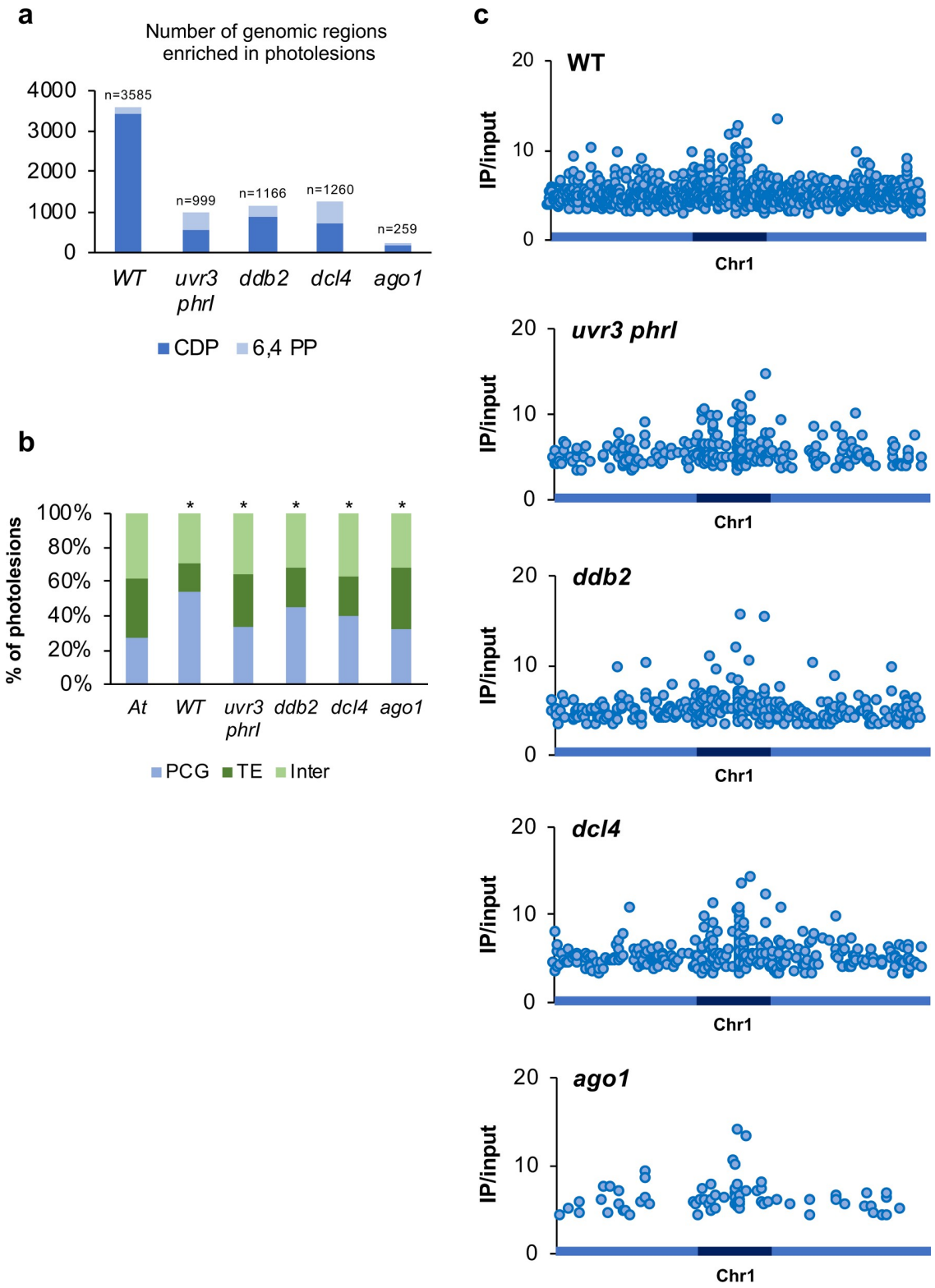

Fig 5. Genome-wide identification of UV-C induced photolesions. a Histograms representing the total number of photolesions identified in WT, *uvr3 phrI*, *ddb2*, *dcl4* and *ago1* using IPOUD. **b** Histograms representing the percentage of the identity (protein-coding genes: PCG, TE and intergenic) of photolesions identified in WT, *uvr3 phrI*, *ddb2*, *dcl4* and *ago1* plants. *A. t* represents the overall distribution in the Arabidopsis genome. * $p < 0.01$ compared to *A. t* according the chi2 test. **c** Distributions of photolesions along chromosome 1 (light blue: chromosome arms, dark blue: pericentromeric regions).

https://doi.org/10.1371/journal.pgen.1008476.g005

Interestingly, in all mutant plants, photolesions overlap with chromatin states 4, 5, 6, 8 and 9 with even a stronger enrichment compared to those of WT plants (S21 Fig). Thus, these observations highlight that photolesions formation rely on a complex interplay between genomic (di-pyrimidines) and epigenomic (chromatin states) features.

Given that small RNAs also contribute to the repair of UV-induced DNA lesions [16] we mapped the canonical siRNA populations (21-, 22- and 24-nt) to the photodamaged regions. Around 50% of the photolesions-containing regions overlap with small RNAs. They display POL IV dependency (S22 Fig) supporting the idea that these populations of siRNAs likely originated from POL IV precursors [16, 49]. Importantly, we could also observe that, in mutant plants, biogenesis of the 21-nt siRNA population does not fully rely on RNA POL IV (S22 Fig). These analyses highlight that the damaged loci are either under the transcriptional control of different types of RNA POL (i.e. RNA POL II and POL IV) or that defect in DNA repair processes may activate alternative small RNA biogenesis pathways [49].

Hence, these results suggest that, although the formation of photolesions depends primarily on the presence of di-pyrimidines, repressive chromatin states also influence the formation of photodamage. Moreover, our data confirm that both canonical and non-canonical siRNA biogenesis pathways interconnect at many damaged loci likely to contribute to maintain genome/methylome integrity.

DNA methylation changes at UV-damaged sites

Upon induction of DNA damage and following DNA repair, epigenome integrity should be maintained by an accurate re-establishment of the pre-existing DNA methylation patterns. We aimed at determining at the genome-wide level whether regions that have undergone UV damage exhibit significant changes in their DNA methylation levels and how DNA repair pathways contribute to the maintenance of methylome integrity. In others words we are interested in determining if DNA damage could be a source of methylome changes.

For this, we compared the genomic location of photolesions with those of the identified DMRs. Using the cross-comparison of these genomic data we identified that 94 to 98.2% of the photodamaged regions did not exhibit methylome alterations (Fig 6A). Conversely, it implies that several genomic regions that have been UV-C-damaged exhibit significant DNA methylation changes. Indeed, the overlap between DNA damage and methylome change does not occur by chance, as supported by a representation factor >1 (Fig 6A). In WT plants, 0.9% of the damaged regions (33/3585) exhibited changes in DNA methylation (Fig 6A). This proportion exceeded 2.7% in all tested mutant plants, suggesting that specific DNA repair machinery efficiently coordinates re-establishment of DNA methylation upon repair (Fig 6A). In all plants, damaged genomic regions exhibiting DNA methylation changes, mapped predominantly to TE and to centromeric/pericentromeric regions, consistent with the enriched number of photolesions and DMRs identified in these parts of the genome (Figs 6B and S23).

In order to understand the role of the DNA methylation/demethylation pathways in the maintenance of methylome integrity upon UV exposure we extracted the DNA methylation level of each overlapping DMR from *met1*, *cmt2*, *cmt3* and *drm1/2* mutant plants [38]. For hyper-DMRs we found that, in all plants, the gain of methylation relies mainly on CMT2 and on the RdDM pathway, consistent with their roles in maintenance of CHH methylation and in *de novo* DNA methylation, respectively (Fig 7A, [18]). Interestingly, we also observed that, at few loci, CHH DNA methylation is also under the influence of MET1 in agreement with the ectopic gain of CHH methylation reported in *met1* plants [38] and the down regulation of *MET1* expression measured in WT, *ddb2* and *dcl4* plants (Figs 3A and S11). For hypo-DMRs the same trends could be observed with an additional role for CMT3 (S24A Fig) consistent

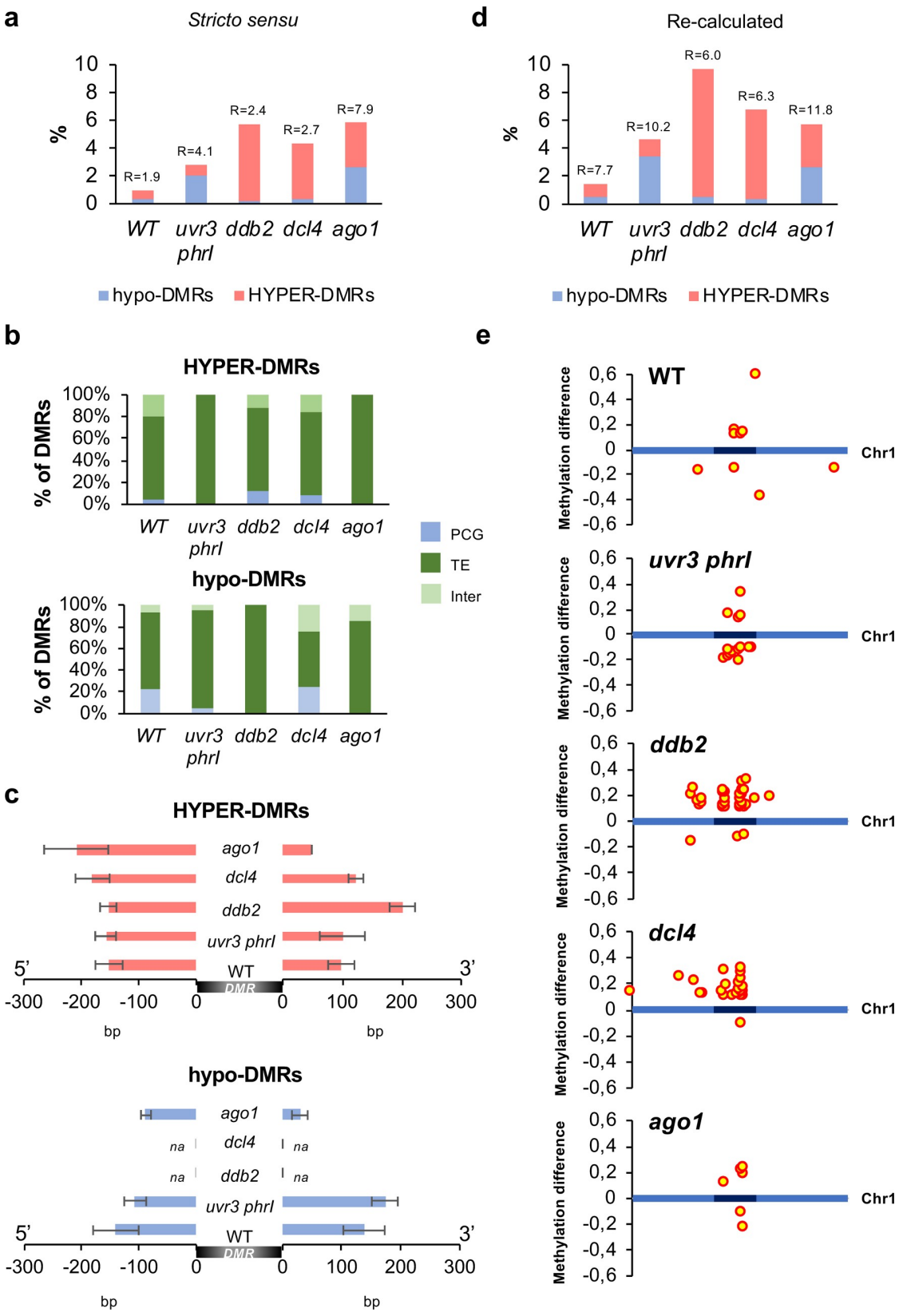
a
Stricto sensu
%
R=1.9
R=4.1
R=2.4
R=2.7
R=7.9
WT
uvr3 phrl
ddb2
dcl4
ago1
hypo-DMRs
HYPER-DMRs
d
Re-calculated
R=7.7
R=10.2
R=6.0
R=6.3
R=11.8
b
HYPER-DMRs
% of DMRs
PCG
TE
Inter
hypo-DMRs
c
HYPER-DMRs
5'
3'
WT
DMR
bp
hypo-DMRs
na
e
Methylation difference
WT
uvr3 phrl
ddb2
dcl4
ago1
Chr1

Fig 6. DMRs overlapping with photolesions. a Histograms representing the percentage of hypo- and hyper-DMRs overlapping with photolesions (*stricto sensu*) in WT, *uvr3 phrI*, *ddb2*, *dcl4* and *ago1* plants. R: Representation factor showing the statistical significance of the overlap between DMRs and photolesions (*stricto sensu*). **b** Histograms representing the percentage of the identity (protein-coding genes: PCG, TE and intergenic) of hyper- and hypo-DMRs overlapping with photolesions in WT, *uvr3 phrI*, *ddb2*, *dcl4* and *ago1* plants. **c** Histograms representing the average length (base pair: bp) of hypo- and hyper-DMRs spreading outside photolesions in WT, *uvr3 phrI*, *ddb2*, *dcl4* and *ago1* plants. na: non-applicable. **d** Histograms representing the percentage of the corrected hypo- and hyper-DMRs overlapping, with photolesions in WT, *uvr3 phrI*, *ddb2*, *dcl4* and *ago1* plants. R: Representation factor showing the statistical significance of the overlap between DMRs and photolesions. **e** Distributions of the corrected DMRs overlapping with photolesions along chromosome 1 (light blue: chromosome arms, dark blue: pericentromeric regions). Hyper- and hypo-DMRs are shown above and below each chromosome, respectively.

https://doi.org/10.1371/journal.pgen.1008476.g006

with the well-established link between CHG and CHH methylation [37]. Surprisingly, none of the damaged loci that have lost DNA methylation are target of the active DNA demethylation pathway, suggesting that defect in maintenance of DNA methylation may have predominantly led to hypo methylation (S24A Fig).

Importantly, genomic regions, such as TEs, can acquire DNA methylation through spreading from adjacent siRNA-targeted regions [52]. Given that 100% of the photodamaged regions exhibiting DMRs contain small RNAs, we investigated whether immediate adjacent regions gained or lost DNA methylation. Interestingly, we found that hyper-DMRs spread over 100 bp in 3' and 5' from the damaged sites in WT plants (Fig 6C). This holds true for all the mutant plants with a more pronounced effect in *ddb2* mutant plants (>200 bp in 3'; Fig 6C). We found the same trends for hypo-DMRs in WT, *uvr3 phrI* plants and to a lower extent in *ago1* plants (Fig 6C). In order to provide a more realistic view of the overlap between DNA damage and DMRs, we took into account this parameter and we recalculated the number of UV-damaged regions exhibiting DMRs. As expected, we observed that the proportion of photodamaged regions exhibiting methylation alterations increased for each plant (Fig 6D). Importantly, 75 to 100% of these regions are located within the centromeric/pericentromeric regions (Figs 6E, S25A and S25B).

To go further in the characterization of the UV-damaged regions exhibiting altered DNA methylation patterns, we analyzed their epigenomic features [36]. We realized that, in all plants, these genomic regions overlap predominantly with the chromatin state 5, enriched in the repressive H3K27me3 mark, representative of facultative heterochromatin and with the constitutive heterochromatic states 8 and 9 (S25C Fig). These observations are in agreement with the role of GGR in the repair of poorly transcribed or un-transcribed genomic regions [14]. In addition it highlights that DR likely contributes to the maintenance of methylome integrity in response to the formation of photolesions in silent genomic regions.

Given that RdDM likely plays an important role in the maintenance of proper DNA methylation level at photo-damaged sites, we determined the correlations between the different populations of canonical small RNAs (21-, 22- and 24-nt siRNA) mapping at these regions. Using circles of correlation, we found that for WT and *ddb2* hyper-DMRs, 21-nt and 22-nt populations positively correlated (Fig 7B). Conversely, 24-nt siRNA did not show linear correlation with the 2 other populations suggesting independent roles (Fig 7B). This holds true for hypo-DMRs in WT and *uvr3 phrI* plants (S24B Fig). In *dcl4* hyper-DMRs 22- and 24-nt small RNA positively correlated whilst 21-nt did not show linear correlation (Fig 7B). These observations suggest that in *dcl4* plants the canonical populations of small RNA may have different roles compared to WT and *ddb2* plants and that DCL4-independent processes exist to produce 21-nt (Fig 7B, [53]). Consistent with this, *dcl3dcl4*, *dcl2dcl3dcl4* and *nrpd1nrpe1* mutant plants displayed higher UV-C sensitivity than single mutant plants (S26A and S26B Fig), shedding light on synergism between 21-, 22- and 24-nt siRNA biogenesis/mode of action in response to UV-C irradiation. Hence, these analyses suggest that 21-, 22- and 24-nt siRNA likely act in

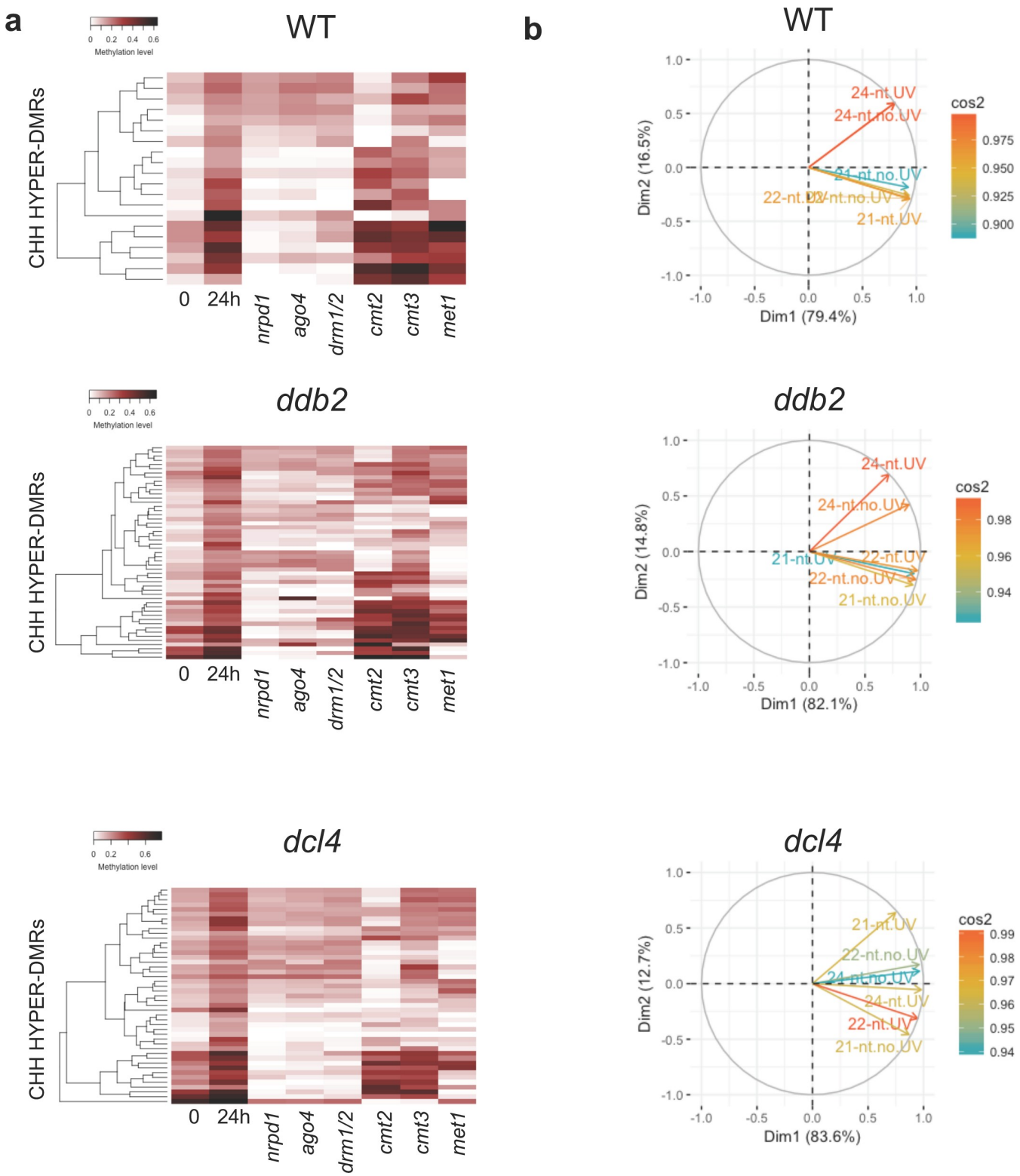

Fig 7. Characteristics of hyper-DMRs overlapping with photolesions. a Heatmaps of CHH methylation levels within hyper-DMRs identified in WT, *ddb2* and *dcl4* plants before, 24h upon UV-C exposure. Columns represent data for each indicated genotype (white, 0; black, 0.6) **b** Circles of correlations between 21-, 22- and 24-nt small RNAs mapping to the hyper-DMRs overlapping with photolesions in WT, *ddb2* and *dcl4* plants.

https://doi.org/10.1371/journal.pgen.1008476.g007

DNA repair and in DNA methylation, in agreement with the role of POL IV-dependent siRNA in DNA repair of UV-induced DNA lesions and in DNA methylation [16, 49].

Collectively, our data show that, in WT plants, UV-C irradiation leads to un-proper re-establishment of DNA methylation pattern in 1.5% of the damaged sites, which therefore correspond to the background level. The altered methylation profiles predominantly map to repressive chromatin and allows speculating that DNA damage are likely source of DNA methylation changes in silent chromatin. Moreover, these results revealed that a relationship exists between DNA damage/repair and methylome landscape with a strong contribution of the photodamage DNA repair pathways, including small RNA-mediated repair.

Discussion

UV-C irradiation induces DNA methylome alterations

Modifications of DNA methylation patterns have been characterized under different stress conditions and in several plant species [20]. Most of these studies were conducted using rather long exposure to biotic or abiotic stresses (several hours to few days) making difficult to determine a primary causal effect of the treatment on DNA methylation status [27, 28, 29, 30]. Here, we aimed at characterizing the effect of DNA damage/repair on methylome landscape. For this, we determined the DNA methylation profiles of *Arabidopsis thaliana* plants 24h upon few seconds of UV-C irradiation. In order to uncouple DNA damage/repair from light sensing/signaling [54] we used a short UV wave length (UV-C: 254 nm) that efficiently reacts with di-pyrimidines to form photodamage [3]. We found that UV-C irradiation, alters asymmetric DNA methylation landscape predominantly at centromeric and pericentromeric regions and that methylome changes are more pronounced in plants defective in the expression of specific repair factors of photolesions. Hence, we identified that DDB2, DCL4 and AGO1 prevent gain of DNA methylation and that UVR3-PHRI photolyases prevent loss of DNA methylation upon UV-C exposure.

DDB2 is involved in the recognition of photolesions during GGR [15, 40]. Although exclusively described as DNA repair factor, DDB2 was shown to form a complex with AGO4 to regulate the abundance of 24-nt siRNA at TE and repeats [23]. Indeed, in absence of applied stress, *ddb2* mutant plants displayed hundreds of hyper-DMRs [23]. Here we identified that *ddb2* mutant plants exposed to UV-C irradiation exhibit around 10,000 hyper-DMRs. Taken together these data show that DDB2 represses *de novo* DNA methylation during plant growth and also in response to UV exposure. In other words, it suggests that DDB2 may act as a general regulator of *de novo* DNA methylation during development and likely in response to stress. Recently, UVH6, a NER factor, was shown to be required for proper heat stress–induced transcriptional activation of heterochromatic TEs together with the mediator subunit MED14 [55]. These observations suggest that components of the DNA repair machinery play an important role in the regulation of silencing processes under stress conditions in addition to their canonical roles in DNA repair. These observations strengthen the notion that genome and methylome surveillance are coordinated.

Our methylome analyses revealed that *dcl4* and *ago1* deficient plants exhibit methylation changes closely related to those of *ddb2* plants. This supports the idea that both GGR and small RNA-mediated GGR cooperatively act in the maintenance of methylome integrity. Conversely to *ddb2*, *dcl4* and *ago1* plants, photolyases deficient plants mainly display hypo-DMRs upon UV-C exposure. In such plants the predominant repair pathway used is the NER, including GGR and small RNA-mediated GGR. Thus, the loss of DNA methylation may reflect the saturation of both GGR pathways including a strong reduction of the DDB2 contents due to its bias use. Upon induction of bulky DNA lesions, DDB2 is mobilized on chromatin to

recognize the DNA damage and is subsequently targeted to the 26S proteasome [15, 40, 56]. Such rapid DNA damage-dependent turnover suggests that DDB2 content is likely a limiting factor. Given that DDB2 also represses both ROS1 expression and activity [24], the UV-induced modulation of the DDB2 pool may lead to the misregulation of ROS1 content/activity in addition to AGO4 availability. Hence, DDB2 may fine tune the antagonist effect of active DNA demethylation and RdDM in response to UV exposure and therefore control methylome landscape at particular loci.

Importantly, our data show that specific DNA repair pathways, DNA synthesis-independent (DR) and -dependent (GGR and small RNA mediated-GGR), coordinate the efficient re-establishment of DNA methylation upon repair, linking the maintenance of genome and methylome integrities.

Interestingly, we identified that UV-C induced gain of CHH methylation as well as up-regulation of *CMT2* and *DRM2* expression, consistent with their roles in CHH DNA methylation [18]. Therefore, UV-C-induced deregulation of DNA methyltransferases may positively correlate with gain or loss of DNA methylation. Conversely, we observed that *MET1* expression was down-regulated in WT, *ddb2* and *dcl4* plants. Although CG methylation remained unaffected upon UV-C exposure, *met1* plants showed ectopic gain of CHH methylation [38]. This phenomenon could be due to UV-C release of expression of particular genomic regions (i.e. TE) followed by an expression-dependent gain of DNA methylation to trigger their silencing. In addition, we cannot exclude that DNA methyltransferases activity could have been modulated by UV-C treatment, even transiently.

The gain of DNA methylation observed in all plants predominantly relies on RdDM, consistent with its role in *de novo* DNA methylation [19]. Although, measurements of 24-nt siRNA abundance did not show significant increase 24h upon UV-C irradiation we cannot exclude that the 24-nt siRNA population was precociously and transiently modulated, reflecting a fast control of their biogenesis or of their mobilization into AGO4 to direct maintenance and/or *de novo* DNA methylation. Importantly the biogenesis of photoproduct-associated siRNAs involves a non-canonical pathway including RNA POL IV, RDR2 and DCL4 [16]. We identified that the biogenesis of 21-, 22- and 24-nt siRNA overlapping with the photodamaged regions predominantly relied on POL IV, in agreement with the hypothesis that such populations of siRNA originate from the same precursor and may serve for DNA repair and for DNA methylation [16].

Combination of post-transcriptional gene silencing (PTGS) and transcriptional gene silencing (TGS) processes acts to repress active plant retrotransposons [49, 57, 58]. Therefore, non-canonical siRNA biogenesis pathways and interconnections between RNA POL II and RNA POL IV biogenesis pathways may coexist at particular loci that need to be repaired and whose DNA methylation status needs to be tightly regulated [49]. This suggests that DR, GGR and small-RNA-mediated GGR coordinately act with the different DNA methylation pathways to maintain both genome and methylome integrities as a general (epi)genome immunity process [8,17].

Photolesions are sources of DNA methylation changes in heterochromatin

In order to characterize the relationship between photoproducts locations and methylome changes, the genomic map of photolesions was produced using immunoprecipitation of both CPD and 6,4 PP followed by next generation sequencing. We found, in all tested plant, that photodamage were located genome wide, albeit a significant enrichment could be characterized in repressive chromatin, stressing the point that these genomic regions are more prone to form photoproducts. Interestingly, 5-mC adjacent to pyrimidine has higher absorbance in the UV-B range and is more prone to form pyrimidine dimers compared to the combination

with unmethylated cytosines [59]. Such feature is consistent with the higher enrichment of photodamage identified in constitutive heterochromatin where DNA methylation is concentrated. In addition, UV-C damages both euchromatin and heterochromatin whilst other genotoxic agents inducing bulky DNA lesions, like cisplatin, acts mostly in euchromatin [60]. Therefore, all these parameters allow considering that, in addition to the presence of di-pyrimidines, DNA methylation, nucleosome density and histone variants/PTM may synergistically contribute to favor photolesions formation in heterochromatin *vs* euchromatin. Collectively these studies highlight that heterochromatin likely displays higher genome/methylome flexibility than euchromatin and that DNA repair pathways (DR, GGR. . .) contribute to different extents to maintain its integrity.

We identified changes in CO and release of silencing of particular repeats consistent with heterochromatin reorganization observed during dark-light transition [61]. Interestingly, the photomorphogenic factor DE-ETIOLATED 1 (DET1) and DDB2 act together in the GGR pathway [62]. Thus, the light-induced chromocenters reorganization likely reflects the existence of a complex interplay between light signaling, induction/processing of photodamage and maintenance of methylome integrity.

The differential accessibility of euchromatic and heterochromatic regions for the DNA repair machinery implies that DNA repair is slower in compacted heterochromatin compared to relaxed euchromatin due to the kinetics of recruitment of the DNA repair factors to the damaged sites [63, 64]. Therefore, chromocenters reorganization upon UV-C exposure may reflect this slower repair kinetics and highlights that heterochromatic photodamage repair may require complex strategies as compared to euchromatic repair [64].

By comparing photolesions locations and DMRs we identified a significant overlap between DNA damage and methylation changes suggesting that photodamage are source of DNA methylation alterations. Interestingly, this un-proper re-establishment of methylome landscape is concentrated in repressed genomic regions (constitutive and facultative heterochromatin) and the DNA repair pathways prevent these exacerbated changes. The presence of TE and repeats in heterochromatin may explain such changes of DNA methylation levels in response to UV stress to further repress TE mobilization, genomic rearrangement that may affect genome integrity. Indeed, tight regulation of chromocenters compaction through specific epigenetic marks is important for chromosome architecture and segregation [65].

Importantly, we have to consider the effect of DNA damage on DNA methylation landscape may have been underestimated because UV-C irradiation also generates oxidatively induced DNA damage (i.e. 8-oxoguanine: 8-oxo-G) and DSB [10, 66]. Therefore, and similarly to photolesions, the proper re-establishment of DNA methylation profiles upon specific repair of these other types of damage could have also been affected.

UV-C exposure leads to the de-regulation of hundreds of genes, TE and repeats, within the first 24h hours following the treatment [35, 45, 48]. Heterochromatin-associated silencing was shown to be released in plants exposed to environmental cues, such as prolonged heat stress [48]. The temperature-induced release of silencing is transient, rapidly restored without the involvement of factors known to be required for silencing initiation [6]. Interestingly, we found that UV-C irradiation induced constitutive heterochromatin reshaping concomitantly with transcriptional reactivation of TE and repeats. Transposon bursts was reported in maize exposed to UV-B [44, 67] and light was shown to trigger changes in nuclear architecture including heterochromatin de-condensation [45, 48, 61]. Moreover, the *ONSEN* RNA steady state level increased upon UV-C exposure showing that such TE up-regulation reports both elevated temperature and high light stress, a characteristic of the global warming [43, 68, 69]. This reflects the complex interplays between environmental-induced transcriptional regulation, heterochromatin reorganization, DNA methylation and DNA damage-repair.

This study highlights that DNA repair pathways of UV-induced DNA lesions, namely DR, GGR and small-RNA mediated GGR, prevent excessive methylome alterations upon UV-C exposure. Moreover, we identified that photolesions are sources of DNA methylation changes in silent genomic regions suggesting that the efficiency of photodamage repair might play a significant role in the variation of DNA methylation landscapes likely contributing to reflect the evolutionary and life histories of plant species.

Materials and methods

Plant materials and growth conditions

The *Arabidopsis thaliana* wild-type (WT); *ddb2-3* [23], *uvr3 phrI* (WiscDsLox334H05 and WiscDsLox466C12, [39]), *nrpd1* (Salk_583051), *nrpe1* (Salk_029919), *dcl2-1* (Salk_064627), *dcl3-1* (Salk_005512), *dcl4-2* (GABI_160G05), *ago1-27* [42] plants used in this study are in the Columbia ecotype (Col0). Plants were grown *in vitro* on solid GM medium [MS salts (Duchefa), 1% sucrose, 0.8% Agar-agar ultrapure (Merck), pH 5.8] in a culture chamber under a 16 h light (light intensity ~150 μmol m^{-2} s^{-1}; 21˚C) and 8 h dark (19˚C) photoperiod.

UV-C treatment

In order to prevent formation of photolesions, induced by the source of light, Arabidopsis WT and mutant plants were germinated and grown *in vitro* on solid GM medium for 10 days. Seedlings were subsequently transferred in larger Petri dishes (145 x 200 mm) at a density of 1 plant/cm and grown in the culture chamber for 11 additional days. Plants (40 plants/plate) were irradiated with UV-C (3,000 J/m^2) using Stratalinker. Immediately upon UV-C exposure 40–50 leaves from 2 different plates were harvested and pooled (time point 0). Remaining plants were put back in the growth chamber and 40–50 leaves from the same 2 different plates were harvested 24h upon UV-C exposure (time point 24h). Leaves samples of two biological replicates were pooled for genome wide studies.

Immunoprecipitation of photodamaged DNA

Genomic DNA was extracted immediately upon UV-C exposure (time point 0) using the Plant DNA Extraction kit (Qiagen). Five μg of genomic DNA were sonicated (Diagenode Bioruptor: 18 x 30 s) and denatured 10 min at 95˚C in Buffer 1 (10 mM Tris HCl pH 7.5, 500 mM NaCl, 1 mM EDTA). Immunoprecipitation (IP) was performed by adding 5 μg of either anti-CPD mouse monoclonal antibody (CAC-NM-DND-001, Cosmo Bio, Japan) or anti-6,4 PPs (CAC-NM-DND-002, Cosmo Bio, Japan) and incubated on rotating wheel (8 rpm) overnight at 4˚C. Afterwards the suspension was incubated with M280 Dynabeads (Invitrogen) 4h at 4˚C under rotation (8 rpm). The pellet was washed 4 times with Buffer 1. The immunoprecipitated DNA was eluted with Buffer 2 (30 mM Tris HCl pH: 8.0; 150 μg Proteinase K) during 1h at 42˚C. DNA from the IP and input fractions was purified using the Nucleospin Gel and PCR clean-up kit (Macherey-Nagel). DNA from IP and input were used for library preparation and sequencing by Illumina Hi-Seq (paired-end 2*75 bp; FASTERIS, Switzerland). Sequences were mapped (input and IP) onto the Arabidopsis nuclear genome (TAIR10) using Bowtie 1.1.2 (-v2 –m1). Both CPD and 6,4 PP enriched regions were determined using MACS2 (version 2.1).

Whole-genome bisulfite sequencing and mapping

Genomic DNA was prepared from the same set of plants used for photolesions immunoprecipitation (time point 0) and also from plants 24h upon UV-C exposure (time point 24h). Purified genomic DNA was bisulfite-treated and sequenced by Illumina Hi-Seq (paired-end 2*125

bp) by the FASTERIS Company (Switzerland). Conversion efficiency was determined using an unmethylated internal control (FASTERIS). For all samples conversion efficiency was >99.99%. Mapping on the arabidopsis genome (TAIR10) was performed using Bsmap (Bsmapz version) using default options (S2 Table).

DMRs calling

Upon mapping, the methylation levels were calculated with methratio.py. Differentially Methylated Regions (DMRs) between untreated and treated plants of the same genotype were determined according Daccord et al. (2017) [70] considering 200 bp sliding-windows with an overlap of 50 bp (sliding-window-pipeline). DMRs were identified using the difference between identical windows and upon filtering. Consecutive windows exhibiting the same methylation change (gain or loss) were joined and methylation level recalculated. DMRs were called for a DNA methylation difference ($p < 0.05$ according Wilcoxon signed-rank test), within the same genotype, higher or equal than 0.4 for CG, 0.2 for CHG and 0.1 for CHH methylation contexts. We re-analyzed with our method previously published BS-seq datasets [38] for *met1* (GSM981031), *cmt2* (GSM981002), *cmt3* (GSM981003), *drm1/2* (GSM981015), *nrpd1* (GSM981039), *ago4* (GSM980991) and *ago6* (GSM980993). Methylation levels were also calculated from chosen genomic coordinates.

The overlaps between the characterized DMRs, the photolesions enriched genomic regions and the chromatin states [36] were performed using the web assisted tool (https://usegalaxy.org/; "Operate on genomic intervals") with an overlap size of 50%.

Small RNA sequencing

Small RNAs were prepared from the untreated and UV-C treated plants (time points 0 and 24h) using the Tri-Reagent (Sigma), used for library preparation and sequencing by Illumina Hi-Seq (single end 50 bp; FASTERIS, Switzerland). Reads were aligned and mapped onto the Arabidopsis genome (TAIR10) using Bowtie (version 1.2.1.1; parameters: -y -e 50 -n 0 -a—best—strata –nomaqround; S2 Table). Upon conversion with samtools (version 1.5), reads overlapping with either the UV-damaged loci or the DMRs (50% overlap) were calculated with intersectBed (BED tools version 2.27.1). The read counts are divided by the "per million" scaling factor (RPM).

RT-qPCR

Reverse transcription (RT) was performed on total RNA extracted using Tri-Reagent (Sigma) from untreated and UV-C treated plants (time points 0, 2h and 24h). The RT reaction was performed on 5 μg of total RNA using a mixture of random hexamers-oligo d(T) primers and the cDNA reverse transcription kit (Applied Biosystems). 100 ng of the RT reaction was used for quantitative PCR (qPCR). qPCR was performed, including technical triplicates, using a Light Cycler 480 and Light Cycler 480 SYBR green I Master mix (Roche) following manufacturer's instructions. All primers are listed in Supplemental S3 Table. Experiments were at least duplicated using independent biological replicates.

UV-C root growth assay

UV-C sensitivity was performed using 7-day-old *in vitro* germinated WT and mutant plants. Plants were grown vertically on square plates containing GM medium. Root length was measured 24h upon UV-C exposure (900 J/m^2) using the Stratalinker 2400 (Stratagene). The relative root growth was calculated: (root length treated/ root length untreated) ×100 (±SD). Eight plants per replicate were used. Experiments were performed in triplicates.

Tissue fixation and 5-mC immunolocalization

Leaves numbers 3 and 4 of 21-old day Arabidopsis WT and mutant plants were collected before irradiation (time point 0) and 24h upon UV-C exposure as described above. The collected leaves were fixed in 4 successive washing steps of at least 5 min in fixative solution (3:1 ethanol / acetic acid) and stored at -20˚C. Fixed leaves were washed twice with demineralized water and incubated 3h at 37˚C in a digestion mix (0.3% cellulase, 0.3% pectolyase 10 mM Na-citrate pH = 4.5). Digested leaves were spread on poly-lysine slides using 20 μl of acetic acid solution (60%) at 46˚C for 1 min. Slides were washed 3 times in fixative solution and once in sterilized demineralized water. Post fixation was performed in a 2% paraformaldehyde PBS solution for 5 min. Slides were washed with demineralized water and incubated for 1h at room temperature in permeabilization buffer (8% BSA, 0.01% Triton-X in Phosphate Buffer Saline x1). For 5-mC immunolocalization slides were first incubated over night at 4˚C with a monoclonal anti-5-mC-antibody (Diagenode C15200003; 1/1000 dilution in 1% BSA, Phosphate Buffer Saline x1). Upon incubation slides were washed 3 times with PBS and goat anti-mouse antibody coupled to FluoProbes488 (Interchim FP-GAMOTTGO488; 1/200 dilution in 1% BSA, Phosphate Buffer Saline x1) was added for 90 min at room temperature. Finally, slides were washed 3 times with Phosphate Buffer Saline x1 and 15 μl of Fluoromount-G (Southern Biotechnology CAT NO 0100–01) with 2 μg/ml DAPI were added as mounting solution for the coverslip.

Image quantification

Whole image acquisition was performed on a Zeiss LSM 780 confocal microscope using a 64X oil immersion objective. 405 nm and 488 nm laser excitation wavelengths were used for DAPI and for the FluoProbes488, respectively. DAPI emission was measured between 410 nm and 585 nm wavelength on a first track. FluoProbes488 emission was measured between 493 nm and 630 nm wavelength on a second track. The same acquisition gain settings were used for all slides of a same genotype. Slight adjustment was performed due to labeling differences in between experiences. Acquisition gain for DAPI and FluoProbes488 in WT, *uvr3 phrI*, *ddb2*, *dcl4* and *ago1* were [650, 500], [750, 698], [800, 615], [750, 698] et [800, 615] respectively. Each image acquisition consists in a Z-stack capture with a 0.43 μm slice distance. All pictures had a final voxel size of 0.1014 x 0.1014 x 0.4300 μm^3.

The image quantification was performed on ImageJ1.52o using a homemade plugin called Nucl.Eye (https://github.com/mutterer/Nucl.Eye). This plugin allows either an automatic or a manual delimitation of all nuclei on the z-max compiled image in order to quantify size and signal intensity of each nuclei and all internal spot like entities. Using the information of individual spot (intensity, surface) and nuclei surface, the Chromocenter Occupancy (CO) was defined as percentage of surface occupied by all bright DAPI spots (chromocenters) in the corresponding nucleus. Intensities and surfaces of each chromocenter and those of the whole nucleus were used to calculate their relative intensities and surface.

Statistics

Mann-Whitney U or Wilcoxon Matched-Pairs Signed-Ranks tests were used as non-parametric statistical hypothesis tests (http://astatsa.com/WilcoxonTest/). Chi 2 test was used to determine significant difference between categories distribution (https://goodcalculators.com/chi-square-calculator/). Representation factor (R) was used to determine the statistical significance of the overlap between 2 independent groups of genomic regions (http://nemates.org/MA/progs/overlap_stats.html). t-test was used as parametric statistical hypothesis test.

Supporting information

S1 Fig. DMRs and chromatin states. a Histograms representing the percentage of hypo-DMRs (red) and hyper-DMRs (blue) identified in WT, *uvr3 phrI*, *ddb2*, *dcl4* and *ago1* plants 24h upon UV-C exposure.
b Histograms representing the distribution of the chromatin states overlapping with DMRs identified in WT, *uvr3 phrI*, *ddb2*, *dcl4* and *ago1* plants. *A*. *t* represents the overall distribution of the 9 chromatin states in the Arabidopsis genome (*A*. *t*). * Chi square test < 0.01 compared to the Arabidopsis genome.
c Histograms representing the distribution of TE families overlapping with DMRs identified in WT, *uvr3 phrI*, *ddb2*, *dcl4* and *ago1* plants. *A*. *t* represents the overall distribution of the TE families in the Arabidopsis genome (*A*. *t*). * Chi square test < 0.01. compared to the Arabidopsis genome.
(TIFF)

S2 Fig. Genome wide distribution of DMRs and methylation changes. a Circos representation of the DMRs identified in WT, *uvr3 phrI*, *ddb2*, *dcl4* and *ago1* plants 24h upon UV-C exposure.
b Boxplots representing the CHH methylation changes in WT, *uvr3 phrI*, *ddb2*, *dcl4* and *ago1* plants 24h upon UV-C exposure.
(TIFF)

S3 Fig. DNA methylation levels. CHH DNA methylation levels along chromosomes(light grey: chromosome arms, dark gray: pericentromeric regions) in WT, *uvr3 phrI*, *ddb2*, *dcl4* and *ago1* plants prior (0) and 24h upon UV-C exposure.
(TIFF)

S4 Fig. DMRs features. a Boxplots representing the size (bp) of hyper-DMRs (left panel) and hypo-DMRs (right panel) identified in WT, *uvr3 phrI*, *ddb2*, *dcl4* and *ago1* plants. Exact p values according Mann Whitney test are indicated above each graph.
b Genome browser views of hyper- and hypo-DMRs identified in WT, *uvr3 phrI*, *ddb2*, *dcl4* and *ago1* plants upon UV-C exposure. Upper panel: Chr1: 15, 023, 000 bp-15, 027, 000 bp intergenic region. Lower panel: Chr5: 20, 127, 000 bp-20, 130, 000 bp intergenic region/PCG. Red line: HYPER-DMRs; blue line: hyo-DMRs.
c Histograms representing the distribution of methylation levels prior UV-C irradiation in genomic regions exhibiting hypo- (left panel) and hyper-DMRs (right panel).
d Boxplots representing the CHH methylation levels prior UV-C irradiation in genomic regions exhibiting hypo- (left panel) and hyper-DMRs (right panel) identified in WT, *uvr3 phrI*, *ddb2*, *dcl4* and *ago1* plants. Exact p values according Mann Whitney test are indicated above each graph.
e Boxplots representing the CHH methylation difference of hypo- (left panel) and hyper-DMRs (right panel) identified in WT, *uvr3 phrI*, *ddb2*, *dcl4* and *ago1* plants 24h upon UV-C exposure. Exact p values according Mann Whitney test are indicated above each graph.
(TIFF)

S5 Fig. *ONSEN* RNA level and DMRs. a Genome browser showing the density graph 24-nt siRNA abundance and DMRs at *ONSEN* locus in WT, *uvr3 phrI*, *ddb2*, *dcl4* and *ago1* plants prior UV-C irradiation (0) and upon UV-C exposure (24h).
b RNA steady state level of *ONSEN* transcripts determined by RT-qPCR in WT, *uvr3 phrI*, *ddb2*, *dcl4* and *ago1* plants before (0), 2h and 24h following UV-C irradiation.
(TIFF)

S6 Fig. Genome browser views. Examples of hyper- and hypo-DMRs identified in WT, *uvr3 phrI*, *ddb2*, *dcl4* and *ago1* plants upon UV-C exposure in TE enriched region (**a**) and in intergenic regions surrounding protein coding genes (**b**) or TE (**c**).
(TIFF)

S7 Fig. Overlap between hyper-DMRs. Venn diagrams representing the overlap of hyper-DMRs between WT plants and either *uvr3 phrI*, *ddb2*, *dcl4*, *ago1* or WT drought plants as well as in between mutant plants. R: Representation factor and exact p value showing the statistical significance of the overlap.
(TIFF)

S8 Fig. Overlap between hypo-DMRs. Venn diagrams representing the overlap of hypo-DMRs between WT plants and either *uvr3 phrI*, *ddb2*, *dcl4*, *ago1* or WT drought plants as well as in between mutant plants. R: Representation factor and exact p value showing the statistical significance of the overlap.
(TIFF)

S9 Fig. Comparisons of DNA methylation levels. Boxplot of CHH methylation levels within DMRs identified in WT, *uvr3 phrI*, *ddb2*, *dcl4* and *ago1* plants 24h upon UV-C exposure. The CHH methylation levels of each of these DMRs are reported before and upon UV-C exposure for each plant. Exact p values according Wilcoxon signed rank test are indicated above each graph. Blue significant decrease of DNA methylation level, red significant increase of DNA methylation level, black non-significant change.
(TIFF)

S10 Fig. Relative fluorescence intensities of chromocenters, chromocenters and nuclei surfaces. Boxplots representing the relative fluorescence intensities of chromocenters (**a**), chromocenter surface (**b**) and nucleus surface (**c**) of untreated (time point 0) and UV-C treated (time point 24h) WT, *uvr3 phrI*, *ddb2*, *dcl4* and *ago1* plants. Exact p values according Mann Whitney test are indicated above each graph. Number of chromocenters analyzed: 252 to 601; Number of nuclei analyzed: 44 to 109.
(TIFF)

S11 Fig. *180 bp* and *5S* RNA levels. Relative RNA steady state level (±SD) of *180 bp* **(a)** and *5S* RNA **(b)** transcripts determined by RT-qPCR in WT, *uvr3 phrI*, *ddb2*, *dcl4* and *ago1* plants before (0), 2h and 24h following UV-C irradiation.
(TIFF)

S12 Fig. DNA methyltransferases RNA levels. Relative RNA steady state level (±SD) of *MET1*, *CMT2*, *CMT3* and *DRM2* transcripts determined by RT-qPCR in WT, *uvr3 phrI*, *ddb2*, *dcl4* and *ago1* plants before (0), 2h and 24h following UV-C irradiation.
(TIFF)

S13 Fig. DNA demethylases RNA levels. Relative RNA steady state level (±SD) of *ROS1*, *DML2* and *DML3* transcripts determined by RT-qPCR in WT, *uvr3 phrI*, *ddb2*, *dcl4* and *ago1* plants before (0), 2h and 24h following UV-C irradiation.
(TIFF)

S14 Fig. RNA-directed DNA methylation and hypo-DMRs. a Heatmaps of CHH methylation levels within hypo-DMRs identified in WT, *uvr3 phrI*, *ddb2*, *dcl4* and *ago1* plants before, 24h upon UV-C exposure. The CHH methylation levels of each of these hypo-DMR are reported for RNA POL IV (*nrpd1*) and AGO4 (*ago4*) deficient plants. (white: 0; black: 1). **b** Boxplots representing the abundance of 24-nt siRNAs mapping to the CHH hypo-DMRs

identified in WT, *uvr3 phrI*, *ddb2*, *dcl4*, *ago1* plants for protein-coding genes (PCG), TE and intergenic regions. For each genotype the abundance of 24-nt siRNAs is shown in RNA POL IV deficient plants (*nrpd1*). The 24-nt siRNA abundance is normalized against global small RNA content and expressed as reads per million (RPM). p-values are calculated according to Wilcoxon Matched-Pairs Signed-Ranks.
(TIFF)

S15 Fig. DMR, active DNA demethylation and 24-nt siRNA. a Histograms representing the percentages of hypo-DMRs identified in WT, *uvr3 phrI*, *ddb2*, *dcl4*, *ago1* plants overlapping with *rdd* hyper-DMRs.
b Boxplots representing the global 24-nt siRNA abundance before and 30 min following UV-C exposure. p-value is calculated according to Wilcoxon Matched-Pairs Signed-Ranks.
(TIFF)

S16 Fig. 21-nt, 22-nt siRNA abundances at hyper-DMRs. Boxplots representing the abundance of 21-nt **(a)** and 22-nt **(b)** siRNAs mapping to the CHH hyper-DMRs identified in WT, *uvr3 phrI*, *ddb2*, *dcl4*, *ago1* plants for protein-coding genes (PCG), TE and intergenic regions. For each genotype the abundance of 21-nt and 22-nt siRNAs is shown in RNA POL IV deficient plants (*nrpd1*). The 21-nt and 22-nt siRNA abundance are normalized against global small RNA content and expressed as reads per million (RPM). p-values are calculated according to Wilcoxon Matched-Pairs Signed-Ranks.
(TIFF)

S17 Fig. 21-nt, 22-nt siRNA abundances at hypo-DMRs. Boxplots representing the abundance of 21-nt **(a)** and 22-nt **(b)** siRNAs mapping to the CHH hypo-DMRs identified in WT, *uvr3 phrI*, *ddb2*, *dcl4*, *ago1* plants for protein-coding genes (PCG), TE and intergenic regions. For each genotype the abundance of 21-nt and 22-nt siRNAs is shown in RNA POL IV deficient plants (*nrpd1*). The 21-nt and 22-nt siRNA abundance are normalized against global small RNA content and expressed as reads per million (RPM). p-values are calculated according to Wilcoxon Matched-Pairs Signed-Ranks.
(TIFF)

S18 Fig. DMRs in *ago4* and *ago6*. Heatmaps of CHH methylation levels within hyper- **(a)** and hypo-DMRs **(b)** identified in WT, *uvr3 phrI*, *ddb2*, *dcl4* and *ago1* plants before and 24h upon UV-C exposure. The CHH methylation levels of each of these DMRs are reported for AGO4 (*ago4*) and AGO6 (*ago6*) deficient plants. Columns represent data for each indicated genotype (white: 0; black: 1).
(TIFF)

S19 Fig. Photolesions location. Circos representation of photolesions identified in WT, *uvr3 phrI*, *ddb2*, *dcl4* and *ago1* plants.
(TIFF)

S20 Fig. Di-pyrimidines frequencies at photolesions. Boxplots representing the di-pyrimidines frequencies (CC, TT, TC and CT) for each DNA strand (+ and–strand) in photodamaged regions (intergenic, TE and protein-coding genes: PCG) identified in WT, *uvr3 phrI*, *ddb2*, *dcl4* and *ago1* plants. The frequency of di-pyrimidine in the *Arabidopsis thaliana* (*A. t*) genome is also represented.
(TIFF)

S21 Fig. Photolesions and chromatin states. Boxplots representing the chromatin states overlapping with photolesions enriched regions in WT, *uvr3 phrI*, *ddb2*, *dcl4* and *ago1*

plants.
(TIFF)

S22 Fig. siRNA overlapping photodamaged regions. Boxplots representing the abundance of 21-, 22 and 24-nt siRNAs mapping to the photodamaged genomic regions in WT, *uvr3 phrI*, *ddb2*, *dcl4*, *ago1* plants. For each genotype the abundance of 21-, 22 and 24-nt siRNAs is shown in RNA POL IV deficient plants (*nrpd1*). siRNA abundances are normalized against global small RNA content and expressed as reads per million (RPM). p-values are calculated according to Wilcoxon Matched-Pairs Signed-Ranks.
(TIFF)

S23 Fig. Photolesions and DMRs. Distributions of DMRs overlapping (*Stricto sensu*) with photolesions along the Arabidopsis chromosomes (light blue: chromosome arms, dark blue: pericentromeric regions). Hyper- and hypo-DMRs are shown above and below each chromosome, respectively.
(TIFF)

S24 Fig. Characteristics of hypo-DMRs overlapping photolesions. a Heatmaps of CHH methylation levels within hypo-DMRs identified in WT and *uvr3 phrI* plants before, 24h upon UV-C exposure. Columns represent data for each indicated genotype (white, 0; black, 0.6).
b Circles of correlations between 21-, 22- and 24-nt small RNAs mapping to the hypo-DMRs overlapping with photolesions in WT and *uvr3 phrI* plants.
(TIFF)

S25 Fig. DMRs overlapping photolesions. a Distributions of DMRs overlapping with photolesions along the arabidopsis chromosomes (light blue: chromosome arms, dark blue: pericentromeric regions). Hyper- and hypo-DMRs are shown above and below each chromosome, respectively.
b Histogram representing the percentage of hyper- and hypo-DMRs overlapping with photolesions located within centromeric and pericentromeric regions.
c Histograms representing the distribution of the 9 chromatin states of DMRs overlapping with photolesions.
(TIFF)

S26 Fig. UV sensitivity of DCLs and RNA POL IV/V loss of function arabidopsis plants. a Genetic interaction between *dcl2*, *dcl3 and dcl4*. Seven-day-old WT, single (*dcl2*, *dcl3* and *dcl4*) and double (*dcl2/3*, *dcl2/4*, *dcl3/4* and *dcl2/3/4*) mutant plants were exposed to UV-C (900 J/m^2). Root growth was calculated relative to the corresponding untreated plants (±SD). Eight plants per replicate were used and experiments were triplicated. t-test $^{*}p<0.01$ compared to WT; ** $p<0.01$ compared to *dcl3 and dcl4*; ns: non-significant.
b Genetic interactions between *nrpd1* and *nrpe1*. Seven-day-old WT, single (*nrpd1* and *nrpe1*) and double (*nrpd1nrpe1*) mutant plants were exposed to UV-C (900 J/m^2). t-test $^{*}p<0.01$ compared to WT; ** $p<0.01$ compared to each single mutant.
(TIFF)

S1 Table. Statistics of di-pyrimidines frequencies.
(DOCX)

S2 Table. NGS statistics.
(DOCX)

S3 Table. qPCR primers.
(DOCX)

Acknowledgments

We thank Amina Mehidi for her help in statistical analyses and members of the Schmit-Chabouté's group.

Author Contributions

Formal analysis: Stéfanie Graindorge, Valérie Cognat, Philippe Johann to Berens, Jérôme Mutterer, Jean Molinier.

Funding acquisition: Jean Molinier.

Investigation: Jean Molinier.

Resources: Stéfanie Graindorge, Valérie Cognat, Jérôme Mutterer.

Software: Jérôme Mutterer.

Supervision: Jean Molinier.

Validation: Jean Molinier.

Writing – original draft: Philippe Johann to Berens, Jean Molinier.

Writing – review & editing: Jean Molinier.

References

1. Wang G, Vasquez KM. Effects of Replication and Transcription on DNA Structure-Related Genetic Instability. Genes. 2017; 1: pii: E17.
2. Eberhard S, Finazzi G, Wollman FA. The dynamics of photosynthesis. Annual Review of Genetics. 2008; 42: 463–515. https://doi.org/10.1146/annurev.genet.42.110807.091452 PMID: 18983262
3. Molinier J. Genome and Epigenome Surveillance Processes Underlying UV Exposure in Plants. Genes. 2017; 11: pii: E316.
4. Britt AB. Repair of DNA damage induced by ultraviolet radiation. Plant Physiol. 1995; 108: 891–896. https://doi.org/10.1104/pp.108.3.891 PMID: 7630970
5. Tsukahara S, Kobayashi A, Kawabe A, Mathieu O, Miura A, Kakutani T. Bursts of retrotransposition reproduced in Arabidopsis. Nature. 2009; 7262: 423–426.
6. Tittel-Elmer M, Bucher E, Broger L, Mathieu O, Paszkowski J, Vaillant I. Stress-induced activation of heterochromatic transcription. PLoS Genet. 2010; 6: e1001175. https://doi.org/10.1371/journal.pgen.1001175 PMID: 21060865
7. Bennetzen JL. Transposable elements, gene creation and genome rearrangement in flowering plants. Curr Opin Genet Dev. 2005; 6: 621–627.
8. Kim MY, Zilberman D. DNA methylation as a system of plant genomic immunity. Trends Plant Sci. 2014; 5: 320–326.
9. Spampinato CP. Protecting DNA from errors and damage: an overview of DNA repair mechanisms in plants compared to mammals. Cell Mol Life Sci. 2017; 9: 1693–1709.
10. Schuch AP, Garcia CC, Makita K, Menck CF. DNA damage as a biological sensor for environmental sunlight. Photochem. Photobiol. Sci. 2013; 8: 1259–1272.
11. Mullenders LHF. Solar UV damage to cellular DNA: from mechanisms to biological effects. Photochem Photobiol Sci. 2018; 12: 1842–1852.
12. Tomura T, van Lancker JL. DNA repair of U.V.-damage in heterochromatin and euchromatin of rat liver. Int J Radiat Biol Relat Stud Phys Chem Med. 1980; 2: 231–235.
13. Sancar A. Photolyase and cryptochrome blue-light photoreceptors. Adv. Protein Chem. 2004; 73–100. https://doi.org/10.1016/S0065-3233(04)69003-6 PMID: 15588840
14. Schärer OD. Nucleotide Excision Repair in Eukaryotes. Cold Spring Harb. Perspect. Biol. 2013; 5: a012609. https://doi.org/10.1101/cshperspect.a012609 PMID: 24086042
15. Chu G and Chang E. Xeroderma pigmentosum group E cells lack a nuclear factor that binds to damaged DNA. Science. 1988; 4878: 564–567.

16. Schalk C, Cognat V, Graindorge S, Vincent T, Voinnet O, Molinier J. Small RNA-mediated repair of UV-induced DNA lesions by the DNA DAMAGE BINDING protein 2 and ARGONAUTE 1. PNAS. 2017; 14: E2965–E2974.
17. Rigal M, Mathieu O. A "mille-feuille" of silencing: epigenetic control of transposable elements. Biochim Biophys Acta. 2011; 1809: 452–458. https://doi.org/10.1016/j.bbagrm.2011.04.001 PMID: 21514406
18. Law JA and Jacobsen SE. Establishing, maintaining and modifying DNA methylation patterns in plants and animals. Nat. Rev. Genet. 2010; 11: 204–220. https://doi.org/10.1038/nrg2719 PMID: 20142834
19. Matzke MA and Mosher RA. RNA-directed DNA methylation: an epigenetic pathway of increasing complexity. Nat. Rev. Genet. 2014; 15: 394–408. https://doi.org/10.1038/nrg3683 PMID: 24805120
20. Zhang H, Lang Z, Zhu JK. Dynamics and function of DNA methylation in plants. Nat Rev Mol Cell Biol. 2018; 8: 489–506.
21. Zhu JK. Active DNA demethylation mediated by DNA glycosylases. Annu Rev Genet. 2009; 43: 143–66. https://doi.org/10.1146/annurev-genet-102108-134205 PMID: 19659441
22. Virdi KS, Laurie JD, Xu YZ, Yu J, Shao MR, Sanchez R, Kundariya H, Wang D, Riethoven JJ, Wamboldt Y, Arrieta-Montiel MP, Shedge V, Mackenzie SA. Arabidopsis MSH1 mutation alters the epigenome and produces heritable changes in plant growth. Nat Commun. 2015; 6: 6386. https://doi.org/10.1038/ncomms7386 PMID: 25722057
23. Schalk C, Drevensek S, Kramdi A, Kassam M, Ahmed I, Cognat V, Graindorge S, Bergdoll M, Baumberger N, Heintz D, Bowler C, Genschik P, Barneche F, Colot V, Molinier J. DNA DAMAGE BINDING PROTEIN 2 (DDB2) Shapes the DNA Methylation Landscape. Plant Cell. 2016; 9: 2043–2059.
24. Córdoba-Cañero D, Cognat V, Ariza RR, Roldán Arjona T, Molinier J. Dual control of ROS1-mediated active DNA demethylation by the DNA DAMAGE BINDING protein 2 (DDB2). Plant J. 2017; 6: 1170–1181.
25. Le May N, Fradin D, Iltis I, Bougnères P, Egly JM. XPG and XPF endonucleases trigger chromatin looping and DNA demethylation for accurate expression of activated genes. Mol Cell. 2012; 4: 622–632.
26. Schalk C, Molinier J. Global Genome Repair factors control DNA methylation patterns in Arabidopsis. Plant Signaling & Behavior. 2016; 12: e1253648.
27. Dowen RH, Pelizzola M, Schmitz RJ, Lister R, Dowen JM, Nery JR, Dixon JE, Ecker JR. Widespread dynamic DNA methylation in response to biotic stress. Proc. Natl. Acad. Sci. USA 2012; 109: E2183–E2191. https://doi.org/10.1073/pnas.1209329109 PMID: 22733782
28. Yu A, Lepère G, Jay F, Wang J, Bapaume L, Wang Y, Abraham AL, Penterman J, Fischer RL, Voinnet O, Navarro L 2013. Dynamics and biological relevance of DNA demethylation in *Arabidopsis* antibacterial defense. Proc Natl Acad Sci U S A. 2013; 6: 2389–2394.
29. Yong-Villalobos L, González-Morales SI, Wrobel K, Gutiérrez-Alanis D, Cervantes-Peréz SA, Hayano-Kanashiro C, Oropeza-Aburto A, Cruz-Ramírez A, Martínez O, Herrera-Estrella L. Methylome analysis reveals an important role for epigenetic changes in the regulation of the Arabidopsis response to phosphate starvation. Proc. Natl. Acad. Sci. USA. 2015; 112: E7293–E7302. https://doi.org/10.1073/pnas.1522301112 PMID: 26668375
30. Liu TK, Li Y, Duan WK, Huang FY, Hou XL. Cold acclimation alters DNA methylation patterns and confers tolerance to heat and increases growth rate in Brassica rapa. J. Exp. Bot. 2017; 68: 1213–1224. https://doi.org/10.1093/jxb/erw496 PMID: 28158841
31. Secco D, Wang C, Shou H, Schultz MD, Chiarenza S, Nussaume L, Ecker JR, Whelan J, Lister R. Stress induced gene expression drives transient DNA methylation changes at adjacent repetitive elements. eLife, 2015; 4: e09343.
32. Eichten SR, Springer NM. Minimal evidence for consistent changes in maize DNA methylation patterns following environmental stress. Front. Plant Sci. 2015; 6: 308. https://doi.org/10.3389/fpls.2015.00308 PMID: 25999972
33. Schuermann D, Molinier J, Fritsch O, Hohn B. The dual nature of homologous recombination in plants. Trends in Genetics. 2005; 21: 172–181. https://doi.org/10.1016/j.tig.2005.01.002 PMID: 15734576
34. Molinier J, Ramos C, Fritsch O, Hohn B. CENTRIN 2 modulates Homologous Recombination and Nucleotide Excision Repair in Arabidopsis. Plant Cell. 2004; 16: 1633–1643. https://doi.org/10.1105/tpc.021378 PMID: 15155891
35. Molinier J, Oakeley EJ, Niederhauser O, Kovalchuk I, Hohn B. Dynamic response of plant genome to ultraviolet and other genotoxic stresses. Mutation Research. 2005; 571: 235–247. https://doi.org/10.1016/j.mrfmmm.2004.09.016 PMID: 15748650
36. Sequeira-Mendes J, Aragüez I, Peiró R, Mendez-Giraldez R, Zhang X, Jacobsen SE, Bastolla U, Gutierrez C. The Functional Topography of the Arabidopsis Genome Is Organized in a Reduced Number of Linear Motifs of Chromatin States. Plant Cell. 2014; 6: 2351–2366.

37. Cao X, Jacobsen SE. Locus-specific control of asymmetric and CpNpG methylation by the DRM and CMT3 methyltransferase genes. Proc. Natl. Acad. Sci. U S A. 2002; 4: 16491–16498.

38. Stroud H, Greenberg MV, Feng S, Bernatavichute YV, Jacobsen SE. Comprehensive analysis of silencing mutants reveals complex regulation of the Arabidopsis methylome. Cell. 2013; 1–2: 352–364.

39. Castells E, Molinier J, Genschik P, Drevensek S, Barneche F, Bowler C. *det1-1* induced UV-C hyposensitivity through *UVR3* and *PHR1* photolyase overexpression. Plant J. 2010; 63: 392–404. https://doi.org/10.1111/j.1365-313X.2010.04249.x PMID: 20487384

40. Molinier J, Lechner E, Dumbliauskas E, Genschik P. Regulation and role of *Arabidopsis* CUL4-DDB1A-DDB2 in maintaining genome integrity upon UV stress. Plos Genet. 2008; 6: e1000093.

41. Ries G, Buchholz G, Frohnmeyer H, Hohn B. UV-damage-mediated induction of homologous recombination in Arabidopsis is dependent on photosynthetically active radiation. Proc Natl Acad Sci U S A. 2000; 24: 13425–13429.

42. Morel JB, Godon C, Mourrain P, Béclin C, Boutet S, Feuerbach F, Proux F, Vaucheret H. Fertile hypomorphic ARGONAUTE (ago1) mutants impaired in post-transcriptional gene silencing and virus resistance. Plant Cell. 2002; 3: 629–639.

43. Ito H, Gaubert H, Bucher E, Mirouze M, Vaillant I, Paszkowski J. An siRNA pathway prevents transgenerational retrotransposition in plants subjected to stress. Nature. 2011; 7341: 115–119.

44. Walbot V. UV-B damage amplified by transposons in maize. Nature. 1999; 6718: 398–399.

45. Xu W, Wang T, Xu S, Li F, Deng C, Wu L, Wu Y, Bian P. UV-C-Induced alleviation of transcriptional gene silencing through plant-plant communication: Key roles of jasmonic acid and salicylic acid pathways. Mutat Res. 2016; 790: 56–67. https://doi.org/10.1016/j.mrfmmm.2016.04.003 PMID: 27131397

46. Van Dooren TJM, Bortolini Silveira A, Gilbault E, Jiménez-Gómez JM, Martin A, Bach L, Tisné S, Quadrana L, Loudet O, Colot V. Mild drought induces phenotypic and DNA methylation plasticity but no transgenerational effects in Arabidopsis. bioRxiv 370320; https://doi.org/10.1101/370320.

47. Fransz P, De Jong JH, Lysak M, Castiglione MR, Schubert I. Interphase chromosomes in Arabidopsis are organized as well defined chromocenters from which euchromatin loops emanate. Proc Natl Acad Sci U S A. 2002; 22: 14584–14589.

48. Pecinka A, Dinh HQ, Baubec T, Rosa M, Lettner N, Mittelsten Scheid O. Epigenetic regulation of repetitive elements is attenuated by prolonged heat stress in Arabidopsis. Plant Cell. 2010; 9: 3118–3129.

49. Cuerda-Gil D and Slotkin RK. Non-canonical RNA-directed DNA methylation. Nat. Plants. 2016; 11: 16163.

50. Pontier D, Picart C, Roudier F, Garcia D, Lahmy S, Azevedo J, Alart E, Laudié M, Karlowski WM, Cooke R, Colot V, Voinnet O, Lagrange T. NERD, a plant-specific GW protein, defines an additional RNAi-dependent chromatin-based pathway in Arabidopsis. Mol Cell. 2012; 1: 121–132.

51. McCue AD, Panda K, Nuthikattu S, Choudury SG, Thomas EN, Slotkin RK. ARGONAUTE 6 bridges transposable element mRNA-derived siRNAs to the establishment of DNA methylation. EMBO J. 2015; 1: 20–35.

52. Ahmed I, Sarazin A, Bowler C, Colot V, Quesneville H. Genome-wide evidence for local DNA methylation spreading from small RNA-targeted sequences in Arabidopsis. Nucleic Acids Res. 2011; 16: 6919–6931.

53. Ye R, Chen Z, Lian B, Rowley MJ, Xia N, Chai J, Li Y, He XJ, Wierzbicki AT, Qi Y. A Dicer-Independent Route for Biogenesis of siRNAs that Direct DNA Methylation in Arabidopsis. Mol Cell. 2016; 2: 222–235.

54. Ulm R, Jenkins GI. Q&A: How do plants sense and respond to UV-B radiation? BMC Biol. 2015; 13: 45. https://doi.org/10.1186/s12915-015-0156-y PMID: 26123292

55. Bourguet P, de Bossoreille S, López-González L, Pouch-Pélissier MN, Gómez-Zambrano Á, Devert A, Pélissier T, Pogorelcnik R, Vaillant I, Mathieu O. A role for MED14 and UVH6 in heterochromatin transcription upon destabilization of silencing. Life Sci Alliance. 2018; 6: e201800197.

56. Groisman R, Polanowska J, Kuraoka I, Sawada J, Saijo M, Drapkin R, Kisselev AF, Tanaka K, Nakatani Y. The ubiquitin ligase activity in the DDB2 and CSA complexes is differentially regulated by the COP9 signalosome in response to DNA damage. Cell. 2003; 3: 357–367.

57. Marí-Ordóñez A Marchais A, Etcheverry M, Martin A, Colot V, Voinnet O. Reconstructing de novo silencing of an active plant retrotransposon. Nat. Genet. 2013; 45: 1029–1039. https://doi.org/10.1038/ng.2703 PMID: 23852169

58. Nuthikattu S, McCue AD, Panda K, Fultz D, DeFraia C, Thomas EN, Slotkin RK. The initiation of epigenetic silencing of active transposable elements is triggered by RDR6 and 21–22 nucleotide small interfering RNAs. Plant Physiol. 2013; 1: 116–131.

59. Rochette PJ, Lacoste S, Therrien JP, Bastien N, Brash DE, Drouin R. Influence of cytosine methylation on ultraviolet-induced cyclobutane pyrimidine dimer formation in genomic DNA. Mutat Res. 2009; 665: 7–13. https://doi.org/10.1016/j.mrfmmm.2009.02.008 PMID: 19427505

60. Hu J, Lieb JD, Sancar A, Adar S. Cisplatin DNA damage and repair maps of the human genome at single-nucleotide resolution. Proc Natl Acad Sci U S A. 2016; 41: 11507–11512.

61. Bourbousse C, Mestiri I, Zabulon G, Bourge M, Formiggini F, Koini MA, Brown SC, Fransz P, Bowler C, Barneche F. Light signaling controls nuclear architecture reorganization during seedling establishment. Proc Natl Acad Sci U S A. 2015; 21: E2836–E2844.

62. Castells E, Molinier J, Benvenuto G, Bourbousse C, Zabulon G, Zalc A, Cazzaniga S, Genschik P, Barneche F, Bowler C. The conserved factor DE-ETIOLATED 1 cooperates with CUL4-DDB1DDB2 to maintain genome integrity upon UV stress. EMBO J. 2011; 6: 1162–1172.

63. Fei J, Kaczmarek N, Luch A, Glas A, Carell T, Naegeli H. Regulation of nucleotide excision repair by UV-DDB: prioritization of damage recognition to internucleosomal DNA. PLoS Biol. 2011; 10: e1001183.

64. Feng W, Michaels SD. Accessing the Inaccessible: The Organization, Transcription, Replication, and Repair of Heterochromatin in Plants. Annu Rev Genet. 2015; 49: 439–459. https://doi.org/10.1146/annurev-genet-112414-055048 PMID: 26631514

65. Simon L, Voisin M, Tatout C, Probst AV. Structure and Function of Centromeric and Pericentromeric Heterochromatin in *Arabidopsis thaliana* Front Plant Sci. 2015; 6: 1049. https://doi.org/10.3389/fpls.2015.01049 PMID: 26648952

66. Puchta H, Swoboda P, Gal S, Blot M, Hohn B. Somatic intrachromosomal homologous recombination events in populations of plant siblings. Plant Mol Biol. 1995; 2: 281–292.

67. Questa J, Walbot V, Casati P. UV-B radiation induces Mu element somatic transposition in maize. Mol Plant. 2013; 6: 2004–2007. https://doi.org/10.1093/mp/sst112 PMID: 23877058

68. Ito H, Yoshida T, Tsukahara S, Kawabe A. Evolution of the ONSEN retrotransposon family activated upon heat stress in Brassicaceae. Gene. 2013; 2: 256–261.

69. Masuda S, Nozawa K, Matsunaga W, Masuta Y, Kawabe A, Kato A, Ito H. Characterization of a heat-activated retrotransposon in natural accessions of Arabidopsis thaliana. Genes Genet Syst. 2017; 6: 293–299.

70. Daccord N, Celton JM, Linsmith G, Becker C, Choisne N, Schijlen E, van de Geest H, Bianco L, Micheletti D, Velasco R, Di Pierro EA, Gouzy J, Rees DJG, Guérif P, Muranty H, Durel CE, Laurens F, Lespinasse Y, Gaillard S, Aubourg S, Quesneville H, Weigel D, van de Weg E, Troggio M, Bucher E. High-quality de novo assembly of the apple genome and methylome dynamics of early fruit development. Nat Genet. 2017; 7: 1099–1106.

4. Chapter II - Advanced methods for segmentation of Arabidopsis nuclei and chromocenters

4.1. Introduction

Visualization of cellular structures is an efficient approach for deciphering biological processes. In the last decades, cytochemistry protocols and microscopes have been improved a lot, allowing detailed observation and study on many kinds of cellular structures such as organelles (Weigel et al. 2021; Keuenhof et al. 2022), cytoskeleton (Steblyanko et al. 2020), extracellular vesicles (Colombo et al. 2021), stress granules (Van Treeck and Parker 2019) and chromatin (Birk 2019). The increasing interest in epigenetics and thus for chromatin contributed to develop a large repertoire of tools for visualization and analysis. Cytogenetics studies chromosomes structures and the features of particular genomic regions. For example, genomic DNA condensation is revealed by 4',6-Diamidino-2-phenylindol (DAPI) staining (Soppe et al. 2002). Fluorescent *in situ* Hybridization (FISH), immunostaining of specific epigenetic marks or proteins, are also routinely used to decipher mechanisms within the nucleus. The improvement of cytogenetic techniques, together with high-quality images acquisition, needs reliable quantification for accurate interpretations. For this, many open-source software, web-assisted applications and plug-ins are regularly developed and improved, to facilitate image analysis and quantification. Indeed, assistance or automatization of image analysis through basic principles such as intensity thresholding, edge detection and mathematical image transformation, have been implemented (Landini et al. 2017; Hunt et al. 2020; Schroeder et al. 2021; Zhang et al. 2021). However, the segmentation of structures of higher complexity, exhibiting irregular shapes and intensities, remains challenging and generally requires a lot of human decision-making. Regretfully, any human decision-making is associated with an observer/user-specific cognitive bias, which, in worst-case scenarios, may false the conclusion of a well-designed experiment. Despite manual segmentation is often seen as the golden standard in medical image segmentation, reducing human decision making in image analysis process is a big issue for experimental reproducibility and accuracy (Renard et al. 2020).

Recently the breakthrough in the development of Deep Learning (DL) tools brought new opportunities for image analyses. Generally speaking, a DL method, derived from machine learning, is defined by its ability to learn on its own by which decision-making, a task of interest can be optimally performed. When applied to image analysis, DL was shown to outperform classical methods in different tasks, such as simple image classification (Seeland et al. 2019), denoising (Song et al. 2021), or the more complex segmentation (Zhou et al. 2021). Especially, segmenting objects of interest is a recurrent task for scientists during images analysis. A common approach to perform such trimming steps using DL is semantic segmentation, which consists in linking each pixel to a label. A fundamental requirement to do so is the use of enough training images in which objects of interest (for example, nuclei or sub-nuclear entities) are labeled. Such a training set is used as a reference to feed an artificial neuronal network, thereby learning the characteristics by which a given pixel can be linked to a specific label. Neuronal networks can have many different structures depending on the task of interest (Ithapu et al. 2017). A mile-stone network-structure, specially developed for semantic segmentation of biological images, is the Convolutional Neuronal Network (CNN) U-Net (Ronneberger et al. 2015). The U-net structure is built to perform end-to-end segmentation by contraction of the input image through successive down-convolutions, nonlinear activation function and Max-pooling steps, and follow-up expansion of the image by successive up-convolutions, non-linear activation function, and concatenation (Ronneberger et al. 2015). During the learning process, the mathematical changes applied to the pixel values of the input image upon contraction and expansion process are progressively optimized in such a way that the output image approaches the binary annotation mask. Unfortunately, despite its added value, deep learning-based image analysis approaches remain substantially weakly used due do the lack of programming expertise in many laboratories. Hence, the development of user-friendly open-source tools, democratizing the use of deep learning, was recognized as an essential objective by the scientific community (Godec et al. 2019; Shepley et al. 2021; Gómez-de-Mariscal et al. 2021). In plant research, increasing efforts have been devoted to develop DL-based tools for species identification (Seeland et al. 2019), phenotypic analysis of arial parts (Atanbori et al. 2020), roots (Yasrab et al. 2019), cells (Li et al. 2022) and analysis of organellar morphology (Li et al. 2021).

Meanwhile, in plant cytogenetics, a growing interest and efforts have been devoted to detect nuclei and subnuclear structures within microscopy images (Kalyanikrishna et al. 2020; Tatout et al. 2022). In *Arabidopsis thaliana*, interphasic nuclei centromeric and pericentromeric DNA sequences are highly condensed, building the so-called chromocenters (Simon et al. 2015). Nucleus and chromocenters morphologies undergo major changes during several biological processes such as development (Benoit et al. 2013; Bourbousse et al. 2015), cell differentiation (Goto et al. 2021), cell division (Pecinka et al. 2020), or exposure to environmental stresses (Pecinka et al. 2010; Graindorge et al. 2019). Thus, the accurate analysis of nuclear phenotypes is necessary to better describe many relevant biological mechanisms.

The following study aims at providing user-friendly tools to perform the segmentation of *Arabidopsis thaliana* nuclei and chromocenters to further quantify several of their features. After showcasing the inter-user differences in the segmentation, the semi-automatic plug-in ICRAQ, was evaluated to reduce user-specific behaviors. Finally, our study will present the ready-to-use Nucl.Eye.D script, developed for the segmentation of *Arabidopsis thaliana* nuclei and chromocenters using a DL approach. The Nucl.Eye.D script was written by biologists for biologists and is conceptualized so that it can be used and adapted with beginner programming knowledge. Additionally, an essential part of the described methods addresses the daily-life application problems such as the availability of few annotated training images and the aim of comparing very different image types with a minimum of effort. Firstly, different ways of annotating the training set will be compared (by hand or using the semi-automated plug-in ICRAQ). Secondly, the Nucl.eye.D script will be evaluated, depending on the training set used. Finally, its relevance is exemplarily showcased on the well-known variability in chromocenter morphologies between WT and DECREASED DNA METHYLATION 1 (*ddm1*) mutant plants (Vongs et al. 1993).

This study wishes to raise awareness and to present several advantages of DL-based analysis applied to plant cytogenetics and, more importantly, to provide tools for biologists to analyze nuclear features.

4.2. Results & Discussion

In this study, different sets of images will be used to evaluate the variability occurring in-between users and segmentation methods. Fifty images containing around 135 DAPI-stained nuclei prepared from Arabidopsis plants grown either in darkness or in light have been used (Bourbousse et al. 2015). Hereafter this Light/Dark image set will be called "L/D set". Previous studies using the same growth condition revealed a decreased Heterochromatin Indexes (HX, chromocenter surface in % of nuclear surface), Relative Chromocenter Intensities (RCI, Mean chromocenter intensity divided by Mean Nuclear Intensity), and Relative Heterochromatin Fraction (RHF, HX multiply by RCI) for nuclei grown in darkness (Bourbousse et al. 2015). Consequently, the L/D set brings the advantage of containing a well-described variety of nuclear phenotypes, allowing to compare the accuracy of different segmentation methods. Our first interest was to evaluate the inter-user variability using manual, semi-automated, and DL-based segmentation in order to demonstrate the issues associated with human decision-making.

4.2.1. Manual Segmentation of nucleus and chromocenters

The segmentation of the L/D set was performed manually using ImageJ (Schroeder et al. 2021) by three independent users proficient in image analysis of Arabidopsis nuclei. This manual approach produced binary masks (Fig. S1) of nuclei and chromocenters that were used for inter-user comparisons. As shown in Figure 1 on representative nuclei from L/D set, differences in the segmentation of nucleus and chromocenters can be observed by all non-overlapping-colored regions. Unsurprisingly, whereas the segmentations only slightly differ in edge regions of chromocenters representative of the light condition (Fig. 1), users do not always agree on chromocenter segmentation of more complex structures with an intermediate intensity as observed in the dark condition (Fig. 1). More importantly, when analyzing chromocenter morphology, manual segmentations of all three users measured the expected trend with a significant decrease of RCI, HX, and RHF for nuclei prepared from plants grown in darkness (Bourbousse et al. 2015) (Fig. 2).

However, the measured mean RHF for Light and Dark nuclei ranges between 18% - 15% and 11 - 8%, respectively, depending on the user (Fig. 2). This RHF value is higher than the one reported in the literature with 13% and 7% (Bourbousse et al. 2015). These observations illustrate the significant effect of the user-specific decision-taking during the segmentation steps. Hence priority should, as far as possible, be given to the reproducibility of relative differences in-between samples segmented by the same method. Our approach reports the variability observed between three users, performing nucleus and chromocenter segmentation tasks during 3h. However, the cognition and cognitive biases of each user may fluctuate depending on physical, psychological, and emotional conditions. Consequently, the accuracy of user performance likely differs from one day to another, inducing additional biases, especially on large and time-consuming datasets. In the following step, we will investigate the ability of a semi-automatic plug-in to perform an assisted segmentation that may reduce Inter-user biases.

4.2.2. ICRAQ: a plug-in assisted segmentation of nucleus and chromocenters

Here above, we observed and described the inter-user variability upon manual segmentation of nuclei and chromocenters on images from the L/D set. In order to prevent a significant effect of inter-user variability and human decision-taking in the process of nuclei and chromocenter segmentation, several open-access tools, with different degrees of automatization, have been developed in the last years (Iannuccelli et al. 2010; Graindorge et al. 2019; Dubos et al. 2020). To illustrate the performance of such tools, the same three users performed the segmentation of nuclei, and chromocenters from L/D set using the ICRAQ plugin (https://github.com/gschivre/iCRAQ) (Fig. 3). The ICRAQ tool provides semi-automatic segmentation assistance, detecting nuclei via global-variable thresholding of the median filtered z-projection, and chromocenters through an interactive H-watershed (Fig. 3). Interestingly the ICRAQ tool also includes options for a potential free-hand correction of the segmentation in case of need. As shown by the overlays in Figure 1, the nuclear perimeter shows a close overlap in-between all three users. In addition, users more easily agree about the chromocenter segmentations. However, their delimitations remain slightly different (Fig. 1). This feeling is confirmed by the calculation of the mean-distance in between segmentation masks from 2 different users (Fig. 4).

Indeed, for all possible user pairs, the mean distance between perimeters of nuclear masks shows a significant decrease when segmentation was performed using ICRAQ (Fig. 4). The same trend can be observed for the mean distance between chromocenter entities (Fig. 4). Altogether, these results show that the ICRAQ plug-in tends to globally reduce the inter-user variability, even though this effect remains dependent on user behavior and the degree of manual re-adjustment of the segmentations. Necessarily, if the inter-user difference appears to be reduced with ICRAQ, the overlay between manual and ICRAQ assisted segmentation of the same nucleus by the same user show remarkable changes (Fig. 1). These differences reveal how easily users' decision-making can be influenced by the proposition of assisted segmentation tools (Sensakovic et al. 2010). Thus, it can be questioned to which extent the decreased number of inter-user differences is accompanied by a gain of plug-in/algorithm-sourced bias. Finally, when ICRAQ segmentation masks are used to measure RCI, HX, and RHF, a significant decrease in RHF and RCI can be identified in dark nuclei compared to light nuclei, independently on the user (Fig. 2). In contrast, when measuring the HX, only two out of three users observed a significant decrease in dark nuclei (Fig. 2). Interestingly, for all users, the observed RHF differed between manual and ICRAQ segmentation (Fig. 2). These observations highlight the known cognitive biases a trendline/segmentation-assistance may induce, regardless of user expertise (Sensakovic et al. 2010). In addition, these comparative analyses put emphasis on the fact that measures of nuclear morphology should not only rely on mean RCI, HX, or RHF, but always need to be expressed as relative to an internal control (*i.e.,* nuclei from Col-0 plants grown in control condition).

In summary, this analysis shows how assisted segmentation tools such as ICRAQ can significantly reduce inter-user differences. However, this does not imply that human decision-making becomes irrelevant in the processes, as shown by the slight changes that may interfere with the biological meaning of the results.

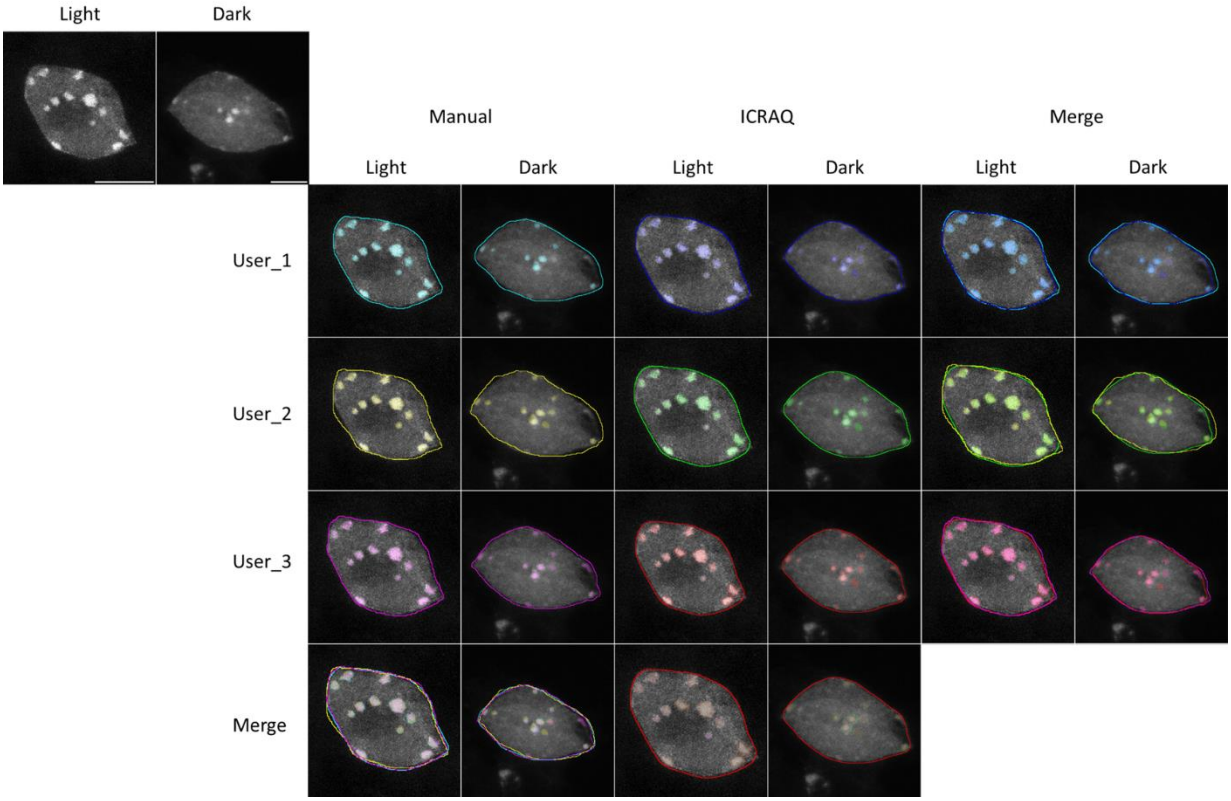

Figure 1: Segmentation of nuclei and chromocenters by three different users

Representative DAPI stained WT (Col-0) nuclei from Light/Dark set (top left) segmented by three different users either manually or by using the ICRAQ plug-in. Border of nucleus segmentation masks are shown as lines, and chromocenter masks as transparent color overlays. Merged images show the overlap between masks, comparing differences between users and differences associated to the segmentation method. Scale bar = 5µm.

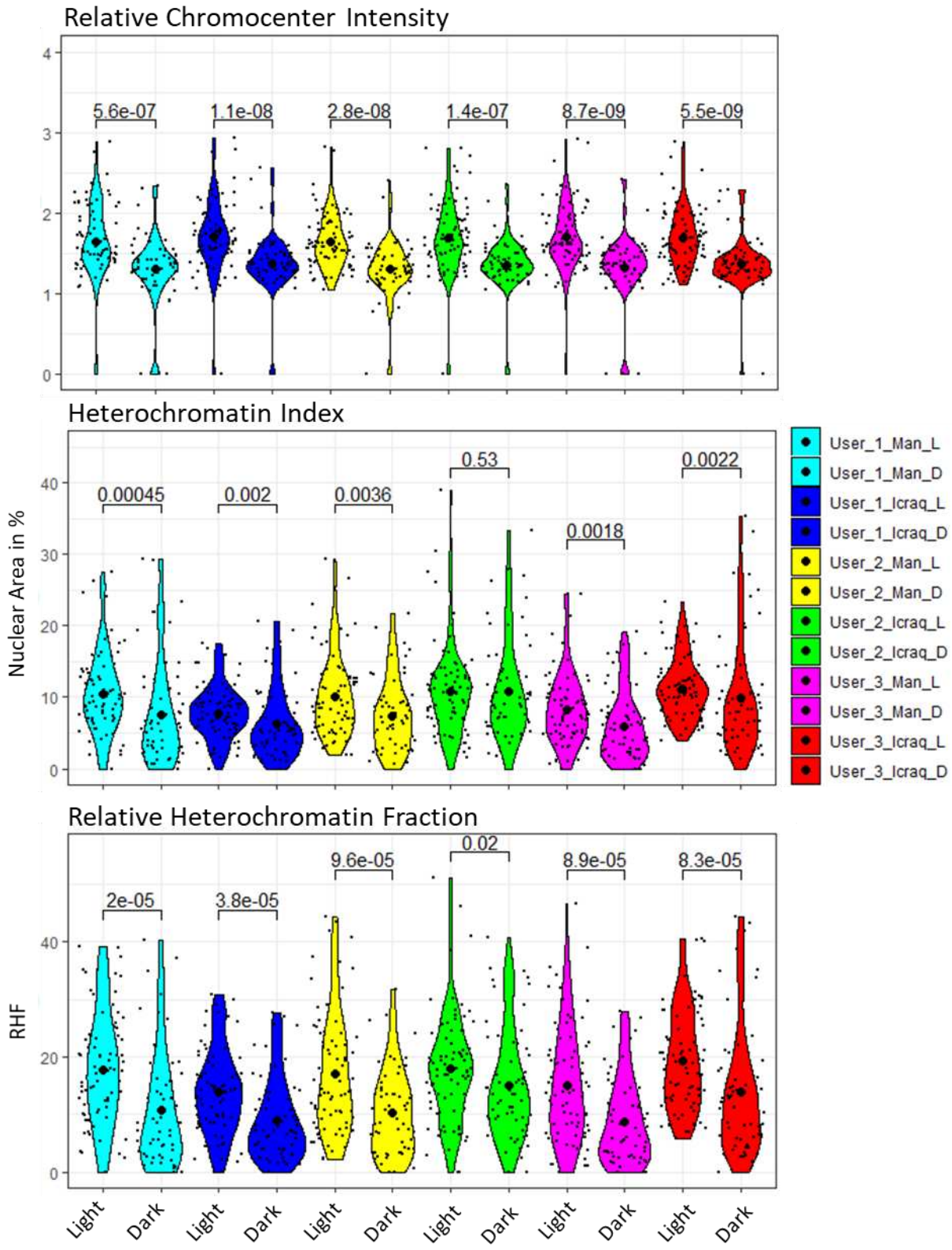

Figure 2: Comparison of heterochromatin features depending on users and segmentation methods

Violin plots illustrating the distribution of relative chromocenter intensity, chromocenter index, and relative heterochromatin fraction in a population of at least 50 nuclei per condition (all nuclei from Light/Dark set). Each black dot represents the measure for one nucleus. The large dot shows the mean value. Exact p values are shown (Mann Whitney Wilcoxon test).

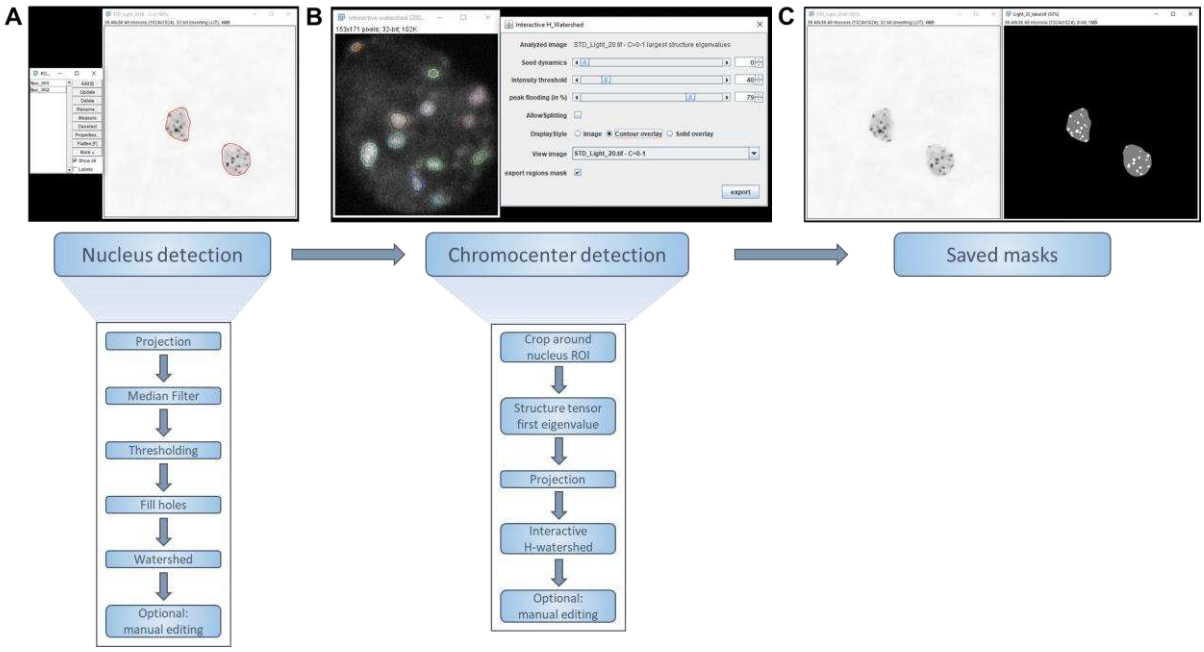

Figure 3: iCRAQ workflow

(A) iCRAQ's first step is to detect the nuclei on the 2D projection of 3D z-stack images based on intensity thresholding. Two examples of segmented nuclei are shown as regions of interest (ROIs) outlined in red. **(B)** A region surrounding each nucleus is set and cropped from the original stack. On each single-nucleus stack, the first eigenvalue of the structure tensor is calculated at each pixel in the image stack and projected in z. This projected image is segmented interactively via the H-watershed plugin. **(C)** The final result is an image mask with three levels of gray: *black* for the image background, *gray* for the nuclear interior outside of chromocenters, and *white* for the chromocenters. See Materials & Methods for more details.

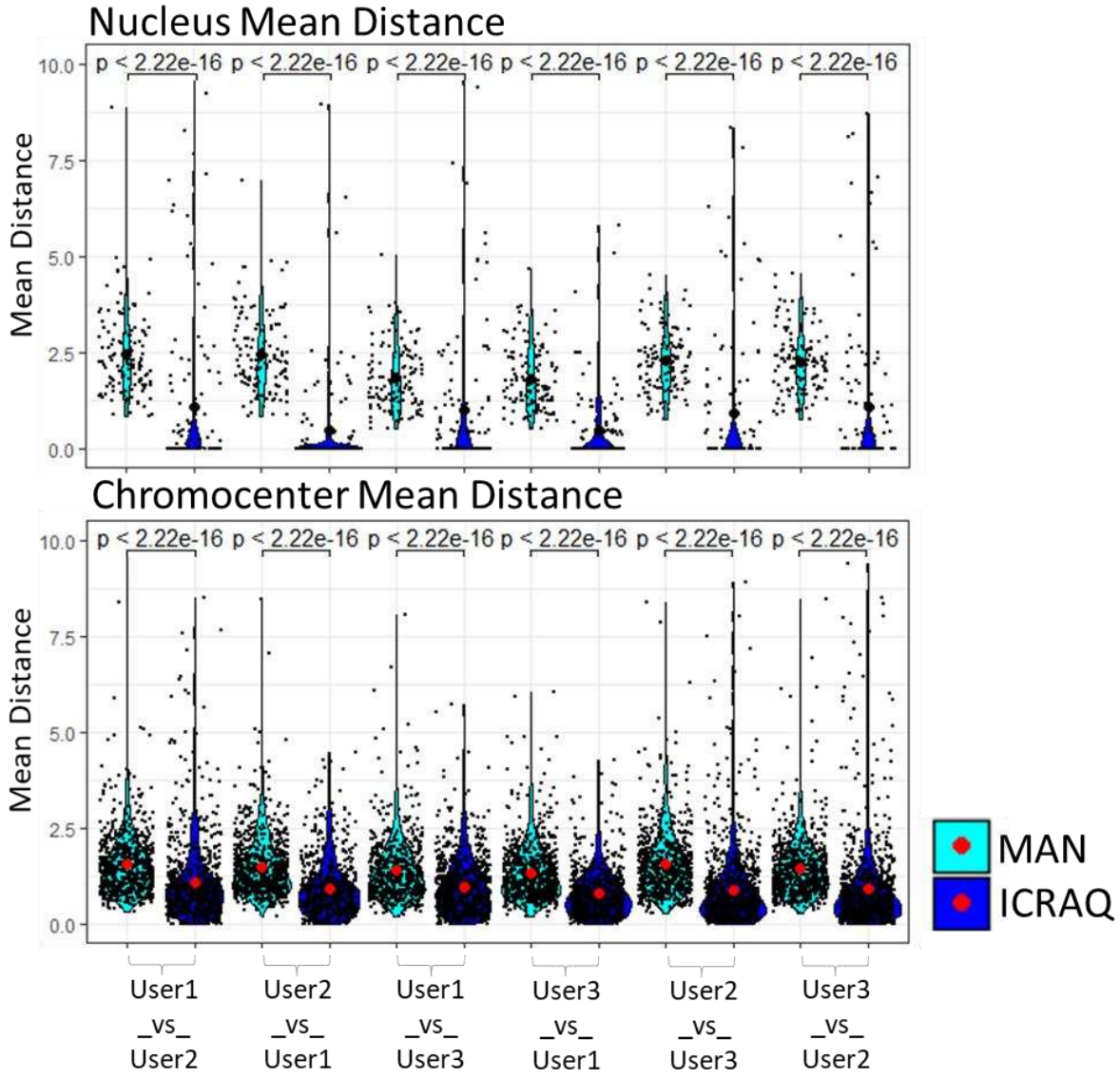

Figure 4: Mean distance in between segmentation masks

All objects from segmentation masks are compared between users and methods. In the constellation "User_A_vs_User_B" the segmentation mask from user A serve as the reference point. The mean distance (in pixel) represents the distance between the perimeters of the same object segmented by two different users. For mean distance calculation, entities with an overlap of 0 were excluded. Statistical comparison was performed in between the segmentation methods. Exact p values are shown (Mann Whitney Wilcoxon test).

4.2.3. Presentation of a fully automized Deep-Learning pipeline for segmentation of nucleus and subnuclear structures

We demonstrated how human decision-taking influenced the segmentation of nuclei and chromocenter structure. To overcome the lack of segmentation reproducibility linked to intra- and inter-user variability, the next part is devoted to the description of a fully automated Deep-Learning-based tool: Nucl.Eye.D (https://tinyurl.com/NuclEyeD) (Fig. 5). As a tool developed by biologists, for biologists, our approach and design tried to reproduce realistic average-lab conditions, disposing of a relatively small training dataset, potential problems of inter-user diversity in sample preparation and image acquisition, and basic programming skills. Another key goal of this tool development was to build a script that includes all necessary code and explanations to easily teach your own model with your own images, in case the provided pre-trained model does not fit your probe preparation (https://tinyurl.com/NuclEyeD).

Each DL tool starts with a training data set that needs to be properly thought. In our example, the training sets are composed of 300 and 150 images (with an average of 5 nuclei/image) to train nuclear and chromocenters segmentations, respectively. This training sets originates from several different experiments, including mutant plants, abiotic treatments…(Soppe et al. 2002; Graindorge et al. 2019), providing a high variability of nuclear morphologies. Slides preparation and images acquisition of this training set were performed as described in § 4.4. The annotation of the training set is the first critical step. Indeed, in contrast to common expectations, deep-learning algorithms are far from being deprived of human-like bias (Cazes et al. 2021; Kliegr et al. 2021). Indeed, the segmentation of a DL-based tool can only be efficient if the provided training annotation is of high quality. Therefore, the first step for preventing algorithm bias consists in reducing user-specific bias in the annotation of the training set (Alzubaidi et al. 2021; Cazes et al. 2021; Paullada et al. 2021). In order to study the effect of inter-user differences on the Nucl.Eye.D pipeline, the same training images get annotated in three different ways. The first set of annotations was performed manually by a single user (User3 in previous parts: One_User, OU). The second set of annotations was produced manually by ten different users (Ten_Users, TU), and the third set of annotations was displayed by ten users with the ICRAQ plug-in (Ten_Users_Icraq, TUI).

After several optimization steps, the Nucl.Eye.D tool finally was released as a pipeline composed of 3 successive U-net neuronal networks (Ronneberger et al. 2015) (Fig. 5). To prevent model overfitting (Alzubaidi et al. 2021) as consequence of small training data sets, the pipeline includes optional data-augmentation steps. In a first step, the 300 nuclei trained images are fed into a Region Proposal U-Net Model (RPM) (Fig. 5), which aims at making a raw prediction of the regions of the image that contains nuclei to define bounding boxes, ideally containing a single nucleus. In a second step, the predicted bounding boxes are used to produce small image fragments, which will, in turn, feed the nuclei segmentation U-Net model (Fig. 5). This second model precisely predicts the borders of each single nuclei, previously identified by the RPM, redefining a more accurate bounding box (Fig. 5). Finally, nuclei from the 150 chromocenter-trained images are successively segmented using the RPM and nuclear segmentation models, providing small image fragments which will be used to train the chromocenter segmentation U-Net (Fig. 5).

Once trained, models can be loaded and used to predict nuclear and chromocenter structures on a test data set. In our case, we primarily use the L/D set (Fig. 5). Upon prediction process, input images are also refined into image fragments, with one nucleus per image, as previously described for the training process. A full-image prediction mask is automatically reconstructed from the different image fragments for output in order to deliver a user-friendly format where masks can easily be overlayed to the original input images (Fig.5). To fully exploit the potential of the Nucl.Eye.D pipeline, it needs to be considered that prior being released as a binary segmentation mask, each prediction output is an uncertainty heat map, with intensities ranging from 0 to 1 (Fig. S1). Increased intensity means a high certainty of the pixel for being a part of the target object. Thus, in order to obtain a binary mask, a threshold needs to be set. This threshold can be chosen by a trial-and-error process until the segmentation fits the best with the user's expectations. However, to avoid as much human decision-making as possible, the threshold is by default set at 0.5. With this threshold, as soon as the model reaches a higher probability for a pixel to be part of the object than being part of the background, the pixel is kept for the segmentation step. The training of the three successive models takes around 12h. In contrast, once trained, the prediction of large data sets (1000 images) can be performed within a few minutes.

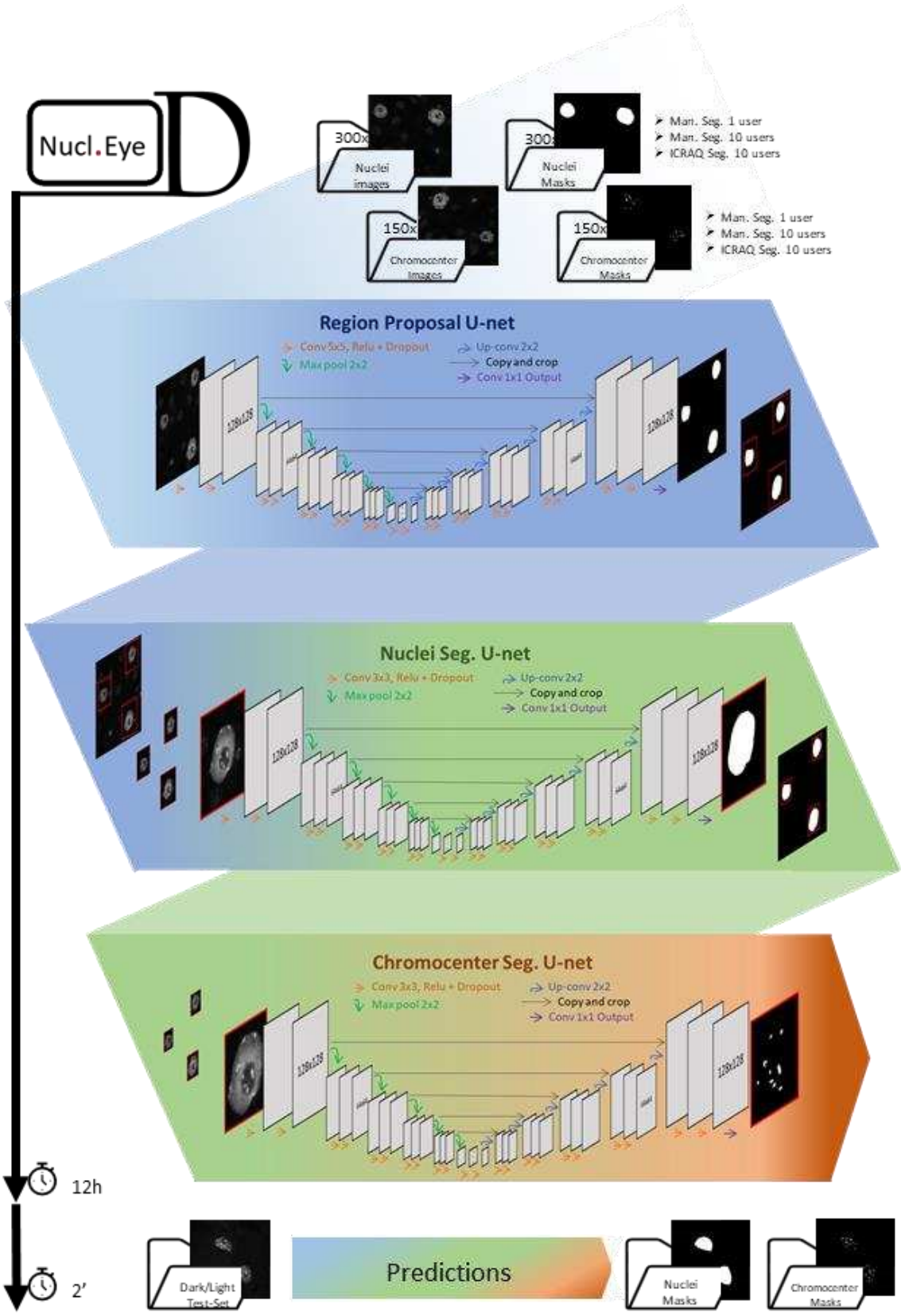

Figure 5: Nucl.Eye.D Pipeline

Graphical abstract of the Nucl.Eye.D pipeline, subdivided into three successive neuronal U-networks. The training period takes around 12h for the detection of both nuclei and chromocenters. Prediction takes 2 min for 50 Dark/Light test-set images.

4.2.4. Nucl.Eye.D based segmentation of nucleus and chromocenter

To evaluate the accuracy of nuclear and chromocenter segmentations performed by the Nucl.Eye.D pipeline, all images of the L/D set were predicted using a threshold of 0.5. Importantly, the L/D set was produced using different sample preparation and image acquisition protocols than the one used for the training set. Consequently, its segmentation may be less accurate. As shown in Figure 6, the segmentation performed by the Nucl.Eye.D pipeline slightly varies depending on the training set used. Nevertheless, it shows a coherent overlay. Interestingly, whereas OU and TU models lead to relatively similar results, TUI model-based predictions recognize a few more chromocenters in the dark nuclei and slightly reduce the nuclear perimeter (Fig. 6).

When calculating RCI, HX and RHF using the segmentation masks produced by the Nucl.Eye.D pipeline, the expected decrease of all three features could be observed in dark nuclei, independently of the training set initially used (Fig. 7A). The mean RHF values range from 8% to 10% and 4% to 6% in light and dark nuclei, respectively (Fig. 7A). This indicates that the Nucl.eye.D pipeline tends to globally underestimate the HX of nuclei from the L/D set when compared to the manual segmentations (Fig. 2). This result reflects a globally high uncertainty for chromocenter prediction of the L/D set and may notably be linked to the differences in sample preparations protocols. However, a close overlap with the results obtained with the manual segmentation could be observed when defining a lower threshold for the chromocenter model (Fig. S2). Interestingly, despite the close segmentations identified for OU, TU and TUI pipelines, an influence of the training set can be observed (Fig. 6 and 7A). Indeed, RHF values obtained from manual segmentation, ICRAQ, and from the 3 Nucl.Eye.D pipelines vary (Fig. 7B). However, it can be noticed that manual segmentation performed by three different users correlates, showing that such an approach is accurate although time-consuming (Fig. 7B). In contrast, a higher variability is observed in between the 3 ICRAQ segmentations (Fig. 7B). The TUI tends to reproduce the mean RHF calculation observed for ICRAQ users (Fig. 7B). Importantly, the User3 ICRAQ segmentation correlates with the manual segmentations, suggesting that human decisions may have occurred (Fig. 7B).

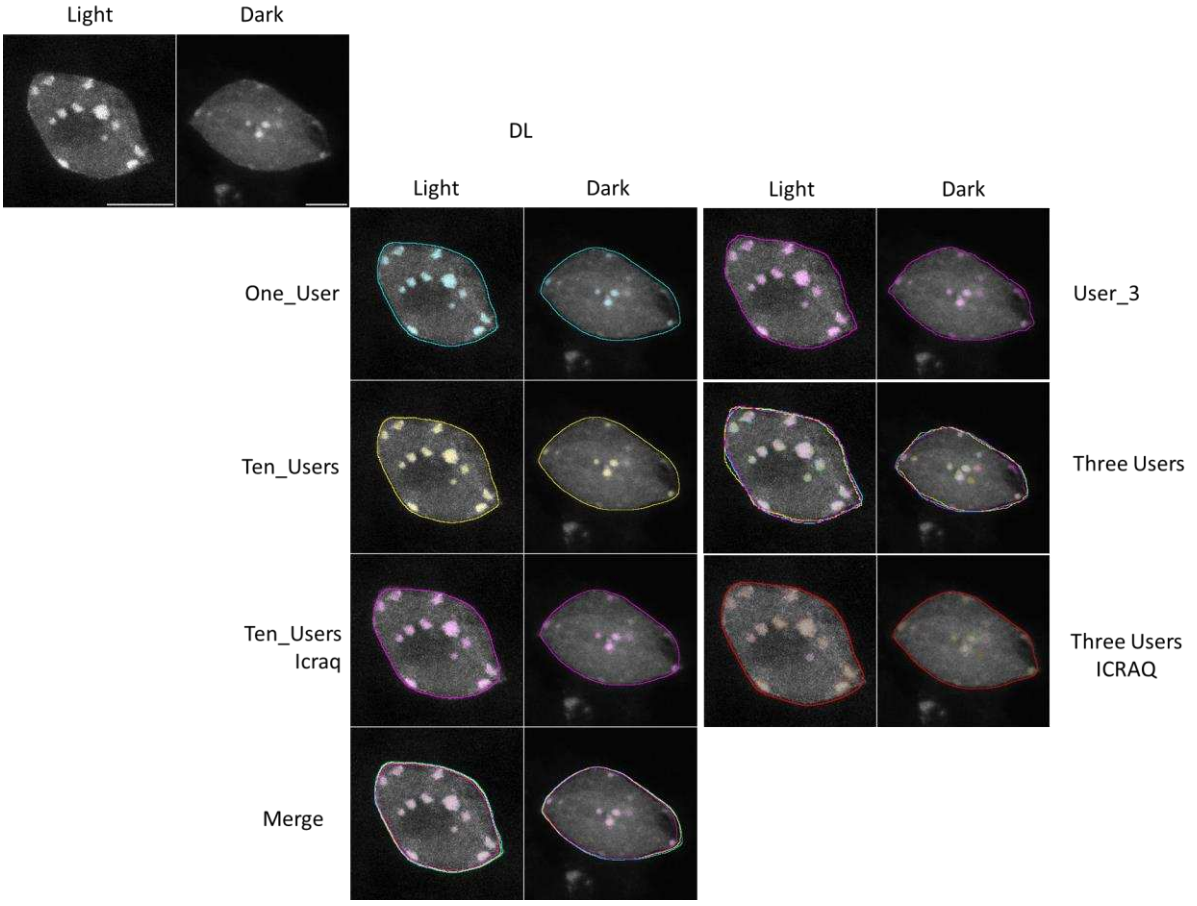

Figure 6: Segmentation of nuclei and chromocenters using the Nucl.Eye.D tool

Representative DAPI stained WT (Col-0) nuclei from Light/Dark set (top left) segmented by three different Nucl.Eye.D pipelines. The "One_User" pipeline was trained with an image set manually segmented by a single user. The "Ten_User" pipeline was trained with the same image set manually segmented by ten different users. The "Ten_User_ICRAQ" pipeline was trained with the same image set segmented by ten different users with the ICRAQ tool. Border of nucleus segmentation masks are shown as lines, and chromocenter masks as transparent color overlay. In comparison to "One_User" the segmentation of the same nuclei performed by User_3 who produced the training set for the "One_User" pipeline, was added. As a comparison to "Ten_User" the merge of manual segmentations from 3 users was added. Finally, as a comparison to "Ten_User_ICRAQ" the merge of ICRAQ segmentations from 3 users was added. Merged images show the overlap between masks, comparing the different pipelines. Scale bar = 5µm.

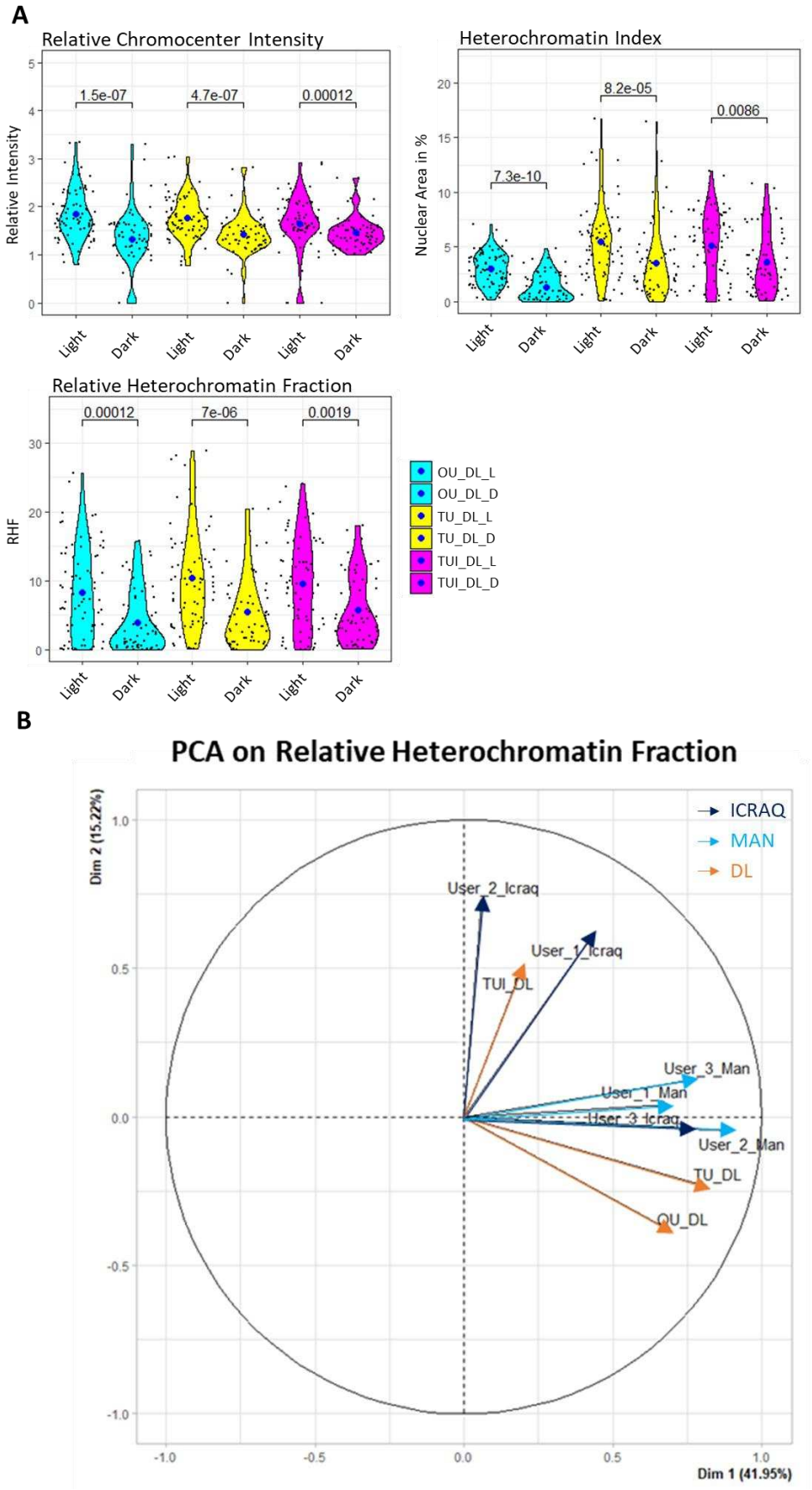

Figure 7: Comparison of heterochromatin features using Nucl.Eye.D segmentation pipelines

(A) Violin plots illustrating the distribution of relative chromocenter intensity, chromocenter index and relative heterochromatin fraction in a population of at least 50 nuclei per condition (all nuclei from Light/Dark Set).

OU: one user; TU: ten users; TUI: ten users ICRAQ. Each black dot represents the measure for one nucleus. The large dot shows the mean value. Exact p values are shown (Mann Whitney Wilcoxon test). **(B)** Circular correlation plots of RHF between different users and segmentation methods.

4.2.5. Application of the Nucl.Eye.D tool: analysis of the *ddm1* data set

In order to demonstrate the ability of the Nucl.Eye.D pipelines to accurately measure nuclear features, we used Decreased DNA Methylation I (*ddm1*) Arabidopsis plant exhibiting well-described alterations of heterochromatin structure (Soppe et al. 2002; Mathieu et al. 2003). For this, we used three different Nucl.Eye.D pipelines to automatically segment a data set of more than 150 WT (Col-0) and 150 *ddm1* Arabidopsis nuclei, prepared following the same procedure as the one used to produce the training images. As shown in Figure 8, the OU and TU pipeline presents a coherent segmentation of low contrasted nuclei and small atypical *ddm1* chromocenters. However, with a TH of 0.5, the TUI pipeline shows a weakness for the detection of nuclear borders, especially in low contrasted images (Fig. 8). This behavior is probably linked to the fact that ICRAQ users tend to apply the basic thresholding mechanism for nuclear detection (Fig. 2). This observation perfectly summarizes (i) the necessity of building a bias-free training set and (ii) the effort needed to provide good quality test sets.

However, for the RCI, HX, and RHF measures, despite the observed weakness of nuclear detection, the TUI, as well as the TU and OU pipelines, allow detecting the well-described chromocenter morphology of the *ddm1* mutant (Soppe et al. 2002; Mathieu et al. 2003) (Fig. 9). Indeed, the mean RHF in WT (Col-0) plants ranges between (12.5 and 14) as usually described in the literature (Soppe et al. 2002; Snoek et al. 2017), whereas *ddm1* nuclei exhibit an expected mean RHF of 5 to 8 (Soppe et al. 2002) (Fig. 9). The analysis of this test set demonstrates the convincing performance of the Nucl.Eye.D pipeline for fast Arabidopsis nuclei and chromocenter segmentation to identify significant differences in nucleus morphologies and phenotypes. Importantly, the Nucl.Eye.D pipeline could be trained with a new set of images specific of particular mutant plants or biological processes, providing an added value to build a highly accurate automated segmentation method. In addition, to the detection of DAPI stained structures, Nucl.Eye.D tool offers the possibility to perform the segmentation of any sub-nuclear structures revealed by FISH- or Immuno-staining (*i.e.,* histone PTMs).

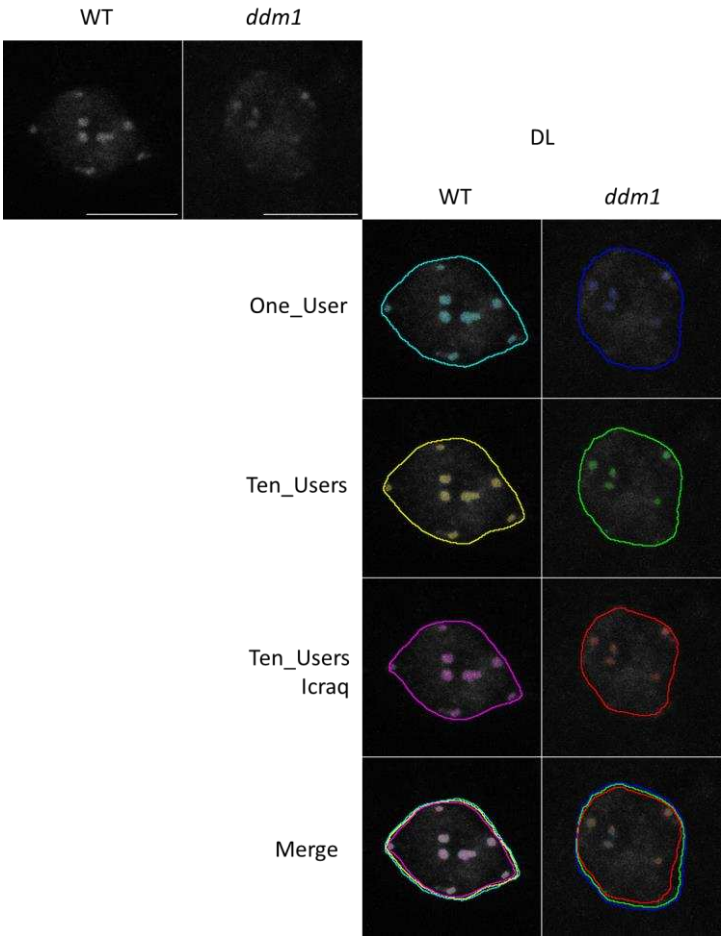

Figure 8: Segmentation of *ddm1* Nuclei and Chromocenters using the Nucl.Eye.D tool

Representative DAPI stained WT (col-0) and *ddm1* nuclei extracted from leaves (top left) segmented by three different Nucl.Eye.D pipelines. The "One_User" pipeline was trained with an image set manually segmented by a single user. The "Ten_User" pipeline was trained with the same image set manually segmented by ten different users. The "Ten_User_Icraq" pipeline was trained with the same image set segmented by ten users with the ICRAQ tool. Border of nucleus segmentation masks are shown as lines, and chromocenter masks as transparent color overlay. Merged images show the overlap between masks, comparing the different pipelines. Scale bar = 5µm.

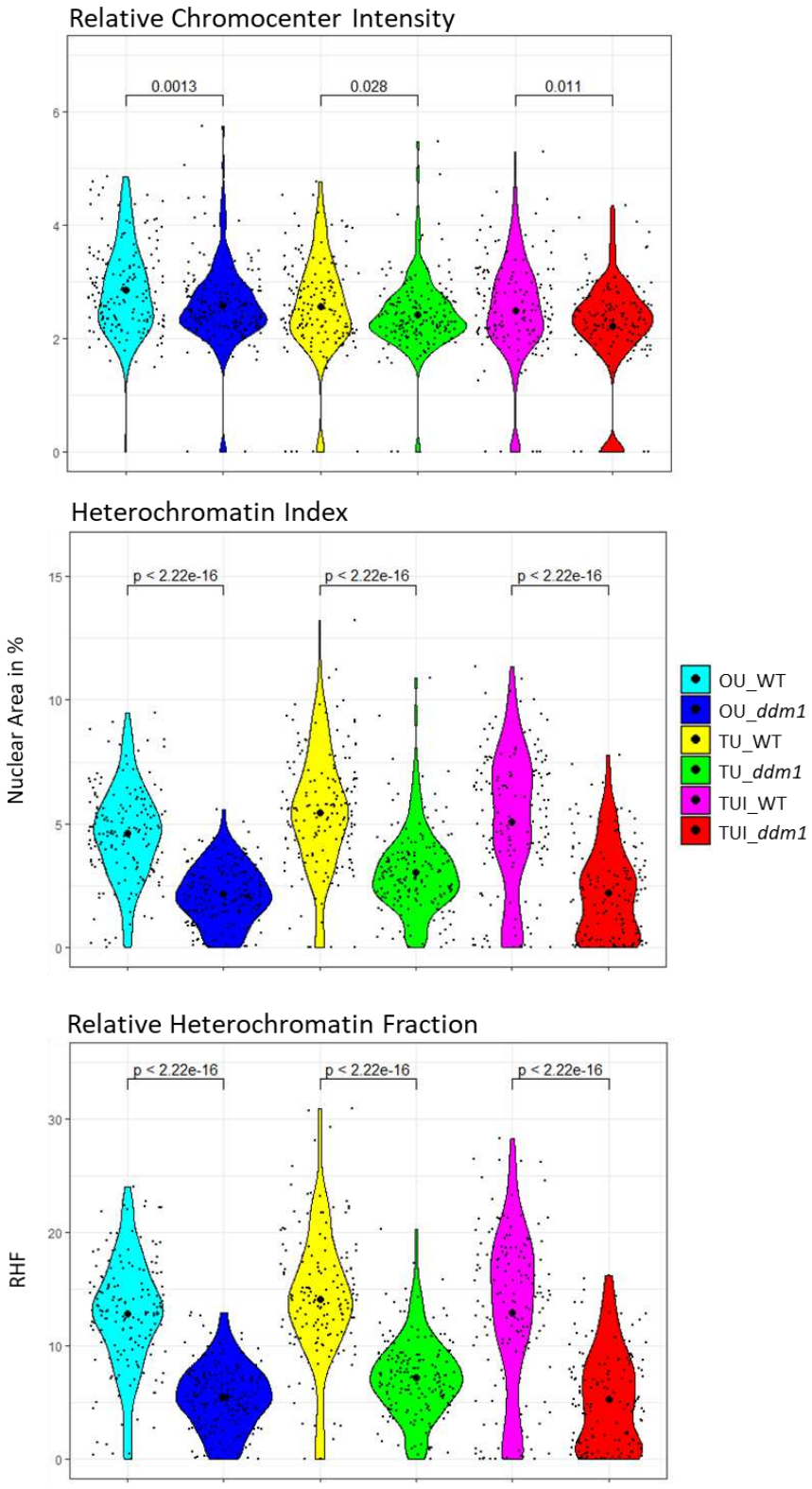

Figure 9: Comparison of heterochromatin features between WT and *ddm1* plants

(A) Violin plots illustrating the distribution of Relative chromocenter Intensity, Chromocenter Index, and Relative Heterochromatin Fraction in a population of at least 150 nuclei per genotype. OU: one user; TU: ten users; TUI: ten users ICRAQ. Each black dot represents the measure for one nucleus. The large dot shows the mean value. Exact p values are shown (Mann Whitney Wilcoxon test).

4.3. Conclusions

Our work describes user-linked issues in manual nuclei-chromocenter detection and the need to improve tools for accurate segmentation. A semi-automatic plug-in, ICRAQ, and a DL-based approach, Nucl.Eye.D, which reduced this variability, have been developed and highlight the important steps to consider for the segmentation task. Although the Nucl.Eye.D tool was trained with a relatively small data set (around 300 images); it provides convincing segmentations, even on images produced from different protocols witnessing its adaptability. Nucl.Eye.D as DL-based approach for segmentation of nuclear and subnuclear structures provide an interesting step-froward in the field of plant science cytogenetics, and complete the existing range of DL-based tools already existing for phenotypic analysis in roots (Yasrab et al. 2019), leaves (Atanbori et al. 2020) and cells (Li et al. 2022). Our work assists nuclei and subnuclear structure segmentation and encourages biologists to consider DL-based methods in their experimental approaches.

Importantly, it must be kept in mind that any algorithm- and DL-based tool is far from being free of human bias. Obviously, bias can be introduced during the training process due to image choice and data labeling but additionally, the “programmer”-based bias starts to be investigated as a potential explanation for data-set specific performance (Sun et al. 2020; Cazes et al. 2021).

Conclusively, according to our thoughts, the growing trend of automatizing image segmentation and analysis, should be accompanied by substantial efforts in verifying the efficiency of these segmentation methods (Robinson et al. 2019).

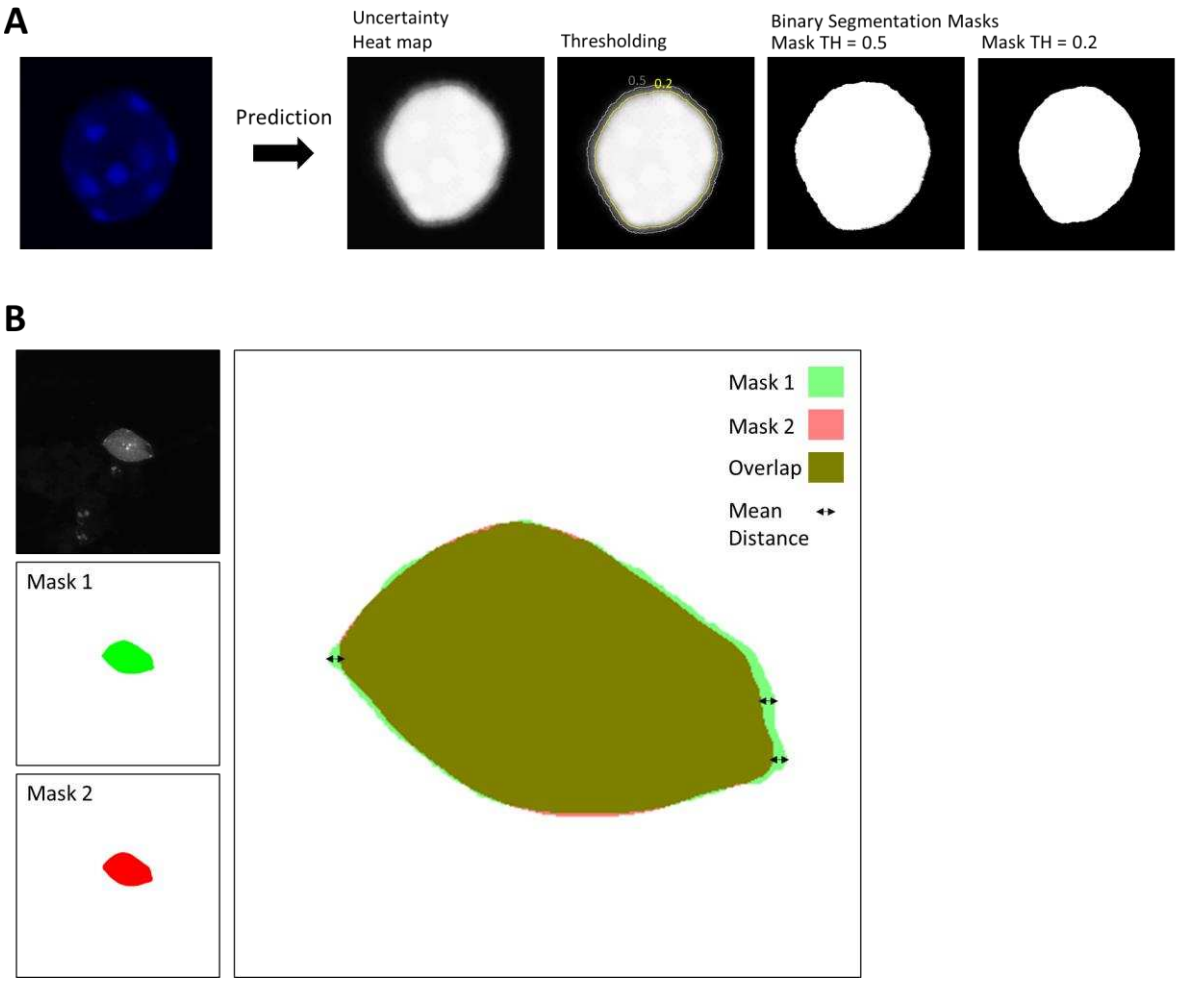

Supplemental figure 1: From prediction to the comparison of binary segmentation masks

(A) Graphical representation of the predicted uncertainty heat map, Thresholding process to obtain binary segmentation masks. **(B)** Graphical representation of overlap and mean distance between binary segmentation masks.

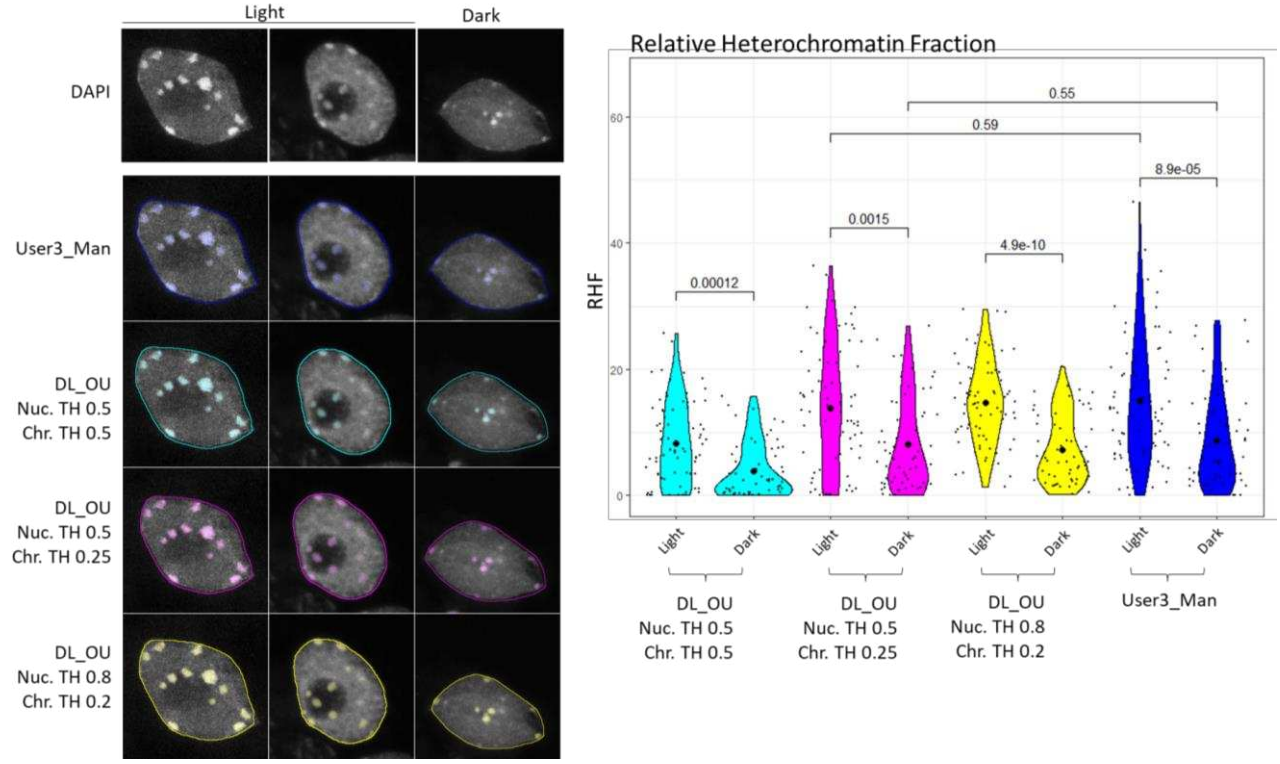

Supplemental figure 2: Segmentation of nuclei and chromocenters using different TH in the Nucl.Eye.D tool

Left panel: representative DAPI stained WT (Col-0) nuclei from Light/Dark set segmented by Nucl.Eye.D. The "One_User" (DL_OU) pipeline was trained with an image set manually segmented by User3. The manual segmentation of User3 was consequently added as a comparison. The prediction was performed using three different Threshold (TH) Settings. The first segmentation (cyan) was performed with a TH of 0.5 for nucleus (Nuc.) and 0.5 for chromocenter (Chr.) The second segmentation (magenta) with a TH for Nuc. 0.5 and for Chr. 0.25. The third segmentation (yellow) with a TH for Nuc. = 0.8 and for Chr. = 0.2. Border of nucleus segmentation masks are shown as lines, and chromocenter masks as transparent color overlay. Right panel: violin plots of the relative heterochromatin fraction in a population of at least 50 nuclei per condition (all nuclei from Light/Dark Set) depending on the segmentation tool used. Each black dot represents the measure for one nucleus. The large dot shows the mean value. Exact p values are shown (Mann Whitney Wilcoxon test).

4.4. Materials & Methods

4.4.1. Plant material and growth conditions

Seeds from wild-type (Col-0) Arabidopsis plants are surface-sterilized, plated on filter papers lying on MS medium supplemented with 0.9% agar, and exposed to either a 16-/8-h (23/19 °C) white light/dark photoperiod or constant-dark conditions (wrapped in 3 layers of aluminum foil). White light is generated by fluorescent bulbs (100 µmol·m−2·s−1). Seedlings are harvested under light conditions or under safe green light for dark condition (Bourbousse et al. 2015). Arabidopsis Col-0, *ddm1-2* (Jeddeloh et al. 1999) plants are grown *in vitro* on solid GM medium [MS salts (Duchefa), 1% sucrose, 0.8% Agar-agar ultrapure (Merck), pH 5.8] in a culture chamber under a 16 h light (light intensity ∼150 µmol m^{-2} s^{-1}; 21°C) and 8h dark (19°C) photoperiod.

4.4.2. Tissue fixation and nuclei preparation

Leaves 3 and 4 from 21-days-old Col-0 and *ddm1* plants are washed four times (4°C), at least 5 min, in fixative solution (3:1 ethanol/acetic acid; vol/vol). Leaves nuclei are extracted by chopping fixed tissue in LB-01 Buffer (15 mM Tris-HCl pH 7.5, 2 mM EDTA, 0.5 mM spermine, 80 mM KCl, 29 mM NaCl, 0,1% Triton X-100) with a razor blade. The nuclei-containing solution is filtered through 20 µm nylon mesh and centrifugated 1 min (1000g). The supernatant is spread on poly-lysine slides (thermofisher 631-1349) and post-fixation is performed using a 1:1 acetone/methanol (vol/vol) solution for 2 min. Slides are washed with Phosphate Buffer Saline x1 and incubated for 1h at room temperature in permeabilization buffer (8% BSA, 0.01% Triton-X in Phosphate Buffer Saline x1). Finally, 15 µl of Fluoromount-G (Southern Biotechnology CAT NO 0100–01) with 2 µg/ml 4',6-Diamidino-2-phenylindol (DAPI) are added as a mounting solution before deposing the coverslip. Image acquisition is performed on a Zeiss LSM 780 confocal microscope using a 64X oil immersion objective. 405 nm laser excitation wavelength is used for DAPI. Emission is measured between 410 nm and 585 nm wavelength each image acquisition consists of a Z-stack capture. For training sets different gain and slice distances are used on purpose to diversify the set. All images are available at: https://tinyurl.com/NucleyeSD

4.4.3. Tissue fixation and nuclei preparation of dark/light test set

Seedlings are fixed in 4% formaldehyde for 3h under light or dark condition and treated with a solution containing 0.5% cellulose Onozuka R10 (Yakult), 0.25% macerozyme R10 (Yakult), and 0.1% Triton X-100 for 1h and 30 min. Cotyledons are isolated and squashed on a glass slide, flash-frozen in liquid nitrogen, and incubated with PEMSB [50 mM Pipes pH 7.3, 5 mM EGTA pH 7.1, 5 mM MgSO4, 0.05% saponin, 5% (wt/vol) BSA] before being mounted with Vectashield (Vector Laboratories) supplemented with 2 µg/mL−1 DAPI (4',6'-diamidino-2-phenylindole). Images are acquired using a confocal laser-scanning microscope (SP5, Leica). All images are available at: https://tinyurl.com/NucleyeSD

4.4.4. Mask preparation

Manual segmentation of nuclei and chromocenters is performed on ImageJ using the freehand tool and converted into binary masks. Image names are randomized before annotation. For training sets #1 the segmentation was performed by a single user. For the training sets #2, ten different users segmented 10% of the total set of images. For training sets #3, ten different users segmented 10% of the total set using the ICRAQ tool.

4.4.5. iCRAQ analysis

iCRAQ is a tool written in ImageJ macro language which relies on the FeatureJ (http://imagescience.org/meijering/software/featurej/) and Interactive H_Watershed (https://imagej.net/plugins/interactive-watershed) plugins; here we use a version adapted from https://github.com/gschivre/iCRAQ to annotate images. Nuclei are detected via global thresholding of the median filtered z-projection (either standard deviation or maximum intensity) of the stack, and the corresponding regions are saved as ImageJ regions of interest (ROIs). Incorrectly detected nucleus ROIs are suppressed manually. Likewise, missed nuclei are added manually. The input stack is cropped around each nucleus ROI. For chromocenter segmentation, the largest 3D structure tensor eigenvalue is calculated using the FeatureJ plugin, and its z-projection serves as an input for the interactive H-watershed plugin.

Image regions labeled as chromocenters are also saved as ROIs. Chromocenter ROIs can also be manually added or removed. Finally, binary masks of the nucleus and chromocenter ROIs are used to produce an annotated image with three gray levels: 0 for the background, 128 for the nucleus, and 255 for the chromocenters.

4.4.6. Nucl.Eye.D

Nucl.Eye.D script is written in python using Keras and TensorFlow libraries for Neuronal network designing. U-net networks are built according to the original paper from Olaf Ronneberger (Ronneberger et al. 2015). Model training was performed using Google Colab with access to Tesla P100 - 16 Go HBM2 GPU (Bisong 2019). The full script is available on https://tinyurl.com/NuclEyeD, user guide and trained models are available on https://tinyurl.com/NucleyeSD.

4.4.7. Masks comparisons

The comparison between masks from the same image was performed using a self-developed ImageJ plug-in “compare2masks” (available at https://tinyurl.com/JotoBe). The mean distance was calculated by measuring the minimal distances of each point of the perimeter of a first object to the closest point of the perimeter from the same object on the second mask. The lower the mean distance, the closer the compared objects' perimeters.

4.4.8. Data display and statistics

Violin plots, Principal Component Analysis, and statistics (Mann Whitney Wilcoxon test) are done with RStudio, using the ggPlot2 and FactoMineR Libraries (http://www.rstudio.com/).

4.5. References

Alzubaidi L, Zhang J, Humaidi AJ, Al-Dujaili A, Duan Y, Al-Shamma O, Santamaría J, Fadhel MA, Al-Amidie M, Farhan L (2021) Review of deep learning: concepts, CNN architectures, challenges, applications, future directions. J Big Data 8:53. https://doi.org/10.1186/s40537-021-00444-8

Atanbori J, French AP, Pridmore TP (2020) Towards infield, live plant phenotyping using a reduced-parameter CNN. Mach Vis Appl 31:2. https://doi.org/10.1007/s00138-019-01051-7

Benoit M, Layat E, Tourmente S, Probst AV (2013) Heterochromatin dynamics during developmental transitions in Arabidopsis - a focus on ribosomal DNA loci. Gene 526:39–45. https://doi.org/10.1016/j.gene.2013.01.060

Birk UJ (2019) Super-Resolution Microscopy of Chromatin. Genes (Basel) 10:493. https://doi.org/10.3390/genes10070493

Bisong E (2019) Google Colaboratory. In: Bisong E (ed) Building Machine Learning and Deep Learning Models on Google Cloud Platform: A Comprehensive Guide for Beginners. Apress, Berkeley, CA, pp 59–64

Bourbousse C, Mestiri I, Zabulon G, Bourge M, Formiggini F, Koini MA, Brown SC, Fransz P, Bowler C, Barneche F (2015) Light signaling controls nuclear architecture reorganization during seedling establishment. Proc Natl Acad Sci U S A 112:E2836-2844. https://doi.org/10.1073/pnas.1503512112

Cazes M, Franiatte N, Delmas A, André J-M, Rodier M, Kaadoud IC (2021) Evaluation of the sensitivity of cognitive biases in the design of artificial intelligence. 9

Colombo F, Norton EG, Cocucci E (2021) Microscopy approaches to study extracellular vesicles. Biochim Biophys Acta Gen Subj 1865:129752. https://doi.org/10.1016/j.bbagen.2020.129752

Dubos T, Poulet A, Gonthier-Gueret C, Mougeot G, Vanrobays E, Li Y, Tutois S, Pery E, Chausse F, Probst AV, Tatout C, Desset S (2020) Automated 3D bio-imaging analysis of nuclear organization by NucleusJ 2.0. Nucleus 11:315–329. https://doi.org/10.1080/19491034.2020.1845012

Godec P, Pančur M, Ilenič N, Čopar A, Stražar M, Erjavec A, Pretnar A, Demšar J, Starič A, Toplak M, Žagar L, Hartman J, Wang H, Bellazzi R, Petrovič U, Garagna S, Zuccotti M, Park D, Shaulsky G, Zupan B (2019) Democratized image analytics by visual programming through integration of deep models and small-scale machine learning. Nat Commun 10:4551. https://doi.org/10.1038/s41467-019-12397-x

Gómez-de-Mariscal E, García-López-de-Haro C, Ouyang W, Donati L, Lundberg E, Unser M, Muñoz-Barrutia A, Sage D (2021) DeepImageJ: A user-friendly environment to run deep learning models in ImageJ. Nat Methods 18:1192–1195. https://doi.org/10.1038/s41592-021-01262-9

Goto C, Hara-Nishimura I, Tamura K (2021) Regulation and Physiological Significance of the Nuclear Shape in Plants. Front Plant Sci 12:673905. https://doi.org/10.3389/fpls.2021.673905

Graindorge S, Cognat V, Johann to Berens P, Mutterer J, Molinier J (2019) Photodamage repair pathways contribute to the accurate maintenance of the DNA methylome landscape upon UV exposure. PLoS Genet 15:e1008476. https://doi.org/10.1371/journal.pgen.1008476

Hunt GJ, Dane MA, Korkola JE, Heiser LM, Gagnon-Bartsch JA (2020) Automatic Transformation and Integration to Improve Visualization and Discovery of Latent Effects in Imaging Data. J Comput Graph Stat 29:929–941. https://doi.org/10.1080/10618600.2020.1741379

Iannuccelli E, Mompart F, Gellin J, Lahbib-Mansais Y, Yerle M, Boudier T (2010) NEMO: a tool for analyzing gene and chromosome territory distributions from 3D-FISH experiments. Bioinformatics 26:696–697. https://doi.org/10.1093/bioinformatics/btq013

Ithapu VK, Ravi SN, Singh V (2017) On architectural choices in deep learning: From network structure to gradient convergence and parameter estimation. arXiv:170208670 [cs, math, stat]

Jeddeloh JA, Stokes TL, Richards EJ (1999) Maintenance of genomic methylation requires a SWI2/SNF2-like protein. Nat Genet 22:94–97. https://doi.org/10.1038/8803

Kalyanikrishna null, Mikulski P, Schubert D (2020) Measurement of Arabidopsis thaliana Nuclear Size and Shape. Methods Mol Biol 2093:107–113. https://doi.org/10.1007/978-1-0716-0179-2_8

Keuenhof KS, Larsson Berglund L, Malmgren Hill S, Schneider KL, Widlund PO, Nyström T, Höög JL (2022) Large organellar changes occur during mild heat shock in yeast. J Cell Sci 135:jcs258325. https://doi.org/10.1242/jcs.258325

Kliegr T, Bahník Š, Fürnkranz J (2021) A review of possible effects of cognitive biases on interpretation of rule-based machine learning models. Artificial Intelligence 295:103458. https://doi.org/10.1016/j.artint.2021.103458

Landini G, Randell DA, Fouad S, Galton A (2017) Automatic thresholding from the gradients of region boundaries. J Microsc 265:185–195. https://doi.org/10.1111/jmi.12474

Li J, Peng J, Jiang X, Rea AC, Peng J, Hu J (2021) DeepLearnMOR: a deep-learning framework for fluorescence image-based classification of organelle morphology. Plant Physiol 186:1786–1799. https://doi.org/10.1093/plphys/kiab223

Li S, Li L, Fan W, Ma S, Zhang C, Kim JC, Wang K, Russinova E, Zhu Y, Zhou Y (2022) LeafNet: A Tool for Segmenting and Quantifying Stomata and Pavement Cells. Plant Cell koac021. https://doi.org/10.1093/plcell/koac021

Mathieu O, Jasencakova Z, Vaillant I, Gendrel A-V, Colot V, Schubert I, Tourmente S (2003) Changes in 5S rDNA chromatin organization and transcription during heterochromatin establishment in Arabidopsis. Plant Cell 15:2929–2939. https://doi.org/10.1105/tpc.017467

Paullada A, Raji ID, Bender EM, Denton E, Hanna A (2021) Data and its (dis)contents: A survey of dataset development and use in machine learning research. Patterns (N Y) 2:100336. https://doi.org/10.1016/j.patter.2021.100336

Pecinka A, Chevalier C, Colas I, Kalantidis K, Varotto S, Krugman T, Michailidis C, Vallés M-P, Muñoz A, Pradillo M (2020) Chromatin dynamics during interphase and cell division: similarities and differences between model and crop plants. J Exp Bot 71:5205–5222. https://doi.org/10.1093/jxb/erz457

Pecinka A, Dinh HQ, Baubec T, Rosa M, Lettner N, Scheid OM (2010) Epigenetic Regulation of Repetitive Elements Is Attenuated by Prolonged Heat Stress in Arabidopsis. The Plant Cell 22:3118–3129. https://doi.org/10.1105/tpc.110.078493

Renard F, Guedria S, Palma ND, Vuillerme N (2020) Variability and reproducibility in deep learning for medical image segmentation. Sci Rep 10:13724. https://doi.org/10.1038/s41598-020-69920-0

Robinson R, Valindria VV, Bai W, Oktay O, Kainz B, Suzuki H, Sanghvi MM, Aung N, Paiva JM, Zemrak F, Fung K, Lukaschuk E, Lee AM, Carapella V, Kim YJ, Piechnik SK, Neubauer S, Petersen SE, Page C, Matthews PM, Rueckert D, Glocker B (2019) Automated quality control in image segmentation: application to the UK Biobank cardiovascular magnetic resonance imaging study. J Cardiovasc Magn Reson 21:18. https://doi.org/10.1186/s12968-019-0523-x

Ronneberger O, Fischer P, Brox T (2015) U-Net: Convolutional Networks for Biomedical Image Segmentation. arXiv:150504597 [cs]

Schroeder AB, Dobson ETA, Rueden CT, Tomancak P, Jug F, Eliceiri KW (2021) The ImageJ ecosystem: Open-source software for image visualization, processing, and analysis. Protein Sci 30:234–249. https://doi.org/10.1002/pro.3993

Seeland M, Rzanny M, Boho D, Wäldchen J, Mäder P (2019) Image-based classification of plant genus and family for trained and untrained plant species. BMC Bioinformatics 20:4. https://doi.org/10.1186/s12859-018-2474-x

Sensakovic WF, Starkey A, Roberts R, Straus C, Caligiuri P, Kocherginsky M, Armato SG (2010) The influence of initial outlines on manual segmentation. Med Phys 37:2153–2158. https://doi.org/10.1118/1.3392287

Shepley A, Falzon G, Lawson C, Meek P, Kwan P (2021) U-Infuse: Democratization of Customizable Deep Learning for Object Detection. Sensors 21:2611. https://doi.org/10.3390/s21082611

Simon L, Voisin M, Tatout C, Probst AV (2015) Structure and Function of Centromeric and Pericentromeric Heterochromatin in Arabidopsis thaliana. Front Plant Sci 6. https://doi.org/10.3389/fpls.2015.01049

Snoek BL, Pavlova P, Tessadori F, Peeters AJM, Bourbousse C, Barneche F, de Jong H, Fransz PF, van Zanten M (2017) Genetic Dissection of Morphometric Traits Reveals That Phytochrome B Affects Nucleus Size and Heterochromatin Organization in Arabidopsis thaliana. G3 (Bethesda) 7:2519–2531. https://doi.org/10.1534/g3.117.043539

Song T-A, Yang F, Dutta J (2021) Noise2Void: unsupervised denoising of PET images. Phys Med Biol 66. https://doi.org/10.1088/1361-6560/ac30a0

Soppe WJJ, Jasencakova Z, Houben A, Kakutani T, Meister A, Huang MS, Jacobsen SE, Schubert I, Fransz PF (2002) DNA methylation controls histone H3 lysine 9 methylation and heterochromatin assembly in Arabidopsis. EMBO J 21:6549–6559. https://doi.org/10.1093/emboj/cdf657

Steblyanko Y, Rajendraprasad G, Osswald M, Eibes S, Jacome A, Geley S, Pereira AJ, Maiato H, Barisic M (2020) Microtubule poleward flux in human cells is driven by the coordinated action of four kinesins. EMBO J 39:e105432. https://doi.org/10.15252/embj.2020105432

Sun W, Nasraoui O, Shafto P (2020) Evolution and impact of bias in human and machine learning algorithm interaction. PLoS One 15:e0235502. https://doi.org/10.1371/journal.pone.0235502

Tatout C, Mougeot G, Parry G, Baroux C, Pradillo M, Evans D (2022) The INDEPTH (Impact of Nuclear Domains On Gene Expression and Plant Traits) Academy - a community resource for plant science. J Exp Bot erac005. https://doi.org/10.1093/jxb/erac005

Van Treeck B, Parker R (2019) Principles of Stress Granules Revealed by Imaging Approaches. Cold Spring Harb Perspect Biol 11:a033068. https://doi.org/10.1101/cshperspect.a033068

Vongs A, Kakutani T, Martienssen RA, Richards EJ (1993) Arabidopsis thaliana DNA methylation mutants. Science 260:1926–1928. https://doi.org/10.1126/science.8316832

Weigel AV, Chang C-L, Shtengel G, Xu CS, Hoffman DP, Freeman M, Iyer N, Aaron J, Khuon S, Bogovic J, Qiu W, Hess HF, Lippincott-Schwartz J (2021) ER-to-Golgi protein delivery through an interwoven, tubular network extending from ER. Cell 184:2412-2429.e16. https://doi.org/10.1016/j.cell.2021.03.035

Yasrab R, Atkinson JA, Wells DM, French AP, Pridmore TP, Pound MP (2019) RootNav 2.0: Deep learning for automatic navigation of complex plant root architectures. Gigascience 8:giz123. https://doi.org/10.1093/gigascience/giz123

Zhang J, Li C, Rahaman MM, Yao Y, Ma P, Zhang J, Zhao X, Jiang T, Grzegorzek M (2021) A comprehensive review of image analysis methods for microorganism counting: from classical image processing to deep learning approaches. Artif Intell Rev 1–70. https://doi.org/10.1007/s10462-021-10082-4

Zhou W, Yang Y, Yu C, Liu J, Duan X, Weng Z, Chen D, Liang Q, Fang Q, Zhou J, Ju H, Luo Z, Guo W, Ma X, Xie X, Wang R, Zhou L (2021) Ensembled deep learning model outperforms human experts in diagnosing biliary atresia from sonographic gallbladder images. Nat Commun 12:1259. https://doi.org/10.1038/s41467-021-21466-z

5. Chapter III - DDB2 and JMJ27 contribute to H3K9me2 dynamic at chromocenters in response to UV-C exposure

5.1. Introduction

We identified that ionizing (protons) and non-ionizing (UVs) irradiations alter both genomic and epigenomic integrities (Chapter I). Indeed, UV-C and protons that generate different types of DNA lesions affect the structure of constitutive heterochromatin 24h upon exposure. As shown for UV-C, these changes in constitutive heterochromatin shape depend on DNA repair processes and are accompanied by alterations of the DNA methylation landscape (Graindorge et al. 2019). The analysis of early time points upon UV-C exposure (*i.e.,* 2h), showed that the chromocenter shape undergoes an important restructuration, which likely includes modifications of several epigenetic marks aside from DNA methylation. Additionally, this phenomenon indicates that the late changes in constitutive heterochromatin structure (24h) might result from the precocious reshaping process.

In the last decades, many studies reported evidence for multiple interplays between DNA repair pathways and epigenome landscape (Agarwal and Miller 2016; Sharma and Hendzel 2019). This includes the epigenetically related DNA damageability (Johann to Berens and Molinier 2020), the specific damage repair processes (Conconi et al. 2002; Johann to Berens and Molinier 2020), and the role of these interconnected mechanisms in the maintenance and plasticity of the epigenome (Graindorge et al. 2019).

UV-C irradiation induces predominantly CPDs and 6,4-PPs (Rastogi et al. 2010; Johann to Berens and Molinier 2020). The localization of both types of photolesions seems partially influenced by the epigenetic context (Johann to Berens and Molinier 2020)(Chapter I). Indeed, 5mC within cytosine-containing di-pyrimidines (CT, TC and CC) (Rochette et al. 2009; Banyasz et al. 2016) and nucleosome binding sequences are more prone to form photolesions (Gale et al. 1987; Gale and Smerdon 1990). In addition, microscopical approaches highlighted an enrichment of photolesions in chromocenter regions, containing high 5mC levels and specific histones PTMs (Chapter I).

Therefore, constitutive heterochromatin appears to be a showcase to analyze DNA repair and epigenetic remodeling upon lesions formation and processing.
The maintenance of (epi)genome integrity relies on the efficient recognition of the DNA damage, on the accurate re-establishment of both nucleotide and epigenetic marks identity. Interestingly, the epigenetic context of the damaged genomic regions would define by which repair pathways the lesions would be processed (Johann to Berens and Molinier 2020). Indeed, the Transcription Coupled Repair (TCR) pathway relies on the damage recognition by the RNA-POL II and thus mainly excises lesions in regions with an epigenetic landscape allowing transcription (Al Khateeb et al. 2019). The nucleosome rich, heterochromatic regions, in turn, are predominantly repaired by the Global Genome Repair (GGR) pathway involving DDB2 (Fei et al. 2011; Johann to Berens and Molinier 2020), and by the direct photoreactivation repair (DR) pathway, involving the 2 photolyases PHR1 and UVR3 (Ahmad et al. 1997; Nakajima et al. 1998; Guintini et al. 2015). The exact mechanisms by which both repair pathways process photodamaged DNA sequences wrapped around nucleosomes remain speculative and are controversially discussed (Duan and Smerdon 2010; Hauer and Gasser 2017; Matsumoto et al. 2019). *In vitro* experiments described how nucleosome hinders the DNA repair by photolyases and NER factors (Schieferstein and Thoma 1998; Liu 2015). Interestingly, Cryo-Electron Microscopy approaches demonstrated how DDB2 recognizes photolesions at loci wrapped around nucleosomes, suggesting that only slight shifts may be required for the first damage recognition step (Matsumoto et al. 2019).

According to several reports and working models, the DNA repair in compacted heterochromatic regions acts in concert with mechanisms involved in active nucleosome sliding (Dinant et al. 2012; Matsumoto et al. 2019; Nodelman and Bowman 2021) and in histones/nucleosome depletion (Chakraborty et al. 2021). Importantly, the recognition step of the GGR, involving DDB2, occurs in two temporally controlled steps: one precocious, in nucleosome free regions and the other, later, in nucleosome containing DNA sequences (Fei et al. 2011). Once bound to the DNA damage, DDB2 is targeted by the CULLIN4 E3 ubiquitin ligase complex (Cavadini et al. 2016) to be (i) released from the DNA and (ii) degraded (Luijsterburg et al. 2007). The DNA repair protein XPC (*Xeroderma pigmentosum* complementation group C) and histones are also targeted by the CULLIN4 E3 ubiquitin ligase complex (Sugasawa et al. 2005; Wang et al. 2006).

Interestingly, this mechanism has been demonstrated to occur preferentially in the nucleosome-free DDB2-pool, whereas DDB2 dynamics in core nucleosomes is ubiquitin-independent (Fei et al. 2011). Additionally, the human UV-DDB complex allows the recruitment of chromatin remodelers (Zhao et al. 2009; Jiang et al. 2010; Pines et al. 2012) and histone writer such as: the histone H3K4 methyltransferase ASH1L (*A*bsent, *S*mall, or *H*omeotic discs *1*-*L*ike) (Balbo Pogliano et al. 2017) and the H3K79 methyltransferase DOT1L (Disrupter of telomere silencing protein 1 Like) (Zhu et al. 2018; Kari et al. 2019). In Drosophila, the NER pathway was shown to be increased by H3K9me3 demethylation of heterochromatic regions depending on the Lysine-9 demethylase 4B (KDM4B) (Palomera-Sanchez et al. 2010). This histone demethylation most likely enhances the NER efficiency by chromatin remodeling/relaxation (Shu et al. 2012). Finally, the role of DDB2 in heterochromatin decompaction upon UV-C was deeply investigated in human cell lines, revealing displacement of histone H1, incorporation of new core histones, and strict maintenance of histone H3K9me3 upon UV-C irradiation (Fortuny et al. 2021).

In contrast to DDB2, the binding of photolyases to nucleosome-DNA complexed structures remains elusive. Consequently, its relevance for photolesion repair in heterochromatic regions with dense nucleosome packaging could be addressed. As shown in yeast strains overexpressing photolyases, all damages even in dense chromatin are finally cleared (Bucceri et al. 2006). Thus, due to their mono-enzymatic mode of action (Zhang et al. 2017), photolyases may efficiently participate in the DNA repair within heterochromatin assisted by nucleosome sliding/shifting mechanisms (Guintini et al. 2015). Alternatively, it could be assumed that photolyases can take advantage of the relaxed microenvironment formed by DDB2 during the recognition step of the GGR to revert photolesions.

In *Arabidopsis thaliana,* the constitutive heterochromatin is mainly characterized by two repressive histone PTMs, H3K27me1, and H3K9me2, as well as by high DNA methylation (Roudier et al. 2011). The lack of one of these marks leads to a decompaction of the chromocenter regions (Jacob et al. 2009; Shu et al. 2012). Thus, it could be assumed that the decreased Chromocenter Occupancy observed 2h upon UV-C exposure (Chapter I) might reflect changes in the amount of H3K27me1 and/or H3K9me2 and/or 5mC.

In most eukaryotes, the methylation of H3K27 depends on different E(z)/PRC2 (Polycomb Repressive Complex 2). In Arabidopsis, only H3K27me2 and H3K27me3 depend on PRC2 complex activity (Jiao and Liu 2015), whereas H3K27me1 was shown to mainly depend on the SET-domain histone methyltransferase trithorax-related protein 5 and 6 (ATXR5 / ATXR6), independently of the DNA methylation status, but in a replication-dependent manner (Jacob et al. 2009; Jacob et al. 2014; Ma et al. 2018). Although it was reported that mutations of ATXR5 and ATXR6 induce genomic instability as a consequence of TE reactivation (Potok et al. 2022), no link has been established with photodamage repair.

Whereas in other organisms, constitutive heterochromatin formation goes ahead with H3K9me3 deposition (Burton et al. 2020; Wei et al. 2021), in Arabidopsis, heterochromatin H3K9 is predominantly di-methylated (H3K9m2) (Xu and Jiang 2020). Arabidopsis genome encodes 15 potential H3K9, SET-domain containing methyltransferases, homologous of the Su(Var)3-9 Suppressor of variegation 3-9 proteins (Su(Var)3-9) from Drosophila (Baumbusch et al. 2001). However, the H3K9 di-methylation mainly depends on SUVH4 (Suppressor of variegation 3-9 homolog protein 4 hereafter also called KRYPTONITE: KYP) and to some extent on SUVH5 and SUVH6 (Jackson et al. 2002; Ebbs and Bender 2006; Li et al. 2018). Interestingly, in contrast to H3K27me1, H3K9m2 correlates with 5mC due to the affinity of the SET and RING-associated (SRA) domain of SUVH4/5/6 to methylated DNA (Stroud et al. 2014; Li et al. 2018; Xu and Jiang 2020). Respectively, H3K9me2 enhances DNA methylation by several pathways including CMT2/3 (Chromomethylases 2 and 3), ADCP1 (AGENET DOMAIN (AGD)-CONTAINING P1) and SHH1 (DNA TRANSCRIPTION FACTOR 1/SAWADEE HOMEODOMAIN HOMOLOG 1)/RdDM (RNA directed DNA methylation) (Law et al. 2013; Stroud et al. 2014; Zhang et al. 2018). H3K9me2 establishment was also shown to alternatively occur in a DNA methylation-independent manner through the activity of the histone methyltransferases SUVR5 and SUVR4 (Veiseth et al. 2011; Caro et al. 2012).

As counterpart, regulation of H3K9me2 content is mediated by specific demethylases. Arabidopsis carries 3 H3K9me2 demethylases with Jumonji (JMJ) C domain-containing: JMJ29, JMJ25, and JMJ27 (Fan et al. 2012; Dutta et al. 2017; Hung et al. 2020). Whereas JMJ29 was recently described as a regulator of trichome development, JMJ25, also called IBM1 (*INCREASE IN BONSAI METHYLATION 1),* was the first H3K9me2 demethylase studied.

IBM1 was shown to prevent heterochromatinization of particular genic regions (Saze et al. 2008; Miura et al. 2009), to regulate Arabidopsis immunity (Chan and Zimmerli 2019) and RdDM (Fan et al. 2012). JMJ27 was reported to coordinate defense against Pseudomonas, to control flowering time (Dutta et al. 2017), and, more recently, to respond to drought stress (Wang et al. 2021b).

Despite the increasing amounts of studies related to Arabidopsis histone methylases/demethylases, the interplays between factors involved in H3K27me1/H3K9me2 homeostasis and DNA repair within constitutive heterochromatin is poorly documented.

To address this question, we investigated:

- Whether UV-C irradiation induces heterochromatin dynamics
- Whether interplays between photodamage repair and H3K27me1-H3K9me2 homeostasis exist
- Which factors act in this process.

Through cytogenetic, genetic, and biochemical approaches, we aimed at identifying the underlying molecular mechanisms contributing to the repair of photolesions within heterochromatic regions.

5.2. Results

We described how UV-C and the DNA repair mechanisms control DNA methylation landscape and chromocenter shape (Graindorge et al. 2019) (Chapter I). Indeed, constitutive heterochromatin shows UV-C induced dynamics, and its reshaping relies on the GGR and DR photodamage repair pathways (Chapter I). We also demonstrated that the structural changes in constitutive heterochromatin are linked to DNA methylation. To better decipher the underlying molecular processes of chromocenter reshaping upon UV-C irradiation, we followed the dynamics of particular histone marks known to associate with constitutive heterochromatin, namely H3K9me2 and H3K27me1 (Roudier et al. 2011).

5.2.1. Immunolabeling of H3K27me1 and H3K9me2 upon UV-C exposure

5.2.1.1. H3K27me1 and H3K9me2 dynamics in WT plants upon UV-C exposure

In order to follow the putative correlation between alteration of chromocenter shape and histone PTMs, we monitored H3K9me2, and H3K27me1 occupancy in WT (Col-0) plants prior (0) and upon UV-C irradiation (30', 2h, 24h) using immunolabeling (Fig. 1A). Chromocenter-like structures of both epigenetic marks were segmented using Nucl.Eye.D models specially trained for H3K9me2 and H3K27me1 signal recognition (see chapter II for details). This segmentation enabled the calculation of PTM Occupancies, PTM Relative chromocenter intensities, and PTM contents (Fig. S1). As a negative control, *kyp suvh-5,6* and *atxr-5,6* mutant plants were specifically used for H3K9me2 and H3K27me1 detection, respectively.

In WT plants, before UV-C irradiation, both H3K9me2 and H3K27me1 signals are, as expected, located in the chromocenter regions (Fig. 1A). These signals are reduced, even absent, in both control mutant plants (*kyp suvh-5,6* and *atxr-5,6*), highlighting the specific immunolabeling of these histone marks (Fig. 1B). The H3K9me2 content significantly increases 30 min upon UV-C exposure and is followed by a decrease at 2h (Fig. 1C). As shown in Fig. 1D, the differences in H3K9me2 contents are mainly due to changes in occupancy, whereas H3K9me2 relative intensity remains stable. 24h upon irradiation, the H3K9me2 content is re-established even higher than prior irradiation (Fig. 1C). Thus, the amount of H3K9me2 in chromocenter regions is highly dynamic upon UV-C exposure. These H3K9me2 dynamics fit with the previously observed changes in chromocenter structures observed in DAPI stained nuclei, suggesting the potential involvement of H3K9me2 homeostasis in constitutive heterochromatin reshaping upon UV-C exposure. The H3K27me1 contents show slight differences, with a significant decrease 30 min upon UV-C exposure (Fig. 1C). We can observe at 24h that the H3K27me1 occupancy increase and the relative intensity decrease, whereas comparable content values are detected (Fig. 1D). This observation indicates that the spatial distribution of H3K27me1 containing loci may change whilst the global amount per nucleus remains stable.

Altogether, these data demonstrate that UV-C irradiation induces predominantly H3K9me2 dynamics, which follow chromocenters reshaping. These observations are in agreement with the well-described high correlation between H3K9me2 and DNA methylation, whereas correlation is lower between H3K27me1 and DNA methylation (Roudier et al. 2011). Moreover, our results highlight that histone and/or specific histone PTMs undergo either eviction/sliding or erasure during the photodamage repair processes.

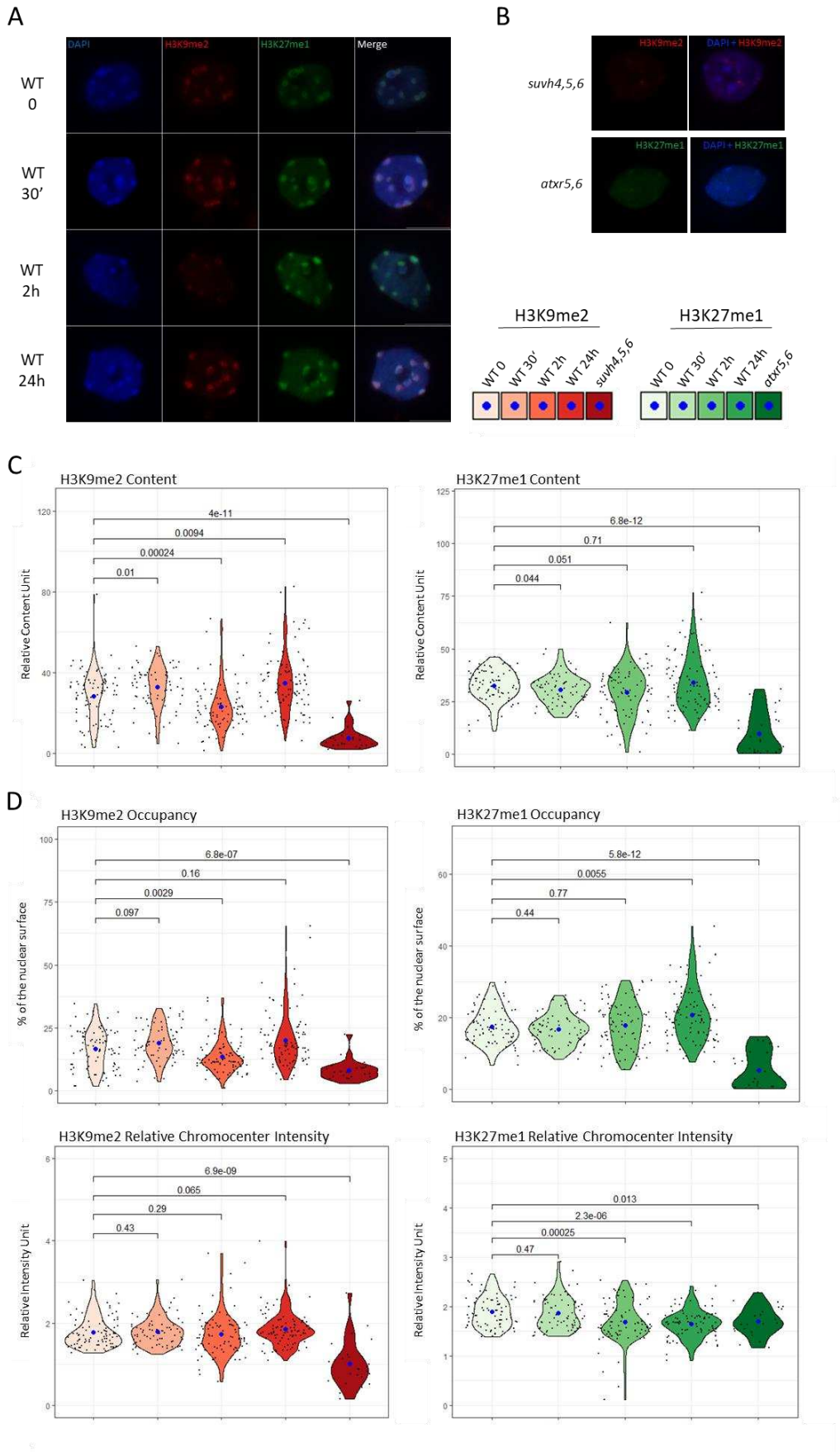

Figure 1: H3K9me2 and H3K27me1 patterns in WT plants upon UV-C exposure

(A) Microscopy images of DAPI, H3K9me2, and H3K27me1 immuno-stained Arabidopsis nuclei isolated from WT (Col-0) leaves in control condition (0) or upon UV-C irradiation (30min, 2h, 24h). Scale bar = 5µm. **(B)** Microscopy images of DAPI / H3K9me2 and DAPI / H3K27me1 immuno-stained Arabidopsis nuclei isolated from *kypsuvh-5,6* and *atxr-5,6* respectively in control. Scale bar = 5µm. **(C)** Violin plots of the H3K9me2 and H3K27me1 Content (Occupancies * Relative Intensities). Each black dot represents the measure for one nucleus. The blue dot shows the mean value. Exact p values are shown (Mann Whitney Wilcoxon test). **(D)** Violin plots of H3K9me2 and H3K27me1 occupancy (percent of the nuclear surface occupied by chromocenter-like structure) and Relative Intensity (ratio of mean chromocenter structure intensity / Mean nuclei intensity) in a population of at least 80 nuclei per condition as described in (A). Each black dot represents the measure for one nucleus. The blue dot shows the mean value. Exact p values are shown (Mann Whitney Wilcoxon test).

5.2.1.2 H3K27me1 and H3K9me2 dynamics upon UV-C in photodamage repair-deficient plants

We observed how H3K9me2 and H3K27me1 contents evolved in WT nuclei upon UV-C exposure. To further investigate if the observed changes depend on DNA repair pathways, an immunostaining of H3K9me2 and H3K27me1 marks was performed on WT (Col-0), *ddb2, uvr3phr1,* and *ddb2uvr3phr1* plants prior (0) and upon UV-C irradiation (2h, 24h) (Fig. 2).

As shown in Figure 3, the H3K27me1 contents remain stable in *ddb2* and *uvr3phr1* mutant plants exposed to UV-C. Only minor changes in relative chromocenter intensity of H3K27me1 could be observed in *ddb2*, at 2h and 24h (Fig. 3). Interestingly, in the triple mutant *ddb2uvr3phr1,* affected in both DR and GGR pathways, nuclei show a higher H3K27me1 occupancy and content compared to the WT nuclei prior UV-C exposure (Fig. 3). Interestingly, H3K27me1 content significantly decreases 2h upon irradiation (Fig. 3). This observation suggests that DDB2 and the UVR3/PHR1 photolyases may have a redundant role in the stabilization of the H3K27me1 landscape in response to UV-C irradiation.

The H3K9me2 dynamics, in turn, seem to depend on DDB2 (Fig. 4). Indeed, in *ddb2* mutant plants, H3K9me2 content remains stable 2h upon UV-C (Fig. 4). Additionally, the observed increase of H3K9me2 content 24h upon irradiation in WT plants, is suppressed in *ddb2* plants and mainly depends on a decrease of H3K9me2 occupancy (Fig. 4).

This likely suggests a role for DDB2 in the re-establishment of the H3K9me2 landscape at chromocenter upon repair (Fig. 4). In *uvr3phr1* mutant plants, the H3K9me2 dynamic is closely related to the one observed in WT plants, with a significant decrease in H3K9me2 content and occupancy 2h upon UV-C (Fig. 4). 24h upon exposure, the H3K9me2 content again reaches the level observed in the control condition (0) but does not show further increase as observed in WT plants (Fig. 4). In *ddb2uvr3phr1* mutants, like in *ddb2,* no decrease in H3K9me2 content could be observed (Fig. 4). Surprisingly a significant increase could be measured at 24h, suggesting that alternative repair processes may have stimulated H3K9me2 deposition (Fig. 4).

Taken together, these observations highlight an essential role for the photodamage repair machinery in H3K9me2 homeostasis upon UV-C irradiation. Especially, DDB2 seems to initiate the early decrease of H3K9me2 and in its proper re-establishment upon repair.

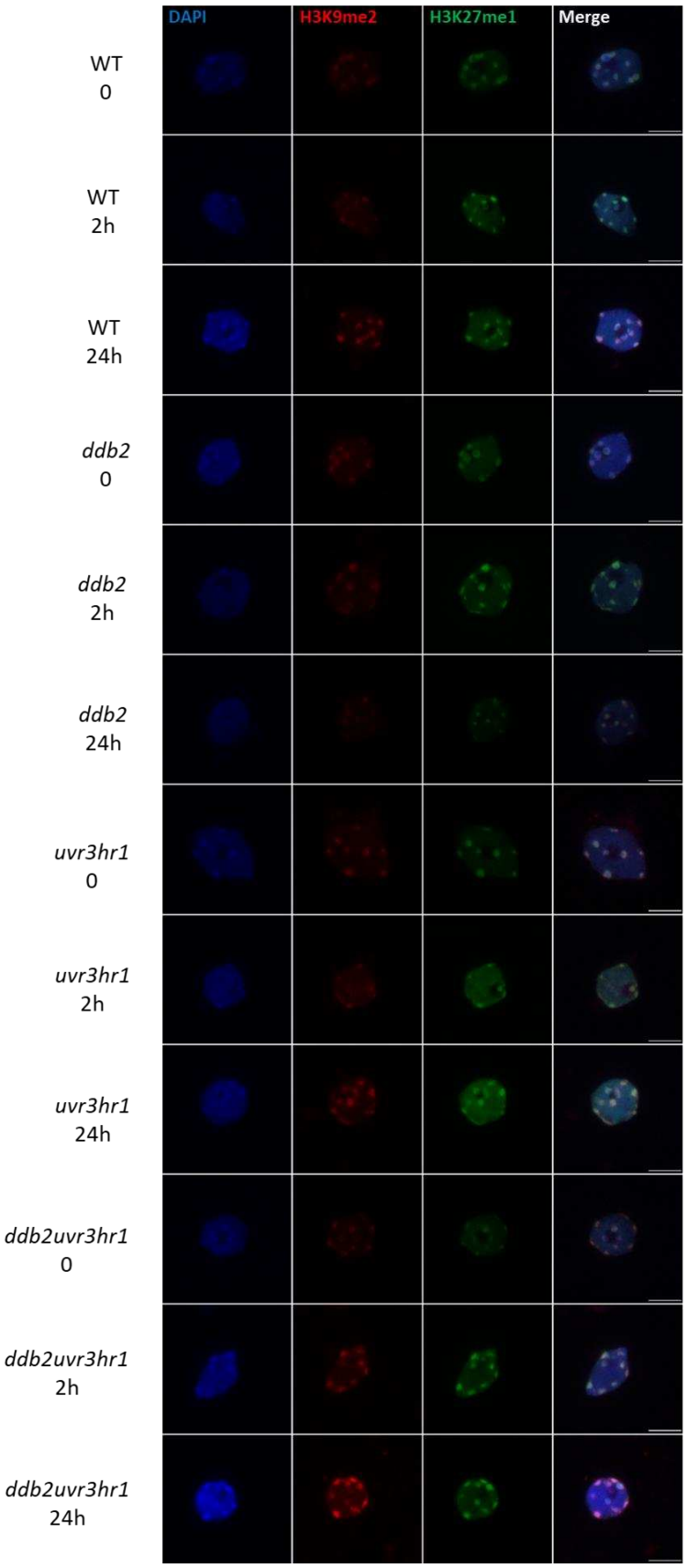

Figure 2: UV-C induced H3K9me2 and H3K27me1 dynamic in *ddb2*, *uvr3phr1,* and *ddb2uvr3phr1* mutants

Microscopy images of DAPI, H3K9me2 and H3K27me1 immuno-stained Arabidopsis nuclei isolated from WT (Col-0), *ddb2*, *uvr3phr1* and *ddb2uvr3phr1* leaves in control condition (0) or upon UV-C irradiation (2h, 24h). Scale bar = 5µm.

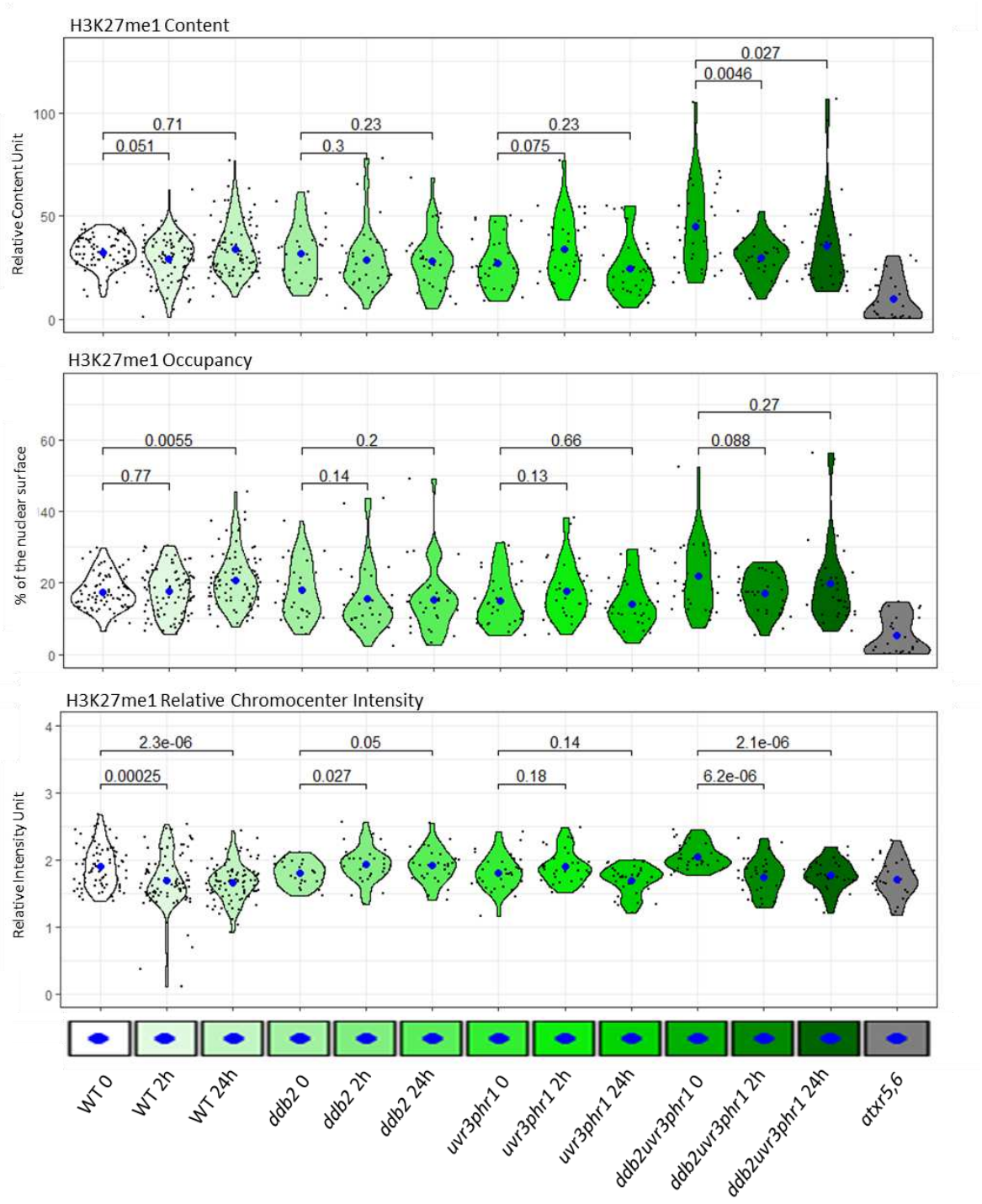

Figure 3: Measurements of H3K27me1 in WT, *ddb2*, *uvr3phr1,* and *ddb2uvr3phr1* mutant plants upon UV-C Exposure

Violin plots of H3K27me1 Occupancy (percent of the nuclear surface occupied by chromocenter like structure), Relative Intensity (ratio of mean chromocenter structure intensity / Mean nuclei intensity), and Content (Occupancies * Relative Intensities) in a population of at least 30 nuclei per condition as described in Figure 2. Additionally, nuclei from *atxr-5,6* mutant, were used as negative control. Each black dot represents the measure for one nucleus. The blue dot shows the mean value. Exact p values are shown (Mann Whitney Wilcoxon test).

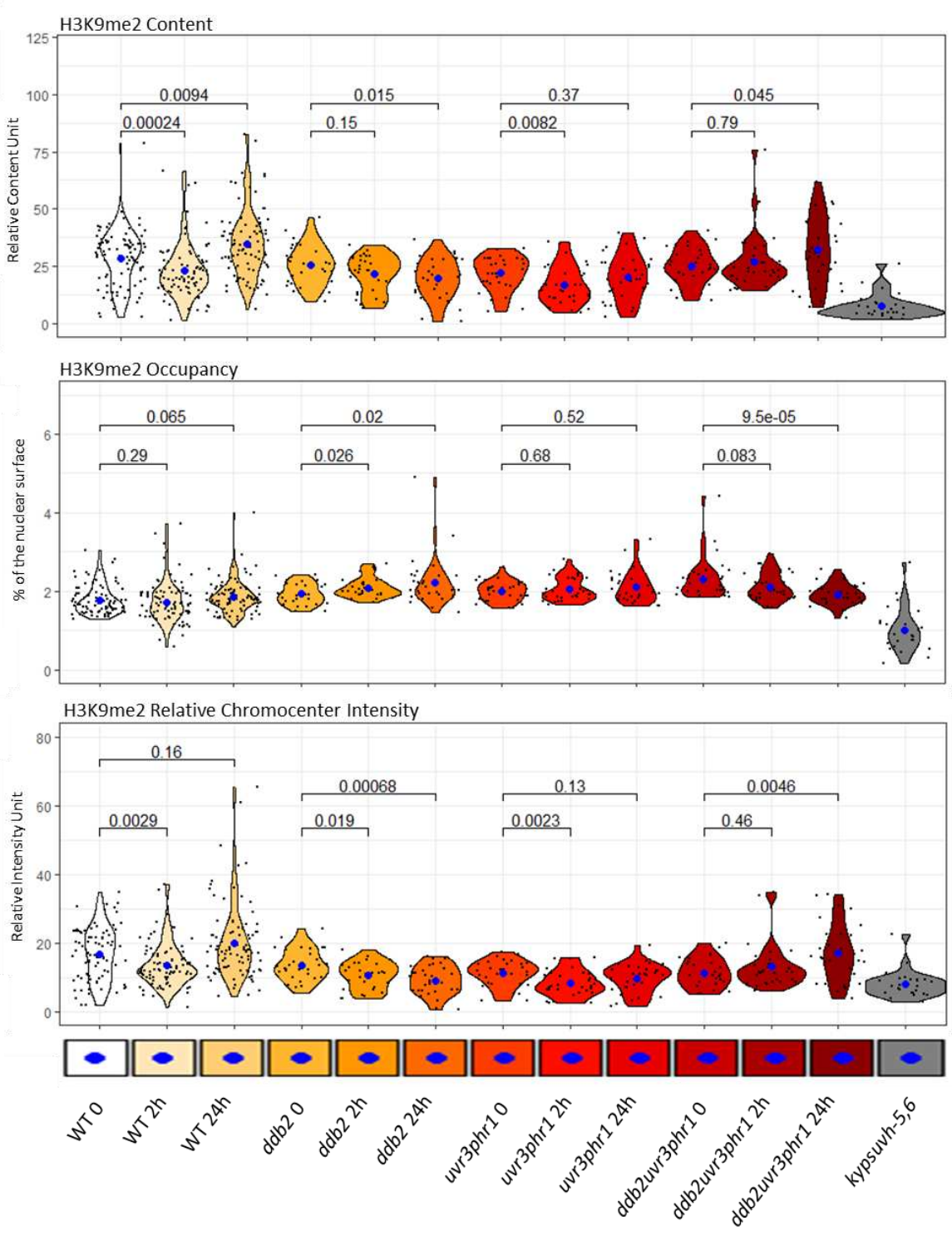

Figure 4: Measurements of H3K9me2 in WT, *ddb2*, *uvr3phr1,* and *ddb2uvr3phr1* mutant plants upon UV-C exposure

Violin plots of H3K9me2 Occupancy (percent of the nuclear surface occupied by chromocenter like structure), Relative Intensity (ratio of mean chromocenter structure intensity / Mean nuclei intensity), and Content (Occupancies * Relative Intensities) in a population of at least 30 nuclei per condition as described in Figure 2. Additionally, nuclei from *kypsuvh-5,6* mutant as described in Figure 1B were used as negative control. Each black dot represents the measure for one nucleus. The blue dot shows the mean value. Exact p values are shown (Mann Whitney Wilcoxon test).

5.2.1.3. H3K27me1 and H3K9me2 nucleoplasmic signals upon UV-C irradiation in WT and photodamage repair-deficient plants

In the previous part, we determined how UV-C affects the H3K27me1 and H3K9me2 marks within chromocenter-like structures. In a complementary approach, we measured the H3K27me1 and H3K9me2 Mean Nucleoplasmic Intensity (MNI) to define their potential dynamics in other parts of the genome (*i.e.* chromosome arms; Fig. S1).

In WT nuclei, the H3K27me1 MNI strongly increases 2h upon UV-C irradiation which is followed by a slight decay at 24h (Fig. 5A). This holds true in *ddb2* plants, whereas this enhancement occurs at 24h in *uvr3phr1* plants (Fig. 5A). In the triple *ddb2uvr3phr1* mutant plants, the H3K27me1 MNI profile behaves like in WT plants (Fig. 5A), suggesting that the nucleoplasmic H3K27me1 dynamics is DDB2-, UVR3- and PHR1-independent. Interestingly, in WT and *uvr3phr1* nuclei, the H3K9m2 MNI significantly decreases at 2h whilst it remains stable in *ddb2* and in *ddb2uvr3phr1* nuclei (Fig. 5B). This observation highlights the putative role of DDB2 in the regulation of H3K9me2 dynamics at a genome-wide level. Importantly, H3K27me1 and H3K9me2 MNIs are not correlated (Fig. 5A), indicating the independent dynamics of both marks.

These changes in histone PTM contents within chromocenter-like structures and in the whole nucleus can be due to a fine-tuning of histone removal/active erasure and writing upon UV-C exposure.

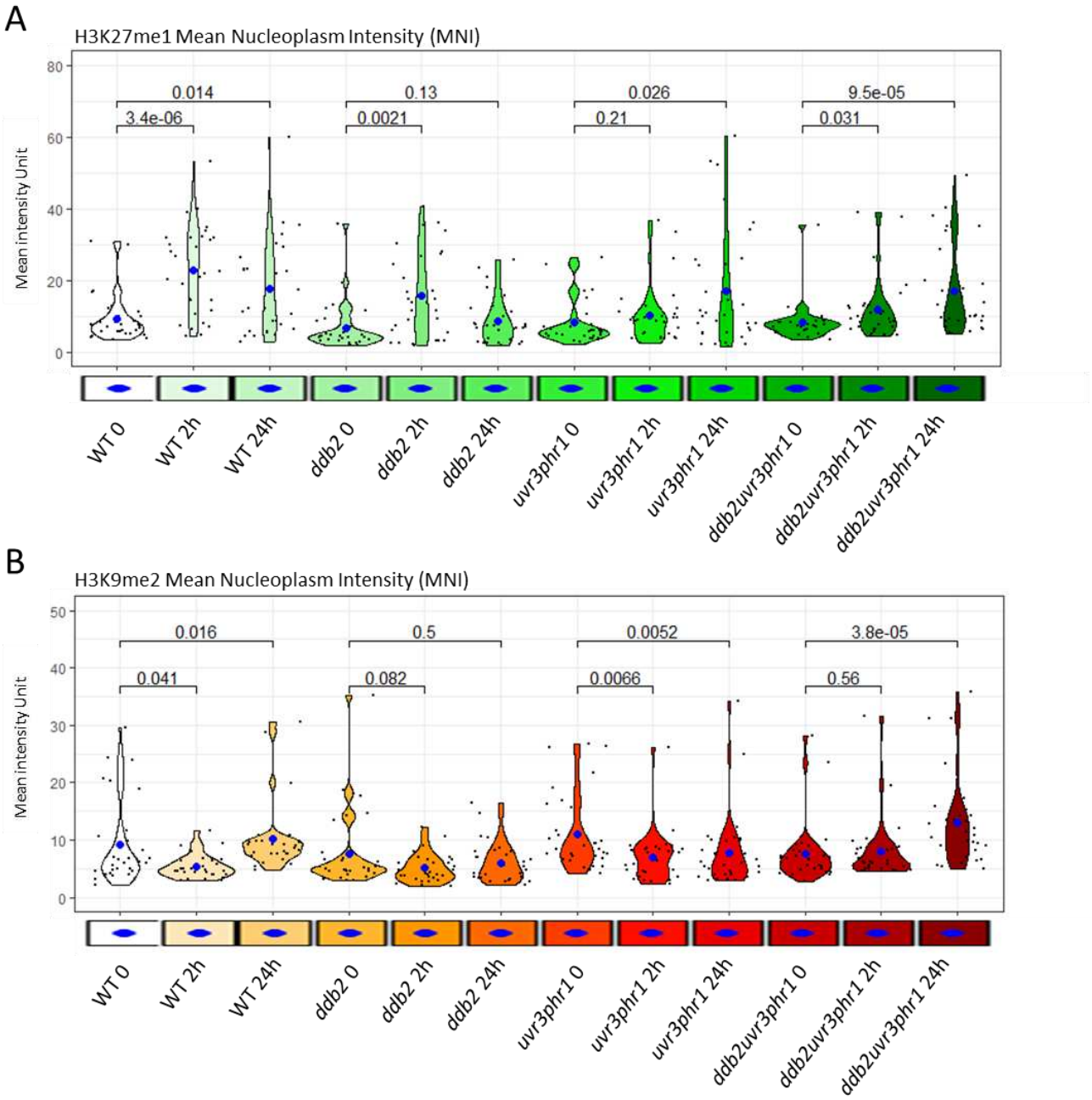

Figure 5: Measurements of H3K9me2 and H3K27me1 nucleoplasmic contents in WT, *ddb2*, *uvr3phr1,* and *ddb2uvr3phr1* plants upon UV-C exposure

Violin plots of H3K9me2 **(A)** and H3K27me1 **(B)** Mean Nucleoplasmic Intensities in a population of at least 30 nuclei per condition as described in Fig.X2. Each black dot represents the measure for one nucleus. The blue dot shows the mean value. Exact p values are shown (Mann Whitney Wilcoxon test).

5.2.2. Role of factors acting in H3K9me2 homeostasis

Given that UV-C induces significant changes of chromocenter and nucleoplasmic H3K9me2 contents, it could be assumed that factors involved in their homeostasis would cooperate with the photodamage repair pathways to ensure genome and epigenome integrities. Thus, the following part aims at characterizing the role of several H3K9me2 writers/erasers in UV-C response.

5.2.2.1 H3K9me2 dynamics in HMTase and histone demethylases deficient plants upon UV-C exposure

In Arabidopsis, KYP, SUVH5, and SUVH6 are the main H3K9me2 methyltransferases (Jackson et al. 2002; Ebbs and Bender 2006; Li et al. 2018). IBM1 and JMJ27 are the most characterized H3K9me2 demethylases (Saze et al. 2008; Wang et al. 2021b). We used these methyltransferases and demethylases deficient plants to monitor H3K9me2 contents, using immunolabeling. H3K9me2 Occupancy, Relative intensity, and Content (Fig. S1) were measured in *kyp suvh5,6*, *jmj27,* and *ibm1* plants prior (0) and 2h upon UV-C exposure.

In the absence of the three main H3K9me2 methyltransferases, in *kyp suvh-5,6*, the H3K9me2 content is, as expected, remarkably low (Fig. 6A and 6B). Interestingly, 2h upon UV-C, a significant increase in H3K9me2 Occupancy, RCI, and Content could be observed (Fig. 6A and 6B). Aside from KYP(SUVH4), SUVH5, and SUVH6, the *Arabidopsis thaliana* genome encodes 12 other SET-domain proteins, which may be responsible for the observed increase in H3K9me2 2h upon UV (Xu and Jiang 2020). The analysis of H3K9me2 content in nuclei isolated from plants deficient in the expression of the H3K9me2 demethylase JMJ27, reveals a loss of dynamic 2h upon UV-C (Fig. 6A and 6B). In *ibm1* plants, deficient for another H3K9me2 demethylase, a WT-like decrease of H3K9me2 Occupancy and content could be observed (Fig. 6A and 6B). Consequently, the decrease of H3K9me2 content at 2h seems to depend on the H3K9me2 demethylase JMJ27. Additionally, it can be observed that in *ibm1* mutant nuclei the H3K9me2 content is highly variable in control conditions when compared to *jmj27* and WT plants, highlighting its potential importance for the maintenance of accurate H3K9me2 patterns, during the daily plant growth.

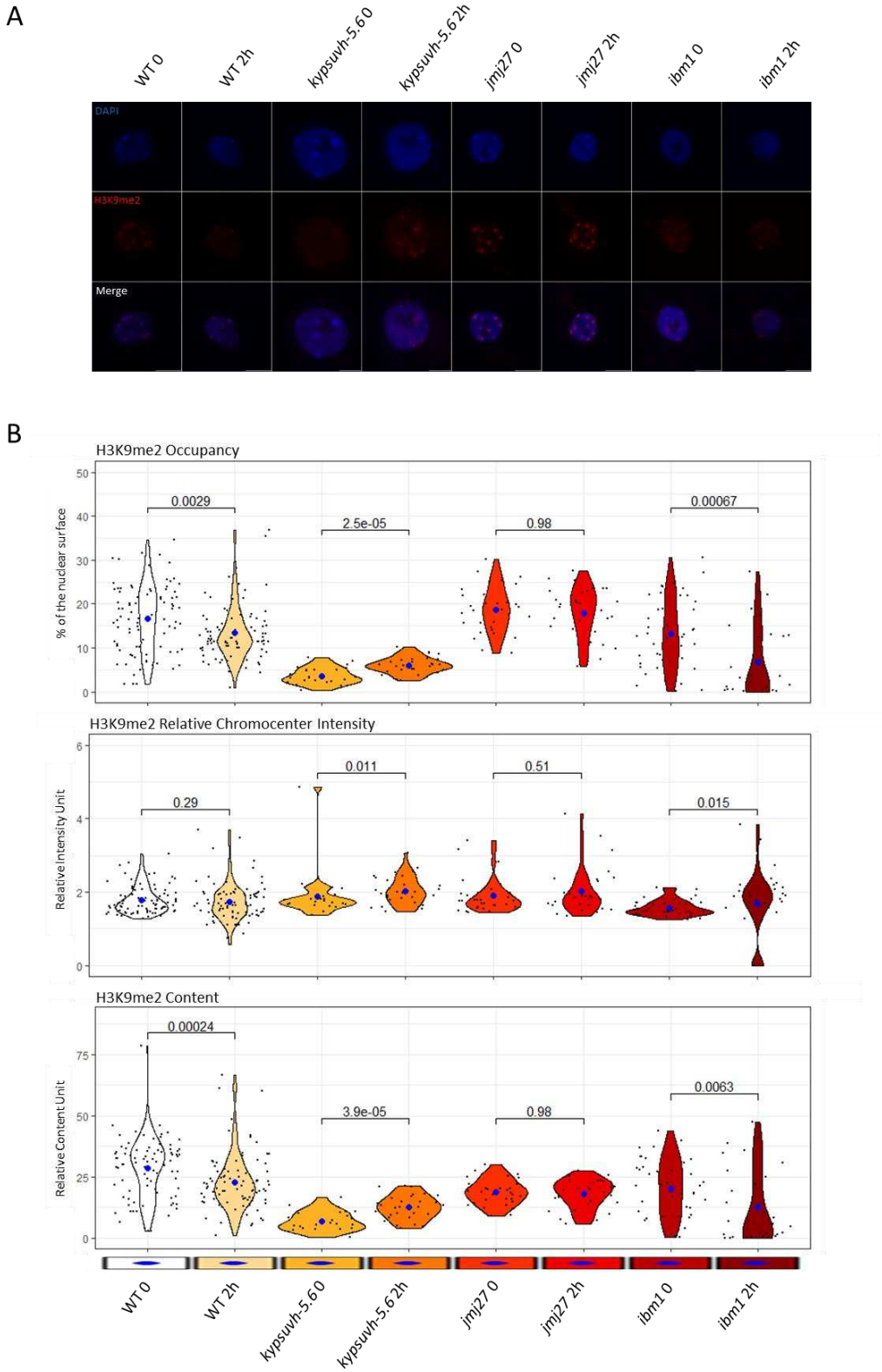

Figure 6 Measurements of H3K9me2 in *kyp suvh-5.6*, *jmj27,* and *ibm1* mutant plants upon UV-C exposure

(A) Microscopy images of DAPI and H3K9me2 immuno-stained Arabidopsis nuclei isolated from WT (Col-0), *kyp suvh-5.6, jmj27,* and *ibm1* leaves in control condition (0) or upon UV-C irradiation (2h). Scale bar = 5µm. **(B)** Violin plots of H3K9me2 Occupancy (percent of the nuclear surface occupied by chromocenter like structure), Relative Intensity (ratio of mean chromocenter structure intensity / Mean nuclei intensity) and Content

(Occupancies * Relative Intensities) in a population of at least 25 nuclei per condition as described in (A). Each black dot represents the measure for one nucleus. The blue dot shows the mean value. Exact p values are shown (Mann Whitney Wilcoxon test).

5.2.2.2 Photolesions repair in H3K9me2 MTase-demethylases deficient plants

In order to decipher the putative role of H3K9me2 MTase-demethylases in the repair of photolesions, we assayed the DNA repair efficiency of H3K9me2 MTase-demethylases mutant plants. For this, we measured the remaining amount of photodamage (CPD and 6,4-PP) 1h upon UV-C. It is expected that photodamage repair-deficient plants will show higher CPD or 6,4 PP contents than WT plants (Schalk et al. 2017).

In WT (Col-0) plants, more than 90% of the UV-C induced CPDs and 6,4 PPs get repaired 1h upon irradiation (Fig. 7). Interestingly, 1h upon irradiation, the amount of both types of photolesions in *kyp* remain high, demonstrating a repair deficiency (Fig. 7). In *ibm1* plants, the remaining amount of CPD 1h upon UV-C exposure is higher than in WT plants, while no clear difference could be observed in *jmj27* plants (Fig. 7). Interestingly both *jmj27* and *ibm1* plants display a 6,4-PP repair deficiency compared to WT plants (Fig. 7), highlighting that both H3K9me2 demethylases likely control the repair of this type of photolesions. Importantly, it could be observed that the amount of photolesions induced by UV-C is reduced in *kyp* mutant plants, whereas in *jmj27* and *ibm1* mutants, only the basal level of induced 6,4-PPs is lower than those measured in WT plants (Fig. 7).

Our results are in agreement with the emerging notion that the epigenetic context may influence DNA damageability. Indeed, the significant decrease in damage accumulation in *kyp*, may be explained by the reduced amount of H3K9me2 in heterochromatin. However, KYP and consequently H3K9me2 deposition also seems essential for efficient photolesion repair. In addition, these results show that both IBM1 and JMJ27 are important for efficient 6,4PP repair.

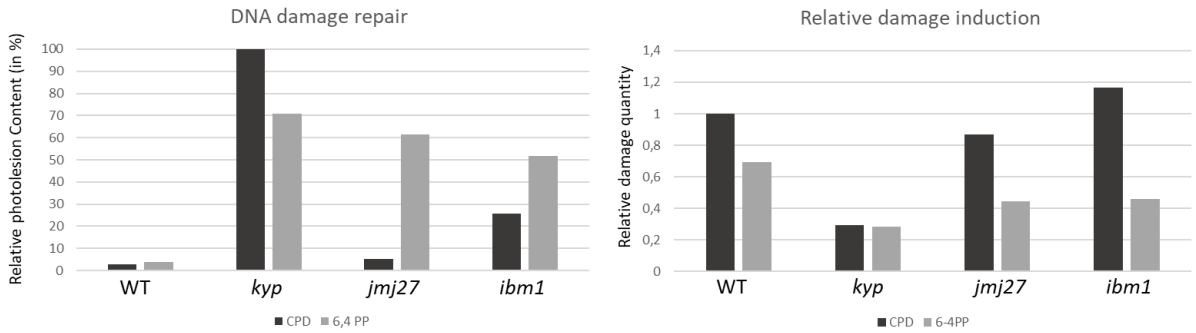

Figure 7: Photolesions repair in H3K9me2 MTase-demethylases deficient plants

Left Panel: histogram of the percentage of remaining photodamages 1h upon UV-C irradiation. Right Panel: histogram of the amount of photolesions measured directly after UV-C treatment normalized to WT plants.

5.2.2.3. Genetic interactions between photodamage repair and H3K9me2 MTase-demethylases mutations.

We provided evidence that factors involved in H3K9me2 homeostasis contribute to the proper dynamics of H3K9me2 content upon UV-C irradiation. However, the interplay between H3K9me2 writers-erasers and the photodamage repair pathways remains elusive. To decipher such putative interconnections, we analyzed the genetic interactions between photodamage repair and H3K9me2 MTase-demethylases mutations. For this, we used the well-established root growth assay (Molinier et al. 2004) that predominantly reflects UV-C repair efficiency.

As shown in Figure 8A, UV-C induces a significant root growth delay in the *jmj27* mutant plant that is suppressed in the complementation line (Fig. 8B and 8C). These observations strengthen the assumption that JMJ27, catalyzing H3K9me2 demethylation, is involved in UV-C response and likely in DNA repair. However, a significant UV-C sensitivity of *kyp* (Fig. 9A) and *ibm1* (Fig. 9B) could also be observed, indicating that both H3K9me2 methylation and demethylation processes are both required for proper root growth upon UV-C irradiation.

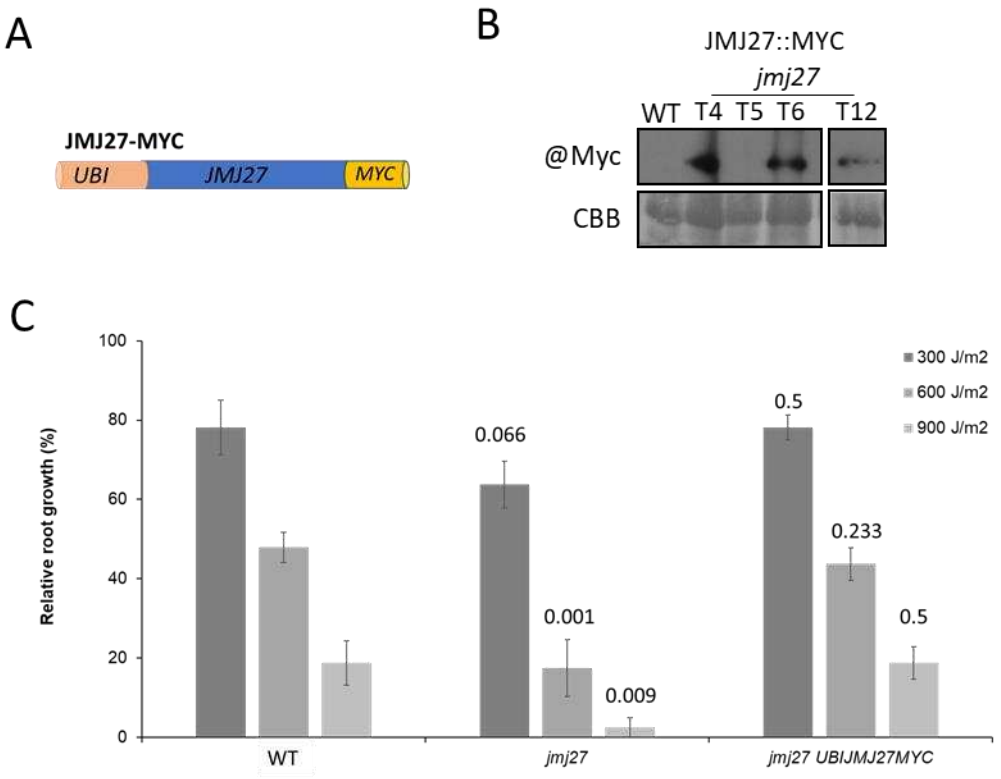

Figure 8: Complementation and UV-C sensitivity assay of the *jmj27* mutant plants

(A) Schematic representation of the construct used to complement the *jmj27* mutant plants. The expression of the genomic *JMJ27* coding sequence fused to the MYC tag was driven by the *UBI10* promoter. Vector used pEAQ_ΔP19 (Fig.SX2). **(B)** Western blot of j*mj27 JMJ27MYC* expressing plants. **(C)** UV-C sensitivity assay of *jmj27* and j*mj27JMJ27MYC* plants Line T12. 3 different UV-C doses were used.

As expected, DNA repair-deficient plants such as *ddb2*, *rad10,* and *uvr3phr1* mutants exhibit a UV-C hypersensitivity compared to WT plants (Fig. 9A and 9D). Interestingly, when *ddb2* and *rad10* mutations are combined with *jmj27*, the UV-C sensitivity does not differ from the one observed in the single *jmj27* mutant plants (Fig. 9A). Therefore *ddb2*, *rad10,* and *jmj27* mutations are epistatic and *JMJ27* acts upstream of *DDB2* and *RAD10* (Fig. 9A). Similar epistasis could be determined with *ddb2* and *kyp* mutations, also revealing that *KYP* acts upstream of *DDB2 (*Fig. 9A). These results show that the KYP HMTase and the JMJ27 demethylase likely act in the GGR pathway. Interestingly, *kyp* and *jmj27* are epistatic (Fig. 9C), suggesting that both act in GGR. *ibm1* shows a synergistic effect when combined with *ddb2*, suggesting that IBM1 and DDB2 act in two parallel pathways (Fig. 9B). *ibm1* also shows a synergistic effect with *jmj27*, highlighting the non-redundant function of both H3K9me2 demethylases in response to UV-C (Fig. 9C).

In order to determine whether KYP and the JMJ27 demethylase may also be involved in the DR pathway, we produced *uvr3phr1 kyp* and *uvr3phr1 jmj27* triple mutant plants. Both combinations show synergistic effects (Fig. 9D) highlighting that KYP and JMJ27 unlikely act in the DR pathway. These data reinforce the hypothesis that KYP and JMJ27 are involved in the GGR pathways, known to process photolesions in parallel to the DR pathway (Johann to Berens and Molinier 2020).

In Arabidopsis, there exists a non-canonical GGR mechanism (Schalk et al. 2017). This pathway involves small RNA and factors of the TGS-PTGS machinery such as DCL4 and RNA-POL IV (Schalk et al. 2017). In order to underpin the role of JMJ27 in this non-canonical DNA repair pathway, *jmj27* was crossed with mutants deficient in the small RNA-mediated GGR pathway *dcl4* and *nrpd1* (Schalk et al. 2017). As shown in Figure 9E, single *dcl4* and *nrpd1* mutant plants exhibit UV-C sensitivity, whereas no significant difference could be measured in *dcl4 jmj27* and *jmj27nrpd1* double mutant plants compared to single mutants (Fig. 9E), revealing epistatic interactions. In addition, we can identify that *DCL4*, and *NRPD1,* act upstream of *JMJ27*. These results demonstrate that JMJ27 is likely involved in the small RNA-mediated GGR pathway. In order to test the potential interplay between JMJ27 and DNA methylation pathways, we used in genetic interaction assays *cmt2*, *cmt3,* and *drm2* mutant plants defective for maintenance and *de novo* DNA methylation (Ashapkin et al. 2016). DNA methylation mutants *cmt2*, *cmt3,* and *drm2,* do not exhibit UV-C sensitivity compared to WT plants (Fig. 9F). Surprisingly, *cmt2* and *cmt3* show UV-C tolerance (Fig. 9F). Both *cmt2jmj27* and *cmt3jmj27* double mutant plants exhibit an intermediate UV-C sensitivity compared to the respective single mutant plants, suggesting that they act in independent processes (Fig. 9F). Although the mode of action of CMT2 and CMT3 is linked to H3K9me2 (Stroud et al. 2014), it reflects that (i) this well-documented interplay might be more complex than expected in plants exposed to UV-C (ii) alternative processes might exist. The double mutant *drm2jmj27* exhibited a *drm2*-like growth upon UV-C irradiation, indicating that *DRM2* and *JMJ27* act in the same pathway with *DRM2* upstream of JMJ27 (Fig. 9F). This observation is in agreement with the role of *DRM2* in the RdDM pathway and the crosstalk between DNA repair factors and the RNA silencing machinery (Schalk et al. 2016; Schalk and Molinier 2016). All together, these genetic interaction assays allow defining that KYP and JMJ27, involved in H3K9me2 homeostasis, contribute to both canonical and non-canonical GGR pathways.

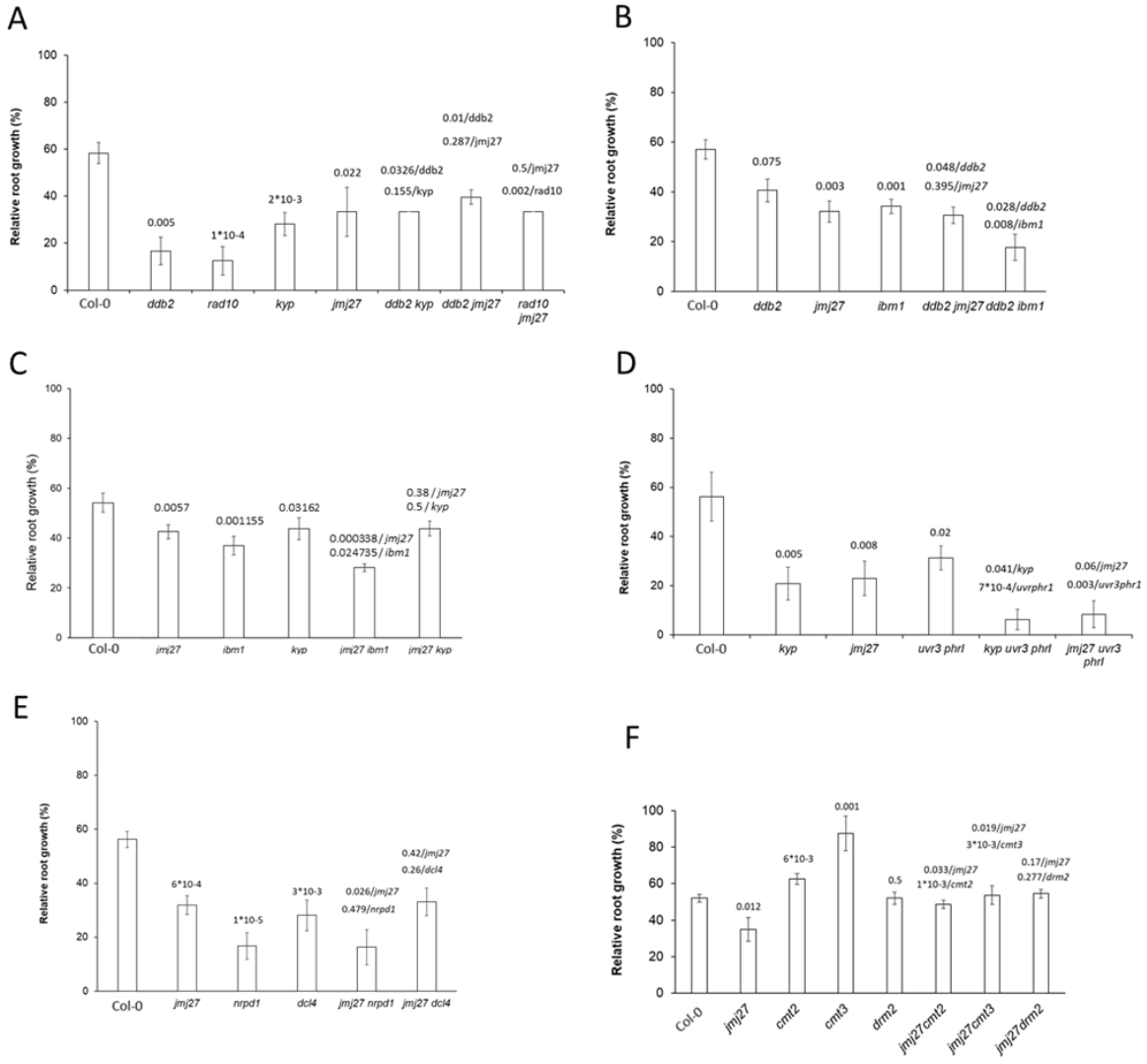

Figure 9: Genetic interactions between *jmj27*, DNA-repair (GGR, DR), H3K9me2 methyltransferase, DNA methyltransferases, and RdDM-PTGS mutations

Root-growth assay of 6-day-old plants exposed to UV-C. Root growth was calculated relative to the corresponding untreated plants (±SD). Eight plants per replicate were used, and three independent biological replicates were performed. Exact p values are shown (t-test). **(A)** Genetic interactions between *ddb2, rad10*, *kyp,* and *jmj27.* **(B)** Genetic interactions between *ddb2*, *jmj27,* and *ibm1*. **(C)** Genetic interactions between *jmj27*, *ibm1,* and *kyp.* **(D)** Genetic interactions between *uvr3phr1*, *kyp,* and *jmj27*. **(E)** Genetic interactions between *jmj27, nrpd1,* and *dcl4*. **(F)** Genetic interactions between *jmj27*, *cmt2, cmt3,* and *drm2.*

5.2.3. Localizations and loadings on chromatin of DDB2 and UVR3

Cytogenetic approach and genetic interactions highlighted that factors regulating H3K9me2 homeostasis contribute to the repair of UV-C-induced photodamages with a predominant role in the GGR pathway. The following study aims at analyzing the role of H3K9me2 homeostasis on DDB2 dynamics to decipher the putative role of this histone mark on DDB2 loading on chromatin to sense photolesions. In addition, the localization and the chromatin loading of the photolyase UVR3, which reverts photolesions in parallel to the GGR pathway, will be analyzed to provide an overview of photodamage repair within genome complexity.

5.2.3.1. DDB2 chromatin loading in H3K9me2 MTase-demethylases deficient plants

The loading of DDB2 on chromatin and its release were already extensively studied (Jones et al. 2010). Importantly, DDB2 recognizes in priority photodamage in the accessible internucleosomal regions and later in the core nucleosome (Fei et al. 2011). Given that H3K9me2 participates in fine-tuning chromatin compaction, we decided to take into account such complexity. For this, we designed experiments to follow the kinetics of DDB2 on chromatin upon UV-C exposure with a particular focus on nucleosomal or internucleosomal DNA fractions prepared from H3K9me2 MTase/demethylases deficient plants. Samples fractionation was performed as shown in Figure 10A (see Materials and Methods for details).

Firstly, the total amount of DDB2 was tracked in a time course upon UV-C irradiation in WT, *jmj27,* and *kyp* plants (Fig. 10B). As expected, in WT plants DDB2 content decreases at 2h, reflecting its ubiquitin-dependent decay (Fig. 10B) (Molinier et al. 2008). In *jmj27* and *kyp* mutant plants, the total amount of DDB2 is slightly lower than in WT plants (Fig. 10B). Upon UV-C exposure, the DDB2 kinetics in *kyp* plants looks like the one observed in WT plants with a decay at 2h (Fig. 10B). Conversely, in *jmj27* mutant plants, the DDB2 content increased at 2h, suggesting a protein stabilization (Fig. 10B).

Secondly, we followed the DDB2 content in soluble (free DDB2) and in insoluble fractions (DDB2 enriched in chromatin). In WT plants, the soluble DDB2 pool, which is not associated with chromatin, slightly increases upon treatment (Fig. 10C). Interestingly, in the insoluble fraction, which reflects the chromatin pool, DDB2 content increases at 30 min/ 1h and decreases at 2h, showing its loading and release from chromatin (Fig. 10C). In *jmj27* and *kyp* plants, no significant differences in DDB2 concentration can be observed in the soluble fraction (Fig. 10C). However, in the insoluble fraction of *jmj27* plants, DDB2 shows a strong peak at 30 min, whereas in *kyp*, the DDB2 signal remains very weak and only displays a slight increase until 2h (Fig. 10C). These observations might indicate that the presence of H3K9me2 and the active demethylation both participate in the regulation of DDB2 loading/release on chromatin.

DDB2 was shown to recognize photolesions on DNA even on sequences wrapped around nucleosomes (Matsumoto et al. 2019). To further decipher DDB2 dynamics within chromatin complexity, the plant nucleosomes have been dissected by micrococcal nuclease (MNase) to reveal the proportion of DDB2 loaded on internucleosomal regions *vs* core nucleosomes. In WT and *jmj27* plants, DDB2 shows a peak of loading to internucleosomal regions at 30 min, indicating that the biding to internucleosomal DNA does not significantly depend on JMJ27 (Fig. 10D). Interestingly, in WT plants DDB2 is progressively loaded on core nucleosomes to reach a maximum at 2h (Fig. 10D). In contrast, in *jmj27* mutant plant the signal of DDB2 loading to nucleosomes is weaker and shows a peak at 30 min (Fig. 10D). Thus, JMJ27 seems to facilitate the progressive loading of DDB2 on DNA wrapped around nucleosome.

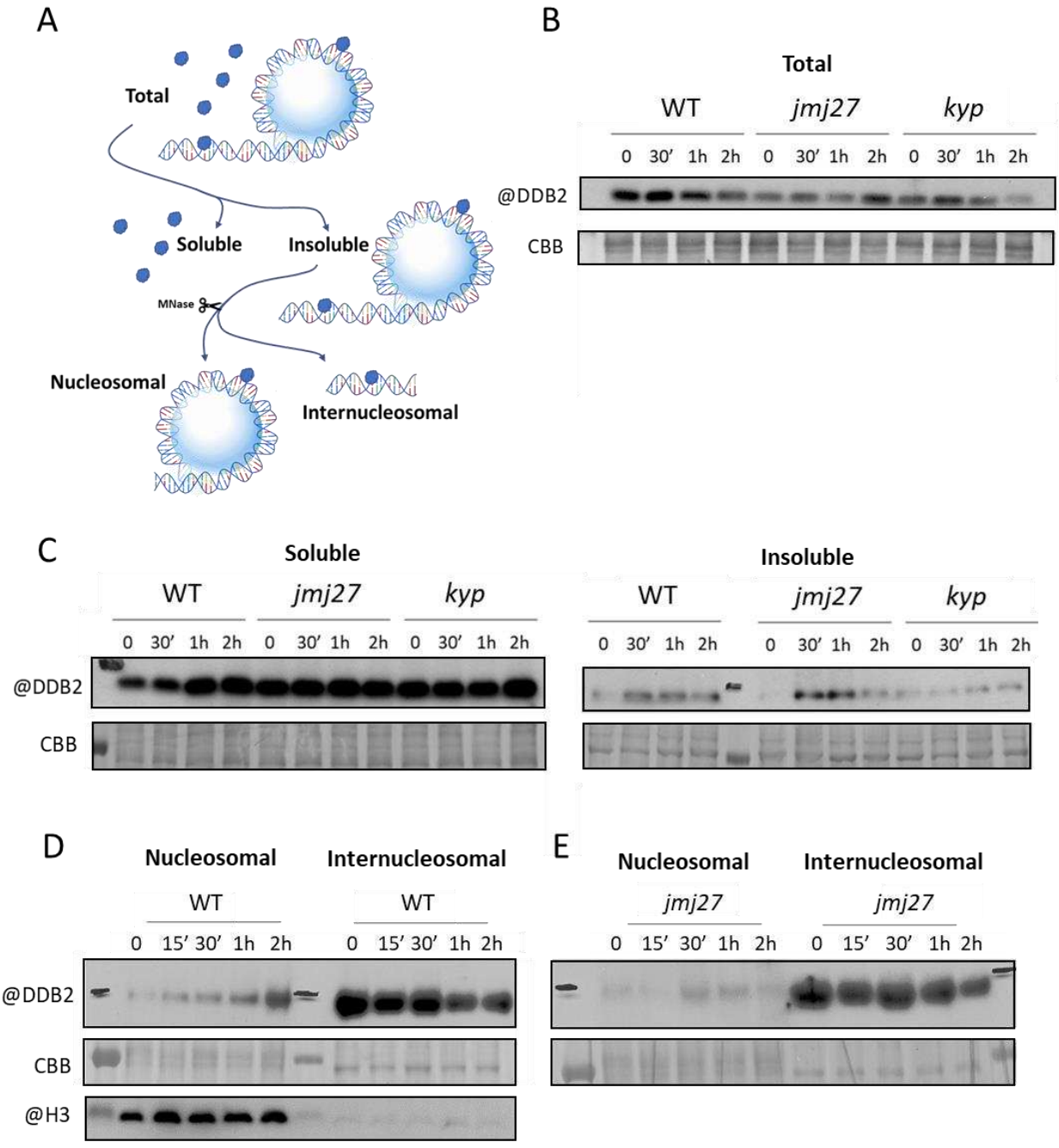

Figure 10: Immunoblotting of DDB2 in H3K9me2 methyltransferase and demethylase mutant plants upon UV-C exposure

(A) Protein fractionation used for immunoblotting. **(B)** DDB2 in total extracts of WT, *jmj27,* and *kyp* plants prior (0) and upon UV-C exposure (30 min, 1h, 2h). **(C)** DDB2 in soluble and insoluble fractions of WT, *jmj27,* and *kyp* plants prior (0) and upon UV-C exposure (30min, 1h, 2h). **(D)** DDB2 in nucleosomal and internucleosomal fractions of WT plants prior (0) and upon UV-C exposure (15min, 30min, 1h, 2h). H3 is shown as control for MNase treatment. **(E)** DDB2 in nucleosomal and internucleosomal fractions in *jmj27* plants prior (0) and upon UV-C exposure (15 min, 30 min, 1h, 2h). Coomassie blue staining are shown as loading controls.

5.2.3.2. UVR3 chromatin dynamics upon UV-C irradiation

The DDB2 loading on chromatin was shown to occur rapidly upon UV-C exposure, predominantly on internucleosomal regions and later on core nucleosomes. Given that the GGR pathway acts cooperatively with the DR pathway to repair photolesions, we decided to follow the dynamics of one of the photolyases, UVR3, that reverts specifically 6,4 PP. Importantly, *jmj27* plants display a delay of 6,4 PP removal compared to WT plants, suggesting a specific role for this histone demethylase in this repair process. Therefore, deciphering UVR3 spatio-temporal dynamics may help in better defining the interplays between GGR, H3K9me2, and DR. To measure UVR3 dynamics, we used UVR3-GFP expressing line (Katarzyna Banas et al. 2018) in microcopy and immunoblotting experiments.

Firstly, the localization of UVR3-GFP was observed in leaf nuclei before (0) and upon UV-C exposure (30 min and 2h). In the absence of UV-C irradiation, a spread GFP signal could be observed within the nucleus (Fig. 11A). Thirty minutes upon irradiation, the GFP signal accumulates at chromocenter regions, indicating a UV-C-induced localization of UVR3 to constitutive heterochromatin (Fig. 11A). This localization persists at 2h upon UV, although at this timepoint, most of the photolesions are already repaired in WT plants (Fig. 11A; Chapter I). Secondly, we used immunoblotting approach to follow UVR3 chromatin loading on soluble and insoluble protein fractions prepared from UVR3-GFP expressing plants. Importantly, UVR3-GFP plants have been grown either in light or in darkness conditions upon UV-C exposure to favor DR or GGR, respectively (Fig. 11B). In light growth conditions, a stable amount of soluble UVR3-GFP can be observed (Fig. 11B). In the insoluble fraction, a peak is visible at 1h, showing UVR3 chromatin loading (Fig. 11B). Interestingly, in dark cultured plants, a UVR3-GFP decay in the soluble fraction is observed, whereas we identified a peak at 2h in the insoluble chromatin fraction (Fig. 11B). These data suggest that light regulates the UVR3 turnover as well as its loading on chromatin.

In parallel, we performed H3K9me2 immunoblotting in nucleosomal fraction of UVR3-GFP expressing plants grown in light or in darkness conditions to allow DR-GGR and only GGR to process photolesions, respectively. This approach confirms that the predominant use of the GGR pathway (dark condition) favors to H3K9me2 decay as observed in WT plants using cytogenetics (Fig. 11C).

Importantly, it also suggests that H3K9me2 alteration (histone eviction/sliding or active demethylation) may contribute to the GGR pathway. This result strengthens the notion that regulation of H3K9me2 content/homeostasis participates in the repair of photolesions.

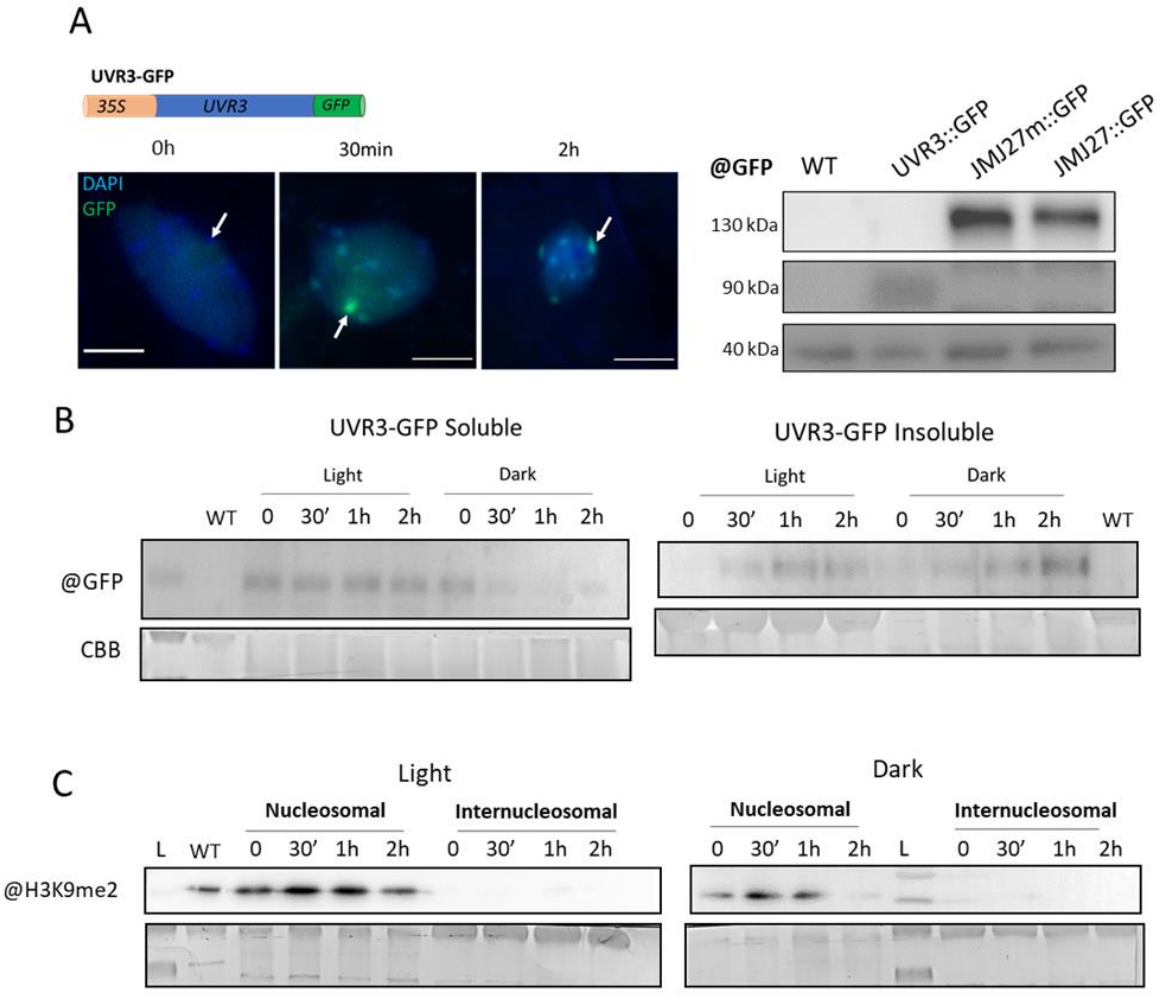

Figure 11: UVR3-GFP localization and loading on chromatin upon UV-C irradiation

(A) Left panel: Schematic representation of the UVR3-GFP constructs expressed in *uvr3* mutant plants (Katarzyna Banas et al. 2018) and immunostaining showing the nuclear localization of UVR3-GFP in control condition and upon UV-C exposure (30 min, 2h). Scale bar = 5µm. Right panel: Immunoblotting of total protein extracts of UVR3-GFP (90 kDa), JMJ27-GFP (130 kDa) or JMJ27m-GFP (130kDa) expressing plants. A Cross-reacting signal was used as a loading control. **(B)** Immunoblotting of UVR3-GFP in plants in control condition (0) and upon UV-C exposure (30 min, 1h, 2h), grown under light or darkness conditions upon irradiation. **(C)** Immunoblotting of H3K9me2 in nucleosomal and internucleosomal fractions of UVR3-GFP expressing plants in control condition (0) and upon UV-C exposure (30 min, 1h, 2h) grown under light or darkness conditions upon irradiation.

5.2.4. JMJ27 and DDB2 dynamics upon UV-C exposure

In the previous part, we described how JMJ27 contributes to the proper chromatin loading of DDB2. According to these results, we further investigated the spatio-temporal localization of JMJ27 and its putative interaction with DDB2.

5.2.4.1. Nuclear localization of JMJ27 and DDB2

The localization of JMJ27 was first analyzed *in planta*, using JMJ27::JMJ27GUS expressing line (Wang et al. 2021b). As previously described, JMJ27 is strongly expressed in shoot and apical meristems (Fig. 12A)(Wang et al. 2021b). Additionally, GUS staining could be observed in leaves nuclei, especially in the vicinity of the vascular bundles (Fig. 12B). Upon UV-C irradiation, the intensity of the GUS staining shows a slight increase in leaves at 2h, followed by a decrease at 6h (Fig. 12C). This indirect approach provides evidence that JMJ27 turnover is stimulated by UV-C irradiation *in planta*.

At the cellular scale, the immunolocalization of JMJ27-GFP (Wang et al. 2021b) reveals a spread nuclear GFP pattern, mostly excluded from nucleoli and with lower intensity in chromocenter regions compared to the nucleoplasm (Fig. 13A). This pattern remains the same upon UV-C exposure (30 min and 2h), indicating that JMJ27 does not drastically re-localize in a UV-C-dependent manner (Fig. 13A).

Immunolocalization of DDB2, using DDB2-FLAG expressing plants (Schalk et al. 2017), shows a nuclear distribution similar to that of JMJ27 (Fig. 13A). Nevertheless, the heterogeneity of signal intensity slightly differs (Fig. 13A). Neither exposure to UV-C, nor *jmj27* defect significantly change the DDB2-FLAG signal distribution (Fig. 13A). Altogether, these observations, highlight that DDB2 and JMJ27 exhibit similar nuclear patterns.

5.2.4.2. DDB2 and JMJ27 chromatin recruitment upon UV-C exposure

DDB2 is loaded on chromatin 30 min upon UV-C exposure to sense photodamage (Fig. 10C; Schalk et al. 2017). In order to investigate the chromatin dynamics of JMJ27 we used immunoblot analyses of JMJ27-GFP expressing plants over a 2h time-course upon UV-C irradiation (Fig. 13B). JMJ27-GFP was indeed progressively enriched in the insoluble chromatin extracts, reaching a peak at 30 min upon UV-C treatment (Fig. 13B). However, when using *jmj27* mutants expressing JMJ27m-GFP, an enzymatically inactivated version of JMJ27-GFP, the total JMJ27m-GFP amount appears to be higher than the amount of JMJ27-GFP (Fig.13B). In addition, no progressive decrease of the JMJ27m-GFP signal could be observed at 2h, suggesting that the protein decay may depend on the enzymatic activity whereas the chromatin loading does not (Fig. 13B).

Collectively, these results show that, upon UV-C exposure, DDB2 and JMJ27 follow comparable UV-C-dependent chromatin dynamics that could be controlled by common mechanisms and factors.

5.2.4.3. Co-immunoprecipitation of DDB2 and JMJ27

Given that DDB2 and JMJ27 act in the same pathway as demonstrated by genetic interactions assay and that both proteins display similar nuclear/chromatin patterns, we thus tested if DDB2 could associate with JMJ27. For this, we used transgenic plants expressing a functional DDB2-FLAG version (Schalk et al. 2016) crossed with JMJ27-GFP expressing plants (Wang et al. 2021b). DDB2-FLAG effectively co-immuno-precipitated with JMJ27-GFP in plant whole-cell extracts prepared before and after UV-C exposure (Fig. 13C). This preliminary experiment suggests that DDB2 and JMJ27 would assemble into a protein complex whose chromatin dynamics relies on UV-C exposure.

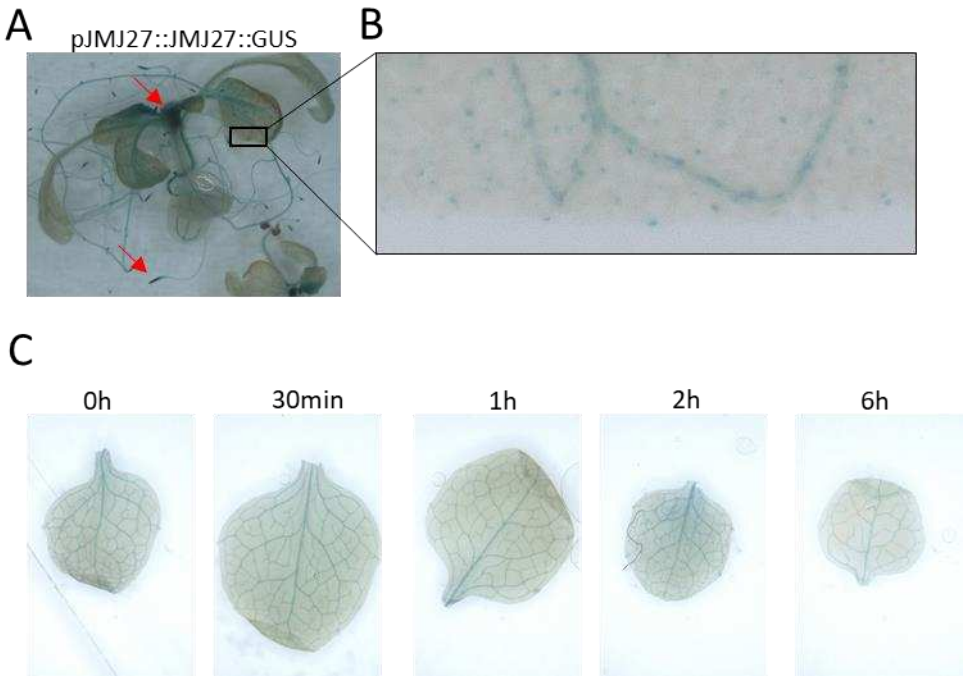

Figure 12: GUS patterns of JMJ27::JMJ27-GUS expressing line upon UV-C exposure

(A) Histochemical GUS staining of 21-day old JMJ27::JMJ27-GUS expressing plants (Wang et al. 2021b). The red arrow shows root and apical meristems. **(B)** Magnified view on a GUS-stained leaf. **(C)** GUS-stained leaves of JMJ27::JMJ27-GUS expressing plants in control condition (0) and upon UV-C exposure (30 min, 1h, 2h, 6h).

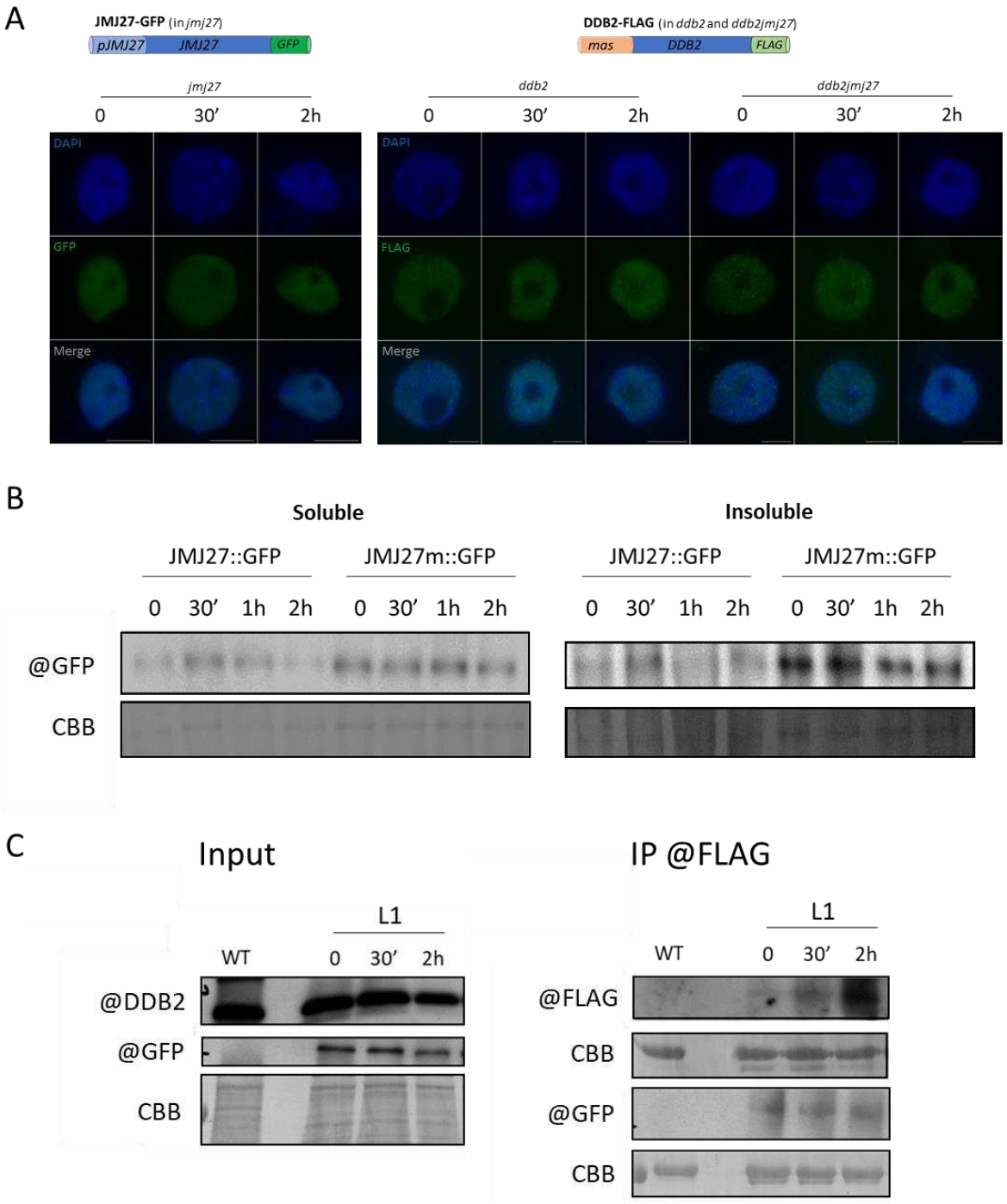

Figure 13: JMJ27-GFP Immuno-labelling, -blotting and -precipitation upon UV-C

(A) Left panel: Schematic representation of the JMJ27-GFP constructs expressed in *jmj27* mutant plants. Microscopy images of DAPI-stained and GFP immuno-labeled Arabidopsis nuclei in control (0) condition and upon UV-C exposure (30 min, 2h). Scale bar = 5µm. Right panel: Schematic representation of the DDB2-FLAG construct expressed in *ddb2* and *ddb2jmj27* mutant plants. Microscopy images of DAPI-stained and FLAG immuno-labeled Arabidopsis nuclei in control (0) condition and upon UV-C exposure (30 min, 2h). Scale bar = 5µm. **(B)** Immunoblotting of JMJ27-GFP and a catalytic loss of function JMJ27m-GFP construct in *jmj27* mutant plants in control condition (0) and upon UV-C exposure (30 min, 1h, 2h).

(C) *In vivo* pull-down of JMJ27-GFP with DDB2-FLAG protein upon UV-C exposure. *ddb2-3* mutant line co-expressing *DDB2-FLAG* and *JMJ27-GFP (*L1*)* was used for immunoprecipitation assay using anti-FLAG antibody prior and upon UV-C irradiation (30 min, 2h). WT plants were used as a negative control. Coomassie blue staining of the blots are shown.

5.3. Discussion

We deciphered the interplay between photodamage repair and H3K9me2 homeostasis in response to UV-C damage. An important reshaping of chromocenter-like H3K9me2 structures was observed upon UV-C irradiation in Arabidopsis leaf nuclei. Further characterization reveals a strong disturbance of H3K9me2 reshaping in DDB2, KYP, and JMJ27 deficient plants, highlighting crosstalk between the GGR pathway and the factors regulating H3K9me2 homeostasis. Indeed, the UV-C-dependent DDB2 loading on chromatin is influenced by the H3K9me2 contents, and its stabilization on DNA packed around nucleosomes relies on the H3K9m2 demethylase JMJ27. Moreover, we found that DDB2 and JMJ27 form a complex, suggesting that the H3K9me2 demethylation would facilitate photodamage recognition by DDB2.

5.3.1. UV-C irradiation induces changes in H3K9me2 contents

We investigated the dynamics of the chromocenter-associated H3K9me2 and H3K27me1 histone marks in a time course following UV-C irradiation. We identified significant alterations of their patterns with an increase of H3K9me2 content at chromocenters 30 min upon exposure, whereas H3K27me1 remains stable. This increase of H3K9me2 could also be observed by immunoblotting, suggesting that the change likely occurs at a genome-wide level. In human cells irradiated with UV, a significant increase of the heterochromatin mark, H3K9me3, could be measured (Fortuny et al. 2021), indicating the early increase of H3K9 methylation would be a conserved mechanism among eukaryotes. In addition, it has been observed in mammals that DOT1L-dependent H3K79me3 or the ASH1L-dependent H3K4me3 occur upon UV exposure to promote damage handover between DDB2 and XPC during NER (Zhu et al. 2018). Arabidopsis lacks a DOT1L homolog (Kari et al. 2019), and ASHH2/SDG8 (the homolog of ASH1L) was, to our knowledge, not reported to be linked to DNA repair, suggesting that some specific processes also exist between kingdoms.

Later upon UV-C irradiation (2h), in parallel to the drop of DAPI-stained chromocenter occupancy (Graindorge et al. 2019), H3K9me2 chromocenter content and occupancy also decreased, reflecting a potential heterochromatin decompaction. Such alteration of chromatin structure occurs during several DNA repair processes and is often described to result from a change in nucleosome density (Waters et al. 2015; Tripuraneni et al. 2021; Chakraborty et al. 2021).

Few emerging models proposed that different chromatin remodeling events facilitate DNA repair. This includes nucleosome PTM erasure (Palomera-Sanchez et al. 2010; Jeon et al. 2020), nucleosome sliding (Dinant et al. 2012; Matsumoto et al. 2019; Nodelman and Bowman 2021), and nucleosome eviction (Chakraborty et al. 2021). Interestingly, the decreased H3K27me1 chromocenter intensity at 2h, indicates that despite the lack of significant changes in its spatial organization, some quantitative changes may also occur at particular loci. Importantly, our results suggest that the characterized heterochromatin dynamics predominantly depend on the modulation of H3K9me2 content upon UV-C exposure. In Arabidopsis, UV-C was found to increase the RNA steady-state levels of 180 bp repeats, *5S rDNA,* and *ONSEN* highlighting that exposure to such genotoxic stress also induces the release of silencing at centromeric and pericentromeric repeats (Graindorge et al. 2019). Indeed, the lack of H3K9me2 was related to the release of silencing and to heterochromatin opening (Zhao et al. 2019; Wang et al. 2019; Kabi and Filion 2021). Given that heterochromatic structures are highly compacted and thus represent a physical barrier for the DNA repair machinery, the transient decrease of H3K9me2 and chromocenter occupancy is likely dependent on the DNA repair activity, allowing the release of the silencing and TE mobilization.

A recent study on human cells irradiated with UV also shows an important relaxation of heterochromatin (Fortuny et al. 2021). However, no significant decrease in the constitutive heterochromatin mark, H3K9me3, has been measured (Fortuny et al. 2021). In contrast, in Drosophila it was shown that the amount of H3K9me3 actively decreased upon UV exposure, from 30 min till several hours (Palomera-Sanchez et al. 2010).

Interestingly the decrease in H3K9me3 in the context of Double Strand Break (DSB) repair was already described, showcasing the induction of such dynamic by factors acting upstream of the DNA repair processes (Jeon et al. 2020). Finally, in *Saccharomyces cerevisiae*, UV was shown to induce H3K9 acetylation at silenced loci to promote chromatin remodeling and GG-NER (Waters et al. 2015), highlighting that several different histone PTMs contribute to the repair of UV-induced DNA lesions.

We also found a significant increase of H3K9me2 content 24h upon UV exposure. At this time point, the photolesion repair is completed, and the H3K9me2 content should be restored together with the chromocenter structure to ensure (epi)genome integrity (Chapter I). However, this “final” H3K9me2 content, as well as the chromocenter occupancy (Chapter I), appears higher than those measured before irradiation. This observation indicates that the H3K9me2 content in chromocenter regions is not accurately maintained 24h upon UV-C irradiation. This alteration of H3K9me2 content might represent a durable scare of the UV-induced dynamics, preventing further release of the silencing and thus strengthening genetic immunity (Kim and Zilberman 2014).

Interestingly, our previous studies identified that UV-C and DNA repair processes introduced differences in the DNA methylation landscape, genome wide and at damage sites predominantly in the CHH context (Graindorge et al. 2019). These changes in H3K9me2 content would likely overlap/correlate with the observed changes in DNA methylation (Law et al. 2013; Stroud et al. 2014; Zhang et al. 2018) and vice versa (Stroud et al. 2014; Li et al. 2018; Xu and Jiang 2020). This hypermethylation of H3K9me2 may also participate in a genome-wide loss of chromatin accessibility following UV exposure (Schick et al. 2015). The hereabove described H3K9me2 dynamic resembles the prime-repair-restore model well described for DSB repair (Soria et al. 2012).

5.3.2. GGR pathway act together with factors involved in H3K9me2 homeostasis

We identified that H3K9me2 dynamic is disturbed in photodamage repair-deficient Arabidopsis plants and that DDB2 plays a predominant role. The photolyases UVR3 and PHR1, in turn, appear to be dispensable, suggesting that the reshaping of H3K9me2 chromocenter signals is predominantly a part of the GGR-NER pathway. This observation is relevant considering the complexity of the GGR pathway compared to the DR process (Johann to Berens and Molinier 2020). Furthermore, these results are in agreement with the DDB2-dependent heterochromatin decompaction reported in human cells exposed to UV (Fortuny et al. 2021) and the interplay between H3K9me3 and NER reported in Drosophila (Palomera-Sanchez et al. 2010).

We identified that the decrease of H3K9me2 content at 2h upon UV depends on the histone demethylase JMJ27 and on the HMTases KYP/SUVH5/SUVH6. Importantly, the well-characterized demethylase IBM1 is unlikely involved in this UV-C-induced dynamics, in agreement with its predominant role in the control of H3K9me2 contents in genic regions (Chan and Zimmerli 2019).

In addition, the observed effect of *JMJ27* mutation on H3K9me2 content can be likely linked to its demethylase activity (Dutta et al. 2017; Wang et al. 2021b). For now, JMJ27 was mainly associated with the regulation of gene expression (Dutta et al. 2017; Wang et al. 2021b); thus, it cannot be excluded that JMJ27 also indirectly modulates the H3K9me2 content at chromocenter regions by regulating the expression of particular genes related to chromatin remodeling and DNA repair. Nevertheless, the transcriptome analysis of *jmj27* deficient plants did not reveal significant deregulation of such candidate genes (Wang et al. 2021b). Alternatively, the observed decrease in H3K9me2 content might be due to chromatin remodeling events, including a histone eviction process. Given that H3K27me1 contents did not show significant changes, the eviction mechanism would need to be specific to the H3K9me2 containing heterochromatin. Therefore, the most plausible explanation remains, an active demethylation process triggered by a H3K9me2 specific histone demethylase. This assumption is supported by the lack of detectable H3K9me2 decrease in *jmj27* mutant plants at 2h as well as their UV-C sensitivity.

In parallel, we found that plants lacking the 3 HMtases KYP, SUVH4/5 exhibit an increase of H3K9me2 content 2h upon UV-C exposure, suggesting that non-canonical HMTase(s) may exist and are activated in such stress conditions. Two putative candidates are the SUVR4 and SUVR5 HMTase, already described for their DNA methylation-independent H3K9 methyltransferase activity (Thorstensen et al. 2006; Caro et al. 2012).

The potential roles of KYP and JMJ27 in the repair of photodamage were strongly supported by our genetic approach. Indeed, we demonstrated that KYP and JMJ27 act together with DDB2 in both canonical and non-canonical GGR pathways. In addition, *kyp* and *jmj27* show a delay in photolesion removal. Thus, H3K9 di-methylation and active H3K9me2 demethylation most likely participate in GGR. Our data are in agreement with the reports showing an increase in H3K9me3 content in human cells upon UV exposure (Fortuny et al. 2021) and the KDM4B-dependent H3K9me3 demethylation acting in the NER in Drosophila (Palomera-Sanchez et al. 2010).

The behavior of heterochromatin during DNA repair relies on antagonist mechanisms. On the one hand, continuous silencing is essential to maintain genome integrity by avoiding TE reactivation (Lisch and Slotkin 2011). On the other hand, the dense heterochromatin structure hinders an efficient DNA repair process and thus needs to be decompacted (Schieferstein and Thoma 1998; Liu 2015). The fine-tuning of H3K9me2 occurring during the first step of GGR (photodamage recognition) reveals the complex Spatio-temporal regulation of chromatin structure enabling genome stability but allowing a transient release of the silencing that might lead to genome flexibility.

5.3.3. Factors involved in H3K9me2 homeostasis contribute to an efficient DDB2 chromatin loading

Considering the results of genetic interactions and photolesions removal assays, both KYP and JMJ27 participate in the GGR pathway upstream of DDB2. Interestingly, chromatin fractionation highlighted a significant decrease/delay of DDB2 chromatin loading in the absence of KYP, suggesting that H3K9me2 enhances the affinity of DDB2 to chromatin.

This result agrees with the role of DDB2 in recognizing photolesions in GGR acting in poorly transcribed and/or un-transcribed genomic regions known to contain high H3K9me2 level (Johann to Berens and Molinier 2020). Interestingly, in the *kyp* plants, we identified: low photolesions induction and weak DDB2 chromatin loading. This suggests that the reduced amount of H3K9me2 would prevent the formation of photolesions and could activate alternative DNA repair pathways (*i.e.* DR). These observations strengthen the emerging notion that the epigenome landscape would contribute to the photodamage formation and to the choice of the repair pathway to process these lesions (Johann to Berens and Molinier 2020). Interestingly, we also observed the localization of the UVR3 photolyase in constitutive heterochromatin in the first 2h following UV exposure. This reveals that the DR pathway likely acts genome-wide, including in heterochromatin.

Chromatin fractionation experiments allowed identifying that DDB2 loads rapidly in nucleosome-free DNA, whereas the core nucleosomal fraction is enriched later by DDB2. Our results fit with the data obtained in mammal cells, reporting the sequential DDB2 loading in internucleosomal regions followed later by its loading in the core nucleosome (Fei et al. 2011). In Drosophila, although it was elusive how the decrease of H3K9me3 triggered by the KDM4B histone demethylase is coupled to NER (Palomera-Sanchez et al. 2010), our study provides this potential connection. Indeed, we propose a model in which both DDB2 and JMJ27 cooperate as a molecular complex to trigger active H3K9me2 demethylation and chromatin relaxation. This complex allows DDB2 loading/stabilization at DNA-damaged sites located in high nucleosome occupancy loci that were initially weakly accessible (Fig. 14). It can be expected that H3K9me2 demethylation is among the first step in DDB2-dependent chromatin remodeling.

In mammals, stabilized DDB2 at damaged sites was shown to recruit the chromatin remodeler ALC1 (Pines et al. 2012; Wang et al. 2021a). Interestingly, reports about the role in DNA repair of its homolog, CHR10 (AtALC1), are still missing. Importantly, the chromatin relaxation observed upon UV-C exposure may reflect the combination of several mechanisms. Indeed, nucleosome sliding and histone eviction enable the recruitment of the full NER machinery together with active H3K9me2 demethylation (Zhao et al. 2009; Jiang et al. 2010; Luijsterburg et al. 2012; Pines et al. 2012).

In addition, we cannot exclude that UVR3 may participate in the heterochromatic DNA repair within the DDB2-JMJ27 relaxed chromatin microenvironments. Such a synergistic mode of action would enhance the repair efficiency by preventing a long-time window of chromatin relaxation, enabling an uncontrolled release of the silencing (*i.e.* TE mobilization).

The transient increase of H3K9me2 content may serve as an anchor for JMJ27 to load together with DDB2 for damage recognition (Fig. 14). Given that DDB2-JMJ27 complex formation is independent of UV irradiation and that the main loading of JMJ27 on chromatin was observed 30 min upon UV, H3K9me2 demethylation could also occur in particular euchromatic regions that would need to be characterized. This possibility holds true regarding the decrease in H3K9me2 signal intensity in the nucleoplasm, 2h upon UV-C, and the delayed repair of the 6,4-PP in JMJ27 deficient plants (Han et al. 2016). In addition, it is well established that DDD2 also recognizes mismatches, abasic sites…. (Wittschieben et al. 2005). Thus, the UV-independent DDB2-JMJ27 complex formation also indicates that active H3K9me2 demethylation may participate in the initiation of the excision repair of other types of DNA lesions.

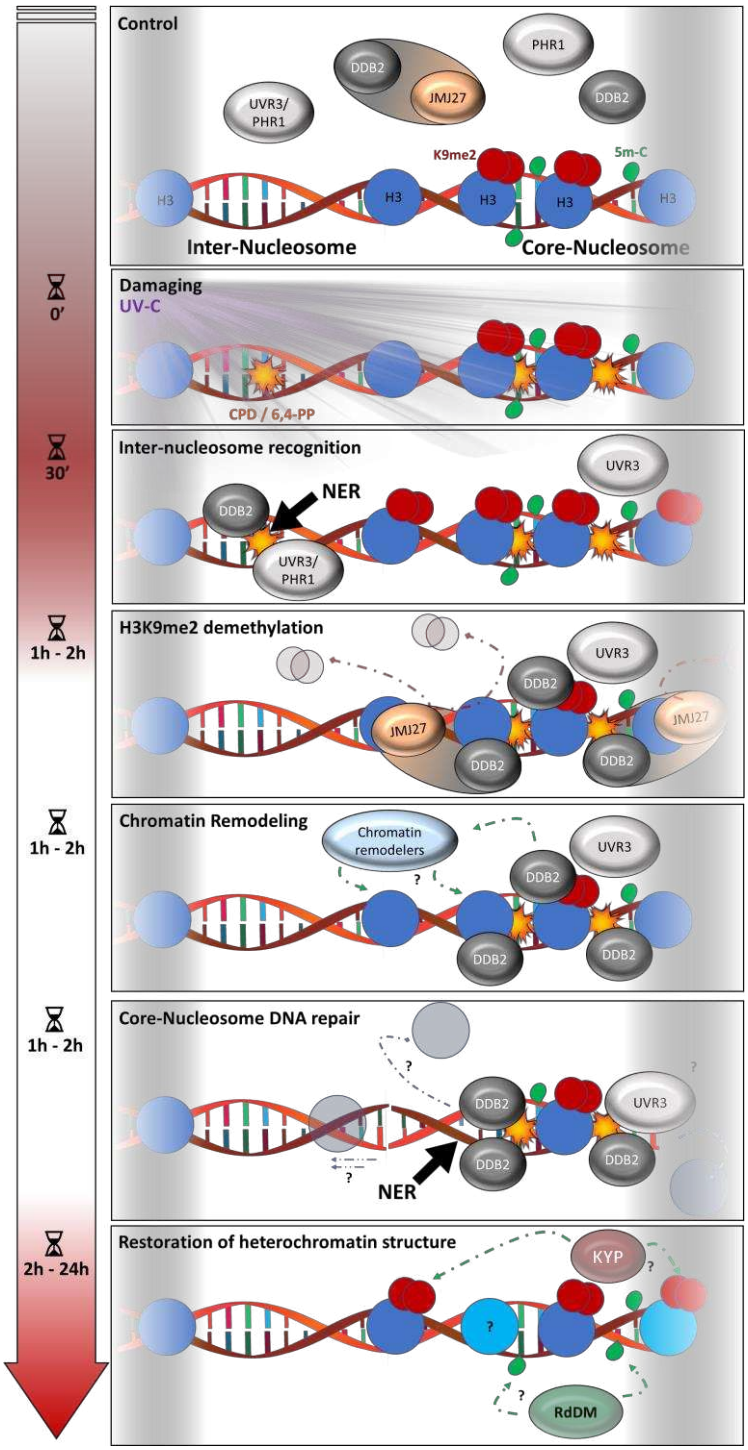

Figure 14: Model illustrating the interplay between photodamage repair and H3K9me2 dynamic upon UV-C exposure

UV-C irradiation induces CPD and 6,4-PPs in internucleosomal regions and in core nucleosomes carrying the H3K9me2 histone mark. 30 min upon UV-C exposure DDB2 and UVR3/PHR1 load at photodamages sites in internucleosomal regions. At 1h, the DDB2-JMJ27 complex is recruited to H3K9me2 enriched regions, and JMJ27 actively demethylated H3K9 me2 to ensure a stable binding of DDB2 to the damaged DNA wrapped into core nucleosomes. The H3K9me2 removal and DDB2 stabilization may induce the further recruitment of chromatin remodelers (*i.e.,* ALC1). The induced chromatin reshaping likely relies on the combination of nucleosome sliding

and eviction. Once an open chromatin microenvironment is built around the damaged site, DDB2 recruits the NER machinery. In parallel, the relaxed chromatin may favor the binding of UVR3 and PHR1 photolyases. After repair, heterochromatin structure is restored, with a slightly different DNA methylation landscape, a higher H3K9me2 content, and potentially different histone variants/ nucleosome occupancy.

5.4. Ongoing work

We provided evidence that GGR and regulation of H3K9me2 homeostasis act together to maintain genome and epigenome integrities upon UV-C exposure. In order to better characterize the precocious dynamics of epigenetic marks and the loading of the photodamage repair factors, several genome-wide analyses are being performed (Fig. 15). These approaches would allow to better decipher the kinetics of the epigenome landscape and the photodamage recognition/processing. Therefore, we are experimentally determining:

- How does the H3K9me2 landscape evolve in the first 2h following UV-C exposure?
- How does the DNA methylation landscape evolve in the first 2h following UV-C exposure?
- Where do DDB2 and UVR3 load?
- Do their loadings depend on the epigenetic landscape?

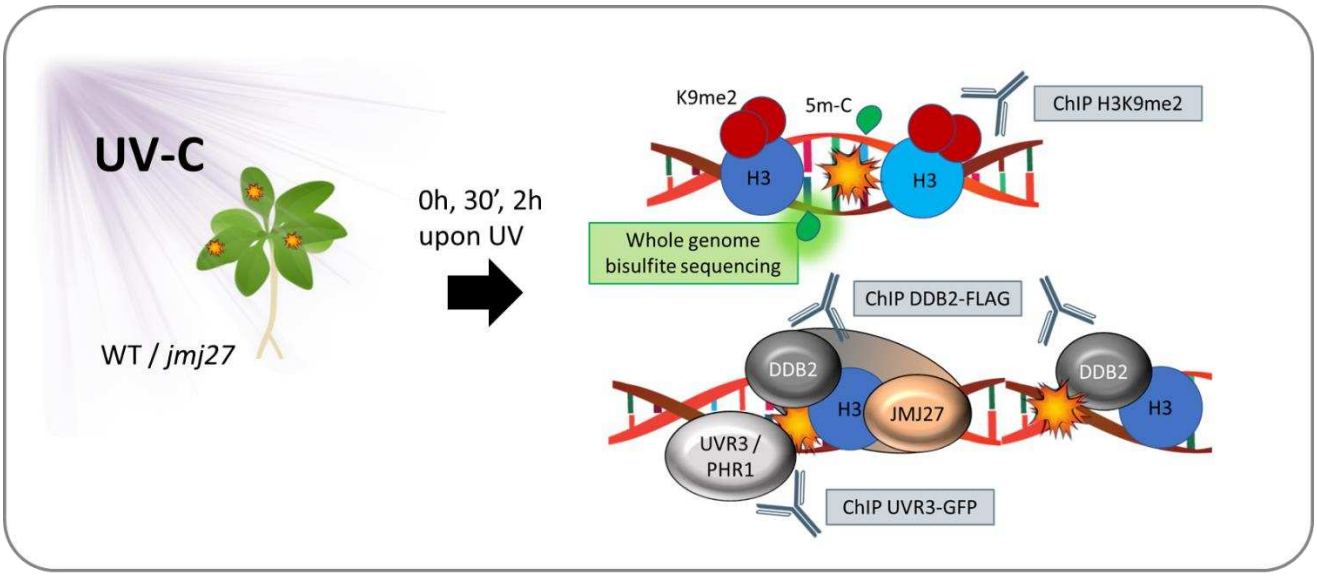

Figure 15: Graphical abstract of the ongoing experiments

H3K9me2 contents, DDB2, and UVR3 binding will be characterized by ChIP prior to UV-C irradiation, 30' and 2h upon UV-C exposure in WT and *jmj27* plants. DNA methylation landscape will be characterized in the same conditions.

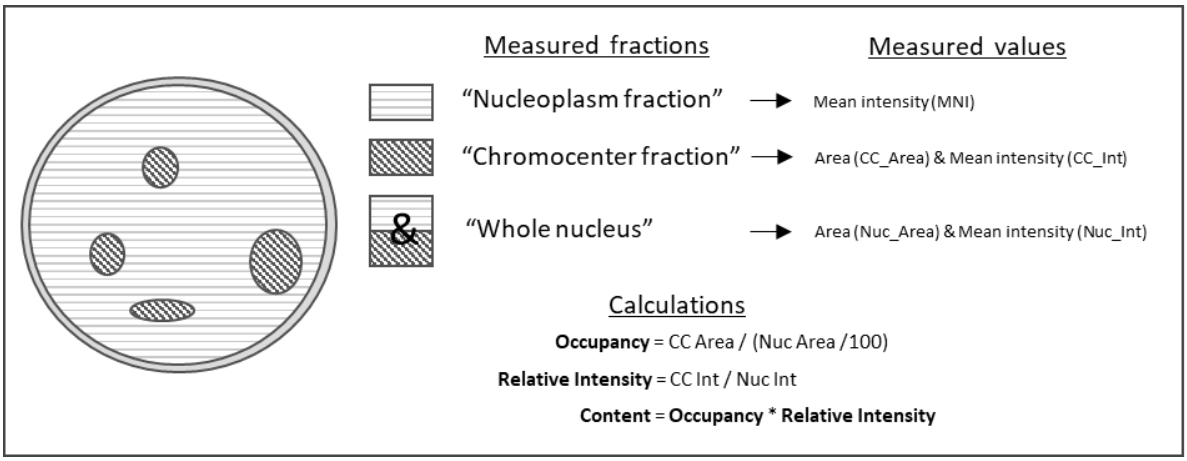

Supplemental Figure 1: Schematic representation of the measurements performed on microscopy images

Scheme of the different nuclear fractions and how their intensities and areas were used to calculate Mean intensity (MNI), Occupancy (OC), Relative Intensity (RI), and Content.

5.5. References

Agarwal P, Miller KM (2016) The nucleosome: orchestrating DNA damage signaling and repair within chromatin. Biochem Cell Biol 94:381–395. https://doi.org/10.1139/bcb-2016-0017

Ahmad M, Jarillo JA, Klimczak LJ, Landry LG, Peng T, Last RL, Cashmore AR (1997) An enzyme similar to animal type II photolyases mediates photoreactivation in Arabidopsis. Plant Cell 9:199–207. https://doi.org/10.1105/tpc.9.2.199

Al Khateeb WM, Sher AA, Marcus JM, Schroeder DF (2019) UVSSA, UBP12, and RDO2/TFIIS Contribute to Arabidopsis UV Tolerance. Front Plant Sci 10. https://doi.org/10.3389/fpls.2019.00516

Ashapkin VV, Kutueva LI, Vanyushin BF (2016) Plant DNA Methyltransferase Genes: Multiplicity, Expression, Methylation Patterns. Biochemistry (Mosc) 81:141–151. https://doi.org/10.1134/S0006297916020085

Balbo Pogliano C, Gatti M, Rüthemann P, Garajovà Z, Penengo L, Naegeli H (2017) ASH1L histone methyltransferase regulates the handoff between damage recognition factors in global-genome nucleotide excision repair. Nat Commun 8. https://doi.org/10.1038/s41467-017-01080-8

Banyasz A, Esposito L, Douki T, Perron M, Lepori C, Improta R, Markovitsi D (2016) Effect of C5-Methylation of Cytosine on the UV-Induced Reactivity of Duplex DNA: Conformational and Electronic Factors. J Phys Chem B 120:4232–4242. https://doi.org/10.1021/acs.jpcb.6b03340

Baumbusch LO, Thorstensen T, Krauss V, Fischer A, Naumann K, Assalkhou R, Schulz I, Reuter G, Aalen RB (2001) The Arabidopsis thaliana genome contains at least 29 active genes encoding SET domain proteins that can be assigned to four evolutionarily conserved classes. Nucleic Acids Res 29:4319–4333. https://doi.org/10.1093/nar/29.21.4319

Bucceri A, Kapitza K, Thoma F (2006) Rapid accessibility of nucleosomal DNA in yeast on a second time scale. EMBO J 25:3123–3132. https://doi.org/10.1038/sj.emboj.7601196

Burton A, Brochard V, Galan C, Ruiz-Morales ER, Rovira Q, Rodriguez-Terrones D, Kruse K, Le Gras S, Udayakumar VS, Chin HG, Eid A, Liu X, Wang C, Gao S, Pradhan S, Vaquerizas JM, Beaujean N, Jenuwein T, Torres-Padilla M-E (2020) Heterochromatin establishment during early mammalian development is regulated by pericentromeric RNA and characterized by non-repressive H3K9me3. Nat Cell Biol 22:767–778. https://doi.org/10.1038/s41556-020-0536-6

Caro E, Stroud H, Greenberg MVC, Bernatavichute YV, Feng S, Groth M, Vashisht AA, Wohlschlegel J, Jacobsen SE (2012) The SET-domain protein SUVR5 mediates H3K9me2 deposition and silencing at stimulus response genes in a DNA methylation-independent manner. PLoS Genet 8:e1002995. https://doi.org/10.1371/journal.pgen.1002995

Cavadini S, Fischer ES, Bunker RD, Potenza A, Lingaraju GM, Goldie KN, Mohamed WI, Faty M, Petzold G, Beckwith REJ, Tichkule RB, Hassiepen U, Abdulrahman W, Pantelic RS, Matsumoto S, Sugasawa K, Stahlberg H, Thomä NH (2016) Cullin–RING ubiquitin E3 ligase regulation by the COP9 signalosome. Nature 531:598–603. https://doi.org/10.1038/nature17416

Chakraborty U, Shen Z-J, Tyler J (2021) Chaperoning histones at the DNA repair dance. DNA Repair (Amst) 108:103240. https://doi.org/10.1016/j.dnarep.2021.103240

Chan C, Zimmerli L (2019) The Histone Demethylase IBM1 Positively Regulates Arabidopsis Immunity by Control of Defense Gene Expression. Front Plant Sci 10:1587. https://doi.org/10.3389/fpls.2019.01587

Conconi A, Bespalov VA, Smerdon MJ (2002) Transcription-coupled repair in RNA polymerase I-transcribed genes of yeast. Proc Natl Acad Sci U S A 99:649–654. https://doi.org/10.1073/pnas.022373099

Dinant C, Bartek J, Bekker-Jensen S (2012) Histone Displacement during Nucleotide Excision Repair. International Journal of Molecular Sciences 13:13322–13337. https://doi.org/10.3390/ijms131013322

Duan M-R, Smerdon MJ (2010) UV damage in DNA promotes nucleosome unwrapping. J Biol Chem 285:26295–26303. https://doi.org/10.1074/jbc.M110.140087

Dutta A, Choudhary P, Caruana J, Raina R (2017) JMJ27, an Arabidopsis H3K9 histone demethylase, modulates defense against Pseudomonas syringae and flowering time. Plant J 91:1015–1028. https://doi.org/10.1111/tpj.13623

Ebbs ML, Bender J (2006) Locus-specific control of DNA methylation by the Arabidopsis SUVH5 histone methyltransferase. Plant Cell 18:1166–1176. https://doi.org/10.1105/tpc.106.041400

Fan D, Dai Y, Wang X, Wang Z, He H, Yang H, Cao Y, Deng XW, Ma L (2012) IBM1, a JmjC domain-containing histone demethylase, is involved in the regulation of RNA-directed DNA methylation through the epigenetic control of RDR2 and DCL3 expression in Arabidopsis. Nucleic Acids Res 40:8905–8916. https://doi.org/10.1093/nar/gks647

Fei J, Kaczmarek N, Luch A, Glas A, Carell T, Naegeli H (2011) Regulation of nucleotide excision repair by UV-DDB: prioritization of damage recognition to internucleosomal DNA. PLoS Biol 9:e1001183. https://doi.org/10.1371/journal.pbio.1001183

Fortuny A, Chansard A, Caron P, Chevallier O, Leroy O, Renaud O, Polo SE (2021) Imaging the response to DNA damage in heterochromatin domains reveals core principles of heterochromatin maintenance. Nat Commun 12:2428. https://doi.org/10.1038/s41467-021-22575-5

Gale JM, Nissen KA, Smerdon MJ (1987) UV-induced formation of pyrimidine dimers in nucleosome core DNA is strongly modulated with a period of 10.3 bases. Proc Natl Acad Sci USA 84:6644–6648. https://doi.org/10.1073/pnas.84.19.6644

Gale JM, Smerdon MJ (1990) UV induced (6-4) photoproducts are distributed differently than cyclobutane dimers in nucleosomes. Photochem Photobiol 51:411–417. https://doi.org/10.1111/j.1751-1097.1990.tb01732.x

Graindorge S, Cognat V, Johann to Berens P, Mutterer J, Molinier J (2019) Photodamage repair pathways contribute to the accurate maintenance of the DNA methylome landscape upon UV exposure. PLoS Genet 15:e1008476. https://doi.org/10.1371/journal.pgen.1008476

Guintini L, Charton R, Peyresaubes F, Thoma F, Conconi A (2015) Nucleosome positioning, nucleotide excision repair and photoreactivation in Saccharomyces cerevisiae. DNA Repair 36:98–104. https://doi.org/10.1016/j.dnarep.2015.09.012

Han C, Srivastava AK, Cui T, Wang Q-E, Wani AA (2016) Differential DNA lesion formation and repair in heterochromatin and euchromatin. Carcinogenesis 37:129–138. https://doi.org/10.1093/carcin/bgv247

Hauer MH, Gasser SM (2017) Chromatin and nucleosome dynamics in DNA damage and repair. Genes Dev 31:2204–2221. https://doi.org/10.1101/gad.307702.117

Hung F-Y, Chen J-H, Feng Y-R, Lai Y-C, Yang S, Wu K (2020) Arabidopsis JMJ29 is involved in trichome development by regulating the core trichome initiation gene GLABRA3. The Plant Journal 103:1735–1743. https://doi.org/10.1111/tpj.14858

Jackson JP, Lindroth AM, Cao X, Jacobsen SE (2002) Control of CpNpG DNA methylation by the KRYPTONITE histone H3 methyltransferase. Nature 416:556–560. https://doi.org/10.1038/nature731

Jacob Y, Bergamin E, Donoghue MTA, Mongeon V, LeBlanc C, Voigt P, Underwood CJ, Brunzelle JS, Michaels SD, Reinberg D, Couture J-F, Martienssen RA (2014) Selective methylation of histone H3 variant H3.1 regulates heterochromatin replication. Science 343:1249–1253. https://doi.org/10.1126/science.1248357

Jacob Y, Feng S, LeBlanc CA, Bernatavichute YV, Stroud H, Cokus S, Johnson LM, Pellegrini M, Jacobsen SE, Michaels SD (2009) ATXR5 and ATXR6 are H3K27 monomethyltransferases required for chromatin structure and gene silencing. Nat Struct Mol Biol 16:763–768. https://doi.org/10.1038/nsmb.1611

Jeon H-Y, Hussain A, Qi J (2020) Role of H3K9 demethylases in DNA double-strand break repair. J Cancer Biol 1:10–15. https://doi.org/10.46439/cancerbiology.1.003

Jiang Y, Wang X, Bao S, Guo R, Johnson DG, Shen X, Li L (2010) INO80 chromatin remodeling complex promotes the removal of UV lesions by the nucleotide excision repair pathway. Proc Natl Acad Sci U S A 107:17274–17279. https://doi.org/10.1073/pnas.1008388107

Jiao L, Liu X (2015) Structural basis of histone H3K27 trimethylation by an active polycomb repressive complex 2. Science 350:aac4383. https://doi.org/10.1126/science.aac4383

Johann to Berens P, Molinier J (2020) Formation and Recognition of UV-Induced DNA Damage within Genome Complexity. Int J Mol Sci 21. https://doi.org/10.3390/ijms21186689

Jones KL, Zhang L, Seldeen KL, Gong F (2010) Detection of bulky DNA lesions: DDB2 at the interface of chromatin and DNA repair in eukaryotes. IUBMB Life 62:803–811. https://doi.org/10.1002/iub.391

Kabi M, Filion GJ (2021) Heterochromatin: did H3K9 methylation evolve to tame transposons? Genome Biol 22:325. https://doi.org/10.1186/s13059-021-02550-5

Kari V, Raul SK, Henck JM, Kitz J, Kramer F, Kosinsky RL, Übelmesser N, Mansour WY, Eggert J, Spitzner M, Najafova Z, Bastians H, Grade M, Gaedcke J, Wegwitz F, Johnsen SA (2019) The histone methyltransferase DOT1L is required for proper DNA damage response, DNA repair, and modulates chemotherapy responsiveness. Clin Epigenetics 11:4. https://doi.org/10.1186/s13148-018-0601-1

Katarzyna Banas A, Hermanowicz P, Sztatelman O, Labuz J, Aggarwal C, Zglobicki P, Jagiello-Flasinska D, Strzalka W (2018) 6,4-PP Photolyase Encoded by AtUVR3 is Localized in Nuclei, Chloroplasts and Mitochondria and its Expression is Down-Regulated by Light in a Photosynthesis-Dependent Manner. Plant Cell Physiol 59:44–57. https://doi.org/10.1093/pcp/pcx159

Kim MY, Zilberman D (2014) DNA methylation as a system of plant genomic immunity. Trends Plant Sci 19:320–326. https://doi.org/10.1016/j.tplants.2014.01.014

Kuhlmann M, Mette MF (2012) Developmentally non-redundant SET domain proteins SUVH2 and SUVH9 are required for transcriptional gene silencing in Arabidopsis thaliana. Plant Mol Biol 79:623–633. https://doi.org/10.1007/s11103-012-9934-x

Law JA, Du J, Hale CJ, Feng S, Krajewski K, Palanca AMS, Strahl BD, Patel DJ, Jacobsen SE (2013) Polymerase IV occupancy at RNA-directed DNA methylation sites requires SHH1. Nature 498:385–389. https://doi.org/10.1038/nature12178

Li X, Harris CJ, Zhong Z, Chen W, Liu R, Jia B, Wang Z, Li S, Jacobsen SE, Du J (2018) Mechanistic insights into plant SUVH family H3K9 methyltransferases and their binding to context-biased non-CG DNA methylation. Proc Natl Acad Sci U S A 115:E8793–E8802. https://doi.org/10.1073/pnas.1809841115

Lisch D, Slotkin RK (2011) Strategies for silencing and escape: the ancient struggle between transposable elements and their hosts. Int Rev Cell Mol Biol 292:119–152. https://doi.org/10.1016/B978-0-12-386033-0.00003-7

Liu X (2015) In vitro chromatin templates to study nucleotide excision repair. DNA Repair (Amst) 36:68–76. https://doi.org/10.1016/j.dnarep.2015.09.026

Luijsterburg MS, Goedhart J, Moser J, Kool H, Geverts B, Houtsmuller AB, Mullenders LHF, Vermeulen W, van Driel R (2007) Dynamic in vivo interaction of DDB2 E3 ubiquitin ligase with UV-damaged DNA is independent of damage-recognition protein XPC. J Cell Sci 120:2706–2716. https://doi.org/10.1242/jcs.008367

Luijsterburg MS, Lindh M, Acs K, Vrouwe MG, Pines A, van Attikum H, Mullenders LH, Dantuma NP (2012) DDB2 promotes chromatin decondensation at UV-induced DNA damage. J Cell Biol 197:267–281. https://doi.org/10.1083/jcb.201106074

Ma Z, Castillo-González C, Wang Z, Sun D, Hu X, Shen X, Potok ME, Zhang X (2018) Arabidopsis Serrate Coordinates Histone Methyltransferases ATXR5/6 and RNA Processing Factor RDR6 to Regulate Transposon Expression. Dev Cell 45:769-784.e6. https://doi.org/10.1016/j.devcel.2018.05.023

Matsumoto S, Cavadini S, Bunker RD, Grand RS, Potenza A, Rabl J, Yamamoto J, Schenk AD, Schübeler D, Iwai S, Sugasawa K, Kurumizaka H, Thomä NH (2019) DNA damage detection in nucleosomes involves DNA register shifting. Nature 571:79–84. https://doi.org/10.1038/s41586-019-1259-3

Miura A, Nakamura M, Inagaki S, Kobayashi A, Saze H, Kakutani T (2009) An Arabidopsis jmjC domain protein protects transcribed genes from DNA methylation at CHG sites. EMBO J 28:1078–1086. https://doi.org/10.1038/emboj.2009.59

Molinier J, Lechner E, Dumbliauskas E, Genschik P (2008) Regulation and Role of Arabidopsis CUL4-DDB1A-DDB2 in Maintaining Genome Integrity upon UV Stress. PLoS Genet 4. https://doi.org/10.1371/journal.pgen.1000093

Molinier J, Ramos C, Fritsch O, Hohn B (2004) CENTRIN2 modulates homologous recombination and nucleotide excision repair in Arabidopsis. Plant Cell 16:1633–1643. https://doi.org/10.1105/tpc.021378

Nakajima S, Sugiyama M, Iwai S, Hitomi K, Otoshi E, Kim ST, Jiang CZ, Todo T, Britt AB, Yamamoto K (1998) Cloning and characterization of a gene (UVR3) required for photorepair of 6-4 photoproducts in Arabidopsis thaliana. Nucleic Acids Res 26:638–644. https://doi.org/10.1093/nar/26.2.638

Naumann K, Fischer A, Hofmann I, Krauss V, Phalke S, Irmler K, Hause G, Aurich A-C, Dorn R, Jenuwein T, Reuter G (2005) Pivotal role of AtSUVH2 in heterochromatic histone methylation and gene silencing in Arabidopsis. EMBO J 24:1418–1429. https://doi.org/10.1038/sj.emboj.7600604

Nodelman IM, Bowman GD (2021) Biophysics of Chromatin Remodeling. Annu Rev Biophys 50:73–93. https://doi.org/10.1146/annurev-biophys-082520-080201

Palomera-Sanchez Z, Bucio-Mendez A, Valadez-Graham V, Reynaud E, Zurita M (2010) Drosophila p53 is required to increase the levels of the dKDM4B demethylase after UV-induced DNA damage to demethylate histone H3 lysine 9. J Biol Chem 285:31370–31379. https://doi.org/10.1074/jbc.M110.128462

Pines A, Vrouwe MG, Marteijn JA, Typas D, Luijsterburg MS, Cansoy M, Hensbergen P, Deelder A, de Groot A, Matsumoto S, Sugasawa K, Thoma N, Vermeulen W, Vrieling H, Mullenders L (2012) PARP1 promotes nucleotide excision repair through DDB2 stabilization and recruitment of ALC1. J Cell Biol 199:235–249. https://doi.org/10.1083/jcb.201112132

Potok ME, Zhong Z, Picard CL, Liu Q, Do T, Jacobsen CE, Sakr O, Naranbaatar B, Thilakaratne R, Khnkoyan Z, Purl M, Cheng H, Vervaet H, Feng S, Rayatpisheh S, Wohlschlegel JA, O'Malley RC, Ecker JR, Jacobsen SE (2022) The role of ATXR6 expression in modulating genome stability and transposable element repression in Arabidopsis. Proc Natl Acad Sci U S A 119:e2115570119. https://doi.org/10.1073/pnas.2115570119

Rastogi RP, Richa, Kumar A, Tyagi MB, Sinha RP (2010) Molecular Mechanisms of Ultraviolet Radiation-Induced DNA Damage and Repair. J Nucleic Acids 2010. https://doi.org/10.4061/2010/592980

Rochette PJ, Lacoste S, Therrien J-P, Bastien N, Brash DE, Drouin R (2009) Influence of cytosine methylation on ultraviolet-induced cyclobutane pyrimidine dimer formation in genomic DNA. Mutat Res 665:7–13. https://doi.org/10.1016/j.mrfmmm.2009.02.008

Roudier F, Ahmed I, Bérard C, Sarazin A, Mary-Huard T, Cortijo S, Bouyer D, Caillieux E, Duvernois-Berthet E, Al-Shikhley L, Giraut L, Després B, Drevensek S, Barneche F, Dèrozier S, Brunaud V, Aubourg S, Schnittger A, Bowler C, Martin-Magniette M-L, Robin S, Caboche M, Colot V (2011) Integrative epigenomic mapping defines four main chromatin states in Arabidopsis. EMBO J 30:1928–1938. https://doi.org/10.1038/emboj.2011.103

Saze H, Shiraishi A, Miura A, Kakutani T (2008) Control of genic DNA methylation by a jmjC domain-containing protein in Arabidopsis thaliana. Science 319:462–465. https://doi.org/10.1126/science.1150987

Schalk C, Cognat V, Graindorge S, Vincent T, Voinnet O, Molinier J (2017) Small RNA-mediated repair of UV-induced DNA lesions by the DNA DAMAGE-BINDING PROTEIN 2 and ARGONAUTE 1. Proc Natl Acad Sci U S A 114:E2965–E2974. https://doi.org/10.1073/pnas.1618834114

Schalk C, Drevensek S, Kramdi A, Kassam M, Ahmed I, Cognat V, Graindorge S, Bergdoll M, Baumberger N, Heintz D, Bowler C, Genschik P, Barneche F, Colot V, Molinier J (2016) DNA DAMAGE BINDING PROTEIN2 Shapes the DNA Methylation Landscape. Plant Cell 28:2043–2059. https://doi.org/10.1105/tpc.16.00474

Schalk C, Molinier J (2016) Global Genome Repair factors controls DNA methylation patterns in Arabidopsis. Plant Signal Behav 11:e1253648. https://doi.org/10.1080/15592324.2016.1253648

Schick S, Fournier D, Thakurela S, Sahu SK, Garding A, Tiwari VK (2015) Dynamics of chromatin accessibility and epigenetic state in response to UV damage. J Cell Sci 128:4380–4394. https://doi.org/10.1242/jcs.173633

Schieferstein U, Thoma F (1998) Site-specific repair of cyclobutane pyrimidine dimers in a positioned nucleosome by photolyase and T4 endonuclease V in vitro. EMBO J 17:306–316. https://doi.org/10.1093/emboj/17.1.306

Sharma AK, Hendzel MJ (2019) The relationship between histone posttranslational modification and DNA damage signaling and repair. Int J Radiat Biol 95:382–393. https://doi.org/10.1080/09553002.2018.1516911

Shu H, Wildhaber T, Siretskiy A, Gruissem W, Hennig L (2012) Distinct modes of DNA accessibility in plant chromatin. Nat Commun 3:1281. https://doi.org/10.1038/ncomms2259

Soria G, Polo SE, Almouzni G (2012) Prime, repair, restore: the active role of chromatin in the DNA damage response. Mol Cell 46:722–734. https://doi.org/10.1016/j.molcel.2012.06.002

Stroud H, Do T, Du J, Zhong X, Feng S, Johnson L, Patel DJ, Jacobsen SE (2014) Non-CG methylation patterns shape the epigenetic landscape in Arabidopsis. Nat Struct Mol Biol 21:64–72. https://doi.org/10.1038/nsmb.2735

Sugasawa K, Okuda Y, Saijo M, Nishi R, Matsuda N, Chu G, Mori T, Iwai S, Tanaka K, Tanaka K, Hanaoka F (2005) UV-induced ubiquitylation of XPC protein mediated by UV-DDB-ubiquitin ligase complex. Cell 121:387–400. https://doi.org/10.1016/j.cell.2005.02.035

Thorstensen T, Fischer A, Sandvik SV, Johnsen SS, Grini PE, Reuter G, Aalen RB (2006) The Arabidopsis SUVR4 protein is a nucleolar histone methyltransferase with preference for monomethylated H3K9. Nucleic Acids Res 34:5461–5470. https://doi.org/10.1093/nar/gkl687

Tripuraneni V, Memisoglu G, MacAlpine HK, Tran TQ, Zhu W, Hartemink AJ, Haber JE, MacAlpine DM (2021) Local nucleosome dynamics and eviction following a double-strand break are reversible by NHEJ-mediated repair in the absence of DNA replication. Genome Res 31:775–788. https://doi.org/10.1101/gr.271155.120

Veiseth SV, Rahman MA, Yap KL, Fischer A, Egge-Jacobsen W, Reuter G, Zhou M-M, Aalen RB, Thorstensen T (2011) The SUVR4 histone lysine methyltransferase binds ubiquitin and converts H3K9me1 to H3K9me3 on transposon chromatin in Arabidopsis. PLoS Genet 7:e1001325. https://doi.org/10.1371/journal.pgen.1001325

Wang H, Zhai L, Xu J, Joo H-Y, Jackson S, Erdjument-Bromage H, Tempst P, Xiong Y, Zhang Y (2006) Histone H3 and H4 Ubiquitylation by the CUL4-DDB-ROC1 Ubiquitin Ligase Facilitates Cellular Response to DNA Damage. Molecular Cell 22:383–394. https://doi.org/10.1016/j.molcel.2006.03.035

Wang L, Chen K, Chen Z (2021a) Structural basis of ALC1/CHD1L autoinhibition and the mechanism of activation by the nucleosome. Nat Commun 12:4057. https://doi.org/10.1038/s41467-021-24320-4

Wang L, Gao Y, Zheng X, Liu C, Dong S, Li R, Zhang G, Wei Y, Qu H, Li Y, Allis CD, Li G, Li H, Li P (2019) Histone Modifications Regulate Chromatin Compartmentalization by Contributing to a Phase Separation Mechanism. Mol Cell 76:646-659.e6. https://doi.org/10.1016/j.molcel.2019.08.019

Wang Q, Liu P, Jing H, Zhou XF, Zhao B, Li Y, Jin JB (2021b) JMJ27-mediated histone H3K9 demethylation positively regulates drought-stress responses in Arabidopsis. New Phytol 232:221–236. https://doi.org/10.1111/nph.17593

Waters R, van Eijk P, Reed S (2015) Histone modification and chromatin remodeling during NER. DNA Repair (Amst) 36:105–113. https://doi.org/10.1016/j.dnarep.2015.09.013

Wei KH-C, Chan C, Bachtrog D (2021) Establishment of H3K9me3-dependent heterochromatin during embryogenesis in Drosophila miranda. eLife 10:e55612. https://doi.org/10.7554/eLife.55612

Winter D, Vinegar B, Nahal H, Ammar R, Wilson GV, Provart NJ (2007) An "Electronic Fluorescent Pictograph" browser for exploring and analyzing large-scale biological data sets. PLoS One 2:e718. https://doi.org/10.1371/journal.pone.0000718

Wittschieben BØ, Iwai S, Wood RD (2005) DDB1-DDB2 (Xeroderma Pigmentosum Group E) Protein Complex Recognizes a Cyclobutane Pyrimidine Dimer, Mismatches, Apurinic/Apyrimidinic Sites, and Compound Lesions in DNA. J Biol Chem 280:39982–39989. https://doi.org/10.1074/jbc.M507854200

Xu L, Jiang H (2020) Writing and Reading Histone H3 Lysine 9 Methylation in Arabidopsis. Frontiers in Plant Science 11

Zhang C, Du X, Tang K, Yang Z, Pan L, Zhu P, Luo J, Jiang Y, Zhang H, Wan H, Wang X, Wu F, Tao WA, He X-J, Zhang H, Bressan RA, Du J, Zhu J-K (2018) Arabidopsis AGDP1 links H3K9me2 to DNA methylation in heterochromatin. Nat Commun 9:4547. https://doi.org/10.1038/s41467-018-06965-w

Zhang M, Wang L, Zhong D (2017) Photolyase: Dynamics and Electron-Transfer Mechanisms of DNA repair. Arch Biochem Biophys 632:158–174. https://doi.org/10.1016/j.abb.2017.08.007

Zhao Q, Wang Q-E, Ray A, Wani G, Han C, Milum K, Wani AA (2009) Modulation of Nucleotide Excision Repair by Mammalian SWI/SNF Chromatin-remodeling Complex. J Biol Chem 284:30424–30432. https://doi.org/10.1074/jbc.M109.044982

Zhao S, Cheng L, Gao Y, Zhang B, Zheng X, Wang L, Li P, Sun Q, Li H (2019) Plant HP1 protein ADCP1 links multivalent H3K9 methylation readout to heterochromatin formation. Cell Res 29:54–66. https://doi.org/10.1038/s41422-018-0104-9

Zhu B, Chen S, Wang H, Yin C, Han C, Peng C, Liu Z, Wan L, Zhang X, Zhang J, Lian CG, Ma P, Xu Z-X, Prince S, Wang T, Gao X, Shi Y, Liu D, Liu M, Wei W, Wei Z, Pan J, Wang Y, Xuan Z, Hess J, Hayward NK, Goding CR, Chen X, Zhou J, Cui R (2018) The protective role of DOT1L in UV-induced melanomagenesis. Nat Commun 9:259. https://doi.org/10.1038/s41467-017-02687-7

6. Chapter IV - UV-B exposure of Arabidopsis natural variants and parental memory

6.1. Introduction

Previous chapters described the impact of UV-C and proton irradiations on the shaping of constitutive heterochromatin (*i.e.,* chromocenters). Both induce changes in chromocenter structure 24h upon exposure (Chapter I). In the case of UV-C, these alterations go along with the remodeling of the epigenetic landscape. DNA methylation and the histone PTM H3K9me2 were previously shown to undergo a dynamic upon UV-C exposure, at least partially, and are related to the photodamage repair pathways (Chapter I and III). However, given that proton irradiation also induces chromocenter reshaping 24h upon exposure, photolesions are not the only type of DNA damage-inducing constitutive heterochromatin reshaping (Chapter I). Hence, it can be hypothesized that the oxidatively-induced DNA damage also affects the epigenetic landscape. Interestingly, as previously introduced, UV-B induces concomitantly photolesions and oxidative stress (Schuch et al. 2017). However, the amount of UV-B-induced photolesions is lower compared to UV-C and the oxidative burst is reduced compared to proton irradiation. Despite such quantitative differences, UV-B irradiation represents an environmental source of DNA damage, combining different types of stresses. Thus, it can be questioned how chromocenters structure evolves upon exposure to this biological relevant genotoxic stress. In addition, several studies revealed robust correlations between light perception, light intensity, and chromocenter shape (Tessadori et al. 2009; Snoek et al. 2017). However, the consequence of the exposure to specific wavelengths such as UV-B was not deeply investigated yet.

As a naturally occurring irradiation, UV-B brings some interesting additional aspects into our working model. For example, plants sense UV-B through the photoreceptor UVR8 (Kliebenstein et al. 2002), enabling the activation of specific cellular mechanisms (physiological adaptation, choice of the repair process...). In the absence of UV-B, UVR8 is present in the cytoplasm as homodimers (Kaiserli and Jenkins 2007; Tossi et al. 2019; Liang et al. 2019).

When activated by UV-B, UVR8 changes its quaternary structure, becoming an active monomer and interreacts with several nuclear partners (Kaiserli and Jenkins 2007; Tossi et al. 2019; Liang et al. 2019). A main target of UVR8 is the Constitutively Photomorphogenic 1 protein (COP1), part of an E3 ubiquitin ligase complex (Lau and Deng 2012). COP1 binding hinders the E3 ubiquitin ligase activity, preventing the ubiquitination and subsequent degradation of ELONGATED HYPOCOTYL 5 (HY5) and HY5 HOMOLOG (HYH), activators of UV-B responsive genes (Cloix et al. 2012). UVR8 monomers also interact with the transcription factors BIM1 (BES1-INTERACTING MYC-LIKE 1) and BES1 (BRI1-EMS-SUPPRESSOR1), regulating Brassinosteroids signaling and promoting hypocotyl growth in the absence of UV-B (Liang et al. 2018).

Interestingly, UVR8 was also described as a potential activator of the PHR1, photolyase, expression (Li et al. 2015), highlighting its role in prioritizing specific DNA repair pathways. Recently, UVR8 was also shown to be involved in the modulation of the DNA methylation landscape. Indeed, UVR8 active monomers can bind DRM2 in the nucleus, inhibiting its DNA methylation activity (Jiang et al. 2021). Thus, UV-B sensing by UVR8 was reported to induce hypomethylation, especially at TE (Jiang et al. 2021). The changes in DNA methylation observed upon UV-B irradiation appear to be enriched in chromocenter regions and rely on DRM2 (Jiang et al. 2021). In addition to its regulatory role in DNA methylation, UVR8 was reported to induce both H3K9 and H3K14 acetylation at several light-responsive genes, such as PHR1 and HYH (Velanis et al. 2016). However, the exact mechanisms by which UVR8 induces these histone PTMs remains unknown (Velanis et al. 2016). In extension, UV-B and UVR8 could also be considered as putative regulators of the epigenetic landscape in constitutive heterochromatin.

Another aspect of UV-B signaling/response is the specific evolution and adaptation of plants that undergo recurrent exposure to the genotoxic effect of the UV-B wavelength. Deciphering the pathways that differentially act in Arabidopsis plants originating from different ecological niches, exposed to particular UV-B regimes, would provide some clues about the biological mechanisms that may have contributed to efficiently cope with this stress (Latta 2010).

A driver of adaptation would be a stress-induced epigenetic memory, which sometimes could even be inherited in the offspring (D'Urso and Brickner 2014; Ashe et al. 2021). UVR8 was recently shown to enhance the establishment of short-term memory (3 days) by transcriptional priming of UV-B responsive genes (Xiong et al. 2021). Studies on clonal plants, such as *Glechoma longituba,* show the existence of an epigenetic memory maintained in genic regions upon UV-B exposure of the parents (Zhang et al. 2021). However, no molecular mechanisms of UV-B-induced parental or transgenerational memory (PTGM) have been described yet. Few examples of epigenetic PTGM in response to abiotic stress have been reported for now (D'Urso and Brickner 2014). A recently characterized model is the heat-memory, driving early flowering in the progeny, through an interplay between the H3K27me3 demethylase RELATIVE OF EARLY FLOWERING 6 (REF6), the HEAT SHOCK TRANSCRIPTION FACTOR A2 (HSFA2), and a tasiRNA (Liu et al. 2019). Unfortunately, even here, the exact mechanism by which the feedback loop is primarily transmitted to the offspring remains unclear (Liu et al. 2019). However, considering these reports together, as well as the environmental cues, it can be expected that UV-B may somehow induce an epigenetic PTGM.

In order to better characterize the adaptive processes to environmental cues, the analysis of hundreds of natural accessions variants of Arabidopsis recently emerged (Ossowski et al. 2008; Weigel and Mott 2009; Gan et al. 2011; Schmitz et al. 2013). Such large-scale resources provide potent tools for ecological and evolutionary studies (Kawakatsu et al. 2016). The 1.001 genome project, for example, gives access to genome sequences, transcriptome and methylome data sets of hundreds of different Arabidopsis ecotypes (Weigel and Mott 2009; Kawakatsu et al. 2016). The methylomes of Arabidopsis natural accessions are correlated with geography and climate of origin (Kawakatsu et al. 2016). Especially, the DNA methylation levels within TEs were positively correlated with latitude (Kawakatsu et al. 2016). In other words, high light intensities / high UV exposure likely participate in the modulation of DNA methylation at TE. This fits with the previous observation that variation in light exposure induces changes in chromocenter structure, where TE are enriched (Tessadori et al. 2009).

Nevertheless, the link(s) between the naturally occurring UV-B regime, DNA methylation, and constitutive heterochromatin structure were not investigated yet. In parallel, the global UV-B radiation data set for macroecological studies are available and would help to perform correlative studies (Beckmann et al. 2014).

Altogether, these observations and resources pave the way for future studies, focusing on the characterization between UV-B and the natural adaptation of *Arabidopsis thaliana* accessions. The following experiments aim at determining whether UV-B, as a biological relevant environmental factor, impacts constitutive heterochromatin shape in different Arabidopsis accessions. To this end, we first investigated whether UV-B can induce chromocenter dynamics. Additionally, Arabidopsis natural accessions exposed to various UV-B regimes were analyzed for UV-B chromocenter shapes and specific transcriptional priming. Finally, the inheritance of chromocenter dynamics will be questioned, using inter-ecotype hybrids and a UV-B-directed evolution approach.

6.2. Results

6.2.1 UV-B and chromocenter shape

We showed the effect of UV-C on chromocenter shape and its epigenetic landscape (Chapters I and III). Interestingly, this dynamic seems to depend, at least, on DDB2 and photolyases (UVR3 and PHR1), which are known to be also involved in the repair of UV-B induced photodamage (Biedermann and Hellmann 2010; Vechtomova et al. 2020). Thus, this observation addresses the broader question related to the effect of the biologically more relevant UV-B wavelength on chromatin shape : "Does UV-B also affect the constitutive heterochromatin structure?". In contrast to the previous chapters, an additional focus will be put on the diversity and heredity of constitutive heterochromatin structures found in natural Arabidopsis accessions. Such an approach wishes at answering the following question:

"Does UV-B exposure participate in the evolution of Arabidopsis heterochromatin in particular ecological niches?"

6.2.2. UV-B-induced structural dynamics of chromocenters

To analyze the chromocenter dynamics upon UV-B exposure leaves nuclei of WT (Col-0) *Arabidopsis thaliana* plants were DAPI stained and analyzed using the Nucl.eye.D script (Chapter II for details), prior (0), 2h, and 24h upon UV-B irradiation. As shown in (Fig. 1A), WT nuclei show an expected Heterochromatin Content (HC) of about 11% in untreated control conditions (0) (Biedermann and Hellmann 2010). Two hours upon UV-B exposure, the HC significantly decreases to reach about 8% (Fig. 1A). The following day (time point 24h), the heterochromatic entities look efficiently restored, reaching the same content as before irradiation (Fig. 1B). This result shows that UV-B irradiation induces HC dynamics similar to those previously described upon UV-C exposure (Chapter I). In order to test whether these UV-B-induced chromocenter dynamics rely on the UVR8 receptor, HC was measured in a similar way in *uvr8* plants (Brown et al. 2005). Prior UV-B exposure, HC content in *uvr8* plants does not significantly differ from WT plants (Fig. 1A). Two hours upon irradiation, the HC in *uvr8* nuclei decreases to 8% like in WT plants (Fig. 1A). Interestingly, 24h upon irradiation, HC does not reach the initial level and remains as low as at 2h (Fig. 1B). These data suggest that the accurate re-establishment of HC depends on the UVR8 receptor whilst its dynamics (at 2h) do not. To better decipher which parameters contribute to HC alteration, the chromocenter occupancies (CO), the relative intensity of chromocenters (RI), and the number of chromocenters (CC) per nucleus have also been evaluated.
In WT plants, the drop of HC at 2h upon irradiation is mainly related to a significant decrease of CO and CC number per nucleus, whereas the RI remains stable (Fig. 1C and 1D).
In *uvr8* plants, the HC decrease seems to be mainly related to the drop of RI 2h and 24 h upon UV-B exposure (Fig. 1C).

To summarize, our results demonstrate that UV-B induces HC dynamics similarly to UV-C irradiation, reinforcing the idea that the chromocenter dynamics are predominantly related to the induction of DNA damage and DNA repair pathways. Interestingly, the restoration of chromocenter shape depends on the UV-B specific receptor, UVR8, likely involved in the regulation of factors acting in heterochromatin reconstruction. This observation is in agreement with the recent study revealing a link between UV-B perception and DNA methylation (Jiang et al. 2021). Indeed, UVR8 represses DRM2 activity upon UV-B exposure (Jiang et al. 2021)

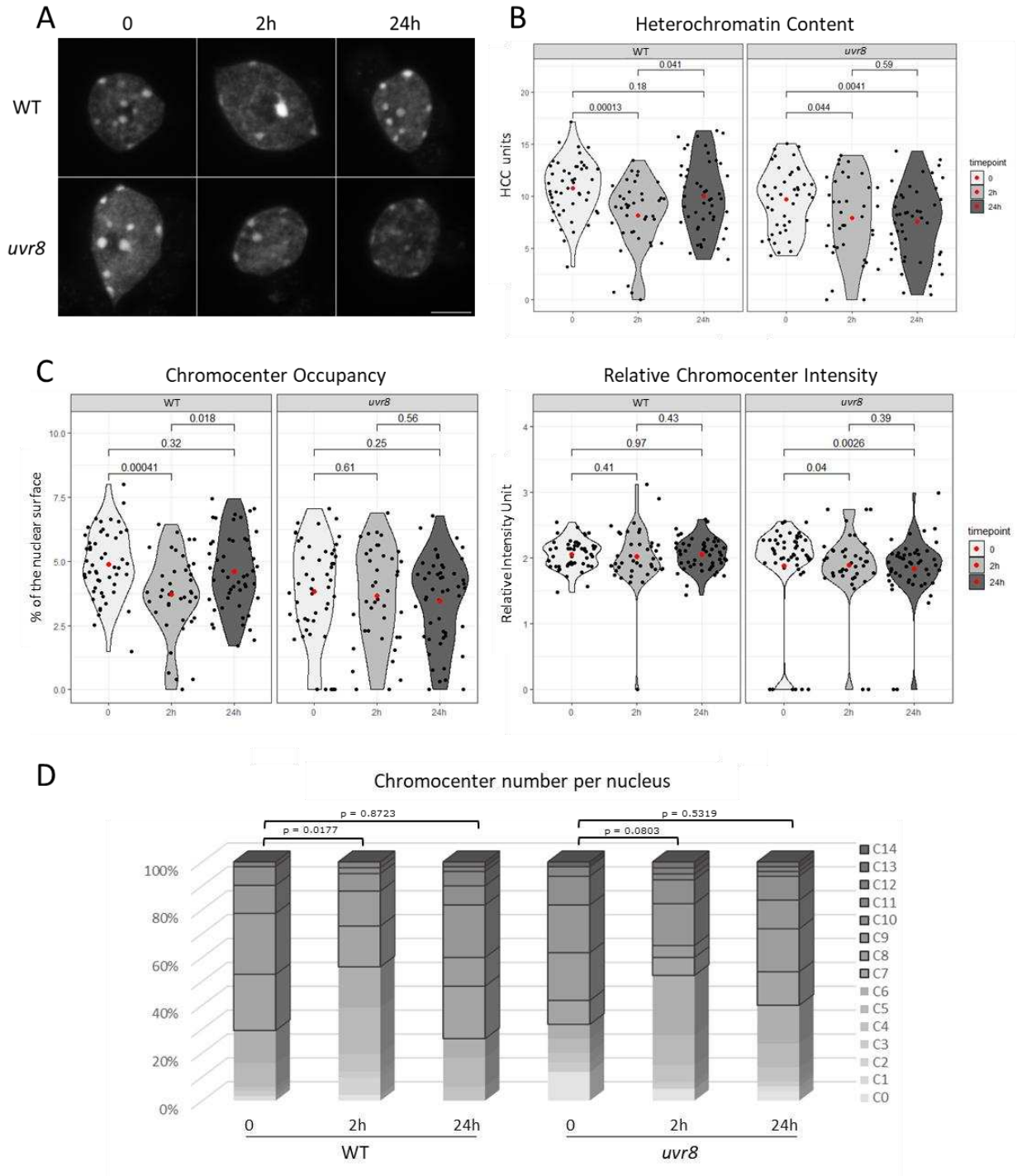

Figure 1: UV-B-induced constitutive heterochromatin dynamics in WT and *uvr8* plants

(A) Microscopy images of DAPI stained Arabidopsis nuclei isolated from WT (Col-0) and *uvr8* leaves in the control condition (0) or upon UV-B irradiation (2h, 24h). Scale bar = 5µm. **(B)** Violin plots illustrating the distribution of heterochromatin content (Chromocenter occupancy * Relative chromocenter Intensity) in a population of at least 45 nuclei per condition as described in (A). Each black dot represents the measure for one nucleus. The red dot shows the mean value. Exact p values are shown (Mann Whitney Wilcoxon test). **(C)** Violin plots showing the distribution of the Chromocenter Occupancies (percent of the nuclear surface occupied by chromocenters) and Relative Chromocenter Intensities (ratio of mean chromocenter intensities / Mean nuclei intensity). Each black

dot represents the measure for one nucleus. The red dot shows the mean value. Exact p values are shown (Mann Whitney Wilcoxon test). **(D)** Stacked pillar diagram comparing the number of chromocenters per nucleus upon UV-B in WT and *uvr8* nuclei. Exact p values are shown (Chi-Square test: χ^2).

6.2.3. DNA repair gene expression in natural Arabidopsis variants

We found that the UV-induced HC dynamics depend on several factors involved in photodamage repair and UV-B perception (Chapter I). Therefore, it can be hypothesized that the chromocenter shape of Arabidopsis ecotypes may correlate with their natural UV-B regimes and with the expression level of particular photodamage repair genes.

Arabidopsis thaliana can be found worldwide in various ecological niches. In addition, the 1001 genome project (https://1001genomes.org/) provides essential information about transcriptomes, methylomes, and SNPs (Single Nucleotide Polymorphisms) for several hundreds of ecotypes (Alonso-Blanco et al. 2016; Kawakatsu et al. 2016). These natural resources and the associated molecular data offer a set of powerful tools to study the putative correlation between UV-B regime, genes expression, and HC shape. In a first analysis, we investigated the correlation between the expression of factors demonstrated to directly or indirectly regulate chromocenter shape and the natural UV-B regime (Table 1). For this, we performed a Principal Component Analysis (PCA) on 561 Arabidopsis ecotypes focusing on DNA repair, H3K9me2 homeostasis, and DNA methylation-related genes.

DNA repair	*DDB2*	Photodamage detection in Global Genome repair (GGR)
	DCL4	21-nt siRNA biogenesis related to small RNA mediated GGR
	PHR1	Cyclobutane pyrimidine dimer (CPD)-specific photolyases
	UVR3	6-4 Photoproduct (6-4PP) -specific photolyases
	CSA	Recruiting NER-machinery for Transcription Coupled Repair (TCR)
	OGG1	Functional 8-oxoguanine DNA glycosylase
DNA methylation/demethylation	*MET1*	Cytosine methyltransferase (CG)
	CMT2	Cytosine methyltransferase (CHH)
	CMT3	Cytosine methyltransferase (CHG)
	ROS1	Cytosine demethylase all contexts
	DML2	Cytosine demethylase all contexts
	DML3	Cytosine demethylase all contexts
RNA directed DNA methylation	*DRM2*	Cytosine methyltransferase (*de novo* and CHH maintenance)
	NRPD1A	Large subunit of RNA Polymerase IV
	NRPD1B	Large subunit of RNA Polymerase V
	RDR2	RNA-dependent RNA polymerase 2
	DCL3	24-nt siRNA biogenesis
	AGO4	Argonaute protein involved in siRNA mediated gene silencing
H3K9me2 homeostasis	*SUVH4 / KYP*	Histone 3 lysine 9 dimethyltransferase (H3K9me2)
	IBM1	H3K9me2 demethylase
	JMJ27	H3K9me2 demethylase

Table 1: List of genes used for PCA analysis

As shown in Figure 2A, *DDB2* and *PHR1* expressions correlate as well as *DCL4*, *OGG1,* and *CSA* expressions. When considering the UV-B doses, both *PHR1* and *DDB2* show the highest correlation with the UV-B regimes (Fig. 2A). Surprisingly, the expression of the *UVR3* photolyase is negatively correlated with the UV-B doses (Fig. 2A) in agreement with its expression occurring during the night (Fig. S1) (Cortijo et al. 2019). Expressions of several factors regulating DNA methylation levels correlate, such as *MET1* and *CMT3* on one hand and *ROS1* and *CMT2* on the other hand (Fig. 2B). However, we cannot observe a linear correlation between UV-B regimes and the expression of most of the factors involved in the control of the DNA methylation landscape (Fig. 2B). The RdDM related genes all show a high correlation to each other, apparently independent of the natural UV-B regimes (Fig. 2C).

Interestingly, expressions of both *JMJ27* and *IBM1* involved in H3K9me2 removal are correlated, whilst no linear correlation can be found with the H3K9me2 methyltransferase *KYP*/*SUVH4* (Fig. 2D). Moreover, the expression of these three genes involved in H3K9me2 homeostasis does not correlate with UV-B regimes (Fig. 2D). When considering the expression level of *UVR8* in the 561 ecotypes in relation to the UV-B doses, no correlation can be observed (Fig. 2E), highlighting the complexity of the regulation of UV-B perception and signaling.

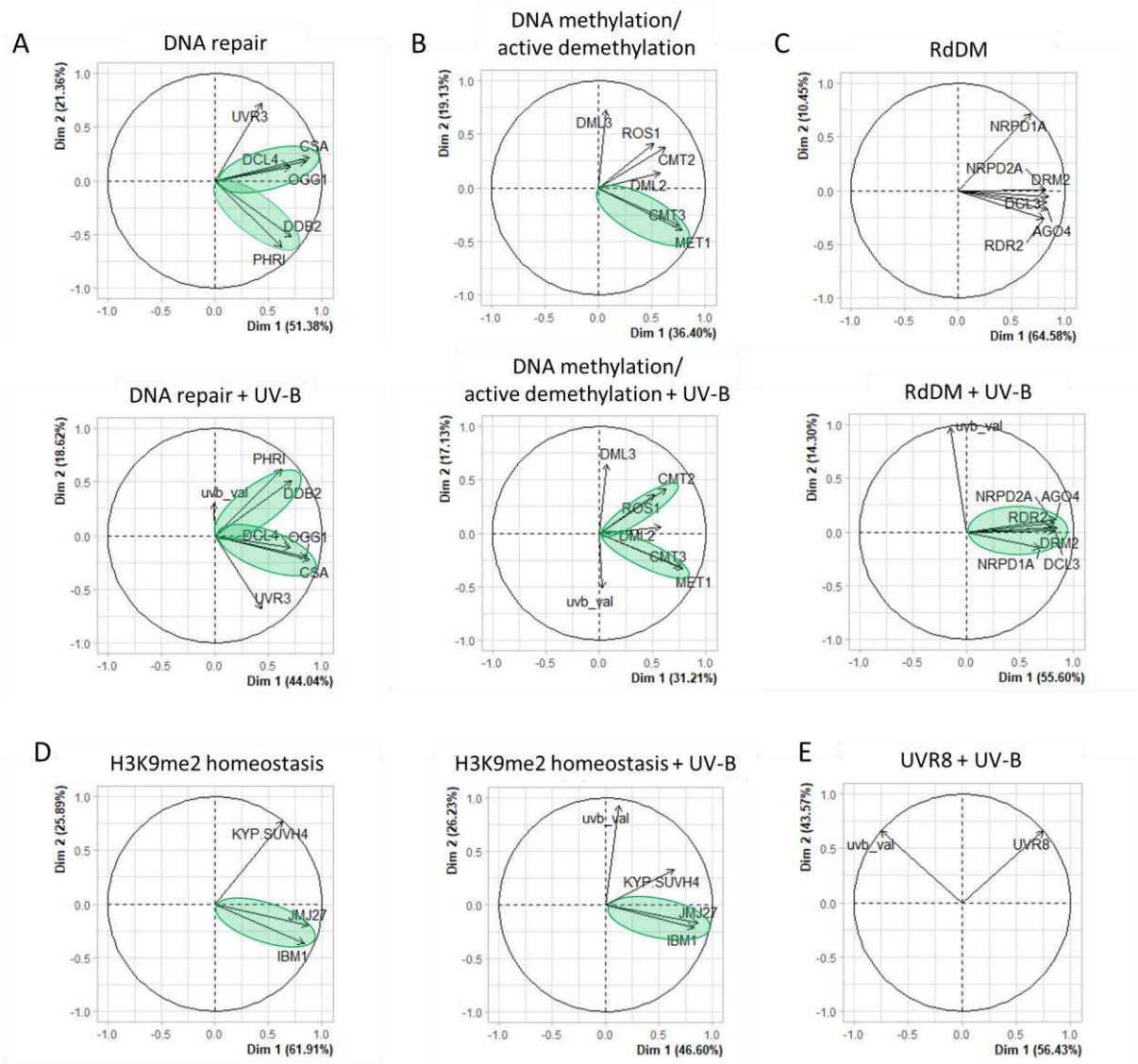

Figure 2: Principal Component Analysis of gene expression data of 561 ecotypes related to the UV-B regime

PCA circular correlation plots of the variables (gene expression) in principal components PC1 and PC2 in 561 ecotypes, with or without naturally encountered UV-B regimes as an additional variable. **(A)** DNA repair genes (*DDB2, DCL4, PHR1, UVR3, CSA,* and *OGG1*). **(B)** DNA methylation / active demethylation genes (*MET1, CMT3, CMT2, ROS1, DML3,* and *DML2*). **(C)** RdDM genes (*DRM2, NRPD1A, NRPD1B, DCL3, AGO4, and RDR2*). **(D)** H3K9me2 homeostasis genes (*KYP/SUVH4, IBM1, and JMJ27*). **(E)** Gene coding for the UV-B receptor *UVR8.* Green areas highlight genes exhibiting correlated expression levels.

In order to experimentally assay the putative correlation between natural UV-B regime and expression profile of photodamage repair genes, we decided to test several Arabidopsis ecotypes in our growth conditions. For this, we analyzed publicly available data for the expression of the photodamage repair genes *DDB2*, *UVR3*, *PHR1* and *CSA* on a set of 14 ecotypes representative of different UV-B regimes (Beckmann et al. 2014). In order to experimentally validate these published expression profiles, we measured by RT-qPCR the mRNA steady-state level of these photolesions repair genes in our growth condition. A particular focus was devoted to the identification of natural variants with altered expression of *DDB2*, *UVR3,* or *PHR1* genes, that have been shown to be involved in both photodamage repair and chromocenter shape (Chapter I). In other words, we aim at identifying low *DDB2*, *UVR3,* or *PHR1* expressing ecotypes (compared to Col-0) to study HC dynamics upon UV-B exposure. They would represent natural hypomorphic mutant plants.

The comparisons of the publicly available transcriptomic profiles with the mRNA steady-state levels measured by qPCR, show that many differences are observed when plants are cultivated under our growth conditions (Fig.3A). Indeed, *PHR1* expression is low in most of the ecotypes compared to Col-0 whilst *UVR3* expression is high (Fig. 3A). Interestingly, under our growth conditions, the Ms-0 ecotype shows low expression levels for all the tested repair genes (Fig. 3A). This hypomorphic phenotype appears interesting, given that Ms-0 ecological niche is under low UV-B regime (Fig.4A). In contrast, two other ecotypes, Can-0, and Cvi growing under a high UV-B regime display high *DDB2* mRNA steady-state level compared to Col-0 (Fig. 4A). Their CSA expressions are low compared to Col-0, suggesting that the GGR repair pathway is likely to be predominant in such natural variants or that the TCR pathway needs to be stimulated (Fig. 4A). This holds true also in Old-2 plants that display the highest DDB2 mRNA steady-state level (Fig. 4A). PCA analyses of *DDB2, UVR3, PHR1,* and *CSA* expression in these 14 ecotypes, show that *DDB2* and photolyases expression are negatively correlated (Fig. 3B).

Importantly, most of the 14 ecotypes cultivated in our growth conditions show different expression patterns than in the transcriptomic data (Fig. 3A). This variability observed between transcriptomic data and qPCR, highlights that growth conditions interfere significantly with the expected expression profiles, adding several layers of complexity in the experimental system.

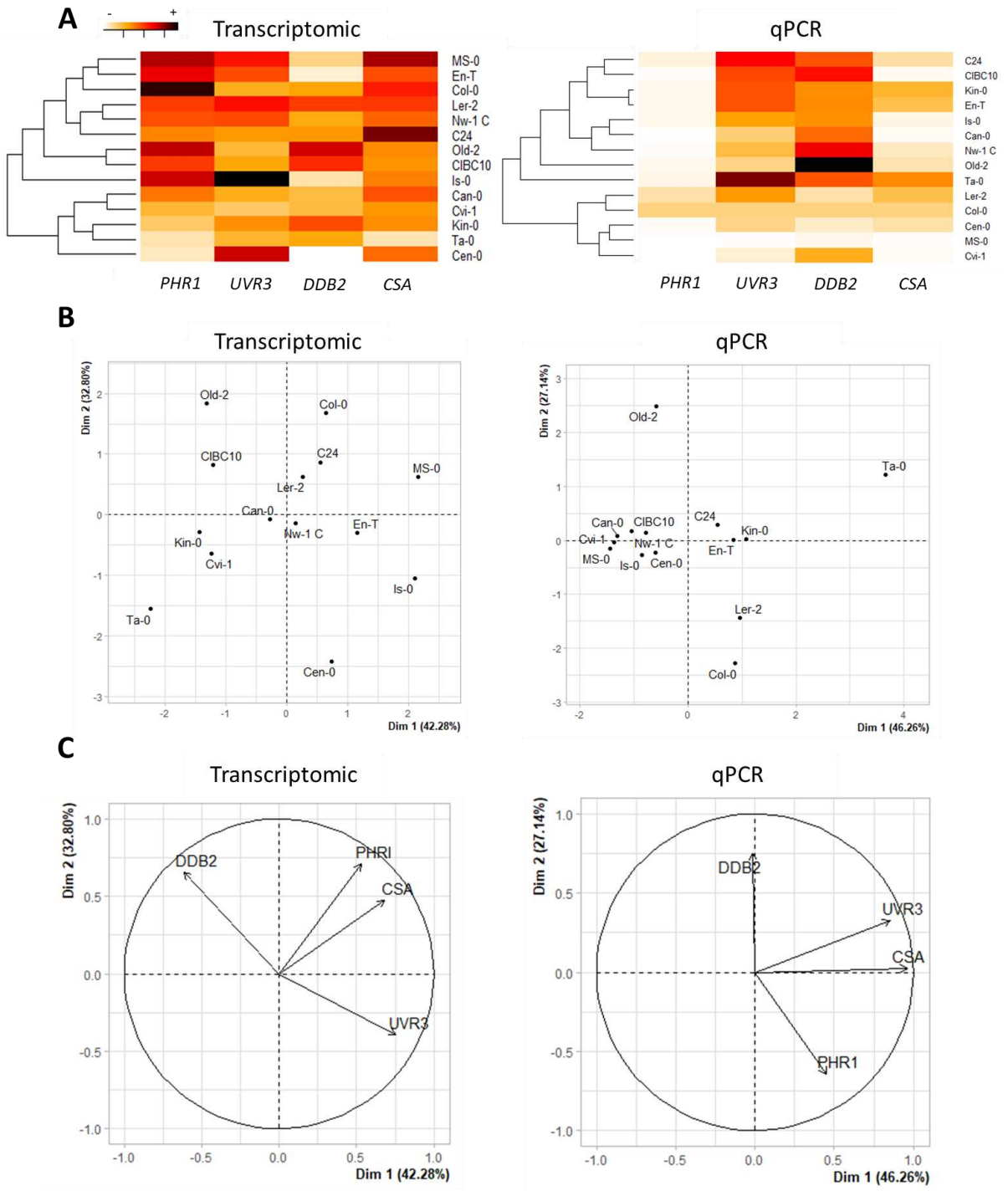

Figure 3: Heatmap of photodamage repair gene expression

(A) Heatmap of mRNA steady-state level of *DDB2*, *UVR3*, *PHR1*, and *CSA* in 14 ecotypes. The left panel shows a heatmap generated according to the expression data from (Beckmann et al. 2014). The right panel shows the heatmap generated from qPCR results in our growth conditions, normalized to Col-0. **(B)** PCA clustering plots of the variables (gene expression of *DDB2*, *UVR3*, *PHR1*, and *CSA*) in principal components PC1 and PC2 for 14 ecotypes using transcriptomic data or RT-qPCR results in our growth condition. **(C)** PCA circular correlation plots associated with **(B)**.

To better analyze the repair efficiency of several ecotypes exhibiting differential expression of photodamage repair genes compared to Col-0, a CPD removal assay was performed. We choose Can, Cvi (high UV-B regime and high GGR), and Ms-0 (low UV-B regime and low expression of photodamage repair genes) plants. This assay allows measuring the remaining amount of photodamage (CPD) 1h upon UV-B exposure and thus reflects the specific repair efficiency (Schalk et al. 2017). As shown in Figure 4 in Col-0 plants, 45% of CPDs are left upon 1h. Can-0 shows a slightly more efficient repair with only 35% of CPD remaining (Fig. 4). Interestingly, Cvi, Ms-0, and *rad10* (photodamage repair-deficient plant) exhibit a high amount of CPDs 1h upon exposure to UV-B (Fig. 4). In *rad10* and Ms-0 plants (low expression of photodamage repair genes, Fig. 3A), this observation could be correlated to a low GGR activity. Aside from DNA repair, we also measured the DNA damageability of these different ecotypes by comparing CPD quantity directly upon UV-B exposure (Fig. 4). When normalized to Col-0, Can-0, MS-0, and *rad10* show a lower CPD accumulation of 0.75, 0.6, and 0.65, respectively (Fig. 4). Strikingly Cvi appears to accumulate only 30% of the CPDs measured in Col-0 plants (Fig. 4).

In conclusion, our study allowed determining the correlative trends between the expression of some genes such as *DDB2, PHR1,* and the natural UV-B regimes. Unfortunately, the qPCR analysis of ecotypes grown in our conditions did not confirm this correlation. However, it should be considered that the accumulation of transcripts in the absence of UV-B treatment does not reflect the protein pools and the mRNA steady-state level that could be induced/repressed upon UV-B exposure. Furthermore, we observed that Arabidopsis ecotypes with different CPD repair efficiency are neither linked to their respective UV-B regime nor to the expression of specific DNA repair genes.

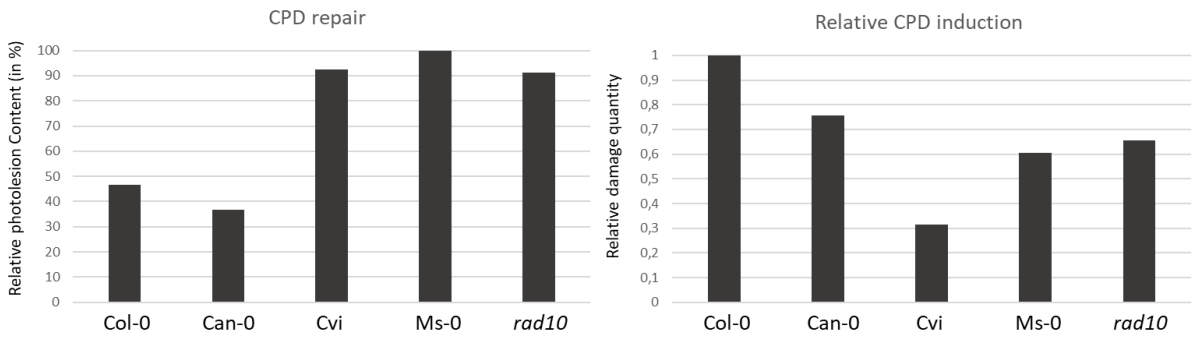

Figure 4: Photolesions repair in different Arabidopsis ecotypes

Left Panel: histogram illustrating the percentage of remaining photodamages 1h upon UV-B irradiation. Right Panel: histogram illustrating the amount of photolesions measured directly after UV-B treatment normalized to the Col-0 plants.

6.2.4. Chromocenter shape in natural variants

We identified that UV-B induces a transient reorganization of constitutive heterochromatin in the first 2h following irradiation. This observation suggests that the UV-B regime may have contributed to the shaping of the heterochromatic structures in Arabidopsis natural variants. Given that heterochromatic structures are the predominant targets for photolesion formation (Chapter I), it may provide an advantage in reducing these structures when plants are naturally exposed to high UV-B doses.

In order to investigate the link between UV-B exposure and chromocenter shape in natural variants, we choose four ecotypes among a range of natural UV-B regimes as shown in Figures 5A and 5B. Ms-0 originates from Moscow, (Latitude 55.75°) and is used to the lowest UV-B exposure with a mean annual dose of 1418 J/m²/day. Col-0 from Columbia (Latitude 38.3°) in turn got exposed to a mean dose of 2721 J/m²/day. For high UV-B exposure, we used Can-0 on the Canary Islands (Latitude 29.21°) with a 4074 J/m²/day and Cvi from Cap-Verde Islands (15.11°) with a mean annual dose of 5582 J/m²/day (Fig. 5B). According to our working hypothesis, if UV-B contributes to a particular dynamic and/or shaping of constitutive heterochromatin, we would expect to observe a gradual distribution of the HC in the four ecotypes. Prior to the analysis of the nuclear traits, we performed a growth assay to compare the effect of UV-B between the four different ecotypes.

As shown in Figure S2 none of the tested ecotypes exhibit UV-B hypersensitivity in our protocol. Indeed, 48h upon irradiation, the growth was reduced by around 40% in all four ecotypes (Fig. S2). Importantly, irradiated *rad10* plants, deficient for the NER pathway, exhibit a similar growth delay to those of the four natural variants, indicating that the UV-B dose used is below a lethal dose.

We next measured, under our growth conditions, CO, RCI, and HC in the four ecotypes. As shown in Figure 5C and D, CO, RCI, and HC in Can-0 and Cvi are significantly lower compared to Col-0. These results are in agreement with published data reporting that Cvi chromocenters are smaller than those of Col-0 (Pavlova et al. 2021). Thus, the lower HC of Can-0 and Cvi compared to Col-0 suggests that a high natural UV-B regime likely contributes to shaping HC structures.

In contrast, Ms-0 exhibits significantly smaller CO whilst its RCI is higher compared to Col-0 (Fig. 5C and 5D). Moreover, HC measurements do not show a significant difference between Col-0 and Ms-0 (Fig. 5C and 5D), suggesting that other environmental parameters may also influence HC, especially for this ecotype originating from a low natural UV-B regime. This approach allowing the identification of ecotypes with different HC provides a useful tool to further characterize chromocenter dynamics and its shaping in nature.

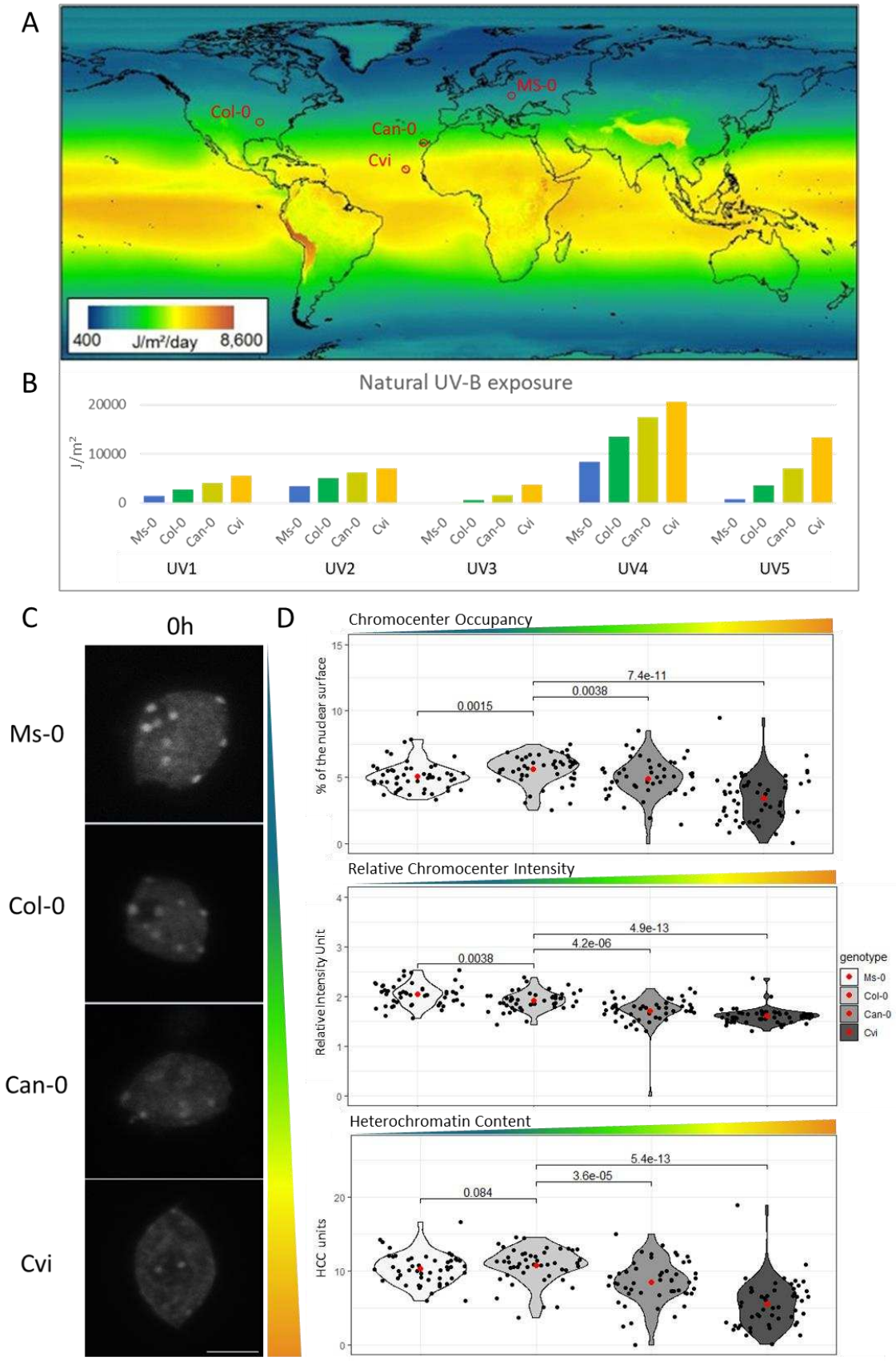

Figure 5: Chromocenter shapes in relation with natural UV-B regimes

(A) Worldwide natural UV-B exposure map showing the location of 4 different *Arabidopsis thaliana* ecotypes: Ms-0 (Moscow), Col-0 (Columbia-0), Can-0 (Canary Islands), Cvi (Cape Verde Islands) (adapted from glUV: A global UV-B radiation dataset for macroecological studies (Beckmann et al. 2014)) **(B)** Histograms displaying UV-B exposure of Ms-0, Col-0, Can-0 and Cvi in their native ecosystem. UV1 = Annual Mean UV-B (in J/m²/day); UV2= Mean UV-B of Highest Month (in J/m²/day); UV3= Mean UV-B of Lowest Month (in J/m²/day); UV4 = Sum of Monthly Mean UV-B during Highest Quarter (in J/m²);); UV5 = Sum of Monthly Mean UV-B during Lowest Quarter (in J/m²) [ref]. **(C)** Microscopy images of DAPI stained Arabidopsis nuclei isolated from Ms-0, Col-0, Can-0, and Cvi leaves. Scale bar = 5µm. **(D)** Violin plots showing the distribution of the Chromocenter Occupancies (percent of the nuclear surface occupied by chromocenters), Relative Chromocenter Intensities (ratio of mean chromocenter intensities / Mean nuclei intensity), and Heterochromatin content (Chromocenter occupancy * Relative chromocenter Intensity) in a population of at least 40 nuclei per ecotype. Each black dot represents the measure for one nucleus. The red dot shows the mean value. Exact p values are shown (Mann Whitney Wilcoxon test).

6.2.5 Inheritance of chromocenter shape

As described in the introduction, the chromocenter entities are characterized by specific sequences, such as centromeric repeats and TEs. In addition, chromocenters are characterized by a specific epigenetic landscape, including the loading of particular histone variants, the deposition of histone PTMs, and high DNA methylation (Simon et al. 2015). Therefore, the inheritance of the heterochromatic chromocenter shape is complex and multifactorial (Snoek et al. 2017). The following part aims at characterizing the inheritance of chromocenter shape and its dynamics upon UV-B exposure in 2 ecotypes with divergent HC: Col-0 and Cvi.

6.2.5.1. Cvi chromocenter dynamics and parental effect

In order to investigate to which extent the chromocenter shape can be inherited in the offspring, inter-ecotype hybrids, produced by crossing Col-0 (high HC) with Cvi (low HC), were analyzed. The crossing was performed in both directions (having Col-0 once as mother and once as father) to test a putative parental effect on HC inheritance.

As shown in Figure 5A, the progeny of both Col-0 ♀ x Cvi ♂ (Hybrids 1: H1) and Cvi ♀ x Col-0 ♂ (Hybrids 2: H2) show an intermediate HC compared to the Col-0 and Cvi parents suggesting that both parents contribute independently and in equal parts to the chromocenter shape in the hybrids progenies. The plotting of the relative intensities and HC for each nucleus in H1 and H2 does not indicate the formation of two strikingly different subpopulations, arguing against a sequence-specific regulation of the chromocenter structures (Fig. S3).

To go further in the characterization of chromocenter dynamics and inheritance, we measured the nuclear traits in both parents (Col-0 and Cvi) as well as in the inter-ecotype hybrids 2h upon UV-B exposure. Surprisingly, Cvi nuclei exhibit a significant increase of HC 2h upon UV-B exposure, whereas Col-0 HC decreases (Fig. 6C). This observation reveals that in Cvi plants, non-canonical chromocenter dynamics exist. This UV-B induced HC increase in Cvi is mainly explained by an increased CO and CC number per nucleus (Fig. 6D and Fig. S3), arguing in favor of *de novo* heterochromatin formation. Significantly, in both H1 and H2 hybrids, CO, RI, or HC do not vary 2h upon UV-B (Fig. 6C), suggesting that independent/antagonist mechanisms acting in *trans*, likely act to regulate CC dynamics. The highly complex, genetic, and epigenetic structure of constitutive heterochromatin seems to "equally" depend on both parents. The Cvi ecotype may have evolved a non-canonical mechanism of HC remodeling to cope with recurrent high UV-B exposure. Therefore, its detailed characterization in comparison to the canonical dynamics observed in Col-0 may be an added value to decipher chromocenter dynamics in response to the induction of photodamages.

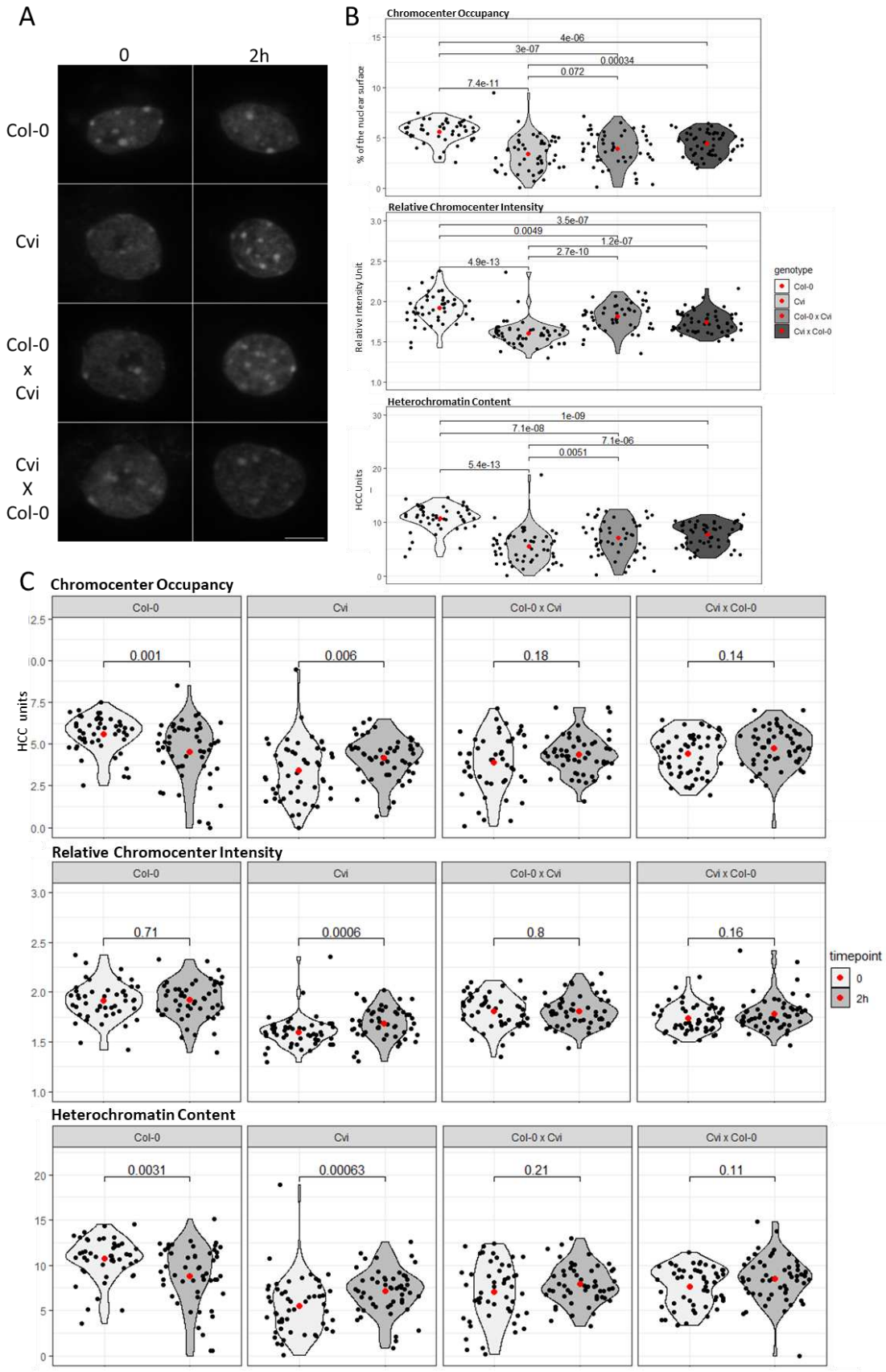

Figure 6: Chromocenter dynamics of Cvi, Col-0 x Cvi and Cvi x Col-0 hybrids following UV-B exposure

(A) Microscopy images of DAPI stained Arabidopsis nuclei isolated from Col-0, Cvi, Col-0 x Cvi and Cvi x Col-0 leaves in control condition (0) or upon UV-B irradiation (2h). Scale bar = 5µm. **(B)** Violin plots showing the

distribution of the Chromocenter Occupancies (percent of the nuclear surface occupied by chromocenters) and Relative Chromocenter Intensities (ratio of mean chromocenter intensities / Mean nuclei intensity), and Heterochromatin content (Chromocenter occupancy * Relative chromocenter Intensity) in a population of at least 45 nuclei per control condition described in (A). Each black dot represents the measure for one nucleus. The red dot shows the mean value. Exact p values are shown (Mann Whitney Wilcoxon test). **(C)** Violin plots showing the distribution of the Chromocenter Occupancies (percent of the nuclear surface occupied by chromocenters) and Relative Chromocenter Intensities (ratio of mean chromocenter intensities / Mean nuclei intensity), and Heterochromatin content (Chromocenter occupancy * Relative chromocenter Intensity) in control condition (0) and two hours upon UV-B (2h) in a population of at least 45 nuclei per sample described in (A). Each black dot represents the measure for one nucleus. The red dot shows the mean value. Exact p values are shown (Mann Whitney Wilcoxon test).

6.2.5.2 Parental effect of UV-B exposure

In order to challenge the hypothesis of an inherited UV-B-dependent chromocenter reshaping, a "directed evolution" experiment was designed, as described in Figure 7A. Col-0 and Cvi S0 parent plants were divided into two groups:

- an unirradiated control group
- an UV-B-irradiated group.

For both groups, the offspring were collected after selfing, generating S1 and S1UV plants (Fig. 7A). We aimed at measuring the differences in HC dynamics observed between Col-0 and Cvi, thereby tracking a UV-B-dependent parental modification of particular genes expressions. For this, we followed by qPCR, in a time course following UV-B exposure, the steady-state levels of *DDB2*, *KYP*, *JMJ27*, *5S rRNA,* and 180 bp repeats transcripts of Col-0 and Cvi S1/S1UV leaves (Fig. 7B). In S1 plants, *DDB2* shows similar profiles in both Col-0 and Cvi ecotypes (Fig. 7B). *KYP* and *JMJ27* also show similar profiles in S1 and S1UV plants (Col-0 and Cvi; Fig. 7B). Interestingly, the steady-state level of transcripts of the centromeric 180-bp repeats in the S1 Cvi plants displays a 5 times higher accumulation compared to Col-0 (Fig. 7B). This trend is reversed in the S1UV plants (Fig. 7B), suggesting an inherited UV-B repressive effect. When analyzing the 180-bp repeats dynamics, transcripts accumulation is strongly reduced in both Col-0 and Cvi S1/S1UV offsprings (Fig. 7B).

In control condition (time point 0), the steady-state level of *5S rRNA* shows a 4 times higher accumulation in Cvi compared to Col-0 S1 plants (Fig. 7B). Similarly to the 180bp-repeats, this trend is reverted in S1UV offspring (Fig. 7B). These results highlight that UV-B induces inherited repression of expression of particular genomic loci located in centromeric and pericentromeric regions in Cvi plants. In the Col-0 S1 plants, the *5S rRNA* steady-state level gradually increases during the time course (Fig. 7B). This effect may be related to a UV-B-induced heterochromatin relaxation enabling a higher transcriptional activity of the pericentromeric regions. In Cvi S1 plants, the amount of *5S rRNA* decreased 30 min upon UV-B irradiation and gradually increased until 6h (Fig. 7B). The dynamics of *5S rRNA* steady-state level is changed in both Col-0 and Cvi S1UV plants (Fig. 7B), highlighting the potential role of UV-B in the modulation of the epigenetic landscape in centromeric/pericentromeric regions of the offspring. These changes may also explain the slight differences in growth and flowering time observed in S1 and S1UV (Fig. S5). Finally, when analyzing the chromocenter structures in Col-0 and Cvi S1/S1UV leaf nuclei, no significant differences related to the UV-B exposure of the parent plants could be observed (Fig. 8). The HC is, as expected, around 11 for Col-0 and around 5 for Cvi (Fig. 8).

Taken together, these results show that a single UV-B exposure in S0 parent plants is not sufficient to induce a significant modulation of the chromocenter structure in their progenies. However, we identified that this single UV-B exposure is enough to alter *5S rRNA* and 180 bp repeats transcripts accumulation in the offspring. Indeed, the Cvi heterochromatic regions look more silenced when parents get exposed to UV-B whilst these Col-0 regions show enhanced transcriptional activity. It highlights that UV-B may have induced local inherited changes of the epigenomic landscape in constitutive heterochromatin, altering the expression levels of particular regions prior to and upon UV-B irradiation.

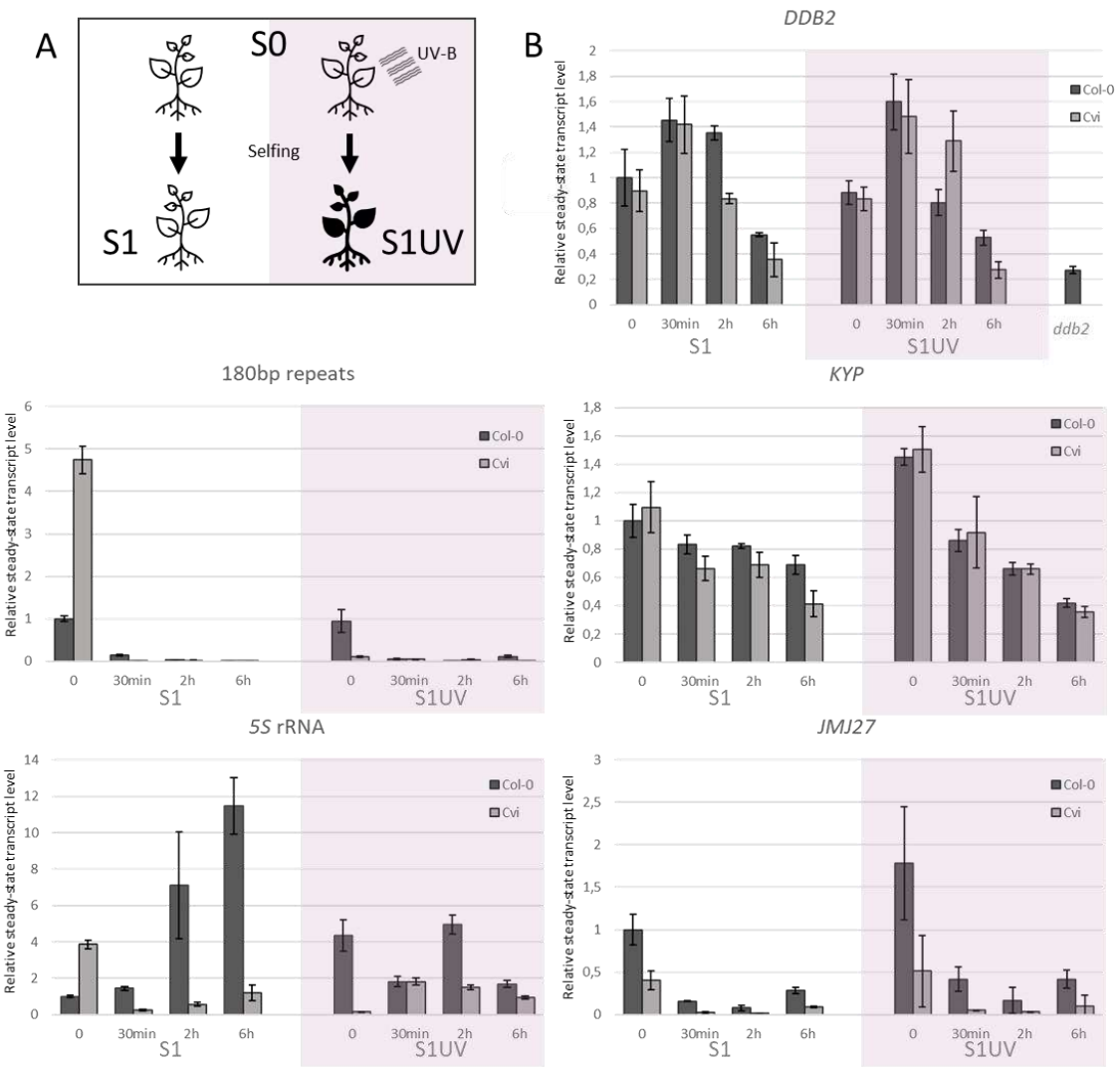

Figure 7: Transcripts levels of *DDB2, KYP, JMJ27*, *5S* rRNA, and 180bp repeats

(A) Schematic representation of the experimental design to produce S1 and S1UV plants. **(B)** Transcripts steady-state levels of *DDB2*, 180bp repeats, *5S rRNA*, *KYP,* and *JMJ27* in Col-0 or Cvi S1/S1UV plants in a time course upon UV-B exposure. All steady-state levels were normalized to Col-0 S1 (0).

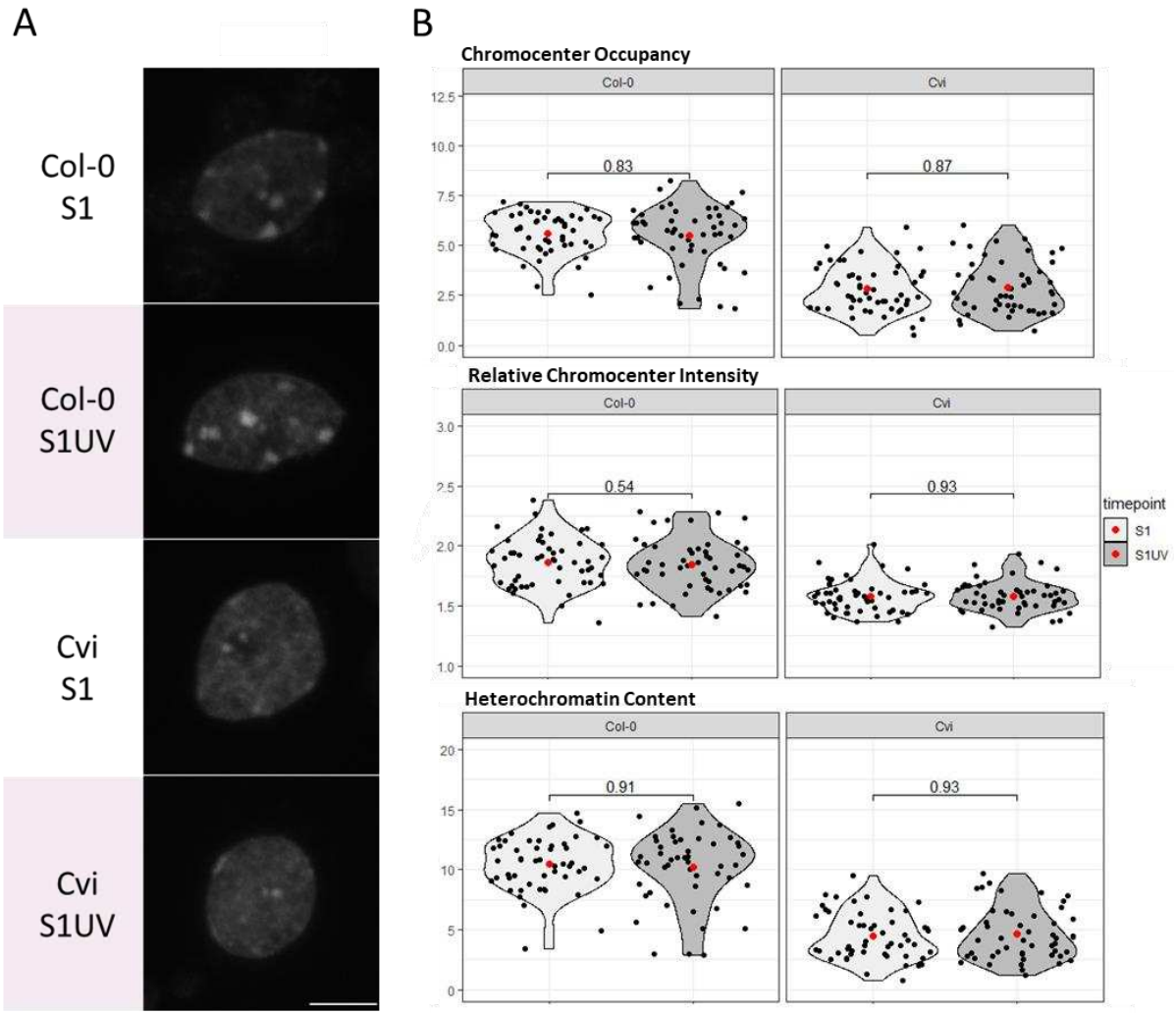

Figure 8: Heterochromatin Content in S1 and S1UV plants

(A) Microscopy images of DAPI stained Arabidopsis nuclei isolated from Col-0 S1, Col-0 S1UV, Cvi S1, and Cvi S1UV leaves in the control condition. Scale bar = 5µm. **(B)** Violin plots showing the distribution of the Chromocenter Occupancies (percent of the nuclear surface occupied by chromocenters) and Relative Chromocenter Intensities (ratio of mean chromocenter intensities / Mean nuclei intensity), and Heterochromatin content (Chromocenter occupancy * Relative chromocenter Intensity) in a population of at least 45 nuclei per control condition described in **(A)**. Each black dot represents the measure for one nucleus. The red dot shows the mean value. Exact p values are shown (Mann Whitney Wilcoxon test).

6.3. Discussion

The effect of UV-B exposure on constitutive heterochromatin was characterized, revealing a dynamic reshaping of the chromocenter structure upon irradiation. In follow-up experiments, the role of this mechanism in a UV-B specific PTGM was also investigated by analyzing expressional priming and chromocenter shape inheritance in natural variants cultivated under our growth conditions.

6.3.1. UV-B induces constitutive heterochromatin dynamics

Col-0 nuclei were analyzed for HC prior and 2h or 24h upon UV-B exposure. This analysis was performed using the fully automated nuclei and chromocenter segmentation performed by the Nucl.Eye.D script (Chapter II). Our analysis reveals a decrease in HC 2h upon UV-B exposure and a structurally restored HC at 24h. This dynamic is mainly related to changes in CO and goes along with a release of silencing of pericentromeric *5S rDNA* in early time points following UV-B irradiation (Fig. 7B; Col-0 S1). These observations indicate that the area identified as chromocenters decreases, whereas the DAPI density in the detected structures remains stable. Consequently, the recognized chromocenter structures do not become more compact, whereas some others decondense and change shapes, interfering with the proper identification of a chromocenter-like structure. UV-B irradiation induces a similar decrease 2h upon exposure as previously described for DAPI and H3K9me2 with UV-C (Chapter I and Chapter III). Therefore, it can be assumed that in both cases, similar pathways are involved in the remodeling of constitutive heterochromatin upon induction of photolesions.

In the case of UV-C, this dynamic seems mainly due to the repair of photodamage (Chapter III). Given that UV-B induces the same type of lesions and may consequently use the same DNA repair pathways: DR, GGR, and TCR, similar mechanisms may act to reshape heterochromatin. Interestingly, we also found that proton irradiation induces significant changes in HC, 24h upon exposure, reflecting alterations of the epigenetic landscape (Chapter I). These changes could not be observed upon UV-B irradiation, suggesting that the effect of UV-B on the remodeling of the chromocenter is less pronounced or delayed in time.

This difference may be due to the relatively high amount of DNA damage expected to be induced by UV-C or proton irradiation compared to UV-B. In other words, only when saturated the DNA repair processes may be the source of durable changes in the epigenetic landscape. Alternatively, it can be hypothesized that UV-B sensing and signaling somehow allows more accurate epigenome maintenance after DNA repair. This hypothesis is strengthened regarding the HC dynamics observed in *uvr8* nuclei. Indeed, *uvr8* nuclei show a decrease of HC 2h upon exposure (like in Col-0), but the chromocenter reshaping 24h after irradiation looks disturbed with a low HC.

UVR8 was recently described as an inhibitor of DRM2 following UV-B exposure (Jiang et al. 2021). Consequently, in *uvr8* plants, DRM2 activity may be higher compared to Col-0. This enhanced activity could, in turn, leads to hypermethylation of particular genomic regions. Surprisingly, in *uvr8* nuclei, CO is relatively stable, whereas a decrease in RCI can be measured 2h and 24h upon UV-B (Fig. 1). These changes in RCI are mainly responsible for the dynamic in HC observed in *uvr8* upon UV-B (Fig. 1). Theoretically, a decrease in RCI should indicate a decreased DAPI/DNA density by surface (Pavlova et al. 2021)(Chapter II). Hypermethylation, in turn, is expected to increase the DNA density. However, it cannot be excluded that DNA methylation highly impacts CO and that the decrease in RCI observed in *uvr8* plants depends on epigenetic marks such as H3K9me2. Future studies may help to clarify how nuclei with a low HC (*i.e.* 8%) and a CO/CRI ratio of 4/2 differ epigenetically from nuclei with an HC of 8% and a CO/CRI ratio of 2/4. Interestingly, a significant difference could be measured when comparing the CO and RCI in Col-0 and *uvr8* control nuclei, indicating that the *uvr8* chromocenters are already in a different epigenetic context, potentially inducing a bias in damageability and repair processes.

In summary, we showed that UV-B induces chromocenter dynamics comparable to those observed upon UV-C, providing evidence for the use of similar pathways. However, both mechanisms seem to, at least partially, differ due to the UVR8 activity, which appears to be essential for the proper dynamic and maintenance of heterochromatic chromatin. This role in epigenome maintenance may also be dependent on the interplay with DRM2 (Jiang et al. 2021). According to these results, it can be proposed that in nature, the activity of UVR8 is an important driver in maintaining constitutive heterochromatin and chromocenter shape.

6.3.2. UV-B-driven variations of expression and chromocenter shaping in natural accessions of Arabidopsis thaliana

In several ecological niches, high UV-B constantly challenges the integrity of genetic information and, according to our observations, the centromeric integrity of plant genomes. Consequently, the above-described dynamics and the modulation of the expression of factors involved in genome and epigenome dynamics may affect adaptation during chronic UV-B exposure.

We considered the expression level of potential actors involved in the maintenance of chromocenter shape, and we observed that in natural accessions, high UV-B exposure in the natural environment somehow correlates with high *KYP*, *CMT3, MET1* expressions and low *DML3* expression (Fig. 2). Consequently, it can be speculated that in accessions exposed to a high UV-B regime, *de novo* H3K9me2 deposition, as well as CG and CHG DNA methylation, are predominant. Interestingly, *DDB2* and *PHR1* expressions show a correlation with the UV-B regimes (Fig. 2A), indicating that GGR and DR are likely required to cope with the UV-B pressure rather than the *CSA*-based TCR and the *UVR3* based DR of 6-4PPs. This observation is in agreement with studies describing PHR1 as the most important actor to avoid genome instability and mutations upon UV-B exposure (Ries et al. 2000; Willing et al. 2016). However, the expression patterns of the photodamage repair genes on a subset of 14 ecotypes vary a lot in our growth conditions (Fig. 3), indicating the multifactorial influence of environmental parameters on the regulation of these genes. Indeed, the expression of *UVR3* and *PHR1*, depends on the circadian clock and UV-B wavelength, respectively (Castells et al. 2010; Li et al. 2015)(Fig. S1).

Epigenetic marks may, on their own, influence the frequency of DNA lesions formed (Johann to Berens and Molinier 2020) (Chapter I). For example, methylated cytosines, in combination with another pyrimidine, are more prone to form pyrimidine dimers (Rochette et al. 2009). Hence, the epigenetic landscape, as well as the nucleotide composition of constitutive heterochromatin, may have evolved in such a way that in ecological niches exposed to high UV, DNA methylation decreased. As a consequence, it can be expected that the HC also decreases in ecotypes exposed to elevated UV-B regimes. This assumption fits with our results.

Indeed, the Col-0 ecotype shows a higher HC than Can-0, which in turn has a higher HC than Cvi (Fig. 3). The Ms-0 HC, naturally exposed to very low UV-B doses, is not higher than the Col-0 HC (Fig. 3), suggesting that (i) UV-B may only affect the chromocenter shape when reaching a biologically relevant dose (ii) other environmental factors such as precipitation, white light and temperature may also influence the HC. For example, heat-stress was also shown to induce 3D remodeling of pericentromeric regions using HI-C analysis (Sun et al. 2020). DNA methylation level within TEs is positively correlated with latitude and precipitation and negatively correlated with warmer temperatures, as described in the 1001 methylome analysis (Kawakatsu et al. 2016). Light intensity was also described as a main actor in heterochromatin shaping in natural variants through regulation of HDA6 (HISTONE DEACETYLASE 6) and PHYB (PHYTOCHROME B) activity (Tessadori et al. 2009; Snoek et al. 2017). Given that light intensity and UV-B irradiance correlate in nature, it would be interesting to combine such light regimes with different natural accessions to follow nuclear phenotypes. Interestingly, if we consider that compacted methylated DNA is more prone to form photolesion (Rochette et al. 2009; Banyasz et al. 2016), the reduction of the amount of dense chromatin may be an efficient strategy to prevent the accumulation of photodamage.

Aside from the constitutive heterochromatin structure itself, the UV-induced dynamics may undergo adaptative changes. The Cvi ecotype, originating from high UV-B regions, displays an increase in HC 2h upon UV-B exposure (Fig. 5C). This increase relies on the rise in CO and RCI, whereas, in Col-0, only CO is significantly changed (Fig. 5C). Interestingly, in the inter-ecotype hybrids H1 (Col-0 ♀ x Cvi ♂) and H2 (Cvi ♀ x Col-0 ♂), the HC remains stable 2h upon UV-B (Fig. 5C). Consequently, a primarily plausible explanation could be that Cvi evolves another, different mechanism that suppresses the one observed in Col-0. This mechanism in Cvi may result from an adaptation to high UV-B irradiance. Reducing HC prior exposure may be an advantage in environments with recurrent high UV-B pressure.

However, it must be considered that Cvi shows a lower basal HC compared to Col-0 in control conditions (Fig. 6A and 6B). According to recent studies, the low HC (RHF) (Biedermann and Hellmann 2010; Pavlova et al. 2021) reported in Cvi also implicates that most of the TEs are not predominantly located in the dense chromocenter regions (Pavlova et al. 2021).

This low TE density would reflect a reduced presence of repressive epigenetic marks leading to more relaxed heterochromatin. Consequently, it is likely that the mechanisms of DNA repair and chromocenter reshaping are similar in both ecotypes but with a different efficiency due to their respective chromocenter compaction and silencing marks. Thus, UV-B-induced chromocenter dynamics may be linked to the amount of TEs contained in constitutive heterochromatin and thus to the epigenetic marks controlling their silencing. In agreement with this, Cvi chromocenters were shown to accumulate less DNA methylation and H3K9me2 compared to Col-0 (Tessadori et al. 2009).

6.3.3. Inheritance of chromocenter shape and parental UV-B effect

Col-0 x Cvi hybrids show an intermediate HC suggesting that the inheritance of chromocenter shape dependents "equally" on both parents. Previous studies analyzing Ler x Cvi hybrids showed HC close to the one observed for Cvi (Tessadori et al. 2009; Snoek et al. 2017), indicating that the Cvi phenotype is dominant for the inheritance of specific nuclear phenotypes (Snoek et al. 2017). However, this dominance was not observed in crosses with Col-0.

The CO measured in H1 plants (Col-0 ♀ x Cvi ♂) is similar to Cvi, indicating a potential paternal dominance of Cvi, likely acting in *trans*, regarding the chromocenter compaction trait (Fig. 6B). This example of inter ecotypes crosses shows cast how changes in chromocenter shape can be inherited and addresses questions about the stress-induced modulation of the epigenetic landscape and its inheritance.

Putative epigenetic changes occur upon UV-B exposure at some loci such as centromeric 180bp repeats (in Cvi) and pericentromeric *5S-rDNA* arrays (in Col-0 and Cvi; Fig. 7B). Interestingly, inactive bulk-rDNA repeats typically show a strong H3K9me2 occupancy (Kutashev et al. 2021). Their release in Col-0 S1UV plants may be explained by an altered Restauration of H3K9me2 upon UV-B exposure. QTL analysis identified several genetic loci related to specific morphological traits of nucleus and chromocenter shape (Tessadori et al. 2009; Snoek et al. 2017).

However, aside from these genetic elements, future studies may also consider epigenetic inheritance as a determinant factor explaining the naturally occurring differences in chromocenter shape. Generally, the mechanisms involved in PTGM remain poorly understood (D'Urso and Brickner 2014). Indeed, epigenetic changes that persist beyond the reprogramming occurring during sexual reproduction remain difficult to decipher (Liu et al. 2019). A prominent explanation for PTGM is the inheritance of small RNA-mediated silencing. The efficient silencing of TE in a transgenerational manner was notably shown to depend on AGO9 and the heritage of small RNAs (Wu et al. 2021). This observation also fits with the fact that UV-C was described to activate the transcription of TE in the progeny in a DCL2/3-dependent manner (Migicovsky and Kovalchuk 2014). Nevertheless, it cannot be excluded that some residual TF, parental DNA methylation or histone PTM are maintained during reproduction and are involved in the priming of the epigenetic landscape of the offspring (Liu et al. 2019).

In addition, S1 and S1UV showed slight differences in growth and flowering time, which may reflect a more global modulation of the transcriptional regulation of particular genomic regions (Fig. S5).

6.4. Conclusions & Perspectives

In this chapter, the UV-B-induced dynamics of constitutive heterochromatin was described. This dynamic shows strong similarities with the one reported with UV-C (Chapters I and III). Given that UV-B induces photolesions that must be efficiently repaired, the early decrease in chromocenter compaction would be likely related to the mobilization of DNA repair processes. Interestingly, we found that the UV-B specific photoreceptor UVR8 is also involved in this dynamic, especially for the proper restoration of constitutive heterochromatin. This highlights the need to integrate and signal the exposure downstream of the photoreceptor. We also addressed the question of whether natural UV-B exposure could be a potential source of epigenetic evolution/variability. Interestingly, the Cvi ecotype originating from a high UV-B irradiance area shows opposite chromocenter dynamics compared to Col-0.

In addition to the described effect of light intensity on chromocenter (De)condensation, we proposed that the UV-B wavelength could be a central natural stimulus determinant for chromocenter structure. The analysis of inter-ecotypes hybrids between Col-0 and Cvi showed that chromocenter shape and UV-B induced chromatin dynamics are inherited by both parents. Finally, using a directed evolution assay, it could be demonstrated that a single UV-B exposure of the parents is not sufficient to induce significant changes in the chromocenter structure of the offspring. However, this approach revealed that centromeric and pericentromeric loci show some UV-B triggered transcriptional changes in the offspring.

It would be of interest to further characterize the different epigenetic layers that are affected by UV-B irradiation and which factors act in their maintenance. According to our observations, a first approach would focus on DNA methylation and H3K9me2 homeostasis.
In addition, S2, S3… generations of the UV-B irradiated plants (Fig. S4) should allow deciphering whether repeated exposures to UV-B would significantly reshape constitutive heterochromatin.

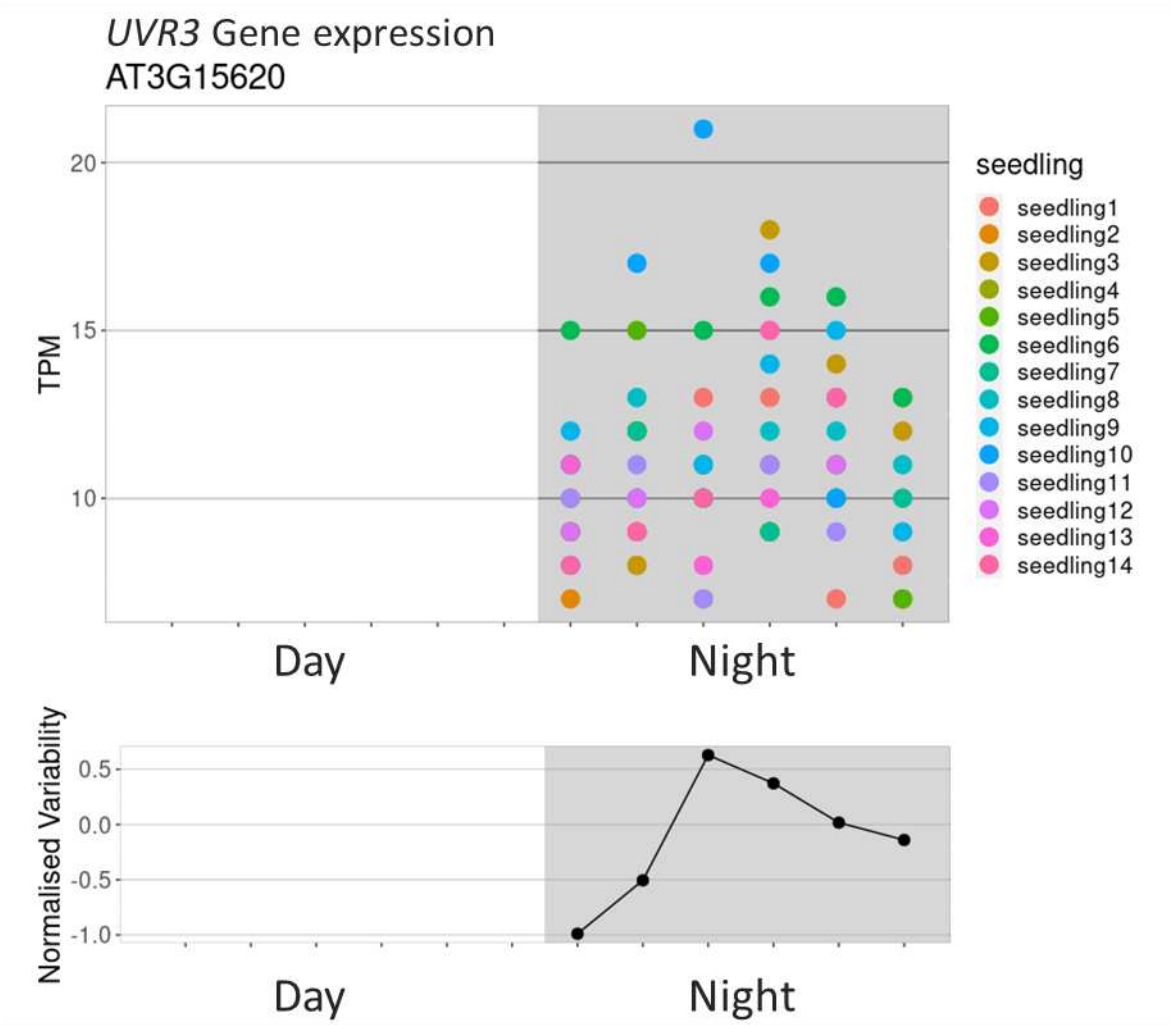

Supplemental Figure 1: *UVR3* gene expression

(A) Dotplot showing the expression level in TPM (Transcripts Per Million) of *UVR3* in 14 independent Arabidopsis Col-0 seedlings (Cortijo et al. 2019). **(B)** Curve of the normalized expression variability of *UVR3*. Both graphs were adapted from (https://jlgroup.shinyapps.io/AraNoisy/) (Cortijo et al. 2019).

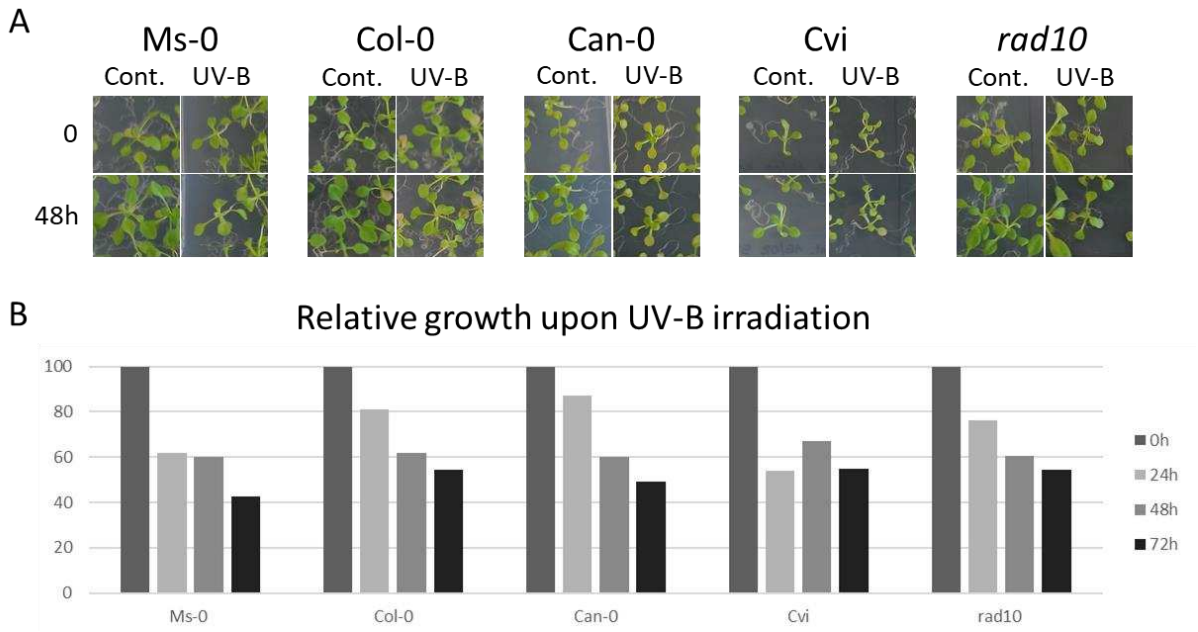

Supplemental Figure 2: UV-B sensitivity assay

(A) Pictures of Ms-0, Col-0, Can-0, Cvi, and *rad10* seedlings. Growth of control (Cont.) and UV-B irradiated plants, 48h upon irradiation. **(B)** Histogram showing the relative growth of each ecotype 24h, 48h, and 72h upon irradiation.

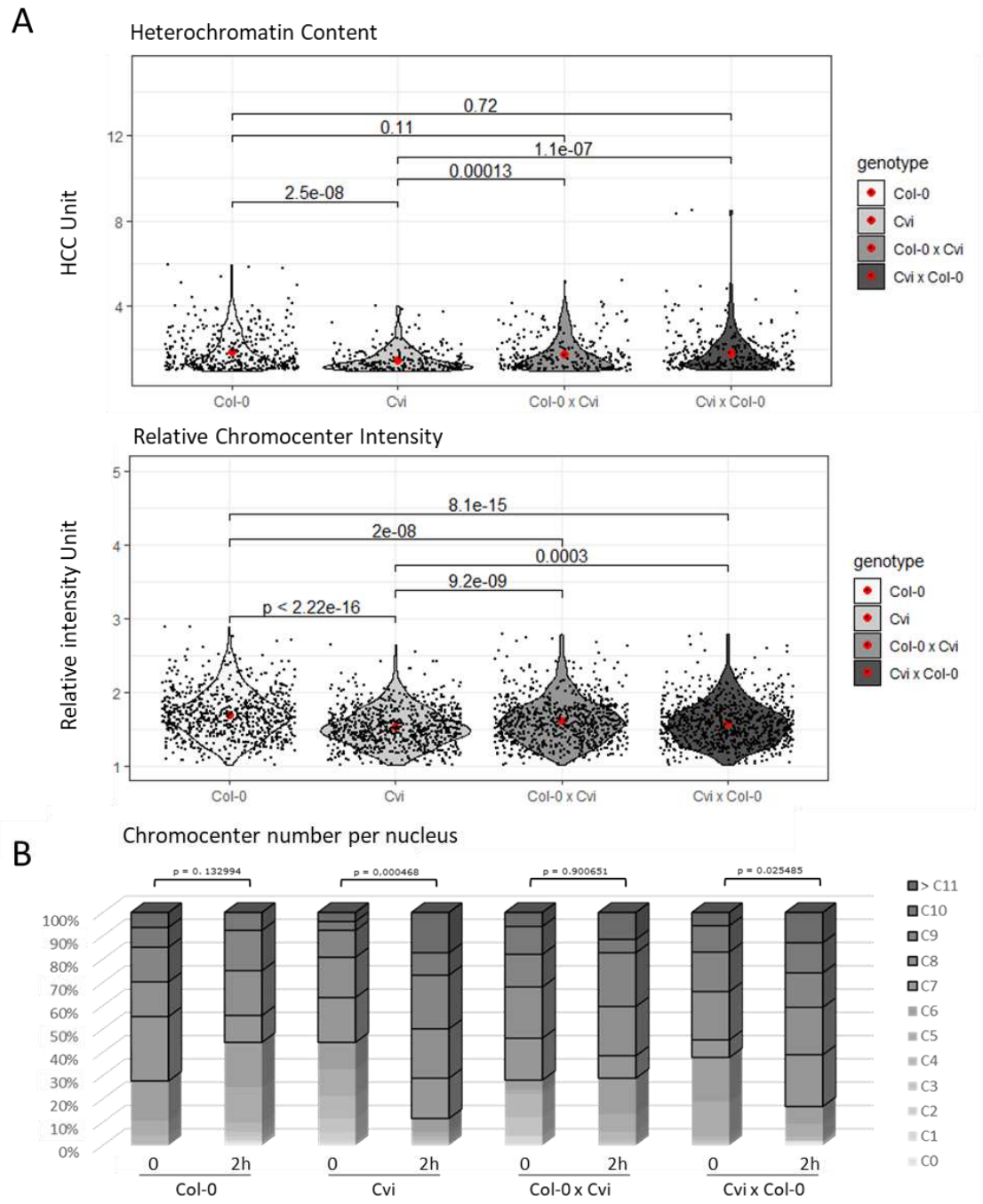

Supplemental Figure 3: Violin plot HC and RI of individually measured chromocenters

(A) Violin plots showing the distribution of Heterochromatin content (Chromocenter occupancy * Relative chromocenter Intensity) and Relative Chromocenter Intensities (ratio of mean chromocenter intensities / Mean nuclei intensity) measured individually for each chromocenter. Each black dot represents the measure for one chromocenter. The red dot shows the mean value. Exact p values are shown (Mann Whitney Wilcoxon test). **(D)** Stacked pillar diagram comparing the number of Chromocenters per nucleus upon UV-B in Col-0, Cvi, Col-0 x Cvi and in Cvi x Col-0 nuclei. Exact p values are shown (Chi-Square test: χ^2).

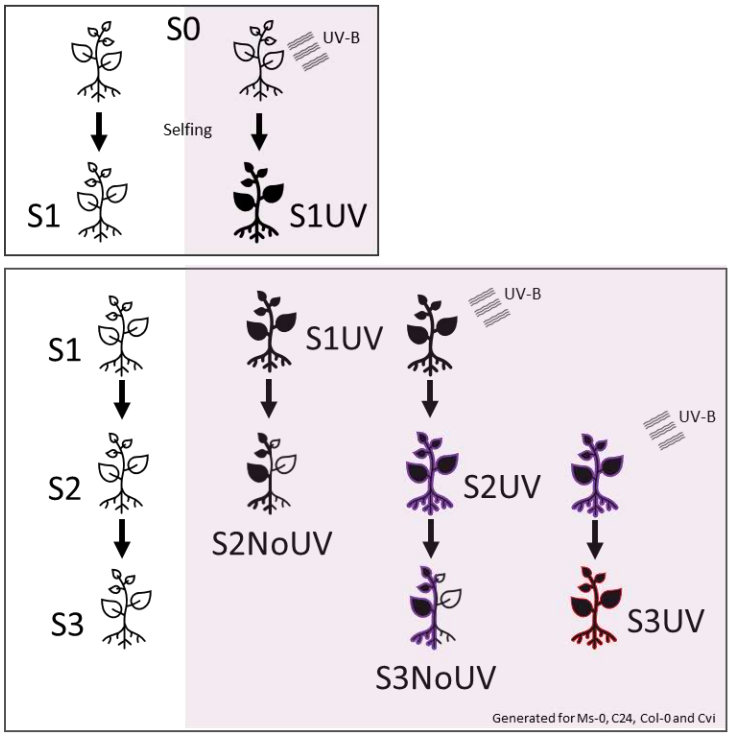

Supplemental Figure 4: Scheme of the "Directed Evolution" – Assay

S0 is the parental plant of ecotypes cultivated under our growth conditions (see Material and Methods for details). Half of the population (n= 15) is kept in control condition, whereas the other half was UV-B irradiated once 21-day-old. S0 plants undergo selfing, generating S1 progeny originating from untreated S0 plants and S1UV progeny originating from UV-B-treated S0 plants. S1UV plants are selfed to generate S2NoUV and S2UV seed. In parallel S1 seeds are grown in the control condition to generate S2 control plants. These steps were already repeated till generation S3 for Ms-0, C24, Col-0, and Cvi ecotypes.

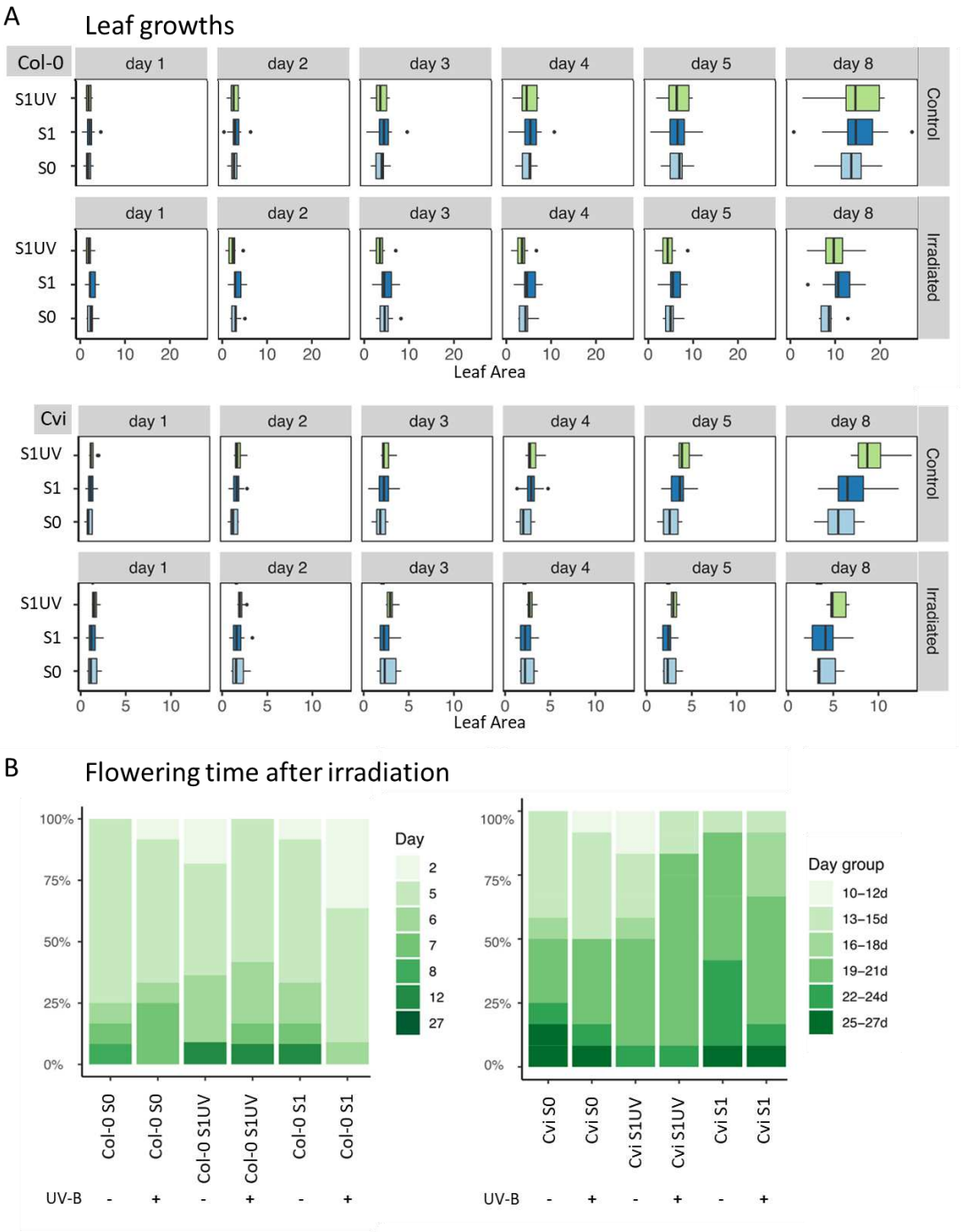

Supplemental Figure 5: Phenotypic analysis of leaf growth and flowering time upon UV-B exposure

(A) Leaf growth of Col-0 S0, Col-0 S1, Col-0 S1UV, Cvi S0, Cvi S1, and Cvi S1UV plants in control condition and upon UV-B exposure (at Day 3). **(B)** Flowering time after irradiation in Col-0 S0, Col-0 S1, Col-0 S1UV, Cvi S0, Cvi S1, and Cvi S1UV plants in control condition and upon UV-B exposure.

6.5. References

Alonso-Blanco C, Andrade J, Becker C, Bemm F, Bergelson J, Borgwardt KM, Cao J, Chae E, Dezwaan TM, Ding W, Ecker JR, Exposito-Alonso M, Farlow A, Fitz J, Gan X, Grimm DG, Hancock AM, Henz SR, Holm S, Horton M, Jarsulic M, Kerstetter RA, Korte A, Korte P, Lanz C, Lee C-R, Meng D, Michael TP, Mott R, Muliyati NW, Nägele T, Nagler M, Nizhynska V, Nordborg M, Novikova PY, Picó FX, Platzer A, Rabanal FA, Rodriguez A, Rowan BA, Salomé PA, Schmid KJ, Schmitz RJ, Seren Ü, Sperone FG, Sudkamp M, Svardal H, Tanzer MM, Todd D, Volchenboum SL, Wang C, Wang G, Wang X, Weckwerth W, Weigel D, Zhou X (2016) 1,135 Genomes Reveal the Global Pattern of Polymorphism in Arabidopsis thaliana. Cell 166:481–491. https://doi.org/10.1016/j.cell.2016.05.063

Ashe A, Colot V, Oldroyd BP (2021) How does epigenetics influence the course of evolution? Philosophical Transactions of the Royal Society B: Biological Sciences 376:20200111. https://doi.org/10.1098/rstb.2020.0111

Banyasz A, Esposito L, Douki T, Perron M, Lepori C, Improta R, Markovitsi D (2016) Effect of C5-Methylation of Cytosine on the UV-Induced Reactivity of Duplex DNA: Conformational and Electronic Factors. J Phys Chem B 120:4232–4242. https://doi.org/10.1021/acs.jpcb.6b03340

Beckmann M, Václavík T, Manceur AM, Šprtová L, von Wehrden H, Welk E, Cord AF (2014) glUV: a global UV-B radiation data set for macroecological studies. Methods in Ecology and Evolution 5:372–383. https://doi.org/10.1111/2041-210X.12168

Biedermann S, Hellmann H (2010) The DDB1a interacting proteins ATCSA-1 and DDB2 are critical factors for UV-B tolerance and genomic integrity in Arabidopsis thaliana. Plant J 62:404–415. https://doi.org/10.1111/j.1365-313X.2010.04157.x

Brown BA, Cloix C, Jiang GH, Kaiserli E, Herzyk P, Kliebenstein DJ, Jenkins GI (2005) A UV-B-specific signaling component orchestrates plant UV protection. Proc Natl Acad Sci U S A 102:18225–18230. https://doi.org/10.1073/pnas.0507187102

Castells E, Molinier J, Drevensek S, Genschik P, Barneche F, Bowler C (2010) det1-1-induced UV-C hyposensitivity through UVR3 and PHR1 photolyase gene over-expression. Plant J 63:392–404. https://doi.org/10.1111/j.1365-313X.2010.04249.x

Cloix C, Kaiserli E, Heilmann M, Baxter KJ, Brown BA, O'Hara A, Smith BO, Christie JM, Jenkins GI (2012) C-terminal region of the UV-B photoreceptor UVR8 initiates signaling through interaction with the COP1 protein. Proc Natl Acad Sci U S A 109:16366–16370. https://doi.org/10.1073/pnas.1210898109

Cortijo S, Aydin Z, Ahnert S, Locke JC (2019) Widespread inter-individual gene expression variability in Arabidopsis thaliana. Mol Syst Biol 15:e8591. https://doi.org/10.15252/msb.20188591

D'Urso A, Brickner JH (2014) Mechanisms of epigenetic memory. Trends Genet 30:230–236. https://doi.org/10.1016/j.tig.2014.04.004

Gan X, Stegle O, Behr J, Steffen JG, Drewe P, Hildebrand KL, Lyngsoe R, Schultheiss SJ, Osborne EJ, Sreedharan VT, Kahles A, Bohnert R, Jean G, Derwent P, Kersey P, Belfield EJ, Harberd NP, Kemen E, Toomajian C, Kover PX, Clark RM, Rätsch G, Mott R (2011) Multiple reference genomes and transcriptomes for Arabidopsis thaliana. Nature 477:419–423. https://doi.org/10.1038/nature10414

Jiang J, Liu J, Sanders D, Qian S, Ren W, Song J, Liu F, Zhong X (2021) UVR8 interacts with de novo DNA methyltransferase and suppresses DNA methylation in Arabidopsis. Nat Plants 7:184–197. https://doi.org/10.1038/s41477-020-00843-4

Johann to Berens P, Molinier J (2020) Formation and Recognition of UV-Induced DNA Damage within Genome Complexity. Int J Mol Sci 21. https://doi.org/10.3390/ijms21186689

Kaiserli E, Jenkins GI (2007) UV-B promotes rapid nuclear translocation of the Arabidopsis UV-B specific signaling component UVR8 and activates its function in the nucleus. Plant Cell 19:2662–2673. https://doi.org/10.1105/tpc.107.053330

Kawakatsu T, Huang S-SC, Jupe F, Sasaki E, Schmitz RJ, Urich MA, Castanon R, Nery JR, Barragan C, He Y, Chen H, Dubin M, Lee C-R, Wang C, Bemm F, Becker C, O'Neil R, O'Malley RC, Quarless DX, 1001 Genomes Consortium, Schork NJ, Weigel D, Nordborg M, Ecker JR (2016) Epigenomic Diversity in a Global Collection of Arabidopsis thaliana Accessions. Cell 166:492–505. https://doi.org/10.1016/j.cell.2016.06.044

Kliebenstein DJ, Lim JE, Landry LG, Last RL (2002) Arabidopsis UVR8 regulates ultraviolet-B signal transduction and tolerance and contains sequence similarity to human regulator of chromatin condensation 1. Plant Physiol 130:234–243. https://doi.org/10.1104/pp.005041

Kutashev KO, Franek M, Diamanti K, Komorowski J, Olšinová M, Dvořáčková M (2021) Nucleolar rDNA folds into condensed foci with a specific combination of epigenetic marks. Plant J 105:1534–1548. https://doi.org/10.1111/tpj.15130

Latta RG (2010) Natural Selection, Variation, Adaptation, and Evolution: A Primer of Interrelated Concepts. International Journal of Plant Sciences 171:930–944. https://doi.org/10.1086/656220

Lau OS, Deng XW (2012) The photomorphogenic repressors COP1 and DET1: 20 years later. Trends Plant Sci 17:584–593. https://doi.org/10.1016/j.tplants.2012.05.004

Li N, Teranishi M, Yamaguchi H, Matsushita T, Watahiki MK, Tsuge T, Li S-S, Hidema J (2015) UV-B-Induced CPD Photolyase Gene Expression is Regulated by UVR8-Dependent and -Independent Pathways in Arabidopsis. Plant Cell Physiol 56:2014–2023. https://doi.org/10.1093/pcp/pcv121

Liang T, Mei S, Shi C, Yang Y, Peng Y, Ma L, Wang F, Li X, Huang X, Yin Y, Liu H (2018) UVR8 Interacts with BES1 and BIM1 to Regulate Transcription and Photomorphogenesis in Arabidopsis. Dev Cell 44:512-523.e5. https://doi.org/10.1016/j.devcel.2017.12.028

Liang T, Yang Y, Liu H (2019) Signal transduction mediated by the plant UV-B photoreceptor UVR8. New Phytol 221:1247–1252. https://doi.org/10.1111/nph.15469

Liu J, Feng L, Gu X, Deng X, Qiu Q, Li Q, Zhang Y, Wang M, Deng Y, Wang E, He Y, Bäurle I, Li J, Cao X, He Z (2019) An H3K27me3 demethylase-HSFA2 regulatory loop orchestrates transgenerational thermomemory in Arabidopsis. Cell Res 29:379–390. https://doi.org/10.1038/s41422-019-0145-8

Migicovsky Z, Kovalchuk I (2014) Transgenerational changes in plant physiology and in transposon expression in response to UV-C stress in Arabidopsis thaliana. Plant Signal Behav 9:e976490. https://doi.org/10.4161/15592324.2014.976490

Ossowski S, Schneeberger K, Clark RM, Lanz C, Warthmann N, Weigel D (2008) Sequencing of natural strains of Arabidopsis thaliana with short reads. Genome Res 18:2024–2033. https://doi.org/10.1101/gr.080200.108

Pavlova P, van Zanten M, Snoek BL, de Jong H, Fransz P (2021) 2D morphometric analysis of Arabidopsis thaliana nuclei reveals characteristic profiles of different cell types and accessions. Chromosome Res. https://doi.org/10.1007/s10577-021-09673-2

Ries G, Buchholz G, Frohnmeyer H, Hohn B (2000) UV-damage-mediated induction of homologous recombination in Arabidopsis is dependent on photosynthetically active radiation. Proc Natl Acad Sci U S A 97:13425–13429. https://doi.org/10.1073/pnas.230251897

Rochette PJ, Lacoste S, Therrien J-P, Bastien N, Brash DE, Drouin R (2009) Influence of cytosine methylation on ultraviolet-induced cyclobutane pyrimidine dimer formation in genomic DNA. Mutat Res 665:7–13. https://doi.org/10.1016/j.mrfmmm.2009.02.008

Schalk C, Cognat V, Graindorge S, Vincent T, Voinnet O, Molinier J (2017) Small RNA-mediated repair of UV-induced DNA lesions by the DNA DAMAGE-BINDING PROTEIN 2 and ARGONAUTE 1. Proc Natl Acad Sci U S A 114:E2965–E2974. https://doi.org/10.1073/pnas.1618834114

Schmitz RJ, Schultz MD, Urich MA, Nery JR, Pelizzola M, Libiger O, Alix A, McCosh RB, Chen H, Schork NJ, Ecker JR (2013) Patterns of population epigenomic diversity. Nature 495:193–198. https://doi.org/10.1038/nature11968

Schuch AP, Moreno NC, Schuch NJ, Menck CFM, Garcia CCM (2017) Sunlight damage to cellular DNA: Focus on oxidatively generated lesions. Free Radic Biol Med 107:110–124. https://doi.org/10.1016/j.freeradbiomed.2017.01.029

Simon L, Voisin M, Tatout C, Probst AV (2015) Structure and Function of Centromeric and Pericentromeric Heterochromatin in Arabidopsis thaliana. Front Plant Sci 6. https://doi.org/10.3389/fpls.2015.01049

Snoek BL, Pavlova P, Tessadori F, Peeters AJM, Bourbousse C, Barneche F, de Jong H, Fransz PF, van Zanten M (2017) Genetic Dissection of Morphometric Traits Reveals That Phytochrome B Affects Nucleus Size and Heterochromatin Organization in Arabidopsis thaliana. G3 (Bethesda) 7:2519–2531. https://doi.org/10.1534/g3.117.043539

Sun L, Jing Y, Liu X, Li Q, Xue Z, Cheng Z, Wang D, He H, Qian W (2020) Heat stress-induced transposon activation correlates with 3D chromatin organization rearrangement in Arabidopsis. Nat Commun 11:1886. https://doi.org/10.1038/s41467-020-15809-5

Tessadori F, van Zanten M, Pavlova P, Clifton R, Pontvianne F, Snoek LB, Millenaar FF, Schulkes RK, van Driel R, Voesenek LACJ, Spillane C, Pikaard CS, Fransz P, Peeters AJM (2009) Phytochrome B and histone deacetylase 6 control light-induced chromatin compaction in Arabidopsis thaliana. PLoS Genet 5:e1000638. https://doi.org/10.1371/journal.pgen.1000638

Tossi VE, Regalado JJ, Iannicelli J, Laino LE, Burrieza HP, Escandón AS, Pitta-Álvarez SI (2019) Beyond Arabidopsis: Differential UV-B Response Mediated by UVR8 in Diverse Species. Frontiers in Plant Science 10

Vechtomova YuL, Telegina TA, Kritsky MS (2020) Evolution of Proteins of the DNA Photolyase/Cryptochrome Family. Biochemistry Moscow 85:131–153. https://doi.org/10.1134/S0006297920140072

Velanis CN, Herzyk P, Jenkins GI (2016) Regulation of transcription by the Arabidopsis UVR8 photoreceptor involves a specific histone modification. Plant Mol Biol 92:425–443. https://doi.org/10.1007/s11103-016-0522-3

Weigel D, Mott R (2009) The 1001 genomes project for Arabidopsis thaliana. Genome Biol 10:107. https://doi.org/10.1186/gb-2009-10-5-107

Willing E-M, Piofczyk T, Albert A, Winkler JB, Schneeberger K, Pecinka A (2016) UVR2 ensures transgenerational genome stability under simulated natural UV-B in Arabidopsis thaliana. Nat Commun 7:13522. https://doi.org/10.1038/ncomms13522

Wu W, Li L, Zhao Y, Zhao Y, Jiang T, McCormick S, Zheng B (2021) Heterochromatic silencing is reinforced by ARID1-mediated small RNA movement in Arabidopsis pollen. New Phytol 229:3269–3280. https://doi.org/10.1111/nph.16871

Xiong Y, Xing Q, Müller-Xing R (2021) A novel UV-B priming system reveals an UVR8-depedent memory, which provides resistance against UV-B stress in Arabidopsis leaves. Plant Signal Behav 16:1879533. https://doi.org/10.1080/15592324.2021.1879533

Zhang X, Li C, Tie D, Quan J, Yue M, Liu X (2021) Epigenetic memory and growth responses of the clonal plant Glechoma longituba to parental recurrent UV-B stress. Funct Plant Biol 48:827–838. https://doi.org/10.1071/FP20303

7. General discussion

7.1. DNA damageability and epigenetic landscape

The first aim of our study was to determine the localization of UV-induced DNA damages to question the influence of the epigenetic context on their formation. We focused our attention on CPDs , 6,4-PPs and the oxidatively-induced DNA damage 8-Oxo-G. In Chapter I, we shed light on the particular distribution of CPDs and 6,4-PP within the Arabidopsis genome. Photolesions localization was analyzed using damage specific antibodies either for immunolabeling of microscopical probes or for the precipitation of DNA fragments followed by new generation sequencing (Graindorge et al. 2019). The thereby generated view confirms the common thought that DNA/histone methylation and nucleosome occupancy correlate with the formation of photolesions (Johann to Berens and Molinier 2020).

Interestingly, both CPD and 6-4-PP overlap significantly with the chromocenters; the chromatin states CS2, CS4, CS5 (facultative heterochromatin), CS8, CS9 (constitutive heterochromatin), CS6 (intergenic regions), and more precisely with H3K9me2 enriched loci. The common feature of these genomic regions is the presence of epigenetic marks related to transcriptional silencing. We questioned whether H3K9me2 favors damageability or if this observation is an indirect correlation linked to the close relation between DNA methylation and H3K9me2 (Jackson et al. 2002; Law et al. 2013). In line with this observation, the *kyp suvh5,6* mutant, deficient for the expression of the main H3K9me2 methyltransferases and the natural variant Cvi, are known to contain reduced H3K9me2 contents and show a reduced accumulation of photolesions compared to the Col-0 wild-type plants. Moreover, *kyp suvh5,6* and Cvi plants also exhibit a decreased DNA methylation level, most likely as a consequence of a reduced H3K9me2 content (Tessadori et al. 2009; Stroud et al. 2013; Pignatta et al. 2014). Consequently, the low photodamage accumulation could be indirectly linked to H3K9me2. Nevertheless, this observation strengthens the idea that photolesion formation is highly influenced by the epigenetic context.

UV-B exposure is thought to induce both photolesions and oxidatively-induced DNA damage (Schuch et al. 2017). Unfortunately, in our experimental conditions, we were unable to generate a detectable amount of 8-Oxo-G using UV-B irradiation. This observation can notably be explained by the strong antioxidant production that we detected upon UV-B thanks to a metabolomic approach. Among these metabolites, we could observe an accumulation of 5-hydroy-L-Tryptophane (5-HTP) which was shown to be a substrate in the melatonin biosynthesis in Arabidopsis (Back et al. 2016). Interestingly, melatonin is enriched upon UV-B exposure in Arabidopsis, thereby regulating several UV responsive genes (Yao et al. 2021). Thus, our experiment may highlight the dual role of 5-HTP as an antioxidant and precursor for further molecular signaling. In addition, it cannot be excluded that the lack of/weak detection of 8-Oxo-G, reflects the short half-life of this modified base.

However, 8-Oxo-G could be detected through a cytochemical approach using an alternative genotoxic source to generate an oxidative burst. Indeed, Arabidopsis leaves exposed to proton irradiation display an 8-Oxo-G spotty signal all over the nucleus. This distribution strongly resembles the pattern observed in human cells upon $KBrO_3$ induced oxidative stress (D'Augustin et al. 2020). Unfortunately, this pattern does not provide robust information about the role of the epigenome in the distribution of 8-Oxo-G. It can be speculated that the spot-like structure may be due to sequence specificities (*i.e.,* G-Quadruplex (Martínez-López et al. 1998; Mullen et al. 2010)) and/or to particular epigenetic landscape (*i.e.,* euchromatin). Additionally, it should be considered that the proton beam, despite its homogenous dose deposition by surface all over the nucleus, most likely introduces a more vigorous oxidative burst in regions with high H_2O concentration. Consequently, the macromolecular crowding effect in heterochromatic regions (dense in DNA and proteins) may lead to comparatively low water radiolysis in comparison to the euchromatic areas (Privett et al. 2017; Malacrida et al. 2017). This local decrease in water radiolysis may, in turn, explain the reduced amount of 8-Oxo-G detected in the heterochromatic area. In addition, the probability for a proton to directly deliver its kinetic energy to proteins and DNA is increased in heterochromatin fractions. This could lead to an accumulation of DNA strand-breaks and crosslinking events (Ibañez et al. 2009; Luitel et al. 2018).

Strikingly, the 8-Oxo-G pattern looks different when leaves get exposed to Paraquat with enrichment of dot-signals around chromocenters. This observation may result from 2 main differences:

Firstly, Paraquat treatment induces an oxidative burst originating from the chloroplasts (Hawkes 2014). Thus, the stress may not be homogeneously distributed in the cell and may show a directionality. It can be postulated that these oxidative waves originating from the cytoplasm encounters the phase-separated heterochromatic chromocenters and pLAD structures, discharging most of their reactional energy before reaching the euchromatin.

Secondly, Paraquat is a chemical compound acting for several hours. Thus, the 8-oxo-G pattern may also result from this chronic exposure and the slower DNA repair of heterochromatic regions (Falk et al. 2010). However, the center of chromocenters always shows exclusion of the 8-Oxo-G signal, indicating that structural and epigenetic characteristics may influence such accumulation patterns. Indeed, human cells exposed to $KBrO_3$ for 30 min, display 8-Oxo-G enrichment at the border of DNA-dense structures (Campalans et al. 2013), arguing in favor of a primarily DNA structure and thereby epigenome-dependent damaging.

Taken together, our observations support the notion that the epigenome influences DNA damageability. In the case of photolesions, we observed a clear tendency for a heterochromatin-dependent enrichment, whereas 8-Oxo-G is mainly excluded from heterochromatin. In addition, our experiments highlight the hyperparametric complexity that needs to be considered for deciphering how epigenetic marks influence DNA damageability depending on the genotoxic source.

7.2. Constitutive heterochromatin is reshaped by genotoxic stress

Our study shed light on the dynamic of *Arabidopsis thaliana* constitutive heterochromatin upon exposure to different sources of genotoxic stresses. These results rely on a robust image analysis approach. Indeed, the accuracy of this analysis was significantly improved by the development of a deep learning-based automatic tool. Such a tool reduces time cost in data mining and enhances reliability in an experimentalist-independent manner.

Interestingly, both UV-C and UV-B exposures lead to early (2h) heterochromatin decompaction followed by a re-compaction, 24h following irradiation. This observation indicates that common molecular processes may act to reshape constitutive heterochromatin. This dynamic reminds the access-repair-restore model mechanism (Polo and Almouzni 2015) and is in agreement with the predisposition of the heterochromatic regions to accumulate photolesions upon UV-C and UV-B exposures.

In addition, we observed an increased heterochromatin content in Arabidopsis nuclei 24h upon exposure to a proton beam, as described upon UV-C exposure. Importantly, proton irradiation neither induces photolesions nor 8-Oxo-G in these heterochromatic regions. The most plausible explanation is that other types of damages (SSB and/or DSB) may have occurred (Ibañez et al. 2009) and thereby promote an access-repair-restore process. In mammalian cell cultures, irradiation-induced DSBs occur in euchromatin (Falk et al. 2010) whilst heterochromatin shows a high chromosome aberration frequency, probably due to a less efficient repair (Surrallés et al. 1997a; Surrallés et al. 1997b; Surrallés et al. 1998). DSB repair was proposed to depend on chromatin movement out of heterochromatin at the more accessible periphery (Falk et al. 2010; Caron et al. 2021; Arnould et al. 2021). This type of movement may be a source of important structural change at constitutive heterochromatin and thereby could partially explain our observations (Falk et al. 2010; Caron et al. 2021; Arnould et al. 2021). Alternatively, it can be questioned to which extent DNA damages occurring in euchromatin can affect the heterochromatic structures, for example, through *de novo* heterochromatin formation at damages loci. To our knowledge, the epigenetic dynamic of heterochromatin upon proton irradiation has not been reported. However, future investigations focusing on the early dynamic of heterochromatin and on the localization of other types of DNA damage (*i.e.* DSB) in proton-irradiated nuclei will be needed to better understand such heterochromatin dynamic. Moreover, our data suggest that constitutive heterochromatic structures can be used as a genotoxic stress sensor and as a quantifiable phenotypic trait.

Thanks to automated tools (Bian et al. 2020), such as Nucl.Eye.D pipeline, High-Throughput Imaging (HTI) (Pegoraro and Misteli 2017), mutant screening may become an interesting perspective to identify new players involved in chromatin remodeling during DNA repair. This type of approach is already used in several domains, notably for the analysis of Fluorescence *in situ* hybridization images or global disease phenotyping (Shachar et al. 2015; Pegoraro and Misteli 2017).

7.3. H3K9me2 homeostasis acts in constitutive heterochromatin dynamics during photodamage repair

In Chapter III of this work, we determined the shape of constitutive heterochromatin histone marks (H3K9me2 and H3K27me1) in a time course following UV-C exposure. In agreement with the DAPI staining (Chapter I), we identified a significant decrease in H3K9me2 content 2h upon UVC irradiation, whereas H3K27me1 contents remain stable. The loss of H3K9me2 content strongly resembles the active H3K9me3 demethylation reported in Drosophila during the repair of UV-induced DNA damage (Palomera-Sanchez et al. 2010). Interestingly, a decompaction of heterochromatin also occurs a few minutes after microtargeting heterochromatic regions with UV-C-Laser (Fortuny et al. 2021). Thus, this process might be conserved among several species, including plants.

Surprisingly, we observed a precocious (30 min) increase of H3K9me2 content. As, the H3K9me2 histone methyltransferase, KYP, acts upstream of DDB2, it can be assumed that such increase in H3K9me2 content labels heterochromatin for efficient recruitment of the DDB2 complex at particular regions as well as in the nucleosome rich regions. Indeed, we found that chromatin DDB2 loading is less efficient in H3K9me2 depleted plants. Moreover, DDB2 loads earlier in nucleosome-free regions than on nucleosomal DNA, in agreement with the mechanisms reported in human cells (Fei et al. 2011). Indeed, a slight increase of the H3K9me3 content was observed 1h after damaging heterochromatic regions with UV-C-Laser (Fei et al. 2011). We propose that H3K9me2 homeostasis likely regulates DDB2 recruitment and photodamage accessibility during GGR. This working hypothesis was further supported by some of our findings. Indeed, we identified that DDB2 and the H3K9me2 demethylase, JMJ27, interact in a complex and are both necessary for the decrease of H3K9me2 content 2h upon irradiation.

Additionally, we showed that JMJ27 is essential to stabilize DDB2 within nucleosomal DNA. Thus, it seems that JMJ27 actively demethylated the histone H3K9m2 in the vicinity of the damage sites, restraining further DNA methylation (Stroud et al. 2014; Li et al. 2018; Xu and Jiang 2020) and leading to a relaxed heterochromatin shape which may allow nucleosome shifting for stable DDB2 loading (Matsumoto et al. 2019).

7.4. H3K27me1, like a rock in the storm

We also analyzed the dynamic of another heterochromatic mark, H3K27me1, that did not exhibit significant alterations upon UV-C exposure. The lack of H3K27me1 dynamic is another evidence indicating that H3K9me2 is specifically targeted during photodamage repair. Moreover, H3K27me1 stability in constitutive heterochromatin rules out for a massive core-histone eviction. Given that H3K9me2 and H3K27me1 largely overlap in heterochromatin (Costas et al. 2011; Roudier et al. 2011), it would strengthen the idea that H3K9me2 fine-tuning plays a key role in UV-C response. The lack of a clear H3K27me1 specific eraser supports these observations (Antunez-Sanchez et al. 2020). H3K27me1 deposition occurs in a replication-dependent manner (Jacob et al. 2009; Jacob et al. 2014; Ma et al. 2018) and is uncoupled from DNA methylation. Indeed, H3K27me1 *de novo* deposition by ATXR5,6 in collaboration with SERRATE even inhibits RDR6-directed DNA methylation (Ma et al. 2018). In addition, the erasure of H3K27me1 may induce K27 acetylation by GCN5 (Dong et al. 2021), preventing the accurate re-establishment of the initial epigenetic landscape.

7.5. A dual role for H3K9me2 in chromosome structure and in transcriptional regulation

Aside from its structural role, H3K9me2 also mediates a regulatory function on the expression of a subset of protein-coding genes (Zhou et al. 2010). Consequently, it cannot be excluded that the dynamic observed in chromocenters also impacts gene regulation in chromosome arms. Indeed, in WT plants 2h upon UV-C exposure, we observed a decrease of the nucleoplasmic H3K9me2 signal, indicating that the subset of H3K9me2 regulated regions may show a release of silencing (Zhou et al. 2010) or a different transcriptional elongation process (Rigal et al. 2012).

Previous studies characterized a subset of 1.100 loci occupied by H3K9me2 and most likely under the antagonistic effect of both H3K9me2 and H3K9ac (Zhou et al. 2010). Among these genes are the photoreceptor UV-B-RESISTANCE 8 (UVR8), the CONSTITUTIVE PHOTOMORPHOGENIC 9 (COP9), and the E3 ubiquitin ligase component CULLIN4 (CUL4) (Zhou et al. 2010). The regulatory role of H3K9me2 was also demonstrated during drought response in Arabidopsis (Wang et al. 2021). In this study, the histone demethylase JMJ27 was shown to positively regulate drought-responsive genes such as GALACTINOL SYNTHASE 2 (GOLS2) and RESPONSE TO DESICCATION 20 (RD20) (Wang et al. 2021). As shown by this study, JMJ27 and RPN1a (REGULATORY PARTICLE NON-ATPASE 1a), a subunit of the 26S proteasome, regulate dynamic H3K9me2 deposition, ensuring proper response to drought stress (Wang et al. 2021).

Interestingly, the regulation of programmed cell death (PCD) genes upon pathogen invasion were also proposed to depend on the regulation of H3K9me2 (Dvořák Tomaštíková et al. 2021). Indeed, PCD induction was shown to induce chromocenter decompaction in a H3K9me2-dependent manner (Dvořák Tomaštíková et al. 2021). This H3K9me2 dynamic deregulates expression of several TEs and PCG (Dvořák Tomaštíková et al. 2021). Indeed, around 800 genes loose H3K9me2 and 500 genes gain H3K9me2 upon pathogen infection (Dvořák Tomaštíková et al. 2021). Interestingly, defect in the expression of the main H3K9me2 histone methyltransferase, KYP, enhances the progression of PCD (Dvořák Tomaštíková et al. 2021). Thus, the authors assumed that the loss of H3K9me2 participates in the regulation of a subset of PCD relevant genes in complement to the predominant role of H3K27me3 in this process (Dvořák Tomaštíková et al. 2021). However, our UV-C treatment did not induce any phenotypic traits associated with senescence, although it is well-established that UV-C irradiation induces transcriptional changes resembling fungal/bacterial elicitations (Molinier et al. 2005).

Altogether these observations are strong indications for a potential role of the UV-C-induced H3K9me2 dynamic in transcriptional regulation of specific stress-responsive genes. These dynamic changes in H3K9me2 landscape need to be further investigated, notably through our ongoing ChIP approaches and by considering the antagonistic histone mark, H3K9ac (Zhou et al. 2010).

7.6. Photodamage repair pathways and genetic immunity

The rather limited pool of DNA repair proteins forces to set priorities between transcriptionally active and silenced loci in order to prevent any deleterious effects such as mutations accumulation or burst of TE mobilization. Importantly, given that DNA repair mechanisms require chromatin opening and that heterochromatin contains many TEs, the repair of this particular genomic region may lead to TE reactivation. Indeed, TE reactivation was reported in Arabidopsis and Maize upon UV exposure (Qüesta et al. 2010; Graindorge et al. 2019). Interestingly, the centromeric 180bp repeats and 5S rDNA transcripts also accumulate 2h upon UV irradiation (Chapter IV).

Thus, heterochromatin repair should be fine-tuned to efficiently maintain genome integrity and to prevent excessive transcriptional activation/mobilization of TE. Therefore, the mobilized molecular mechanisms should cooperate to act in both directions. Interestingly, plants evolved sophisticated pathways to repair photodamage and to ensure silencing. One such pathway is the AGO1 (ARGONAUTE1)/siRNA-dependent recruitment of DDB2 to damaged sites and the DDB2 chaperoning of AGO4 (ARGONAUTE4) to inhibit RdDM (Schalk et al. 2017). Together both mechanisms were proposed to regulate fine-tune DNA repair/methylation in heterochromatic regions (Schalk et al. 2016; Schalk and Molinier 2016; Schalk et al. 2017). Indeed, once DNA repair is completed, DDB2 may release AGO4, thereby allowing RdDM to re-establish DNA methylation at damaged loci and to prevent further TE reactivation. This observation is in agreement with the newly described mechanism by which DDB2 and JMJ27 collaborate in H3K9me2 demethylation (Chapter III). Future studies should investigate by which mechanism the H3K9me2 occupancy is re-established upon repair and if DDB2 also regulates directly or indirectly KYP activity upon repair.

In our study, we observed alterations of the methylome in constitutive heterochromatin. Indeed, 24h upon UV-C exposure, we identified many differentially methylated regions (DMRs) mainly in CHH context (Chapter I (Graindorge et al. 2019)). This equilibrium is disturbed in *ddb2*, and *uvr3phr1* mutant plants, where an increased amount of Hyper- and Hypo-DMRs could respectively be identified (Graindorge et al. 2019).

This observation reveals the complementarity of both repair mechanisms in the maintenance of genome and epigenome integrity (Graindorge et al. 2019). Moreover, it suggests that change of the methylation levels, in addition to the increased H3K9me2 occupancy (Chapter III), may reinforce the silencing of particular loci (*i.e.,* TE) to avoid further mobilization and prevent genome instability.

7.7. GGR and DR in Heterochromatin

We provide evidence that a DDB2-dependent decompaction of heterochromatin and an interplay between GGR and H3K9me2 homeostasis exist. However, in parallel, we also observed that UV irradiation-induced a fast re-localization of the UVR3 photolyase to the chromocenter regions for at least 2h upon UV-C irradiation. These results differ from reports describing that photolyases were inefficient in repairing photodamaged DNA within nucleosomes (Smerdon and Conconi 1999; Thoma 1999; Suter and Thoma 2002). Interestingly, Suter and Thoma revealed that photolyases show a slow repair in the center of nucleosomes rich regions in yeast (Suter and Thoma 2002). Although a discrepancy between these findings exists, it also suggests that nucleosome mobility or its transient disruption could participate in photolyases damage accessibility and repair. Indeed, sequences that are transiently unwrapped or exposed away for nucleosome are proposed to become the target for photolyases (Duan and Smerdon 2010). However, the exact mechanism for this type of interaction is still under debate. According to our results, it can be assumed that the UVR3 photolyase would find opportunities for damage recognition in the vicinity of the chromatin remodeled during the precious steps of the GGR (Matsumoto et al. 2019) (Chapter III). Thus, DDB2 may indirectly participate in DR, through its chromatin remodeling activity, even without a direct damage handover as observed with XPC (Akita et al. 2015). An additional benefit of this process would be to speed up the repair in transcriptionally silenced regions, thereby limiting the use of the invasive NER involving *de novo* DNA synthesis (Johann to Berens and Molinier 2020) as a last resort for sequences within nucleosomes.

Altogether, our study provides an additional piece of the puzzle on the understanding of fundamental mechanisms of photodamage recognition in heterochromatin regions. This data could be easily integrated with the access-repair-restore model. However, most players providing access remain unknown (Kim 2019). Future work is needed to investigate the role of chromatin remodelers and other epigenetic erasers in this process. Additionally, it may be questioned if the fast photolyase re-localization to heterochromatin may depend on an active recruitment mechanism.

7.8. UV-induced parental effects

Interestingly, in the last years, UV-light and especially UV-C became an interesting tool to enhance plant fitness upon environmental stress exposure (Thomas T.T. and Puthur 2017). Indeed, farmers have known UV-C irradiation for several years to have a beneficial effect on stress tolerance, growth, and crop yield, most likely through a transcriptional priming effect (Thomas T.T. and Puthur 2017). However, little is known about the mechanisms linking UV-C irradiation to the expressional priming and the resulting stress resistance. This UV-induced priming effect was even observed to be inherited to the next generation (Thomas T.T. and Puthur 2017). Thus, it is of ecological and economic interest to further investigate to which extent the UV-C-induced epigenetic changes described in our work may participate in such long-term priming. Especially since previous studies provided evidence that transgenerational salt-stress memory notably depends on H3K9me2 (Bilichak et al. 2012).

We hypothesized that the epigenetic changes induced upon DNA repair of UV-B photolesions might trigger an inherited epigenetic memory. More precisely, we investigated whether the UV-B regime may explain the variability of chromocenter structures observed in different natural variants of *Arabidopsis thaliana*. Several studies already reveal correlations between light perception, light intensity, and chromocenter shape (Tessadori et al. 2009; Snoek et al. 2017). However, we could demonstrate that UV-B also modulates chromocenter shape and that this reshaping is different in the “small” chromocenters of Cvi plants than on the “large” ones of Col-0 plants. Indeed, 2h upon irradiation Cvi chromocenter size increases conversely to Col-0 chromocenters. Interestingly, it was shown that increased light intensity leads to enhancement of chromocenter size in both Col-0 and Cvi ecotypes (Tessadori et al. 2009). Thus, UV light regulates chromocenter shape by different mechanisms.

Such behavior is different in Col-0 and Cvi ecotypes and would likely depend on DNA repair pathways as described for chromocenter dynamic upon UV-C irradiation (Chapter I and III). Apparently, one factor involved in the UV-B-dependent chromocenter remodeling is the UV-B photoreceptor UVR8, which was notably shown to inhibit DRM2-dependent DNA methylation (Jiang et al. 2021). In our experiments, *uvr8* mutant plants tend to have smaller chromocenters 24h upon UV-B exposure. Such shape was not expected according to the hypermethylation associated to DRM2 activation reported in *uvr8* plants (Jiang et al. 2021). Consequently, we suppose a potential interplay with other epigenetic regulators.

We also found that chromocenter shape is inherited equally in crossing between Col-0 and Cvi plants. Indeed, the Col-0 x Cvi hybrids exhibit an intermediate chromocenter occupancy. This observation contrasts with previous studies describing a dominant inheritance of Cvi nuclear phenotype in Cvi x Ler hybrids (Tessadori et al. 2009; Snoek et al. 2017). However, it cannot be excluded that in both cases, the nuclear morphology depends on the inheritance of particular loci, for example, nucleotide sequences at centromeres (Ito et al. 2007; Snoek et al. 2017). Thus, the UV-B-induced parental inheritance was investigated (Chapter IV). We observed slight phenotypical and transcriptional changes in the offspring of UV-B irradiated plants indicating that priming, notably in chromocenter regions, may have occurred (Chapter IV). Unfortunately, with a single UV-B exposure of the parent plant at the seedling stage, we could not observe significant changes in chromocenter shape in the offspring. This last observation may indicate that single UV-B irradiation is insufficient to trigger visible structural changes in heterochromatin. Indeed, unlike after UV-C, no changes of chromocenter structure were measured 24h upon UV-B irradiation in parent plants, indicating that both irradiations lead to different heterochromatin reshaping.

Consequently, it can only be speculated that DNA repair-dependent and light-dependent chromocenter remodeling collaborates in the shaping of chromocenter structures in nature. Future experiments will investigate the chromocenter shape in the next generations under consecutive UV-B exposures.

7.9. References

Akita M, Tak Y-S, Shimura T, Matsumoto S, Okuda-Shimizu Y, Shimizu Y, Nishi R, Saitoh H, Iwai S, Mori T, Ikura T, Sakai W, Hanaoka F, Sugasawa K (2015) SUMOylation of xeroderma pigmentosum group C protein regulates DNA damage recognition during nucleotide excision repair. Sci Rep 5:10984. https://doi.org/10.1038/srep10984

Antunez-Sanchez J, Naish M, Ramirez-Prado JS, Ohno S, Huang Y, Dawson A, Opassathian K, Manza-Mianza D, Ariel F, Raynaud C, Wibowo A, Daron J, Ueda M, Latrasse D, Slotkin RK, Weigel D, Benhamed M, Gutierrez-Marcos J (2020) A new role for histone demethylases in the maintenance of plant genome integrity. eLife 9:e58533. https://doi.org/10.7554/eLife.58533

Arnould C, Rocher V, Finoux A-L, Clouaire T, Li K, Zhou F, Caron P, Mangeot PE, Ricci EP, Mourad R, Haber JE, Noordermeer D, Legube G (2021) Loop extrusion as a mechanism for formation of DNA damage repair foci. Nature 590:660–665. https://doi.org/10.1038/s41586-021-03193-z

Back K, Tan D-X, Reiter RJ (2016) Melatonin biosynthesis in plants: multiple pathways catalyze tryptophan to melatonin in the cytoplasm or chloroplasts. J Pineal Res 61:426–437. https://doi.org/10.1111/jpi.12364

Bian Z, Guo C, Jiang S, Zhu J, Wang R, Song P, Zhang Z, Hoshino K, Zheng G (2020) Autofocusing technologies for whole slide imaging and automated microscopy. J Biophotonics 13:e202000227. https://doi.org/10.1002/jbio.202000227

Bilichak A, Ilnystkyy Y, Hollunder J, Kovalchuk I (2012) The progeny of Arabidopsis thaliana plants exposed to salt exhibit changes in DNA methylation, histone modifications and gene expression. PLoS One 7:e30515. https://doi.org/10.1371/journal.pone.0030515

Campalans A, Kortulewski T, Amouroux R, Menoni H, Vermeulen W, Radicella JP (2013) Distinct spatiotemporal patterns and PARP dependence of XRCC1 recruitment to single-strand break and base excision repair. Nucleic Acids Research 41:3115–3129. https://doi.org/10.1093/nar/gkt025

Caron P, Pobega E, Polo SE (2021) DNA Double-Strand Break Repair: All Roads Lead to HeterochROMAtin Marks. Front Genet 12:730696. https://doi.org/10.3389/fgene.2021.730696

Costas C, de la Paz Sanchez M, Stroud H, Yu Y, Oliveros JC, Feng S, Benguria A, López-Vidriero I, Zhang X, Solano R, Jacobsen SE, Gutierrez C (2011) Genome-wide mapping of Arabidopsis thaliana origins of DNA replication and their associated epigenetic marks. Nat Struct Mol Biol 18:395–400. https://doi.org/10.1038/nsmb.1988

D'Augustin O, Huet S, Campalans A, Radicella JP (2020) Lost in the Crowd: How Does Human 8-Oxoguanine DNA Glycosylase 1 (OGG1) Find 8-Oxoguanine in the Genome? Int J Mol Sci 21:E8360. https://doi.org/10.3390/ijms21218360

Dong J, LeBlanc C, Poulet A, Mermaz B, Villarino G, Webb KM, Joly V, Mendez J, Voigt P, Jacob Y (2021) H3.1K27me1 maintains transcriptional silencing and genome stability by preventing GCN5-mediated histone acetylation. Plant Cell 33:961–979. https://doi.org/10.1093/plcell/koaa027

Duan M-R, Smerdon MJ (2010) UV damage in DNA promotes nucleosome unwrapping. J Biol Chem 285:26295–26303. https://doi.org/10.1074/jbc.M110.140087

Dvořák Tomaštíková E, Hafrén A, Trejo-Arellano MS, Rasmussen SR, Sato H, Santos-González J, Köhler C, Hennig L, Hofius D (2021) Polycomb Repressive Complex 2 and KRYPTONITE regulate pathogen-induced programmed cell death in Arabidopsis. Plant Physiology 185:2003–2021. https://doi.org/10.1093/plphys/kiab035

Falk M, Lukasova E, Kozubek S (2010) Higher-order chromatin structure in DSB induction, repair and misrepair. Mutat Res 704:88–100. https://doi.org/10.1016/j.mrrev.2010.01.013

Fei J, Kaczmarek N, Luch A, Glas A, Carell T, Naegeli H (2011) Regulation of nucleotide excision repair by UV-DDB: prioritization of damage recognition to internucleosomal DNA. PLoS Biol 9:e1001183. https://doi.org/10.1371/journal.pbio.1001183

Fortuny A, Chansard A, Caron P, Chevallier O, Leroy O, Renaud O, Polo SE (2021) Imaging the response to DNA damage in heterochromatin domains reveals core principles of heterochromatin maintenance. Nat Commun 12:2428. https://doi.org/10.1038/s41467-021-22575-5

Graindorge S, Cognat V, Johann to Berens P, Mutterer J, Molinier J (2019) Photodamage repair pathways contribute to the accurate maintenance of the DNA methylome landscape upon UV exposure. PLoS Genet 15:e1008476. https://doi.org/10.1371/journal.pgen.1008476

Hawkes TR (2014) Mechanisms of resistance to paraquat in plants. Pest Manag Sci 70:1316–1323. https://doi.org/10.1002/ps.3699

Ibañez IL, Bracalente C, Molinari BL, Palmieri MA, Policastro L, Kreiner AJ, Burlón AA, Valda A, Navalesi D, Davidson J, Davidson M, Vázquez M, Ozafrán M, Durán H (2009) Induction and rejoining of DNA double strand breaks assessed by H2AX phosphorylation in melanoma cells irradiated with proton and lithium beams. Int J Radiat Oncol Biol Phys 74:1226–1235. https://doi.org/10.1016/j.ijrobp.2009.02.070

Ito H, Miura A, Takashima K, Kakutani T (2007) Ecotype-specific and chromosome-specific expansion of variant centromeric satellites in Arabidopsis thaliana. Mol Genet Genomics 277:23–30. https://doi.org/10.1007/s00438-006-0172-2

Jackson JP, Lindroth AM, Cao X, Jacobsen SE (2002) Control of CpNpG DNA methylation by the KRYPTONITE histone H3 methyltransferase. Nature 416:556–560. https://doi.org/10.1038/nature731

Jacob Y, Bergamin E, Donoghue MTA, Mongeon V, LeBlanc C, Voigt P, Underwood CJ, Brunzelle JS, Michaels SD, Reinberg D, Couture J-F, Martienssen RA (2014) Selective methylation of histone H3 variant H3.1 regulates heterochromatin replication. Science 343:1249–1253. https://doi.org/10.1126/science.1248357

Jacob Y, Feng S, LeBlanc CA, Bernatavichute YV, Stroud H, Cokus S, Johnson LM, Pellegrini M, Jacobsen SE, Michaels SD (2009) ATXR5 and ATXR6 are H3K27 monomethyltransferases required for chromatin structure and gene silencing. Nat Struct Mol Biol 16:763–768. https://doi.org/10.1038/nsmb.1611

Jiang J, Liu J, Sanders D, Qian S, Ren W, Song J, Liu F, Zhong X (2021) UVR8 interacts with de novo DNA methyltransferase and suppresses DNA methylation in Arabidopsis. Nat Plants 7:184–197. https://doi.org/10.1038/s41477-020-00843-4

Johann to Berens P, Molinier J (2020) Formation and Recognition of UV-Induced DNA Damage within Genome Complexity. Int J Mol Sci 21. https://doi.org/10.3390/ijms21186689

Kim J-H (2019) Chromatin Remodeling and Epigenetic Regulation in Plant DNA Damage Repair. Int J Mol Sci 20:E4093. https://doi.org/10.3390/ijms20174093

Law JA, Du J, Hale CJ, Feng S, Krajewski K, Palanca AMS, Strahl BD, Patel DJ, Jacobsen SE (2013) Polymerase IV occupancy at RNA-directed DNA methylation sites requires SHH1. Nature 498:385–389. https://doi.org/10.1038/nature12178

Li X, Harris CJ, Zhong Z, Chen W, Liu R, Jia B, Wang Z, Li S, Jacobsen SE, Du J (2018) Mechanistic insights into plant SUVH family H3K9 methyltransferases and their binding to context-biased non-CG DNA methylation. Proc Natl Acad Sci U S A 115:E8793–E8802. https://doi.org/10.1073/pnas.1809841115

Luitel K, Bozeman R, Kaisani A, Kim SB, Barron S, Richardson JA, Shay JW (2018) Proton radiation-induced cancer progression. Life Sciences in Space Research 19:31–42. https://doi.org/10.1016/j.lssr.2018.08.002

Ma Z, Castillo-González C, Wang Z, Sun D, Hu X, Shen X, Potok ME, Zhang X (2018) Arabidopsis Serrate Coordinates Histone Methyltransferases ATXR5/6 and RNA Processing Factor RDR6 to Regulate Transposon Expression. Dev Cell 45:769-784.e6. https://doi.org/10.1016/j.devcel.2018.05.023

Malacrida LS, Ranjit S, Gratton E (2017) Water Activity Inside the Nucleus: Some Clues using ACDAN Fluorescence and its Implications in the Chromatin Supramolecular Organization. Biophysical Journal 112:218a. https://doi.org/10.1016/j.bpj.2016.11.1202

Martínez-López W, Boccardo EM, Folle GA, Porro V, Obe G (1998) Intrachromosomal localization of aberration breakpoints induced by neutrons and gamma rays in Chinese hamster ovary cells. Radiat Res 150:585–592

Matsumoto S, Cavadini S, Bunker RD, Grand RS, Potenza A, Rabl J, Yamamoto J, Schenk AD, Schübeler D, Iwai S, Sugasawa K, Kurumizaka H, Thomä NH (2019) DNA damage detection in nucleosomes involves DNA register shifting. Nature 571:79–84. https://doi.org/10.1038/s41586-019-1259-3

Molinier J, Oakeley EJ, Niederhauser O, Kovalchuk I, Hohn B (2005) Dynamic response of plant genome to ultraviolet radiation and other genotoxic stresses. Mutat Res 571:235–247. https://doi.org/10.1016/j.mrfmmm.2004.09.016

Mullen MA, Olson KJ, Dallaire P, Major F, Assmann SM, Bevilacqua PC (2010) RNA G-Quadruplexes in the model plant species Arabidopsis thaliana: prevalence and possible functional roles. Nucleic Acids Res 38:8149–8163. https://doi.org/10.1093/nar/gkq804

Palomera-Sanchez Z, Bucio-Mendez A, Valadez-Graham V, Reynaud E, Zurita M (2010) Drosophila p53 is required to increase the levels of the dKDM4B demethylase after UV-induced DNA damage to demethylate histone H3 lysine 9. J Biol Chem 285:31370–31379. https://doi.org/10.1074/jbc.M110.128462

Pegoraro G, Misteli T (2017) High-Throughput Imaging for the Discovery of Cellular Mechanisms of Disease. Trends Genet 33:604–615. https://doi.org/10.1016/j.tig.2017.06.005

Pignatta D, Erdmann RM, Scheer E, Picard CL, Bell GW, Gehring M (2014) Natural epigenetic polymorphisms lead to intraspecific variation in Arabidopsis gene imprinting. Elife 3:e03198. https://doi.org/10.7554/eLife.03198

Polo SE, Almouzni G (2015) Chromatin dynamics after DNA damage: The legacy of the access-repair-restore model. DNA Repair (Amst) 36:114–121. https://doi.org/10.1016/j.dnarep.2015.09.014

Privett AJ, Teixeira ES, Stopera C, Morales JA (2017) Exploring water radiolysis in proton cancer therapy: Time-dependent, non-adiabatic simulations of H+ + (H2O)1-6. PLoS One 12:e0174456. https://doi.org/10.1371/journal.pone.0174456

Qüesta JI, Walbot V, Casati P (2010) Mutator transposon activation after UV-B involves chromatin remodeling. Epigenetics 5:352–363. https://doi.org/10.4161/epi.5.4.11751

Rigal M, Kevei Z, Pélissier T, Mathieu O (2012) DNA methylation in an intron of the IBM1 histone demethylase gene stabilizes chromatin modification patterns. EMBO J 31:2981–2993. https://doi.org/10.1038/emboj.2012.141

Roudier F, Ahmed I, Bérard C, Sarazin A, Mary-Huard T, Cortijo S, Bouyer D, Caillieux E, Duvernois-Berthet E, Al-Shikhley L, Giraut L, Després B, Drevensek S, Barneche F, Dèrozier S, Brunaud V, Aubourg S, Schnittger A, Bowler C, Martin-Magniette M-L, Robin S, Caboche M, Colot V (2011) Integrative epigenomic mapping defines four main chromatin states in Arabidopsis. EMBO J 30:1928–1938. https://doi.org/10.1038/emboj.2011.103

Schalk C, Cognat V, Graindorge S, Vincent T, Voinnet O, Molinier J (2017) Small RNA-mediated repair of UV-induced DNA lesions by the DNA DAMAGE-BINDING PROTEIN 2 and ARGONAUTE 1. Proc Natl Acad Sci U S A 114:E2965–E2974. https://doi.org/10.1073/pnas.1618834114

Schalk C, Drevensek S, Kramdi A, Kassam M, Ahmed I, Cognat V, Graindorge S, Bergdoll M, Baumberger N, Heintz D, Bowler C, Genschik P, Barneche F, Colot V, Molinier J (2016) DNA DAMAGE BINDING PROTEIN2 Shapes the DNA Methylation Landscape. Plant Cell 28:2043–2059. https://doi.org/10.1105/tpc.16.00474

Schalk C, Molinier J (2016) Global Genome Repair factors controls DNA methylation patterns in Arabidopsis. Plant Signal Behav 11:e1253648. https://doi.org/10.1080/15592324.2016.1253648

Schuch AP, Moreno NC, Schuch NJ, Menck CFM, Garcia CCM (2017) Sunlight damage to cellular DNA: Focus on oxidatively generated lesions. Free Radic Biol Med 107:110–124. https://doi.org/10.1016/j.freeradbiomed.2017.01.029

Shachar S, Pegoraro G, Misteli T (2015) HIPMap: A High-Throughput Imaging Method for Mapping Spatial Gene Positions. Cold Spring Harb Symp Quant Biol 80:73–81. https://doi.org/10.1101/sqb.2015.80.027417

Smerdon MJ, Conconi A (1999) Modulation of DNA damage and DNA repair in chromatin. Prog Nucleic Acid Res Mol Biol 62:227–255. https://doi.org/10.1016/s0079-6603(08)60509-7

Snoek BL, Pavlova P, Tessadori F, Peeters AJM, Bourbousse C, Barneche F, de Jong H, Fransz PF, van Zanten M (2017) Genetic Dissection of Morphometric Traits Reveals That Phytochrome B Affects Nucleus Size and Heterochromatin Organization in Arabidopsis thaliana. G3 (Bethesda) 7:2519–2531. https://doi.org/10.1534/g3.117.043539

Stroud H, Do T, Du J, Zhong X, Feng S, Johnson L, Patel DJ, Jacobsen SE (2014) Non-CG methylation patterns shape the epigenetic landscape in Arabidopsis. Nat Struct Mol Biol 21:64–72. https://doi.org/10.1038/nsmb.2735

Stroud H, Greenberg MVC, Feng S, Bernatavichute YV, Jacobsen SE (2013) Comprehensive analysis of silencing mutants reveals complex regulation of the Arabidopsis methylome. Cell 152:352–364. https://doi.org/10.1016/j.cell.2012.10.054

Surrallés J, Darroudi F, Natarajan AT (1997a) Low level of DNA repair in human chromosome 1 heterochromatin. Genes Chromosomes Cancer 20:173–184

Surrallés J, Puerto S, Ramírez MJ, Creus A, Marcos R, Mullenders LH, Natarajan AT (1998) Links between chromatin structure, DNA repair and chromosome fragility. Mutat Res 404:39–44. https://doi.org/10.1016/s0027-5107(98)00093-1

Surrallés J, Sebastian S, Natarajan AT (1997b) Chromosomes with high gene density are preferentially repaired in human cells. Mutagenesis 12:437–442. https://doi.org/10.1093/mutage/12.6.437

Suter B, Thoma F (2002) DNA-repair by Photolyase Reveals Dynamic Properties of Nucleosome Positioning in Vivo. Journal of Molecular Biology 319:395–406. https://doi.org/10.1016/S0022-2836(02)00291-7

Tessadori F, van Zanten M, Pavlova P, Clifton R, Pontvianne F, Snoek LB, Millenaar FF, Schulkes RK, van Driel R, Voesenek LACJ, Spillane C, Pikaard CS, Fransz P, Peeters AJM (2009) Phytochrome B and histone deacetylase 6 control light-induced chromatin compaction in Arabidopsis thaliana. PLoS Genet 5:e1000638. https://doi.org/10.1371/journal.pgen.1000638

Thoma F (1999) Light and dark in chromatin repair: repair of UV-induced DNA lesions by photolyase and nucleotide excision repair. EMBO J 18:6585–6598. https://doi.org/10.1093/emboj/18.23.6585

Thomas T.T. D, Puthur JT (2017) UV radiation priming: A means of amplifying the inherent potential for abiotic stress tolerance in crop plants. Environmental and Experimental Botany 138:57–66. https://doi.org/10.1016/j.envexpbot.2017.03.003

Wang Q, Liu P, Jing H, Zhou XF, Zhao B, Li Y, Jin JB (2021) JMJ27-mediated histone H3K9 demethylation positively regulates drought-stress responses in Arabidopsis. New Phytol 232:221–236. https://doi.org/10.1111/nph.17593

Xu L, Jiang H (2020) Writing and Reading Histone H3 Lysine 9 Methylation in Arabidopsis. Frontiers in Plant Science 11

Yao J-W, Ma Z, Ma Y-Q, Zhu Y, Lei M-Q, Hao C-Y, Chen L-Y, Xu Z-Q, Huang X (2021) Role of melatonin in UV-B signaling pathway and UV-B stress resistance in Arabidopsis thaliana. Plant, Cell & Environment 44:114–129. https://doi.org/10.1111/pce.13879

Zhou J, Wang X, He K, Charron J-BF, Elling AA, Deng XW (2010) Genome-wide profiling of histone H3 lysine 9 acetylation and dimethylation in Arabidopsis reveals correlation between multiple histone marks and gene expression. Plant Mol Biol 72:585–595. https://doi.org/10.1007/s11103-009-9594-7

8. Conclusion & Perspectives

This work aimed to decipher the reciprocal crosstalk between epigenetics, UV-induced DNA damages, and DNA repair processes to better understand the molecular mechanisms involved in genome and epigenome integrity maintenance.

The first relationship between epigenome and UV is supported by the predominant localization of photolesions in constitutive heterochromatin characterized by high H3K9me2, high nucleosome occupancy, and high DNA methylation levels. Secondly, we revealed that the GGR pathway follows an access-repair-restore mechanism in constitutive heterochromatin relying on the interplay between H3K9me2 homeostasis regulators and the damage recognition protein DDB2. Finally, we provided evidence for epigenetic changes induced by UV irradiations and controlled by DNA repair factors. These results open perspectives for the study of mechanisms involved in stress-specific transcriptional regulation and epigenetic memory, potentially shaping the chromocenters of natural Arabidopsis variants.

As often, the answers proposed by our work lead to several other open questions. Indeed, it would be of interest to analyze:

- To which extent the dynamic of constitutive heterochromatin involves linker histone displacement and/or core histone eviction
- Which chromatin remodelers act with DDB2
- Whether new histone variants are incorporated at damaged sites and how they regulate the re-establishment of the epigenome landscape
- Whether the non-canonical chromatin dynamic observed in the Cvi ecotype provides an evolutionary advantage

9. Acknowledgments

Life and love are not happening on paper. So those acknowledgments will be brief, in order to have more time to spend with all these people I like.

I would like to give my first *"thank you"* to Jean MOLINIER.
As a thesis Director, who always gave me the right amount of creative freedom and frame. Whose main interest was the intellectual and professional progress of his students and the good science. As a friend, who always communicates straight and accompanied me through the best and worst situations.

My second *"thank you"* goes to the institute IBMP-Strasbourg, to all those smiling faces, that gave me the feeling of being welcome since the very first day as a bachelor student. I want to thank all the different platforms, especially Jerome Mutterer from the microscopy platform, who helped me a lot with great advices, hours of invested time, and a good mood!

My third *"thank you"* goes to the members of lab 526 and external collaborators:
- To the group leader, When-hui SHEN, for his warm welcome and positive spirit!
- To the core members: Sallimata Ousmane SALL, Jackson PETER, Sebastian STAERCK ('de Seppel'), and Kumar Amit SINGH, who made the lab a peaceful and productive place full of joy.
- The Physicists from IPHC Cronenbourg, especially Mark ROUSSEAU and Quentin RAFFY, which was a pleasure to work with.
- To Marius THEUNE and the Team of Fredy BARNECHE for their collaboration in the Nucl.Eye.D Project.
- To Thomas SEXTON from IGBMC for his support and intellectual implication at my mid-thesis committee.

The Fourth *"thank you"* goes to all my friends for filling my life. Especially Denisa TOMKOVA and Simon Yannick NDECKY, with whom I shared my meal, my time, my feelings, my scientific theories, and my love for the last five years. Another particular "thank you" goes to the cleverest guy I've ever met, Marius Theune. A faithfull friend I'm missing daily.

The Fifth *"thank you"* goes to my parents, Karl-Heinz BREUER and Andrea JOHANN TO BERENS, who gave me the opportunity of learning French like a mother tongue despite never speaking it on their own, who taught me to live with my dyslexia, without feeling different. And who never doubted about any of my decisions.

The *Biggest thank* goes to my wife Julie JOHANN TO BERENS, whowalked through rain and fire with me for more than a decade. Who brings me all the love and patience I needed to fulfill this thesis on my best, and with whom any future will be shiny.

And finally, I would like to say for the first time *"thank you"* to Timéo JOHANN TO BERENS, my son who's expected to join our world in June 2022, and who was always awake to give me a high-five when I came to sleep late after a (long) night of work.

Here my thesis ends, and marks the beginning of a new adventure…

drawing by
Julie JOHANN TO BERENS

Dynamic and maintenance of constitutive heterochromatin in response to UV exposure

Key words:

UV-light, Epigenetics, DNA-repair, Chromocenters, Heterochromatin

Summary

Plants are sessile organisms that have evolved sophisticated mechanisms to cope with the sun light, which is mandatory for photosynthesis, and with the deleterious effects of associated UV radiations, inducing cellular and DNA damage. Characterizing the dynamic responses of plants to UV irradiation is of great importance. In particular, it is crucial to understand how genetic and epigenetic mechanisms cooperate with DNA repair to efficiently maintain (epi)genome integrities. In the following study, *Arabidopsis thaliana*, was used as a model organism to understand the interactions between the DNA repair machinery and the epigenome following UV exposure. Through cytological and next-generation sequencing approaches we identified that constitutive heterochromatin is predisposed to form photolesions. Using a self-developed deep-learning-based image segmentation approach, we determined the dynamic of constitutive heterochromatin shape and of two associated epigenetic marks (H3K9me2 and H3K27me1) upon UV exposure. The combination of genetic, cytogenetic and biochemistry approaches allowed demonstrating that component of the Global Genome Repair (GGR) pathway and factors involved in H3K9me2 homeostasis act together to maintain heterochromatin integrity. Interestingly, we found that UV-C exposure induces durable changes of several epigenetic features of constitutive heterochromatin. In the last part of this study, we questioned to which extend the UV-induced structural changes of constitutive heterochromatin could be inherited and could participate to a transcriptional priming. A particular focus was devoted to understand the adaptation to high-UV environments. Collectively, our results shed the light on new factors involved in the crosstalk between epigenome dynamics and DNA repair in Arabidopsis thaliana and paves the way for future investigations about UV-induced memory.